RAY TRACE TOMOGRAPHIC VELOCITY ANALYSIS OF SURFACE SEISMIC REFLECTION DATA

Thesis by
Christof Stork

In Partial Fulfillment of the Requirements
for the Degree of
Doctor of Philosophy

California Institute of Technology
Pasadena, California

March 1988
(Submitted March 3, 1988)

In appreciation of
Heidi Houston

Acknowledgements

The inspiration and initial ideas for this work came from my advisor, Rob Clayton. Much of my approach is based on his insight. It is unfortunate a thesis cannot have a second author because his name deserves to accompany this work.

Rob has continuously amazed me by how quickly he digests details of research results, places the work in a broad perspective, understands my personal ambitions, and makes insightful suggestions--all while thrashing the computer at backgammon. I have considerable respect for him as a computer hacker, scientist, educator, and leader. But, I'll never forgive him for hustling me in a tabletop shuffleboard game at the Houston SEG after a few beers.

I gratefully acknowledge the generosity of three oil company research departments, that of Amoco, Arco, and Chevron, which allowed me to work on this research while employed by them over the summers. Use of their computer resources, the aid of their focused work environments, the exposure they provided to practical considerations, and their scientific feedback have been instrumental to the results presented here. Numerous people at these research labs have my gratitude. I could not have done this work without their help and have learned much in the process.

Amoco, in particular, has been highly supportive by funding the majority of my university support, providing the CRAY-2 and an army of SUNs to produce most all the figures in this thesis, and being very encouraging of the project. My positive experience with Amoco is much a result of the efforts of Sven Treitel. He instills a constructive attitude which is still with me.

In addition to funding from Amoco, I received university support from Rob Clayton's Presidential Young Investigators award. I am grateful to Rob for enabling me to carry out this work without consideration about funding.

I thank my office mates, Heidi Houston and Ann Mori, for their candid thoughts.

This thesis incorporates improvements suggested by Sven Treitel, Larry Lines, and John Scales, all of Amoco. Their interest in this thesis motivated me to improve it beyond what I would have accomplished on my own.

RAY TRACE TOMOGRAPHIC VELOCITY ANALYSIS OF SURFACE SEISMIC REFLECTION DATA

Christof Stork, Ph.D.
California Institute of Technology, 1988

ABSTRACT

Recent development of two technologies allows application of a generalized formulation of travel time inversion to very large data sets, such as the surface reflection surveys collected for oil exploration. This generalized formulation uses very small cell sizes, effectively eliminating discretization effects. Inversion of an effective continuum that has no built-in *a priori* constraints is what places this technique in the category of *tomography*.

In reflection surveys, the generalized formulation investigated here treats the continuous velocity field independently from the reflector locations. The *a priori* assumption, common with travel time inversions in seismic exploration data, is thus not made: that the velocity field is defined as a series of layers with constant or smoothly varying velocity. This assumption restricts significant velocity variations to occur only at reflector locations. Velocity parameterized as layers is merely one of many geologic constraints that can be added optionally in tomographic inversion.

The technologies that enable this generalized approach to travel time inversion are: 1) a computer program capable of tracing rays through a 2-dimensional grid of points and off reflectors with structure, and 2) iterative schemes that efficiently perform damped, constrained generalized matrix inversions over a user-specified wide eigenvalue range for very large model and data sizes. An argument is presented that a variation of Richardson's iteration is preferred to the Conjugate Gradient Iterative Method for performing the matrix inversion.

With this generalized formulation, Ray Trace Tomography is a first approach to tomographic transmission analysis. Travel times and ray paths are a valid approximation to the wave equation for broad velocity variations. The method efficiently addresses the characteristics of more general but much more expensive transmission techniques. For example, Ray Trace Tomography demonstrates that an iterative application of a transmission velocity analysis technique, tomography, and a scattering reflector location technique, migration, do not necessarily converge to the optimal solution. To resolve the ambiguity between velocity-reflector depth, velocity and reflector locations must be coupled in one inversion technique. Ray Trace Tomography is able to couple the two. Using it to indicate the absolute resolution between velocity and reflector depth, we find that for certain geometries, reflector depths cannot be resolved where most recorded energy travels within 45^{o} of vertical.

Poor resolution of the velocity-reflector depth ambiguity and other problems are inherent to reflection surveys. These problems also exist for other transmission techniques and can be solved only through use of inversion

constraints. Ray Trace Tomography can test constraints for possible use in other transmission techniques efficiently.

Ray Trace Tomography has difficulty with non-linearities caused by some types of starting model errors, such as small-scale reflector structure. Improved performance with non-linearities is an objective we should seek in other transmission techniques.

Not only is Ray Trace Tomography a useful intellectual exercise as a preliminary analysis of transmission inversion, but in many cases it is a viable technique for addressing serious problems with surface seismic reflection data. It can determine an accurate two-dimensional velocity field for migration, such as in the case of gas pockets or fault blocks. In addition, it can resolve between certain velocity and reflector ambiguities such as those occuring in the permafrost region of Alaska.

As a comparatively efficient technique, Ray Trace Tomography can serve as a tool for interactive interpretation. The geologist can use the ray tracing to compare various geologic models with the data and then use the inversion to fine-tune the models. The inversion enables the geologist to formulate his geologic knowledge as constraints in the inversion. By analyzing the inversion results, the interpreter will develop an understanding of the validity of the various models and the resolution amoung them.

Table of Contents

Acknowledgements iv
Abstract v
Table of Contents viii

Chapter 1: Introduction and Overview

1.1 Motivation 1
1.2 General Approach of Ray Trace Tomography 2
1.3 Relationship of Ray Trace Tomography to Waveform Inversion Techniques 5
1.4 Implementation 8
1.5 Synthetic Modeling 10
1.6 Eigenvector Analysis of Velocity-Reflector Depth Ambiguity 14
1.7 Constraining the Inversion 16
1.8 Data Examples 18
1.9 Summary 19

Chapter 2: An Implementation of Ray Trace Tomography to Reflection Seismology

2.1 Abstract 21
2.2 Introduction 21
2.3 Ray-Tracing Methodology 23
2.4 Linearization of Travel Time Equation 29
2.5 Analysis of Iterative Tomography and Migration Methods: Should Tomography Include a Reflector Term? 31
2.6 Inclusion of Reflector Perturbations in the Linearized Travel Time Equations 40
2.7 Iterative Matrix Inversion Through Dines & Lytle Back Projection . 43
2.8 Sample Computer Program for Dines & Lytle Back Projection . . . 47
2.9 Summary of Comer & Clayton Matrix Analysis 48
2.10 Acceleration of Dines & Lytle Back Projection with Chebyshev Acceleration Factors 54
2.11 Discussion of Iterative Matrix Inversion and its Relationship to the Conjugate Gradient Method 61
2.12 Including Constraints in Dines & Lytle Back Projection 64
2.13 Improving Non-linear Errors by Updating Incorrect Ray Paths 73
2.14 Conclusion 77

Chapter 3: A Modeling Analysis of Ray Trace Tomography Applied to Reflection Surveys

3.1 Abstract . . . 79
3.2 Introduction . . . 80
3.3 Flaws of the Reflection Seismology Experiment for the Application of Tomography . . . 82
3.4 Dependence of Modeling Results on Inversion Technique Used . . . 84
3.5 Smearing From Limited Angular Ray Coverage . . . 86
3.6 Non-linear Effects of Velocity . . . 89
3.7 Velocity-Reflector Depth Tradeoff . . . 96
3.8 Non-linear Effects of Reflector Position . . . 100
3.9 Additional Stabilizing Effect of Prestack Migration . . . 112
3.10 Edge Effects . . . 113
3.11 Conclusion . . . 117

Chapter 4: Singular Value Decomposition Analysis of the Travel Times of a Surface Reflection Survey

4.1 Abstract . . . 119
4.2 Introduction . . . 120
4.3 Method . . . 122
4.4 Setting up the Matrix for SVD . . . 126
4.5 SVD of a Two Parameter Model . . . 130
4.6 Variance Analysis Example of a Two Parameter Model . . . 136
4.7 SVD Results for the Generic Model . . . 140
4.8 SVD Results for a Model with Edge Effects . . . 148
4.9 Conclusion . . . 151

Chapter 5: Applications of Tomography to Two Data Sets Containing Lateral Velocity Variations

5.1 Abstract . . . 153
5.2 Introduction . . . 153
North Slope Data Set:
5.3 Description . . . 154
5.4 Inversion Procedure . . . 155
5.5 Inversion Results . . . 157
Central Valley Data:
5.6 Description . . . 160
5.7 Inversion Procedure . . . 161
5.8 Inversion Results . . . 161
5.9 Conclusion . . . 164

Conclusions . . . 165

Appendix

A: Additional Examples of Non-linear Effects from Velocity . . . 167
B: Additional Examples of Velocity-Reflector Depth Tradeoff . . . 172
C: SVD Results for Variations to the Generic Model . . . 175

References . . . 183

Chapter 1

Overview of the Application of Ray Trace Tomography to Seismic Surface Reflection Seismology

1.1 Motivation

Knowledge of seismic velocities is essential for transforming data recorded as time sections at the earth's surface into a map of reflector locations as depth sections. Velocity determination is a routine procedure where velocity varies only vertically. When velocity varies laterally, determination of the velocity field becomes complicated. As more interest in complex geology develops, it becomes vital to resolve lateral velocity variations correctly so that the data transformation is performed accurately.

The preferred method for handling velocity variations smaller than a CMP gather width is performing a prestack migration through the correct velocity field. The technology of prestack migration has advanced so far that processed images in areas of complicated structure can be as clear as those in simpler areas, given accurate velocities. However, no effective scheme exists for determining the laterally varying velocity model to input into the migration. As a result, prestack migrations currently do not produce optimal images in may areas. Determination of velocity is the missing link for the application of prestack migration. Ray Trace Tomography has potential for filling the gap.

Poor resolution of lateral velocity variations degrades seismic data quality in a wide range of geologic settings like: permafrost variations, gas pockets, basin edges, lithologic changes in a layer, salt, faults, and "dynamic statics" seen in Saudi Arabia. Surface-consistent statics are applied to some of these problem cases, but the results are generally compromised because the static model is inadequate for these geologic settings.

If uncorrected, these velocity variations, in transforming time sections into depth sections, manifest themselves as false reflector variations. For instance, a false reflector "pull-up" can be caused by a region of unresolved fast material above the reflector. Many times, a structural high has been drilled only to discover that it is merely an artifact of an unresolved velocity variation.

Those velocity variations that are ambiguous with reflector depth variations are generally wider than a CMP gather. When unresolved velocity variations are smaller than the width of a CMP gather, the reflector images in the seismic section are blurred on stacking or migration of the time sections through the false velocity field. In such cases, the waveforms will not overlap each other properly when summed. These non-optimal summations reduce signal-to-noise levels in general, but most significantly in the higher frequencies needed for detailed reservoir mapping. In extreme cases, the summations are so poor that the image is washed out altogether.

1.2 General Approach of Ray Trace Tomography

A common characteristic to the geologic settings targeted by this approach is that the velocity variations are broader than the dominant wavelength of the

seismic signal. Gradual components of velocity variations do not significantly affect the waveform of the seismic signal, but only the travel time of the signal through the media. Thus, the main information in the data about broad velocity variations is the arrival time of transmitted energy from the prestack traces of reflected signals. For instance, the most obvious evidence of a velocity variation is deviation from hyperbolic moveout of reflections from below the velocity variation. Generally, useful reflections off the velocity variations do not exist. A technique using the transmitted energy is the most straightforward approach for resolving these broad velocity variations.

CMP velocity semblance analysis is such a transmission technique. The method is applicable only when velocity does not vary over the width of a CMP gather, however. Toldi (1985) and Fowler (1988) generalized the technique to handle smaller velocity variations, an efficient and effective solution for certain cases. However the use of stacking velocities misses some information and is applicable only when stacking velocities can be obtained.

Ray Trace Tomography is the transmission method investigated here for the determination of velocity. The technique finds the velocity field and reflector depths that statistically best fit the travel times of reflections on the prestack traces. The method works by discretizing the velocity field into a large number of blocks or cells, the size of which is smaller than the desired resolution. The reflector is discretized into a series of points, each free to move perpendicularly to the reflector slope. Velocity and reflector cells are related to travel times through ray paths. Only the capability of the ray tracing code restricts the complexity of the reference velocity and reflector structure that can be handled with this model is dependent.

Ray paths are used to set up a linear system for inversion for the discretized velocity field and reflector locations. A linear system is too large to invert using formal matrix methods (SVD) in most geophysical situations, even with the most powerful of todays computers. RAM storage requirements are in giga-bytes; computation time on a CRAY-2 CPU would take months. Furthermore, these formal techniques are unnecessary: iterative inversion techniques will produce a result similar to formal techniques at a fraction of the computational capability, currently available on today's mini-computers.

Since correct velocity and reflector positions are, of course, unknown at the start, ray paths used for inversion are traced through a *best estimate* model, generally produced using conventional techniques. How well these reference ray paths approximate true ray paths depends upon the accuracy of the starting velocity and reflector position. The linear system and inversion results are imperfect as a result of this approximation.

Solution of the imperfect linear system is generally closer to the correct model than that of the starting model. If this is the case, the linear system can be improved by tracing a new set of rays through the updated velocity and reflector position. A new and improved solution is produced from the updated linear system. The procedure of alternately applying ray tracing and inversion is repeated as many times as necessary until convergence is achieved, which generally occurs after only a few iterations.

The inadequacy of the linear system to simulate the true relation between data and model is known as non-linearity. The repeated ray tracing and linear inversion used to correct non-linear errors are an iteration procedure distinct from

the iteration procedure used to solve the linear matrix equation. It is not guaranteed that these 'non-linear' iterations converge or converge to the correct result. Success is dependent upon the type and magnitude of differences between the starting model and the solution.

Use of ray paths to simulate waveform propagation aggravates some instabilities in the inversion, especially in the reflector position. A more stable method of determining reflector position, given the velocity, is to migrate data through velocity. Our proposed procedure for implementation of Ray Trace Tomography is thus to ignore reflector positions produced from the combined inversion for velocity and reflector depth. The reflector position used for later ray tracing or interpretation is determined by migrating the data through the velocity field portion of the inverted model. This procedure of applying tomography followed by migration is known as iterative migration and tomographic inversion. Figure 2.7 presents a flow chart of the procedure.

1.3 Relationship of Ray Trace Tomography to Waveform Inversion Techniques

A waveform technique developed by Tarantola (1985), based on the Born scattering approximation, has recently been proposed by Mora (1987) as a transmission analysis technique. The technique is an automatic one that involves subtraction of synthetic data of a reference model from the real data. Only arrivals in the data that overlap the corresponding arrivals in the synthetic waveforms produce a constructive contribution to the inversion results. Even when a reference model differs significantly with the true structure, some portions of the waveforms, such as diffractions, overlap. It is presumed that with repeated

iterations, even a seriously inaccurate reference model will drift to the correct model. In time, more waveforms overlap. If this procedure is robust, it would require many iterations, however.

These waveform techniques are most effective when a starting model is accurate enough that many of arrivals of the synthetics overlap corresponding ones in the data. This condition requires a highly accurate starting model, frequently unavailable, however.

In many cases where arrivals in the synthetics fail to overlap those of the data, human processors can identify which waveforms in the synthetics correlate with those in the data. Hence, this waveform inversion technique does not use information that might be plain to the processor of the technique. There is, at present, no robust, automatic method of determining this information relating two non-overlapping arrivals. The processor is best at determining this relationship. To utilize the processor's knowledge relating two non-overlapping arrivals, it must be formulated in some manner as data for use by an inversion technique. Designating a time difference between the two arrivals is the simplest approach and is the data used in Ray Trace Tomography.

Phase shift, the frequency domain expression of a time difference, can be exploited with other transmission techniques, such as the Rytov approximation (Woodward, 1988, Slaney et al, 1984, Soumekh, 1986). These techniques appear to be the wavefield extrapolation of Ray Trace Tomography.

Thus Ray Trace Tomography is a rudimentary reconnaissance technique that can invert the general aspects of a model well. However, the technique does not have the resolution capability of a waveform-based technique, such as that

proposed by Tarantola. It is the opinion of the author that neither technique solves the entire inversion problem of producing the optimal model possible from the raw data. Each technique addresses a separate part of the problem: Transmission tomography is more robust and efficient for inversion of greater and broader scale differences between a starting model and the true model; a Born-based waveform technique produces the optimal resolution available from the data wave field, given a close starting model. The two classes of techniques, however, nicely complement each other. Transmission tomography can be used to invert the broad velocity variations, those greater than several wavelengths of the seismic signal. The inversion result will serve as an accurate starting model for a scattering inversion technique that significantly improves the chance for successful convergence and the number of iterations needed for convergence. It is this complementary nature of scattering and transmission techniques that iterative tomography and migration attempt to utilize.

Work presented here is directed toward understanding the formulation using travel times picked from the prestack data. It is expected that techniques similar to John Toldi's (1985) method of using a semi-automated procedure for chosing stacking velocities can be applied to travel times. These techniques would be statistically analogous to the present process of CMP velocity determination, except that deviations from non-hyperbolic paths relating to velocity variations would be included.

1.4 Implementation of Ray Trace Tomography

Seismic Ray Trace Tomography shares the same principles as the medical CAT (Computer Axial Tomography) scanner, which automatically produces images of exceptional quality. To perform a CAT scan, the patient is placed in an x-ray device, and a few moments later the doctor has his pictures on a TV screen. The use of CAT scanners is so simple because the data collection process is ideal. The ray paths are straight, data coverage is uniform, sources and receivers are rotated completely around the object, and the X-rays are of high enough frequency that they are considered narrow beams with high resolution. Producing the image from this complete data set is straightforward using either an inverse Radon Transform or the ART iterative inversion technique.

However, seismic data collection and restricted surface reflection geometry have many complications that prevent the application of these simple and efficient techniques of CAT scanners. Complications inherent to seismic data are: curved ray paths; ray path locations are only approximate; and the average seismic wavelength is of significant size compared to the desired level of resolution. Complications specific to surface reflection geometry are: ray density is non-uniform; sources and receivers are constrained to the earth's surface; and a reflector is included in the problem. Other techniques must be implemented to overcome these obstacles.

Advanced computer programs are one means of overcoming these obstacles. To handle curved ray paths, rays must be traced through potentially complicated velocity fields. This thesis uses the method of Langan & Lerche

(1985) which traces rays through cells rather than the more conventional method of using semiconstant velocity layers. To handle the non-uniform ray density, inversion theory must be used. Applying inverse methods to such a large data volume requires use of efficient iterative methods. The inversion is performed here using the SIRT iterative method of Dines & Lytle (1979) coupled with Chebyshev acceleration factors (Olson, 1986). This iterative matrix inversion method is preferable to the more popular Conjugate Gradient Iterative Method, (Scales, 1987; Hestenes & Stiefel, 1952), because the eigenvalue range inverted can be controlled and because data inversions can be compared directly with synthetic inversions. To improve on the smearing from the limited angular ray coverage and large wavelength of the seismic signal, the reflector is imaged by migrating the data through the inverted velocity model. To take into account the effect of the reflector on the data, reflector depth is included in the inversion. To improve the approximation of the ray paths, the whole process of ray tracing, iterative inversion, and migration is repeated using the previous inversion result as the reference model.

These programs are based on simple principles, but are complicated in practice. Chapter 2 describes the implementation used for all the applications in this thesis. The implementation is based on the approach of being as general as possible and placing as little emphasis as possible on computational efficiency or programming simplicity. Inversion instability and other problems are handled on an individual basis through program parameters.

When these computer programs are applied to address problems of seismic data and surface reflection geometry, Ray Trace Tomography can produce an image as readily as CAT scanners. Ray Trace Tomography results

where, bright colors highlight the different image aspects, can be as dramatic as those CAT scanners produce. Regardless, the computer programs cannot solve all problems from the more complicated data collection geometry. As a result of the inherent limitations of seismic data and a reflection survey, the inversion is incomplete. Certain aspects are missing from the image; others are corrupted by artifacts.

To utilize transmission tomography properly, the characteristics of the technique must be understood. Resolution limits must be known to avoid overinterpretation of the result. To make sense of a distorted result and improve upon it, artifact generation must be understood. This thesis focuses upon analysis of the characteristics of Ray Trace Tomography applied to surface reflection data. The analysis is performed by synthetic example in Chapter 3 and by theoretical analysis in Chapter 4.

1.5 Synthetic Modeling

The problems of the data collection procedure of a seismic reflection survey are summarized in Figure 3.1 by comparing it with that of a CAT scanner. This thesis addresses several of these complications: 1) smearing resulting from limited angular ray coverage; 2) errors caused by using ray paths traced through an approximate model for the inversion; 3) image distortion by limited ray coverage at the edges of a survey; and 4) poor resolution between reflector depth and velocity. Additional complications uninvestigated here are: 1) differences between waveform propagation and ray tracing; 2) difficulty of picking travel times from a reflection survey; and 3) additional processes affecting seismic

propagation unaccounted for with our model, such as anisotropy, 3-D effects, diffractions, and attenuation.

Vertical smearing of the tomography results from a reflection survey is inevitable. Reflected signals travel within a limited angular range around vertical. Without horizontal ray paths, images are smeared by streaking anomalies along the ray paths. Geology is frequently horizontal, so the tomography-produced image may bear little resemblance to actual geology. However, transmission tomography is not designed to generate an end product, but rather to produce input velocity for a migration or other scattering techniques. Chapter 3 shows that migration is insensitive to vertical smearing of tomography.

Both limited angular ray coverages and the relatively large dominant wave length of the seismic signal serve to smear the image. A propagating wave field will see merely the average of velocity variations smaller than the characteristic wavelength of the signal. The size of the seismic pulse is approximately the limit to the possible resolution of the inversion. Normal seismic pulse width is about 100-500 feet, which does not produce resolution sharp enough for direct interpretation of the inversion. Subsequent application of scattering techniques such as migration, best at resolving velocity variations smaller than the size of a seismic wavelength, will produce higher resolution.

Ray paths used for the linear matrix inversion are only approximate because the true velocity and reflector positions are unavailable. Ray paths represent a linear approximation to the true non-linear relationship between data and model. This non-linearity does not lend itself to explicit mathematical formulation and can be approximated only by repeated linearization of the

curvature by a series of points in the region of interest. Relinearization corresponds to redefining the linear matrix equation by retracing rays through the results of the previous inversion. The non-linear iteration process, schematically diagrammed in Figure 2.8, is commonly used in geophysics to solve these complicated non-linear systems. Similar non-linear iteration is proposed by Tarantola (1984), Mora (1987), Toldi (1985), and Sword (1987) among many others.

A common analogy used to describe non-linear iteration procedure is trying to find the lowest point in a valley while blind but able to jump great distances. Each jump or step corresponds to one non-linear iteration. Lacking any other knowledge, the best direction to jump would be the direction of the maximum gradient from our present position. The distance to jump is determined by estimating the location of the low point from the curvature and slope of the valley at our present position. Unfortunately, the optimal distance to jump cannot be determined except through repeated forward modeling, an expensive procedure. If the valley is smooth, the lowest point will be located quickly. But, topography encountered along the way will cause problems by sending us off in a wrong direction. We could also be fooled by finding a local minima. Without the ability to see the rest of the valley, we would assume that the local minimum is the low point of the valley and that the search is over.

This analogy is two dimensional and is significantly more complicated than the one dimensional case of Figure 2.8. Typical inversions would involve thousands of dimensions. Clearly, this non-linear iteration procedure cannot be taken for granted. It may take an unreasonably large number of jumps to find the low point, or it might not be possible to find it at all. The trick to finding the low

point of the valley is simply to start close enough to the low point so that no intermediate complicated topography is encountered. What distance defines *close* will vary greatly with the topography of the valley, which will differ in each case.

Trial-and-error synthetic modeling of insightful cases is the only method of analyzing the non-linear iteration behavior. When the inversion procedure is expensive, extensive studies are impossible. Since ray tracing and iterative matrix inversion are relatively inexpensive, it is possible to perform numerous examples of the non-linear iteration for Ray Trace Tomography, which are presented in Chapter 3. For broad velocity variations, the results here may be applicable to other, more expensive, transmission techniques similar to Ray Trace Tomography.

In Chapter 3, we show that the non-linear iteration procedure is stable in the presence of simple, horizontally-shaped inaccuracies in the starting velocity model. However, the procedure is less stable in the presence of simple vertically-shaped starting model and starting reflector model inaccuracies. Vertically-shaped velocity variations cause more problems than horizontally-shaped ones because they have a greater effect on the vertical ray paths of a reflection survey.

Reflector inaccuracies cause significant non-linearities because slight errors in reflector structure can significantly alter ray paths. The sensitivity of the reflector position in the inversion is a motivation to position the reflector by migrating the data through the inverted velocity field and to ignore the reflector position from the inversion itself. We find that even when the reflector appears unstable in the inversion, the subsequent migration generally produces a stable result.

Velocity inaccuracies between the reference and true model that are either high in amplitude or complicated in structure appear not to converge well with non-linear iteration. Non-linearity in these cases reduces the potential of the technique. Non-linear iteration appears to work well only for cases where the objective is well-defined and most of the other geology is known. Such an objective might be the location and velocity of a gas pocket. When the problems are more complicated, such as in the overthrust region, useful results may be difficult to produce.

At the edges of a reflection survey, insufficient ray coverage exists to produce a proper inversion. Anomalies at the edges of the ray coverage will smear into the center of the ray coverage and anomalies away from the edges will smear toward the edges. Smearing is a complicated phenomenon that may be difficult to predict or identify. It is highly dependent upon ray geometry and the type of anomaly. Chapter 3 presents some inconclusive examples that suggest edge effects may seriously distort the inversion a significant distance away from the edges.

Application of transmission tomography to a reflection survey is effected by the relatively small region of inhomogeneous ray coverage at the edges. Other applications such as VSP or cross-hole geometries, which have greater regions of inhomogeneous ray coverage, may have greater effects.

1.6 Eigenvalue Analysis of Velocity-Reflector Depth Ambiguity

The accurate resolution of reflector depth in cases where an ambiguity exists between velocity and reflector depth is a main goal of Ray Trace

Tomography. These ambiguities are frequently broad features on the order of a cable length of a reflection survey. Because of their size, they frequently do not affect the waveform or cause non-linearities. Thus, travel times and ray paths are an adequate approximation for the analysis of the velocity-reflector depth ambiguities, whether we choose to invert them using tomography or some other technique.

Ambiguity between velocity and reflector depth occurs because a change in velocity can completely negate the travel time effect of a shift in reflector depth for vertical rays. Addition of rays at angles other than vertical will resolve this ambiguity, but the difference in signature between velocity and reflector depth can be subtle. For laterally invariant cases, the different signature between velocity and reflector depth corresponds to different hyperbolic moveout curves in Common Midpoint Gathers, something generally apparent in the data. When velocity varies laterally, the difference is less apparent. The velocity can be adjusted to mimic the hyperbolic moveout signature of a reflector depth change. Just how subtle this signature is depends on many items: the level of noise in the data, the angular ray coverage available, edge effects, non-linearities, and the geologic information available to each particular case.

Chapter 4 performs the analysis of the velocity-reflector depth ambiguity with the use of Singular Value Decompositions of the model space for a small generic reflection survey (1400 model space parameters), which is the largest reasonably possible on a CRAY-2 computer. This theoretical analysis of the linear system can categorize resolution in the quantitative but abstract terms of eigenvalues and eigenvectors. By relating geologic objectives to certain eigenvalues, we can determine whether the objective can be resolved. If it can be

resolved, we can carry out the inversion over the proper range to ensure that the desired objective is achieved yet contaminated with as little noise as possible.

Theoretical analysis can directly determine the resolution of the model in common units such as depth or velocity, given the accuracy of the data and the noise content. The abstract nature of the theoretical analysis enables easy quantitative comparison of different recording geometries and geologic structures. Thus, the effect of recording parameters, inversion constraints, and geologic characteristics on the resolution are available for analysis.

Chapter 4 focuses on characterizing what types of velocity variations are most ambiguous with reflector variations and what information is needed to resolve ambiguity. The theoretical analysis of Chapter 4 produces results in terms of eigenvectors, difficult entities to relate to geologic structures. Simple examples of the ability of Ray Trace Tomography to resolve sample velocity-reflector depth ambiguities are presented in Chapter 3.

1.7 Constraining the Inversion

Several processes have been mentioned that degrade the inversion: limited angular ray coverage, non-linearities caused by inaccuracies of the starting model, edge effects, the poor resolution of ambiguous velocity and reflector depth, and processes unaccounted for by our ray tracing model (3-D effects, anisotropy, & attenuation). There may be other aspects that further contribute to distort the inversion, such as practical problems in implementing the technique, or special problems caused by unique geometries. Frequently, these problems can be resolved with geologic constraints or just plain common sense.

For instance, by knowing that the geology in an area is mostly horizontal, vertical features can be attributed to being artifacts of the limited angular ray coverage. Kknowledge that certain geologic units are unlikely to contain velocity variations can be used to resolve certain velocity-reflector depth ambiguities. The assumption that there are no velocity variations at the edges of the model can serve to reduce edge effects.

To produce the best result from the data, the interpreter's knowledge must be entered quantitatively into the inversion in the form of mathematical constraints. Ray Trace Tomography can easily implement many of these constraints. Several examples are presented throughout Chapter 3 on solving problems with edge effects, the velocity-reflector depth ambiguity, and non-linear effects. The ability to couple seismic data with alternative information may be very beneficial in certain areas.

It is preferable that the interpreter have as much control as possible over the implementation of constraints. He/she may want to vary them for each case. As we explore more complicated areas and desire greater accuracy in present areas, the need grows for flexibility in implementing our techniques. Moreover, in many cases, inversion results will be dependent upon the constraints used, which are not always correct. For instance, one can rarely say with certainty that a particular layer contains significant internal velocity variations. An understanding of the resolution of the results is crucial before making economic decisions based on those results.

To facilitate programming and processing, we sometimes implement techniques using assumptions that amount to *a priori* constraints. Though often

valid, these constraints are not always appropriate. It is important to carefully separate the information in the data from the constraints implemented by a person. This separation is clearest to a processor when the constraints must be deliberately implemented in the processing and are not "hard-wired" into a program. For example, sometimes a constraint with questionable validity will produce a result that looks "cleaner," which will incorrectly suggest greater accuracy of the result. It may be better to leave the artifacts in a distorted result so that it is not overinterpreted.

1.8 Data Examples

Examples of the implementation of Ray Trace Tomography to two industry reflection data sets are presented in Chapter 5. One data set, from the north slope of Alaska, contains a velocity-reflector depth ambiguity caused by permafrost variations. The other data set from the central valley of California contains a gas pocket that washes out the data beneath it on stacking. These data set examples were performed without with the full capability of industry or the thoroughness necessary for industry interpretation. However, the results show that tomography can be implemented with some success even with the limited resources available to a graduate student. The practical problems, such as travel time picking, are not too great, and useful results are achieved. In particular, examples are presented on how careful application of tomography is used to indicate how well the geological objective was achieved. For the North Slope data set, this objective is the resolution of the velocity-reflector depth ambiguity. For the Central Valley data set, this objective is the accurate determination of the velocity input for migration. The examples also demonstrate some of the

problems involved with the implementation, such as the image distortion from the artifacts.

1.9 Summary

Ray Trace Tomography has solid potential. From an applied perspective, the technique can solve present pressing problems with the processing of seismic surface reflection data. From a general perspective, it serves as a model for more advanced transmission tomography techniques.

However, Ray Trace Tomography also has many drawbacks. It is an inversion procedure with a large number of parameters. The procedure is intolerant of data or starting model errors. Artifacts will generally dominate the solution unless constraints are implemented.

Not only are there questions about the technique's effectiveness, but it is difficult to implement and execute, and it does not fit well into the present structure of oil exploration or other detailed seismic analyses. Several extensive programs need to be written to pick the travel times from prestack traces, trace rays through cells, to invert travel times, to interact with a person to input constraints, and to perform prestack migration. Considerable human interaction is needed to choose a starting reference model, run programs, identify artifacts, and input geologic information.

This thesis attempts to introduce the complications involved in implementing and executing Ray Trace Tomography, characterize their seriousness, and present approaches for dealing with the problems. The analysis

is performed with synthetic modeling in Chapter 3, by theoretical analysis in Chapter 4, and with sample data applications in Chapter 5.

Chapter 2

An Implementation of Ray Trace Tomography to Reflection Seismology

2.1 Abstract

Travel times are linearized with respect to slowness and reflector depth using a cell-based ray-tracing method to set up a very large linear system for inversion. Because of its size and desired high bandwidth inversions, an efficient iterative inversion technique, Dines and Lytle (1979) back-projection, with the application of Chebyshev acceleration factors, is used. This technique has advantages over the conventional conjugate gradient iterative inversion technique. Several methods for constraining the inversion are presented.

2.2 Introduction

Computer implementation of Ray Trace Tomography is essentially a two-step process: setting up the inverse equation through use of ray-tracing and then solving the equation. The mechanics of both steps are generally well understood. Numerous ray tracers and iterative matrix inversion schemes exist. Implementation issues generally involve practicalities such as efficiency and ease of

programming and use. The best method will probably be determined only through devising and attempting several different types of ray tracers and inversion schemes. Here, the implementation presented is based on the philosophy of making the method as general as possible, with no built-in assumptions, but many optional ones.

A form of this philosophy allows every point of a model to vary independently of others. This general formulation enables a wide variety of constraints to be implemented so that they adjusted for each individual case. This approach is the most general, but creates numerous difficulties for ray-tracing and inversion by disqualifying much of the layer-based ray-tracing technology that has been developed.

The cell-based approach creates large model spaces, which require efficient iterative inversion techniques. A modification of the Dines and Lytle (1979) back-projection technique performs this function well and has advantages over the conjugate gradient technique. The algorithm for this technique is presented in pseudocomputer language form. The technique has advantages over the conjugate gradient technique.

The flexible cell-based approach gives the inversion dangerously many degrees of freedom. Generally, some constraints must

implemented to guide the inversion. Several methods for implementing geologic assumptions as inversion constraints into back-projection are introduced.

The formulation presented here is based exclusively on travel times. This approach enables efficient modeling of the technique to analyze its characteristics in a wide variety of settings, one goal of this thesis. The picking of travel times from real data, while possible as shown in Chapter 5, limits the application of the technique to high-quality data. The potential application can be broadened by using a waveform driven technique analogous to Toldi's (1985) method of using a semi-automated procedure for chosing stacking velocities or a similar technique by Sherwood (1987).

Since ray paths used to set up the linear system for inversion are traced through an approximate reference model, they have errors that affect the inversion result. Repeated application of ray-tracing will reduce these errors, but not eliminate them. A description of this strategy and some of its pitfalls is presented at the end of this chapter.

2.3 Ray-Tracing Methodology

The ray-tracing method implemented here is based on the method of Langen et al. (1985). Its approach is to trace rays through a velocity field discretized into a large number of cells, each with a linear

velocity gradient. To find the path between two points, a shooting method must be employed that iterates to the desired ending point.

Simpler and faster ray-tracing methods exist, but the cell-based method is preferred for its flexibility and compatibility with tomographic inversion. A two-dimensional grid of points is the most general formulation for representing a velocity field. Any velocity field can be represented in this way. With a flexible cell-based ray tracer, additional complications are not introduced into the inversion process and the capability of the tomographic inversion is left uncompromised by ray-tracing considerations.

The purpose of ray-tracing for this application is to provide the tomographic inversion with ray paths to be used for the inversion. Since the inversion also uses a cell-based representation of the velocity field, this quantity is easily computed with this ray tracer. Cells used for the ray-tracing are the same as those used in the inversion.

This flexibility of the ray tracer and the duality between the two velocity fields also enable the inverted velocity field to be easily re-ray-traced to update the ray paths. This capability to improve the non-linear effects resulting from ray path errors is important for accurate inversions, as shown in Chapter 3. Moreover, the ray tracer can be easily used to determine travel times in velocity fields for modeling

with tomographic inversion.

Figure 2.1 illustrates the cell-based ray-tracing approach. The points of the velocity grid are the corners of rectangular cells. The cells are further subdivided into triangles so that the three corner points define a unique velocity gradient in each triangle. Neighboring cells are subdivided in different directions to avoid an artificial bias from the subdivision direction.

By using cells with gradients, the velocity is continuous across triangle boundaries, and thus is continuous across the entire velocity field. Without velocity discontinuities, rays are not diffracted but only curved. Eliminating diffractions helps make the ray set smooth and continuous.

Rays are traced through each triangle using the fact that ray paths are arcs of circles in a linear velocity gradient. This procedure involves the computation of an arctangent, a logarithm, and a square root. Since the curvature of a ray in each cell is generally low, these functions can be approximated by their polynomial expansions. However, we find the trigonometric functions on the computers to be as efficient as polynomial approximations. Moreover, the use of these functions ensures robustness of the method in the presence of strong gradients. Care must be taken to avoid numerical round-off errors.

With the velocity continuous across triangle boundaries, the ending point and direction of a ray are carried over from one triangle to the next, and thus, through the entire velocity field.

Smoothly varying reflectors are handled by defining them as a series of third-order polynomials in each cell. The four coefficients of the polynomial enable the position and slope to be continuous across the two cell sides, and thus across the entire velocity field. Distance of a ray to the reflector in a cell is determined by finding the smallest positive root of a third-order polynomial through iteration.

Examples of the ray tracer are shown in Figures 2.2 through 2.3. In routine applications, the cell size used is much smaller than that shown in the figures. Examples of the ray tracer in more complicated velocity fields are presented in Chapter 3.

Figure 2.3 presents ray paths traced through random media of different-sized velocity variations. Some of the figures show an evenly spaced ray fan; the others show paths to receivers. Rays of the fan curve away from the high velocity regions and are concentrated in the low velocity regions. If ray density is taken as a measure of amplitude, the low velocity regions have greater amplitude energy. The rays to receivers, however, are concentrated in the high velocity regions because the paths of least travel time are used. These paths will have

low amplitude.

One of the basic approximations Ray Trace Tomography makes is that it simulates waveform propagation by optical ray-tracing. Optical rays cannot simulate some phenomena of waveform propagation such as diffractions and refractions. Figures 2.3e & f demonstrate that for certain velocity fields, optical rays can become complicated to the point of being meaningless.

Optical rays are the high frequency limit of waveform propagation. Such rays are an adequate approximation to waveform propagation where the velocity variations are broader than the wavelength content of the wave field. If a very high frequency source had been used in the velocity fields of Figures 2.3e & f, the wave field too would be broken up and become complicated, similar to the ray paths shown.

A lower frequency source, however, remains more intact. In transmission, a wave field does not "see" the small scale velocity variations that are shorter than the wavelength content of the wave field. The effect of the smaller scale velocity variations on the transmitted longer wavelength wave field would be similar to a smoothed version of the velocity variations. Thus, the ray-tracing approximation for smaller scale velocity variations can be improved by

smoothing the velocity field to remove those components that are greater than the characteristic wavelength of the signal. The accuracy of this simulation of using a smoothed version of the velocity field for ray-tracing low frequency energy is not analyzed.

In cases where the source content is of high enough frequency that the ray paths of Figures 2.3e & f are an accurate description of wave propagation, any transmission inversion scheme will have serious problems and may not produce a useful result. With high frequency data, it may be possible to perform only a statistical analysis of the velocity variations in the field. To image the velocity fields of Figures 2.3e & f accurately would require the use of a scattering technique with a lower frequency source.

This ray-tracing approach lends itself to simple extrapolation to three dimensions. In three dimensions, the points of a discretized velocity field form a cubic volume that can be subdivided into 5 tetrahedrons as shown in Figure 2.4a. The four corners of the tetrahedron will specify a unique linear velocity gradient within each tetrahedron, and continuous velocity across the sides of neighboring tetrahedrons. Extrapolation of reflectors to three dimensions is more complicated, but can be performed. The reflector in two-dimensions is a third order polynomial in each cell. This polynomial has twelve

coefficients, ensuring that the position and slope are continuous across cell boundaries. Examples of three-dimensional ray-tracing are presented in Figure 2.4b.

Ray-tracing extends nicely to three dimensions, but the shooting method for iterating to a receiver does not. A robust method could not be developed for solving the two-point problem. In two dimensions, when two rays span a receiver, they effectively *captured* the ray. We know that the ray to the receiver lies in between the two unless some unusual situation exists, such as the receiver being in a shadow zone or near a caustic. However, in three dimensions, the receiver cannot be similarly *captured.* No robust descent methods could be devised to work with lateral velocity variations.

2.4 Linearization of the Travel Time Equation

Travel times are a linear integral of the slowness along the ray path.

$$t = \int_{ray\ path} s \cdot dl,$$

where

$s = \dfrac{1}{velocity}$, which is the slowness along the ray path.

l = the distance along the ray path.

With the slowness field discretized into cells and a reference problem subtracted out, the forward problem of the travel time deviations from the reference model is expressed for the kth ray as:

$$\Delta t_k = \sum_j l_{kj} \cdot \Delta s_j,$$

where

l_{kj} = the path length of the kth ray in the jth cell, and

Δs_j = the slowness variation of the jth cell.

The kth ray path is represented here only by the segment lengths, l_{kj}, in the cells that were crossed. These segment lengths are computed by ray-tracing through the best estimate of the velocity field available. The formulation does not take into account that changing the slowness will change the ray path. This approximation will introduce an error into the inversion. The magnitude of this error and methods for reducing it are discussed in Chapter 3.

The discretized travel time equation can be written in matrix notation for numerous ray paths as

$$\Delta \mathbf{t} = \mathbf{L}\Delta \mathbf{s},$$

where

$\Delta \mathbf{t}$= vector of travel times deviations predicted from reference model;

Δs= vector of slowness deviations from reference model; and

L= matrix where a row contains the path lengths of a ray in each cell.

The **L** matrix is generally unbearably large for seismic exploration applications of tomography. A typical reflection survey will have 500 shot points of 96 traces producing about 50,000 data points. The model will have 500 cells across and 40 down producing about 20,000 cells. The resulting **L** matrix is (50,000 $\times$ 20,000), a billion elements.

For a standard situation, a ray will cross only a few of the cells in the model producing a sparse matrix, generally consisting of 95-99% zeros. For the example above, a ray may cross 100 cells down to the reflector and another 100 back up, giving it 200 cells out of the model space of 20,000. Naturally, this matrix can be compacted by only storing non-zero elements and their locations. Since consecutive cells in the ray path must be neighbors, after the first cell, only a cell position relative to the previous one must be stored.

2.5 Analysis of Iterative Tomography and Migration Methods: Should Tomography Include a Reflector Term?

An example of the iterative application of a velocity analysis technique, (tomography), and a reflector location technique, (migration), is carried out on a simple two-parameter model. Using the simple model will enable the iterative application to be performed analytically. A quantitative convergence rate for an incorrect reflector position can then be determined. The iterative application is carried out on more realistic models in Chapter 3.

The two-parameter model, shown in Figure 4.3, consists of: 1) a uniform slowness, and 2) a uniform reflector depth. While this model is a highly simplified version of a realistic case, it can represent a localized case, such as in Figure 4.2. The two- parameter model isolates the velocity-reflector depth ambiguity.

Travel time deviations of the rays of a CMP gather over this two parameter model can be written as

$$\Delta t = \frac{2}{\cos(\theta)} \cdot h \cdot \Delta s + 2 \cdot \cos(\theta) \cdot s \cdot \Delta h$$

where the variables are defined as in Figure 4.3.

The $\frac{2}{\cos(\theta)} \cdot h$ is the distance the ray travels in the slowness field. The $2 \cdot \cos(\theta) \cdot \Delta h$ is the extra distance a ray travels as the result of a reflector depth deviation, Δh. The deviations, Δs, Δh are assumed to be small enough to ignore higher order terms.

Let us consider a starting model with the correct reflector depth, $\Delta h^{(0)} = 0$, but an incorrect slowness deviation, $\Delta s^{(0)} \neq 0$. This model will cause travel time variations, $\Delta t^{(0)}$ of

$$\Delta t^{(0)} = \frac{2}{\cos(\theta)} \cdot h \cdot \Delta s^{(0)} .$$

Assuming the reflector location method (migration) is first applied, it will adjust the reflector depth to match the travel times by

$$\Delta h^{(1)} = f\left(\Delta t^{(0)}\right)$$

where

$f()$ = the migration function that produces the reflector depth from the collection of travel times of a CMP gather.

Later, several different migration functions will be considered. The travel time deviations resulting from this new model will be

$$\begin{aligned} \Delta t^{(1)} &= \Delta t^{(0)} - 2 \cdot \cos(\theta) \cdot s \cdot \Delta h^{(1)} \\ &= \frac{2}{\cos(\theta)} \cdot h \cdot \Delta s^{(0)} - 2 \cdot \cos(\theta) \cdot s \cdot f\left(\Delta t^{(0)}\right) \\ &= 2\left(\frac{1}{\cos(\theta)} - \cos(\theta) \cdot \frac{s \cdot f\left(\Delta t^{(0)}\right)}{h \cdot \Delta s^{(0)}} \right) \cdot h \cdot \Delta s^{(0)} . \end{aligned}$$

We now apply the velocity determination method, tomography. The least-squares determination of the single slowness parameter is written as

$$\Delta s^{(1)} = \frac{\sum_{i=1}^{nrays} l_i \Delta t_i^{(1)}}{\sum_i l_i^2} ,$$

where

$l_i = \frac{2}{\cos(\theta)} \cdot h$, which is the path length of the ray.

Using the following relationship, the summations are changed to integrals

$$\sum_{i=1}^{nrays} g(\theta_i) = \int_{\theta=0}^{\theta_{max}} d\theta \; g(\theta) \cdot \frac{\text{nrays}}{\theta_{max}} ,$$

where

nrays = the number of rays

producing

$$\Delta s^{(1)} = \frac{\int_{\theta=0}^{\theta_{max}} d\theta \; l_\theta \Delta t_\theta^{(1)} \cdot \frac{nrays}{\theta_{max}}}{\int_{\theta=0}^{\theta_{max}} d\theta \; l_\theta^2 \cdot \frac{nrays}{\theta_{max}}}$$

where

$l_\theta = l_i$ of before.

Summations are changed to integrals under the assumption that enough

rays exist to approximate a continuum. This enables analytic computations of the summations. We ignore the complication that even coverage with offset of a CMP gather does not translate into an even coverage in angle, θ. We also assume equal weighting of the rays.

Substituting in for $\Delta t^{(1)}$ and l_θ

$$\Delta s^{(1)} = \left(\frac{4h^2 \int_{\theta=0}^{\theta_{max}} \frac{d\theta}{\cos^2(\theta)}}{4h^2 \int_{\theta=0}^{\theta_{max}} \frac{d\theta}{\cos^2(\theta)}} - \frac{4h^2 \frac{s \cdot f\left(\Delta t^{(0)}\right)}{h \cdot \Delta s^{(0)}} \int_{\theta=0}^{\theta_{max}} d\theta}{4h^2 \int_{\theta=0}^{\theta_{max}} \frac{d\theta}{\cos^2(\theta)}} \right) \Delta s^{(0)} .$$

The expression is simplified using

$$\int_{\theta=0}^{\theta_{max}} \frac{d\theta}{\cos^2(\theta)} = \tan(\theta_{max}) .$$

So,

$$\Delta s^{(1)} = \left(1 - \frac{\theta_{max}}{\tan(\theta_{max})} \cdot \frac{s \cdot f\left(\Delta t^{(0)}\right)}{h \cdot \Delta s^{(0)}} \right) \Delta s^{(0)} .$$

The expression in brackets represents the portion of the original slowness perturbation, $\Delta s^{(0)}$, that has been inverted after one loop of iterative tomography and migration. This will be dependent on the

choice of migration function, $f()$, that determines how inconsistent data maps into reflector depths.

We will examine three different choices of $f()$: $f^1()$, $f^2()$, & $f^3()$. The first function considered is a time-to- depth conversion of the zero-offset time which is analogous to post-stack migration. The function is produced from the reflector portion of the earlier travel time equation

$$\Delta t = 2 \cdot s \cdot \cos(\theta) \cdot \Delta h, \qquad \theta = 0 ,$$

and is written as

$$f^1(\Delta t^{(0)}) = \frac{\Delta t_{\theta=0}}{2 \cdot s}$$

$$= \frac{2 \cdot h \cdot \Delta s^{(0)}}{2 \cdot s} .$$

Plugging this into the expression for $\Delta s^{(1)}$ produces:

$$\Delta s^{(1)} = \left(1 - \frac{\theta_{max}}{\tan(\theta_{max})} \right) \Delta s^{(0)}$$

$$= 0.21 \cdot \Delta s^{(0)} \quad \text{for } \theta_{max} = 45°$$

$$= 0.09 \cdot \Delta s^{(0)} \quad \text{for } \theta_{max} = 30° .$$

Alternatively, we can perform the time to depth conversion using the far offset time. Again using the reflector position of the travel

time equation

$$\Delta t = 2 \cdot s \cdot \cos(\theta) \cdot \Delta h, \qquad \theta = \theta_{max}$$

$$f^2(\Delta t^{(0)}) = \frac{\Delta t_{\theta_{max}}^{(0)}}{2 \cdot \cos(\theta_{max}) \cdot s}$$

$$= \frac{\frac{2}{\cos(\theta_{max})} \cdot h \cdot \Delta s^{(0)}}{2 \cdot \cos(\theta_{max}) \cdot s}$$

$$= \frac{h \cdot \Delta s^{(0)}}{s \cdot \cos^2(\theta_{max})} .$$

Plugging this expression into the equation for $\Delta s^{(1)}$ above produces

$$\Delta s^{(1)} = -0.57 \cdot \Delta s^{(0)} \quad \text{for } \theta_{max} = 45°$$
$$= -0.21 \cdot \Delta s^{(0)} \quad \text{for } \theta_{max} = 30°$$

These negative values mean that the system is actually diverging.

The third choice for $f\,()$ considered is determining the reflector depth by considering all the offsets with a least-squares approach. Similar to prestack migration, this method performs a time to depth conversion of all the travel times and then takes some average of the resulting depths. The least-squares formula of the reflector depth is written as

$$f^3(\Delta t^{(0)}) = \frac{\sum_{i=1}^{nrays} 2 \cdot \cos(\theta) \cdot s \cdot \Delta t_i^{(0)}}{\sum_{i=1}^{nrays} (2 \cdot \cos(\theta) \cdot s)^2}$$

$$= \frac{h \cdot s \cdot \Delta s^{(0)} \cdot \int_{\theta=0}^{\theta_{max}} d\theta}{s^2 \cdot \int_{\theta=0}^{\theta_{max}} d\theta \cos^2(\theta)}$$

$$= \frac{h \cdot \Delta s^{(0)} \cdot \theta_{max}}{s \cdot \left(\frac{\theta_{max}}{2} + \frac{\sin(2 \cdot \theta_{max})}{4} \right)} .$$

Plugging this expression in with the equation for $\Delta s^{(1)}$ above produces

$$\Delta s^{(1)} = 0.04 \cdot \Delta s^{(0)} \quad \text{for } \theta_{max} = 45°$$
$$= 0.008 \cdot \Delta s^{(0)} \quad \text{for } \theta_{max} = 30°$$

The fast convergence rate of the zero offset time to depth conversion is because it has arbitrarily ignored a certain portion of the data. While a zero offset migration scheme is efficient to code on the computer and simple to conceptualize, there is nothing inherent about the zero offsets that makes them preferred here. A more complete reflector location method is one that uses some average of all the data

to determine reflector depth.

The fastest convergence rate of these three techniques is the first one which requires 10 iterations to produce an inversion of 90% accuracy for a maximum ray angle of 45° $(0.1=(1.0-0.21)^{10})$. This maximum ray angle is generally unavailable. Examples of the iterative application of a velocity-only analysis technique and post-stack migration on more realistic models in Chapter 3 that allow velocity variations, show similar behavior. The use of an averaging reflector location technique, such as a post-stack migration scheme with the same maximum ray angle, would require 115 iterations $(0.1=(1.0-0.02)^{115})$.

These convergence rates are far too slow. The iterative application of a velocity-only analysis method and a reflector location method is effectively unable to properly position a reflector at the correct depth. Properly resolving reflector depth requires that reflector depth and velocity be coupled in one inversion technique. This can be done easily with Ray Trace Tomographic inversion by including a reflector term.

2.6 Inclusion of Reflector Perturbations in the Linearized Travel Time Equation

We desire to include the reflector position in the linearized travel time equation. For the forward problem, the effect of small reflector position variations on travel time is expressed as

$$\Delta t_k = \frac{2 \cdot \cos(\theta_k) \cdot \Delta \tilde{h}}{vel},$$

where

θ_k = the angle of reflection from vertical of the *kth* ray;

vel = the velocity above the reflector perturbation; and

$\Delta \tilde{h}$ = the reflector perturbation perpendicular to its slope.

The numerator represents the extra distance traveled by a ray as the result of a small reflector perturbation

$$\Delta l = 2 \cdot \cos(\theta) \cdot \Delta \tilde{h},$$

where

Δl = the extra distance a ray must travel due to a reflector perturbation, $\Delta \tilde{h}$.

This relationship can be easily shown to hold for flat reflectors and laterally invariant velocity, as demonstrated in Figure 2.5a.

This result is also valid for sloping reflectors and an arbitrary velocity field as shown in Figures 2.5a & b with the use of Hyugen's principle. It demonstrates that surfaces of constant travel time are

perpendicular to the ray path. The result is valid only for small reflector perturbations.

The reflector is parameterized by discretizing it into a series of points with line segments joining the points. Point of reflection is an arbitrary one located between two points of discretization, where the reflector position is defined. With the linear approximation between these two points, the perturbation at the point of reflection is related to that of the discretized points by

$$\Delta\tilde{h} = \frac{\beta \cdot \Delta h_1 + \alpha \cdot \Delta h_2}{\alpha + \beta},$$

where

α & β= the distance of the point of reflection from discretized point 1 & 2, respectively.

Δh_1 & Δh_2= the reflector perturbations of discretized points 1 & 2, respectively.

This handling of the reflector is identical to that of Bishop et al. (1984). A simpler method for handling the reflector was attempted, which related the point of reflection to only the closest of the discretized reflector positions. This method models the reflector perturbations as a series of piece-wise steps. Additional errors caused by this method are very small for small cells, but they were found to

affect the inversion results drastically.

To keep the simple formulation, $\Delta \mathbf{t} = \mathbf{L}\Delta \mathbf{s}$, of the forward problem intact, discretized reflector points are treated analogously to slowness cells and are called *reflector cells*. Rays have *simulated* path lengths in the reflector cells as given by

$$\tilde{l}_k = \cos(\theta_k) \cdot p_o ,$$

where

$\tilde{l}_k$ = the simulated path length in the reflector cell for the k*th* ray;

θ_k = the angle of reflection from vertical of the *kth* ray; and

p_o = an inversion parameter representing the simulated path length for a vertical ray ($\theta_k = 0$) in the reflector. Choice of this parameter is discussed below in the section on back-projection.

The $\tilde{l}_k$ path length is proportionately subdivided between the two reflector points on either side of the reflection point, depending on the distance from each point. These two values for the reflector points, or *cells*, are the entries in the **L** matrix of the forward problem.

Simulated path length in the two reflector cells varies only with

the angle of reflection. As a rule, wide-angle rays are affected less by a reflector perturbation than by vertical rays, as shown in Figure 2.5c.

Use of this simulated path length in the reflector cells will cause the solution, $\Delta \mathbf{s}$, of this inverse problem to produce a result of simulated slowness updates to the reflector cells. To be meaningful, these simulated slownesses must be converted into reflector depth deviations by

$$\Delta h = \Delta s \cdot p_o \cdot \frac{vel}{2} ,$$

where

Δh = reflector depth variation;

vel = the velocity just above the reflector cell;

Δs = simulated slowness variation from solution; and

p_o = inversion parameter representing the *simulated* path length for a vertical ray ($\theta_k = 0$) in the reflector.

2.7 Iterative Matrix Inversion Through Dines and Lytle Back Projection

The Dines and Lytle (1979) back-projection scheme is written as

$$\Delta s_j = \frac{\sum_k l_{kj} \cdot \Delta \tilde{sp}_k}{\sum_k l_{kj} + \varepsilon},$$

and

$$\Delta \tilde{sp}_k = \frac{\Delta t_k}{P_k}$$

where

$\Delta \tilde{sp}_k$= the desired slowness perturbation for the k*th* ray. The desired slowness perturbation of a ray is the cumulative slowness change made all along the ray path that would correct its travel time deviation.

P_k= $\sum_i l_{ki}$, which is the total path length of the k*th* ray, including that of the reflector cells.

l_{ki} = the elements of matrix **L**

$\sum_k l_{ki}$ = the sum of the ray segment lengths in the i*th* cell.

ε = a damping factor to stabilize the division for empty or nearly empty cells.

This back-projection scheme can be written as a matrix equation

$$\mathbf{\Delta s = S L^T D \Delta t}$$

where

l_{kj} are the elements of matrix **L**, and

S and **D** are diagonal matrixes:

$$\mathbf{D}_{kk} = P_k^{-1}$$
$$\mathbf{S}_{ii} = (\sum_k l_{kj} + \varepsilon)^{-1} .$$

This formulation is a conceptually simple one that takes the weighted average in a given cell of the desired slowness perturbations of each ray through that cell. The weight is the ray's path length in the cell.

This formula can also be thought of as back-projection, where a certain amount of the desired slowness perturbation of each ray is deposited into each cell that it crosses. The amount deposited is proportional to the path length in the cell. After all the rays are back-projected, the accumulated slowness in each cell is divided by the sum of the path lengths of all the rays through that cell.

One application of the Dines and Lytle back-projection formula will produce a seriously-smeared result of the original image. Smearing will depend mostly upon ray coverage. Image is improved by repeated application of the formula on the travel time residuals uncorrected by the previous result.

Despite the simplicity of this formula, it is shown later that with the addition of Chebyshev scaling factors, it has the desirable properties of: 1) convergence to least-squares solution, 2) speed, 3) stability, 4) control over the eigenvalue range inverted, and 5) flexibility for including constraints.

From this formulation, it can be seen that the p_o parameter designated above as the simulated path length in the reflector cell for a vertical ray, controls the relative weight between slowness and reflector cells. A large value for p_o will increase the simulated path length in the reflector cells, and tend to account for more of the travel time deviations with reflector depth variations. To weight the slowness and reflector cells equally, we want to back-project about half of the travel time deviations into the reflector and the other half into the slowness. Thus, p_o should be chosen so that the sum of the path lengths in all the reflector cells will be equal to that of the slowness cells sum. This criterion is met with a p_o of approximately the path length of an average ray in the slowness field, assuming that the rays reflects only once. Since there are generally fewer reflector cells than slowness cells, the simulated path length in a reflector cell is generally much greater than that in a slowness cell.

Whether the velocity and reflector should be equally weighted or not is a subjective decision the processor will have to make for each case. The appendix presents examples of inversions with differing values of p_o. Chapter 4 performs an analytic analysis of the effect of the choice of p_o upon the resolution between ambiguous velocity and reflector depth variations.

2.8 Sample Computer Program for Dines and Lytle Back Projection

An example program in pseudo-computer language form for implementing the Dines and Lytle back-projection formula is presented:

```
main()
{
    read(Δt^(0) vector)
    /* read total path lengths of each ray including its reflector cell */
    read(total_path_length vector)

    /*  set Δs vector equal to 0    */
    for (l =  1 to number of cells)
        Δs(l) =  0

    for (i= 1 to number of iterations)
    {
        rewind(ray path file)

        for (k= 1 to number of rays)
        {
            /*  read ray paths from disk    */
            read(cell_positions for ray k)
            read(path_lengths for ray k)

            /* Compute forward problem: Δt^(i) = Δt^(0) – LΔs^(i)   */
            for (j =  1 to number of cells touched by ray number k)
                Δt(k) =  Δt^(0)(k) - path_lengths(j) · Δs(cell_position(j))

            for (j =  1 to number of cells touched by ray number k)
            {
                /* perform back-projection  L^T DΔt^(i)      */
                numerator(cell_positions(j)) + =
                                    path_lengths(j) · Δt(k) / total_path_length(k)

                /* accumulate denominator (Σ_k l_kj)        */

                denominator(cell_positions(j)) + =  path_lengths(j)
            }
        }   /* end loop over rays     */
        for (l =  1 to number of cells)
```

$$\Delta s(l) \mathrel{+}= \frac{\textbf{numerator}(l)}{\textbf{denominator}(l) + \varepsilon}$$

```
    }
    /* end of iterations, write result */
    write(Δs vector)
}.
```

The program is not directly vectorizable because a ray can cross the same cell more than once, causing a loop to repeat access to an $\Delta\mathbf{s}()$, **numerator**(), and **denominator**() storage locations. To vectorize, duplicate listings of the same cell in a ray path need to be compacted into one listing with a pre-processing step.

In data applications, the **L** matrix is generally several gigabytes in size, but 95%-99% sparse. The use of recursive addressing has taken advantage of the sparseness of the **L** matrix to avoid unnecessary multiplications by zero in the forward modeling, $\mathbf{L}\Delta\mathbf{s}$, and the back-projection, $\mathbf{L}^T\Delta\mathbf{t}$ matrix operations. Note that the **L** matrix, even in its compacted form, does not need to be stored in memory.

2.9 Summary of Comer and Clayton Matrix Analysis

Analysis of the behavior of the Dines and Lytle technique we rewrite

$$\Delta s_j = \frac{\sum_k l_{kj} \cdot \frac{\Delta t_k}{P_k}}{\sum_k l_{kj} + \varepsilon},$$

as

$$\Delta \mathbf{s} = \mathbf{S}\mathbf{L}^{\mathrm{T}}\mathbf{D}\Delta \mathbf{t},$$

where **S** and **D** are diagonal matrixes:

$$\mathbf{D}_{kk} = P_k^{-1}$$

and

$$\mathbf{S}_{ii} = (\sum_k l_{kj} + \varepsilon)^{-1},$$

Comer and Clayton (1985) demonstrate that this back-projection scheme converges to the solution of the following variation of the original forward problem, $\Delta \mathbf{t} = \mathbf{L}\Delta \mathbf{s}$, with weights applied to data and model spaces

$$\mathbf{D}^{1/2}\Delta \mathbf{t} = (\mathbf{D}^{1/2}\mathbf{L}\mathbf{S}^{1/2})\mathbf{S}^{-1/2}\Delta \mathbf{s} .$$

We define the square root of a diagonal matrix to be the square root of its elements.

A summary of Comer and Clayton's development demonstrating convergence follows.

Repeated iterations of the Dines and Lytle scheme are written as:

$$\Delta \mathbf{s}^{(n+1)} = \Delta \mathbf{s}^{(n)} + \mathbf{S}\mathbf{L}^{\mathrm{T}}\mathbf{D}\Delta \mathbf{t}^{(n)}$$

and

$$\Delta \mathbf{t}^{(n)} = \Delta \mathbf{t}^{(0)} - \mathbf{L}\Delta \mathbf{s}^{(n)},$$

where

$\Delta s^{(n)}$ = result after n iterations;

$\Delta s^{(0)} = 0$; and

$\Delta t^{(0)}$ = the original travel time deviations between data and that predicted by the reference model.

Performing some simple substitution and rearrangement produces the following equation

$$\begin{aligned}\Delta t^{(n)} &= \Delta t^{(0)} - L\Delta s^{(n-1)} - L\, SL^T D\Delta t^{(n-1)} \\ &= \Delta t^{(n-1)} - L\, SL^T D\Delta t^{(n-1)} \\ &= \left(I - LSL^T D\right)\Delta t^{(n-1)} \\ &= \left(I - LSL^T D\right)^n \Delta t^{(0)}.\end{aligned}$$

It follows that numerous iterations can be displayed in one compact form as

$$\Delta s^{(n)} = \sum_{m=0}^{n-1} SL^T D\left(I - LSL^T D\right)^m \Delta t^{(0)}.$$

Careful consideration demonstrates that the following is equivalent:

$$\Delta s^{(n)} = \sum_{m=0}^{n-1} \left(I - SL^T DL\right)^m SL^T D\Delta t^{(0)}.$$

The essence of this development is forcing symmetry on the expression in brackets of the above equation:

$$\Delta \mathbf{s}^{(n)} = \mathbf{S}^{1/2} \sum_{m=0}^{n-1} \left(\mathbf{I} - \mathbf{S}^{1/2} \mathbf{L}^T \mathbf{D} \mathbf{L} \mathbf{S}^{1/2} \right)^m \mathbf{S}^{1/2} \mathbf{L}^T \mathbf{D} \Delta \mathbf{t}^{(0)}.$$

By substituting $\mathbf{x} = \mathbf{S}^{-1/2} \Delta \mathbf{s}$, $\mathbf{b} = \mathbf{D}^{1/2} \Delta \mathbf{t}$, and $\mathbf{A} = \mathbf{D}^{1/2} \mathbf{L} \mathbf{S}^{1/2}$, we achieve a more compact form:

$$\mathbf{x}^{(n)} = \sum_{m=0}^{n-1} \left(\mathbf{I} - \mathbf{A}^T \mathbf{A} \right)^m \mathbf{A}^T \mathbf{b}.$$

Substituting in the singular value decomposition representation for $\mathbf{A}$, $\mathbf{A} = \mathbf{U} \Sigma \mathbf{V}^T$, produces:

$$\mathbf{x}^{(n)} = \sum_{m=0}^{n-1} \left(\mathbf{I} - \mathbf{V} \Sigma^2 \mathbf{V}^T \right)^m \mathbf{V} \Sigma \mathbf{U}^T \mathbf{b}.$$

Rearranging the previous equation produces

$$\mathbf{x}^{(n)} = \mathbf{V} \sum_{m=0}^{n-1} \left(\mathbf{I} - \Sigma^2 \right)^m \Sigma \mathbf{U}^T \mathbf{b}.$$

Since Σ is a diagonal matrix of eigenvalues ($\Sigma_{ii} = \lambda_i$), the above power series consists of I independent algebraic equations:

$$\mathbf{x}^{(n)} = \sum_{i=1}^{I} \mathbf{v}_i \sum_{m=0}^{n-1} \left(1 - \lambda_i^2 \right)^m \lambda_i \mathbf{u}_i^T \mathbf{b} \,,$$

where $\mathbf{v}_i$, $\mathbf{u}_i$, and λ_i are the individual model space eigenvectors, data space eigenvectors, and eigenvalues, respectively.

For infinite iterations, this equation converges when all eigenvalues of $\mathbf{A}^T\mathbf{A}$ are less than 2.0 and greater than 0.0

$$\sum_{m=0}^{\infty} \left(\mathbf{I}-\Sigma^2\right)^m = \left(\Sigma^2\right)^{-1}.$$

This convergence relationship is derived from

$$\frac{1}{r} = \frac{1}{1-(1-r)} = 1 + (1-r) + (1-r)^2 + (1-r)^3 \cdots ,$$

which converges for $|1-r| < 1.0$.

Thus, the iterations converge to

$$\mathbf{x}^{(\infty)} = \mathbf{V}\Sigma^G\mathbf{U}^T\mathbf{b},$$

which is identical to

$$\mathbf{x}^{(\infty)} = \mathbf{A}^G\mathbf{b},$$

where

$\mathbf{A}^G$ = the generalized inverse.

The general inverse is defined as

$$\Sigma_{ii}^G = \frac{1}{\lambda_i}, \text{ for: } \lambda_i > \lambda_{\min}\tilde{}, \text{ and}$$

$$\Sigma_{ii}^G = 0, \text{ for: } \lambda_i < \lambda_{\min}.$$

This last equation is, of course, the least-squares solution for the original problem

$$\mathbf{Ax} = \mathbf{b},$$

or by back-substituting

$$\mathbf{x} = \mathbf{S}^{-1/2}\Delta\mathbf{s},\ \mathbf{b} = \mathbf{D}^{1/2}\Delta\mathbf{t},\ \text{and}\ \mathbf{A} = \mathbf{D}^{1/2}\mathbf{L}\mathbf{S}^{1/2}$$

the equation is written as

$$(\mathbf{D}^{1/2}\mathbf{L}\mathbf{S}^{1/2})\mathbf{S}^{-1/2}\Delta\mathbf{s} = \mathbf{D}^{1/2}\Delta\mathbf{t}.$$

These weights of $\mathbf{D}^{1/2}$ applied to the data space, and $\mathbf{S}^{-1/2}$ applied to model space, have statistical justification based on gaussian noise. Longer rays are deweighted because, as a function of more slowness cells, they are more susceptible to the inaccuracy of the slowness model. Similarly, slowness cells with more rays, are more susceptible to travel time noise. Their weight is increased to keep their amplitude to a minimum. The square root factor is consistent with the characteristic that error goes by the square root of gaussian noise accumulation. (Least squares inversion minimizes $\sum_i D_{ii}\cdot(\Delta t_i^{data} - \Delta t_i^{model})^2$ and $\sum_j S_{jj}\cdot\Delta s_j^2$.)

Another justification for the data weights is that they speed convergence. For a ray with a short path, there is less doubt about where the slowness anomaly is than for a longer ray. The weight of the shorter ray is therefore increased. It will be shown later how additional weights that can counteract these constraints can be added.

Performing a finite number of iterations will produce a result of

$$\lambda_i^G = \sum_{m=0}^{n-1} \left(1-\lambda_i^2\right)^m \lambda_i,$$

$$= \left(\sum_{m=0}^{\infty} \left(1-\lambda_i^2\right)^m - \sum_{m=n}^{\infty} \left(1-\lambda_i^2\right)^m \right) \cdot \lambda_i,$$

or,

$$\lambda_i^G = \frac{1 - (1 - \lambda_i^2)^n}{\lambda_i},$$

where

n= the number of iterations; and

λ_i= the *ith* eigenvalue.

This equation is stable when $\lambda_i^2 < 2$ and converges the fastest for $\lambda_i^2 = 1.0$. Comer and Clayton (1985) demonstrate that the eigenvalues of $\mathbf{D}^{1/2}\mathbf{L}\mathbf{S}^{1/2}$ are between 0.0 and 1.0. This ensures that performing a finite number of iterations inverts the larger eigenvalues first, and suppresses the inversion of smaller eigenvalues.

The stability of the Dines and Lytle scheme can be easily confirmed from the perspective of considering it as an averaging formula, which is an inherently stable procedure.

2.10 Acceleration of Dines and Lytle Back Projection with Chebyshev Acceleration Factors

Rate of convergence of the Dines and Lytle back-projection scheme is extremely slow for small eigenvalues. Number of iterations, n, required to achieve a 90% inversion of a certain eigenvalue can be computed using:

$$0.9 = 1 - (1 - \lambda_i^2)^n$$

$$(1 - \lambda_i^2)^n = 0.1$$

$$n = \frac{\log(0.1)}{\log(1 - \lambda_i^2)}$$

$$n \approx \frac{2.3}{\lambda_i^2}$$

for small λ_i, say $\lambda_i < 0.3$.

Thus, a 90% inversion of an eigenvalue of 0.3 is performed in about 25 iterations. An eigenvalue of 0.1 is inverted in 230 iterations, and the eigenvalue of 0.05 in 920 iterations. We will generally desire to invert to an eigenvalue of at least 0.1. Chapters 3 and 4 suggest that one would frequently need to invert to the eigenvalue of 0.05 and perhaps lower.

The Dines and Lytle formula is easy and efficient to apply, but it is unbearably slow. Performing thousands of iterations is impractical. However, the number of iterations can drastically be reduced with Chebyshev acceleration factors developed by Olson (1986).

The acceleration factors scale the result of each back-projection

$$\Delta \mathbf{s}^{(n+1)} = \Delta \mathbf{s}^{(n)} + \sigma_n \cdot \mathbf{S}\mathbf{L}^T \mathbf{D} \Delta \mathbf{t}^{(n)},$$

where

σ_n = the amount by which the nth iteration is scaled:

$(\sigma_n > 1)$.

The effect of the scaling factors on the inversions can be determined by carrying it through the Comer and Clayton analysis presented earlier

$$\Delta \mathbf{t}^{(n)} = \prod_{j=0}^{n-1} \left(\mathbf{I} - \sigma_j \mathbf{L}\mathbf{S}\mathbf{L}^T \mathbf{D} \right) \Delta \mathbf{t}^{(0)}$$

and

$$\Delta \mathbf{s}^{(n)} = \sum_{m=0}^{n-1} \sigma_m \prod_{j=0}^{m-1} \left(\mathbf{I} - \sigma_j \mathbf{S}\mathbf{L}^T \mathbf{D}\mathbf{L} \right) \mathbf{S}\mathbf{L}^T \mathbf{D} \Delta \mathbf{t}^{(0)} ;$$

$$\mathbf{x}^{(n)} = \mathbf{V} \sum_{m=0}^{n-1} \sigma_m \prod_{j=0}^{m-1} \left(\mathbf{I} - \sigma_j \Sigma^2 \right) \Sigma \mathbf{U}^T \mathbf{b} ;$$

and

$$\lambda_i^G = \sum_{m=0}^{n-1} \sigma_m \prod_{j=0}^{m-1} (1 - \sigma_j \lambda_i^2) \ \lambda_i .$$

The product operator, $\prod$, applies only to the term in brackets immediately following it.

The last equation for λ_i^G can be rearranged by adding $(1 - 1)$

$$\lambda_i^G = \sum_{m=0}^{n-1} \lambda_i^{-2} \left(1 - (1 - \sigma_m \lambda_i^2) \right) \prod_{j=0}^{m-1} (1 - \sigma_j \lambda_i^2) \lambda_i$$

$$= \lambda_i^{-2} \sum_{m=0}^{n-1} \left(\prod_{j=0}^{m-1} (1 - \sigma_j \lambda_i^2) - \prod_{j=0}^{m} (1 - \sigma_j \lambda_i^2) \right) \lambda_i .$$

Most terms cancel each other out, leaving only

$$\lambda_i^G = \frac{1 - \prod_{j=0}^{n-1}(1 - \sigma_j \lambda_i^2)}{\lambda_i}.$$

This result is very similar to the previous one in the Comer and Clayton analysis for λ_i^G without scaling factors.

For the inversion, the objective is to have $\lambda_i^G = \frac{1}{\lambda_i}$ over the desired eigenvalue range, $\lambda_{min} < \lambda_i < \lambda_{max}$, and some smooth transition to $\lambda_i^G = 0$ for very small eigenvalues, $\lambda_i << \lambda_{min}$. This is best achieved by minimizing

$$\prod_{j=0}^{n-1}(1 - \sigma_j \lambda_i^2) \qquad \text{for } \lambda_{min} < \lambda_i < \lambda_{max}.$$

The unmodified Dines and Lytle formula uses no scaling ($\sigma_j = 1$) that inverts larger eigenvalues faster than small ones. Unfortunately, the 230 iterations necessary to invert an eigenvalue of 0.1 to an error of 10% invert the eigenvalue of 0.5 to an error of 10^{-27}%, which is overkill. We can afford to trade off some of the accuracy of the larger eigenvalue for improving the accuracy of the lower ones. Olson (1986), by relating the polynomial above that we desire to minimize to Chebyshev's polynomial, shows how to determine the optimal acceleration factors, σ_j, so that the inversion

error

is approximately even over the predetermined eigenvalue range. This inversion error will be the minimum attainable for the given number of iterations and eigenvalue range.

The acceleration factors from Olson (1986) are:

$$\sigma_j = \frac{2}{\cos\left(\frac{(2j+1)\pi}{2n}\right)\cdot(\lambda_{max}^2-\lambda_{min}^2) + (\lambda_{max}^2+\lambda_{min}^2)}$$

$$\text{for } j = 0, 1, 2, \cdots, n-1,$$

where

n = the number of iterations to perform, and

$\lambda_{min} < \lambda < \lambda_{max}$ = the eigenvalue range to invert over.

Generally, λ_{max} should be 1.0 for the Dines and Lytle formula.

The maximum error over this eigenvalue range will be:

$$Error = 2^{-(n-1)} \prod_{i=0}^{n-1} \frac{\lambda_{max}^2 - \lambda_{min}^2}{2}\sigma_i.$$

Since the σ_i's change with the number of iterations, this equation cannot be inverted to give the number of iterations necessary to achieve a certain accuracy. Instead, one must simply apply this forward error equation for successively increasing the number of iterations until desired accuracy is reached.

Using these acceleration factors with the Dines and Lytle back-projection, the number of iterations necessary to achieve a 99% inversion over an eigenvalue range of (1.0-0.3) is 8 instead of 25 for a 90% inversion without the scale factors. An eigenvalue of (1.0-0.1) is 24 instead of 230, and an eigenvalue of (1.0-0.05) is 46 instead of 960. The number of iterations necessary for inversion to smaller eigenvalue is now proportional only to the inverse of the eigenvalue instead of the square of the inverse as before. The number of iterations necessary for inversion to greater accuracy goes by the square root of the accuracy.

In general, use of the Chebyshev acceleration factors reduces the number of iterations to about the square root of the number necessary without them. Inversion to small eigenvalue is now feasible.

With acceleration factors, however, one cannot see the inversion improve with each successive iteration. The iterations must be continued to completion or abandoned.

Common methods for determining the range of eigenvalues to be inverted are based on an estimate of expected model variance and estimated data noise. These parameters are very difficult to determine and involve subjective decisions-- the processor is urged not to choose these parameters arbitrarily! Test inversions of the data can indicate the bearing data noise has on a particular geologic objective. Modeling

can indicate expected model variance of the objective. Chapter 5's first data example demonstrates how the eigenvalue range must be chosen carefully and how the eigenvalue range inverted can change significantly with the objective.

When inverting over a wide eigenvalue range, say $0.1 < \lambda < 1.0$, or to high accuracy, computer numerical accuracy affects the result when applying acceleration factors in sequential order. Olson (1986) presents an ordering scheme that has been successfully tested here.

For an original order of acceleration factors from smallest to largest of

$$(1, 2, 3, 4, 5, 6, 7, 8) ,$$

the order must be rearranged in the following manner to avoid numerical round-off error:

$$(7, 5, 3, 1) , \ (2, 4, 6, 8)$$

$$(3, 7) , \ (5, 1) , \ (6, 2) , \ (4, 8) .$$

This ordering sequence requires the number of iterations to be a power of 2.

2.11 Discussion of Iterative Matrix Inversion and its Relationship to the Conjugate Gradient Method

The Dines and Lytle back-projection scheme without acceleration factors is merely a form of Richardson's method (Olson, 1986) for solving the least-squares normal equations. Richardson's method, in turn, is a form of the steepest descent iterative method for locating the bottom of a quadratic, multi-dimensional surface that represents error between data and model. The steepest descent method is generally taken to be the worst of many possible iterative methods for solving least-squares normal equations. The present, most popular method for iterative matrix inversion is probably the conjugate gradient method (Scales, 1987).

However, the decision to use Richardson's method with Chebyshev acceleration factors is deliberate for several reasons. First, the application of the Chebyshev acceleration factors makes Richardson's method competitive with the alternative techniques for very large model spaces. Second, the scheme produces a greater likelihood inverse (Aki & Richards, 1980) than conjugate gradient, by using the eigenvalue range as its basis and not data variance. Last, and most important, the scheme used here allows control over the inversion and enables direct comparisons with synthetics. However, Chebyshev acceleration factors require the maximum eigenvalue and that the number of iterations be known before starting them,

something not always available.

Minimizing data variance is the objective of conjugate gradient iteration, which it does very well. However, in its quest to reduce data variance in the minimum number of iterations, conjugate gradient will not bother to invert eigenvalue ranges with little corresponding energy in the data. These eigenvalues may correspond to the better-resolved components of the model, however. Iterative methods are efficient enough so that we can perform a few additional iterations to invert these eigenvalues.

An additional conjugate gradient iteration may start to invert the smaller eigenvalues, or may invert the partially-inverted larger eigenvalues more accurately. In some cases, inversion below a certain eigenvalue is unjustified based on the signal-to-noise level in the data. Moreover, an objective for the inversion may only exist above a certain eigenvalue. One may want to accurately invert the eigenvalues above a certain point, but not below. Conjugate gradient fails to allow this control.

Furthermore, one frequently wants to compare inversions of synthetic data with rear data directly. This cannot be done with conjugate gradient because it is affected by data components.

A common theme in all of these issues is that we desire an inversion scheme defined from an eigenvalue perspective rather than one based on variance reduction. Richardson's iteration with Chebyshev acceleration parameters is an efficient method defined in the eigenvalue perspective.

Chebyshev factors, unfortunately, do not allow the luxury of starting inversions with little knowledge of the problem's characteristics. In addition, one cannot to stop the method when convenient. When one doesn't know which range of eigenvalue to invert over, using Chebyshev scale factors can be cumbersome. After starting a series of iterations, one must continue through completion to analyze the results. If the results are unsatisfactory and another range of eigenvalues must be inverted, one has to start over. Backtracking or continuing is impossible with the Chebyshev factors, unlike with conjugate gradient.

In many applications such as the tomographic one here, inversion should not be performed without familiarity of the special characteristics of the intended application. This familiarity is especially important for proper interpretation of the result. Several synthetics inversions should be performed as well as several data inversions with different parameters. Chapters 3 and 4 demonstrate how the resolution

of certain features can be related to certain eigenvalue ranges. The North Slope data example of Chapter 5 presents way in which control of the eigenvalues can be useful for inversion.

Lacking knowledge of the maximum eigenvalue, it is impossible to choose Chebyshev scale factors. Data and model weights imposed by the Dines and Lytle back-projection formula ensure that the maximum eigenvalue will be close to but below 1.0. In other situations where the maximum eigenvalue cannot be controlled through weighting, one can generally produce an estimate of the maximum eigenvalue by performing short test inversions of random noise. If the resulting iterations diverge, the maximum eigenvalue is greater than estimated. A lower one should be attempted.

2.12 Including Constraints in Dines and Lytle Back Projection

Chapter 3 presents numerous examples of how inversion artifacts result from limitations in the reflection seismology geometry. Frequently, these artifacts suggest structures that are geologically unlikely. The artifacts can be discounted using either plain common sense or knowledge of the geologic characteristics of a region. For instance, the bizarre velocity variations that occasionally occur at the edges of the model are clearly artifacts from inhomogeneous ray coverage. Small-scale velocity variations that occur just above a

reflector are probably the result of small-scale variations in the reflector instead. Location of velocity variations can be controlled from knowledge of which geologic units are less likely to be homogeneous. To remove the artifacts, geologic information must be included into an inversion quantitatively through the use of constraints.

Constraints can be variously defined: Two of the more general formats are those of weights and penalty functions. Weights and penalty functions are related to each other in that their effect of can generally also be produced by the other. Their difference lies mainly in the perspective from which the constraint is easier to formulate. Both can be implemented in the Dines and Lytle formula.

The earlier program example is altered to include the Chebyshev acceleration factor and several methods for constraining the inversion:

```
main()
{

    read( Δt vector )
    read( Δt_weight vector )
    read( Δs_weight vector )

    /*  set Δs vector equal to 0    */
    for (l =  1 to number of cells)
        Δs(l) =  0

    for (i= 1 to number of iterations)
    {
```

```
rewind(ray path file)

for (k= 1 to number of rays)
{
    /*  read ray paths from disk    */
    read(cell_positions for ray)
    read(path_lengths for ray)

    if (i= 1)
        total_path_length(k)= 0

    for (j =  1 to number of cells touched by ray number k)
    {
        /* Compute forward problem: Δt^(i) = Δt^(0) – LΔs^(i)   */
        Δt(k) =  Δt^(0)(k) - path_lengths(j) · Δs(cell_position(j))

        if (i= 1)
            /* Compute total_path_length(k)  */
            total_path_length(k)+ =
                path_lengths(j) · Δs_weight(cell_position(j))
    }

    for (j =  1 to number of cells touched by ray number k)
    {
        /* perform back-projection  L^T D Δt^(i)      */
        numerator(cell_positions(j)) + =
                            Δs_weight(cell_position(j))·path_lengths(j)
                            Δt(k)·Δt_weight(k)/total_path_length(k)

        /* accumulate S matrix       */
        denominator(cell_positions(j)) + =
                            path_lengths(j) · Δt_weight(k)·
                            Δs_weight(cell_position(j))
    } /*  end j loop over number of cells touched by ray k  */
} /* end k loop over the rays  */

/*  Apply F1() filter to numerator and denominator  */
numerator =  F1(numerator)
denominator =  F1(denominator)
for (l =  1 to number of cells)
    Δs_temp(l) =  numerator(l) / (denominator(l) + ε)

/*  Apply F2() filter   */
```

```
        Δs_temp= F2(Δs_temp)

        /* filter running total */
        Δs= Δs − σi·F3(Δs)
        /* It will be shown later that F3 is a penalty function. */

        /* Apply Chebyshev scaling factor, σi, to back-projection result
        before adding to running total */
        Δs+ = σi·Δs_temp

    } /* end i loop over number of iterations */

    write(Δs vector)

} /* end program */ .
```

Additional data weights, **Δt_weight**, and additional model weights, **Δs_weight**, do not alter the maximum eigenvalue of the problem, keeping it at 1.0. This fact can be confirmed by considering the Dines and Lytle formula from the averaging perspective

$$\mathbf{S'L}^T\mathbf{D'}\Delta\mathbf{t} = \frac{\sum_k \omega_j^s \cdot l_{kj} \cdot w_k^t \cdot \frac{\Delta t_k}{P_k}}{\sum_k \omega_j^s \cdot w_k^t \cdot l_{kj} + \varepsilon} ,$$

where

w_k^t = the weights applied to the data points, $\Delta\mathbf{t}_k$;

ω_j^s = the weights applied to the model cells, $\Delta\mathbf{s}_j$; and

$\mathbf{S'}$ & $\mathbf{D'}$ = the modified model and data weights.

Having a $w_k^t = 2$ is identical to including the same data point twice. Changing ω_j^s is identical to changing the path length of each ray in the cell and the corresponding total path length for each ray. With shorter

path lengths, the cell is represented less, as if it were of smaller size. Clearly, the weights do not affect the structure or stability of this averaging formula: the eigenvalues of the problem remain between 0.0 & 1.0. Off-diagonal model weighting is considered later with the filter $\mathbf{F}_2()$.

One potential use of data weighting is to implement a type of pseudo-norm1 objective function with this norm2 inversion technique (Scales et al., 1987). This variation is implemented by performing repeated inversions, each using data weights proportional to the inverse of the starting travel time deviations ($w_k^t = \frac{1}{\Delta t_k^{(0)}}$).

The algorithm of the program above can be represented with the matrix equation

$$\Delta \mathbf{s}^{(n)} = (\mathbf{I} - \sigma_n \cdot \mathbf{F}_3)\Delta \mathbf{s}^{(n-1)} + \sigma_n \cdot \mathbf{F}_2 \{\mathbf{F}_1 \mathbf{S}^{\leftarrow 1}\}^{-1} \mathbf{F}_1 \mathbf{L}^T \mathbf{D}' \Delta \mathbf{t}^{(n-1)},$$
$$\text{where } \Delta \mathbf{t}^{(n-1)} = \Delta \mathbf{t}^{(0)} - \mathbf{L}\Delta \mathbf{s}^{(n-1)}.$$

The filters, $\mathbf{F}_i$, have been recast as matrices. They can be implemented in the form of a subroutine that performs complex constraints. Input to these subroutines that defines the constraints can be developed on a graphics work station, where the operator specifies the constraints using a picture of the model with an overlay of the previous inversion result.

$\{\mathbf{F}_1 \mathbf{S}^{\leftarrow 1}\}$ is a strange beast that defies matrix notation. It is

meant to denote the $\mathbf{F}_1$ filter operating on the diagonal elements of diagonal matrix $\mathbf{S}^{\leftarrow 1}$, which produces a diagonal matrix result. Note that $\{\mathbf{F}_1\mathbf{S}^{\leftarrow 1}\}^{-1} \neq (\mathbf{F}_1\mathbf{S}^{\leftarrow 1})^{-1}$.

The $\mathbf{F}_1$ matrix is an operator that changes the cell configuration. Consider the $\mathbf{F}_1$ operator adding the values of two neighboring cells and replacing each by the result. Performing this operation for the **numerator** and the **denominator** of the back-projection formula combines two cells into one. In this way, a horizon can be defined to have constant slowness by treating it all as one cell. Similarly, horizontal variations can be disallowed by defining all the cells at the same depth to have identical values.

Another choice for the $\mathbf{F}_1$ operator is for it to be a two-dimensional Gaussian low-pass filter in the wavenumber domain. This operator would tend to smear the values of one cell into its neighbors, as well as effectively reduce high wavenumber variations in the model. This filter can be used to avoid the effects of overparameterizing a model when using very small cell sizes to avoid discretization effects. This type of filter for $\mathbf{F}_1$ has been used for the model inversions in Chapter 3, and for the data inversions of Chapter 5. The effect of this filter upon the eigenvalues and eigenvectors of the problem are addressed by Chapter 4.

The $\mathbf{F}_2$ operator is used to adjust both the diagonal and off-diagonal model weights. The operator can be used to increase the weight at the edges in an attempt to reduce edge effects, or can be used to restrict slowness variations near a borehole where velocity is accurately known. The operator can also be used to set the slowness variations of some blocks to zero, effectively taking them out of the inversion.

The $\mathbf{F}_2$ operator can be used for diagonal weighting to relate two or more cells to one another. For example, the $\mathbf{F}_2$ operator can be used to define two neighboring cells to have identical slowness.

To ensure the stability of the inversion, the back-projection operator acting on $\Delta\mathbf{t}^{(n)}$ must have eigenvalues between 0.0 and 1.0. Since $\mathbf{S}'^{1/2}\mathbf{L}\mathbf{D}'^{1/2}$ have eigenvalues between 0.0 & 1.0, the $\mathbf{F}_1$ & $\mathbf{F}_2$ filters must also have eigenvalues between 0.0 and 1.0. This criterion is upheld when the filters have a band pass or averaging structure that do not introduce, but just remove energy from the system.

The $\mathbf{F}_3$ filter acts as a penalty function, which can be seen with some matrix manipulation. The algorithm of the above program is written as

$$\Delta\mathbf{s}^{(n)} = (\mathbf{I} - \sigma_n \cdot \mathbf{F}_3)\Delta\mathbf{s}^{(n-1)} + \sigma_n \cdot \mathbf{L}^{\mathbf{b}}(\Delta\mathbf{t}^{(0)} - \mathbf{L}\Delta\mathbf{s}^{(n-1)}),$$

where

$\mathbf{L}^{\mathbf{b}} = \mathbf{S}''\mathbf{L}^T\mathbf{D}'$, the back-projection operator, and

$\mathbf{S}'' = \mathbf{F}_2\{\mathbf{F}_1\mathbf{S}^{\leftarrow 1}\}^{-1}\mathbf{F}_1$.

Reducing the indices by one and rearranging produces

$$\Delta\mathbf{s}^{(n)} = \sigma_n\mathbf{L}^{\mathbf{b}}\Delta\mathbf{t}^{(0)} + \left(\mathbf{I} - \sigma_n\cdot\mathbf{F}_3 - \sigma_n\cdot\mathbf{L}^{\mathbf{b}}\mathbf{L}\right)\cdot\Delta\mathbf{s}^{n-1}.$$

Substituting in recursively for $\Delta\mathbf{s}^{n-1}$ produces

$$\Delta\mathbf{s}^{(n)} = \sigma_n\mathbf{L}^{\mathbf{b}}\Delta\mathbf{t}^{(0)} + \left(\mathbf{I} - \sigma_n\cdot(\mathbf{F}_3+\mathbf{L}^{\mathbf{b}}\mathbf{L})\right)\cdot\sigma_{(n-1)}\mathbf{L}^{\mathbf{b}}\mathbf{L}\Delta\mathbf{t}^{(0)} + \left(\mathbf{I} - \sigma_n\cdot(\mathbf{F}_3+\mathbf{L}^{\mathbf{b}}\mathbf{L})\right)\cdot\left(\mathbf{I} - \sigma_{(n-1)}\cdot(\mathbf{F}_3+\mathbf{L}^{\mathbf{b}}\mathbf{L})\right)\cdot\Delta\mathbf{s}^{(0)},$$

or,

$$\Delta\mathbf{s}^{(n)} = \sum_{l=0}^{n}\prod_{j=l+1}^{n}\left(\mathbf{I} - \sigma_j\cdot(\mathbf{F}_3 + \mathbf{L}^{\mathbf{b}}\mathbf{L})\right)\cdot\sigma_l\mathbf{L}^{\mathbf{b}}\Delta t^{(0)} + \prod_{l=0}^{n}\left(\mathbf{I} - \sigma_j(\mathbf{F}_3 + \mathbf{L}^{\mathbf{b}}\mathbf{L})\right)\cdot\Delta\mathbf{s}^{(0)}.$$

$\Delta s^{(0)}$ is defined to equal zero, eliminating the second product. By performing a similar substitution to that of the Comer and Clayton analysis, $\mathbf{x}= \mathbf{S}^{-1/2}\Delta\mathbf{s}$, $\mathbf{b}= \mathbf{D}^{1/2}\Delta\mathbf{t}$, $\mathbf{A}= \mathbf{D}^{1/2}\mathbf{L}\mathbf{S}^{1/2}$, and $\mathbf{R}= \mathbf{S}''^{\leftarrow 1/2}\mathbf{F}_3\mathbf{S}''^{1/2}$, we produce:

$$\Delta\mathbf{x}^{(n)} = \sum_{l=0}^{n}\prod_{j=l+1}^{n}\left(\mathbf{I} - \sigma_j\cdot(\mathbf{A}^T\mathbf{A} + \mathbf{R})\right)\sigma_l\mathbf{A}^T\Delta\mathbf{b}^{(0)},$$

which converges to

$$\mathbf{x}^{(\infty)} = \left(\mathbf{A}^T\mathbf{A}+\mathbf{R}\right)^{-1}\mathbf{A}^T\mathbf{b},$$

which is the least-squares solution of the forward problem, $\Delta \mathbf{x} = \mathbf{A}\Delta \mathbf{b}$, with a penalty function, $\mathbf{R}$.

The penalty function, $\mathbf{R}$, changes the objective function that least-squares inversion seeks to minimize to

$$Error_{data} = (\Delta \mathbf{b} - \mathbf{A}\Delta \mathbf{x})^{\mathbf{T}}(\Delta \mathbf{b} - \mathbf{A}\Delta \mathbf{x}) + \Delta \mathbf{x}^{T} \mathbf{R} \Delta \mathbf{x}.$$

We need to determine the maximum eigenvalue of the matrix $(\mathbf{A}^{T}\mathbf{A} + \mathbf{R})$ to ensure convergence of the iteration formula with the Chebyshev acceleration factors. The minimum eigenvalue of the matrix must be non-negative to ensure stability of the iteration formula. An estimate of these eigenvalues can be made as follows:

$$\lambda_{max} \leq \lambda_{max}^{\mathbf{A}^{T}\mathbf{A}} + \lambda_{max}^{\mathbf{F}_3}$$
$$\lambda_{min} \geq \lambda_{min}^{\mathbf{A}^{T}\mathbf{A}} + \lambda_{min}^{\mathbf{F}_3},$$

where

$\lambda^{\mathbf{A}^{T}\mathbf{A}}$= the eigenvalues of $\mathbf{A}^{T}\mathbf{A}$, and

$\lambda^{\mathbf{F}_3}$= the eigenvalues of $\mathbf{F}_3$.

The eigenvalue range for $\mathbf{F}_3$ is identical to that for $\lambda^{\mathbf{R}}$. Since we know that $\lambda_{min}^{\mathbf{A}^{T}\mathbf{A}} = 0$ & $\lambda_{max}^{\mathbf{A}^{T}\mathbf{A}} = 1.0$,

$$\lambda_{max} = 1.0 + \lambda_{max}^{\mathbf{F}_3}$$
$$\lambda_{min} = \lambda_{min}^{\mathbf{F}_3}.$$

The eigenvalues of the filter $\mathbf{F}_3$ cannot be less than 0.0 to keep $\lambda_{min} > 0.0$ and to ensure the stability of the iterations. The greater

number of large eigenvalues of F_3, the stronger the penalty function **R** is.

A λ_{max} greater than 1.0 can be easily accommodated with the Chebyshev acceleration factors. But, this requires that the maximum eigenvalue of F_3 be known. If the operator F_3 is a high-pass or similar filter, its eigenvalues are between 0.0 and 1.0, resulting in final eigenvalues of

$$\lambda_{max} \leq 2, \qquad \lambda_{min} = 0.$$

The min-max constraint is a very desirable one to implement. This constraint limits the slowness from varying beyond certain reasonable limits, thereby stabilizing wild fluctuations that can occur. Such a constraint is appropriate when concrete information exists about typical rock velocities in a region, something frequently attained from a borehole. Unfortunately, there is no simple direct way to implement the constraint with Dines and Lytle back-projection.

2.13 Improving Non-linear Errors by Updating Incorrect Ray Paths

The inversion approach used here does not analytically take into account that changing velocity changes ray paths. The linear relationship between data and model derived from the ray paths of the reference model is only an approximation of the complicated true non-

linear relationship. A solution based on this approximated linear relationship contains errors, called non-linear errors.

Accuracy of the linear system used for inversion is dependent upon the accuracy of the ray paths through the reference model to the true ray paths. For some reference models, either very accurate to the true model or containing only broad-scale differences, ray paths are an excellent approximation and the inversion is barely compromised. In other cases, where ray paths differ significantly, inversion can be severely affected: there is little point to producing an accurate inversion of the linear system by carrying it out to small eigenvalue. Non-linear errors for many different models are analyzed in Chapter 3.

So as to improve non-linear errors, one must improve the ray paths. By assuming that the result of the latest inversion is closer to the correct model than the reference model, the ray paths can be improved by re-tracing them through the inversion.

The result of the previous inversion can generally be improved upon before it is used for re-tracing the rays. Noticeable artifacts should be removed. The model can be adjusted to reflect regional geologic characteristics. Items that significantly affect ray paths and may be artifacts should be carefully considered for removal. Moreover, reflector depths can generally be improved through migration.

Inversion determines reflector depths from data through the use of ray paths. This relationship is analogous to using ray-tracing for migration, an unpopular procedure rarely used since it has a tendency to create high frequency artifacts. These false small-scale reflector deviations can affect the ray path positions significantly. For instance, a small bump can move rays reflecting from nearby locations onto the bump. A host of waveform migration procedures exist that are stabler than ray-tracing for relating reflector position to the velocity field. Thus, the recommended procedure is not to use reflector positions from the inversion and instead to determine reflector positions by performing a waveform migration through the velocity field of the inverted model. This recommended procedure is called iterative tomographic and migration reconstruction. A flow chart of iterative tomography and migration is in Figure 2.7.

Figure 2.8 depicts the general approach of reducing non-linear effects by improving ray paths. The data, which in our case are travel times, are a non-linear function, ($\mathbf{d}=\mathbf{F}(\mathbf{m})$), of the model. In general, this function is too complicated to be invertible. Although we cannot invert the function, we can determine its slope at a given point. Using this slope, we can perform Newtonian iteration to the desire solution.

The point at which we choose to first linearize the function,

m_o, is our best guess of the desired solution and compromises the reference model. The slope of the function, **F**(m), is determined from ray-tracing. The slope predicts a new point, m_1, based on the assumption of linearity. This point will not be the correct result because of the curvature of the function, **F**(). However, if the function is well-behaved and if our starting point, m_o, was close enough to the correct result, we will eventually converge by performing repeated iterations.

This approach appears well-behaved for one dimension, but it is significantly more complicated for multi-dimensions. The two-dimensional case can be described using the analogy of trying to find the lowest point in a valley being blind, but able to jump great distances. Each jump corresponds to one non-linear iteration. Without additional knowledge, the best direction to jump seems to be the direction of the maximum gradient at one's present position. Distance to jump is determined by estimating the location of the low point from the curvature and slope of the valley at one's present position. Unfortunately, one cannot determine the optimal distance to jump except through repeated forward modeling, an expensive procedure. If the valley is smooth, one will find the lowest point quickly. Any topography along the way will cause problems, however, such as sending one off in a wrong direction. One could also be fooled by

finding a local minimum. Without the ability to see the rest of the valley, one would assume that the local minimum is the valley low point and end the search prematurely.

2.14 Conclusion

Dines and Lytle Back Projection with Chebyshev acceleration factors is an efficient and effective iterative inversion technique. Good control can be exercised over the inversion, constraints can be included, and the method is simple to program. Despite problems associated with a cell-based approach and large matrix sizes, travel time inversion can be implemented to reflection seismology without serious compromises.

However, effective use of this inversion technique involves more than computer implementation. Execution of the method and interpretation of the results require knowledge of its behavior, particularly its artifacts, which is discussed in Chapter 3. Chapter 4 examines questions of its resolution.

Chapter 3

A Modeling Analysis of Ray Trace Tomography Applied to Reflection Surveys

3.1 Abstract

Because of inherent problems with the seismic reflection experiment, tomographic inversion has potential of creating serious artifacts. Problems identified from synthetic tests are: **1)** the limited angular ray coverage smearing images, **2)** edges affecting the central part of the survey, **3)** the ambiguity between reflector depth and velocity, and **4)** errors from using approximate rays traced through a "best guess" model.However, these problems appear to be surmountable. Migration is insensitive to some artifacts of tomography. Modeling demonstrates that the iterative application of tomography and migration is able to correct some of the problems of an inaccurate starting model. The remaining artifacts can generally be controlled through the use of simple constraints. Numerous examples of artifact generation and some methods for their control are presented in this chapter.

3.2 Introduction

Reflection seismology geometry is a far less than perfect for the application of tomography. Shortcomings of the data acquisition method, summarized below, create several types of artifacts in the resulting image that may distort the velocity image enough that it bears little resemblance to the actual structure. In most cases, the image still contains valuable information, however. Isolating the valuable information requires identifying the useful parts, devising methods for distinguishing it from the artifacts, and interpreting the results. This process requires an understanding of how artifacts are caused and how constraints can be used to control them.

Synthetic modeling, the only method of analyzing many of these artifact generation methods, is the focus of this chapter. A theoretical analysis of the linear problem using Singular Value Decomposition is presented in Chapter 4.

Many of the artifacts presented here are not unique to Ray Trace Tomography. Ray tracing is an adequate modeling technique for broad velocity variations. Waveform transmission techniques will have similar characteristics as Ray Trace Tomography for broad velocity variations. Ray Trace Tomography is a comparitively efficient method for forward modeling complex structure. The method can be used to address issues of transmission tomography unfeasible to address with other methods. For example, most methods are too expensive to address how well the repeated application of a linear inversion solves the true complicated non-linear problem.

Methods of artifact generation addressed in this chapter are: 1) smearing from limited angular ray coverage, 2) non-linear effects caused by an incorrect reference velocity field, 3) poor resolution of velocity-reflector depth ambiguity, 4) non-linear effects caused by incorrect reference reflector position, and 5) distortion from inhomogeneous ray coverage at the edges of the ray coverage. Control of these artifacts through several inversion constraints and application of iterative tomography and migration are analyzed.

Because of the limited nature of modeling and the large variety of geologic characteristics, the results are not quantitative and the approaches suggested are not universal. This chapter is intended to provide the reader only with a conceptual understanding of the processes that distort an inversion. Models used here generally bear a relationship to a geological structure, but this chapter is not intended to be a catalog of geologic models. For each individual data case, the tomographer will have to identify artifacts, judge their seriousness, and formulate individual solutions.

It is emphasized that the velocity inversion itself is meant not for interpretation, but rather as input for migration. Migration, after all, is the result that is finally interpreted. Measure of the success of tomography is the improvement of the migration through inverted velocity over a migration through a conventional velocity model.

3.3 Flaws of the Reflection Seismology Experiment for the Application of Tomography

A comparison of the data acquisition method with that of CAT scanners in Figure 3.1 reveals many of the shortcomings of a surface reflection survey for transmission tomography:

1) Wavelength of the signal used for tomography is the approximate minimum length scale that can be resolved. X-rays of CAT scanners are of very small wavelength compared to the image they sample, resolution is therefore unaffected. However, the wavelength of the seismic signal is generally on the order of 100-400 feet, significant size compared to potential images.

2) CAT scanners can rotate around the object, producing a full angular ray coverage of information. Reflection seismology, however, is restricted to having sources and receivers on the earth's surface, producing a ray coverage lacking in horizontal rays. As a result, the image is smeared vertically.

3) X-rays of CAT scanners travel in straight paths, producing a uniform ray coverage. However, ray bending by velocity variations and reflector structure in the earth cause seismic ray coverage to be non-uniform. Non-uniform ray coverage requires the use of inversion theory.

4) Ray paths of X-rays in CAT scanners are largely unaffected by the images they sample. Seismic ray paths, however, are affected by the very image that tomography is trying to resolve. Approximate rays are used for the inversion, which causes errors.

5) CAT scanner objects can be placed only in the region of complete ray coverage. This luxury does not exist in reflection seismology. Velocity variations may exist at the edges of a reflection survey where ray coverage is incomplete. Velocity variations at the edge will be poorly inverted and may affect an image toward the central area of a survey.

6) Seismic rays are affected not only by velocity, but also by a reflector, which complicates the tomographic formulation and potential resolution.

7) Data from reflection seismograms used for applying tomography are the travel times picked from the reflected waveforms. These waveforms may be corrupted by other arrivals overlapping the one of interest. As a result, travel times may be difficult to pick.

8) The reflector further complicates the formulation. The reflector structure is also unknown which increases the errors of the ray path approximations. Moreover, reflector depths may be ambiguous with velocity variations.

9) The formulation of the problem does not take into account certain physical processes that will affect the data: anisotropy, 3-D effects, and attenuation. Moreover, the formulation approximates wave propagation with ray tracing.

3.4 Dependence of Modeling Results on Inversion Technique Used

Of the many available iterative methods for solving the linear system of tomography, none is yet generally accepted by the scientific community as most suitable for seismic reflection seismology. Results using the SIRT technique of Dines and Lytle (1979), described in Chapter 2, are expected to be to valid for most of the other techniques, however. Since perfect data is used and iterations are generally continued to small eigenvalue, the synthetic examples are essentially analyzing the model null space of the linear system, which is independent of the norm of the objective function used ro of the data weights.

Null space is dependent upon the weights applied to the model space. Ray coverage is generous and uniform in the models run here and for a reflection survey. Therefore, weights on the model space should be uniform for any inversion technique, which they are for Dines and Lytle SIRT.

The Dines and Lytle SIRT used here weights rays by the inverse of the square root of the path lengths. Justification for this de-weighting is presented in Chapter 2. For a reflection survey with a generous maximum ray angle of 45^{o},

the far offset rays would have a weight of 84% of the near offset rays, an insignificant amount.

To curb the effects of noise, iterative techniques must be stopped on the path to convergence before effective convergence is reached. Since the path to convergence differs amoung the various techniques, results will be dependent upon the technique used. One of the reasons the Dines and Lytle SIRT inversion technique is used here is because its incomplete inversion can be carefully controlled and succinctly described by the eigenvalue range inverted, more so than that for conjugate gradient (Stork, 1988).

As shown in Chapter 2, the Dines and Lytle SIRT technique uses a Norm 2 objective function. This conventional approach is widely used; however, it appears that a Norm 1 basis may be more desirable for the noise expected to be encountered in a reflection survey (Scales et al, 1987). Scales et al shows how a Norm 1 objective function can be implemented using data weights of an iterative norm 2 inversion scheme.

The inversion procedure is dependent on errors introduced by ray tracing through potentially complex velocity fields. The ray-tracing program used here, that of Langan et al (1985), described in Chapter 2, is a flexible one; it accurately represents and traces almost any structure where ray paths are meaningful. The method is quite robust in finding the ray paths between source and receiver. As a ray-based method, however, it has inherent problems with non-optical arrivals such as refractions and diffractions. In some cases of complex structure, it cannot find the ray path between a source and receiver.

Travel time picking problems are avoided by computing travel times in the true model using ray tracing rather than full waveform propagation and subsequent travel time picking. When duplicate ray paths exist between a source and receiver off a given reflector, the path of shortest travel time is used. This first arrival is the easiest to pick on a seismogram of direct ray paths, but may be difficult to pick on reflection seismograms where other reflections and direct arrivals overlap one another. Since the first arrival is generally also the lowest amplitude arrival, it may be especially difficult to pick. It might have been more practical to use the path of largest amplitude rather than the path of shortest travel time.

Unless otherwise noted, the maximum ray angle used for the inversion is 45°; the models have square cells 150 feet on a side. Using this cell size produces a model with about 35 cells in a vertical column between the surface and the reflector, and about 200-400 cells in a horizontal column. Thus, the number of model parameters is generally around 10,000. High frequency velocity variations in the inversion are damped. All models are run with a dense ray set of several shots and receivers per cell so that the rays can be considered an effective continuum.

3.5 Smearing from Limited Angular Ray Coverage

It is a well-known phenomenon that a limited angular ray coverage smears images along the ray paths. An example of this process is described with Figure 3.2. In the figure, each ray path travels the same distance in each of the two

velocity variation strips shown. Thus, if the velocity variations are equal in amplitude, they have an identical effect on the travel times of the ray paths. An inversion of the travel times is unable to resolve between which of the two strips or any similar velocity variation caused the travel time effect. Without horizontal rays, there is no way of determining the depth of the anomaly. An unbiased inversion will smear the anomaly over the entire depth range down to the reflector. Velocity variations that have a finite horizontal width will endure less vertical smearing.

Examples of the smearing of limited angular ray coverage of various structures is shown in Figures 3.4, 3.5b, 3.13b & 3.21b. For these examples, there are no ray path errors since straight ray paths were used for both the forward problem and the inversion.

Inversion of the "**OIL**" and "**GAS**" models in Figures 3.5b and 3.13b shows that the vertical aspects of the letters have been well-resolved. However, the horizontal aspects, particularly the bar of the "**A**" and "**G**," have been smeared so as to be virtually unrecognizable. Smearing of the horizontal aspects near the top or bottom of the model, such as upper and lower sections of the "**O**," has been "blocked" by the reflector or the surface to create a "build-up" of smeared image. The word "**OIL**" contains more vertical features than the word "**GAS**," and thus is inverted better. Vertical smearing of the horizontal blocks in Figure 3.21b is generally diamond-shaped, with the slope of the edges of the diamond controlled by the maximum angular ray coverage in the data.

For straight rays of uniform coverage, the smearing characteristic of limited angular ray coverage can be demonstrated mathematically using the central slice theorem of Radon transforms (Kjartansson, 1979). A Radon transform of a two-dimensional image is a slant stack over all angles. Straight rays of uniform coverage in a reflection survey will perform this slant stack over only a limited range of angles. The central slice theorem shows that the resolution of a slant stack over a limited range corresponds to resolving only that portion of the wavenumber domain shown by Figure 3.3. Resolution of the horizontal variations would correspond in the wavenumber domain to components on the horizontal axis, which lies in the middle of the resolved region. Resolution of the vertical variations, however, lies in the vertical wavenumber axis, which lies in the unresolved region.

An example of removing the wavenumber components that lie in the unresolved wavenumber region of an image is shown Figure 7.13 on Page 127 of Einar Kjartansson's thesis (1979). His figure appears as Figure 3.4 here, and can be compared with the tomographic inversion of a similar structure in Figure 3.5b. The results should be identical, and appear to be.

Removal of the limited angular ray coverage smearing requires filling in that portion of the wavenumber domain about which we have no information. Any method to remove the smearing would increase the energy in the model and might not be robust. However, the fact that geologic structure tends to be horizontal suggests that the collapsing of the vertical smearing of tomography would be geologically justifiable. Another constraint besides the minimum

energy criterion, like minimum entropy, should be considered for determination of the null space. This possibility is not investigated here.

These results show that smearing from limited angular ray coverage significantly distorts images. However, migration through the inverted velocity is the final result upon which to judge the success of the method, not intermediate result of the inverted velocity field. The vertical smearing from the limited angular ray coverage is not considered to be of serious consequence, since migration is insensitive to the smearing. This insensitivity results from migration being essentially a vertical integration process upon the velocity.

Migrations through the initial and smeared velocity fields in Figures 3.5b, 3.13b, & 3.21b of the **GAS**, **OIL**, and horizontal block models are shown in Figures 3.9, 3.17, & 3.28. The migrations through the smeared images are virtually identical to those through the original images. A comparison of the migration through the smeared image to that through the constant background velocity shows a dramatic improvement.

3.6 Non-linear Effects of Velocity

Non-linear effects are caused by the inaccuracies of the system of linear equations used in the inversion to compute the slowness model from the travel times. The correct linear equations cannot be determined, since they are defined by the ray paths through the correct velocity and reflector model which, as the objective of the inversion, are unknown beforehand. Instead, an approximate system of linear equations, defined by the ray paths through a "best guess"

reference model, is used. The inversion produced from this approximate system of linear equations, though imperfect, will most likely be an improvement over the original reference model. It is expected that the procedure of repeated ray tracing through the most recent model followed by an inversion will correct the non-linear effects in a short number of steps, generally 2 to 5, depending on the accuracy of the original reference model.

The expectation that repeated ray tracings and inversions will converge is a conjecture that may not always be true. The validity of this hypothesis depends upon the individual characteristics of the model and the accuracy of the initial reference model. The process cannot be formulated mathematically, so convergence behavior and other characteristics can be explored only empirically, using synthetic examples, which are performed here in this section.

Generally, the repeated ray tracing and inversion is stable and produces a largely accurate result, but does not converge to the correct solution. The problems with the result can generally be identified by the unreasonable structure of the final solution or experience with the phenomenon. The only remedy for correcting these problems is to start over, using another reference model. It is hoped that, a careful analysis of the inversion results of the original reference model will provide useful information for the determination of a new reference model.

Errors in both the velocity field and the reflector structure will affect the ray paths and create non-linear artifacts. The non-linear artifacts produced by an incorrect velocity field or by incorrect reflector positions in the reference model

are quite different and will be analyzed separately. In this section, the non-linear artifacts caused only by errors in the velocity of the reference model are analyzed. The reflector position used in all the reference models will be the correct flat one and will not be a parameter in the inversion. This geometry is nearly identical to the pure transmission tomography geometry. The artifacts will be directly comparable to those often encountered in whole earth applications. The non-linear artifacts caused by errors in the reflector of the reference model are analyzed later.

Inversions of the **GAS, OIL**, and horizontal block models used in the previous section are repeated in Figures 3.5c, 3.13c, & 3.21c where non-linear effects of using incorrect ray paths are also shown. The effect of these velocity variations on the ray paths is shown in Figures 3.6, 3.14, & 3.22 respectively. These rays were approximated with straight rays through constant velocity reference models.

The inversions contain vertical smearing from the limited angular ray coverage as well as non-linear artifacts from the incorrect ray paths. For distinguishing the non-linear effects, the inversions can be compared with the straight ray inversions, in Figures 3.5b, 3.13b, & 3.21b, that suffer only from vertical smearing. The migrations of the zero offset sections through the non-linear inversions are shown in Figures 3.11, 3.19, & 3.25 and can be compared with the migrations through the linear inversions in previous figures.

Although the original positive and negative velocity variations of Figure 3.21a have identical shape and are located at the same depths, they have been

inverted differently in Figure 3.21c because of non-linear effects. The ray bending in the true model (shown in Figures 3.22) has caused narrowing of the inversion of the slow velocity blocks and widening of the fast velocity blocks. This artifact, which increases with depth, occurs because the paths of fastest travel times avoid the slow velocity blocks and gravitate toward the fast velocity blocks.

Non-linear artifacts grow with depth because the rays, being farther from the source or receiver, have more freedom to adjust their ray paths. This characteristic is apparent from the lower velocity variations, which are not as well-inverted as the upper ones. The migrations in Figures 3.25-3.28 demonstrate clearly that the faster blocks are inverted better than the slow ones, and that the upper blocks are inverted better than the lower ones.

The repeated ray tracings and inversions have been successful in correcting most of the non-linear artifacts in the first inversion caused by ray path errors. The velocity blocks are their proper width and the migration is close to a continuous flat reflector. However, a significant migration artifact still exists under the lowest slow velocity block. The inversion of the slow velocity blocks is poor because they have less effect on the travel times than the fast velocity block. For example, a ray that, in the absence of velocity variations passes at the edge of the block position, will adjust its path the slight amount necessary to avoid a slow block, resulting in very little travel time variation. However, if the block instead were fast, the ray would adjust its path to cross through the block, giving it the full acceleration of that block.

The ray paths in Figures 3.22a & b show that no rays pass through the edges of the slow velocity block. With fewer rays traversing the slow blocks than the fast ones, there is less information in the travel times about the slow block than the fast ones. Once a velocity variation is slow enough that all rays avoid the region, there will be no information about how slow it is below that threshold.

If ray paths of maximum amplitude had been used rather than minimum travel time, they would better resolve the slow velocity anomalies to which they tend to be attracted. However, rays of maximum amplitude also tend to avoid the fast velocity anomalies, causing the latter to suffer from a similar distortion as the slow velocity anomalies. Ideally, to have complete ray coverage of fast and slow velocity variations, both maximum amplitude and minimum travel time arrivals should be used in the inversion. Unfortunately, this complicates the matter significantly and may be impractical. An advantage of Tarantola-style inversion is that all arrivals are automatically included. Continuing the inversion with Tarantola's inversion method from this point forward may improve the non-linear artifacts.

Several additional examples are presented in the Appendix. A model in Figures 3.21 with a maximum ray angle of just 25^{o} instead of 45^{o} shows that although the vertical smearing is more severe with a more limited angular ray coverage, the non-linear artifacts are not more severe and the migrations in Figures 3.29 & 3.30 are accurate. The inversion of horizontal blocks in Figures 3.33 & 3.34 with velocity variations of +/-3000 ft/sec rather than +/-1000 ft/sec shows that the non-linear effects from stronger velocity variations are more

severe, but can be mostly corrected through additional ray tracings. The inversions of non-horizontal velocity blocks in Figures 3.38 & 3.39 show that even though vertical blocks are less affected by vertical smearing and that their inversion appears much better than the horizontal block inversion, the vertical block inversion is actually much worse. It does not have the proper amplitude and significantly distorts the subsequent migration, as seen in Figures 3.40-3.42. This deception underscores the fact that migration is generally a better test for the success of tomographic inversion than the velocity field itself. The visual comparison of velocity fields is a qualitative analysis while migration through the velocity field is a quantitative analysis.

The non-linear effect of more complicated velocity variations is demonstrated using the **GAS** and **OIL** models presented earlier. The inversions show that the non-linear artifacts from using straight rays to approximate the curved ones are quite significant for ray bending caused by velocity variations of only 10%.

The complexities of the velocity variations make the inversions difficult to analyze in detail, but some general features are apparent. The migration of the **GAS** inversion is better than the **OIL** migration. This result is a consequence of the letters of the word **GAS** containing more horizontal features than the word **OIL**. This phenomenon results from the vertical features affecting ray paths more than horizontal ones thereby causing greater non-linear effects. An example in the Appendix highlights this problem.

Two more ray tracings and inversions are performed for each model. The final velocity models are shown in Figures 3.5d & 3.13d. The migrations, shown in Figures 3.12 & 3.20, are improvements over the previous migrations, but still contain significant distortions. The migration through the **GAS** inversion is more coherent, especially on the right side under the **S**, than the **OIL** migration. This result is again attributed to the more horizontal nature of the letters in the word **GAS**, especially the letter **S**. Thus, even though horizontal features are more distorted by vertical smearing, they cause smaller non-linear effects and produce a more accurate result.

Although the velocity contrasts of 10% are not unreasonably large, the complicated nature of the velocity variations, the fact that they are vertical, and their small size, render these two models very difficult test cases for tomographic inversion.

Tomographic inversion is not very successful in many cases, such as: vertically oriented velocity, negative velocity variations at depth, or strong velocity variations. It is clear that tomographic inversion needs some help to invert these types of structures adequately. By carefully analyzing the artifacts of an unsuccessful inversion, an interpreter can use his knowledge of the geologic characteristics of the region to devise a better reference model for these difficult cases.

For less difficult cases, tomography has produced velocity models that produce very accurate migrations. Repeated application of ray tracing and inversion has been successful at removing some non-linear effects.

3.7 Velocity-Reflector Depth Tradeoff

The previous chapters have addressed how well velocity variations can be resolved when the correct reflector structure is known. Except in certain situations, the reflector structure can generally not be determined without an accurate knowledge of the velocity field, however. Thus, we can expect incorrect reflector structure to accompany unresolved velocity variations in the reference model.

In many cases, one will not know *a priori* whether travel time deviations between the data and a model are caused by velocity field errors or reflector position errors in the model. In performing the inversion, one runs the risk of trading off velocity field errors into the reflector structure and vice-versa. This is a velocity-reflector depth ambiguity.

In this section, the linear effects are isolated from the non-linear effects by using small model perturbations to avoid ray path errors. The availability of perfect data enables us to use these small perturbations. For all the inversions performed in this section, the reference model has a constant velocity of 8000 ft/sec and a flat reflector at a depth of 5000 feet.

The inversions are all carried out to at least two minimum eigenvalues: 0.05 and 0.02, which are representative for what can be achieved for a real data case. The optimum minimum eigenvalue inverted will depend on the resolution desired and the noise present in the data. A minimum eigenvalue of 0.05 is

probably achievable for average data. 0.02 is an optimistic goal that may be achieved only with high quality data sets.

Figures 3.44-3.47 show the results of simultaneous inversions for velocity and reflector depth over several eigenvalue ranges for reflector bumps with different widths.

The inversion in Figure 3.46b of the narrow reflector bump over a limited eigenvalue range shows that most of the bump has been inverted, but some velocity artifacts appear just above the reflector bump. The inversions to smaller eigenvalue do not improve the result.

The bump is well inverted in the inversion over limited eigenvalue range in Figure 3.46b because most of the travel time deviations have been arbitrarily put into the reflector rather than into velocity. The velocity-reflector depth ambiguity has not been resolved over the limited eigenvalue range of (1.0-0.3) of this inversion. This result demonstrates that the inversion has a reflector bias for a narrow bump which has arbitrarily aided the inversion of the bump. Had the travel time deviations instead been the result of velocity variations similar to the velocity artifacts of Figure 3.46f, the bias would have hindered the inversion.

The size of the velocity region with which the bump is ambiguous explains this bias. The velocity region ambiguous with a bump is the region where the velocity artifacts appear, which is only a small region, as seen in Figure 3.46f. Since the weighting is initially set up so that the reflector is equivalent with the entire height of the velocity field from the surface down to the reflector,

a smaller velocity region of less height will have less net weight than the corresponding reflector bump. The relative weight between a reflector and its ambiguous velocity region determines how much of the travel time deviations are initially placed in reflector and velocity.

To remove the reflector bias for small bumps, the inversion is repeated with increased velocity emphasis. This will serve to increase the velocity artifacts and better illustrate how inversions to smaller eigenvalues affect the artifact.

The inversion in Figure 3.46g with velocity emphasis of the narrow bump over a limited eigenvalue range shows half of the bump to be inverted with a more significant velocity artifact than the previous inversions. Continuing the inversion to smaller eigenvalue improves the result only marginally. The amplitude of the reflector bump has been improved from 50% to about only 75%. For the broadest eigenvalue range, which is probably too broad for the noise level generally present in real data, the velocity-reflector depth ambiguity for this narrow bump has not been fully resolved.

However, the velocity artifact associated with the narrow bump has a non-geologic shape. To suppress this velocity artifact, an inversion is performed that does not allow the velocity to vary laterally in the bottom third of the velocity model. The inversion with velocity emphasis appears in Figures 3.46j-l. Most of the reflector bump is inverted over the limited eigenvalue range. Continuing the inversion to a smaller eigenvalue significantly improves the result, almost entirely removing the velocity artifacts. The constraint has been successful in resolving the velocity-reflector depth ambiguity.

Some velocity artifact appears at the edges of the velocity field. They are most notable in Figures 3.46f, 3.46m, and 3.46n. These artifacts are edge effects, that are discussed in a later section of this chapter.

The inversions of the wide reflector bump of Figure 3.47a differ greatly from those of the above narrow bump. Only half of the reflector bump is inverted without velocity emphasis over the limited eigenvalue range of Figure 3.47b, whereas most of the narrow bump was inverted under the same conditions. The velocity artifact associated with the wide bump extends up to the surface of the velocity model rather than being in the lower part as with the narrow bump.

Continuing the inversion to a smaller eigenvalue greatly improves the result, leaving little velocity artifact. For the wide reflector bump, the velocity-reflector depth ambiguity has been resolved without the use of constraints. The small velocity artifact that remains has been shifted mostly into the upper part of the model, a shift that did not occur for the narrow bump.

Figure 3.48a analyzes the velocity-reflector depth ambiguity with three horizontal velocity blocks at different depths. These velocity blocks can be considered the reverse case of the reflector bumps used in the previous test cases. The lower block on the right is similar to the velocity artifacts of the narrow bump, while the higher block on the left is similar to those of the wider bump.

An inversion in Figure 3.48b for reflector depth shows only the reflector variations with which the velocity blocks are ambiguous. The upper velocity is more ambiguous with broader reflector variations that have lower amplitude.

The combined inversion in Figure 3.48c for velocity and reflector depth over a limited eigenvalue range has placed half of the travel time deviations into reflector depth, producing artifacts half the amplitude as in Figure 3.48b. Inverting to smaller eigenvalue removes most of the reflector artifacts on the left side of the model, but leaves the ones on the right side. The long wavelength aspects of the velocity-reflector depth ambiguity have been inverted, but not the short wavelength aspects, consistent with the previous inversions. This is apparent under the right velocity block, where the initial reflector square trough of Figure 3.48c remains, but the entire region has been raised so that the average reflector depth is correct. The velocity has been smeared vertically, as was expected.

Additional examples of the velocity-reflector depth ambiguity are presented in the Appendix. An example shows that the addition of a second, deeper reflector to the model significantly helps the inversion of the lower velocity block. Another example applies incorrect velocity constraints to this model and indicates the subsequent consequences. Different-sized velocity variations are also presented.

3.8 Non-linear Effects of Reflector Position

Reflector inaccuracies of the reference model will affect the ray paths that cause non-linearities in the inversion. Reflector inaccuracies are generally caused when velocity variations are interpreted as reflector variations. This would occur when data is migrated through an incorrect velocity field. Thus, errors in the

velocity field of the reference model will most likely accompany errors in the reflector position. Errors in both the velocity and reflector affect the ray paths and contribute to the non-linear effects. However, to isolate the non-linear effect of reflector position errors, most of the reference models here will not contain errors in the velocity field. To analyze a data case that contains both types of errors, an interpreter will have to synthesize the results of this subsection with the previous one on velocity-caused non-linearities.

Non-linear effects are caused by using only approximate ray paths through a reference model. The correct ray paths will, of course, remain unknown until the correct model is determined. The non-linear effects from velocity errors are generally a predictable blurring effect that bears some identifiable relationship with the proper linear inversion. Non-linear effects from reflector position errors have the potential for being unstable, however. In some cases, they will vary wildly with little resemblance to the correct reflector structure.

Inversion instabilities result from use of the limited physical model of adjusting the reflector depths to the travel times along ray paths. This method is analogous to ray trace migration, an unpopular technique. However, wave equation migration is a stable technique that will generally only smear the reflector position in the presence of data or velocity model errors rather than potentially cause wild gyrations.

Thus, to stabilize the process of alternately ray tracing and inversion, migration is used to image the reflector after the inversion. It is expected that the inverted velocity field and updated reflector position will be an improvement over

the reference model used for ray tracing. Tracing rays through the new velocity and reflector position will improve their accuracy. Using these updated ray paths in the inversion should improve the result. The process of repeated ray tracing, inversion, and migration, which should reduce non-linear artifacts, is called iterative tomographic inversion and migration.

The two approaches of implementing iterative tomographic inversion and migration differ as to whether to perform the tomographic inversion for velocity only, or for both velocity and reflector depth. The method preferred by the author uses the combined inversion for velocity and reflector depth. Evidence in Chapter 2 indicates that the combined inversion is necessary to resolve the velocity-reflector depth ambiguity. In this method, the reflector position produced from the tomographic inversion is discarded and the reflector position produced from the migration is used.

The other variation of iterative tomographic inversion and migration performs the tomographic inversion for velocity only. This method avoids the instabilities of the reflector position by eliminating the reflector from the inversion. The reflector position is then updated with the migration through the velocity. Examples of both of these variations of iterative tomography and migration are presented.

Reflector variations that affect ray paths can be grouped into two types: sharp and gradual variations. Figure 3.51 shows the ray paths for a "hill" with a gradual slope. Gradual reflector variations change the angle of reflection of the rays and alter their position and density by shifting all the ray paths upslope. The

angle of reflection is used by the inversion to determine the proper reflector depth. Errors in the angle of reflection will translate into errors in reflector depth. Shifting the position of the rays will shift the position of an anomaly with the rays, while changing the ray density will change the size of the structures.

Sharp changes in reflector depths will cause a discontinuous ray distribution by attracting rays from the neighboring deeper reflector positions. Figure 3.50 shows the paths of least travel time in the presence of a sharp bump. Rays to neighboring receivers can take vastly different paths, creating a discontinuous ray set. Note that no rays reflect near the sides of the bump. In addition, a fault is also a typical sharp change that can cause a discontinuous ray set. The effect of sharp reflector inaccuracies causing discontinuous ray distributions is difficult to generalize and can be bizarre in some cases.

These types of reflector variations, bumps, troughs, faults, and gradual hills are considered to be the generic types of reflector variations that can cause non-linear effects. They will be used to determine reflector non-linear artifacts of tomography and how well the artifacts are solved with iterative tomography and migration.

Figures 3.53 addresses the non-linear effect of gradual reflector errors. The reflector position in Figure 3.53a contains significant vertical exaggeration. Sample ray paths for the model are shown in Figures 3.56a, b, & c without any vertical exaggeration. The ray paths are continuous for near offset rays, but are discontinuous for the far offset rays. The far offset ray paths are more susceptible to reflector structure than the near offset ray paths. Because of the discontinuity

of the far offset rays, this reflector bump is not quite smooth enough to be classified completely as a *gradual* reflector variation, but rather, it is a transitional one between sharp and gradual.

Figures 3.53c and 3.53d show the ray densities for the two models. The attraction of rays to a bump and repulsion from a trough are apparent, with the ray density being about twice the background over the bump and almost zero over the trough. As expected, the ray density for the flat reflector is even across the model.

Figure 3.53e performs an inversion that allows only the reflector position to vary. Because of the ray path differences between the two models, the bump has been widened and the trough narrowed. These artifacts occur because of the tendency of rays to move upslope.

This inversion is a transformation of time data to depth using a given velocity field, which amounts to performing a migration using predetermined ray paths. Since the correct velocity is used, a more conventional wave propagation migration scheme would have produced the correct result. That the inverted reflector position contained artifacts demonstrates a weakness of ray-based methods and is a reason migration is included in the tomographic process to image the reflector.

The inversions in Figures 3.53f & g of the bump-and-trough model using the plain model as the reference produce a reflector with similar artifacts to that of Figure 3.53e, but slightly lower amplitude reflector perturbations. A noticeable

velocity artifact appears above the bump and a lesser one appears above the trough. The fact that the inverted reflector is so similar to that in Figure 3.53e is a consequence of the natural reflector bias for smaller sized bumps also seen in inversions of Figures 3.46b.

Figure 3.57c shows the migration through the inverted velocity field, which can be compared with migration through the correct constant velocity in Figure 3.57b. The bump in the reflector has the right shape but not the proper amplitude. The trough is inverted almost perfectly.

Figure 3.54a represents the picked reflector from the migration plotted with the velocity. This model is used for ray tracing for another inversion, the results of which are shown in Figures 3.54c & d. The velocity artifact over the bump appears to have been reduced but not eliminated. The artifact reduction can be expected since the re-ray tracing should be significantly more accurate and should reduce non-linear effects. However, the artifact above the trough appears to have worsened. A migration through the inverted velocity in Figure 3.57d is significantly worse than the previous migration in Figure 3.57c. This degradation of the migration is surprising considering that the velocity artifacts have not increased that significantly.

The iterative tomography and migration are repeated with the reference model and the true model switched. The inversion should now remove the bump and trough of the reference model and produce a flat reflector. The results in Figures 3.53h & i show that the inversion has progressed in the proper direction. If there were no non-linearities, the velocity artifacts would be merely the

negative of those encountered in the previous inversion in Figure 3.53f, which they are not.

The migration in Figure 3.57f through the inverted velocity again produces a reflector with fewer artifacts than that of the inverted reflector. The picked reflector is shown in Figure 3.54b.

A subsequent ray tracing through the improved model and inversion produces almost no change to the model result in Figure 3.57g. This is unfortunate since the improved model is so accurate that the non-linear effects should be minimal. The lack of improvement is most likely a consequence of the inability to resolve the linear velocity-reflector depth ambiguity over the eigenvalue range inverted. This is a shortcoming of the linear aspect of the inversion, addressed in the previous section.

The 2nd form of iterative tomography and migration--the one where the tomographic inversion adjusts only the velocity, not the reflector--is performed on the bump-and-trough model, using the plain model as the reference model in Figure 3.55a. Comparing the results with those of Figure 3.53f shows the results to be significantly inferior. The velocity artifacts are more pronounced because the inversion could not adjust the reflector position. Since the velocity has been adjusted to match the reflector position of the reference reflector, the migration through the velocity has reproduced most of the reference reflector position, especially the long wavelength features. Additional ray tracings and inversions do not significantly improve the result. If this 2nd form of iterative tomography and

migration does indeed converge, it would take a prohibitive number of repeated ray tracings, inversions, and migrations to achieve the conversion.

The non-linearity of the mild bump and trough of the model used above does not appear to affect the inversion significantly. Most of the unremoved artifacts can be attributed to the inability of the linear system to resolve the velocity-reflector depth ambiguity over the eigenvalue range inverted. Even though these reflector variations were transitional between gradual and sharp and caused some discontinuities in the ray paths, the inversion did not contain any significant artifacts that created new structure or that might cause the inversion to diverge. These types of reflector variations do not cause serious non-linear problems.

Iterative tomography and migration are performed on non-linearities from sharp reflector variations in Figures 3.61. The sharp reflector variations of model J-1 in Figure 3.61a are the three generic kinds: a narrow bump, a narrow trough, and a fault. The plot of the ray density in Figure 3.61b shows how the rays are significantly affected. Sample ray paths through this model exist in Figure 3.50, which also presents the reflector position without vertical exaggeration. The reference model used for the inversion in Figure 3.61c has a flat reflector.

The reflector-only inversion in Figures 3.61d & e of Model J-1 using J-2 as the reference again demonstrates how the higher features of the reflector are enlarged and the lower features are reduced.

The combined inversion in Figures 3.61f & g shows the same general broad reflector features as that of the reflector-only inversion above. The features are, however, lower in amplitude and corrupted with some high frequency artifacts. There is a wide slump in the middle of the reflector. The origin of this artifact is unknown. The velocity artifacts are almost all positive. In general, the artifacts are moderate or minor and a fairly reasonable, stable result was produced.

The migration through the velocity field of the above inversion, shown in Figure 3.63c is very different from the reflector of the inversion itself. This difference underscores the distinction between ray tracing and waveform migration. Most geophysics will trust the waveform migration results more. The reflector picked from the migration is shown with the velocity in Figure 3.61h, which can be compared directly with the inversion in Figure 3.61g. The reflector position from the migration contains many fewer artifacts and is surprisingly close to the correct result.

Using this improved model for additional ray tracing and inversion does not produce a result closer to the correct model. The second inversion is shown in Figures 3.61i & j and the migration through the velocity in Figure 3.63d. The inversion contains no noticeable improvements and several new artifacts. The migration is significantly worse than the previous one. If the first inversion produced an encouraging result, considering the non-linearities present, the additional ray tracings, inversions and migrations did not improve the model.

Another inversion is performed with the reference and the true model switched. The inversion should produce a flat reflector. The results in Figures 3.61k & l show very severe artifacts. The velocity anomalies above the bump and fault have large amplitude and the reflector position is unreasonable. For the non-linearities associated with this reference and the true model, the inversion is unstable. The damping factor used in each back-projection step was 30% of the average ray density. The inversion was not attempted with higher damping factors.

The author speculates that the previous inversion, where the reference model contained a flat reflector, was stable because the fault reflector of the reference produced a very even and uniform ray path set. However, when the model with a sharp structure was used as the reference model, the reflector structure caused a very uneven and inhomogeneous ray path set that enabled portions of the model to gyrate.

The migration in Figure 3.63e through the velocity field of Figure 3.61k does not contain the wild artifacts of the reflector position from the inversion. Again, the migration has produced a more stable and reasonable result than the inversion. In the migration, the reflector position is improved over that of the reference model, but does contain some artifacts, noticeably the troughs next to the bump and the fault.

The picked reflector position is plotted with the velocity field in Figure 3.61m. This model is used for an additional ray tracing and inversion, the result of which appears in Figures 3.61n & o. This inversion, curiously, does not

contain the bizarre artifacts of the previous inversion. However, it has hardly improved the model. Some high frequency artifacts have been introduced, while the reflector position is still far from flat. To the inversion's credit, the slope next to the fault has been reduced to the correct general flat structure.

The migration in Figure 3.63f through the velocity field of the inversion has very significant artifacts, which are probably the result of the high amplitude velocity anomalies. In this case, the reflector position is worse in the migration than in the inversion.

In an attempt to improve upon the poor inversion results of the bumps and fault, the inversions are repeated with velocity constraints that do not allow the lower third of the velocity field to vary laterally. The inversion in Figures 3.61p & q of the bumps and fault, using the flat reflector model as the reference has done very well, with a reflector position nearly identical to the reflector-only inversion in Figure 3.61d. However, some velocity artifacts are created. The migration through the velocity field in Figure 3.63g is very accurate, with only minor artifacts.

Figure 3.61t plots the picked reflector position with the velocity field, the model used for an additional ray tracing, inversion, and migration. The inversion contains significant reflector artifacts next to the bump and fault. However, the velocity artifacts appear to have been reduced. The migration in Figure 3.63h is a nearly perfect result and does not contain any hint of the reflector artifacts in the inversion. With the use of these simple velocity constraints, the additional ray tracing through the updated model has improved the inversion.

Identical velocity constraints are used for the inversion of the flat reflector model using the reflector with bumps and faults as the reference model. The inversions in Figures 3.61r & s contain the artifacts similar to those of the inversion without velocity constraints in Figures 3.61k & l. The migration in Figure 3.63i through the inverted velocity field does not contain these reflector artifacts. Although the result is still far from the correct result of a flat reflector, the initial bump and fault reflector position has been adjusted in the correct direction with no significant artifacts. An additional ray tracing through the updated model shown in Figure 3.61w is used for the inversion in Figures 3.61x & y. The result is a further, significant improvement. The bump is nearly flat and the fault has been reduced and smoothed. For this case, the subsequent migration produces a reflector position similar to the inverted reflector position.

The second form of iterative tomography and migration, where the tomographic inversion is for velocity only, is performed on the bump-and-fault model. Figures 3.62a-e show the successive inversion results and Figures 3.64a-c show the migration results. After three sets of tomography and migration, the model has not approached the correct result and contains many serious artifacts. Most of the velocity artifacts were created in the first inversion and have not been corrected in subsequent inversions. In the first velocity inversion, the velocity was best adjusted to match the fixed reflector position. The subsequent migration then reproduced the flat reflector position of the reference model. The broader reflector features are most consistent between the migration and inversion, with no hint of the gradual slope next to the fault in any of the inversions. However, the small-scale features are resolved.

These examples have shown how migration is needed to stabilize the potential serious non-linear effects in the inversion resulting from an incorrect reflector position. It appears that errors on the smoother side of the reflector structure in the reference model are less serious than the reverse.

3.9 Additional Stabilizing Effect of Prestack Migration

The zero-offset poststack migration examples presented above show that they have a stabilizing effect on the instabilities of the reflector position from the inversion. Preliminary results here demonstrate that prestack migration has an additional stabilizing effect.

Poststack migration propagates one wave field along a single azimuth, generally the vertical direction. Thus, the effect of a velocity artifact near the surface can be propagated down in depth to the reflector, although diffraction will cause some wave front healing. However, with a prestack migration, numerous wave fronts are propagated over a suite of angles. The redundant information will lessen the effect of a single localized velocity artifact on the image.

Examples of the sensitivity of prestack migration to errors of the velocity field is shown in Figures 3.65 & 3.66. The model in Figure 3.65a contains vertically oriented velocity channels, which are the type that most significantly affect ray paths and cause serious non-linear artifacts. Poststack and prestack data from this model is migrated through a laterally uniform velocity model in Figure 3.65g. The results in Figures 3.65h & 3.65i show that the prestack

migration results more accurately reproduce the flat reflector than post-stack migration.

The procedure is repeated for velocity variations shown in Figure 3.66a, which have a sharp velocity contrast in a layer. A poststack migration through a similar velocity model is shown in Figures 3.67d. It shows a sharp reflector jump just below the velocity contrast that can easily be interpreted as a fault. However, the migration of the prestack data from the velocity variations through a constant velocity smears the effect over a wider range. The reflector is smooth just below the velocity contrast.

In general, prestack migration has a smearing effect in the presence of an incorrect velocity model, which will smooth out the structure. This smearing results from the imperfect superposition of the various wave fronts. Previous examples show that tomography is better behaved when the reference model errs on the smoother side of the true model.

3.10 Edge Effects

At the edges of any tomographic data collection geometry, there is a transition region from complete ray coverage to no ray coverage that has a low ray density and poor azimuthal coverage. This inhomogeneous ray distribution can serve to distort images in a complicated way.

Distortion of images at the edges is generally not considered serious since it is expected and will not be misinterpreted. The target of interest is generally in

the central part of the survey, and the images at the edges of a reflection survey are ignored.

Of greater concern is that the edges may affect parts of the reflection survey at considerable distance from the edges. Results presented here are inconclusive about quantifying the extent of the complicated nature of edge effects. They suggest that edge effects do not extend very far from the edges. But, some models demonstrate reason for concern.

For instance, the inversion in Figure 3.67b has hardly changed the incorrect reference model. Subsequent figures show that if either a wider reflection survey, a second reflector, or velocity constraints are used, the inversion is considerably improved, however. Proximity of the edges to the structure of interest has caused failure of the original inversion.

In a previous inversion, presented in Figure 3.46f, artifacts are introduced at the edges of a survey from the structure in the middle of the survey, far from the edges. These inversions show that the edges bear some relationship to aspects of the model a significant distance away from the edges. From this figure, however, it is not known how much the edges affect the inversion of the structure in the middle of the survey.

To gain insight into the magnitude of the edge effects, the inversion is repeated with a narrower reflection surveys in Figures 3.46m & n. If the edges significantly affect the inversion of the bump, the effect should be more serious as the survey becomes narrower. The results show that while the velocity artifacts

increase in magnitude, the bump appears almost equally well inverted suggesting that it has not been corrupted by edge effects.

The recording geometry used for all the examples presented here is a single spread, with the receivers only to the right of the source. The survey is stopped at the right side before any of the receivers are off the model. Thus, the roll-in at the left side of the survey will contain mostly vertical rays while the roll-out at the right side will contain mostly far offset rays. A plot of the ray density of this generic survey in Figure 3.74c shows that the right edge has poorer coverage than the left edge.

The inversions of structure near the edges was found, in general, not to affect the model far from the edges.

The effect of edges on a more regional structure is addressed with models in Figures 3.74. The inversion results in Figures 3.74d, e, & f produced are generally quite accurate and contain few artifacts except near the edges. It appears the roll-out at the right side has caused more serious artifacts than the roll-in at the left side.

The previous example is repeated in Figures 3.73 using narrower reflection surveys. The inversion of the slope in Figures 3.73d & e are severely distorted. Much false structure has been created. When the inversion is repeated in Figures 3.73f & g with the weighting increased from 25% of the average ray density to 100%, the artifacts have been reduced and a slope is noticeable, but serious artifacts still exist. The results of these models suggest that the edge

effects are serious only for narrow surveys. For wider surveys, the effect of the edges does not contaminate the image far from the edges.

In an attempt to improve the inversion of the previous narrow model, velocity constraints were placed at the edges that did not allow lateral variations in the regions marked in Figure 3.73h. The left side of the inversion with these constraints is well-inverted, but not the right side. The roll-out of the survey appears to cause more problems than the roll-in. When the regions of velocity constraints are increased in width, the artifacts have all been nearly removed and the slope is well inverted, as seen in Figures 3.73i & j. The far right side of the model is not inverted because there is no ray coverage there.

The effect of edges or other uneven ray coverages upon an inversion is difficult to predict. Any structure at the edge of a model will be distorted. No explicit examples could be produced that showed an image a reasonable distance away from the edge of a wide survey being distorted by edge effects. However, other models show that the edges are connected to the structure far from the edges, particularly for narrow surveys, suggesting caution.

Edge effect is a serious concern for tomography in surface reflection geometry, even though this is one of the more uniform data sets available in seismology. Results presented here show that inverted images in inhomogeneous ray coverages or located next to them should be interpreted skeptically. The edge effects of transmission tomography may be very serious for these cases. Other seismic applications of tomography such as VSP or cross-hole geometries have

inhomogeneous ray coverage over a significant portion of their entire coverage, somewhat like a narrow reflection survey.

3.11 Conclusion

Numerous inherent factors of a surface reflection survey serve to distort tomographic results and create artifacts, such as non-linear effects from ray path errors, velocity-reflector depth ambiguity, and edge effects. There is no absolute formula for identifying or removing these numerous artifacts. This transmission method cannot be a "black box" for solving problems of seismic data processing. Constraints must be carefully applied to control the artifacts. Other transmission tomography techniques may well also have similar problems that can only be resolved through the use of constraints.

This synthetic modeling analysis is instructive for demonstrating the behavior of the technique, but it is a qualitative approach. In the following chapter, a quantitative study is undertaken of the linear resolution of reflector depth, one main goal of a reflection survey.

Chapter 4

Singular Value Decomposition Analysis of the Travel Times of a Surface Seismic Reflection Survey

4.1 Abstract

Singular Value Decomposition (SVD) of travel time data from a generic reflection seismology geometry indicates that small- and medium-scale reflector depth variations cannot be uniquely resolved from velocity variations. Eigenvector analysis demonstrates that patterns of velocity variation can produce the same travel time variations as a reflector depth perturbation of width approximately twice the depth of the reflector and shorter. Larger-scale reflector perturbations can generally be resolved from velocity variations.

Resolution of the velocity-reflector depth ambiguity is sensitive to the maximum ray angle, but insensitive to the relative weighting between velocity and reflector depth. Velocity variations that are ambiguous with reflector variations form patterns that are unlikely geologic structures, which suggests that the ambiguity can be resolved with the use of constraints.

4.2 Introduction

Recent matrix analysis by Comer & Clayton (1985) have relates the Simultaneous Iterative Reconstruction Technique (SIRT) to the eigenvalues and eigenvectors of a specific matrix inverse formulation. The analysis demonstrates that SIRT can perform an inversion nearly identical to one using SVD, one in which a non-diagonal weighting of model and data space can be applied and the range of eigenvalues inverted can be chosen. Penalty functions can also be included. Quantitative knowledge of the eigenvalues and eigenvectors can thus be directly applied to performing the iterative inversion and interpreting the results.

The relationship between eigenvectors and eigenvalues to structures of interest is valuable knowledge for the application of tomography. For instance, the optimal range of eigenvalues over which to perform an inversion should be just wide enough to include the desired objective, yet as narrow as possible to reduce the effects of noise and keep computer use as low as possible. Moreover, a technique developed by Olson (1986) that significantly accelerates convergence of SIRT for inversion of small eigenvalues, requires the specification of the range of eigenvalues to be inverted.

In some cases, the eigenvalue associated with the structure will be too small, and cannot be effectively inverted. The inability to resolve

certain structural features should be known, so the results of the inversion are cautiously interpreted.

By analyzing the dependence of the eigenvectors upon data collection and inversion parameters, adjustments can be made for individual cases to optimize resolution of a desired feature. Such adjustments could include design of a reflection survey with proper ray coverage at minimum cost, collecting additional data from bore-holes; or implementing inversion constraints based upon geologic knowledge of a region.

Resolving velocity-reflector depth ambiguities is a main goal of the application of tomography to reflection seismology. Knowledge of the eigenvalue range associated with the ambiguity would enable one to relate depth resolution of a reflector with travel time resolution available in the data. This eigenvalue range will depend upon the maximum ray angle and other attributes of the reflection survey.

Bube & Resnick (1985) performed an SVD analysis with goals similar to those of this study, but more limited in scope. Their analysis, limited by computer power, used large cell sizes, narrow data coverage, and contained edge effects. Each of these items is shown here to corrupt the results seriously.

Most reflection seismology problems are far too large for the application of SVD. Analysis is performed here on small generic reflection surveys to generally characterize the resolution of the inverse problem. The results will have to be extrapolated to the more realistic models used in SIRT applications.

Individual eigenvectors from these limited generic models are frequently difficult to correlate with any common geologic structure. Hundreds of eigenvectors are generally necessary for the correlation and significant differences exist between the generic models used for eigenvector generation and the application geometry. The SVD analyses performed here is intended only as a qualitative description of the eigenvector characteristics of a reflection survey. More detailed analysis using larger models and direct analysis of realistic structures are best performed through forward modeling like that shown in Chapter 3.

4.3 Method

Here, SVD analysis is first performed on a model consisting of only 2 parameters: a uniform velocity and a flat reflector. This simplified model represents the laterally-invariant case. It is used to introduce the eigenvector associated with the velocity-reflector depth ambiguity, and to demonstrate how it can be used to relate data accuracy to model accuracy.

The effect on the velocity-reflector depth ambiguity of allowing velocity to vary laterally, is analyzed with a generic two-dimensional model shown in Figure 4.1. To avoid effects of the limited ray coverage at the edges of the survey, ray paths exiting at one side of the model are entered on the other side, producing a continuous, *circular* reflection survey with complete ray coverage everywhere. Consistent results from models run with different circumferences indicate that the results are not affected by the *wrap-around.*

A model size used for SVD (1408) represents the approximate maximum size that could be reasonably run repeatedly on a CRAY-2 computer. Since data space eigenvectors are not computed, storage requirements for the matrix are the square of the model size, about 2 million words for the generic model used above. Model size is itself the square of cell size, so the storage requirement is the 4th power of cell size. It would not take a much smaller cell size until the memory capacity of a CRAY-2 (~100 Mega-words) or a disk is exhausted. With larger storage devices and efficient out-of-memory SVD algorithms, the capability is also becoming more limited by run time, which is proportional to the cube of the model size and therefore the 6th power of cell size. While the model size above executed in only about 90 seconds on one CRAY-2 CPU, smaller cell sizes would quickly prove to be prohibitively expensive to execute. Half the cell size would require

90 minutes of CPU, yet might produce only marginally improved results.

Cell size limitations unfortunately affect possible resolution of the eigenvectors significantly. With only 10 cells down to the depth of the reflector and several cells needed to accurately represent a wavelength, there cannot be much reliable vertical structure in the eigenvectors. Structure that varies significantly over a few cells will have discretization effects from using constant velocity cells. These discretization effects can be reduced by representing the velocity with gradients between the points at which the velocity is defined. This representation was not attempted here.

The matrix for SVD produced by our circular geometry of the generic model, is block diagonally-invariant and block symmetric, and contains similar properties to a standard invariant matrix. An invariant matrix consists of identical rows except that each is shifted over so the elements of a diagonal are identical. The elements from one side are wrapped around to the other side. It can be shown that performing an SVD on an invariant matrix merely performs a Fourier decomposition of the invariant row of the matrix. The eigenvectors are the frequencies and the eigenvalues are the Fourier spectrum. Uniform ray coverage produces a block invariant matrix because for 11 cells in a vertical column (including the reflector cell), every 11th value along a diagonal

of the matrix will be identical. The eigenvectors of our block diagonally-invariant matrix, seen in Figures 4.8-4.11, produce a result with horizontal frequencies that is analogous to that of a purely diagonally-invariant matrix. This analogy suggests that it is possible to perform the SVD of our generic model in the frequency domain, which would significantly improve the attainable resolution. More realistic cases cannot be solved using this method because of the existence of edges and ray coverage inhomogeneities.

The large model spaces used here produce far too many eigenvectors to be analyzed by inspection individually. Automatic methods must be used to characterize the eigenvectors in terms that identify groups and trends within the various groups. Eigenvectors are analyzed here according to the following characteristics: dominant horizontal wavenumber, correlation between reflector depth variations and slowness variations directly above, and fraction of eigenvector component in reflector "cells".

SVD analysis is performed on several variations to this standard recording geometry to analyze the sensitivity of the velocity-reflector depth ambiguity to various parameters. Variations to the standard geometry analyzed are: a strong linear velocity gradient with depth that increases angular ray coverage at the bottom of the model; a velocity

field constrained to vary only in the upper half of the model; a recording geometry with a shorter cable length, one that produces half the angular ray coverage; damping of small-scale horizontal variations; smaller cell sizes; rectangular velocity cells 3 times wider than high; rectangular cells 2 times higher than wide; a second reflector at twice the depth of the other; a pure transmission simulating a cross-hole geometry; and a model without rays wrapping around, which has edge effects.

4.4 Setting up the Matrix for SVD

From Chapter 2, the forward problem of the travel time deviations from the reference model is expressed as:

$$\Delta t_k = \sum_j l_{kj} \cdot \Delta s_j \ ,$$

where:

Δt_k = the travel time deviation of the kth ray;

l_{kj} = the path length of the kth ray in the jth cell; and

Δs_j = the slowness variation of the jth cell.

In matrix notation this system of equations is represented as:

$$\Delta \mathbf{t} = \mathbf{L}\, \Delta \mathbf{s},$$

where

$\Delta \mathbf{t}$= vector of travel times deviations predicted from reference model;

$\Delta\mathbf{s}$= vector of slowness deviations from reference model; and

L= matrix of path lengths of the rays in each cell.

The Dines & Lytle back projection scheme from Chapter 2 is written as:

$$\Delta s_j = \frac{\sum_k l_{kj} \cdot \frac{\Delta t_k}{P_k}}{\sum_k l_{kj} + \varepsilon} .$$

In matrix notation it is

$$\Delta\mathbf{s} = \mathbf{S}\mathbf{L}^{\mathbf{T}}\mathbf{D}\,\Delta\mathbf{t} ,$$

where **S** and **D** are diagonal matrixes:

$$D_{kk} = P_k^{-1}$$

$$S_{ii}^{-1} = (\sum_k l_{ki} + \varepsilon)^{-1},$$

where

l_{ki} = the elements of matrix **L**;

$P_k = \sum_i l_{ki}$, which is the path length, including that in the reflector cells, of the k*th* ray;

$S_{ii}^{-1} \approx \sum_k l_{ki}$, which is the sum of the ray segment lengths in the i*th* cell; and

ε = a damping factor to avoid a zero divide for empty cells.

Comer & Clayton (1985) demonstrate that this back projection scheme converges to the solution of the following variation of the original forward problem, $\Delta t = \mathbf{L}\,\Delta s$, with weights applied to data and model spaces:

$$\mathbf{D}^{1/2}\,\Delta t = (\mathbf{D}^{1/2}\mathbf{L}\mathbf{S}^{1/2})\mathbf{S}^{-1/2}\,\Delta s.$$

D and **S** are the diagonal matrices defined earlier of weights applied to data and model space. We define the square root of a symmetrical matrix as:

$$\mathbf{D}^{1/2} = \mathbf{U}\mathbf{E}^{1/2}\mathbf{U}^{T},$$

where

U= the eigenvectors of **D**. ($\mathbf{U}^{T} = \mathbf{U}$), and

E= diagonal matrix of the eigenvalues of **D**.

Chapter 2 presents analysis of the forward problem and back projection scheme in detail.

All the SVD's presented here are performed on the matrix formulation with the diagonal weighting resulting from the Dines & Lytle (1979) SIRT algorithm. Chapter 2 presents arguments justifying these weights. The results are not expected to vary significantly as a

result of these weights. Since data coverage is uniform throughout the model, model weighting is uniform. The far offset rays are weighted only slightly less than the vertical rays (12% less for rays 45° off vertical). Model null spaces, in particular, are not affected by data weights.

We are interested in only the model space eigenvectors, so the SVD analysis is performed on

$$(\mathbf{U}\Lambda\mathbf{V}^T)^T\,(\mathbf{U}\Lambda\mathbf{V}^T) = (\mathbf{S}^{1/2}\mathbf{L}^T\mathbf{D}^{1/2})\,(\mathbf{D}^{1/2}\mathbf{L}\mathbf{S}^{1/2}),$$
$$\mathbf{V}\Lambda^2\mathbf{V}^T = \mathbf{S}^{1/2}\mathbf{L}^T\mathbf{D}\mathbf{L}\mathbf{S}^{1/2}$$

where:

$\mathbf{V}$= an orthonormal matrix of model space eigenvectors;

$\mathbf{U}$= an orthonormal matrix of data space eigenvectors; and

Λ= a diagonal matrix of the eigenvalues.

Not computing data space eigenvectors generally saves significant computation time, since data space is frequently much larger than model space. Independence from data space size allows use of very large data space so that it is essentially a continuous field and produces no sampling artifacts. Using this formulation, however, has the drawback of dealing with the square of the eigenvalues, presenting numerical problems for small eigenvalues. Double precision was used.

While the computation of $\mathbf{L}^T\mathbf{L}$ is generally an expensive

procedure comparable to the SVD computation itself, the sparseness of the matrix makes the computation relatively inexpensive.

4.5 SVD of a Two-Parameter model

We introduce the velocity-reflector depth ambiguity with the simplified model of Figure 4.2. It shows a slowness variation properly positioned to cancel much of the travel time effect upon all of the rays from a reflector variation. The amplitude of the slowness variation can be chosen to totally cancel the travel time effect of one ray azimuth, but not that of the others. The table in Figure 4.2 determines the amount of residual remaining on the rays for a slowness variation adjusted to negate the reflector variation for vertical rays. Clearly, the greater the offset, the greater residual. This is the information used to resolve the velocity-reflector depth ambiguity.

To analyze this simplified case with SVD, we recast the model into the two-parameter model shown in Figure 4.3, consisting of a slowness variation, Δs, and reflector depth variation, Δh. The travel time deviation, Δt, is expressed as:

$$\Delta t \;=\; \Delta s \cdot 2 \cdot \frac{h}{\cos(\Theta)} \;+\; \Delta h \cdot 2 \cdot \cos(\Theta) \cdot s + O(\Delta s \cdot \Delta h).$$

The $\Delta s \cdot \Delta h$ term is second order and will be ignored. The equation is non-dimensionalized by rewriting it as:

$$\Delta t \;=\; 2\cdot\cos(\Theta)^{-1}\cdot\left(h\Delta s\right) \;+\; 2\cdot\cos(\Theta)\cdot\left(s\Delta h\right).$$

The terms in brackets are now in units of travel time, which will be the variables used in all SVD's performed here. To convert the values of the eigenvectors back to their physical meaning will require taking into account the physical dimensions of the model.

The equation demonstrates that the resolution between velocity variations and reflector variations results from the path length of a ray through the velocity media being proportional to the inverse of the cosine of the angle from vertical, while the effect of the reflector depth is proportional to the cosine of the angle.

Data collected in this model are a ray set spanning evenly from vertical to some maximum angle, Θ, which can be thought of as one CMP gather of a reflection survey.

The matrix for which we seek the SVD is:

$$\mathbf{S}^{1/2}\mathbf{L}^{T}\mathbf{D}\mathbf{L}\mathbf{S}^{1/2} = \mathbf{V}\Lambda^{2}\mathbf{V}^{T} ,$$

where

$\mathbf{V}$= the model eigenvectors;

Λ= the diagonal matrix of the eigenvalues;

$\mathbf{S}^{-1}$= the diagonal matrix of the sum of the path lengths in each cell; and

$\mathbf{D}^{-1}$= the diagonal matrix of the total path lengths of each ray.

For this two-parameter model:

$$\mathbf{S}_{ii}^{-1} = \sum_{k=1}^{n} p \cdot w \cdot \cos(\theta_k) \quad \text{for the reflector cell;}$$

$$\mathbf{S}_{ii}^{-1} = \sum_{k=1}^{n} p \cdot \cos(\theta_k)^{-1} \quad \text{for the slowness cell; and}$$

$$\mathbf{D}_{kk} = \left(p \cdot w \cdot \cos(\theta_k) + p \cdot \cos(\theta_k)^{-1} \right)^{-1}.$$

additionally:

θ_k is the angle from vertical of the k*th* ray;

p= path length of a vertical ray in the slowness cell which will be twice the depth to the reflector; and

w= factor weighting the simulated path length in the reflector cell to the path length in the slowness cell for a vertical ray.

Since the data space will not be computed, we use a continuum of rays evenly spaced in offset. The computations are performed analytically in the Appendix by replacing the summations with integrals.

Using the results of the Appendix, when θ_{max}= 45°:

$$\mathbf{S}_{ii}^{-1} = 0.88 \cdot n \cdot p \cdot w \quad \text{for the reflector cell,}$$

$$\mathbf{S}_{ii}^{-1} = 1.15 \cdot n \cdot p \quad \text{for the slowness cell.}$$

We chose $w = \frac{1.15}{0.88} = 1.31$ so that $\mathbf{S}_{ii}$ is the same for both the reflector cell and the slowness cell. This produces an $\mathbf{S}$ of

$$\mathbf{S} = 1.15 \cdot n \cdot p \cdot \mathbf{I} ,$$

where

$\mathbf{I}$= the identity matrix.

With a w= 1.31, the elements of $\mathbf{D}$ are nearly identical:

$$\mathbf{D}_{kk} = \left(2.31 \cdot p\right)^{-1} \quad \text{for } \theta_k = 0^o ,$$

$$\mathbf{D}_{kk} = \left(2.29 \cdot p\right)^{-1} \quad \text{for } \theta_k = 30^o , \text{ and}$$

$$\mathbf{D}_{kk} = \left(2.34 \cdot p\right)^{-1} \quad \text{for } \theta_k = 45^o .$$

The elements of $\mathbf{L}^T\mathbf{L}$ are

$$(\mathbf{L}^T\mathbf{D}\mathbf{L})_{ij} = \sum_{k=0}^{n} l_{ki} \cdot \mathbf{D}_{kk} \cdot l_{kj} ,$$

where

$$\mathbf{D}_{kk} = \left(p \cdot w \cdot \cos(\theta_k) + p \cdot \cos(\theta_k)^{-1}\right)^{-1} ,$$

$l_{k1} = p \cdot w \cdot \cos(\theta_k)$ for the reflector cell, and

$l_{k0} = p \cdot \cos(\theta_k)^{-1}$ for the slowness cell.

This summation is performed in the Appendix analytically using a continuum of rays.

From the Appendix, we see that the eigenvectors and eigenvalues of this

matrix are:

First Eigenvector: ($\sqrt{0.5}$, $\sqrt{0.5}$) **eigenvalue= 1.000**

Second Eigenvector: ($\sqrt{0.5}$, $-\sqrt{0.5}$) **eigenvalue= 0.01147 ,**

These eigenvalues are the square of the eigenvalues of the inverse problem. The final eigenvalues are: **(1.000, 0.107).**

The first eigenvector corresponds to the constructive interference of travel time from slowness and reflector depth. This eigenvector matches the two-way travel time between model and data by equally adjusting the velocity and reflector depth. The second eigenvector corresponds to the destructive interference between slowness and reflector, or the velocity-reflector depth ambiguity. It has the smaller eigenvalue.

Figures 4.4a & b show the data space eigenvectors corresponding to these model space eigenvectors. These eigenvectors were derived from the **S**, **L**, & **D** matrices of the two-parameter model numerically using one CMP gather with 50 offsets. The first data space eigenvector is essentially the average of the travel times in the data set. The second data space eigenvector is the variation with offset of the data. It relates the hyperbolic moveout of the data to the correct reflector depth and velocity.

The magnitude of the eigenvalue of the second eigenvectors is a measure of the resolution of the reflector depth. It is plotted as a function of the maximum ray coverage of the two-parameter model in Figure 4.5. As could be expected, the eigenvalue is a strong function of the maximum angle available, ranging from 0.1 at 45° to 0.04 at 30°. For curved rays, this angle range of the rays is measured at the point of reflection. The general increase in velocity with depth serves to increase the angular ray coverage, which improves the resolution of the velocity-reflector depth ambiguity for the laterally-invariant case.

The factor w determines the weighting between the velocity and the reflector. Earlier, a value of 1.31 was used for w to equally weight velocity and reflector. Had a different value for w been chosen, say $w=0.1$, the eigenvalues would change:

$$\mathbf{S}^{1/2}\mathbf{L}^T\mathbf{D}\mathbf{L}\mathbf{S}^{1/2} = n \cdot p^2 \cdot \begin{bmatrix} 0.9284 & 0.2566 \\ .2566 & 0.0741 \end{bmatrix}$$

The eigenvectors and eigenvalues of this matrix are:

First Eigenvector: (0.963, 0.269) **eigenvalue= 1.000**

Second Eigenvector: (0.269, −0.963) **eigenvalue= 0.00297 .**

The square root of these eigenvalues are: **(1.000, 0.054)**.

The eigenvectors are now unbalanced: the first one has a greater

velocity component. This imbalance will bias the inversion to placing travel time deviations into slowness variations, a process observed through the modeling performed in Chapter 3. The eigenvalue has also decreased as a result of unbalanced weighting. This effect is analyzed in Figures 4.6a & b which are plots of the magnitude of the smaller eigenvalue as a function of the weight. Weight is defined as the proportion of the simulated path length in a reflector cell to the actual path length in a slowness cell for a *vertical* ray. Optimal weight is greater than 1.0 to compensate for the rays off vertical, which are affected more by velocity variations and less by reflector depth variations.

The plot demonstrates that velocity-reflector depth ambiguity has the largest eigenvalue when the weight is about 1.3 for a vertical ray, which will produce an equal net weight for reflector and velocity when all rays are considered. The eigenvalue is not very sensitive to the relative weighting. As long as the weighting is close to equal, this parameter should not be a serious concern.

4.6 Variance Analysis of a Two-Parameter Model

This eigenvalue of the velocity-reflector depth ambiguity enables a comparison between data variance and model variance. Essentially, for a given data accuracy, the eigenvalue is inversely proportional to the resolution of the model.

A "back-of-the-envelope" calculation of resolution is presented, followed by a more proper formulation. The larger eigenvalue, which equals just about 1.0, is related to matching the two-way travel time. For data accuracy of 4 milliseconds, with a fixed velocity of 7000 ft/sec, our resolution of reflector depth from the first data eigenvector alone is $1.0 \cdot \frac{0.004^{seconds} \cdot 7000^{\frac{feet}{sec}}}{2} =$ 14 feet. With the resolution being the inverse of the eigenvalue, the resolution from the second eigenvector, which has an eigenvalue of 0.1, would be ten times that of the previous eigenvector, or 140 feet. Net resolution is 154 feet. Taking into account redundant information from multiple-fold data and repeated CMP gathers per desired resolution of the velocity-reflector depth ambiguity, data accuracy could be significantly better by a factor of 10 or more, depending on the amount of redundancy and how systematic the noise is. For a more proper analysis of resolution, the eigenvectors of the data space must be analyzed.

The covariance matrices of model and data are related by (Aki & Richards, 1980):

$$< \mathbf{S}^{-1/2} \Delta\mathbf{s} \, \Delta\mathbf{s}^T \mathbf{S}^{-1/2} > \; = \; \mathbf{D} \sigma^2_{\Delta t} \mathbf{V} \Lambda^{-2} \mathbf{V}^T ,$$

where

$\sigma_{\Delta t}$= the variance of the data, Δt.

Using the results from the two-parameter model analysis for $\theta_{max}=45°$

and $w = 1.31$,

$$\mathbf{S} = 1.14 \cdot n \cdot p \cdot \mathbf{I},$$

and the approximation

$$\mathbf{D} = \left(2.31 \cdot p\right)^{-1} \cdot \mathbf{I}$$

gives us

$$< \Delta \mathbf{s}\, \Delta \mathbf{s}^T > = \frac{1}{2.31 \cdot p} \cdot \sigma^2_{\Delta t} \mathbf{V} \Lambda^{-2} \mathbf{V}^T \cdot \frac{1}{1.15 \cdot n \cdot p} .$$

The eigenvectors from before are:

$$\mathbf{V} = \begin{bmatrix} \sqrt{0.5} & \sqrt{0.5} \\ \sqrt{0.5} & -\sqrt{0.5} \end{bmatrix},$$

The eigenvalues are:

$$\Lambda = \begin{bmatrix} 1.00 & 0 \\ 0 & 0.107 \end{bmatrix},$$

These relationships produce:

$$\mathbf{V} \Lambda^{-2} \mathbf{V}^T = \frac{1}{2} \cdot \begin{bmatrix} \lambda_0^{-2} + \lambda_1^{-2}, & \lambda_0^{-2} - \lambda_1^{-2} \\ \lambda_0^{-2} - \lambda_1^{-2}, & \lambda_0^{-2} + \lambda_1^{-2} \end{bmatrix} = \begin{bmatrix} 44.2 & -43.2 \\ -43.2 & 44.2 \end{bmatrix},$$

It is clear that the variance is dominated by the smaller eigenvalue. The resulting generalized model covariance computed for the two-parameter model is:

$$p^2 < \Delta \mathbf{s}\, \Delta \mathbf{s}^T > = \sigma^2_{\Delta t} \cdot \begin{bmatrix} 16.6 & -16.3 \\ -16.3 & 16.6 \end{bmatrix} \cdot \frac{1}{n},$$

The factor of p^2 converts units of travel time into units of

slowness variation. We will ignore it and discuss model variance in units of two-way travel time.

The lower right value of the matrix is the covariance of the reflector depth in two-way travel time. Its resolution ($\sqrt{\text{variance}} \approx$ resolution) is approximated by:

$$\Delta s_{reflector} \approx \frac{4.0}{\sqrt{n}} \cdot \sigma_{\Delta t} ,$$

or in terms of the smaller eigenvalue

$$\Delta s_{reflector} \approx \frac{\lambda_{min}^{-1}}{2.3 \cdot \sqrt{n}} \cdot \sigma_{\Delta t} .$$

For fifty fold data, with a 45° maximum ray angle, 4 millisecond resolution in the data should resolve a reflector depth to 3 milliseconds, which is 10 feet in 7000 ft/sec media. Resolution for other maximum ray angles will be proportional to the inverse of the eigenvalue for the slowness-reflector depth ambiguity.

The author's experience in picking travel times gives him confidence that for a high quality data set, travel times can be picked to an accuracy of 4 milliseconds. The maximum ray angle available in a reflection survey off a reflector is very variable, depending on the cable length, reflector depth, the vertical velocity gradient, and the interference of other arrivals.

Even considering that fifty fold data may contain many fewer effective independent data points, the predicted resolution of this variance analysis of the velocity-reflector depth ambiguity is theoretically quite high.

This analysis demonstrates that potential exists in the raw data for a high accuracy resolution of reflector depth. However, other aspects, such as a laterally variant model, systematic errors in the data (e.g., anisotropy, 3D effects, inelastic effects), edge effects, and non-linearities are probably more serious factors than data accuracy with a travel time inversion.

4.7 SVD Results for the Generic Model

The two-parameter model is generalized to include lateral velocity variations with the two-dimensional generic model shown in Figure 4.1. The model now has the additional capability of varying the velocity laterally to match the effect of a reflector depth variation on the travel times of the rays. This additional capability enables the velocity to match the travel time variation with offset that it is unable to match in the laterally invariant case. As a result, the velocity-reflector depth ambiguity is less well-resolved than with the two-parameter model.

The generic model has 128 columns and 10 rows of square cells, and 128 reflector cells, giving it a model space of 1408. The velocity is

constant and the reflector is flat, so the ray paths are straight. The cable length is twice the depth to the reflector, so the maximum ray angle is 45°. A very dense reflection survey, (5 shots per cell width, 10 receivers per cell width), is modeled such that ray coverage can be considered to be essentially continuous.

The eigenvalues of this model are plotted in descending order in Figures 4.7a, b, & c. As predicted by Comer & Clayton (1985), all eigenvalues are between 1.0 and 0.0. Two distinct changes in the eigenvalue trend occur at the 128th and approximately 750th eigenvalue. The first group corresponds to the first eigenvector of the two-parameter model, which represents the constructive interference between slowness and reflector depth. There are 128 such eigenvectors because there are 128 reflector cells.

Examples of this first group of eigenvectors are presented in Figures 4.8a, b, & c. For each eigenvector, positive slowness variation overlays a positive reflector depth variation, and vice-versa. Each eigenvector represents one frequency of the 128 reflector cells, not surprising, since the model is circular and frequencies are naturally orthogonal to one another. The smaller wavelength models have their slowness components at the bottom of the model because this is the only region that shares the identical ray paths with a small region of the

reflector.

To analyze the resolution of the reflector depth, the fraction of the eigenvectors that lies in the reflector aspect of the model is plotted vs. the eigenvalue of the eigenvector in Figures 4.7d & e. Those reflector components in eigenvectors with very small eigenvalues cannot be inverted.

The group on the far right with the greatest eigenvalues is the same group of 128 eigenvectors in the previous figure that contains constructive interference between velocity and reflector depth. Below this group down to an eigenvalue of about 0.1, none of the eigenvectors contain any significant component in the reflector. This group corresponds to the middle group of Figures 4.7a, b, & c between eigenvalue 129 and about 750. The eigenvectors of this group consist of patterns of velocity variations that are uncoupled with reflector variations. Examples are shown in Figures 4.9a-d.

Below an eigenvalue of about 0.1 on Figure 4.7d, there are two groups: those that have reflector components and those that do not. Both groups continue off the left edge of the plot. The left edge, at an eigenvalue of 0.02, is considered to be the lowest eigenvalue that can be realistically inverted under favorable conditions. The same plot appears on another scale in the subsequent Figure 4.7e.

The group of eigenvectors with significant reflector energy at very small eigenvalue corresponds to the second eigenvector of the two parameter model, the one of the velocity-reflector depth ambiguity. The destructive interference between the velocity and reflector depth of this group is apparent in Figure 4.7f, where the correlation of the reflector variation with the column of slowness above it is plotted against eigenvalue. Examples of the eigenvectors in this group are shown in Figures 4.10a-p.

The eigenvalue derived from the two-parameter model of the velocity-reflector depth ambiguity eigenvector is 0.1, which is the upper limit of the corresponding group from the generic model in Figure 4.7f. However, the eigenvalues decrease significantly below 0.1 for other eigenvectors of the group and are too small to be resolved. Thus, many components of the velocity-reflector depth ambiguity cannot be resolved for this model which allows complete lateral variations of velocity from the surface down to the reflector depth.

The other group of eigenvectors with very small eigenvalues contains no reflector component. This group is similar to a previous one whose eigenvectors consisted of velocity variations that are not coupled with reflector variations. Clearly, the patterns of velocity variation are quite different. Eigenvector examples of the second group are shown in

Figures 4.11b-j. In Figures 4.7g & h horizontal wavenumber is plotted vs. the vertical wavenumber for each group. The two plots do not overlap. The eigenvectors of the group with larger eigenvalues all have vertical wavenumbers smaller than the horizontal one, which corresponds to the vertically-oriented structure. The other group has the reverse. The group with the lower eigenvalue represents the unresolved aspects that cause vertical smearing from the limited angular ray coverage, shown in Chapter 3 not to affect migration. Thus, these eigenvectors of this group are not a serious concern.

The two eigenvectors in Figures 4.11a & b demonstrate the boundary between the groups. They appear to be identical, yet have a significantly different eigenvalue. The only difference between the two eigenvectors is that the one with the larger eigenvalue contains 10 wavelengths across while the other contains only 9. The angle of the diagonal structure of first figure is just below the 45° maximum ray angle of the data; the other figure is just above the boundary.

The most obvious feature of each eigenvector is that it contains a unique horizontal wavenumber. Wavenumber is plotted against the eigenvalue in Figures 4.7i & j. The plot of only those eigenvectors with measurable reflector components in Figures 4.7k & l shows that in the first group with the highest eigenvalue, the eigenvalue decreases

monotonously with decreasing wavelength. This was observed in the eigenvector Figures 4.8a, b, & c.

More interesting, however, is the wavenumber pattern for the group of eigenvectors corresponding to the velocity-reflector depth ambiguity. Figure 4.7l shows the eigenvectors with a very low wavenumber to have an eigenvalue near 0.1. In fact, the 0 wavenumber plots very near 0.1, the result for the laterally invariant two-parameter model. The eigenvalues decrease for a slightly larger wavenumber and have a minimum of 0.006 near a wavenumber of 5. Above this wavenumber, the eigenvalue increases monotonously back to 0.1.

A simple *gedanken* experiment demonstrated with Figure 4.12 shows that shorter wavelengths of reflector variations cannot be better resolved than longer ones. Thus, the entire branch above wavenumber 5 of this trend in Figure 4.7l is an artifact from the finite cell sizes used. The "gedanken" experiment proceeds as follows: If a given eigenvector is shrunken in size, additional slowness field exists above it up to the earth's surface. If the additional slowness field is not allowed to vary, the reflector depth would be equally well resolved as before, since nothing has effectively changed. But when the additional slowness field is allowed to vary, it can aid the original slowness field in imitating the travel time signature of the reflector variations. Thus, the shrunken

reflector variations cannot be better resolved than they were beforehand. Smaller reflector variations must have smaller eigenvalues. Results counter to this trend must be a consequence of finite cell sizes.

This *gedanken* experiment is supported with the tomographic inversions of the velocity-reflector depth ambiguity in Figures 3.46g-i in Chapter 3. Tomographic inversion is able to use much smaller cell sizes than SVD. The modeling results show no increase in the resolution of the smaller reflector structures.

Thus, all but the very long wavelengths of the velocity-reflector depth ambiguity, those below 3, are effectively unresolved for this case without constraints. For this model, a wavenumber of 3 corresponds to a wavelength 4 times the depth to the reflector, or twice the cable length for a maximum ray angle of 45°.

These eigenvectors with a small eigenvalue do not indicate that the reflector structure cannot be resolved, only that it cannot be resolved from the related velocity pattern. To resolve the velocity-reflector depth ambiguity for small wavelengths requires constraining the unresolved eigenvectors by defining their velocity component *a priori*. Analysis of the eigenvectors in Figures 4.10e-p indicates that they do not correspond to common geologic structures. Velocity variations are unlikely to occur just above a reflector.

So as to implement the narrowest possible constraints, it would be useful to characterize the velocity patterns that are ambiguous with reflector variations accurately . No analytic formulation was developed here to achieve this characterization. All the relevant eigenvectors of the velocity-reflector depth ambiguity are plotted so that the reader can empirically develop his or her own characterization. The small number of these eigenvectors is a result of the small model size that could fit on a CRAY-2.

The plot in Figures 4.7m & n of the horizontal wavenumber vs. eigenvalue for those eigenvectors without significant reflector components reveals interesting patterns. There appear to be 10 branches that are horizontal and then swing up and back, which may be related to the 10 slowness cells down to the reflector. The plot is subdivided in Figures 4.7o, p, & q, according to the vertical wavenumber. Trends appear, but their meaning is not entirely clear. A vertical wavenumber does not have a clear meaning for a model with only 10 vertical cells.

In the Appendix, SVD is performed on numerous variations to the generic model in an attempt to determine the sensitivity of various parameters on the velocity-reflector depth ambiguity. Results indicate that reflector resolution is reduced by a shorter cable length, a smaller cell size, and a vertical velocity gradient. Velocity constraints, damping

of small horizontal variations, and a second reflector improve reflector resolution. An example with a different cell size confirms that cell size corrupts the results. Models with different lengths show no indication that the results are corrupted by wrap-around. SVD is also performed on a pure transmission geometry simulating a cross-hole geometry.

4.8 SVD Results for a Model with Edge Effects

A model without the wrap-around of the rays was used for SVD analysis to analyze the effect of the edges upon model resolution. A single-sided spread was modeled where the shot was to the left of the receivers. Figure 4.23 shows the data collection geometry. Therein, the shot started at the left edge of the model and was stopped a cable length from the right edge so that all the rays remained within the model. With this geometry, the left edge contains only vertical rays, while the right side contains only far offset rays. The bottom right hand corner will contain no rays.

The eigenvectors are no longer as "clean" as for the circular models. Sample eigenvectors shown in Figures 4.24a-j and Figures 4.25a-g have a mixing of several frequencies in one eigenvector. The eigenvectors are in two groups: The first in Figures 4.24a-j are largely unrelated to the edges, and should be similar to the eigenvectors of the generic circular model. The second group, Figures 4.25a-g, are

eigenvectors that are related to the edges.

It is this second group that may indicate how the limited coverage at the edges is related to the rest of the model. Of particular interest, is whether the structure near the edges can affect the more central part of the model. Presumably, eigenvectors that contain significant components at the edges and near the center demonstrate that the two areas are connected and that one can affect the other. Analysis of these eigenvectors shows that the edges are connected only to velocity variations away from the edges but not to reflector variations. Since the reflector variations are the ones of interest, these results indicate that edge effects are not serious. These results, particularly the three eigenvectors in Figures 4.25e, f, & g, are consistent with the modeling results of Chapter 3, which showed that velocity variations near the center of the model cause serious artifacts at the edges, but that variations at the edges did not affect the reflector positions near the center.

Characteristics of the eigenvectors, plotted in Figures 4.26a-i, do not show the clear trends seen earlier. Figure 4.26a has lost some sharpness but still displays the inverted "V." Figure 4.26d shows that non-wrap-around eigenvectors with wavenumbers of 3-8 do not have eigenvalues greater than 0.015. Some of the corresponding eigenvectors

with wrap-around in Figure 4.13b have significantly larger eigenvalues.

The fraction of each eigenvector in the reflector and its correlation with the column of slowness above it, shown in Figures 4.26e & f, do not show the clear trends as the corresponding Figures 4.7d & e with wrap-around, but many features are consistent. The eigenvectors near an eigenvalue 0.2 again do not contain any reflector components. Similar to previous results, the correlation between slowness and reflector shows that the eigenvectors with constructive interference between velocity and reflector have large eigenvectors, while those related to the velocity-reflector depth ambiguity have small eigenvalues, many too small to be inverted.

The plot of the proximity of the eigenvector components to the edges in Figures 4.26h & i is produced by summing the elements weighted with a value of 1.0 at the edges, with -1.0 in the center, and a linear slope for the ones in between. Eigenvectors with large components at the edges are in two groups, one near an eigenvalue of 0.2 and the rest below 0.005. These two groups result from the limited angular ray coverage at the edges and are similar to the two eigenvectors of the 2-parameter model.

4.9 Conclusion

SVD analysis determines that the velocity-reflector depth ambiguity is unresolved for all but the very long wavelength variations when the velocity is given total freedom to vary. However, the ambiguity can be partially resolved with the use of constraints to remove some degrees of freedom of the velocity. The absolute resolution possible is strongly dependent upon the maximum ray angle in the data. A careful quantitative study is hindered by the inability to perform SVD on a properly-sized model.

The best indication of the potential of the constraints in solving the problems of Travel Time Tomography is demonstrated through real data applications, two of which are presented in the following chapter.

Chapter 5

Application of Tomography to Two Data Sets Containing Lateral Velocity Variations

5.1 Abstract

Two potential applications of tomography to surface reflection data are: 1) the resolution of a velocity-reflector depth ambiguity, and 2) the determination of an accurate velocity model for migration. Resolution of the velocity-reflector depth ambiguity is necessary to properly map a horizon's depth and to locate the structural high. Accurate velocities are needed for migration to produce high-quality images underneath velocity variations.

Each of these applications is tested on a data set. Resolution of the velocity-reflector depth ambiguity is tested on data over permafrost variations from the North Slope of Alaska. The accurate determination of velocity for migration is tested on data over a gas seep in the Central Valley of California. Tomography was successful in both applications, but only with careful application of the technique. The resolution of the results is checked with a variety of methods.

5.2 Introduction

It is the application to data that serves as the real test for the potential of Ray Trace Tomography. Synthetic examples cannot model the numerous physical processes that affect field data, and they cannot mimic some practical aspects of

implementing the technique. The application of tomography to data will indicate the usefulness in various geological regions and the seriousness of the theoretical and practical problems.

Two data examples are presented for problems where tomography has the potential for making a significant impact: 1) depth resolution of horizons under permafrost variations and 2) locating gas pockets and removing the distortion they cause on the section. These two examples are representative of the two types of broader potential applications of tomography: 1) the resolution of velocity-reflector depth ambiguities to accurately determine reflector depth, and 2) the determination of an accurate velocity model for migration and/or stacking, which enables the production of a sharp image with high frequency content.

Knowledge of the accuracy of the result is vital for interpreting it. Several methods for determining the resolution of the results are applied.

5.3 Description of North Slope Data

Figure 5.1 shows the processed seismic line of the survey over permafrost in the North Slope. An ice lake, unfrozen water because of a high concentration of salts, which is a strong slow-velocity anomaly, is known to be near CMP 475. Even though surface static corrections have been applied, a broad slump of the reflectors appears underneath the ice lake. The goal of tomography is to determine whether this slump is indeed real or is an artifact of statics.

A comparison of the near and far common offset sections in Figure 5.2 shows the effect of the ice lake on prestack traces. The near offset section contains

a narrow slump. Of the two slumps in the far offset section, one results from the shots being over the ice lake, the other results from the receivers being over the ice lake. Between the two slumps, the rays undershoot the ice lake and avoid its slow velocity. The broad slump in the stacked section is absent in both common offset sections.

Analysis of the two common offset sections indicates that the broad slump is indeed an artifact of the application of statics to the ice lake effects. Thus, our objective has essentially been achieved. However, it is difficult to use this qualitative knowledge in processing. The migration still needs an accurate velocity field containing the ice lake anomaly. Moreover, in other cases it is not so simple to resolve the objective. For example, in this case there may be other reflector artifacts from smaller variations in the permafrost that are not readily apparent. This data example, where the answer in known, serves as a test of whether tomography can resolve an ambiguity between permafrost velocity and reflector depth that statics cannot.

5.4 Inversion Procedure for North Slope Data

For the first data set, travel times of 126 shot gathers were picked from the two reflectors marked in Figure 5.13, one at 1.0 seconds and one at 1.3 seconds. For the lower reflector, travel times off all 48 traces could be picked; for the upper reflector the mute removed the arrivals on the far offset traces. Travel times from only the 30 near-offset traces could be picked. For both reflectors, the maximum ray angle available is approximately 30 degrees. After editing of bad picks, 8300 remained. Examples of the picks are shown in Figures 5.3a, b, & c.

Travel time picking and careful editing took about 16 hours on a 3D interactive work station provided by Arco in 1985. The work station had some auto picking capability and allowed analysis of the data in all possible sections: common offset, common shot, and common midpoint.

The reference velocity model varied only with depth and was determined from CMP velocity analysis. The reference reflector positions were mostly picked from the migration of the near offset traces through the reference velocity model. The reflector was assumed to be flat across the slump artifact from the ice lake. Figure 5.4 shows the reference model used for ray tracing. Ray coverage of the survey in the reference model is shown in Figure 5.5.

The travel time variations between data and the model in Figure 5.6 clearly demonstrate the effect of the ice lake on travel time variations.

The discretized model contains 400 cells in the X direction and 60 cells in the Z direction. The square cells are 110 feet square, half the receiver and shot spacing. In retrospect, the cell size could have been doubled, but the small size was chosen so that the resolution would not be limited by a decision this early in the process. Cell size must be an integral number of receiver spacing so that the grid can be easily used for migration. The **L** matrix has 8300x400x60 = 200 million elements. Strong damping of small-scale variations during the inversion avoided effects of an over-parameterized model.

Rays were traced using the method of Langan et al. (1985) from the source off the reflector to within 5 feet of the receiver location. The Dines & Lytle (1979) back-projection technique with the application of Chebyshev acceleration factors developed by Olson (1986) was used for the inversion. Both of these techniques

are described in Chapter 2. The back projections of both models were performed with a damping factor of about 20% of the average ray density. To reduce the effect of erratic picks, travel time deviations greater than 0.01 second from the final result were discarded.

5.5 Inversion Results of North Slope Data

Two inversions of the North Slope data set are shown in Figures 5.7a & b. The inversions were performed with the constraint that allowed velocity variations only in the permafrost layer.

The two inversions are performed with opposite bias to address the question of the ambiguity between velocity and reflector depth. A biased inversion attempts to match the data with only one part of the model, the velocity or reflector, and adjusts the other parts only if necessary. The velocity-biased inversion is achieved by first attempting to fit all the travel times by adjusting only the velocity. Then both the velocity and reflector are allowed to vary to fit that portion not explained by allowing only velocity variations. The reflector-biased inversion does the reverse. Any difference between the two biased inversions represents the velocity-reflector depth ambiguity that could not be resolved by the data over that eigenvalue range.

Similarities and differences between the two biased inversions in Figure 5.7a &b are apparent. To better compare the two inversions, they are subtracted with the result shown in Figure 5.8. The subtraction shows that the velocity-reflector depth ambiguity for these inversion parameters consists almost entirely of long wavelength components. The fact that the intermediate and short wavelength

aspects of the inversions are well-resolved is a result of the constraint that did not allow the velocity to vary below the permafrost layer.

To confirm that the unresolved velocity-reflector depth ambiguity is indeed the result of the ice lake, a sample ice lake of Figure 5.9a is inverted. The result in Figure 5.9b matches that of Figure 5.8 very well. Thus, to resolve the ambiguity, one would have only to make a geologic assumption concerning the ice lake and no other portion of the model. This exercise has helped to indicate the constraints that are necessary to resolve the ambiguity.

The broad, unresolved feature is bothersome at this point since it is the main objective of this study. We would prefer to resolve it without any assumptions. Theoretical results in Figure 4.5 of Chapter 4 suggest that the eigenvalue range of the very long wavelength velocity-reflector depth ambiguity is (0.04-0.02) for the maximum ray angle of about 30^{o} of the data. To attempt to resolve the long wavelength velocity-reflector depth ambiguity, the two biased inversions are carried out to smaller eigenvalues of 0.02 and 0.01. The subtractions of the two biased inversions are shown in Figure 5.10a & b. The amplitude of the velocity-reflector ambiguity has been reduced over the eigenvalue range of (1.0-0.02) and has been nearly eliminated over the range of (1.0-0.01). Thus, the velocity-reflector depth inversion has been resolved by inversion to a smaller eigenvalue.

Carrying out the inversion to such a small eigenvalue may increase the effects of data noise to serious levels. To address this concern, the travel times are split into two separate groups such that each group contains every other shot gather. Without sharing any common data points, the two groups represent independent

data sets. A comparison of the inversions of each set is a measure of the noise in the data.

The two inversions are performed over the ranges of (1.0-0.05) and (1.0-0.01) and then are subtracted from each other. The subtractions are plotted in Figures 5.11a & b. Since each data set contained only half the original data and the results were subtracted, these figures represent a generous upper bound of the effect of random noise and shot coherent noise in the data. To amplify the effect of the noise on the reflectors, the inversions are performed with the reflector bias described above. The figures show that the effect of random noise on the inversion is not serious over the eigenvalue ranges used.

The amplitude of the reflector variations does not increase in the inversion to smaller eigenvalue inversions because of the initial reflector bias of the inversion. The inversions to a smaller eigenvalue trade off reflector variations into velocity variations, which offset the natural increase of the reflector variations when inverting to a smaller eigenvalue.

In contrast to the velocity-reflector ambiguity, the random noise causes mostly high-frequency errors in the reflector position. Thus, with these velocity constraints, the optimal range of eigenvalues to invert is dependent on whether the main objective is the resolution of the long frequency reflector variations or the short ones. To resolve short reflector variations, the inversion is not taken to a small eigenvalue since the velocity-reflector depth ambiguity is resolved early to avoid the more serious effect of noise. Inversions for broader scale variations must be taken to a smaller eigenvalue to resolve the velocity-reflector depth ambiguity and are not affected as much by noise.

The long wavelength feature that crops up in Figure 5.11b is a bothersome component and may indicate other problems. The change between carrying out the velocity-biased inversion from an eigenvalue of 0.02 to 0.01, shown in Figure 5.12, is dominated by this component. It is of large amplitude and seriously affects the inversion. The reflector-biased inversion has the identical feature. Thus, the inversion has indeed been corrupted by continuing to a too-small eigenvalue.

The feature is assumed to be an artifact from spurious data points at the edges of the model. Data quality at both edges of the model was poor and created strong edge effects. This artifact could probably be controlled by removing the data points, or by simply removing one wavelength component.

5.6 Description of Central Valley Data

The seismic line of a survey over a gas seep in the Central Valley of California is shown in Figure 5.13. The effect of the gas seep is apparent as the region where the shallow reflectors have a significant slump and the deep reflectors are washed out. The purpose of tomography will be to calculate an accurate velocity model to input into prestack migration. The resulting migration should image the reflector underneath this velocity variation.

This data example simulates a production situation where the main objective is not the accurate resolution of reflector depth, but attainment of the sharpest migration possible, rich in high frequencies, to perform a detailed analysis of a reservoir.

This data example was also used in the thesis by John Toldi (1985).

5.7 Inversion Procedure for Central Valley Data

For the Central Valley data set, approximately 29,750 picks were taken off the five reflectors marked in Figure 5.13. With a cable length of only 1850 feet, the maximum ray angle for the lower reflector was only 27°. The maximum ray angle for the upper reflector was near 45°, but the picking proved to be difficult at the far offsets, where several arrivals, some possibly being refractions, would join and overlap. Figures 5.14c & d are examples of this problem. In retrospect, many more picks from these upper reflectors should have been discarded. The picking of travel times was performed on an interactive work station using software written by John Toldi. The picking took about 5 days, which is little time compared to other aspects of implementing tomography. All picks were reviewed for accuracy.

The reference velocity model is laterally invariant. The gradient with depth is taken from the reference model used by Toldi (1985). The reference reflectors were flat with depths computed using the reference-velocity model. The ray coverage of the data is shown in Figure 5.15.

The model for the Central Valley survey had 275x40 cells 135 feet square, which was the shot and receiver spacing. Later smoothing during the inversion made the effective size approximately 3 times larger. The L matrix has 275x40x29750 = 327 million elements.

5.8 Inversion Results of Central Valley Data

A preliminary inversion is performed to guide the result based on certain geologic assumptions. First, on the assumption that the gas pocket anomaly is the

dominant feature, the velocity near the presumed position of the gas pocket is inverted. Then, based on the assumption that most of the remaining travel time variations are the result of large wavelength errors of our flat reference reflectors, we invert for broad scale reflector variations and constant velocity changes in the layers. The result of this preliminary inversion is presented in Figure 5.16. It will be used as input to the following inversion but without the retracing of the rays.

Figure 5.17 shows the inversion to a very small eigenvalue without constraints. Many of the velocity variations are undoubtedly the artifact of unresolved velocity-reflector depth ambiguities, which cannot be resolved for such a narrow ray angle without the use of constraints. In retrospect, perhaps a reflector-biased inversion should have been performed that allowed greater reflector variations than the preliminary one performed above. These artifacts are not considered serious since the objective is not the correct determination of reflector depth, but the sharp imaging of the migration through the velocity model.

Figure 5.18 shows the prestack migration through the velocity field of the inversion in the previous figure. The reflectors underneath the gas seep are now imaged, and the break in continuity of the reflectors has been healed.

The fact that the upper reflectors now have a lower amplitude than in the original section in Figure 5.12 is the result of two possible factors: 1) the migration is plotted in real amplitude without AGC, and 2) the travel time picks for the upper reflectors may be seriously corrupted. The lower reflectors may have increased in amplitude so much that the relative amplitude of the upper ones have been reduced. The sample travel time picks from the upper reflectors shown in Figures 5.13c & d show potential problems with two arrivals merging into one.

To compare this migration with another possible result, an inversion is performed that allows only the velocity to vary, not the reflectors. The motivation for this inversion is to test whether including the reflector depths aided the solution even though the velocity-reflector depth ambiguity could not be resolved in the previous inversion.

Figure 5.19 shows the inversion result. The prestack migration through the velocity field of the inversion is shown in Figure 5.20. All the reflectors are nearly perfectly flat, as they were in the reference model. This result is not surprising since the velocity model was adjusted to match the reference reflectors.

As before, migration has imaged the reflectors underneath the gas pocket. Figure 5.21 compares this migration with the previous one by plotting the energy in each trace of the migrations. Migration through the velocity-only inversion is uniformly lower than the migration through the inversion for both velocity and reflector depth. This lower energy results from weaker constructive interference of the data from the traces. Since this effect increases with greater frequency, the migration through the velocity-only inversion will be deficient in high frequency content.

Comparison of the energy of the migration indicates that the combined inversion for velocity and reflector depth has produced a better velocity model for migration.

5.9 Conclusion

The inversion of the North Slope data set produces mixed results. The velocity-reflector depth ambiguity has been resolved through the use of constraints, but corrupts the result by noise at the edges. The inversion must be performed very carefully. The objective can be achieved with only very careful application of constraints.

For the Central Valley data, a velocity model was produced to image effectively the reflector underneath the gas seep.

Conclusion

Travel Time Tomography is an efficient ray-based method for using the information of transmitted waves for determining broad scale velocity features, those larger than the wavelength of the seismic signal. The technique has promise for solving some of the basic problems of surface reflection seismology, such as the velocity-reflector depth ambiguity and the determination of an accurate two-dimensional velocity model for migration. However, this technique has many shortcomings that seriously distort the inversion if implemented without some form of guidance. An inaccurate reference model, (especially one with small scale reflector inaccuracies), the inability to resolve between ambiguous velocity and reflector depths, spurious travel time picks, narrow reflection surveys, anisotropy, and three-dimensional effects all serve to compromise the result by producing artifacts.

The travel time transmission technique can presently be of use in simple areas where a clear, well-defined objective exists that is uncompromised by the problems of picking travel times, corruption by artifacts, and choosing an accurate starting model.

Most of the shortcomings are not particular to this implementation using travel times and ray paths, but are inherent to surface reflection seismology. The travel time and ray-based method is instructive for demonstrating the characteristics of transmission techniques in general.

Whether the artifacts can be controlled is dependent upon what concrete geologic information is available and whether they can be applied as constraints in the inversion. It is apparent that successful application of transmission tomography to reflection seismology involves many subjective decisions that only a person can make--not a computer. Creativity and insight is necessary to identify artifacts, input geologic information to control artifacts, choose a starting reference model, pick and edit data, and choose parameters to execute complex computer programs.

These abstract decisions may be difficult to make, but represent the potential of tomography. Use of a flexible technique that can be adjusted to individual situations is required to realize the full information available in seismic data.

Appendix

Additional Examples of Non-linear Effects from Velocity

The inversion in Figures 3.21g and 3.21h are identical to the inversions of Figures 3.21c and 3.21f except that the maximum ray angle of the reflection survey is only 25^{o} rather than 45^{o}. As expected with the more limited angular ray coverage, the images are smeared more vertically. However, the migrations through the inversions, shown in Figures 3.29 & 3.30, are no worse than the migrations through the 45^{o} inversions. In fact, the migration after four ray tracings and inversions appears to be better, especially under the lowest slow velocity block. This less serious non-linear effect could be attributed to vertical rays being less affected by horizontal velocity blocks than wide angle rays. Despite these results, the reader is cautioned not to assume that the smaller maximum ray angle is more advantageous. Using a smaller maximum ray angle produces less raw data. This example had the luxury of perfect data and the correct reflector was used for these examples.

Two inversions are performed to address the errors in the inversion of the velocity field caused by ray path errors from incorrect reflector position. The original model with the horizontal blocks is inverted using reference models with constant velocity, but non-flat reflectors. The modeling procedure will not allow the false reflector positions to affect the travel times or the velocity to affect ray paths, so that the artifacts from wrong reflector positions affecting the velocity inversion are isolated. The first reference model, in Figure 3.21k, contains a

sinusoidal reflector with relatively long wavelengths, which are meant to mimic broad, structural interpretation errors. The second model, in Figure 3.21l, contains the smaller scale reflector variations that would have been chosen from the constant velocity depth migration of Figure 3.24. It is meant to mimic small scale structural errors. The effect of these reflector structures on the ray paths is shown in Figures 3.22c & d. The inversion results are presented in figures 3.21m & n.

The inversion of the upper blocks is affected less by the incorrect ray paths than the lower blocks. This result can be expected since the reference ray paths deviate from the actual rays less near the top of the model and more at the bottom at the model. Also, some artifacts appear near the bottom of the model just above the reflector. In general, these types of mild reflector inaccuracies have not significantly affected the inversion of the velocity variations. Migrations through the inverted velocity fields in Figures 3.31 & 3.32 show some artifacts.

An inversion of horizontal velocity blocks with larger velocity variations is performed in Figures 3.33. The velocity variations are +/- 3000 ft/sec rather than +/- 1000 ft/sec. As before, the non-linear effects of the inversion cause the fast block to be wider than it should be, while the slow block is thinner. Additional ray tracing and inversions improve the artifacts, but do not eliminate them completely. Analysis of the ray paths in Figures 3.34 shows how very few of the vertical rays and none of the wide angle rays traverse the slow velocity block. The rays are strongly attracted to the fast velocity block.

The migrations through the inversions demonstrate that the slow velocity block has been poorly inverted, even after three ray tracings and inversions.

Without any rays even traversing the slow velocity block, especially at the edges, one cannot expect to properly resolve it.

As in earlier examples, the inversion of the fast velocity block causes less of an artifact on the migration than the slow one. The additional ray tracings and inversions significantly improve the artifacts, but not entirely.

It is not expected that all of the non-linear artifacts will be ever removed with additional ray tracings and inversions. The ray paths through a smeared velocity is not identical to that in the true model. The vertically smeared velocity variations will not be able effect the wide angle ray paths as much as the true velocity variations do in Figure 3.34b.

Although the ray coverage and velocity variation is identical at both edges of the fast velocity block, the migration through the inversion is not symmetric in Figure 3.37. This non-symmetry most likely results from ray tracing error and demonstrates the sensitivity of the results on small numerical factors of the ray tracing code.

The non-linear effects of velocity variations with non-horizontal orientation are investigated in Figures 3.38. The first inversion shows the typical fattening of the fast velocity anomalies and thinning of the slow ones, but the effect appears to be more pronounced than with the horizontal variations of the previous models. Additional ray tracings and inversions appear to almost entirely remove this effect to produce a result that appears highly accurate, at least in the shape of the velocity variations. For vertical velocity variations, the vertical smearing is minimal.

However, the migrations through the inverted velocity fields contain significant artifacts under the vertical velocity blocks. The additional ray tracings and inversions do not significantly improve the migrated image under the vertical velocity blocks. Analysis of the ray paths in Figures 3.39 shows that they are more significantly distorted than the velocity blocks of equal magnitude and depth but horizontal orientation of Figure 3.22a & b. No rays cross the slow vertical block, but some do cross the slow horizontal block. Velocity variations oriented vertically have a greater effect on ray paths and cause more significant non-linear effects. These non-linear artifacts apparently cannot be corrected with additional ray tracings and inversions.

Even though the inversion of the vertical blocks appears better than the horizontal block inversion, it is worse because it does not have the proper amplitude and significantly distorts the subsequent migration. This deception underscores that migration is generally a better test for the success of tomographic inversion than the velocity field itself. The visual comparison of velocity fields is a qualitative analysis while migration through the velocity field is a quantitative analysis.

The blocks oriented 45^{o} represent an intermediate case. They are inverted better than the vertical blocks, but worse than the horizontal blocks. Most important, however, is that the additional ray tracings and inversions do seem to remove most of the artifacts from the migration. As seen earlier, the fast velocity block is inverted better than the slow one.

A large, strong velocity contrast in Figure 3.43a is used for the analysis of velocity induced non-linearity. The true model used for data collection contains a

large wedge shaped region of velocity 11000 ft/sec in a background velocity of 8000 ft/sec. The border of the velocity region is vertical on one side and low angle on the other side. The model used for ray tracing is a plain model with constant velocity of 8000 ft/sec and the same flat reflector as the true model.

The inversions in Figures 3.43d, e, & f produce a result that does not resemble the velocity variations of the true model. It seems that the velocity variations have concentrated in certain areas at the expense of others. Inversion to smaller eigenvalue worsens the artifacts. An additional ray tracing and inversion has not improved the non-linear artifacts.

The velocity variations of the inversion results, some of which go off the high end of the scale at 13000 ft/sec, are geologically unreasonable. It is clear that this inversion needs some guidance, such as knowledge of the characteristic velocity of the rocks in the area. An imposition of a maximum allowed absolute velocity would discourage the concentration of the velocity variations into concentrated regions and would produce a more uniform and correct result. A more uniform image will effect rays less and subsequent inversions may further improve the non-linear effects. Such a maximum limit constraint is not easy to implement with the Tchebychev acceleration factors and was not attempted.

Additional Examples of Velocity-Reflector Depth Tradeoff

To attempt to better resolve the velocity block on the right side of the model in figure 3.48a than the inversion in figure 3.48e, the inversion is repeated with a second, deeper reflector at 9000 feet. Ray paths off of both reflectors are used for the inversion. Since the cable length remains unchanged, the angular ray coverage for the lower reflector will be only about half the 45º angular ray coverage for the upper reflector. The reference model and true model are shown in Figures 3.48f & g respectively.

The inversion in Figure 3.48h over the limited eigenvalue range contains the same artifacts as before. But the inversions to smaller eigenvalues shows considerable improvement of the right side of the model. The addition of rays off of a second reflector has significantly aided the inversion. Artifacts of very short wavelength remain in the reflector position. However, these artifacts are not symmetric around the velocity blocks as they should be. It appears that they are the result of ray tracing errors.

The inversion with two reflector is repeated with the use of a constraint that does not allow the velocity below the first reflector to vary. This constraint would be valid if one knew the horizon to be uniform based on outside geologic information. The artifacts in Figure 3.48k & l are somewhat less than in Figure 3.48i & j, but the overall difference between the inversions is not very significant.

In the inversion of the narrow reflector bump in Figure 3.46l, a velocity constraint that did not allow the velocity to vary in the lower third of the velocity model was added to resolve the velocity-reflector depth ambiguity. To analyze the consequences from when these constraints are applied when not justified, they are

applied to the inversion in Figures 3.48m & n. These constraints do not harm the left side of the model where the original velocity blocks are above the constraints. However, in the center and the right side, serious reflector artifacts are created by the incorrect constraints.

To further focus on the velocity-reflector depth ambiguity, the inversions in Figures 3.49 are performed on a model with a narrow and a broad velocity variation at the bottom of the field. The inversion of the narrow velocity variation hardly changes from the first inversion to the inversion to smaller eigenvalues. However, the broad velocity variation changes significantly from the first inversion in Figure 3.49b to the smallest eigenvalue in Figure 3.49f. It appears that most of the broad aspects are already inverted in the inversion to the eigenvalue of 0.10 in Figure 3.49c. Further inversion seems to sharpen up the reflector artifacts, but the effect is minor. The results indicate of the boundary between the longer resolved wavelengths that the velocity-reflector depth ambiguity and the shorter unresolved ones is of wavelength about the depth to the reflector.

Repeating the inversion with an increased velocity emphasis changes the bias between velocity and reflector, but does not improve the resolution of the velocity-reflector depth ambiguity.

When a second reflector is added to the inversion, the reflector artifacts are reduced significantly, as seen in Figures 3.49i & j. The non-symmetry of the reflector artifacts, attributed earlier to ray tracing inaccuracies, is again present. The lower reflector contains some subtle but broad artifacts.

SVD Results for Variations to the Generic Model

SVD is performed on numerous variations to the generic model in an attempt to determine the sensitivity of various parameters on the velocity-reflector ambiguity. The results are not as clear and enlightening as could be hoped for because of the discretization effects from the large cell sizes used.

Figures 4.13a & b demonstrate that increasing the velocity-reflector weight to a factor of 4:1 does not significantly effect results. These figures are included for comparison with subsequent SVD's which all use this 4:1 weight of velocity to reflector.

In an attempt to better resolve the velocity-reflector depth ambiguity, a strong vertical velocity model was used in Figures 4.14a & b. The gradient curves the rays with depth increasing the angles of reflection at the reflector. With the same cable length as before of twice the reflector depth and a gradient that doubles the velocity from the surface to the reflector, the maximum angle of reflection increases from 45° to almost 60°. The plot of the horizontal wavenumber versus eigenvalue produces a slightly different pattern, but the eigenvalues for the velocity-reflector depth ambiguity in Figure 4.14b are not improved. The eigenvalues for the laterally invariant low wavenumbers are greater than for corresponding Figure 4.13b, but others appear to be smaller. The reason the smaller wavenumbers have smaller eigenvalues than for

the constant velocity case is unknown.

In a further attempt to improve the resolution of the velocity-reflector depth ambiguity, a constraint is imposed to not allow any velocity variations in the lower half of the model. This reduces our model size from 128 $\times$ 10 velocity cells to 128 $\times$ 5. Figure 4.15d show the eigenvalues corresponding to the reflector components of the eigenvectors. The identical figure for the generic model is 4.7d. The constraints have moved most of the reflector components to higher eigenvalues, but some still exist with low eigenvalue. The clear trends that identify separate groups of eigenvectors in Figure 4.7d are obscured in Figure 4.15d. Figure 4.15e of the correlation of the reflector variation with the slowness column above shows that both positive and negative values overlap in the high eigenvalue region unlike in Figure 4.7f for the generic model.

Figures 4.15b & c demonstrate that it is the high wavenumber components that are very well resolved. This result is expected since the high wavenumber reflector variations are most strongly coupled with velocity variations just above the reflector, which are removed with the constraints. The smaller horizontal wavenumbers appear to be only slightly better inverted with some eigenvalues still having values near 0.01. Thus, this constraint has not totally resolved all the velocity-reflector depth ambiguity.

The effects of using a shorter cable length, shown in Figures 4.16a & b, has a dramatic effect on the eigenvectors. The plot of the horizontal wavenumber versus eigenvalue has entirely different trends from that in Figure 4.13a. The narrower ray angle should significantly reduce the resolution of the velocity-reflector depth ambiguity. From Figure 4.5, the simple two parameter model predicts an eigenvalue of only 0.02 for the lateraly earlier case. This value is confirmed on Figure 4.16c from eigenvalue corresponding to a horizontal wavenumber of 0. The eigenvalues drop for the next larger wavenumbers, but then start to rise at a wavenumber of 4. This branch of increasing eigenvalue with larger wavenumber is shown earlier to be an artifact of finite cell sizes. The points with low wavenumber to the far right, near eigenvalues of 0.1, contain very small reflector components and do not correspond to the velocity-reflector depth ambiguity.

The damping of high horizontal wavenumbers strongly reduces the eigenvalues of the high horizontal eigenvectors in Figures 4.17a & b. The damping is performed with a gaussian low pass filter in the frequency domain and is identical to that presented in chapter 2 as a possible constraint.

An effect of the finite cell sizes and wrap around effects on the SVD results is addressed through the use of several different models. First, a model with velocity cells is used. This model is only $\frac{128}{16} = 8$

times wider than high or 4 cable lengths across rather than 12.8 times wider than high. This model has cell sizes 40% smaller than the generic model, which should reduce discretization effects of the finite cell sizes and decrease eigenvalues. The model also has a shorter *circumference* for the circular reflection survey, which should discourage some sizes of velocity variations that are not periodic in the circumference and increase their eigenvalues. With 128 reflector cells, this model size is 2176 and the matrix size is nearly 5 million, making it difficult to execute.

Figure 4.18a of horizontal wavenumber versus eigenvalue is denser but similar to that in Figure 4.13a for the 128 $\times$ 10 model. The eigenvalue range of the top of the inverted "V" is a little lower than in Figure 4.13a. Figure 4.18b with the eigenvalues of the eigenvectors corresponding to the velocity-reflector depth ambiguity shows a clear reduction of eigenvalues over the identical Figure 4.13b for the generic model. There are no signs of the artifacts from the smaller circumference of the model.

Figures 4.19a & b show the SVD results for a model of 128 $\times$ 10 with rectangular velocity cells three times wider than high instead of square ones. That the plots bear a resemblance to those produced using a shorter cable length in Figures 4.16a & b is explained by that neighboring wide velocity cells will share rays in a similar manner as square cells with a narrower maximum ray angle. With these wide cells, the circumference of the circular reflection survey is 38.4 times the depth

where we can be relatively sure there is no artifact from the circular nature of the model. However, the larger cell sizes will cause additional artifacts. Figure 4.19b with the eigenvectors of the velocity-reflector depth ambiguity show that there is a small group with low wavenumber near an eigenvalue of 0.085. For such a wide model all of these wavenumbers are essentially laterally invariant eigenvectors and should have similar eigenvalues. The group of eigenvectors that start at an eigenvalue of 0.01 has increasing eigenvalue with increasing wavenumber and is corrupted by the finite cell sizes.

The model used for Figures 4.20a & b contains 256 $\times$ 5 rectangular velocity cells two times higher than wide. This produces a wide model that will again contain few effects from its circular nature similar to the previous one, but with different discretization effects. This shape of velocity cell has justification from the vertical smearing from the limited angular ray coverage. Figure 4.20a is similar to Figure 4.13a with square cells except that some of the left, upper branches in the inverted "V" are missing. The eigenvalues of the velocity-reflector depth ambiguity in Figure 4.20b do not appear significantly different from those in Figure 4.13b with square cells.

The previous model is to be compared with another having similar rectangular velocity cells, but with a second reflector at twice the depth. With twice the depth, the width is reduced by half so the model contains 128 $\times$ 10 of the rectangular velocity cells. Being deeper with the

same cable length, the second reflector has a narrower maximum ray angle of reflections. The second reflector complicates the results in Figures 4.21a-c. Figure 4.21a shows two branches corresponding the constructive interference of velocity and reflector depth, one for each reflector.

The objective of this model is to analyze the improvement of reflector resolution that results from the addition of a second, deeper reflector. Numerous more eigenvectors now have some reflector components and it is difficult to identify trends. However, Figures 4.21b & c shows that the eigenvalues relating to reflector components of the upper reflector have generally increased, although there still are a few with eigenvalue below 0.01. The second reflector has helped resolve the upper one, but not completely.

The pure transmission cross bore hole experiment is modeled in Figures 4.22a-e. The bore hole geometry is modeled on its side with the sources at the bottom of the field shooting up to receivers at the surface with maximum ray angle of 45°. Wrap around was performed at the edges. A model size of 128 × 8 rectangular velocity cells twice as high as wide were used giving a width 8 times the height. The rectangular cells were used to optimize the geometry in the presence of vertical smearing from the limited angular ray coverage.

Figure 4.22a with the distribution of the eigenvalues shows that

most are above 0.2, with a sharp fall off after eigenvector 800. This sharp fall off represents the inability to resolve the vertical smearing from the limited angular ray coverage. If square cells were used, there would be a greater number of unresolved eigenvectors, below the eigenvector of 0.2. Figures 4.7g & h and Figures 4.11a & b for the generic model with a reflector demonstrate that the eigenvectors after the sharp fall off correspond to the unresolved region of wavenumber space predicted by the central slice theorem of the radon transform, presented in chapter 3 and Figure 3.3. The central slice theorem indicates these eigenvectors should not be inverted at all, which would correspond to an eigenvalue of 0.0. That they do not have a 0.0 eigenvalue is the result of the finite cell sizes.

Figures 4.22d & e indicate that each higher branch in Figure 4.22b most likely corresponds to a greater vertical wavenumber of the eigenvector. For each branch, the eigenvalues increase rapidly with increasing horizontal wavenumber until the horizontal wavenumber is large enough to place the eigenvector in the resolved region of the two dimensional wavenumber domain. The resolved region corresponds to patterns higher than wide. This point of transition is the where the trend reaches its maximum eigenvalue and turns back to the left. The greater the vertical wavenumber of the branch, the greater the horizontal wavenumber of this transition point.

That the minimum eigenvalue of the "resolved" eigenvectors is

about 0.2, a relatively large number, demonstrates that few iterations are needed to resolve velocity components. The velocity variations are resolved quickly while other features, such as the velocity-reflector depth may take much longer, if at all possible.

References

Aki, K. and Richards, P., 1980, *Quantitative Seismology*: W.H. Freeman and Co.

Bishop T. N., Bube, K. P., Cutler, R. T., Shuey, R. T., Kroeger, R. A., Jones, R. C., and Rathbun, M. L., 1984, Tomographic Determination of Velocity and Depth in Laterally Varying Media: *Geophysics*, **50**, 903-923.

Bube, K.P. and Resnik, J.R., 1985, Well determined and poorly determined features in seismic tomography, Part I: SEG Meeting Extended Abstract, Washington, D.C.

Bube, K.P. and Resnik, J.R., 1986, Well determined and poorly determined features in seismic tomography, Part II: SEG Meeting Extended Abstract, Houston, TX.

Comer, R.P. & Clayton R.W., 1985, Reconstruction of Mantle Heterogeneity by Iterative Back-projection of Travel Times, 1: Theory and Reliability, Preprint.

Dines, K. A. and Lytle, R. J., 1979, Computerized geophysical tomography: *Proceedings of the IEEE*, **67**, 1065-1073.

Fowler, P., 1988. Migration Velocity Analysis , Ph. D. Thesis, Stanford University.

Hestenes, M. and Stiefel, E., 1952. Methods of Conjugate Gradients for Solving Linear Systems, *Nat. Bur. Standards J. Res.*, **49**, 409-436.

Ivansson, S., 1983. Remark on an Earlier Proposed Iterative Tomographic Algorithm, *Geophys. J. R. astr. Soc.*, **75**, 855-860.

Kjartansson, E., 1979. Attenuation of Seismic Waves in Rocks, Ph. D. Thesis, Stanford University.

Langan, R. T., Lerche, I., and Cutler, R. T., 1985, Tracing of rays through an heterogeneous media: An accurate and efficient procedure. *Geophysics*, **50**, 1456-1465

Mason, I.M., Algebraic Reconstruction of a Two-dimensional Velocity Inhomogeneity in the High Hazles Seam of Thoresby Colliery, *Geophysics*, **46**, 298-308.

Mora, P., 1987. Nonlinear two-dimensional elastic inversion of multioffset seismic data, *Geophysics*, **52**, 1211-1228.

Olson, A., 1986, A Chebyshev Condition for Accelerating Convergence of Iterative tomographic Methods-Solving Large Least Squares Problems, Preprint.

Scales, J., 1987. Tomographic Inversion via the Conjugate Gradient Method, *Geophysics*, **52**, 179-185.

Scales, J., Gersztenkorn, A., and Treitel, S., 1987. Fast l_p solution of large, sparse linear systems: application to seismic travel time tomography, *J. Computat. Physics* (In press).

Sherwood, J.W.C, Chen, K.C., and Wood, M., 1986, Depths and Interval Velocities From Seismic Reflection Data for Low Relief Structures: Offshore Technology Conference Paper, Houston, TX, **5161**.

Slaney, M., Kak, A.C., & Larsen, L.E., Limitations of Imaging with First-Order Diffraction Tomography, *IEEE Trans. on Microwave Theory*, **MTT-32**, p. 860-873.

Soumekh, M., 1986. An Improvement to the Rytov Approximation in Diffraction Tomography, *IEEE Trans. on Ultraonics, Ferroelectrics, and Freq. Control*, **UFFC-33**, p. 394-401

Stork, C. and Clayton, R. W., 1986, Analysis of the Resolution between Ambiguous Velocity and Reflector Position for Travel Time Tomography: 56th Annual SEG Meeting extended abstract, Houston.

Stork, C., 1988, Comparison of Richardson's Iteration with Chebyshev Acceleration Factors to Conjugate Gradient Iteration, *SEP-Report*, **57**.

Sword, C., 1987. Tomographic Determination of Interval Velocities from Reflection Seismic Data: The Method of Controlled Directional Reception, Ph. D. Thesis, Stanford University.

Tarantola, A., 1984. Linearized Inversion of Seismic Reflection Data, *Geophysical Prospecting*, **32**, 998-1015.

Tarantola, A., 1984. Inversion of Seismic Reflection Data in the Acoustic Approximation, *Geophysics*, **49**, 1259-1266.

Toldi, J., 1985. Velocity Analysis without Picking, Ph. D. Thesis, Stanford University.

Wiggins, R.A., Larner, K.L., and Wisecup, R.D., 1985, Residual Statics Analysis as a general Linear Inverse Problem, *Geophysics*, **50**, 2172-2188.

Woodward, M.J. and Rocca, F, 1988, Wave Equation Tomography I, *SEP report*, **57**.

RAY TRACE TOMOGRAPHIC VELOCITY ANALYSIS OF SURFACE SEISMIC REFLECTION DATA

Volume 2: Figures

Thesis by
Christof Stork

Figures for Chapter 2:

An Implementation of Travel Time Tomography to Reflection Seismology

Figure 2.1

Method used for ray tracing. Velocity field is represented as a two dimensional grid of points. The velocity points define the corners of cells which are subdivided into triangles. The three velocity points at the triangle corners define a unique linear velocity gradient within each cell. Velocity is continuous across triangle boundaries. Using the fact that ray paths are arcs of circles in a triangle, rays are traced through each triangle. Since there are no diffractions, the ray set tends to be smooth.

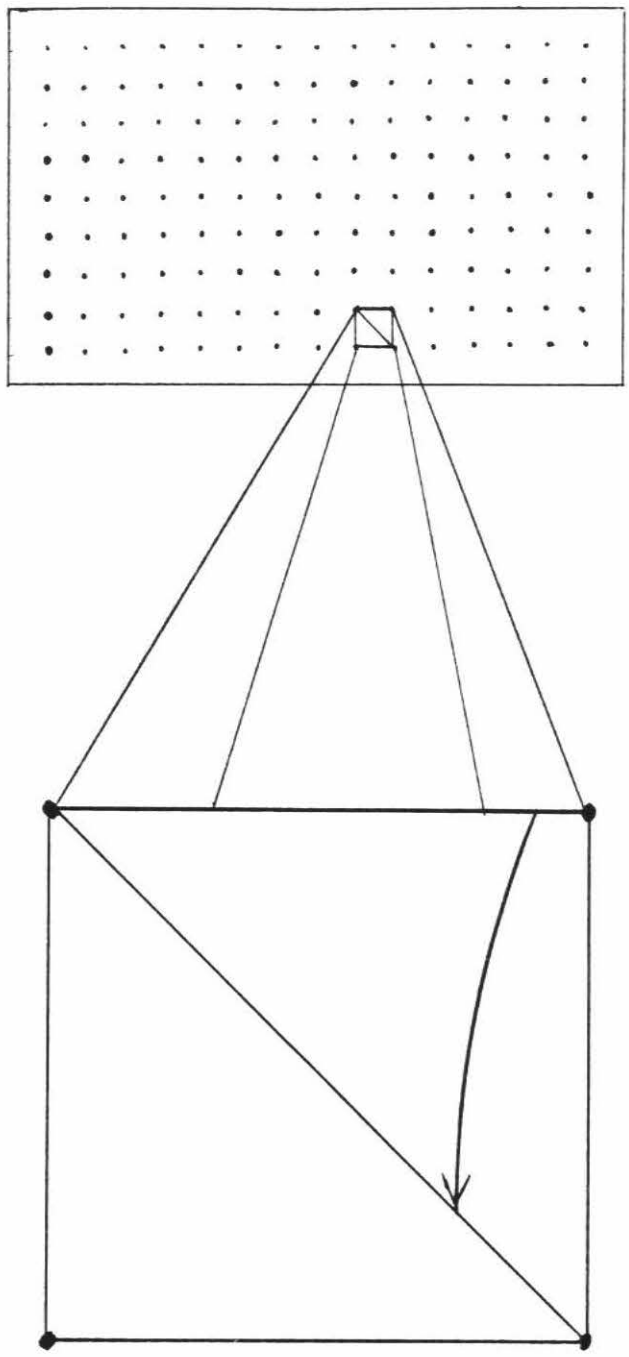

Figure 2.2A

Example of rays through velocity cells, off of a smoothly varying reflector. A linear velocity gradient exists that increases with depth. Shown are the ray paths between a shot and its receivers.

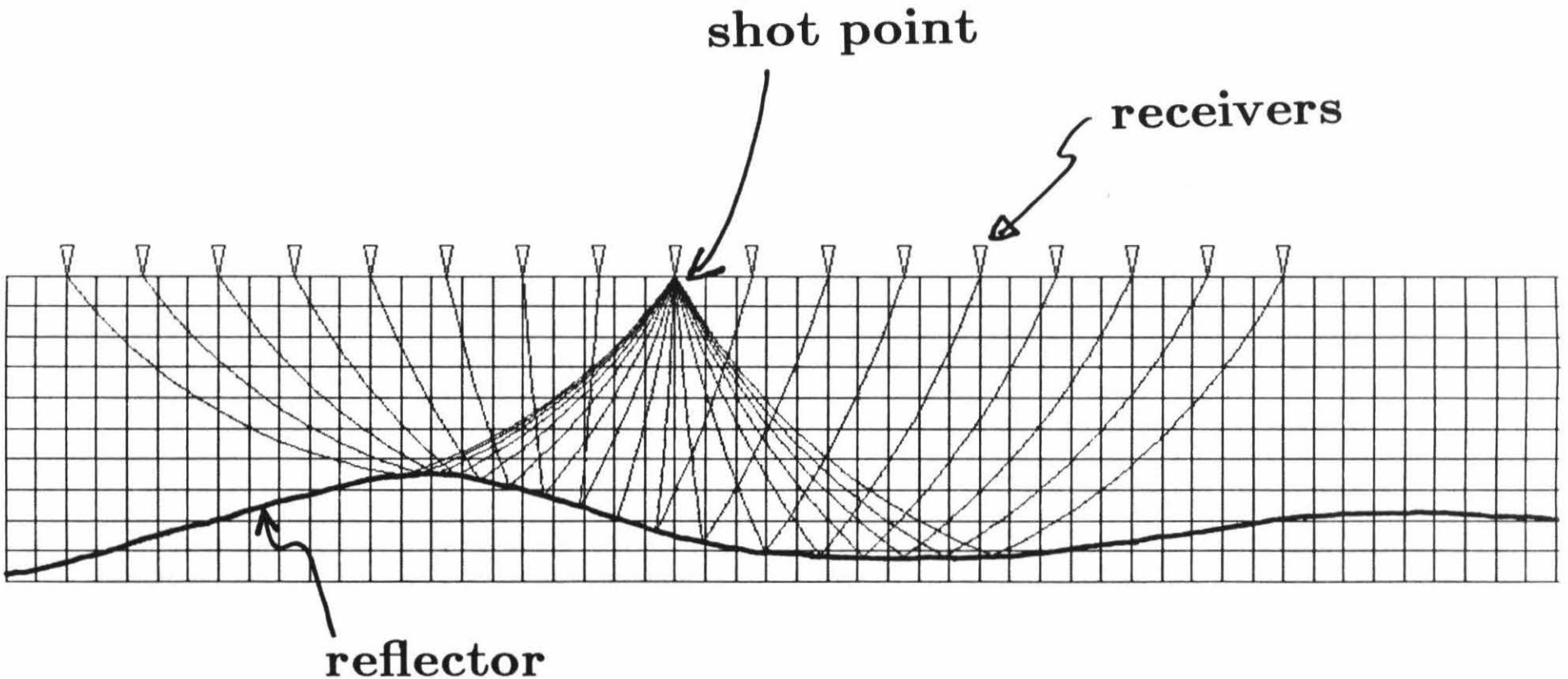
shot point
receivers
reflector

Figure 2.2B

Example of ray paths from a shot point to receivers. Light colored blocks are velocity variations of +/- 10%. Considerable reflector structure exists with tight curves.

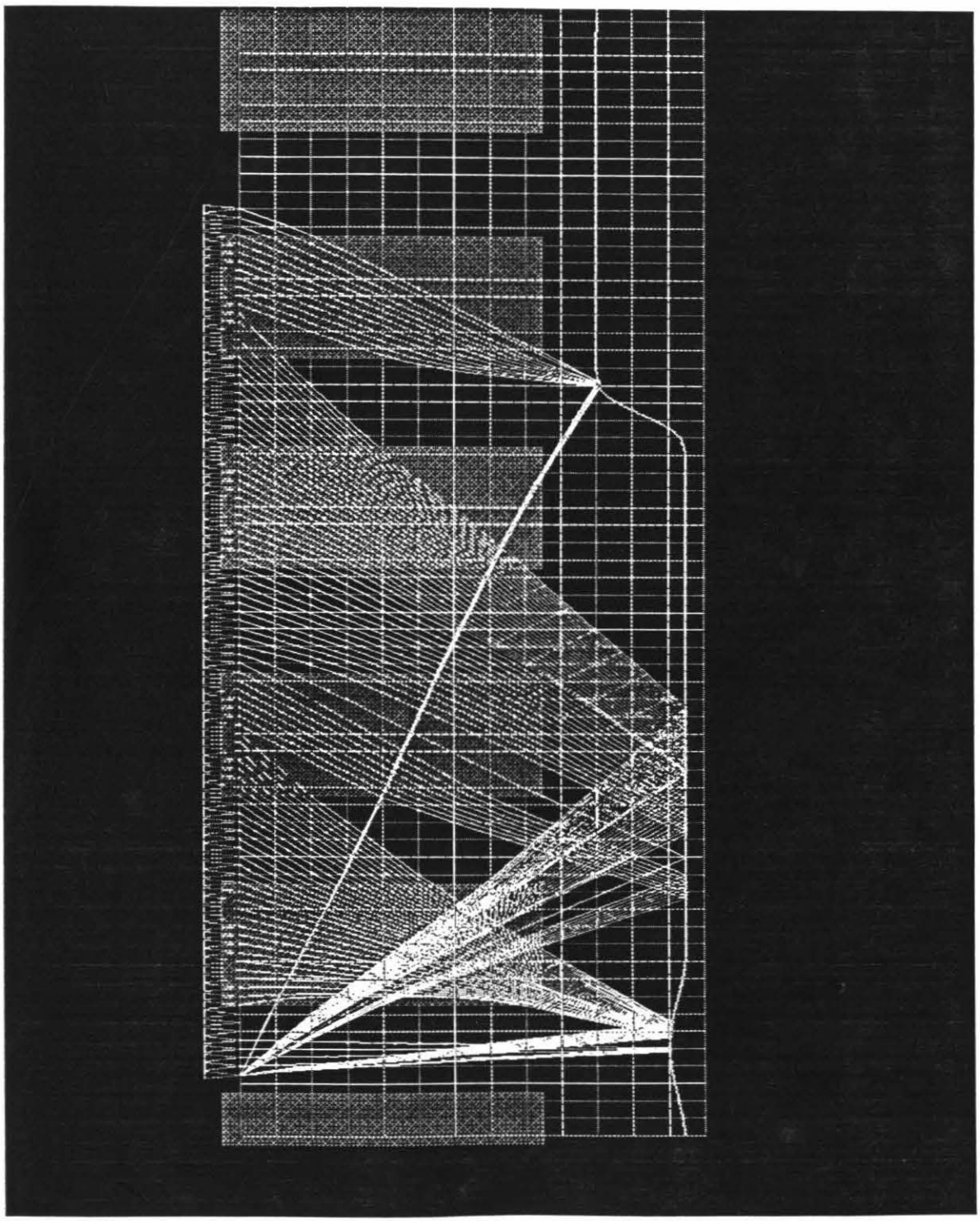

Figure 2.2C

Blowup of lower left corner of previous figure. The triangles are evident from the tick marks that flag where the rays cross a triangle boundary. The points of reflection are clear.

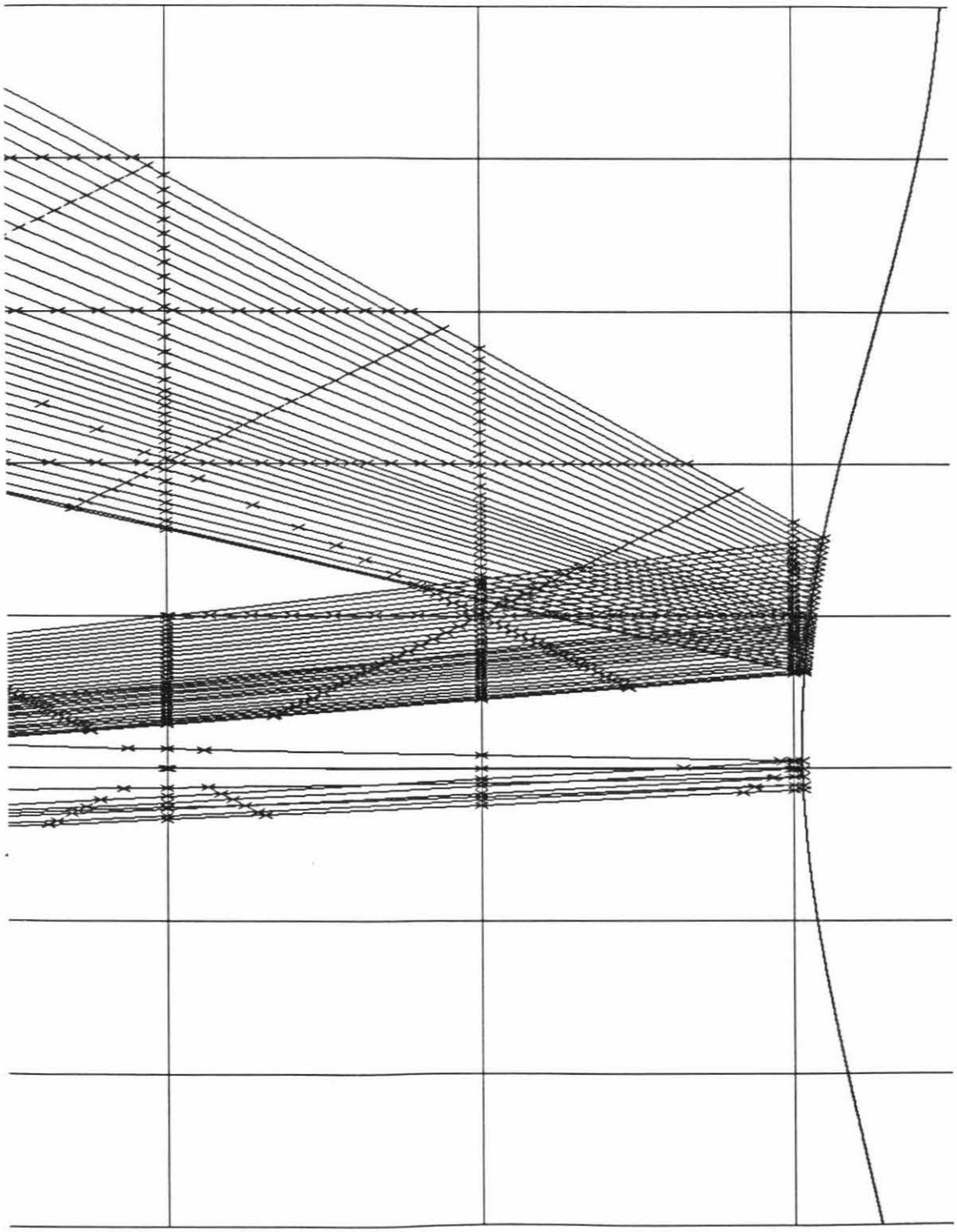

Figure 2.2D

Example of ray tracer with reflector structure and a linear velocity gradient with depth. Ray paths of shortest travel time reflector off only the tops of the bumps.

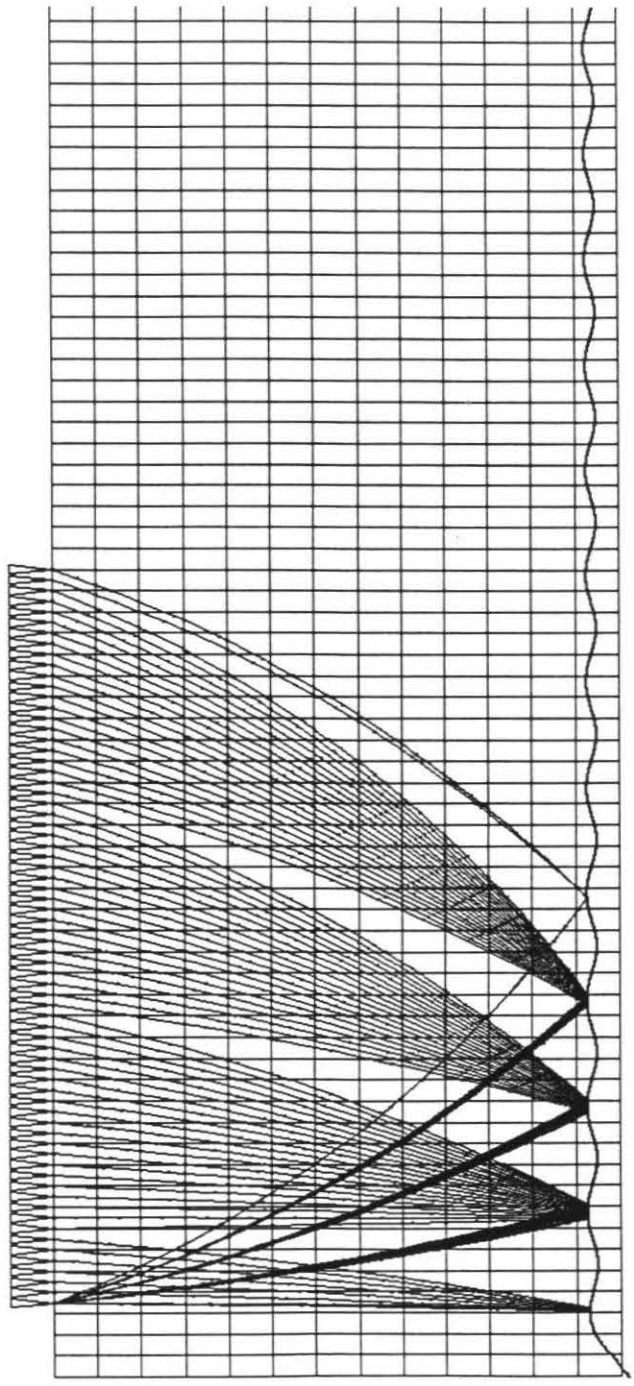

Figure 2.2E

Borehole example of ray tracer. Shot is place at depth. Shown are the paths to receivers in a linear velocity gradient with depth.

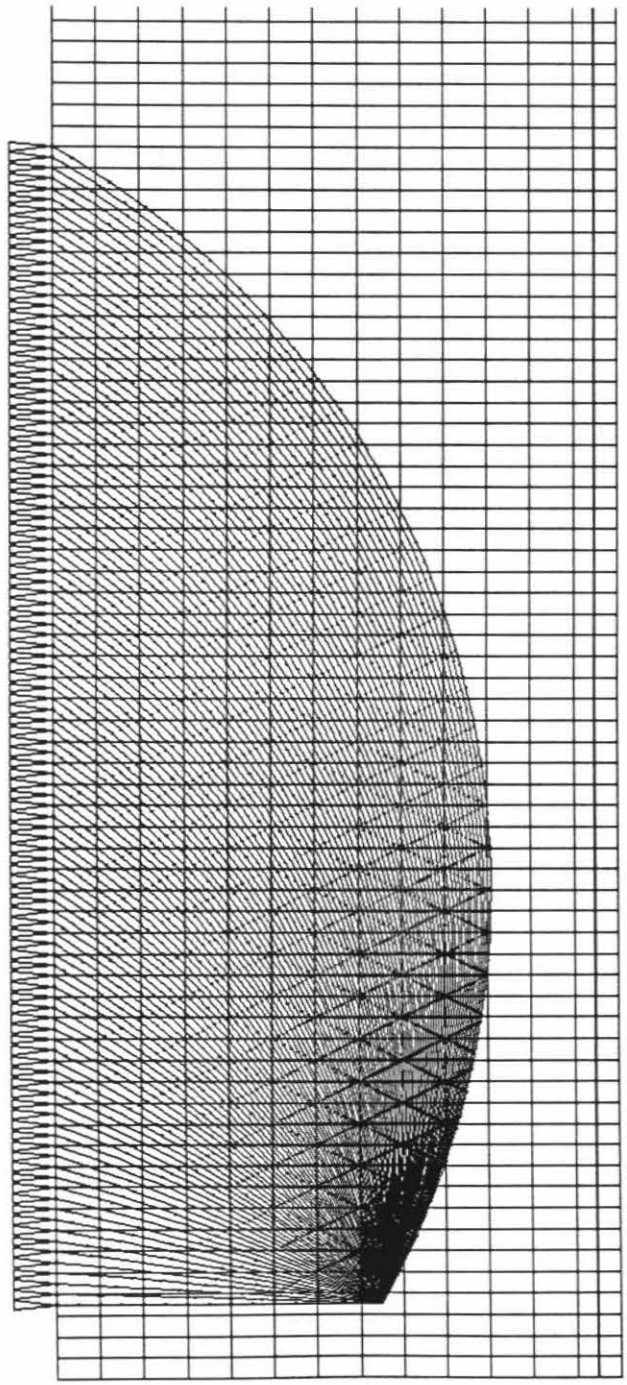

Figure 2.3A

Rays through a large scale random velocity variations of maximum amplitude of +/- 5%. Shown is ray fan produced by shooting rays in constant increments of angle. Rays are bent only mildly, but concentrate toward the low velocity regions. This ray fan is used for iteration to the receivers.

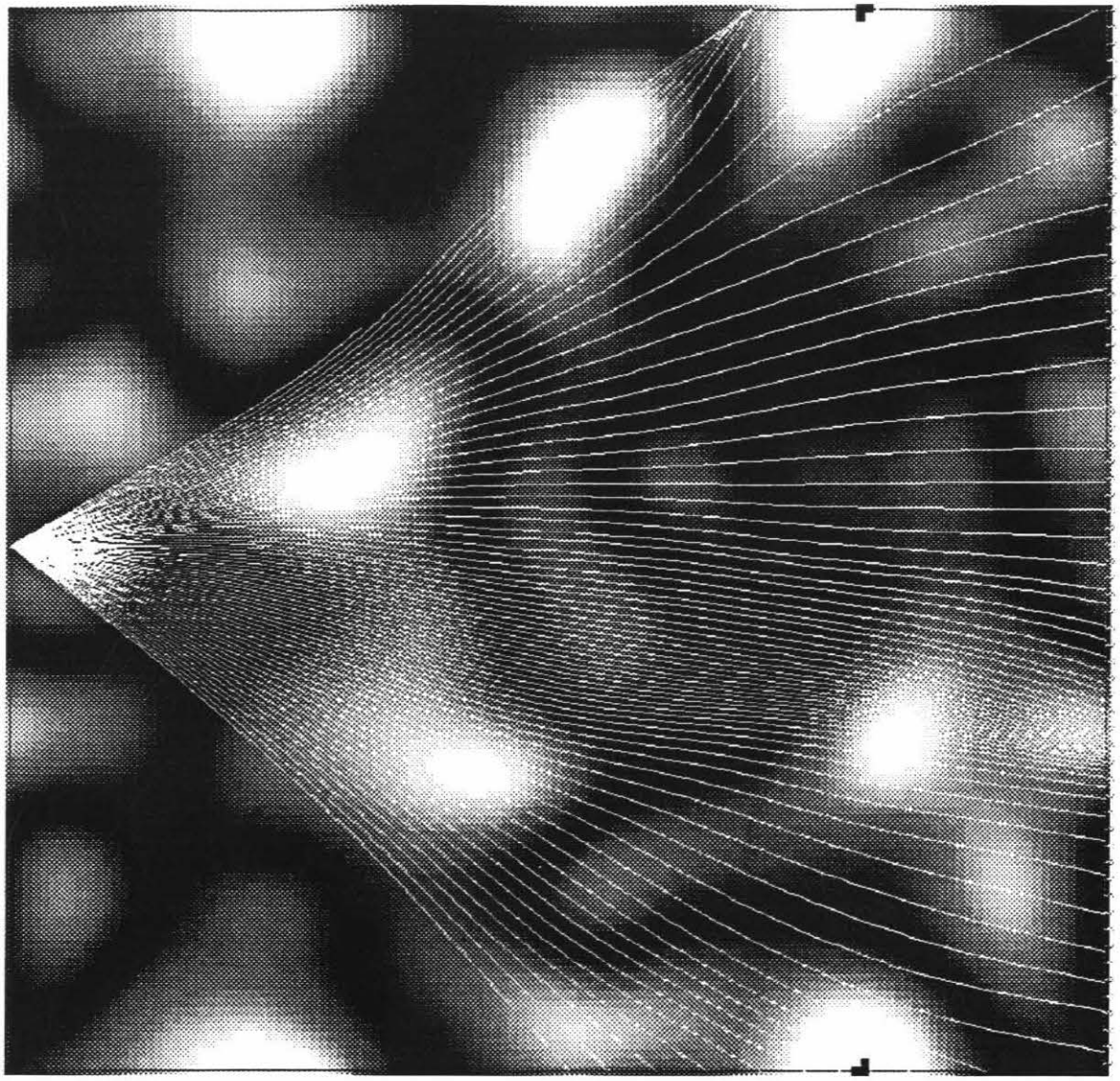

Figure 2.3B

Rays between source and receiver of the same velocity field used in the previous model. Rays of fastest travel time are concentrated toward the fast velocity anomalies.

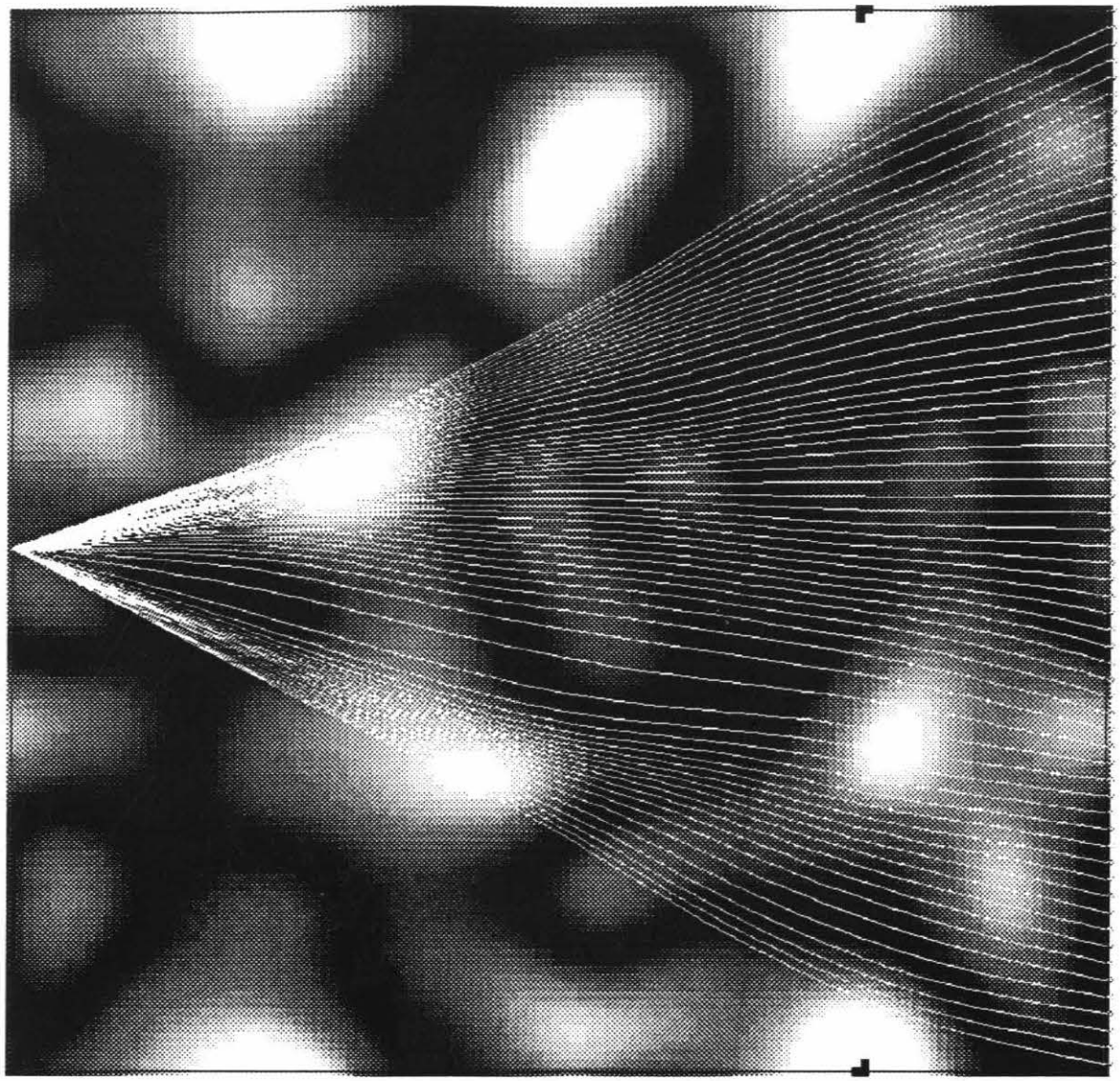

Figure 2.3C

A fan of rays through medium sized velocity variations of amplitude +/-5%. Although velocity variation is the same amplitude as in Figure **2.3a**, the rays are now strongly affected. The ray fan is used for iteration to the receivers.

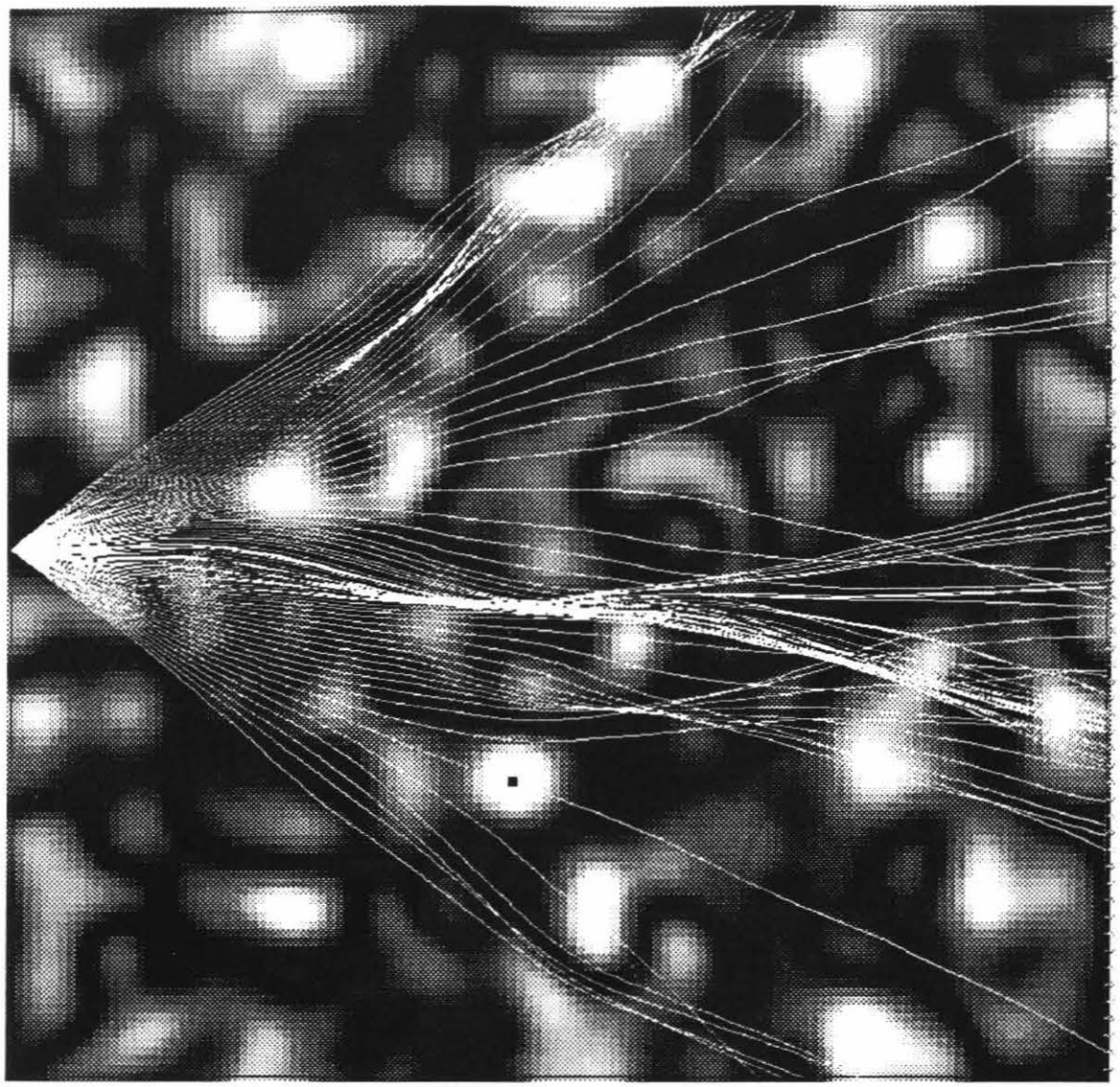

Figure 2.3D

Ray paths between source and receivers through same velocity field used in the previous figure. Ray distribution is very uneven.

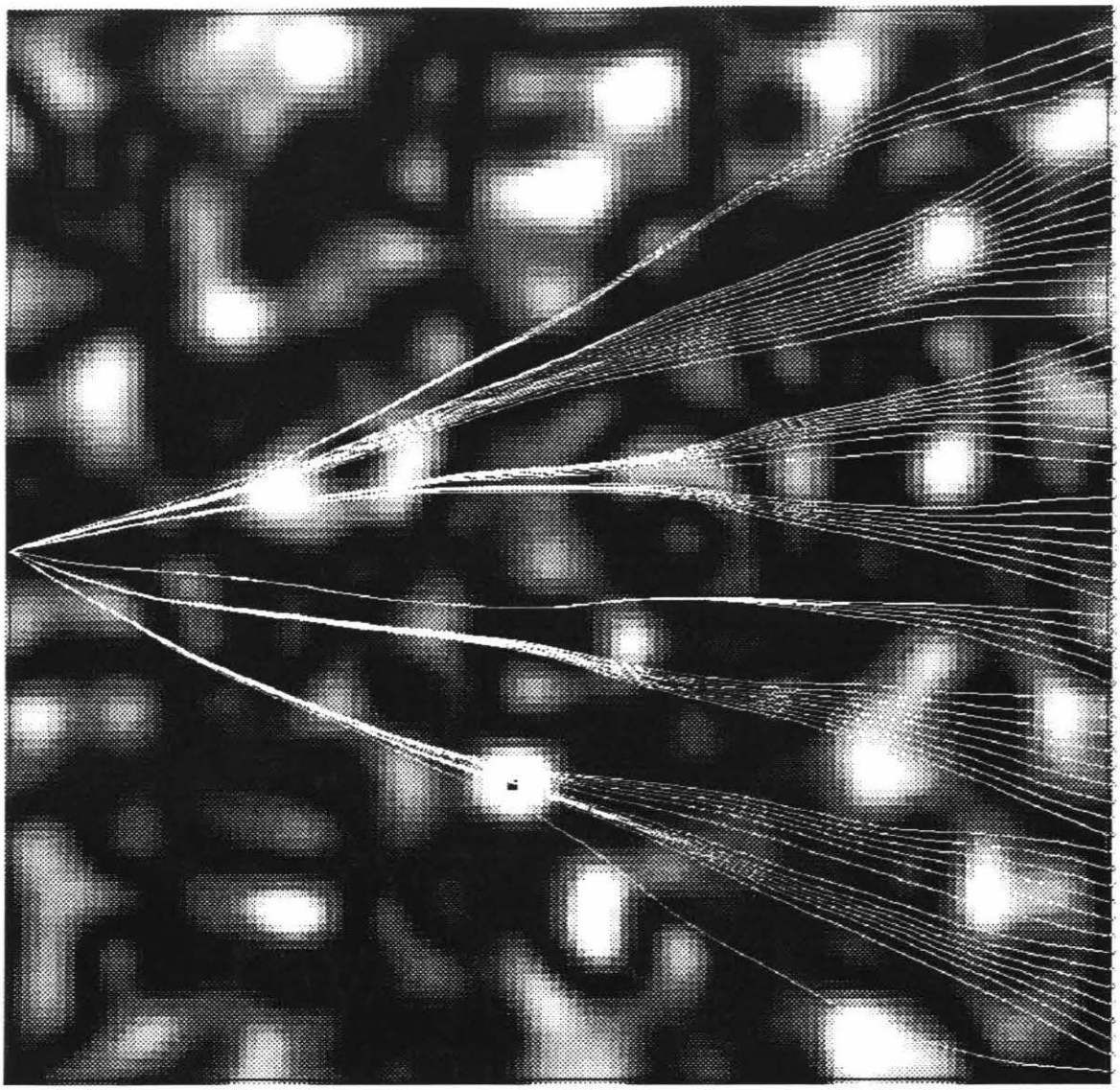

Figure 2.3E

Ray fan through small scale velocity variations of amplitude +/5%. Ray paths are very discontinuous with neighboring rays having no relation to each other. Rays could not be iterated to receivers for this model.

ie1:
spuri
VME 1

Figure 2.3F

Ray fan through small scale veloccity variations of amplitude of +/-15%. Ray paths for this model have little meaning.

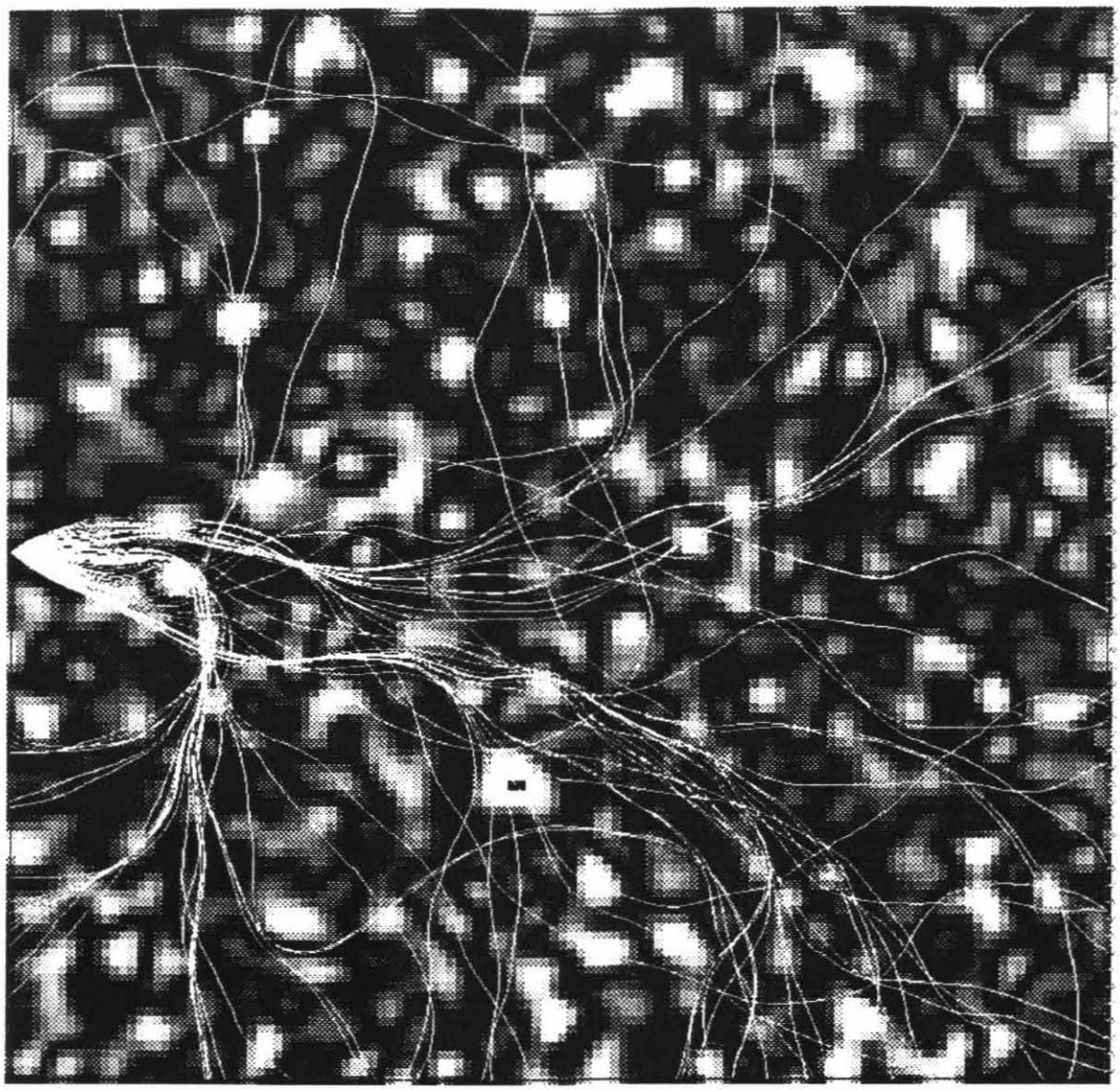

Figure 2.4A

Method for subdividing a cube into 5 tetrahedrons. Four of the tetrahedrons are on the outside and are identical. The fifth is on the inside bounded by the other four. The velocity at the four corner points specify a unique linear velocity gradient within each tetrahedron with the velocity continuous across the sides. Rays are traced through each tetrahedron using the fact that rays are arcs of circles in linear velocity gradients.

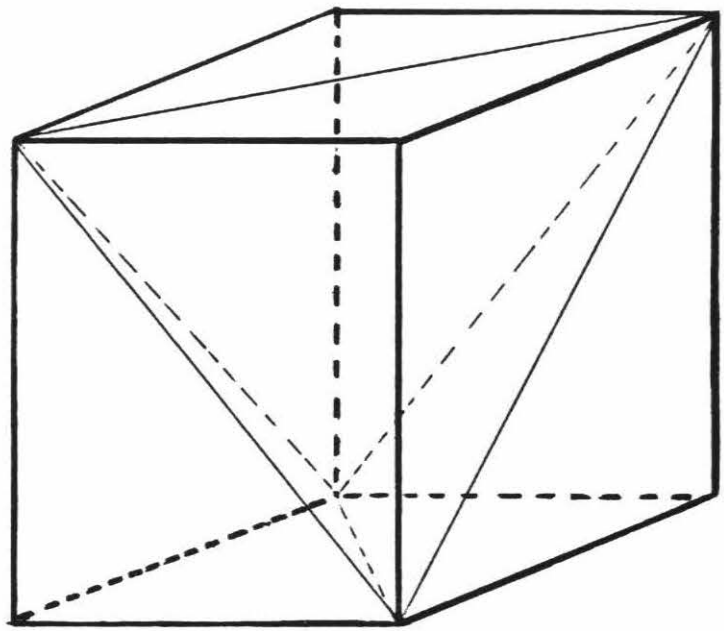

Figure 2.4B

Example of ray tracing through three dimensions with a reflector. In the upper figure that does not have any ray paths is shown from the perspective of looking in from the side of the volume. The top of the volume, the reflector, and the bottom of the volume is shown. The lower figure has added the ray paths. A linear velocity gradient exists.

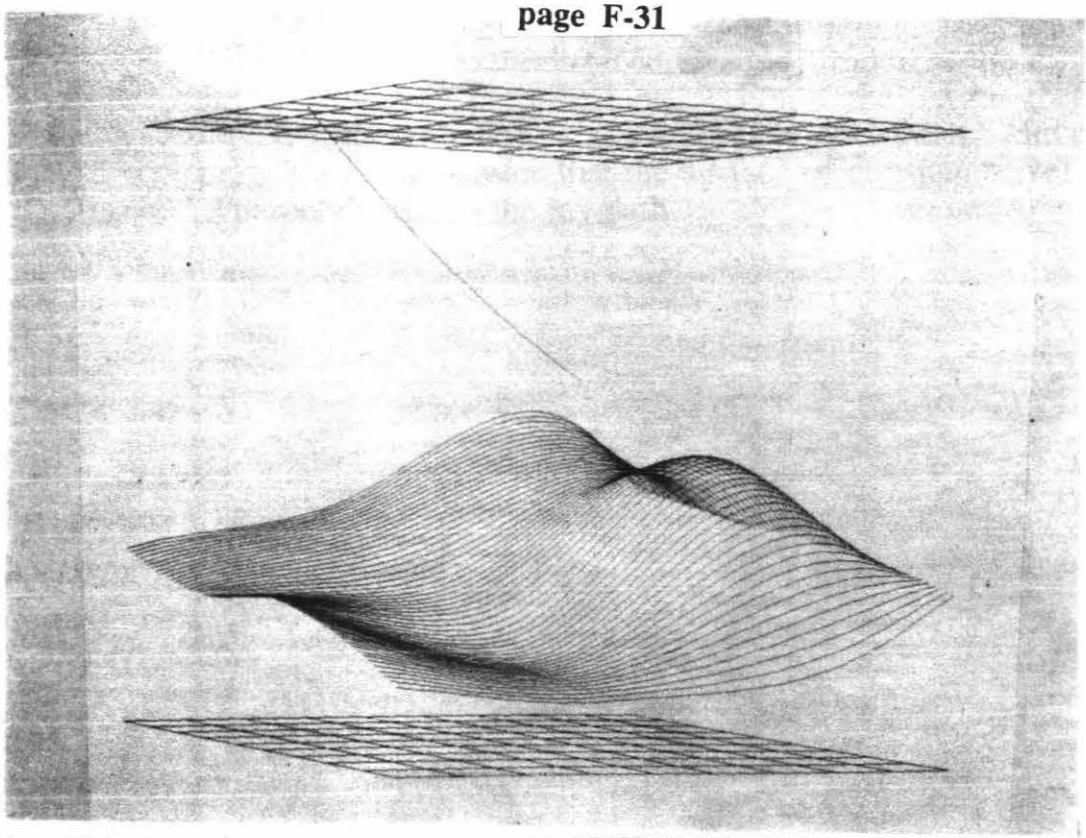

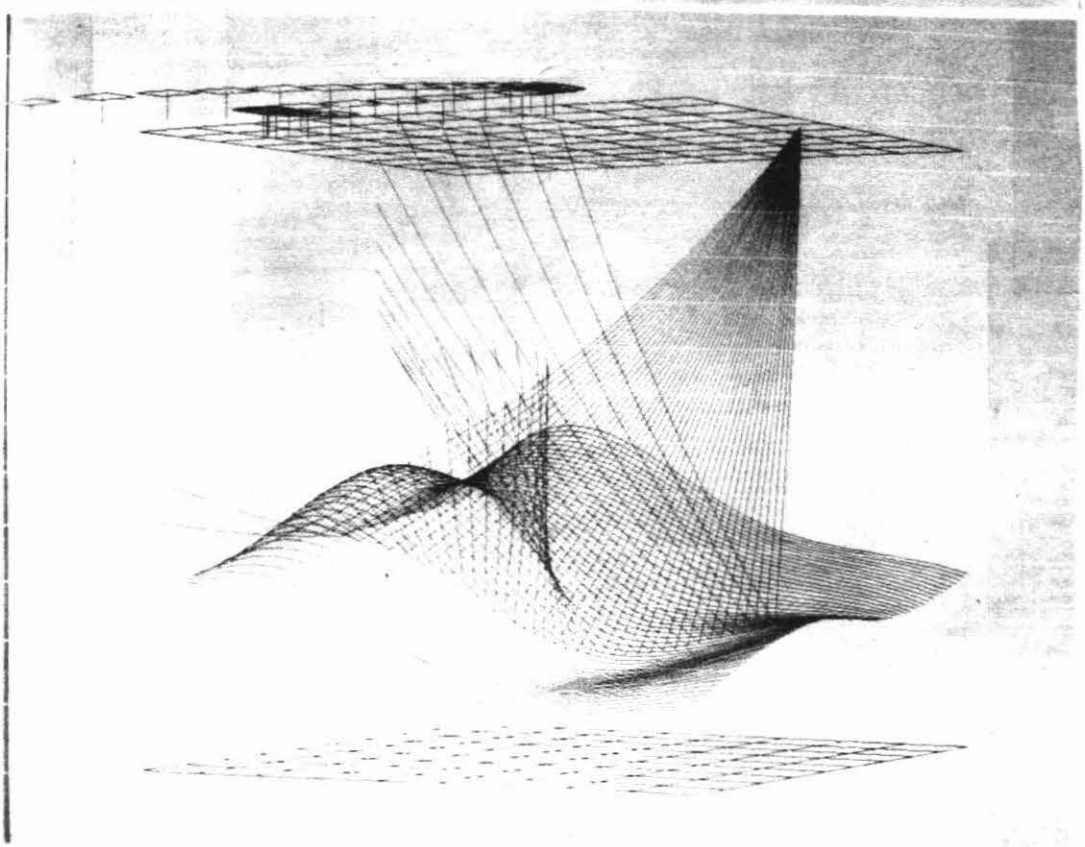

Figure 2.5A

Diagrams of the extra distance rays must travel as the result of small reflector perturbations. From the extra distance traveled, the extra travel time is easily computed. Huygen's principle demonstrates that the surface of constant travel time is perpendicular to the ray path.

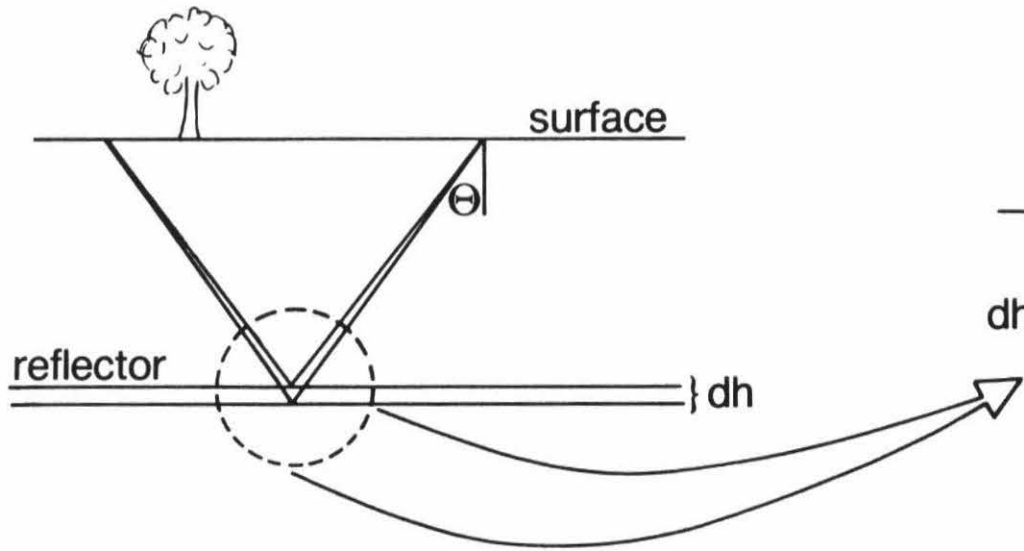

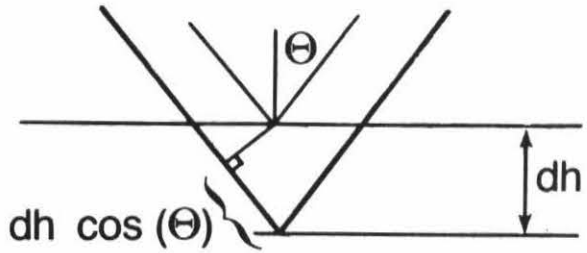

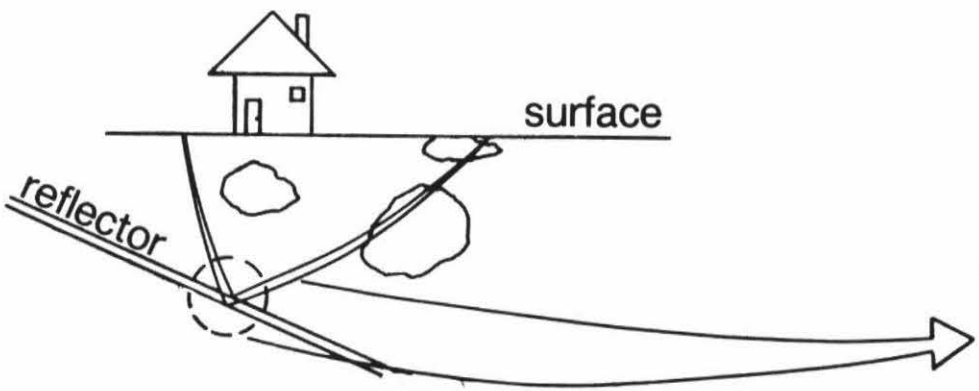

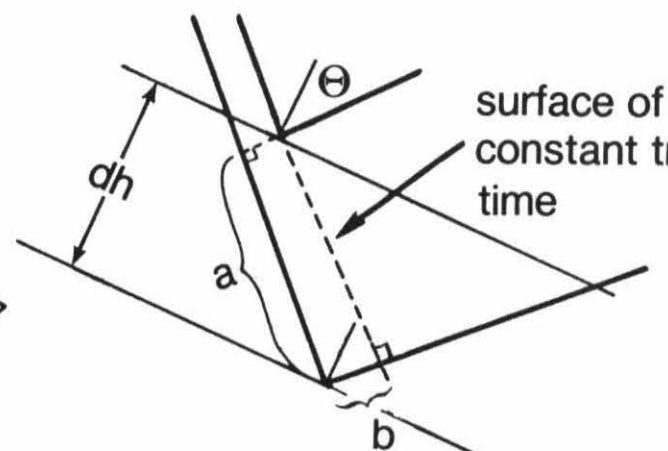

$(a+b) = 2dh \cos(\Theta)$

Figure 2.5B

Diagram demonstrating that the extra distance traveled by a ray due to a reflector perturbation, (a+b), is 2 x dh x cos(theta). No assumption is made about the velocity field or the reflector structure other than small scale reflector perturbation.

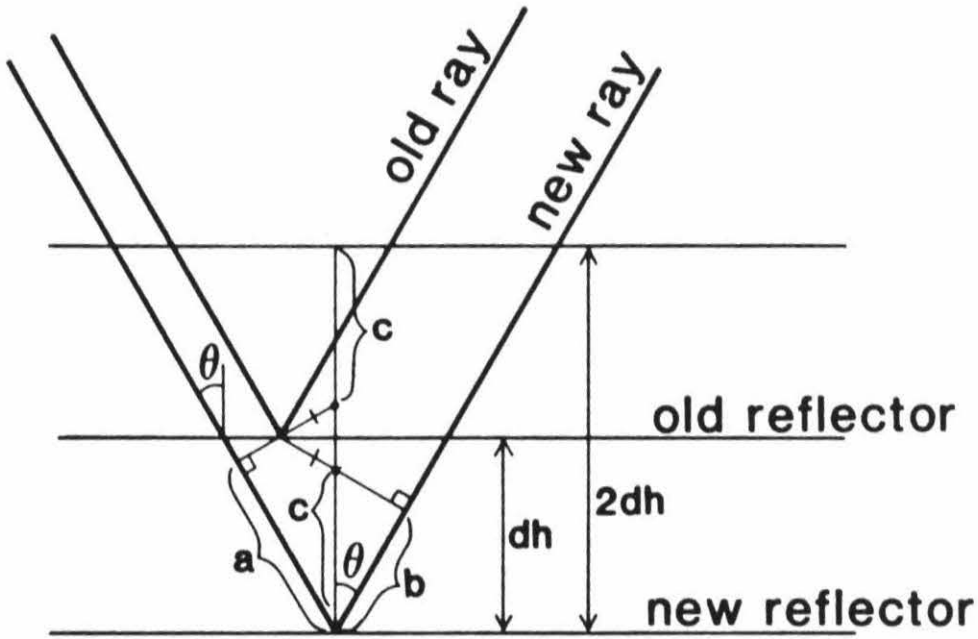

$$\frac{b}{\cos\theta} = C$$

$$\frac{a}{\cos\theta} + c = 2dh$$

$$a + b = 2dh \cos\theta$$

Figure 2.5C

Diagram demonstrating that low angle rays are less affected by reflector depth perturbations than high angle rays.

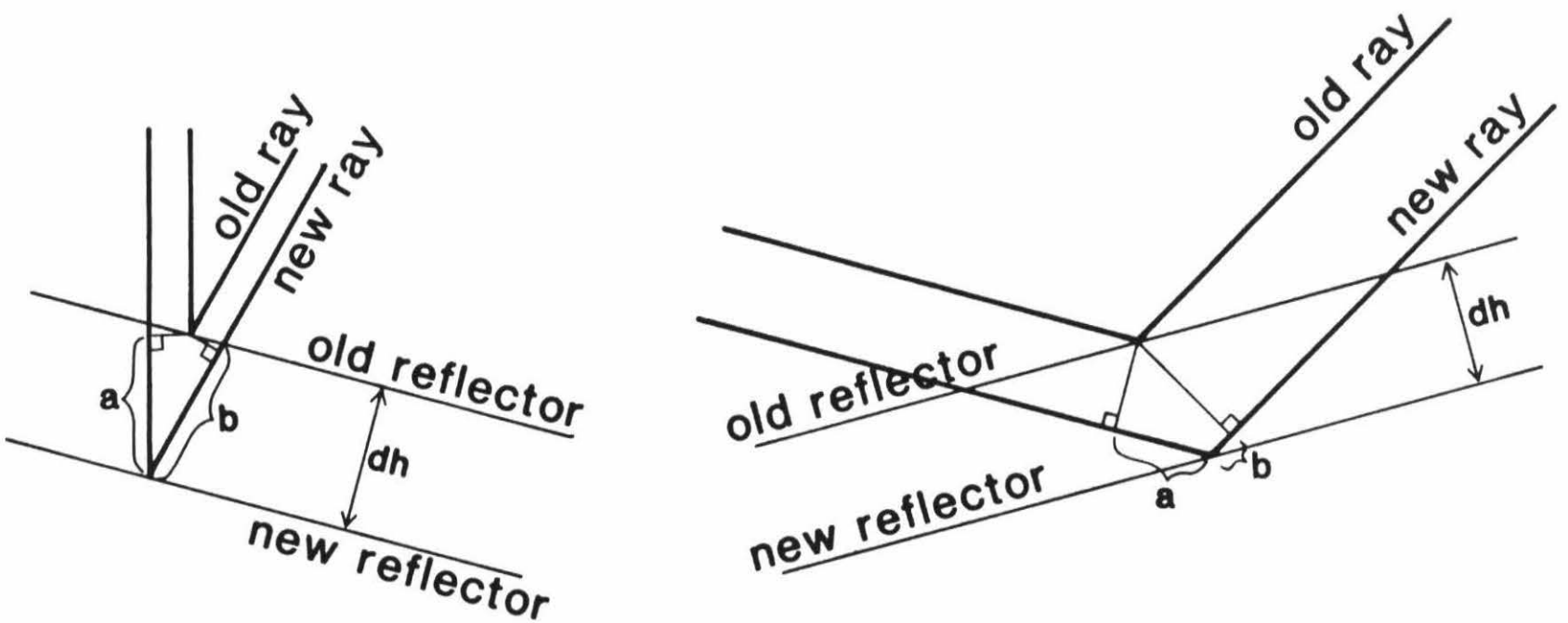

$dh \ll h$

Vertical rays are affected more by reflector depth variations.

Figure 2.6A

Example of structure of $\mathbf{A}^T\mathbf{A}$ matrix. Each figure is one row of the matrix. The matrix is essentially a *connectivity* matrix, indicating how likely cells are to share identical rays.

Row of the [$A^T A$] Matrix for a Generic Survey of square Cells

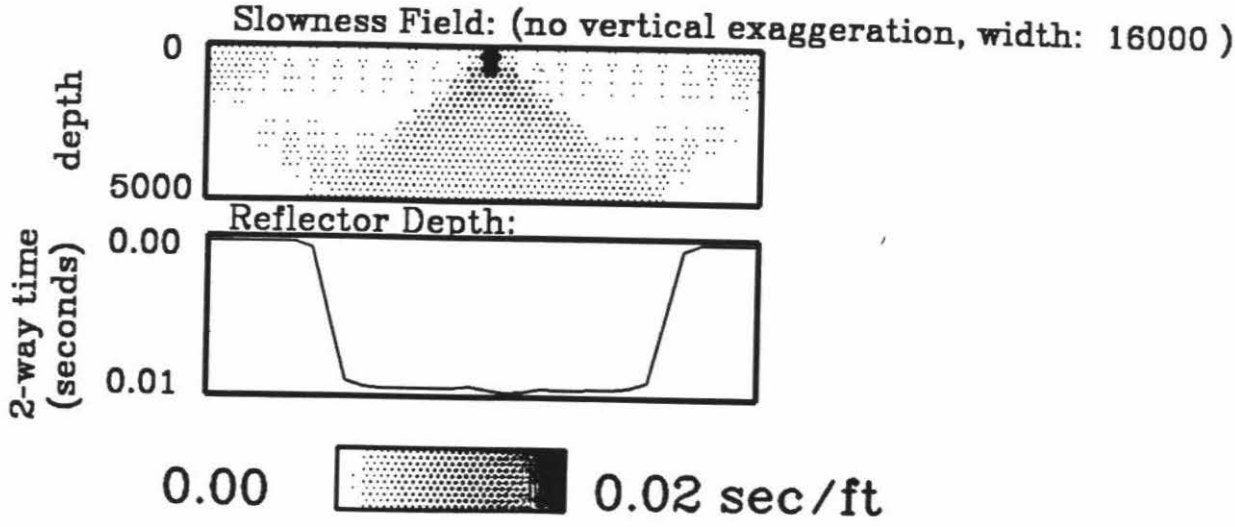

Row of the [$A^T A$] Matrix for a Generic Survey of square Cells

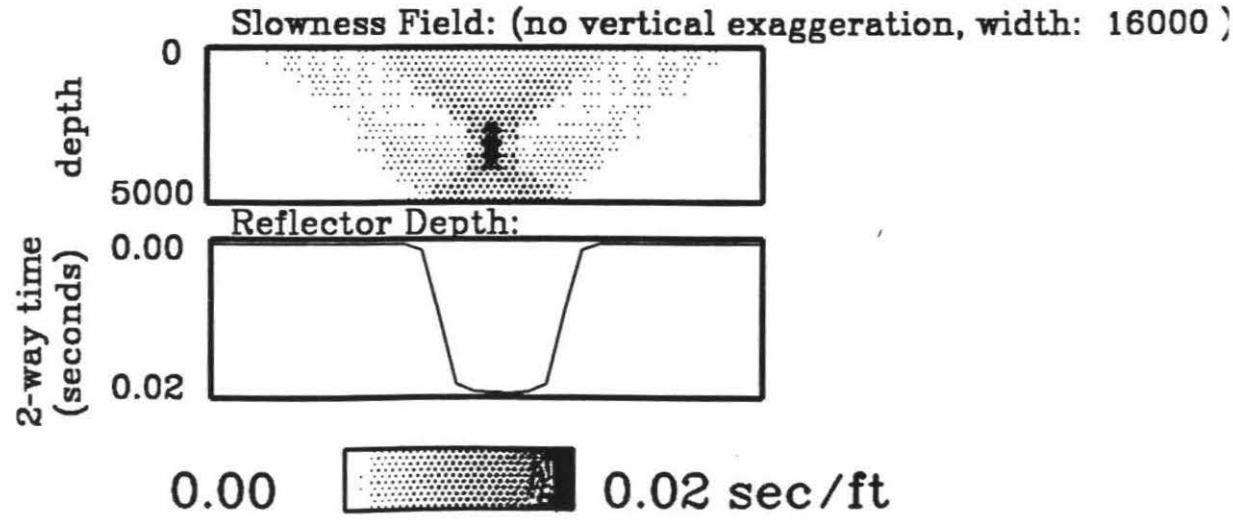

Figure 2.6B

Example of structure of $\mathbf{A}^T\mathbf{A}$ matrix at the edges. Receivers are all to the left of the shot point, so at the right side of the model only vertical rays exist while at the right side only far offset rays exist.

Row of the [$A^T A$] Matrix
for a Generic Survey of square Cells
Analysis of Edges

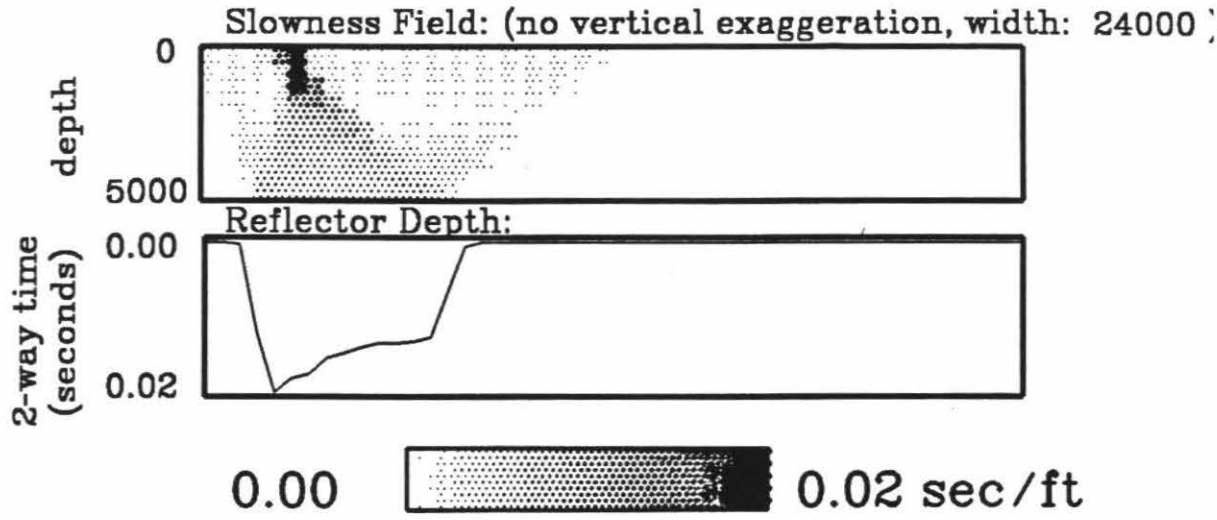

Row of the [$A^T A$] Matrix
for a Generic Survey of square Cells
Analysis of Edges

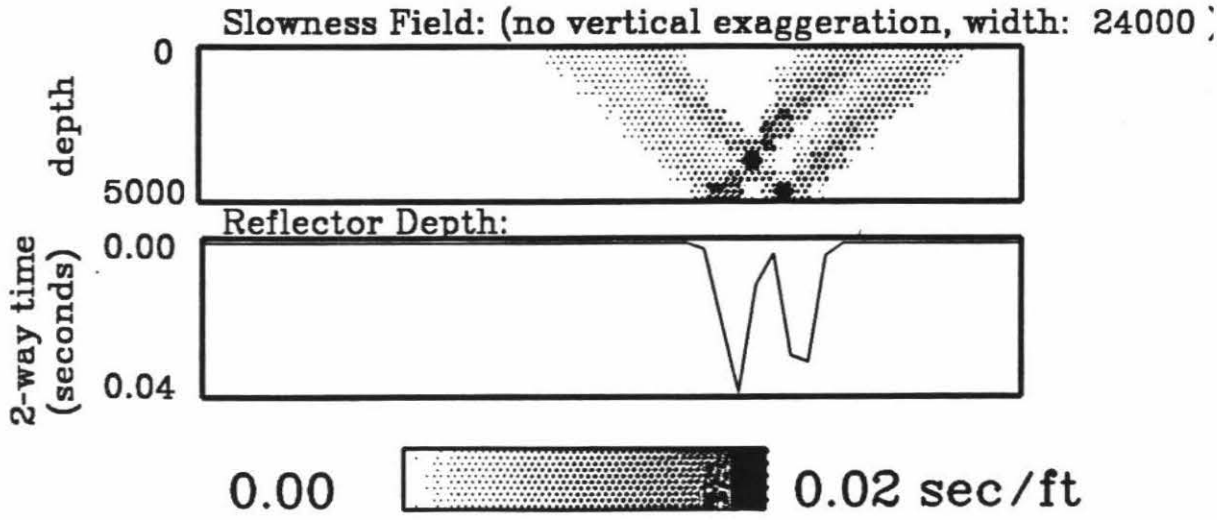

Figure 2.7

Flow chart for the iterative application of tomography and migration.

Iterative Tomographic and Migration Reconstruction of Seismic Images

1) Produce starting velocity model using conventional techniques

2) Migrate data through velocity model; pick reflector.

3) Trace rays through velocity and reflector model.

4) Perform tomographic inversion.

5) Is new velocity model different from old?

YES NO

DONE

Is method stable?

YES NO

Choose a new reference model.

Figure 2.8

Diagram indicating the approach used to solving the non-linear errors.

$$\vec{d} = \mathbf{F}(\vec{m})$$

where:

$\vec{m}$ = **model vector**

$\vec{d}$ = **data vector**

$\mathbf{F}()$ = **a non-linear function**

$$\vec{d} = \mathbf{F}(\vec{m}_o) + \frac{d\mathbf{F}(\vec{m}_o)}{d\vec{m}} \cdot \Delta\vec{m} + \mathbf{O}(\Delta\vec{m}^2)$$

given $\vec{d}$**, solve for** $\Delta\vec{m}$

$$\frac{d\mathbf{F}(\vec{m}_o)}{d\vec{m}} = \text{matrix } \mathbf{L}$$

determined by ray tracing

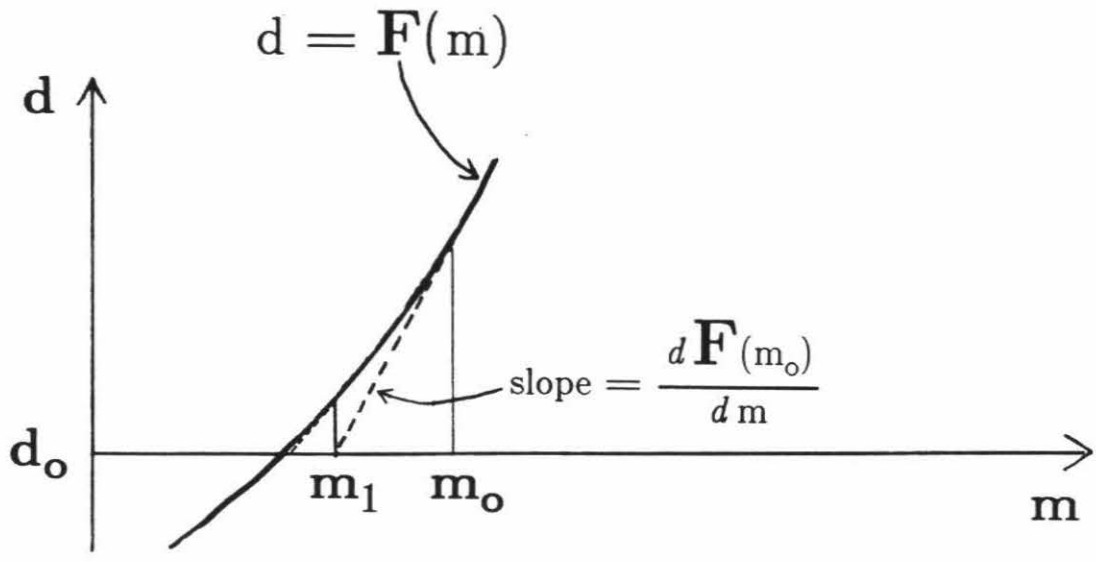

Figures for Chapter 3:

A Modeling Analysis of Ray Trace Tomography Applied to Reflection Seismology

Figure 3.1

A comparison of the data acquisition method of seismic surface reflection surveys to that used in CAT scanners. The CAT scanner has an ideal data collection process while the reflection survey has many complications.

CAT Scanner

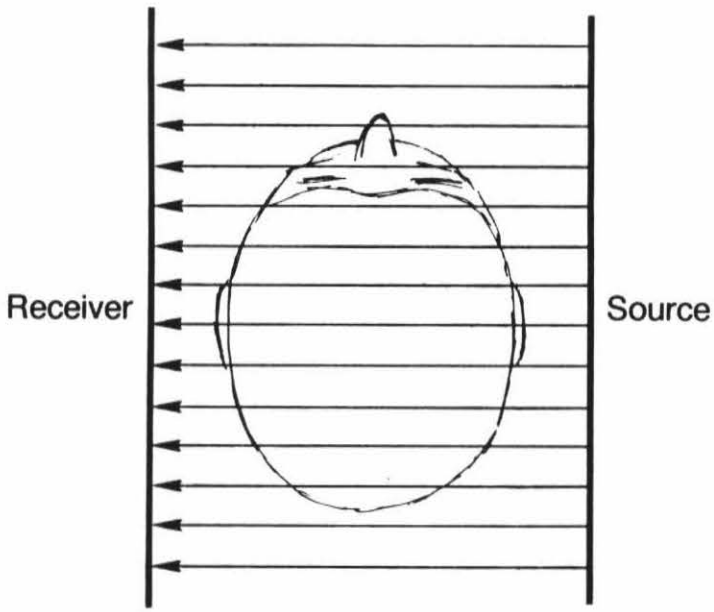

1) X–ray wavelength of ~ Angstroms
2) Experiment can be rotated around object
3) Uniform ray coverage
4) Ray paths unaffected by object
5) Data easily measured, high S/N

Reflection Seismology

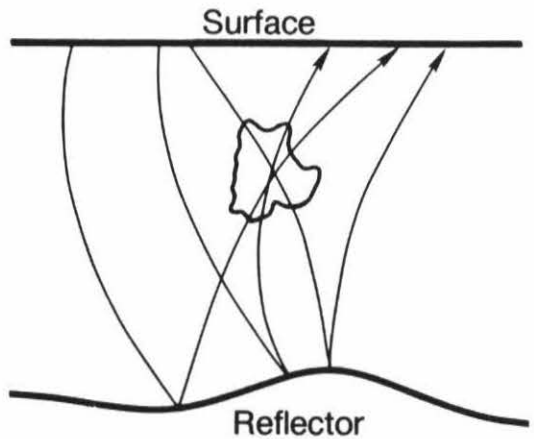

1) Seismic wavelength of ~ 200 feet
2) Only vertical & near vertical rays exist
3) Non-uniform ray coverage
4) Ray paths affected by object
5) Travel time picking from waveforms can be difficult
6) Reflector position effects travel time & ray paths not
7) Model does account for some processes: Anisotropy, 3D effects, Attenuation, Diffraction

Figure 3.2

An example of the inability of the limited angular ray coverage of a reflection survey to resolve the vertical location of velocity anomalies. The ray paths travel the same distance in each of the two velocity variation strips shown. Thus, if the velocity variations are equal in amplitude, they will have an identical effect of the travel times of the ray paths. An inversion of the travel times will be unable to resolve between which of the two strips or any other strip caused the travel time effect.

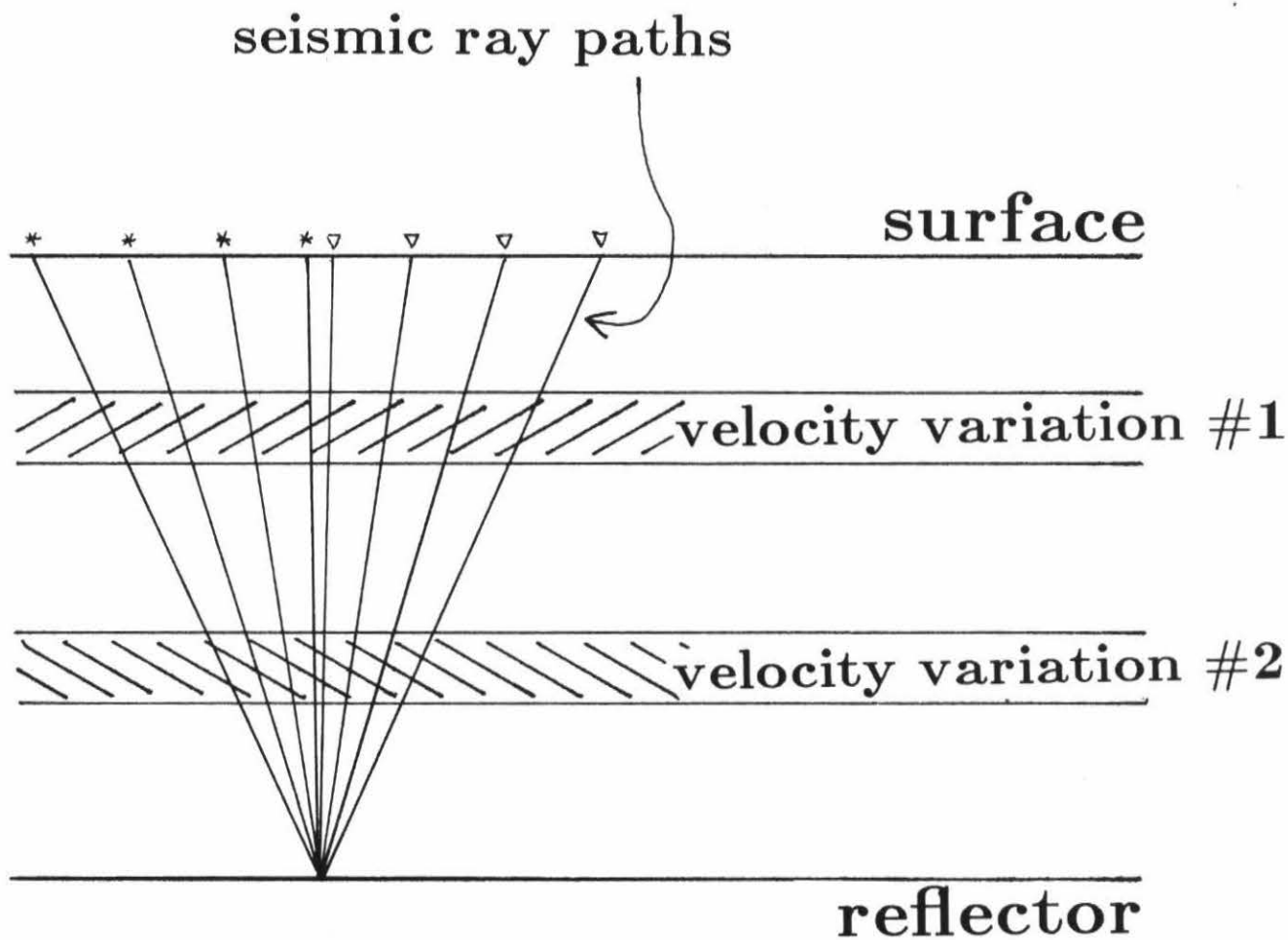
seismic ray paths
surface
velocity variation #1
velocity variation #2
reflector

Figure 3.3

Demonstration of the Central Slice Theorem of Radon Transforms. The resolution of a slant stack with limited angular range is only able to resolve the two cones in wavenumber space. Thus, performing a tomographic inversion with a limited angular ray coverage produces a distorted image with two dimensional "band limiting".

Central Slice Theorem of Radon Transforms

with limited
azimuthal ray coverage,

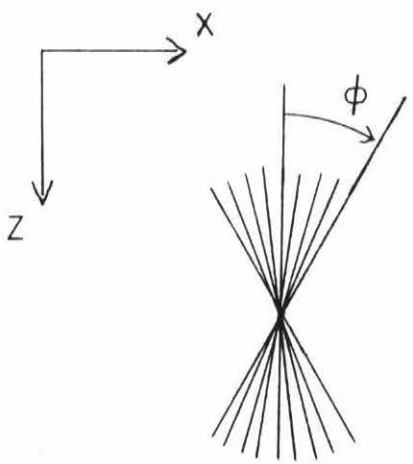

resolution of inversion
in K space is:

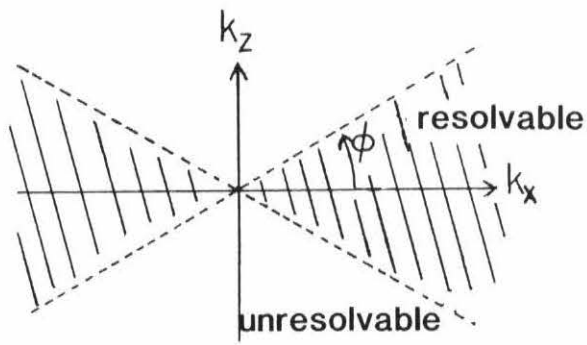

Figure 3.4

Reproduction of Figure 7.13 on page 127 of the thesis by Einar Kjartansson (1979). The bottom figure is an example of removing the wave number components of the upper figure that lie in the unresolved region of the wave number domain as determined by the Central Slice Theorem presented in the previous figure. This figure should be identical to that produced with tomographic inversion in Figure **3.5b**.

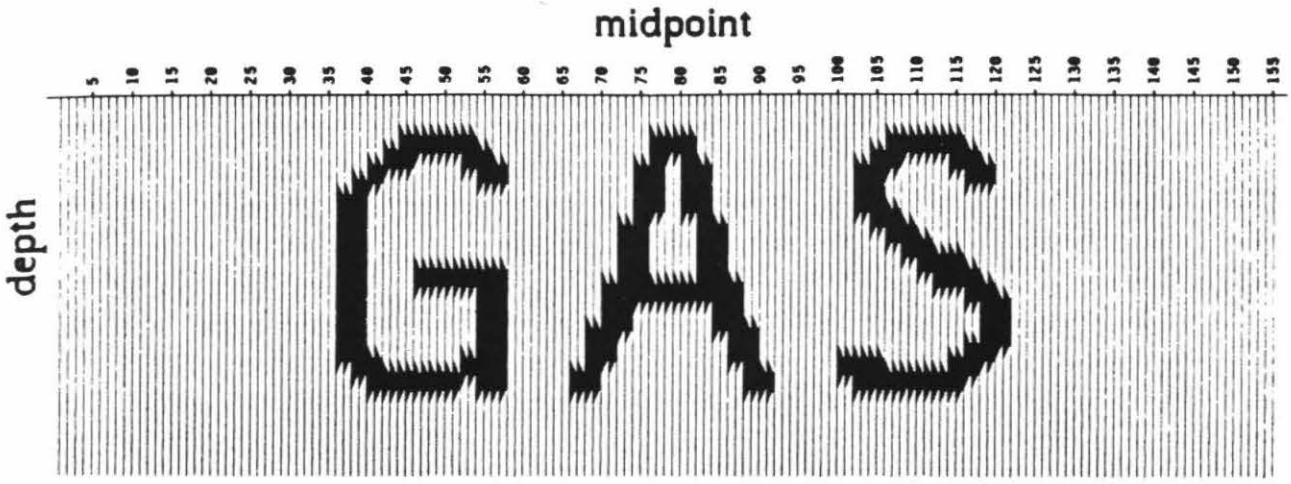
midpoint
depth
5 10 15 20 25 30 35 40 45 50 55 60 65 70 75 80 85 90 95 100 105 110 115 120 125 130 135 140 145 150 155
GAS

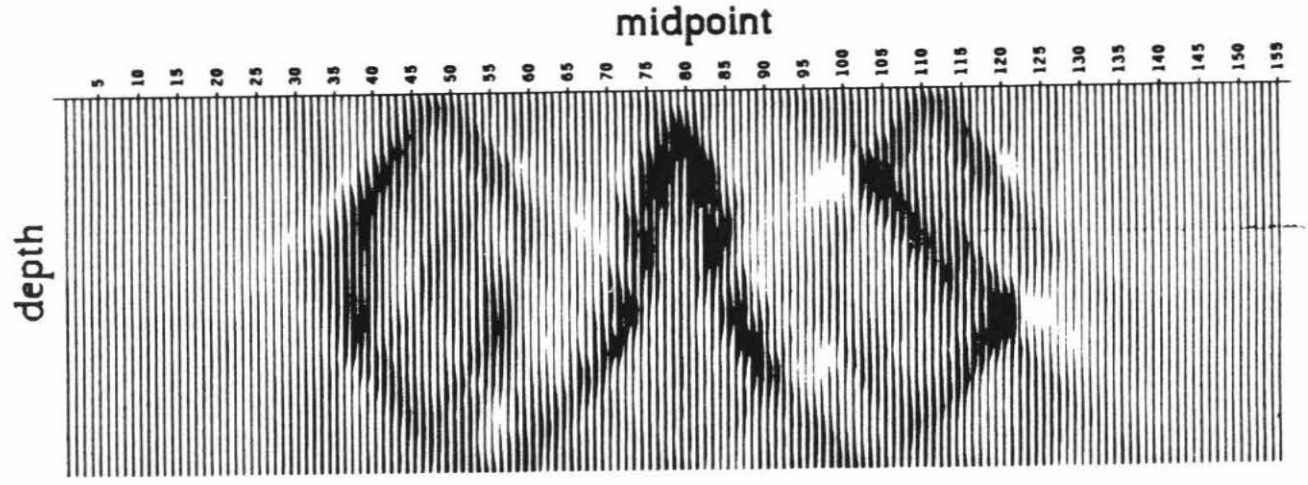
midpoint
depth
5 10 15 20 25 30 35 40 45 50 55 60 65 70 75 80 85 90 95 100 105 110 115 120 125 130 135 140 145 150 155

Figure 3.5

Tomographic inversions of a velocity field that spells **GAS**.

A: The velocity field used for forward modeling. A flat reflector exists at depth 7000 ft. The cable length was 14,000 ft which provides a maximum angular ray coverage of 45°.

B: Inversion with almost no non-linear effects. Most of the artifacts result from the limited angular ray coverage. The non-linear effects are mostly avoided by using ray paths in the inversion that are very close to those used in the forward modeling.

C: Inversion with non-linear effects. The artifacts from the non-linearity can be distinguished from those caused by the limited angular ray coverage by comparing the results with Figure **B** above.

Non-linear effects result from using different ray paths in the inversion from those used for data collection, which are normally not known. The reference model used for ray tracing had a constant velocity field of 8000 ft/sec. An example of the ray paths through the true velocity field is shown in Figure **3.6**.

See text for further discussion.

True 'GAS' Model

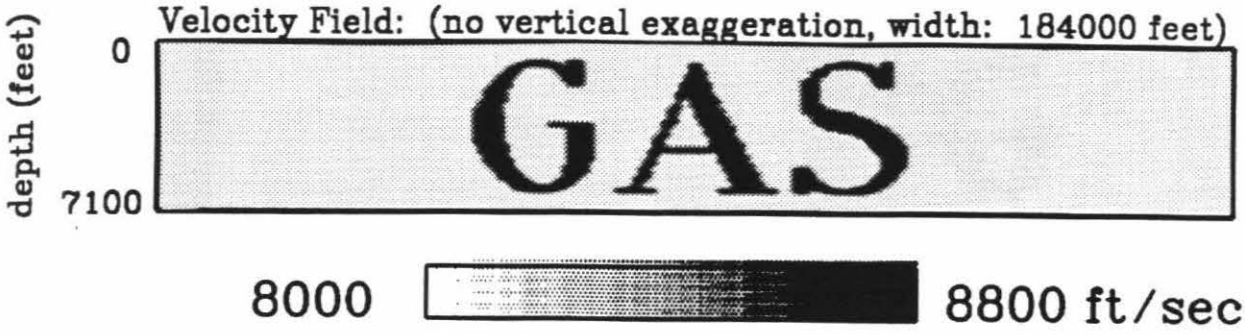

Inversion of 'GAS' Model
with almost no Non-Linear effects

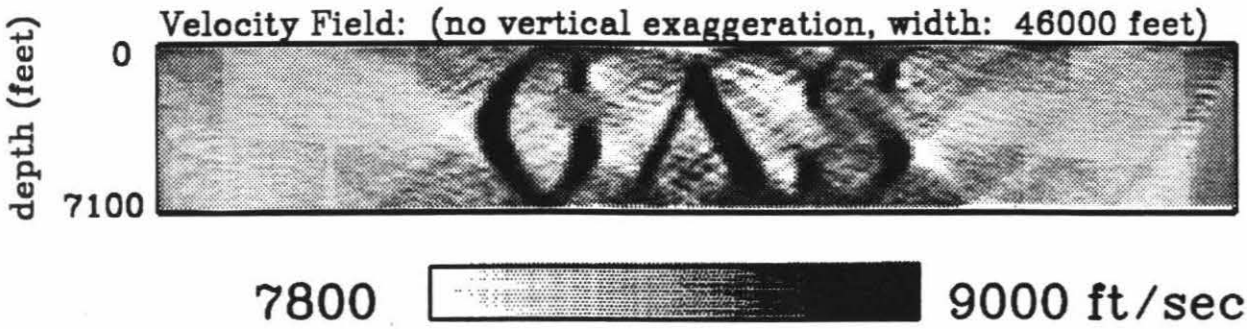

First Inversion of 'GAS' Model

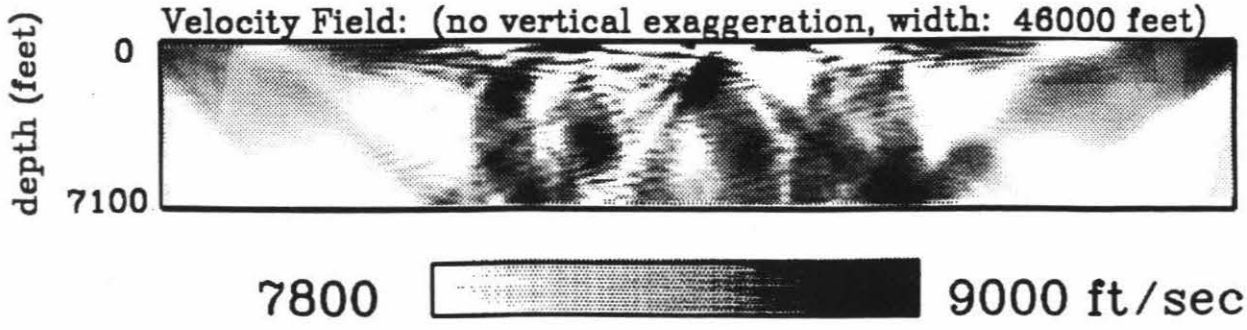

Figure 3.5

D: Result after three ray tracings and inversions. The re-ray tracing is performed through the result of the previous inversion in an attempt to improve the ray paths and reduce non-linear effects. The letters are narrower than in Figure **3.5c**. Serious high frequency artifacts have been introduced and should have been damped.

Inversion of 'GAS' Model
after 3 Ray Tracings and Inversions

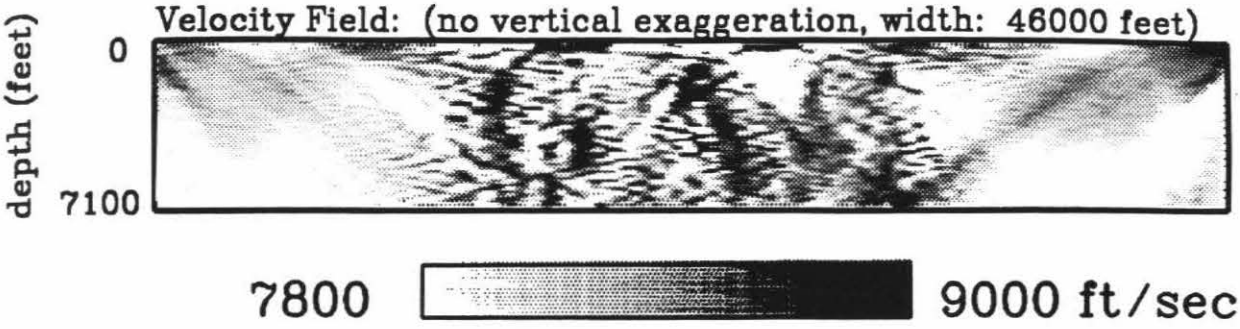

Figure 3.6

Effect the velocity variations of the true model have on the ray paths. Although the velocity variations are only +10% (8800 vs. 8000 ft/sec), they have significantly altered the rays, creating an inhomogeneous ray distribution. Note that no rays can be traced to a group of receivers near the top of the letter **A**.

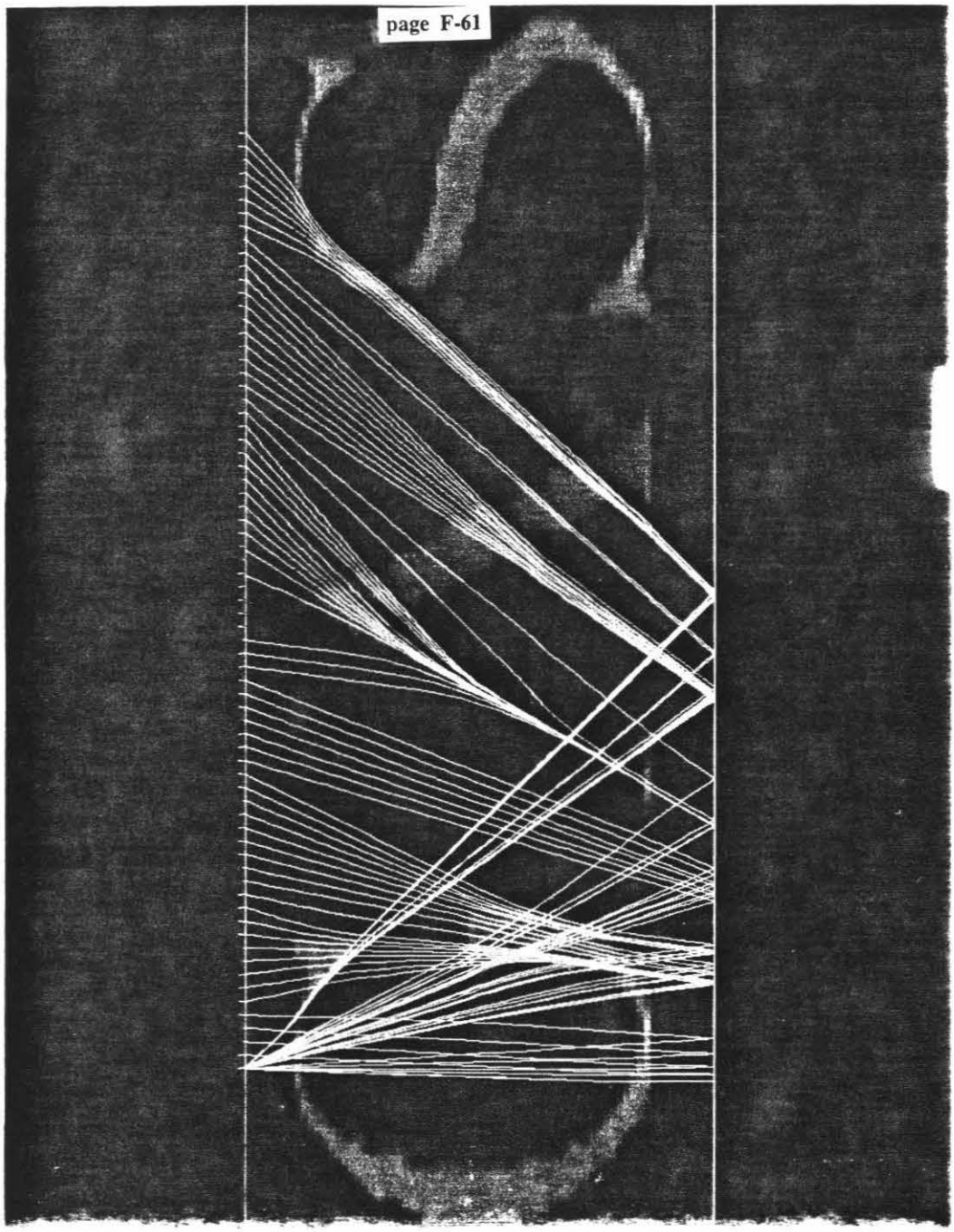

Figure 3.7

Zero offset time section of the central part of the **GAS** model in Figure **3.5a** with a strong reflector at depth 7000 feet. The modeling was performed by reversing a 45^{o} frequency domain finite difference migration program. The velocity variations have caused some clear diffractions. Some low amplitude reflections off of the **GAS** velocity variations can be seen above the reflector.

Note that the waveform of the transmitted energy has hardly been affected by the velocity variations. The main information in the transmitted energy is it's arrival time.

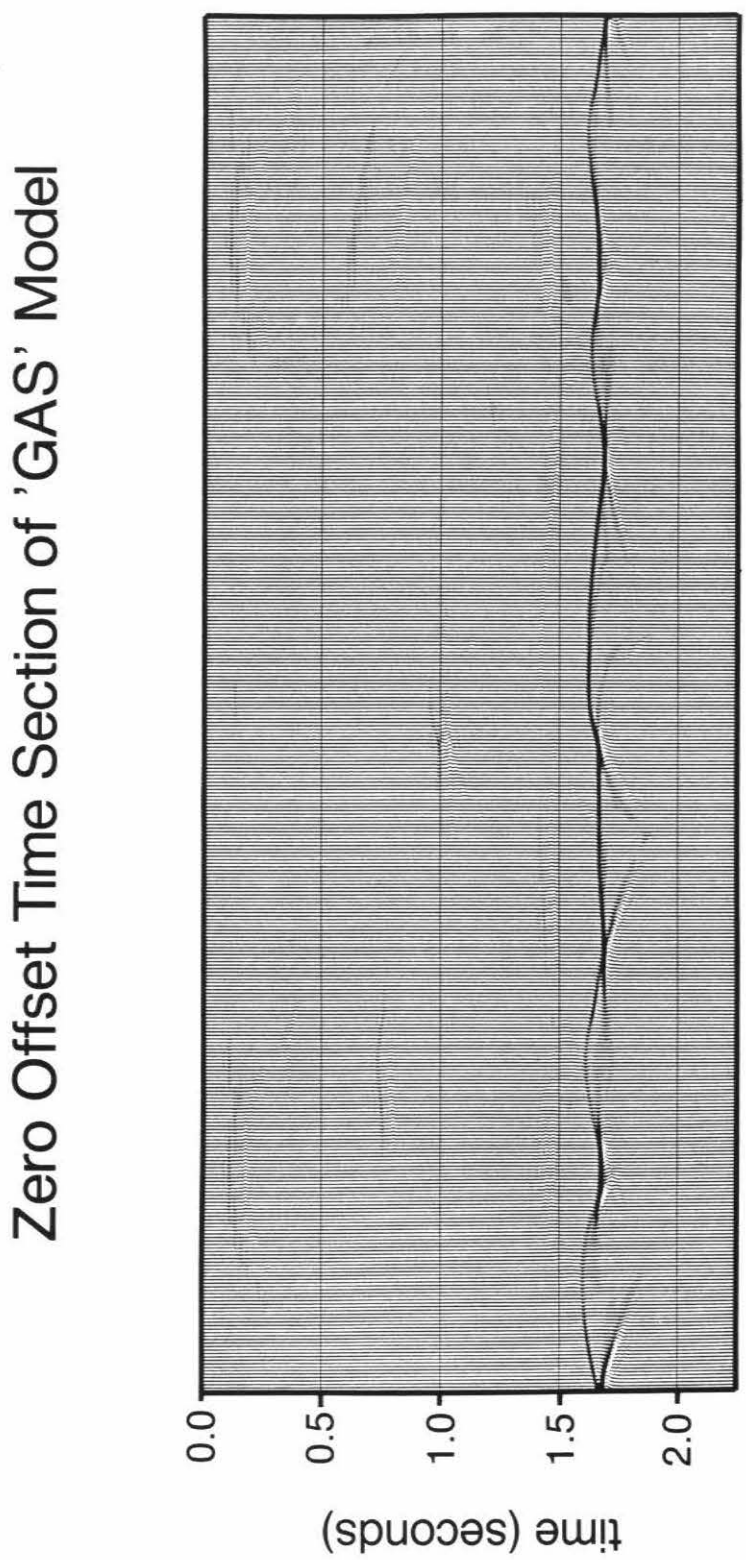
Zero Offset Time Section of 'GAS' Model
0.0
0.5
1.0
1.5
2.0
time (seconds)

Figure 3.8

Migration of the **GAS** zero offset time section of Figure **3.7** through the correct velocity field with the **GAS** velocity variations. The result is close to the correct result of a flat reflector at a depth of 7000 feet. The errors are from numerical artifacts of the modeling and migration programs.

Figure 3.9

Migration of the **GAS** data through the smeared inversion with almost no non-linear effects in Figure **3.5b**. Result is nearly identical to the migration through the correct velocity field in the previous figure. The smearing from the limited angular ray coverage apparently does not affect the migration.

Migration of 'GAS' Time Section Through Correct Velocity

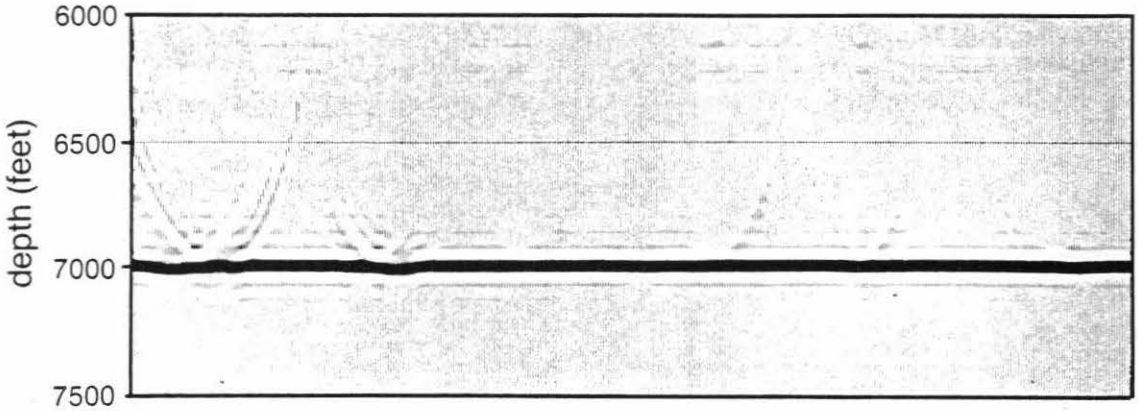

Migration of 'GAS' Time Section Through Inversion With Almost No Non–Linear Effects

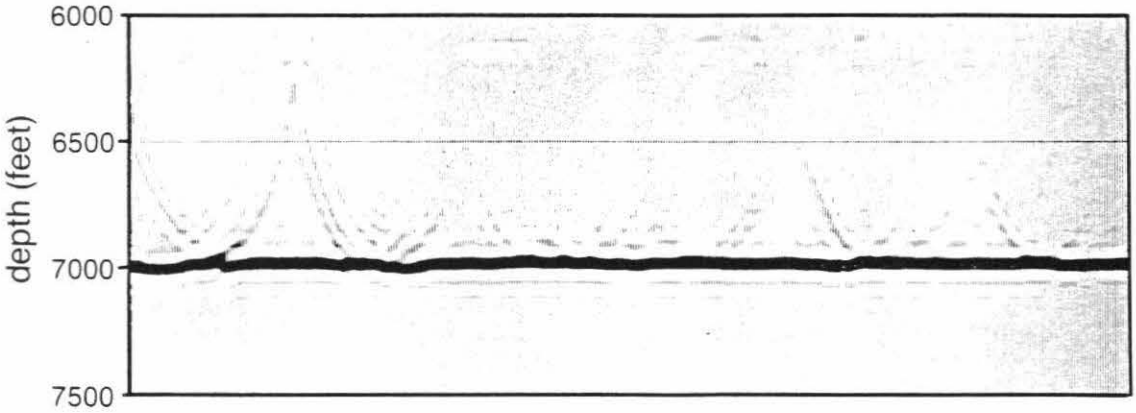

Figure 3.10

Migration of the **GAS** data through a constant velocity field of 8000 ft/sec, which is the reference model used for the ray tracing and inversion of Figure **3.5c**. The migration has been severely corrupted. This is the result that would be produced if the **GAS** velocity variations were not inverted.

Figure 3.11

Migration of the **GAS** data through the inversion with non-linear effects of Figure **3.5c**. The result has many problems, but is still better than the migration through the reference model in the previous figure.

Migration of 'GAS' Time Time Section Through
Constant Velocity Reference Model

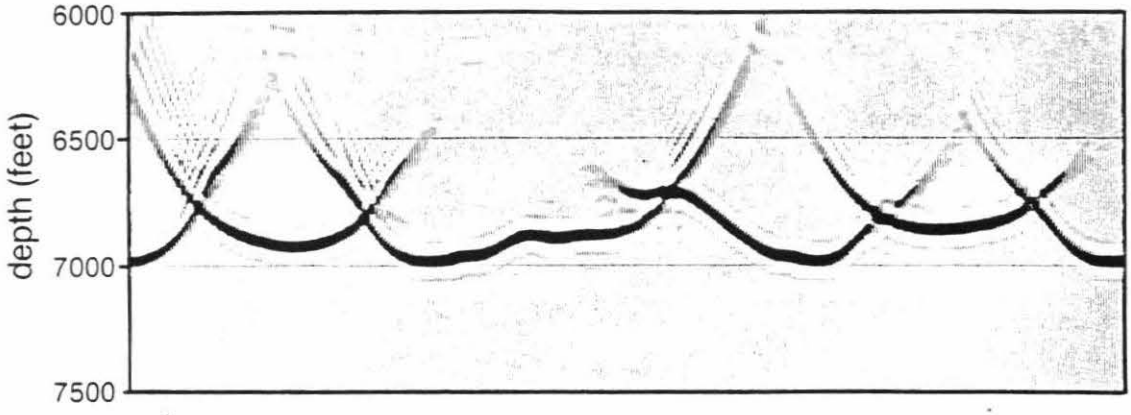

Migration of 'GAS' Time Section Through
First Inversion

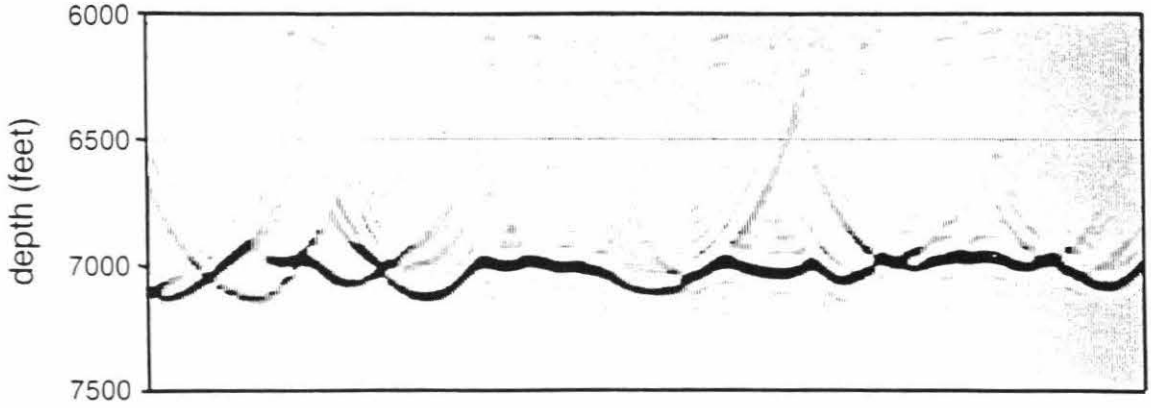

Figure 3.12

Migration of the **GAS** data through the velocity field after 3 ray tracings and linear inversions shown in figure **3.5d**. Note that the migration has improved the most on the right side under the **S**, which contains mostly horizontal features, rather than the left side under the **G**, which contains more vertical features.

Migration of 'GAS' Time Section Through Result After 3 Ray Tracings & Linear Inversions

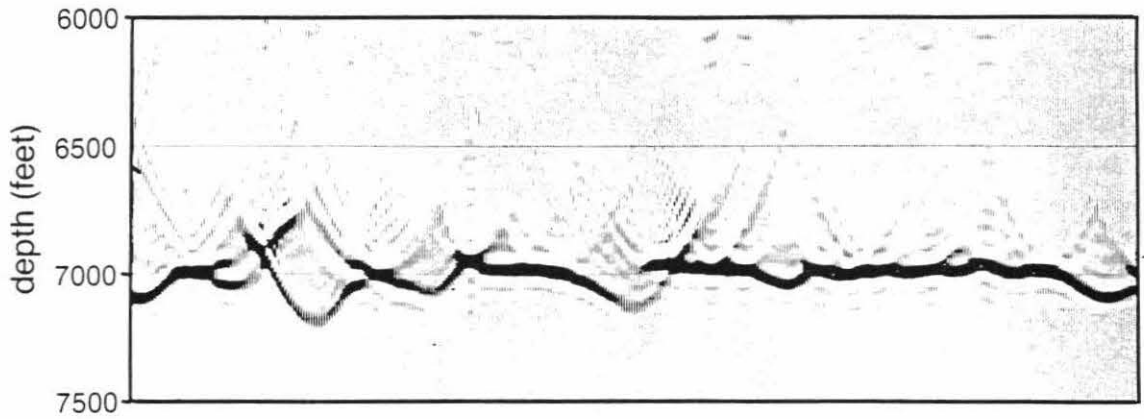

Figure 3.13

Tomographic inversions of velocity field that spells **OIL**.

A: The true model from which synthetic data was collected. Flat reflector exists at 7000 feet depth. The cable length is 14000 feet giving a maximum ray angle of 45°.

B: Inversion of **OIL** velocity field with almost no non-linear effects. The ray paths used for inversion are nearly identical to those in the true model. Dominant artifact is the vertical smearing caused by the limited angular ray coverage.

C: Inversion of **OIL** velocity field with non-linear effects as well as smearing from the limited angular ray coverage. Ray paths used for inversion were traced through a constant velocity (8000 ft/sec) reference model. An example of the true ray paths through the true model are shown in Figure **3.14a & b**. The inversion is severely worse than that in Figure **B**, without non-linear effects.

True 'OIL' Model

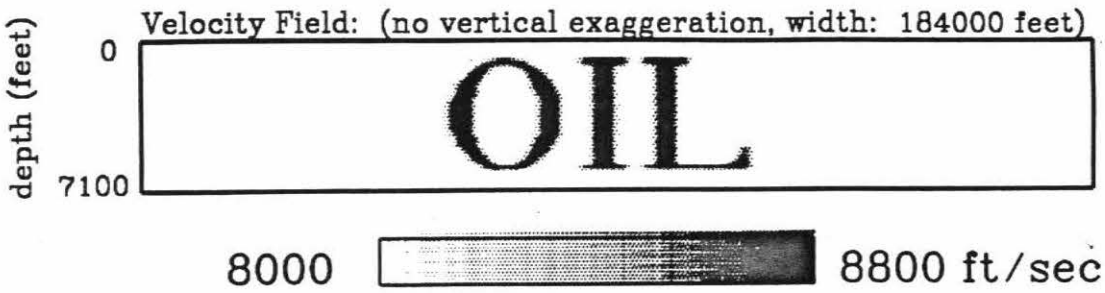

Inversion of 'OIL' Model
with few Non-Linear effects

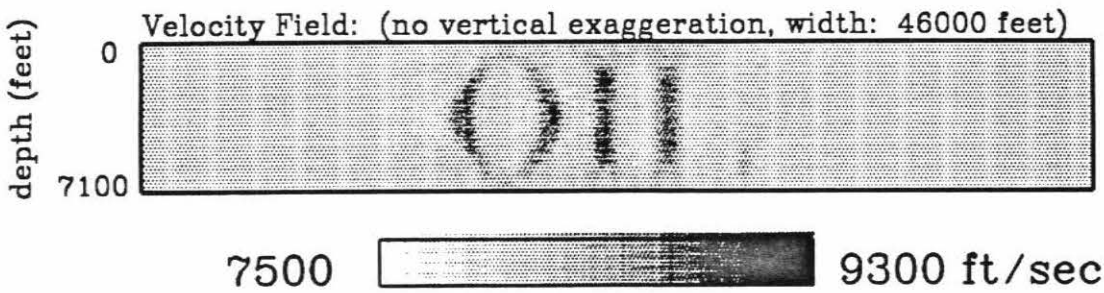

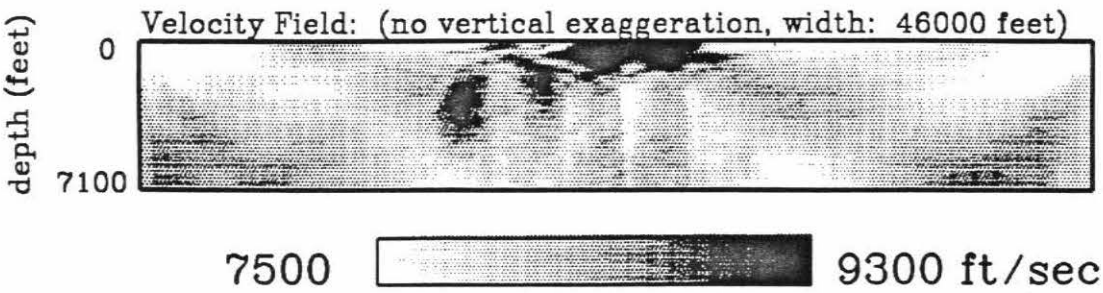

Figure 3.13

D: Inversion of **OIL** model after 3 ray tracings and linear inversions. The additional ray tracings have not helped improve the appearance of the result. High frequency noise has been added to the inversion.

Inversion of 'OIL' Model
after 3 Ray Tracings and Inversions

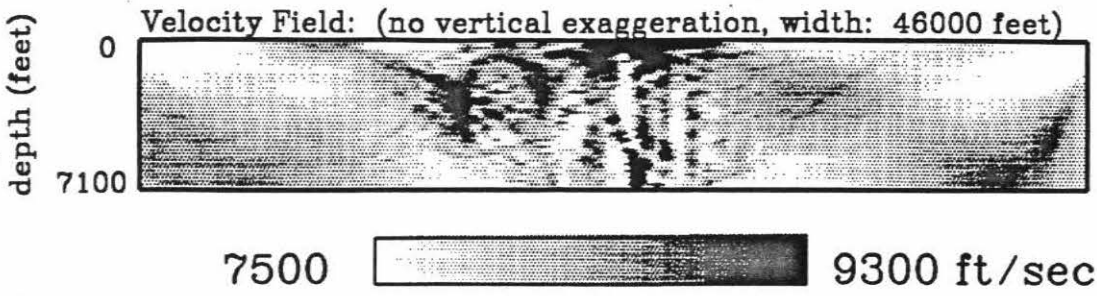

Figure 3.14

A: Sample ray paths through the **OIL** model. Velocity contrast is only +10% yet the rays have been significantly affected, producing an inhomogeneous ray distribution.

B: Sample ray paths of another shot in the **OIL** model.

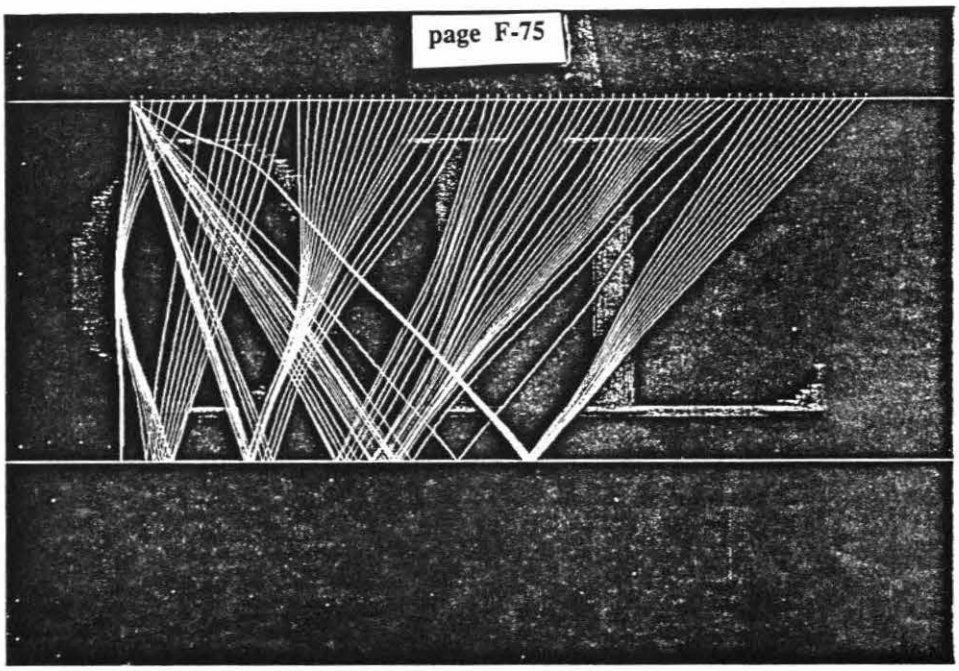

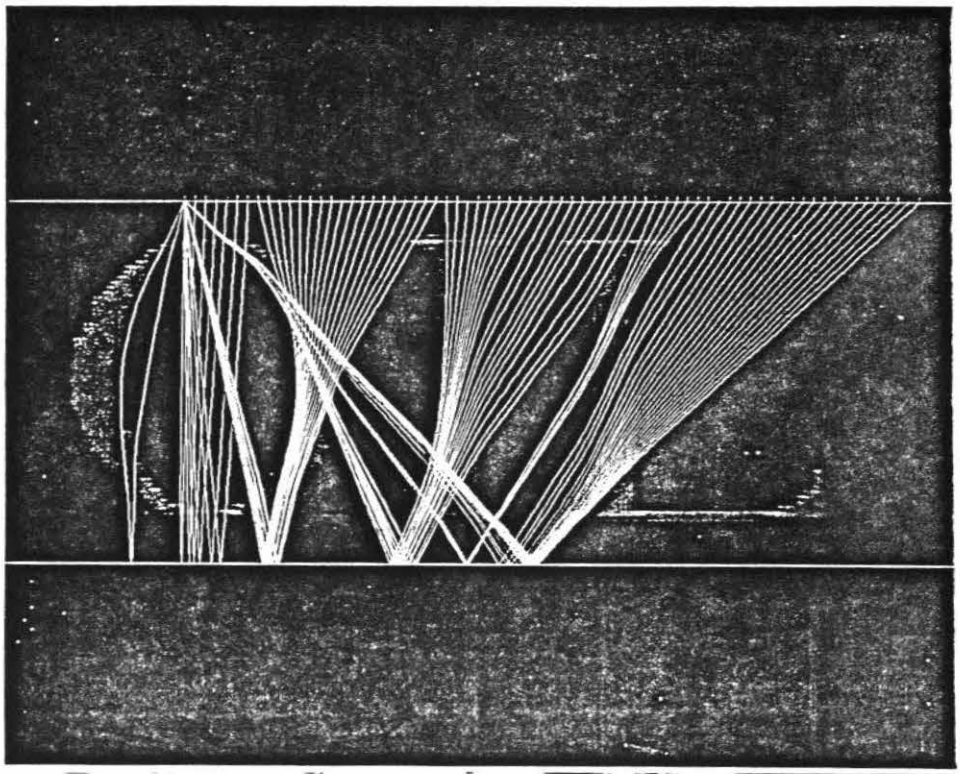

Figure 3.15

Zero offset time section for the **OIL** model with a strong reflector at a depth of 7000 feet. Time section was produced using a 45o frequency domain finite difference migration program.

Figure 3.16

Migration of zero offset time section from **OIL** model through the correct velocity model. Result should be a flat reflector at depth 7000 feet. Diffractions are numerical artifacts of program from the sharp vertical velocity contrast on the sides of the letters.

Zero Offset Time Section of 'OIL' Model

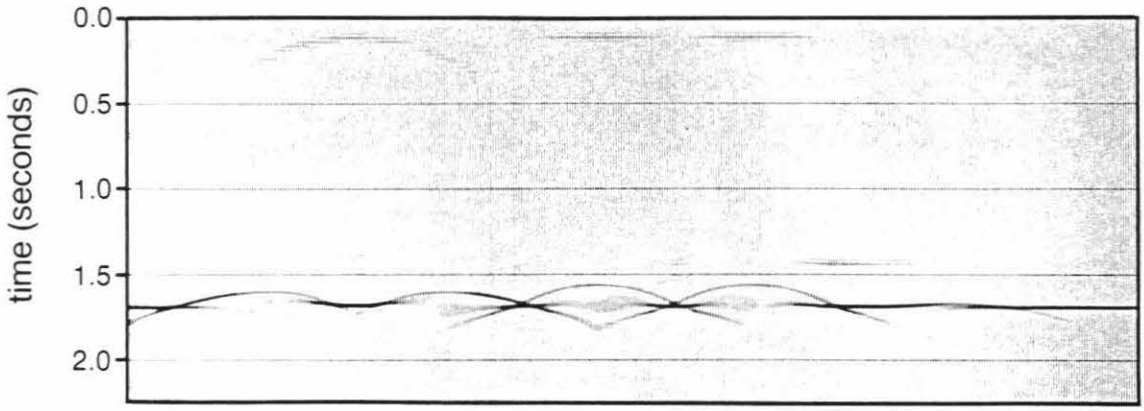

Migration of 'OIL' Time Section Through Correct Velocity

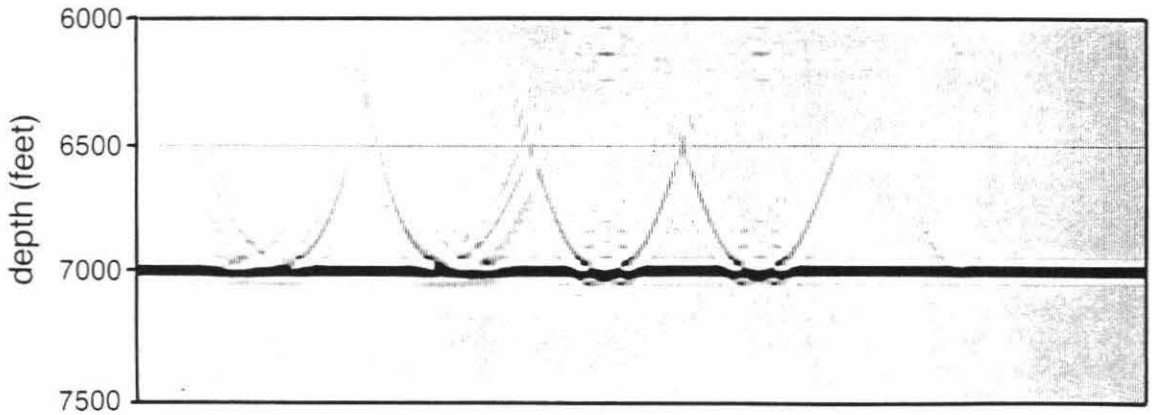

Figure 3.17

Migration of **OIL** data through smeared velocity inversion with almost no non-linear effects. Result is close to the correct flat reflector model. The diffractions that exists are similar to those in the previous figure through the correct model.

Figure 3.18

Migration of **OIL** data through constant velocity field used as the reference model. The result is severely distorted.

Migration of 'OIL' Time Section Through Inversion With Few Non–Linear Effects

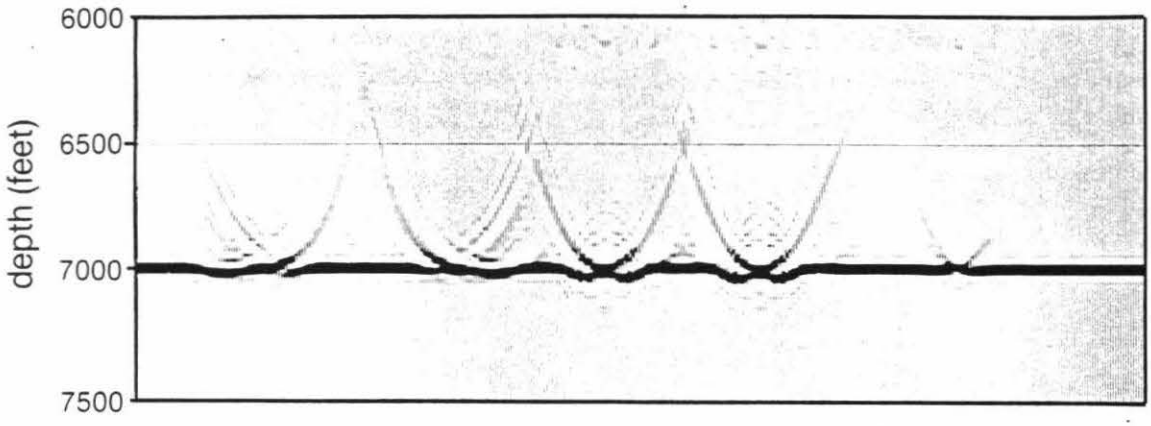

Migration of 'OIL' Time Section Through Constant Velocity Reference Model

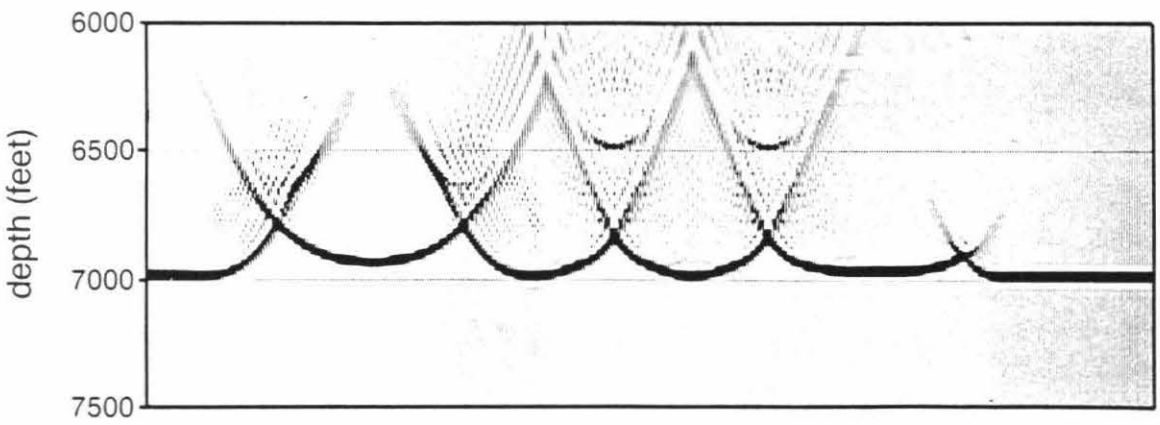

Figure 3.19

Migration of **OIL** data through velocity field inverted with non-linear effects, shown in Figure **3.13c**. The image does not appear to be an improvement over the migration through the reference model used for inversion.

Figure 3.20

Migration of **OIL** data through velocity field after 3 ray tracings and linear inversions, shown in Figure **3.13d**. Image appears to have improved on the left side, under the letter **O**, compared to the previous figure. The central part of the figure, under the letters **I** & **L**, has worsened.

Migration of 'OIL' Time Section Through First Inversion

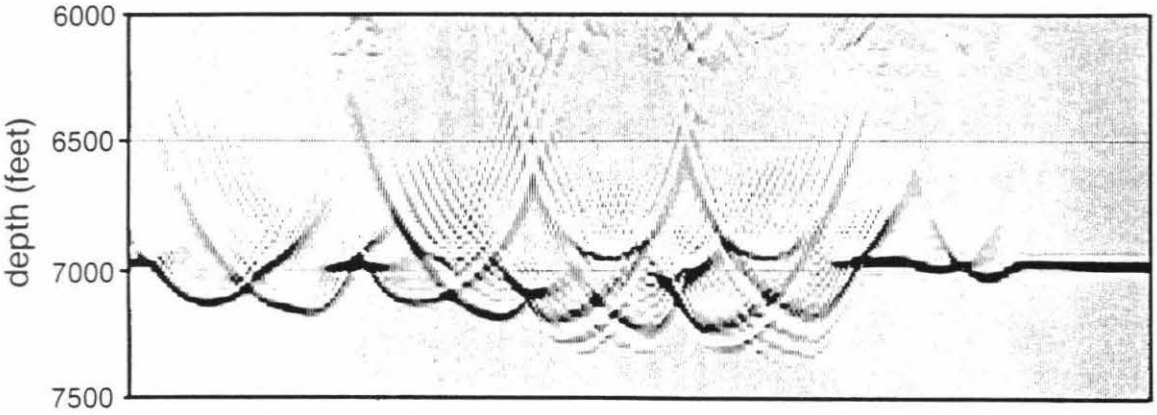

Migration of 'OIL' Time Section Through Result After 3 Ray Tracings & Linear Inversions

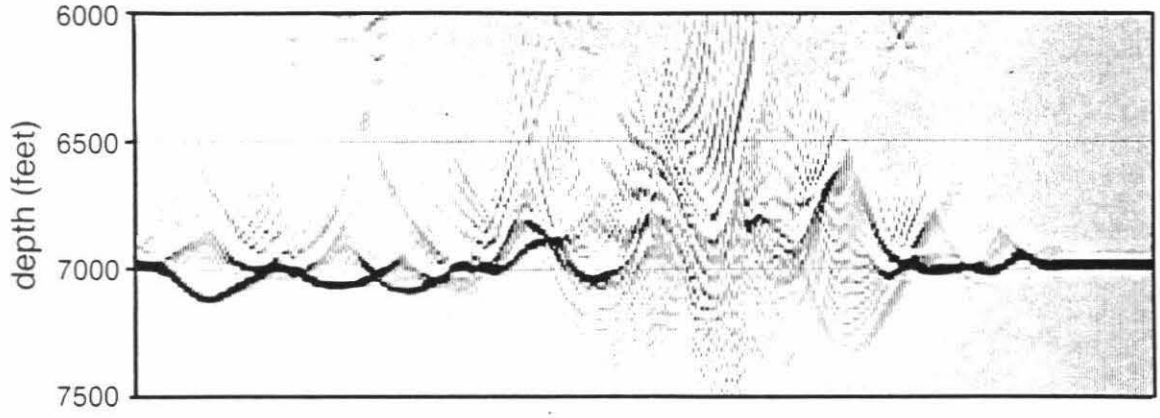

Figure 3.21

Tomographic inversions of horizontally shaped blocks of opposite sign velocity variation and at different depth.

A: Velocity field used for forward modeling. Velocity variations are +/- 1000 ft/sec. Flat reflector exists at depth 5000 feet, maximum ray angle was 45o.

B: Inversion with few non-linear effects produced using accurate ray paths. The blocks have been smeared vertically and their amplitude has been reduced. Note the change in scale.

C: Inversion with non-linear effects. The non-linear artifacts are much less severe than for the **OIL** and **GAS** models of Figures **3.5** & **3.13**. The lower blocks appear to have been affected more, with the fast block being widened, and the slow block being narrower.

True Model B

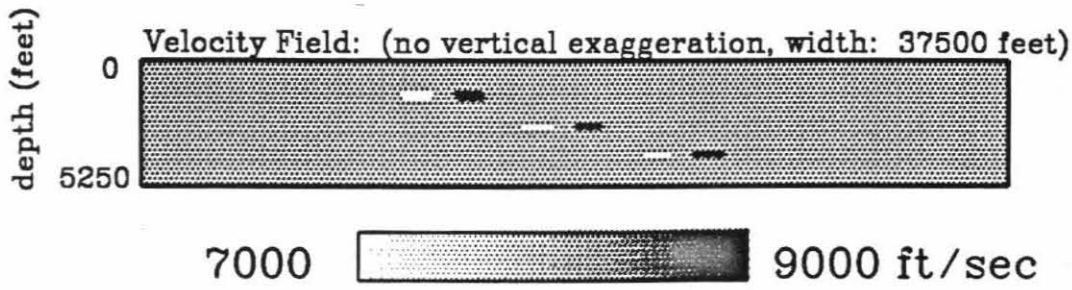

Inversion of Model B with few Non-Linear Effects, eigenvalue range: (1.0-0.02)

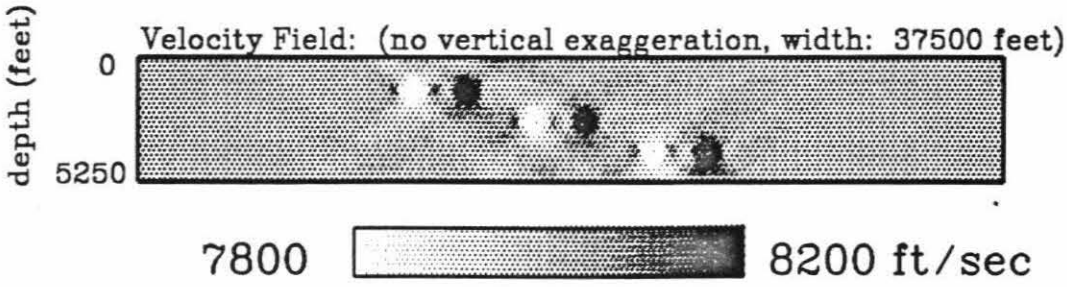

First Inversion of Model B eigenvalue range: (1.0-0.02)

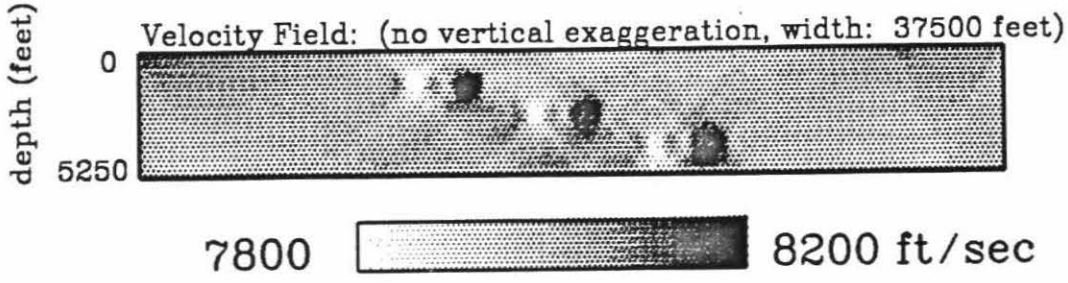

Figures 3.21

D, E, & F: The inversion of the horizontal velocity blocks after successive ray tracings and linear inversions. The lower velocity blocks have been corrected to their proper widths. The greatest noticeable difference occurs with the second ray tracing, but more subtle effects of the additional inversions appear in the migrations through the inversion, shown in Figures **3.25-3.28**.

Inversion of Model B after
2 Ray Tracings and Inversions

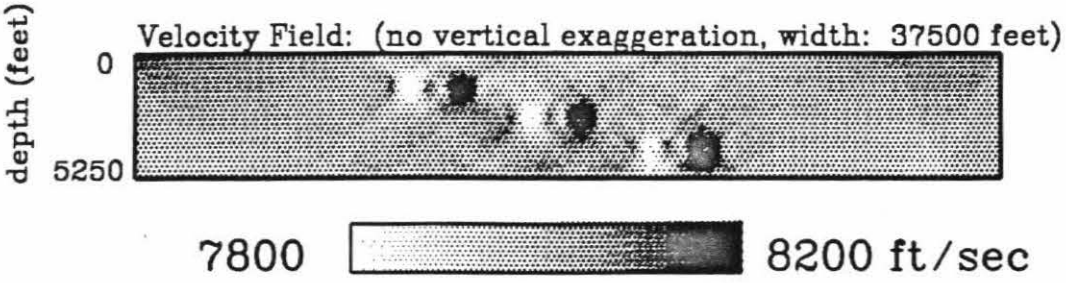

Inversion of Model B after
3 Ray Tracings and Inversions

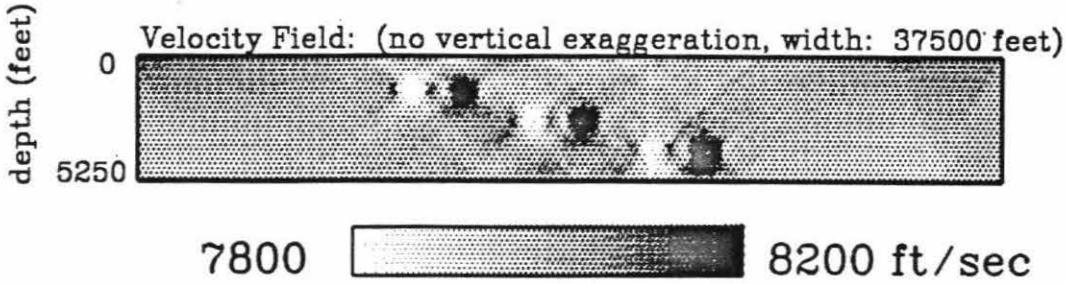

Inversion of Model B after
4 Ray Tracings and Inversions

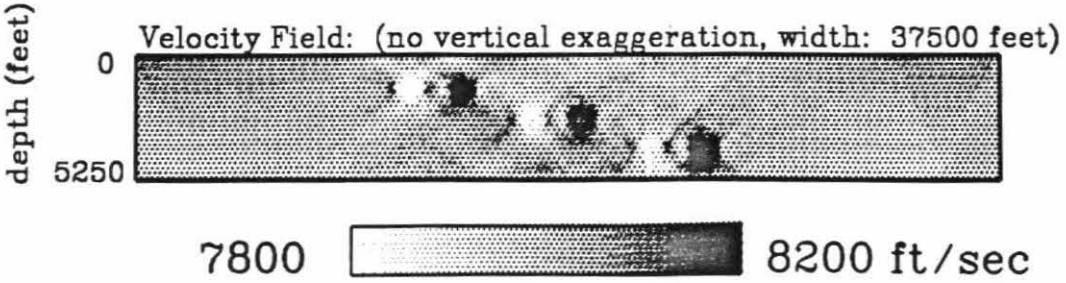

Figures 3.21

Inversion of horizontal blocks using different parameters.

G: Inversion with non-linearities using a maximum ray angle of only 22°. The vertical smearing is more pronounced than in the inversion in Figure **3.21c** produced using a maximum ray angle of 45°. Two non-linear artifacts, the widening of the lower fast block and the thinning of the lower slow block, are also more pronounced.

H: Velocity field after 4 ray tracings and inversions where the maximum ray angle used was 22°. The velocity anomalies have greater amplitude than the previous inversion in Figure **3.21g**.

J: Inversion with a maximum ray angle of 45° where the reflector depth was allowed to vary along with the velocity field. The reference reflector was flat at the correct depth of 5000 feet. The reflector is plotted separately so that it can be vertically exaggerated. Some of the lower velocity variations have traded off into reflector depth variations while none of the upper velocity variations have.

First Inversion of Model B using
Maximum Ray Angle of 22 degrees, eigenvalue range: (1.0-0.02)

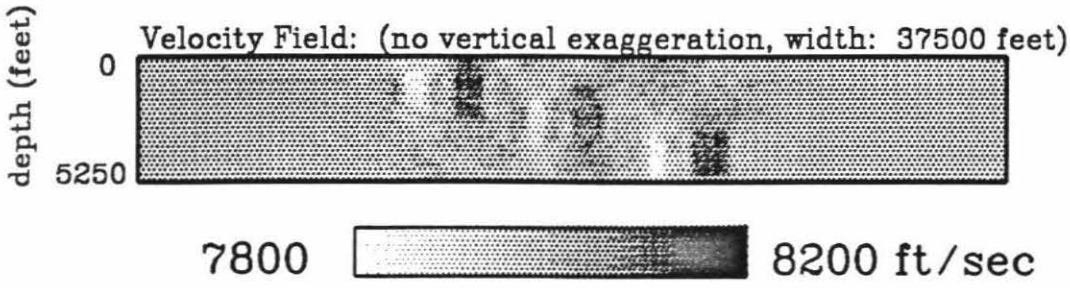

Inversion of Model B after 4 Ray Tracings and
Inversions with Maximum Ray Angle of 22 degrees

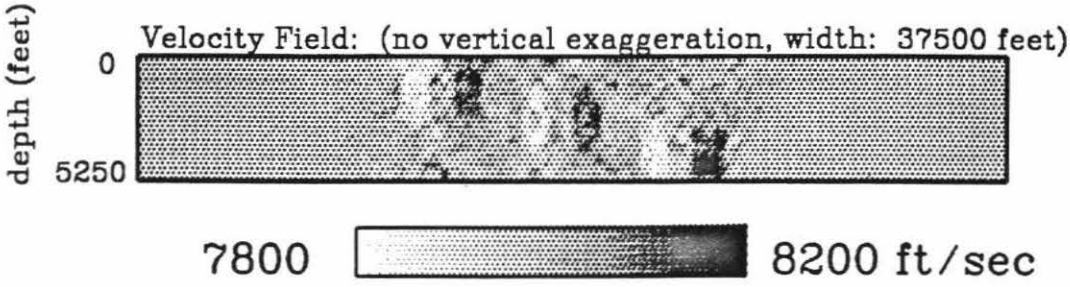

Inversion of Model B for Velocity and Reflector
eigenvalue range: (1.0-0.02)

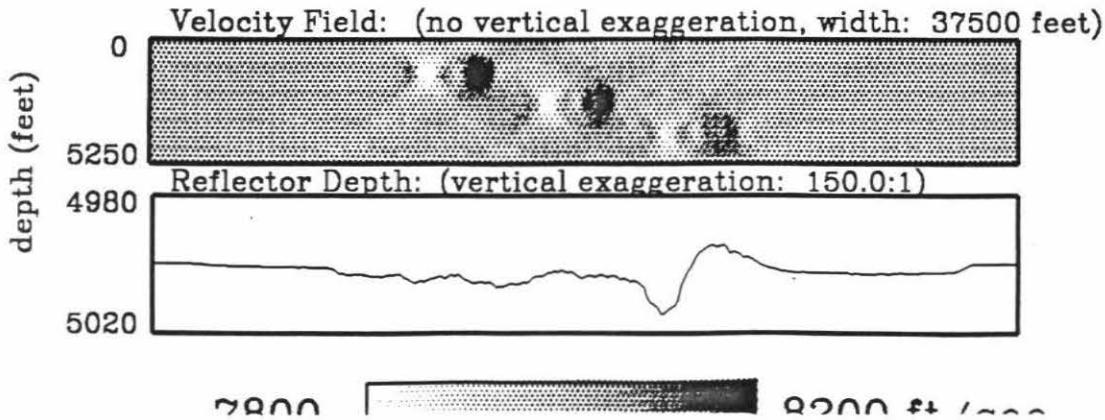

Figures 3.21

K & L: Reference models with incorrect reflector structure used for inversions. Note the vertical exaggeration of the scale used for plotting the reflectors. Examples of how this reflector structure effects the ray paths is shown in Figures **3.22c & d**.

Reference Model B1

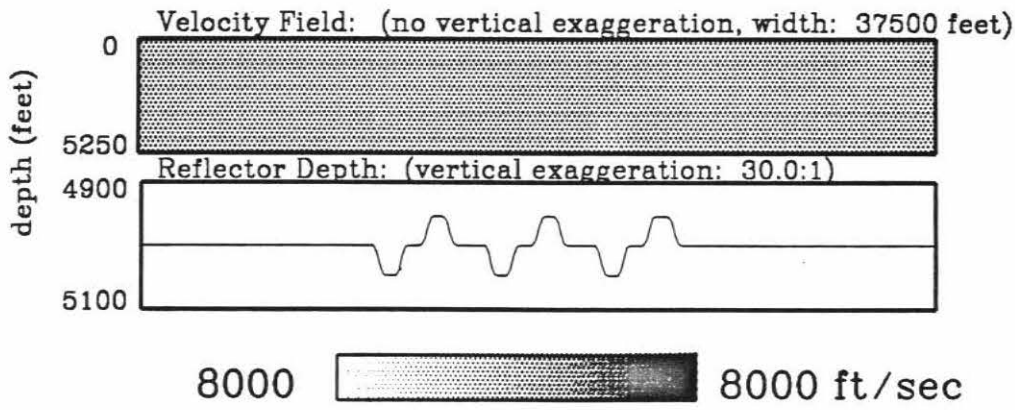

Reference Model B2

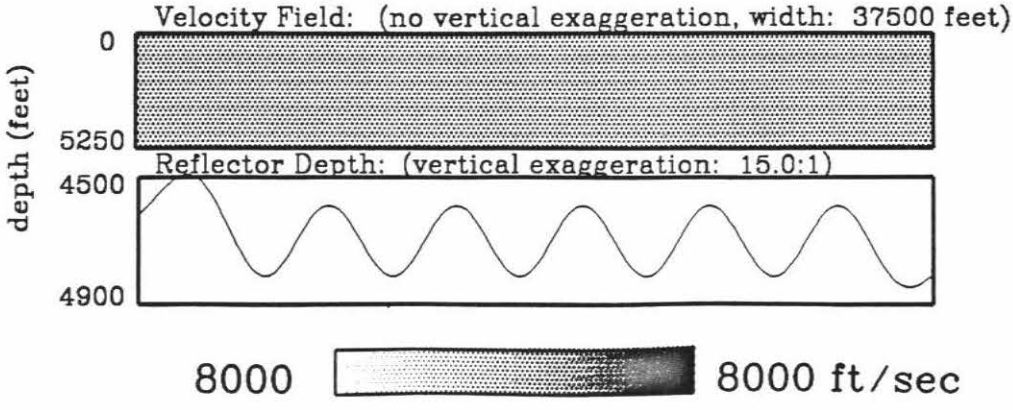

Figures 3.21

M & N: Inversions using reference models with incorrect reflector structure. The inversions are performed such that the incorrect reflector structure does not affect the travel times, but only the ray paths. Conversely, the velocity anomalies affect only the travel times but not the ray paths. Thus these inversions address only the affect of the ray paths errors caused by incorrect reflector structure. The inversions are not severely corrupted.

The lower velocity variations, closer to the reflectors are distorted more by the incorrect reflector structure.

Inversion of Model B using
Reference Model B1 (few Non-linear effects)

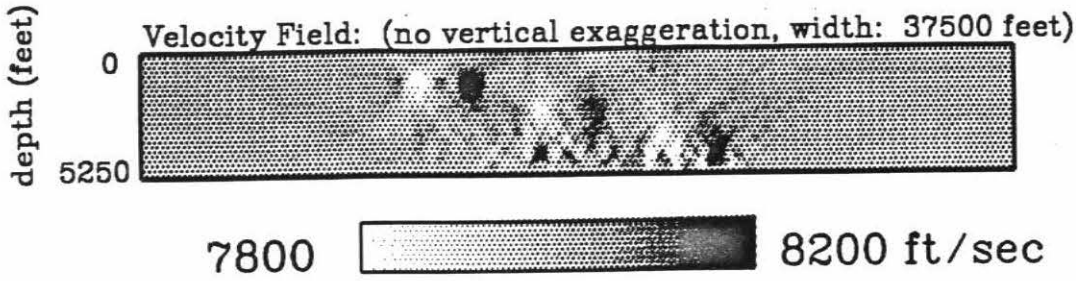

Inversion of Model B using
Reference Model B2 (few Non-linear effects)

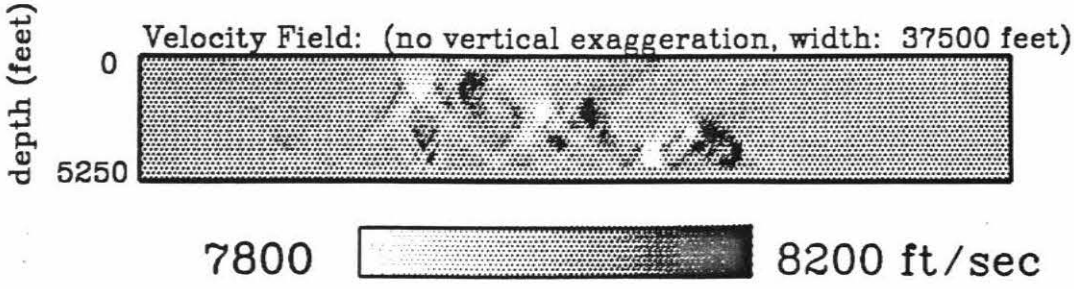

Figure 3.22

A: Sample ray paths from a shot to receivers for the true model in Figure **3.21a**. Slow blocks are lighter.

B: More sample ray paths from a shot to receivers for the true model.

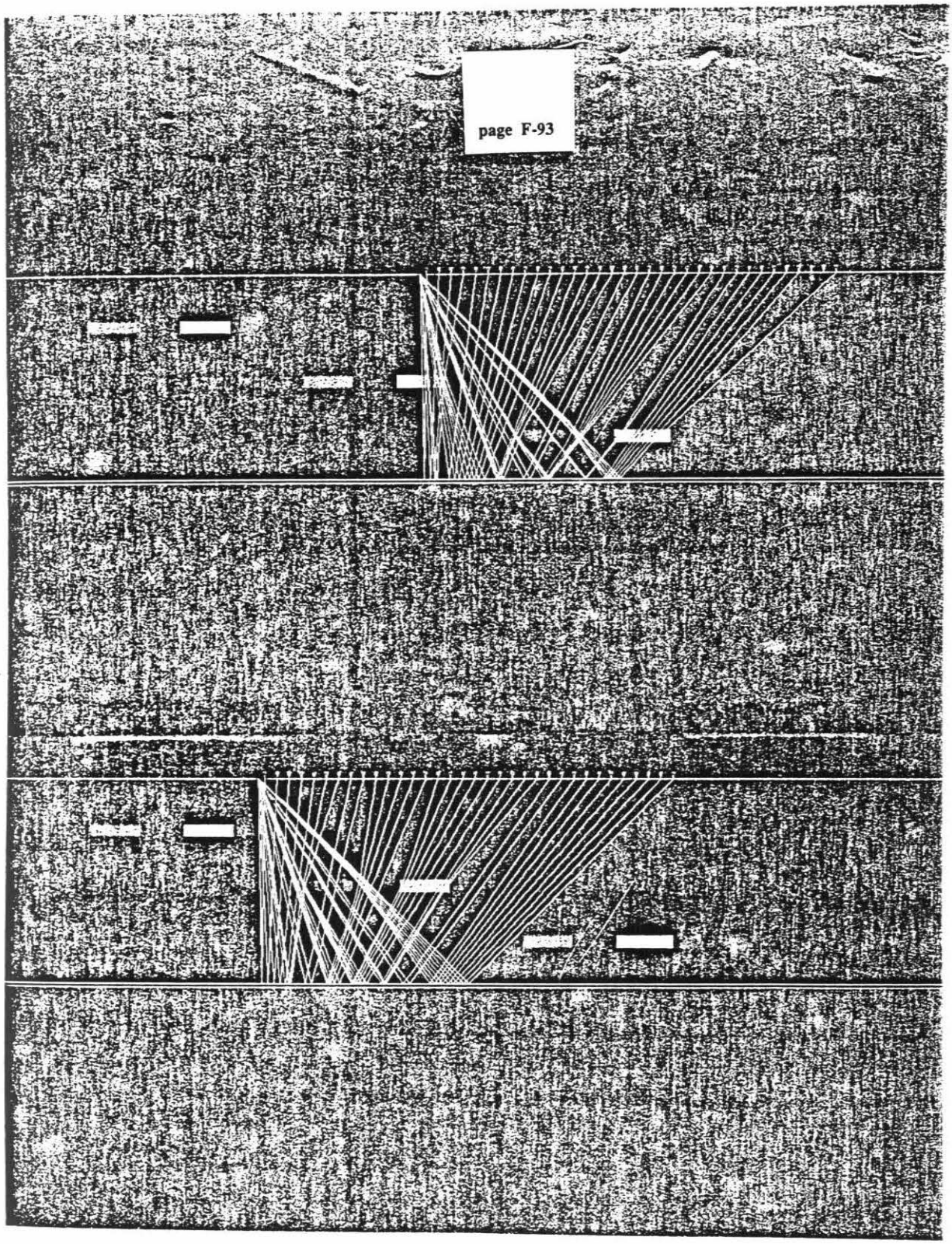

Figure 3.22

C: Sample ray paths from a shot to receivers for reference model B-1 of Figure **3.21k**. Even though the reflector structure is quite small, it has significantly affected the ray paths.

D: Sample ray paths from a shot to receivers for reference model B-2 of Figure **3.21l**. Rays density increases near the reflector peaks and decreases at the troughs.

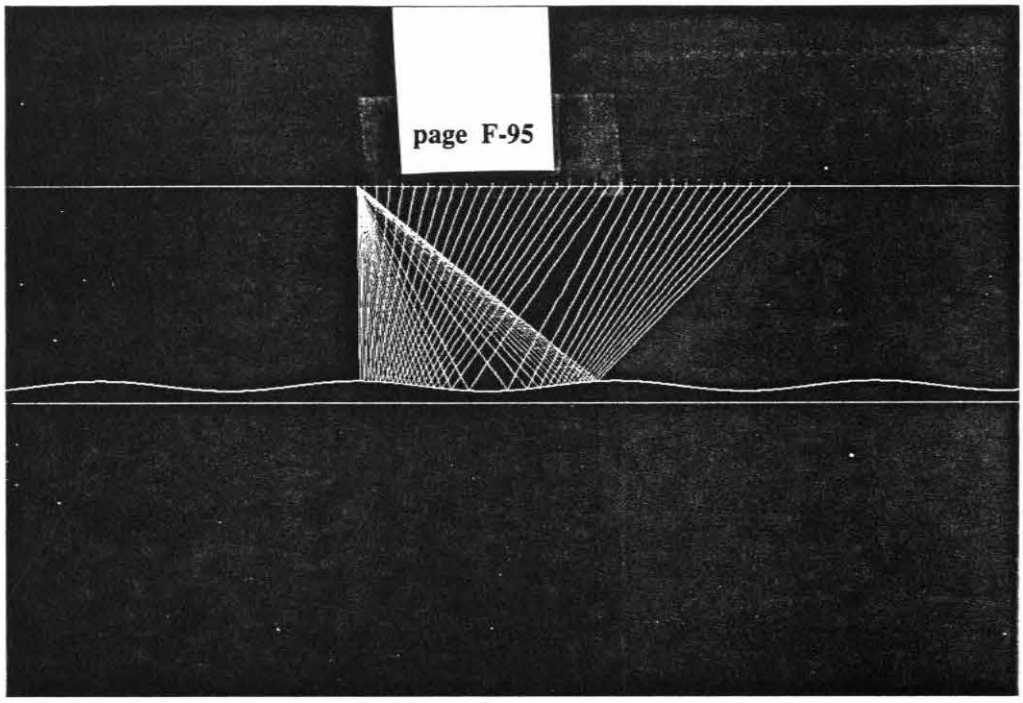

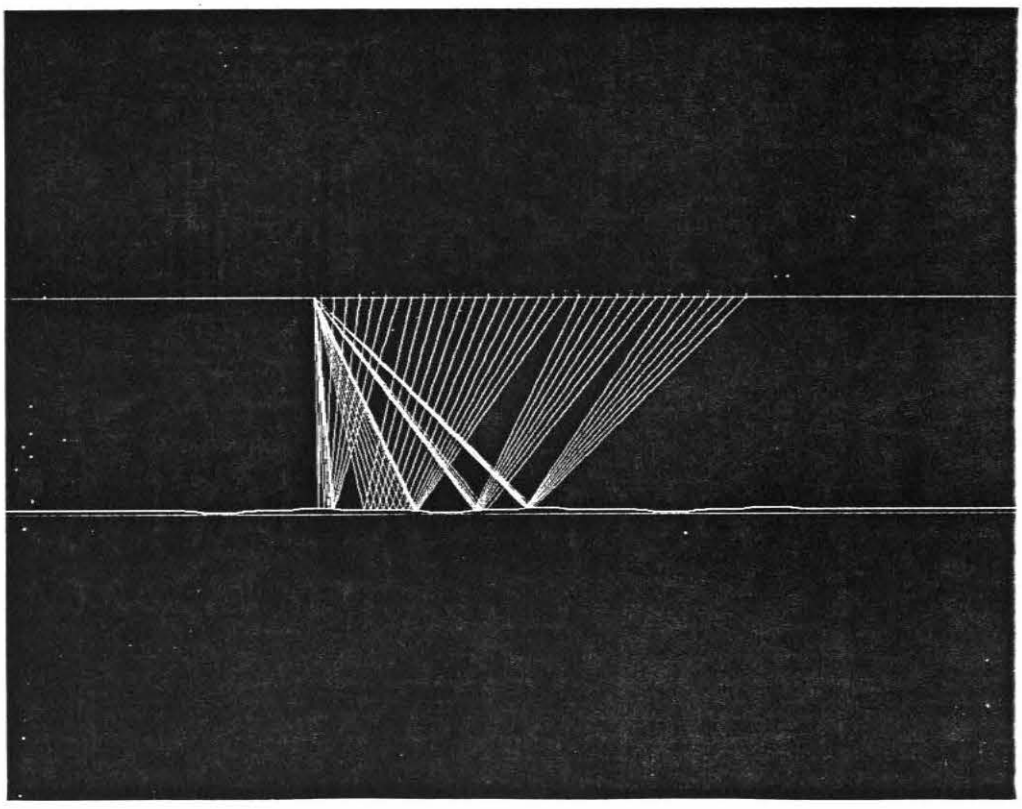

Figure 3.23

Migration of zero offset section from true model through the correct velocity model. The result is a flat reflector at 5000 feet depth.

Figure 3.24

Migration of zero offset section through the constant velocity reference model. The unresolved velocity variations cause reflector deviations of about 40 feet. The reflector artifacts from the upper velocity blocks, on the left side of the figure, have larger diffraction tails.

Migration of Model B Zero Offset Section Through Correct Velocity

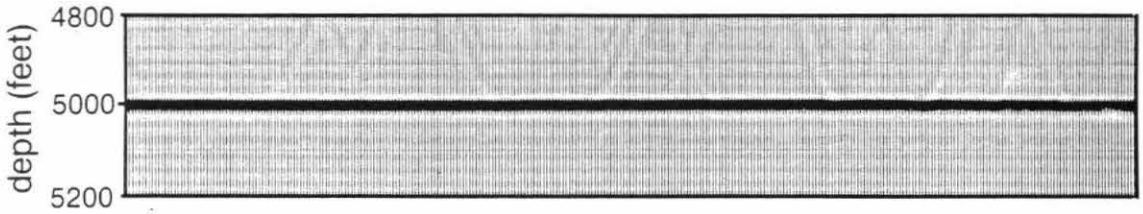

Migration of Model B Zero Offset Section Through Constant Velocity Reference Model

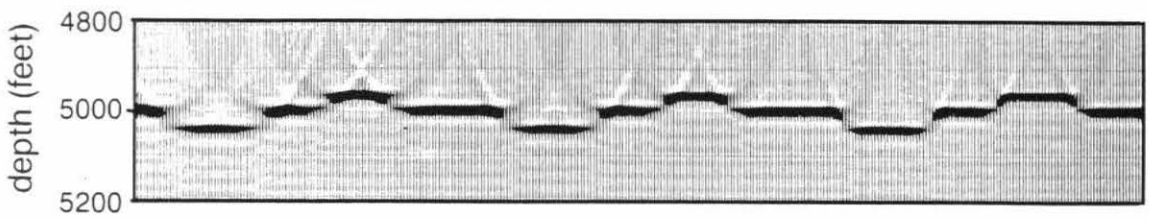

Figure 3.25

Migration through first non-linear inversion, shown in Figure **3.21c**. The non-linear artifacts cause the breaks in the reflector. The artifacts appear greatest on the right side, where the lower velocity blocks are. The artifacts also appear greater for the slow velocity blocks than for the fast ones.

Figure 3.26

Migration through second non-linear inversion shown in Figure **3.21d**, where an additional ray tracing and inversion have been performed over the previous figure. The non-linear effects on the left side, which are under the higher velocity variations, have been almost entirely removed. The other effects have been improved.

Migration of Model B Zero Offset Section Through First Inversion

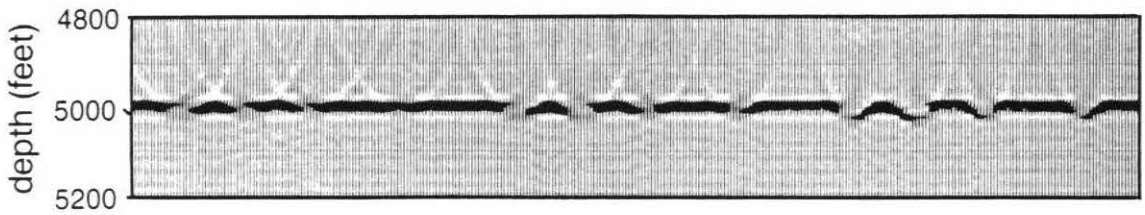

Migration of Model B Zero Offset Section Through Result After 2 Ray Tracings & Inversions

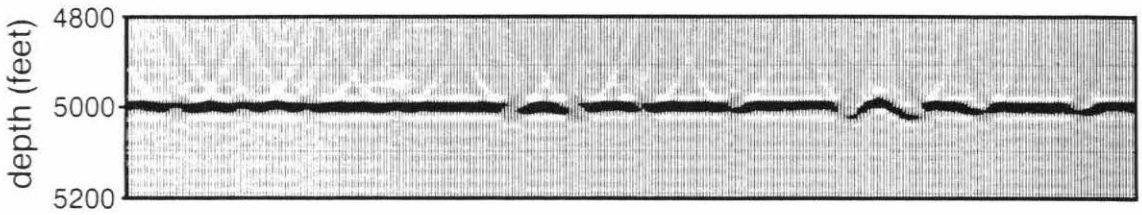

Figure 3.27

Migration through third non-linear inversion, shown in Figure **3.21e**. The non-linear effects have been marginally improved over the previous figure.

Figure 3.28

Migration through fourth non-linear inversion, shown in Figure **3.21f**. There is almost no noticeable change from the previous figure. It is presumed that effective convergence of the non-linear iteration steps has been achieved. Most of the non-linear effects have been removed, even on the far right side under the deep fast velocity block. However, the non-linear effect under the deep slow velocity block has not been removed.

The general success of the migration demonstrates migration is insensitive to the vertical smearing of the images.

Migration of Model B Zero Offset Section Through Result After 3 Ray Tracings & Inversions

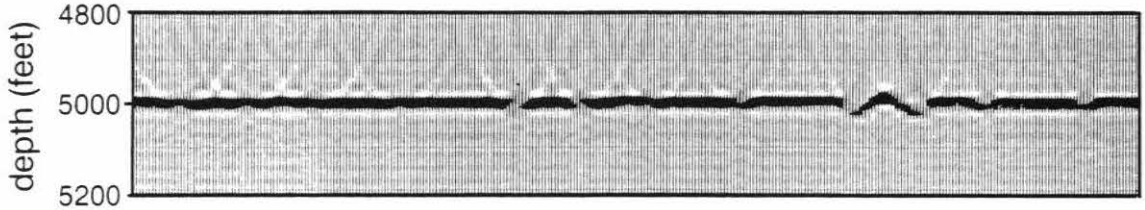

Migration of Model B Zero Offset Section Through Result After 4 Ray Tracings & Inversions

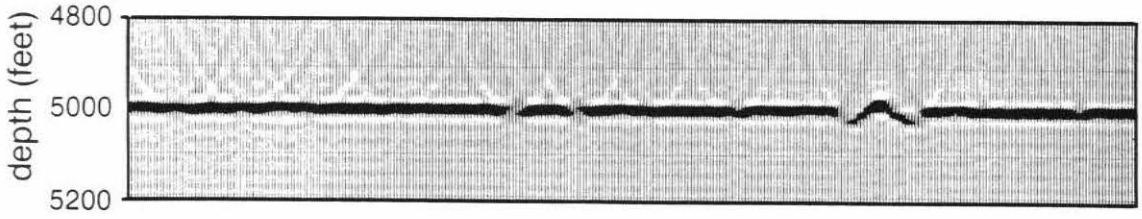

Figure 3.29

Migration through the non-linear inversion produced using a maximum ray angle of 22°, shown in Figure **3.21g**. The artifacts are very similar to the ones of the migration through the first non-linear inversion with a maximum ray angle of 45° in Figure **3.25**.

Figure 3.30

Migration through the fourth non-linear inversion produced using a maximum ray angle of 22°, shown in Figure **3.21h**. Comparing it with the migration in Figure **3.28** through the identical inversion except with a maximum ray angle of 45° shows this migration to have slightly less non-linear effects, especially under the deep slow velocity block on the right side.

This migration also demonstrates migration is insensitive to the vertical smearing of the images, which is especially significant in this case.

Migration of Model B Zero Offset Section Through First Inversion With A Maximum Ray Angle of Only 22°

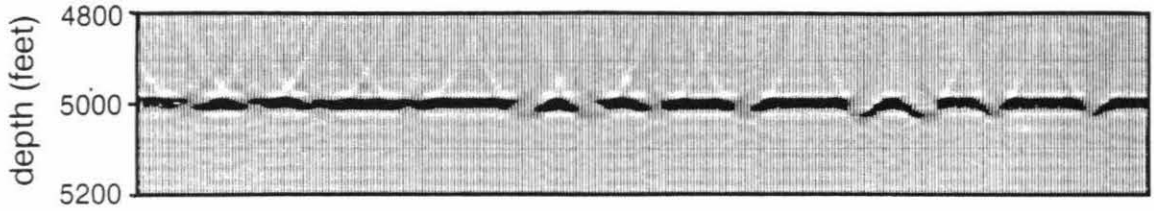

Migration of Model B Zero Offset Section Through Result After 4 Ray Tracings & Inversions With A Maximum Ray Angle of Only 22°

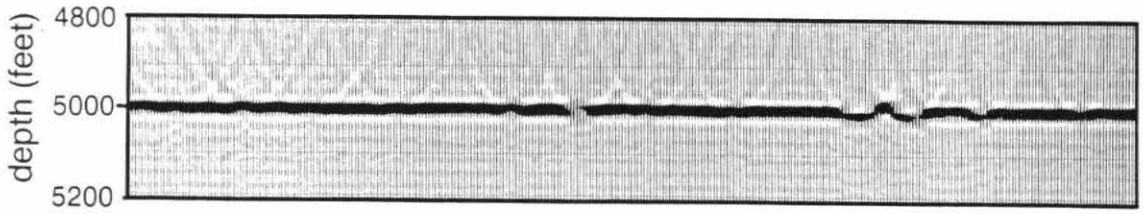

Figure 3.31

Migration through the inversion, shown in Figure **3.21m**, produced using the reference model B-1. The inversion contained no non-linear effects from velocity. The artifacts are a result of the incorrect reflector position of the reference model.

Figure 3.32

Migration through the inversion, shown in Figure **3.21n**, produced using the reference model in figure **3.21l**. As with the previous figure, the artifacts are a result of the incorrect reflector position of the reference model.

Migration of Model B Zero Offset Section Through Inversion Using Reference Model B1

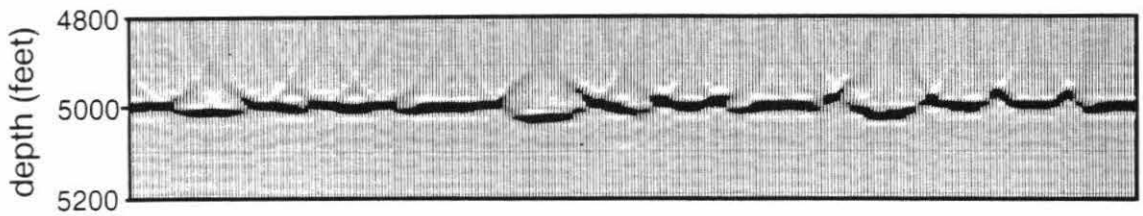

Migration of Model B Zero Offset Section Through Inversion Using Reference Model B2

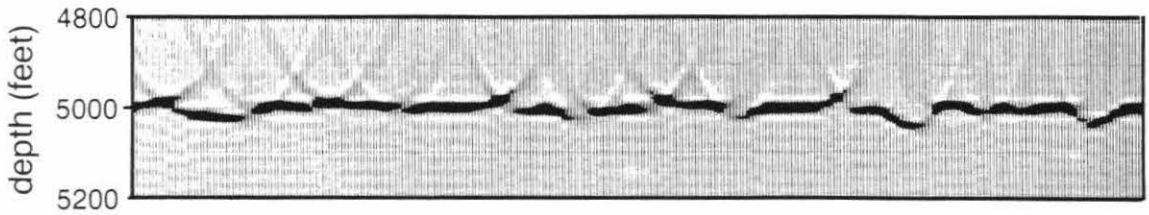

Figures 3.33

Tomographic inversion of horizontal blocks with large amplitude velocity contrasts.

A: The background velocity of the model is 8000 ft/sec; the velocity variation of the blocks are +/-3000 ft/sec. A flat reflector exists at depth 5000 feet. Maximum ray angle is 45o.

B: Inversion with non-linear effects over the eigenvalue range of (1.0-0.05). Reference model used for ray tracing has constant velocity of 8000 ft/sec. The slow block is thinned considerably while the fast block is thickened considerable.

C: Inversion of previous figure carried out to smaller eigenvalue. There is no noticeable change over the inversion in Figure **B**.

True Model A

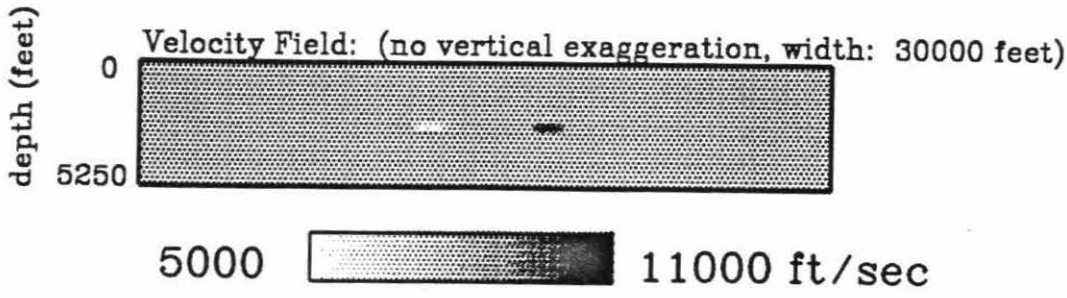

First Inversion of Model A
eigenvalue range: (1.0-0.05)

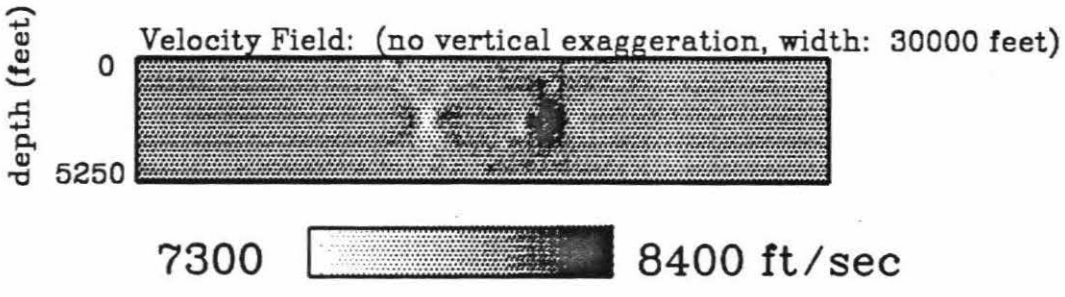

First Inversion of Model A
eigenvalue range: (1.0-0.02)

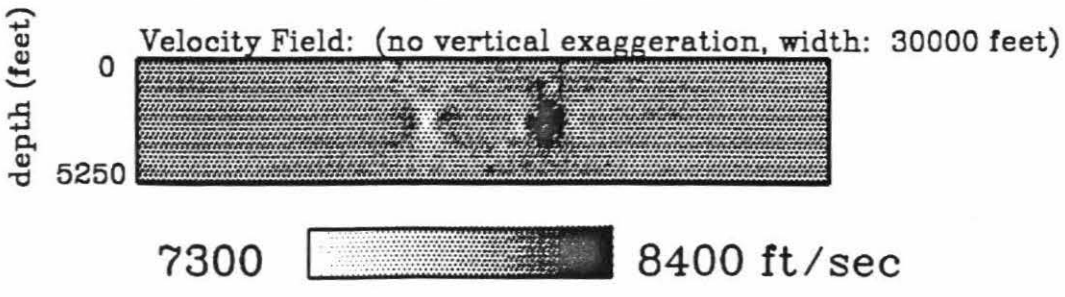

Figure 3.33

D: Inversion after three ray tracings and linear inversions. The slow velocity block has been widened to its approximate correct width and the fast block has been properly narrowed.

E: Inversion with non-linear effects where the reflector was allowed to vary along with the velocity. The reference reflector was flat at the correct depth. The inversion has traded off some of the velocity variations into the reflector depth.

F: Inversion of previous figure carried out to smaller eigenvalue. No noticeable change exists.

Inversion of Model A after 3 Ray Tracings and Inversions

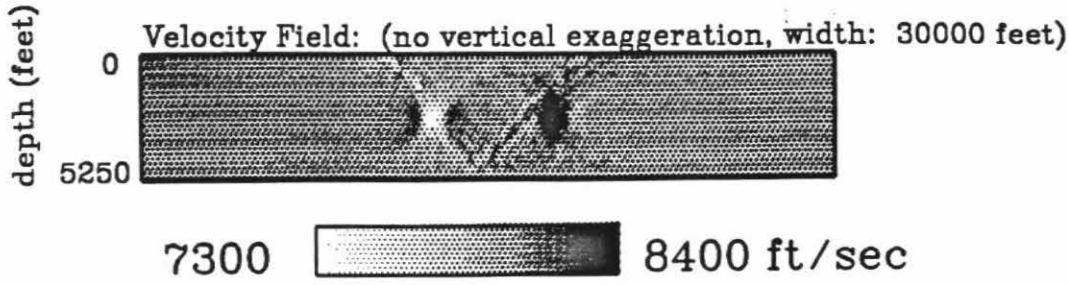

Inversion of Model A for Velocity and Reflector eigenvalue range: (1.0-0.05)

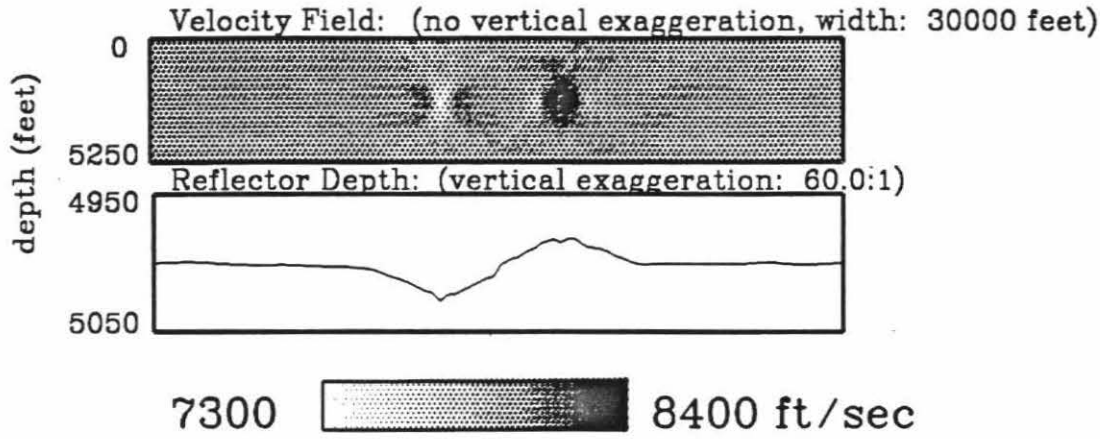

Inversion of Model A for Velocity and Reflector eigenvalue range: (1.0-0.02)

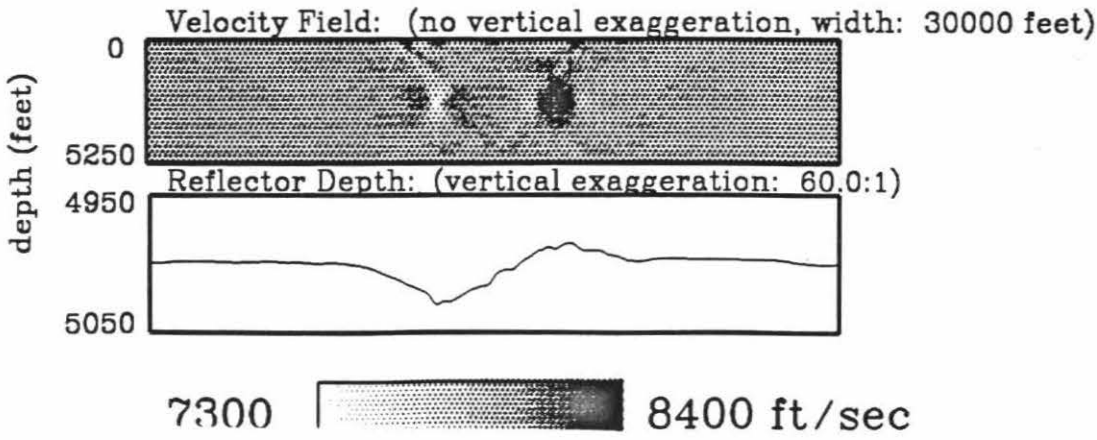

Figure 3.34

A: Sample ray paths between a shot and receivers for the velocity variations of true model in Figure **3.33a**. The rays avoid the slow block and are strongly attracted to the fast block.

B: More sample ray paths for true model in Figure **3.33a**. The rays have totally avoided the slow velocity block. Without any rays crossing the slow velocity variation, there is no information about its absolute velocity. This information is lost when using rays of least travel time.

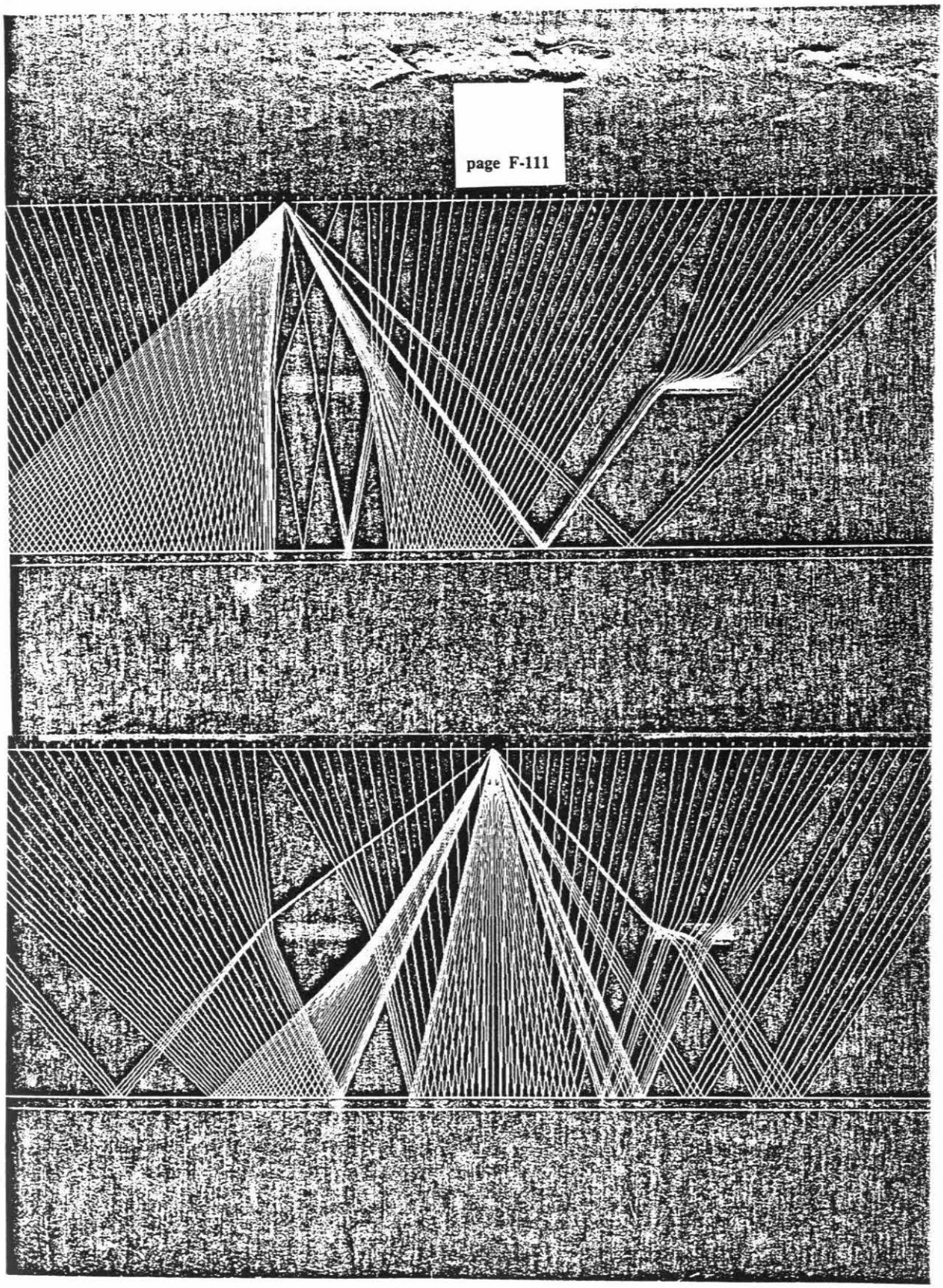
page F-111

Figure 3.35

Migration of zero offset data from true model of Figure **3.33a** through the constant velocity reference model used for the first ray tracing. The effect of the two unresolved velocity variations is clear.

Figure 3.36

Migration of data from model in Figure **3.33a** through first inversion in Figure **3.33b**. Serious non-linear artifacts exist. The migration is better on the right side under the fast block.

Migration of Model A Zero Offset Section Through Constant Velocity Reference Model

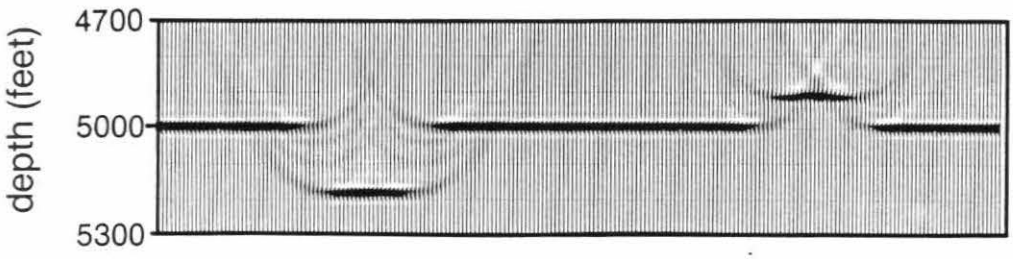

Migration of Model $\tilde{A}$ Zero Offset Section Through First Inversion

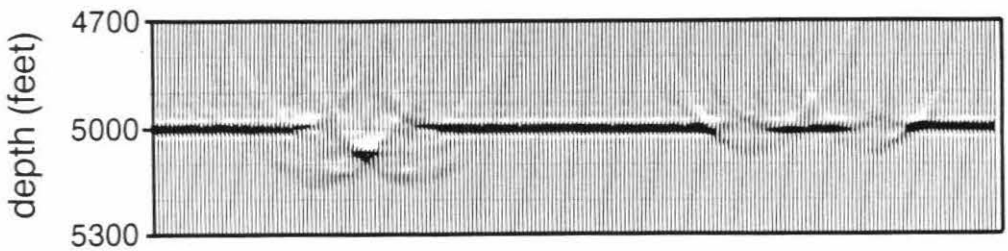

Figure 3.37

Migration through third inversion in Figure **3.33d**. Image is improved over the previous figure with only one inversion. However, some non-linear artifacts still remain. The fast velocity variation, on the right side, has been well inverted, while the slow velocity variation is poorly inverted. The non-linear effects appear to be worse at the edges of the velocity variations.

Migration of Model A Zero Offset Section Through Result After 3 Ray Tracings & Inversions

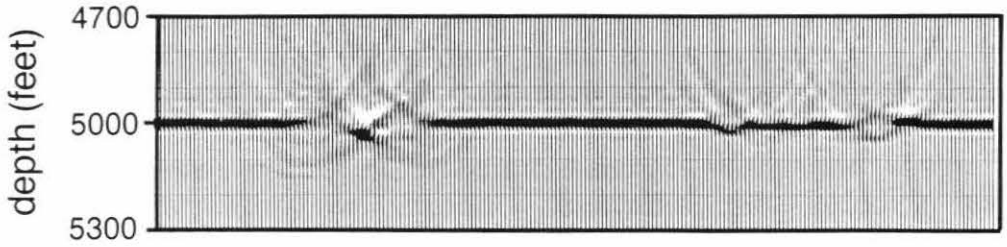

Figure 3.38

Tomographic inversions of blocks oriented differently from horizontal.

A: True model used to collect data. Velocity variations are +/- 1000 ft/sec; a flat reflector exists at depth 5000 feet; maximum ray angle is 45o.

B: First inversion. A constant velocity reference model used for ray tracing. The fast vertical blocks have been considerably thickened, while the slow ones are considerably thinned.

C: Result after 4 ray tracings and linear inversions. The thickness of the blocks have been corrected to their proper widths. The inversion of the vertical blocks looks very good since they have not been smeared much. While the shape appears accurate, we cannot determine the velocity variations amplitude very well with this plot. Note the scale change with that of Figure **A**. The migration in a later figure through this inversion shows it to have serious problems.

True Model C

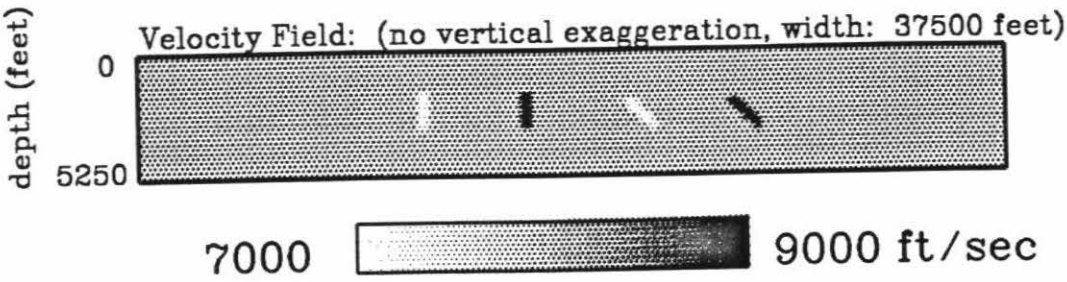

First Inversion of Model C
eigenvalue range: (1.0-0.02)

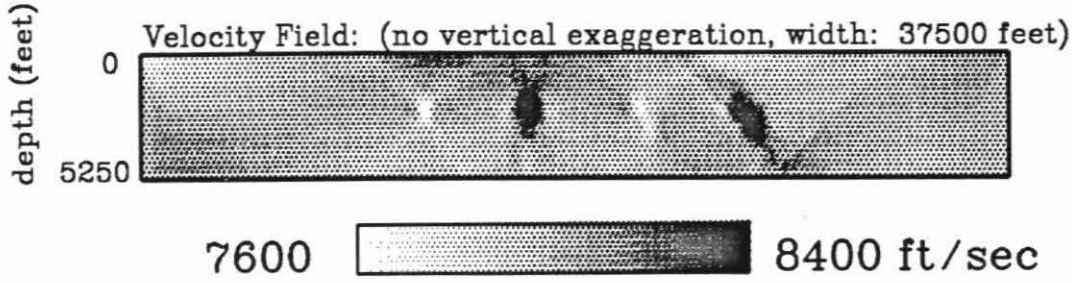

Inversion of Model C after
4 Ray Tracings and Inversions

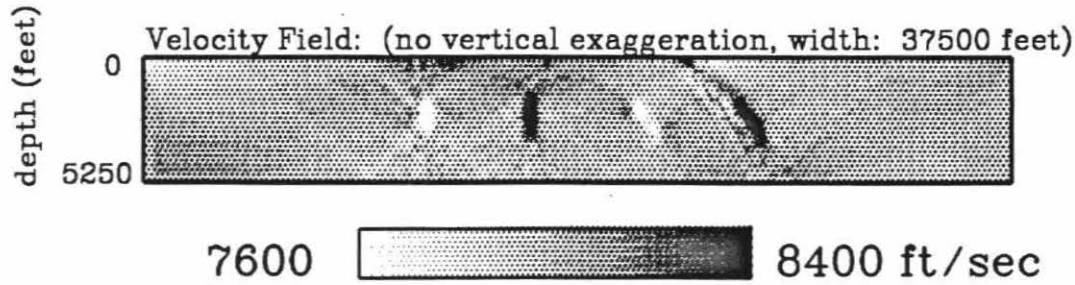

Figure 3.39

A: Sample ray paths through true model of Figure **3.38a**. The paths of least travel time avoid the slow block and are attracted to the fast block.

B: More sample ray paths through true model of Figure **3.38a**.

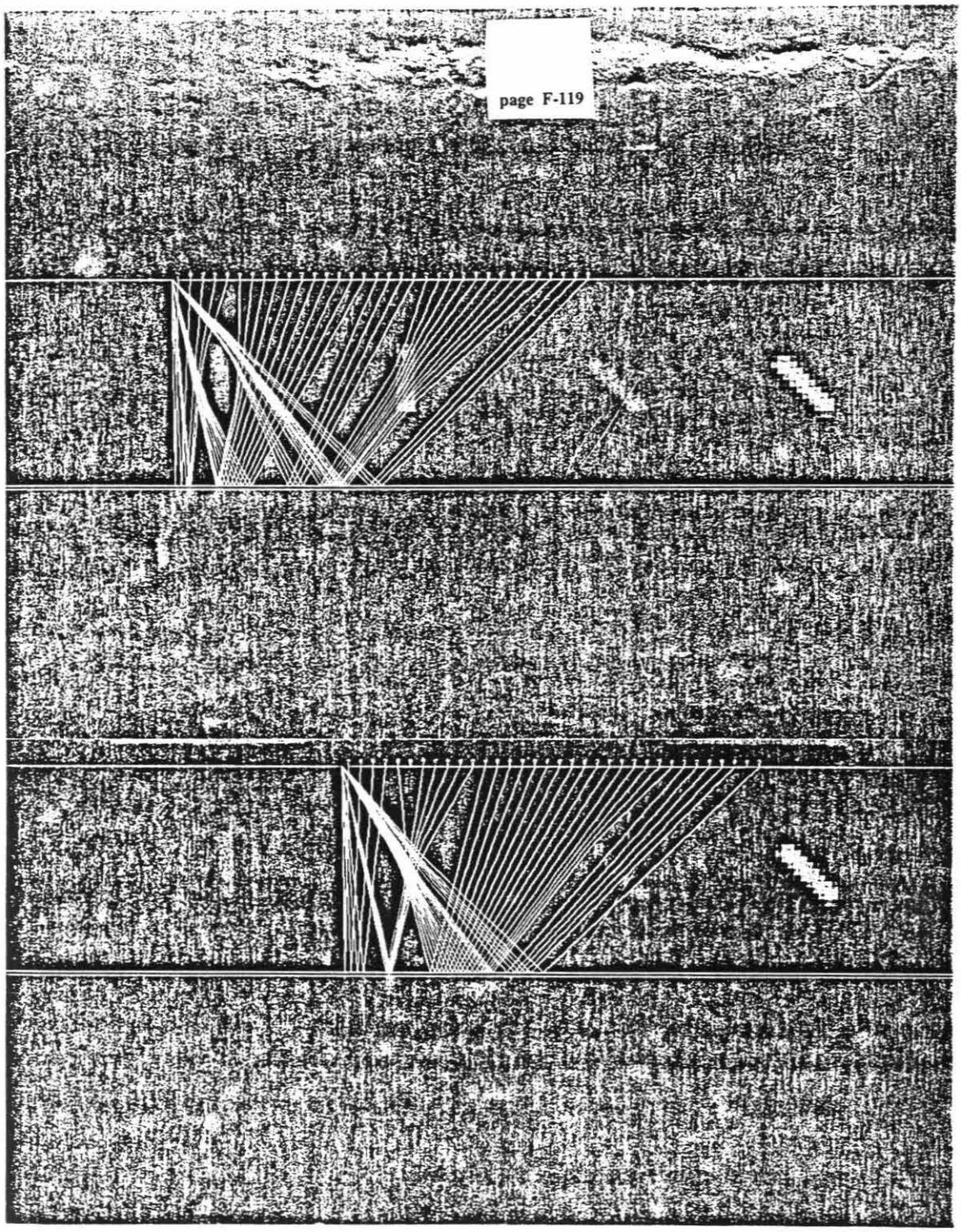
page F-119

Figure 3.39

C: Sample ray paths through true model of Figure **3.38a** that show how rays parallel to velocity variations are affected more by it than those perpendicular to the trend of the velocity variations.

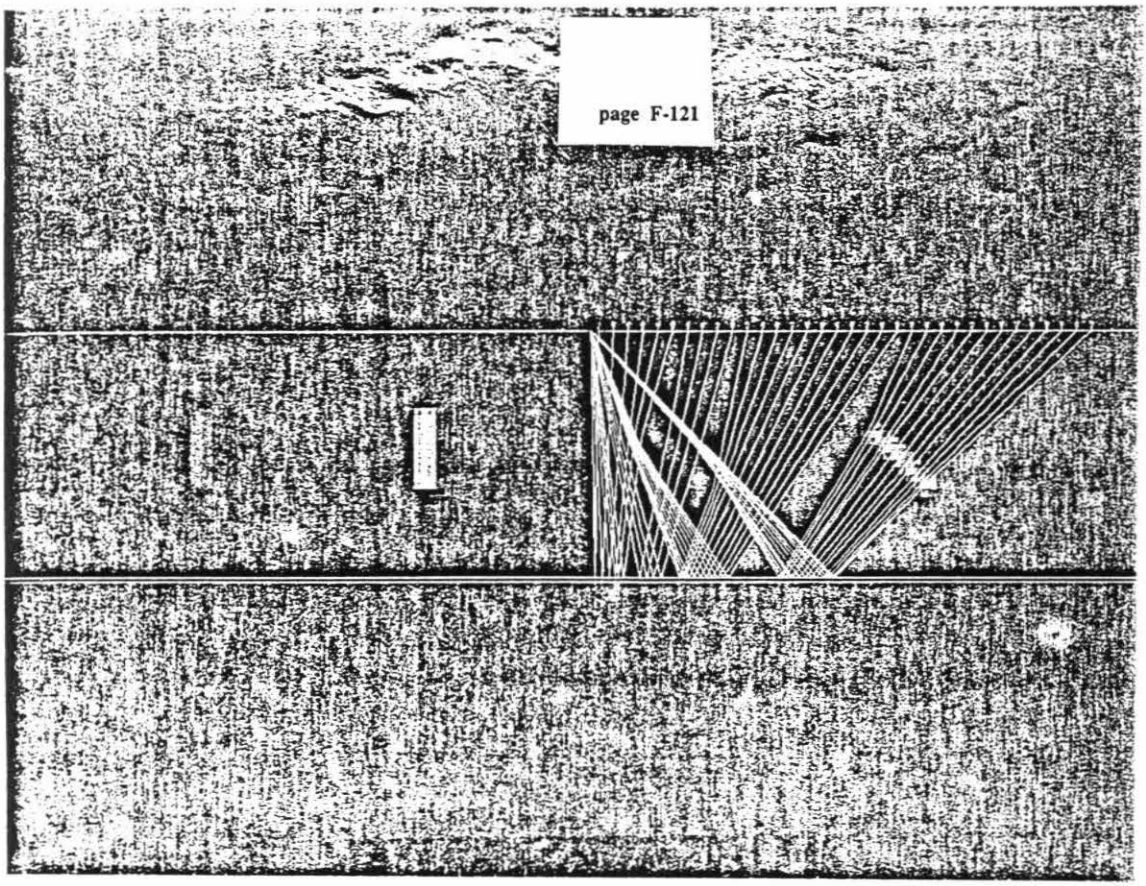
page F-121

Figure 3.40

Migration of zero offset data from true model in Figure **3.38a** through the constant velocity reference model used for ray tracing. The diffractions have mostly healed the reflector on the left side of the plot, under the unresolved vertically oriented velocity variations.

Figure 3.41

Migration of data from true model through first inversion in Figure **3.38b**. The right side of the image, under the slanted velocity variations, is improved over the migration through the reference model. However, the left side, under the vertical velocity variations, is worse. The non-linear effects are stronger for vertical velocity variations.

Migration of Model C Zero Offset Time Section Through Constant Velocity Reference Model

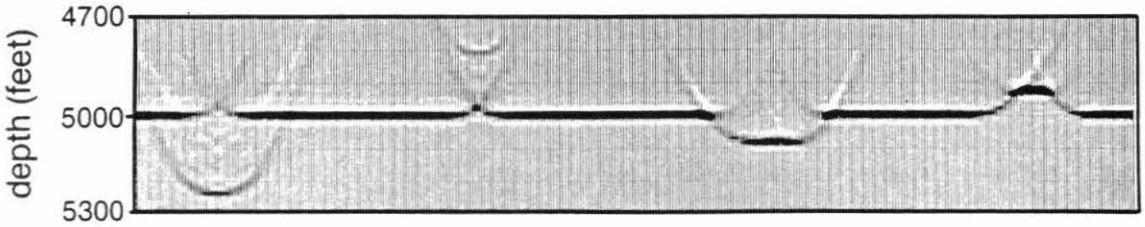

Migration of Model C Section Through First Inversion

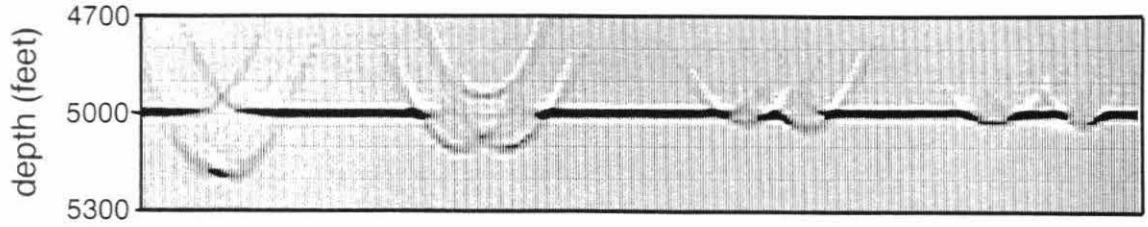

Figure 3.42

Migration through third inversion in Figure **3.38c**. The non-linear effects on the right side of the image, under the slanted velocity variations, have been almost entirely corrected by the repeated ray tracing and inversion. However, the non-linear effects on the left side, under the vertical velocity variations, have not improved significantly from the first inversion. In fact, the image is worse on the left side than in the migration through the constant velocity reference model. From these migrations, the non-linear iterative inversion steps appear to have produced a result for vertical velocity variations worse than what it started with.

Migration of Model C Section Through Result after 4 Ray Tracings & Inversions

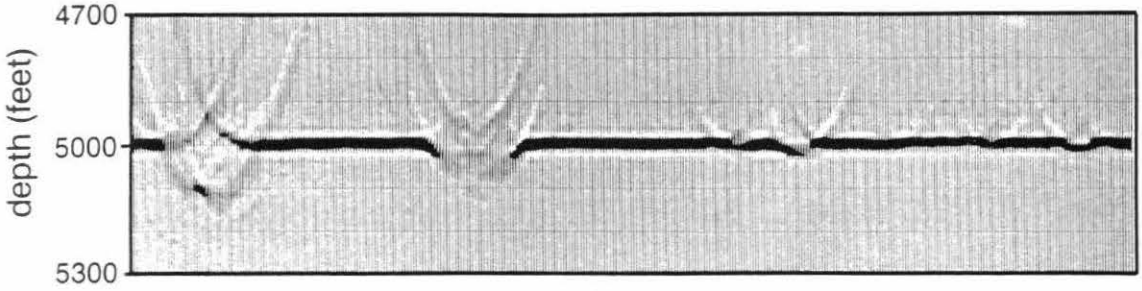

Figure 3.43

Tomographic inversions of a model with strong, large velocity contrasts.

A: True model used for data collection. Wedge in middle has velocity of 11000 ft/sec; surrounding material is 8000 ft/sec. The two boundaries of the velocity contrast have very different slopes.

B: Density of ray paths through true model. The fast velocity strongly attracts the rays creating an inhomogeneous ray coverage at the boundaries of the velocity variations. Ray coverage is more inhomogeneous at the bottom of the model.

C: Constant velocity reference model used for tracing the rays for the inversion. Reflector is at the correct depth and will not be allowed to vary in the inversions.

True Model Q

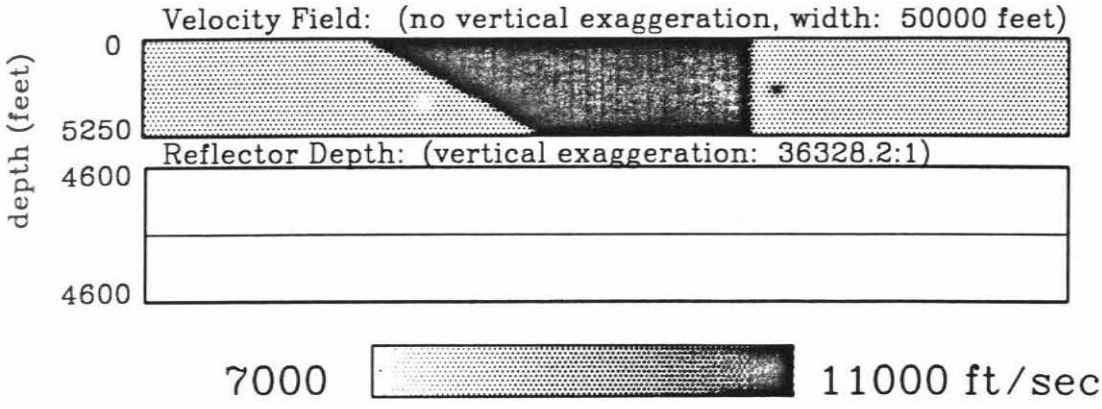

Density of Ray Paths in True Model Q

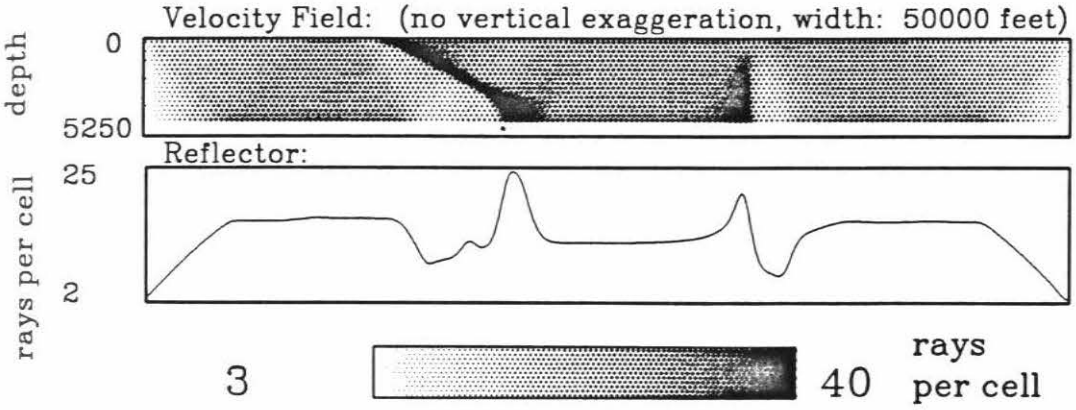

Reference Model Q-1

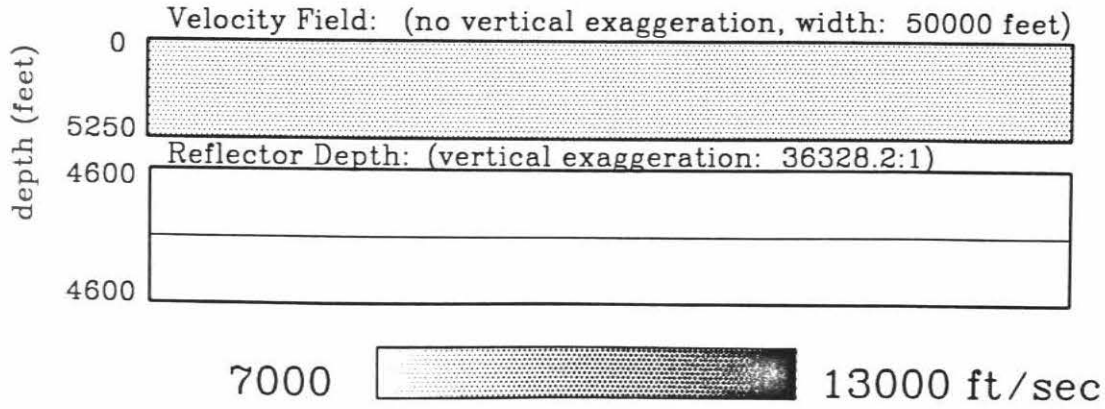

Figure 3.43

D & E: Velocity only inversions of model in Figure **A** using model of Figure **C** as the reference model. The image has been strongly distorted. The artifacts appear to grow with the inversion to smaller eigenvalue.

F: Velocity only inversion after re-tracing rays through the model of Figure **D**. The additional ray tracing and inversion have not improved the result. The only noticeable improvement is that the vertical right border of the velocity contrast is better defined.

The absolute velocities of the inversion are unreasonable. Imposing some reasonable limits on the velocity would improve the inversion.

Inversion Q-1-a of Model Q using Reference Model Q-1
eigenvalue range: (1.0-0.05)

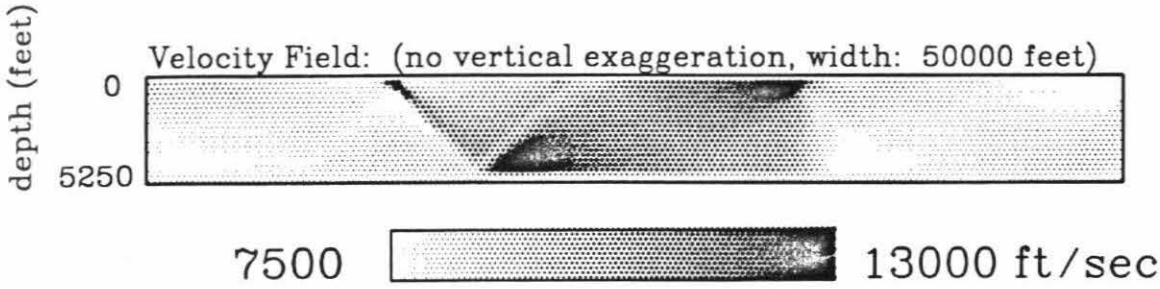

Inversion Q-1-b of Model Q using Reference Model Q-1
eigenvalue range: (1.0-0.02)

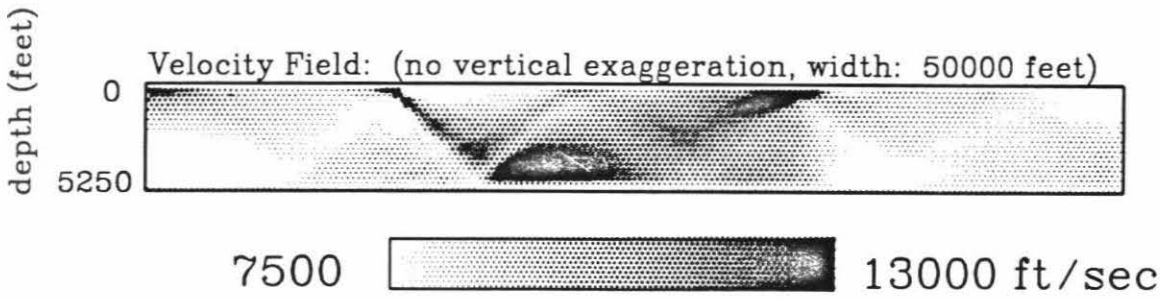

Inversion Q-1-aa of Model Q using Inversion Q-1-a
as the Reference Model, eigenvalue range: (1.0-0.05)

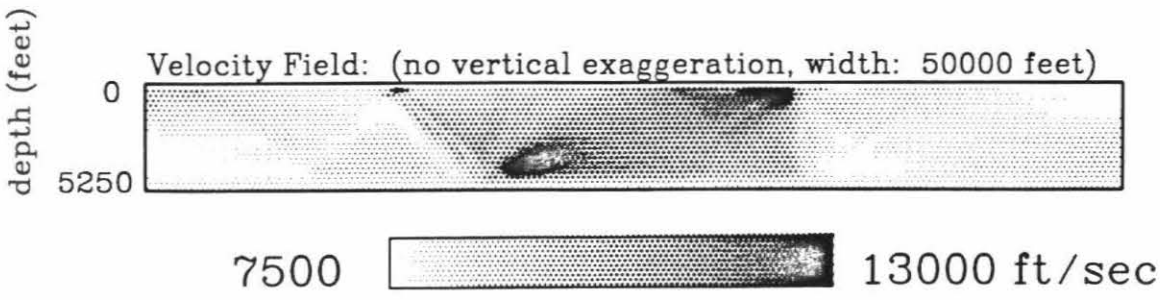

Figure 3.44

Tomographic inversions for velocity and reflector depth of a model that has only broad reflector variations.

A: True velocity and reflector model used data collection. Main feature of model is the broad bump and trough of reflector. Velocity field is a constant 8000 ft/sec. Reflector is plotted on a separate scale so that it can be vertically exaggerated. The amplitude of the reflector topography is very small so that the bump and trough do not effect the ray paths. Without ray paths errors, these inversions address only the linear resolution of the reflector topography.

B: Inversion over a narrow eigenvalue range of true model above. The reference model had a flat reflector and the same constant velocity field as the true model. The ray paths are effectively the same as those used to collect the data.

The reflector bump & trough have been only half inverted. Significant velocity variations have been introduced in the velocity field. Most of the velocity artifacts occur at the bottom of the model, just above the reflector.

C: Inversion to a smaller eigenvalue. The reflector is better inverted and the velocity artifacts are reduced. The velocity variations are now greater at the top of the model.

True Model D

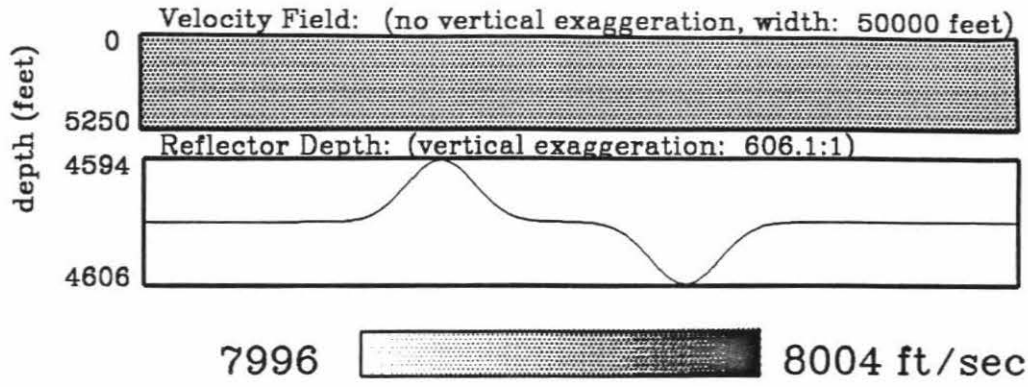

Inversion of Model D
eigenvalue range: (1.0-0.3)

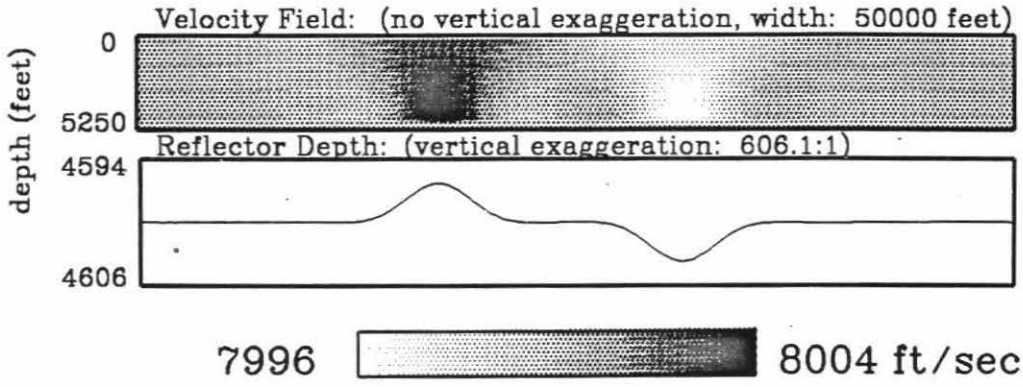

Inversion of Model D
eigenvalue range: (1.0-0.1)

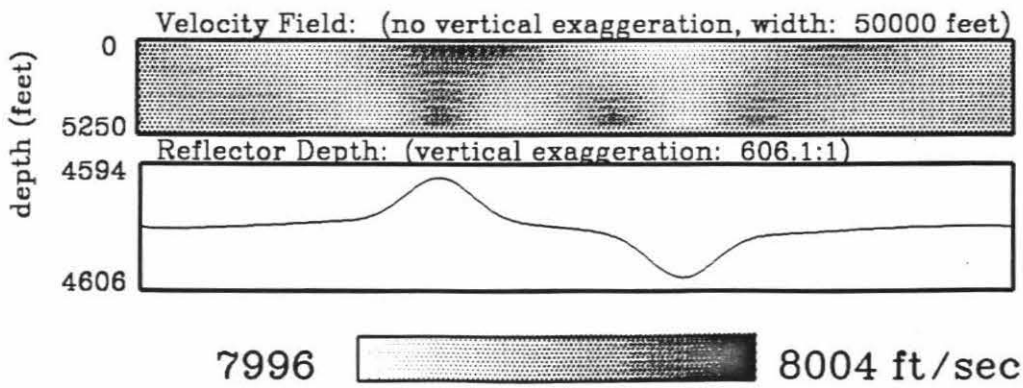

Figures 3.44

D, E, & F: Inversions to yet smaller eigenvalues. The reflector and the velocity artifacts are progressively improved in the successive inversions. In the final inversion, the true model has been almost entirely reproduced, with very few artifacts in the velocity field. This broad scale reflector topography can be mostly resolved from velocity variations over this eigenvalue range.

Inversion of Model D
eigenvalue range: (1.0-0.05)

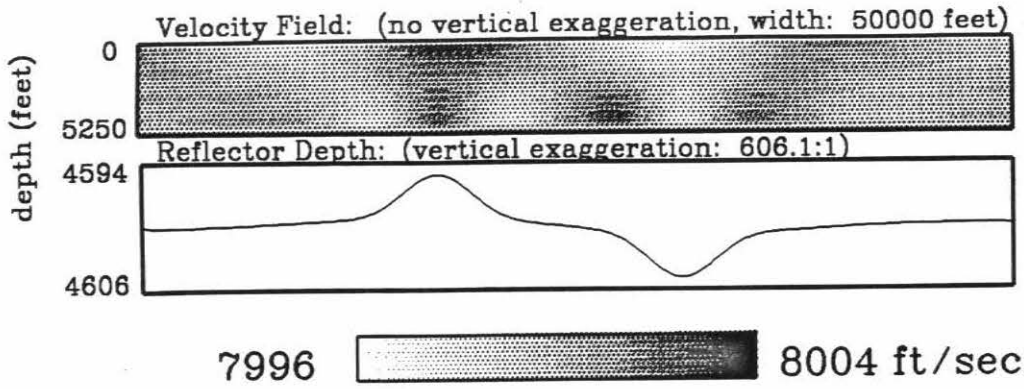

Inversion of Model D
eigenvalue range: (1.0-0.02)

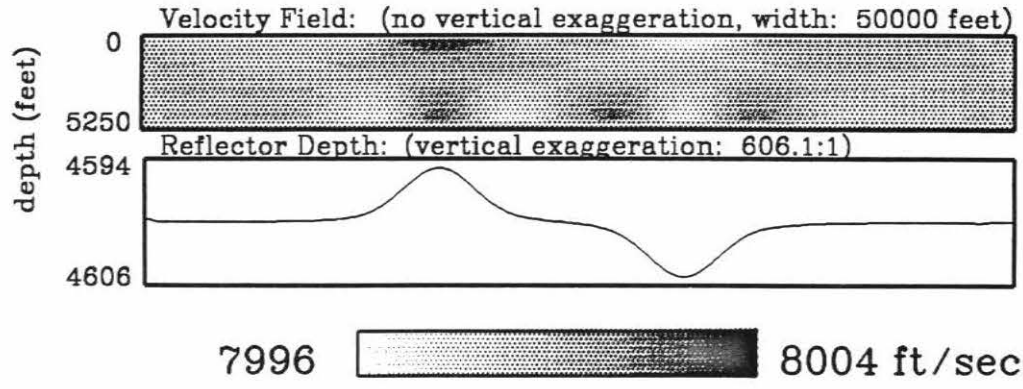

Inversion of Model D
eigenvalue range: (1.0-0.01)

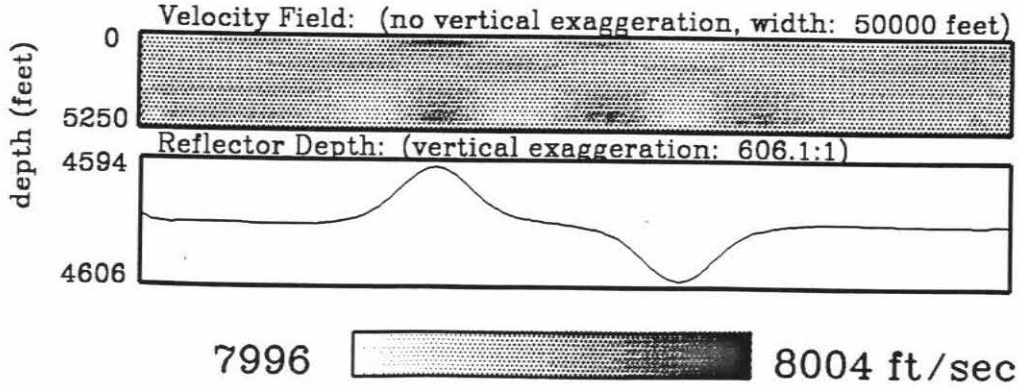

Figure 3.45

Inversions of true model in Figures **3.44** is repeated using a velocity bias to exaggerate velocity artifacts.

A: Inversion over narrow eigenvalue range. Most all of the travel time variations have been accounted for by velocity variation, causing serious artifacts.

B: Inversion to smaller eigenvalue. The reflector is starting to take on correct structure. The velocity variations have been reduced and are starting to take on a pattern.

C: Continued improvement by inversion to smaller eigenvalue.

Inversion of Model D with velocity emphasis eigenvalue range: (1.0-0.3)

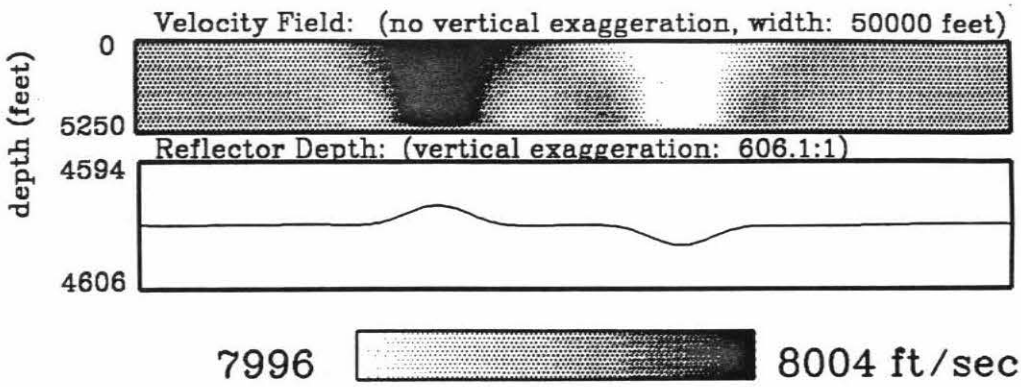

Inversion of Model D with velocity emphasis eigenvalue range: (1.0-0.05)

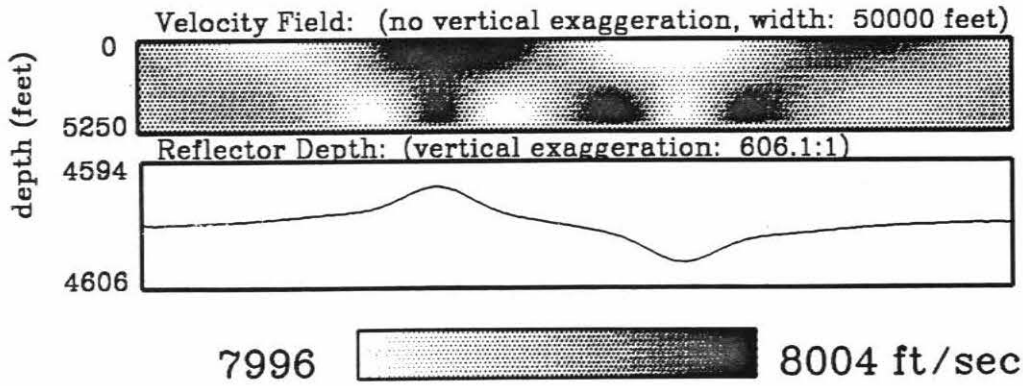

Inversion of Model D with velocity emphasis eigenvalue range: (1.0-0.02)

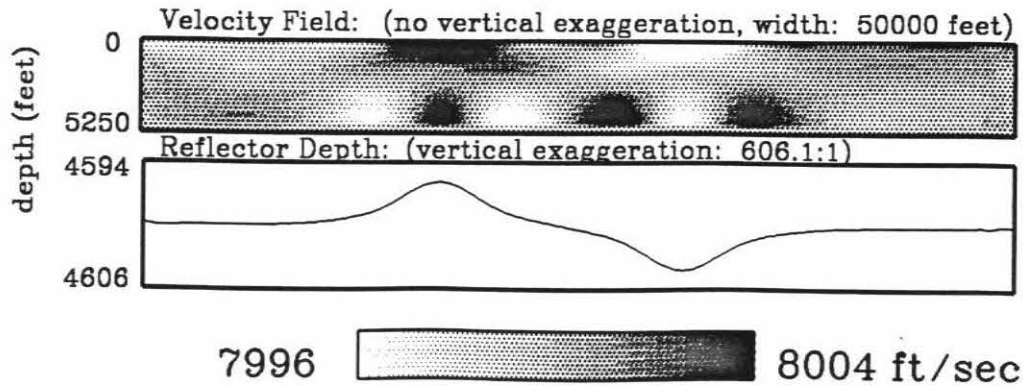

Figure 3.45

D: Inversion to smallest eigenvalue. Reflector structure is accurate, but a characteristic velocity variation still exists. Velocity artifacts appear at the surface and the bottom just above the reflector, but not in the middle. Some artifact also exists on both sides of the bump or trough. In comparison with the identical inversion without velocity bias in Figure **3.44f**, the velocity artifacts have similar shape, but are larger in amplitude and are more apparent.

E: Inversion with velocity bias is repeated with constraints. The constraints do not allow the velocity to vary in the lower third of the velocity field. The inversion over this eigenvalue range has more accurately inverted the reflector than the corresponding inversion without the constraints in Figure **3.45b**.

F: Inversion with velocity bias and constraints to a smaller eigenvalue. The result is improved over the corresponding inversion without constraints in Figure **3.45c**.

Inversion of Model D with velocity emphasis eigenvalue range: (1.0-0.01)

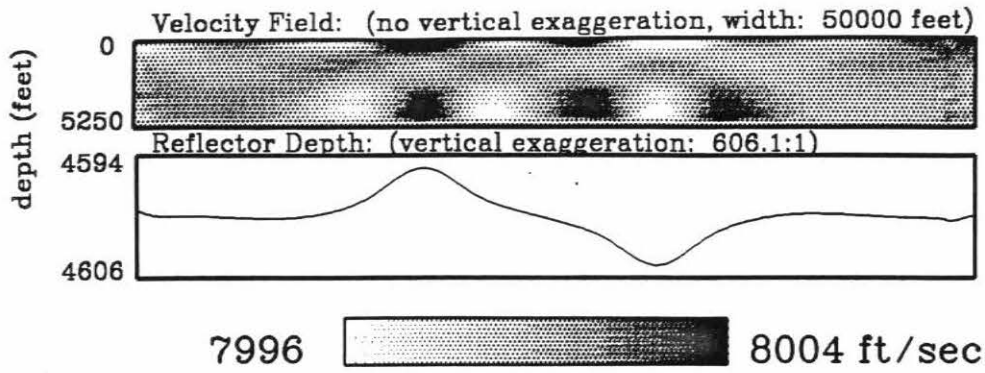

Inversion of Model D with strong velocity emphasis and velocity constraints, eigenvalue range: (1.0-0.05)

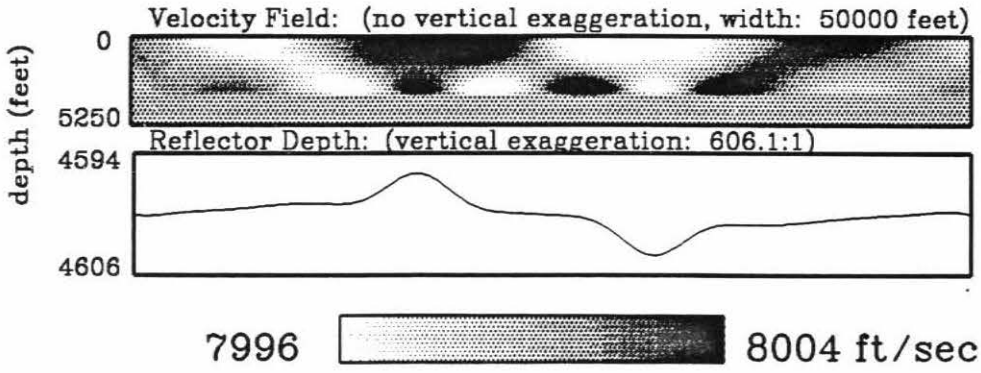

Inversion of Model D with velocity emphasis and velocity constraints, eigenvalue range: (1.0-0.02)

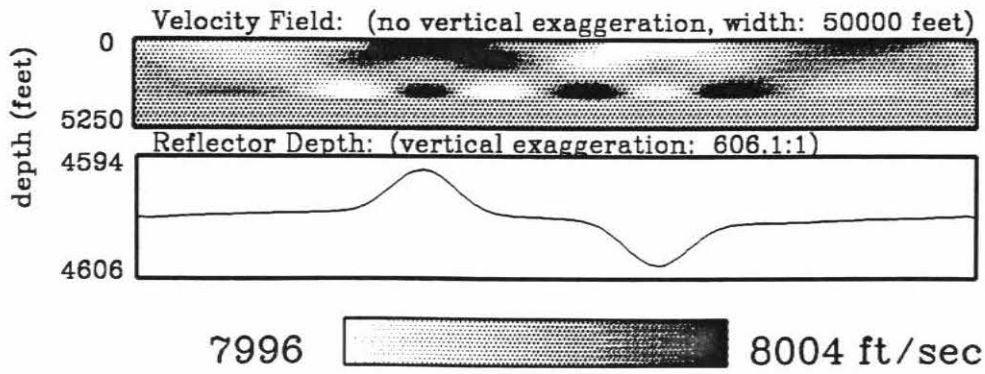

Figure 3.46

Tomographic inversions of model with a narrow reflector bump.

A: True model used for data collection. Bump is very narrow compared with the depth down to the reflector. It's amplitude is very small so that it does not affect the ray paths. Note vertical exaggeration of the reflector scale.

B: Inversion of the true model over a narrow eigenvalue range. Reference model used had the correct constant velocity and a flat reflector. Most of the reflector bump is inverted over this eigenvalue range because of the natural bias toward the reflector for small, deep velocity variations. Some velocity artifact appears at the bottom of the model.

C: Inversion to smaller eigenvalue. The velocity artifacts appear to have been slightly reduced .

True Model E

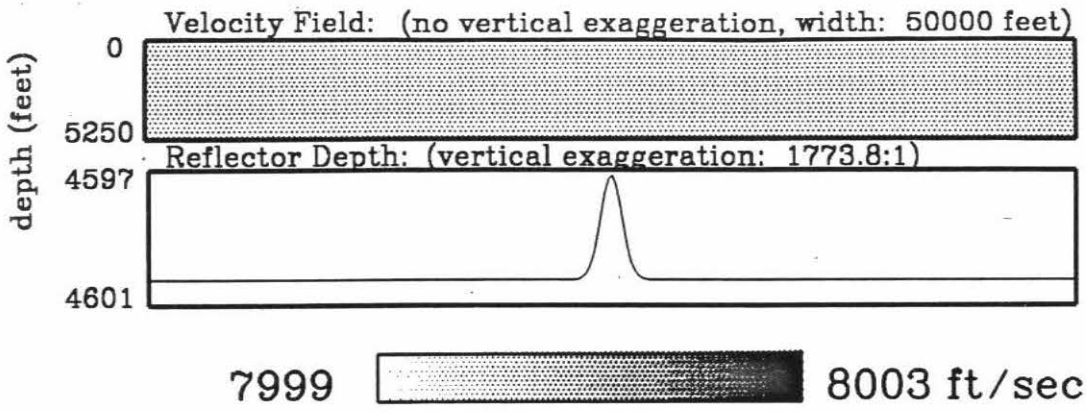

Inversion of Model E
eigenvalue range: (1.0-0.3)

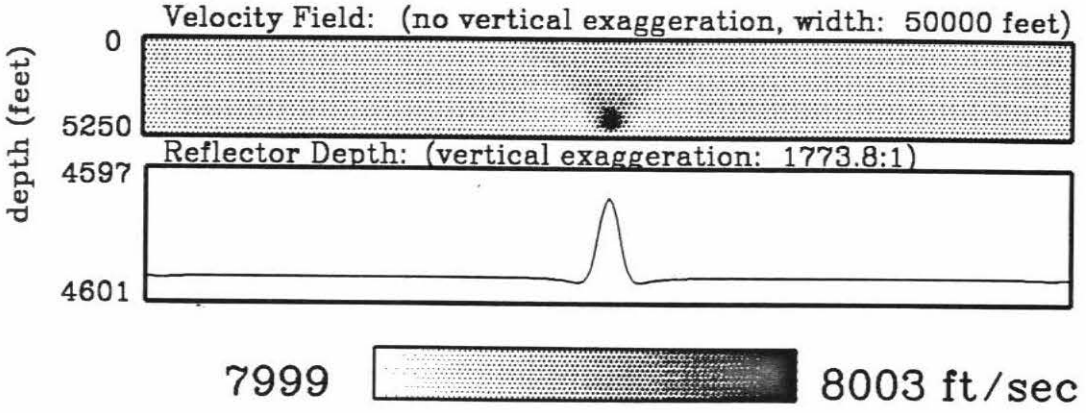

Inversion of Model E
eigenvalue range: (1.0-0.1)

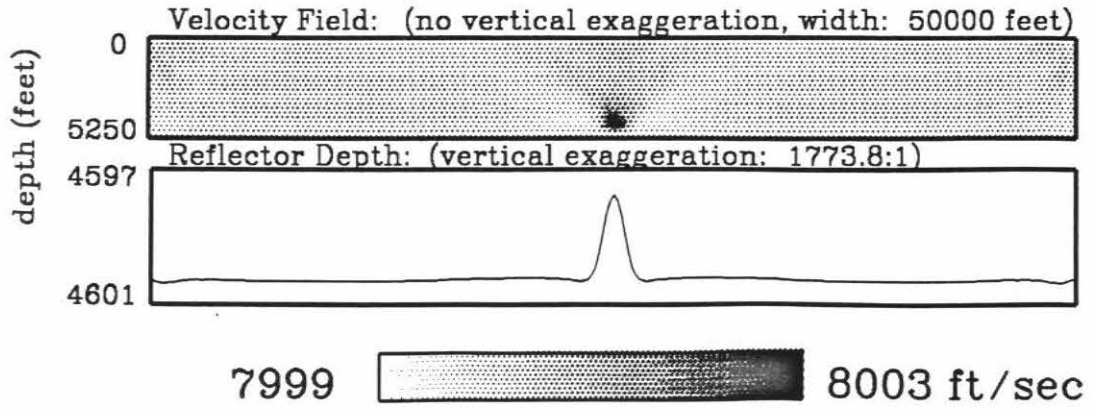

Figures 3.46

D & F: Inversion of narrow bump to yet smaller eigenvalues. Bump appears to be improved slightly and artifacts are reduced slightly, but there is no major improvement.

Note the artifacts that crop up at the edges of the model.

G: Inversion of narrow bump is repeated using velocity bias. This figure should be compared with **3.46b**. The reflector bump has been only half inverted over this small eigenvalue range and the velocity artifacts are greater.

Inversion of Model E
eigenvalue range: (1.0-0.05)

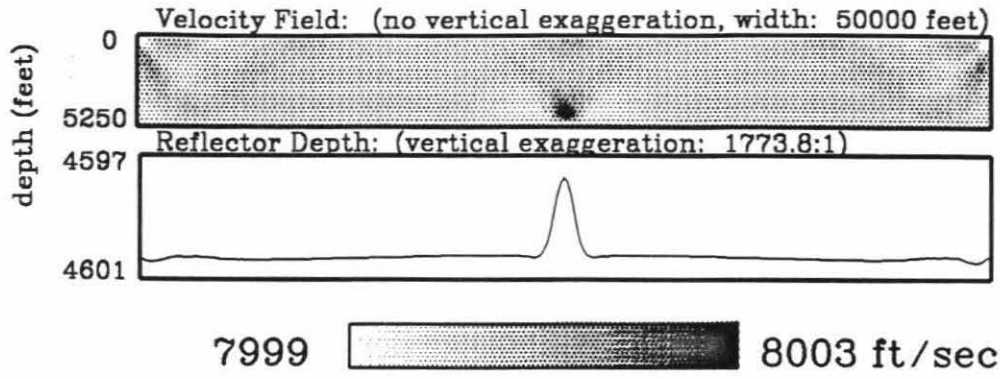

Inversion of Model E
eigenvalue range: (1.0-0.02)

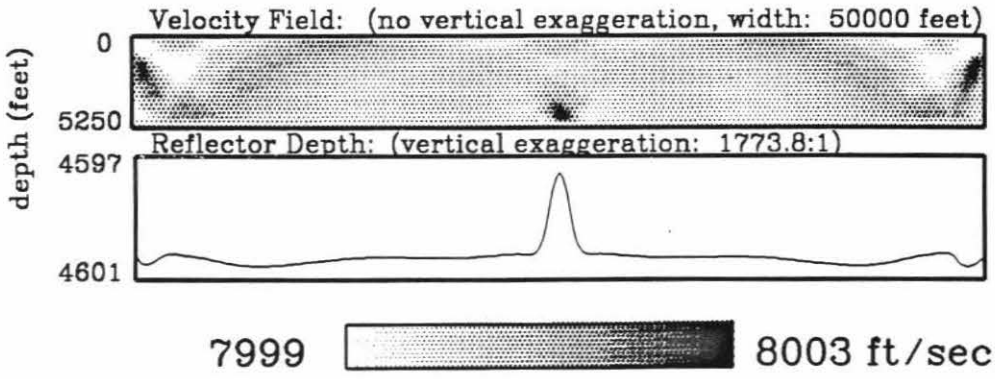

Inversion of Model E with strong velocity emphasis
eigenvalue range: (1.0-0.30)

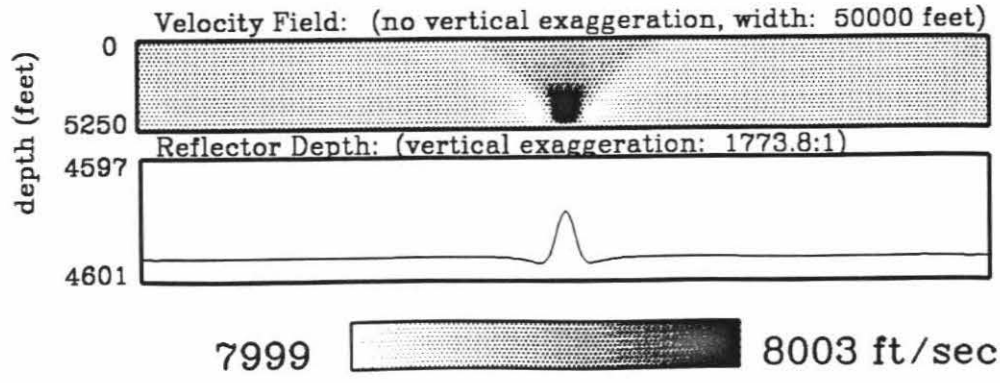

Figures 3.46

H & I: Inversion with velocity bias is continued to smaller eigenvalue. Reflector bump has not been inverted. The velocity artifacts do not change significantly, but a small artifact is created at the surface of the model. These velocity artifacts for a narrow reflector bump can be compared with those for the broad bump in Figure **3.45b & c**. Artifacts again appear at edges.

J: Inversion with velocity bias is repeated with the use of constraints. The velocity was not allowed to vary in the lower third of the model. Reflector is much better inverted than the corresponding inversion without constraints in Figure **3.46g** on the previous page.

Inversion of Model E with velocity emphasis eigenvalue range: (1.0-0.05)

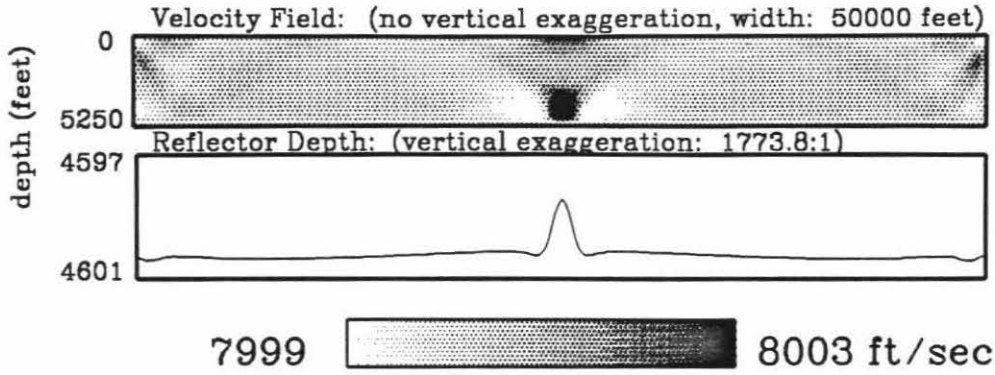

Inversion of Model E with velocity emphasis eigenvalue range: (1.0-0.02)

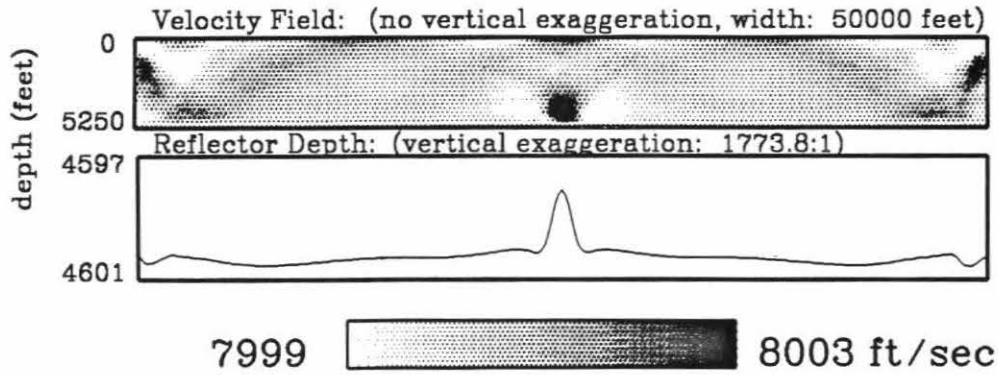

Inversion of Model E with velocity emphasis and Velocity Constraints, eigenvalue range: (1.0-0.30)

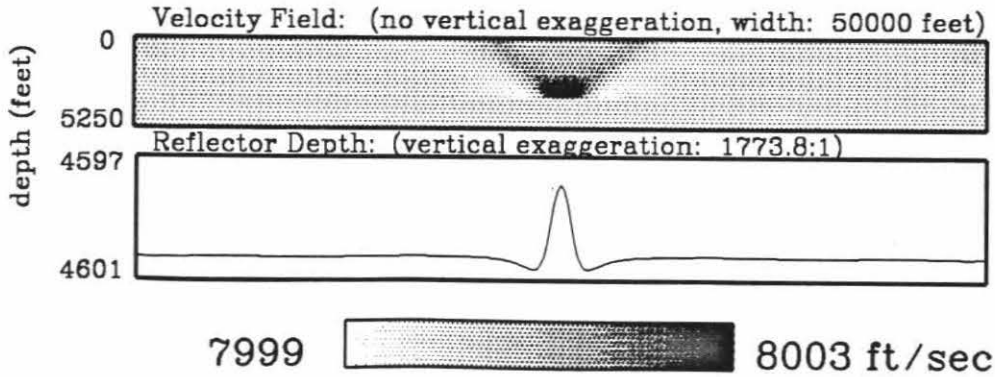

Figures 3.46

K & L: Inversion with velocity bias and constraints continued to smaller eigenvalues. Inversion is significantly improved, with reflector bump almost completely inverted and very few velocity artifacts in the final inversion. Corresponding inversions without constraints are **3.46h & i.**

Inversion of Model E with velocity emphasis and Velocity Constraints, eigenvalue range: (1.0-0.05)

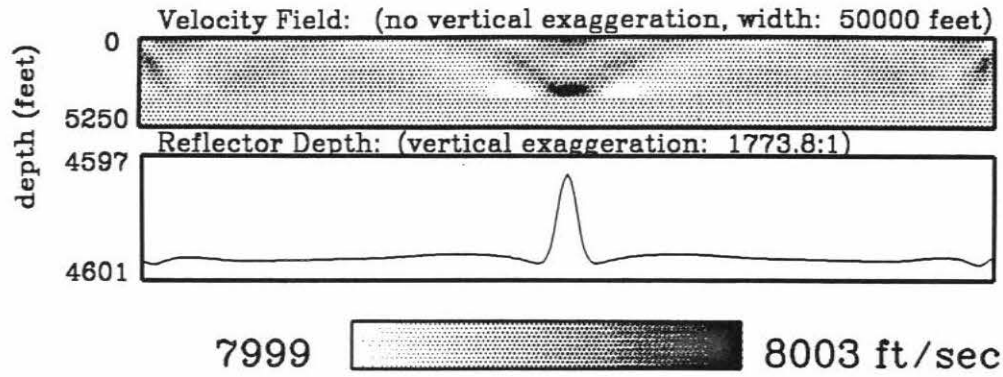

Inversion of Model E with velocity emphasis and Velocity Constraints, eigenvalue range: (1.0-0.02)

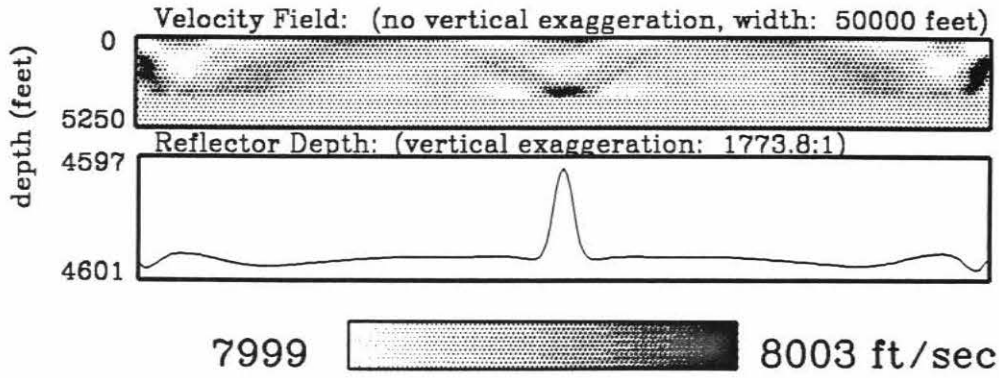

Figures 3.46

M & N: Inversions with velocity bias, no constraints, but a narrower reflection survey. The width of the reflection survey can be identified from the location of the edge effects. The reflector does not appear to be worse inverted or the velocity artifacts do not appear to be greater than the corresponding wider inversion in Figure **3.46i**.

Inversion of Model E with velocity emphasis using a Shorter Reflection Survey, eigenvalue range: (1.0-0.02)

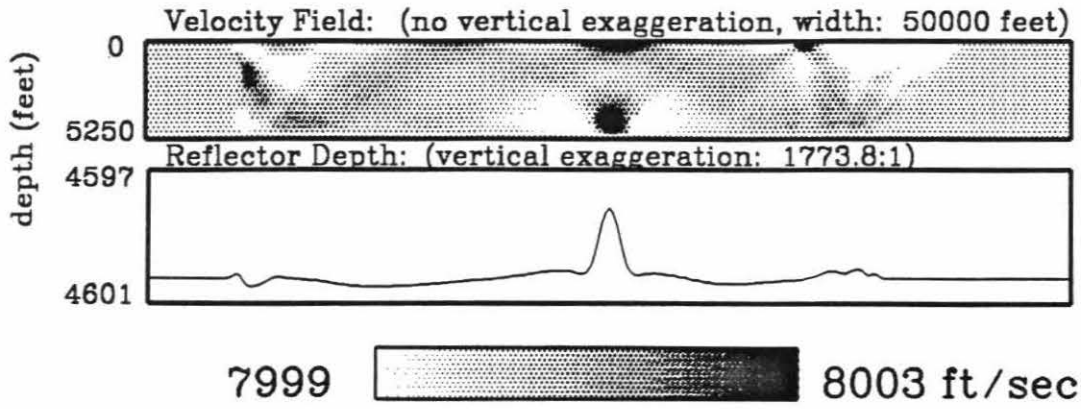

Inversion of Model E with velocity emphasis using a very Short Reflection Survey, eigenvalue range: (1.0-0.02)

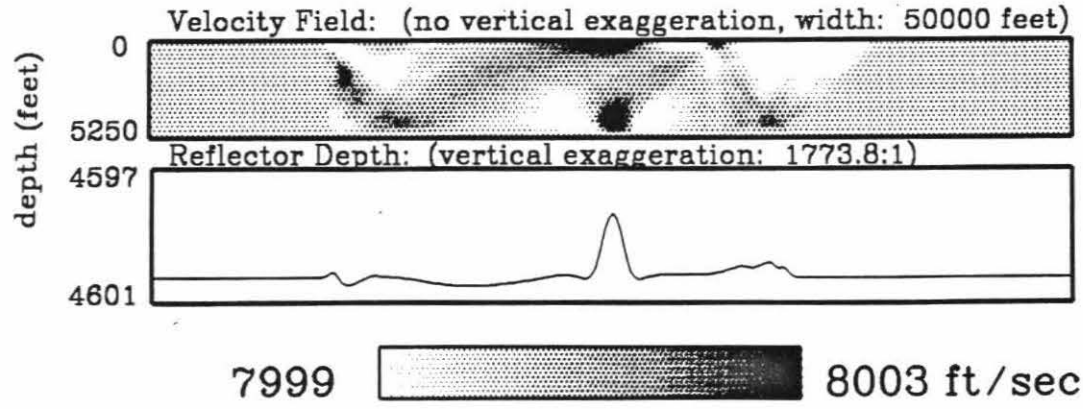

Figure 3.47

Inversion of a very broad reflector bump.

A: True model used for data collection. Velocity is constant; maximum ray angle is 45°; reflector bump is small so that it does not affect ray paths.

B: Inversion over a narrow eigenvalue range. Reference model has the correct constant velocity and a flat reflector. Only half of the broad reflector bump amplitude is inverted. Velocity artifact extends from surface down to the reflector. This result can be compared with the inversion of a narrow bump with identical parameters in Figure **3.46b**.

C: Inversion of broad bump to a smaller eigenvalue. The bump is significantly better inverted and the velocity artifacts have been markedly reduced. This dramatic improvement between this eigenvalue range the one of the previous figure was not experienced in the inversions of narrower bumps.

True Model F

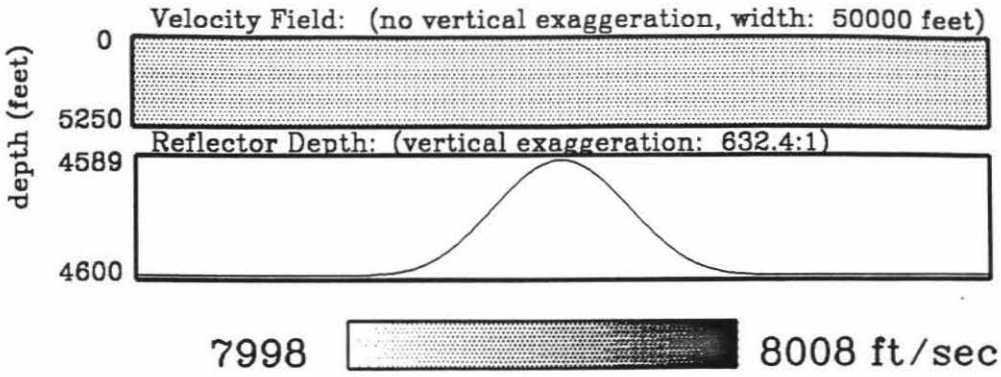

Inversion of Model F
eigenvalue range: (1.0-0.3)

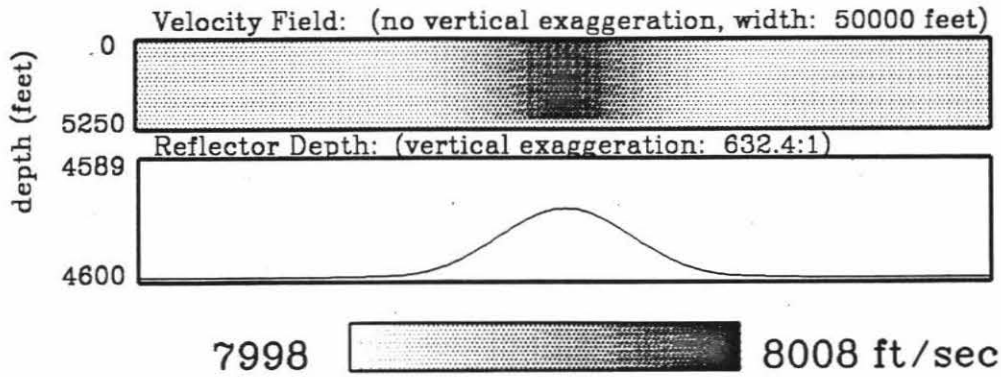

Inversion of Model F
eigenvalue range: (1.0-0.1)

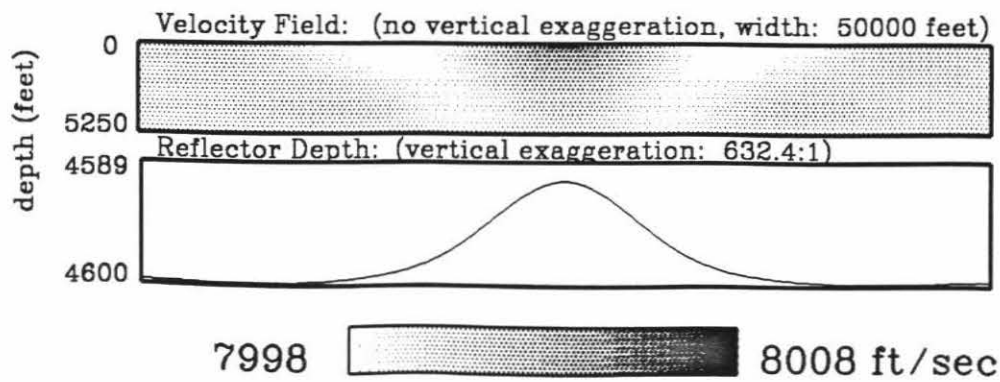

Figures 3.47

D & E: Inversion of broad bump to smaller eigenvalue. Improvement is minor. A small velocity artifact remains at the top of the model.

F: Inversion of broad bump with velocity emphasis over a narrow eigenvalue range. Almost none of the reflector has been inverted and the velocity artifact is large.

Inversion of Model F
eigenvalue range: (1.0-0.05)

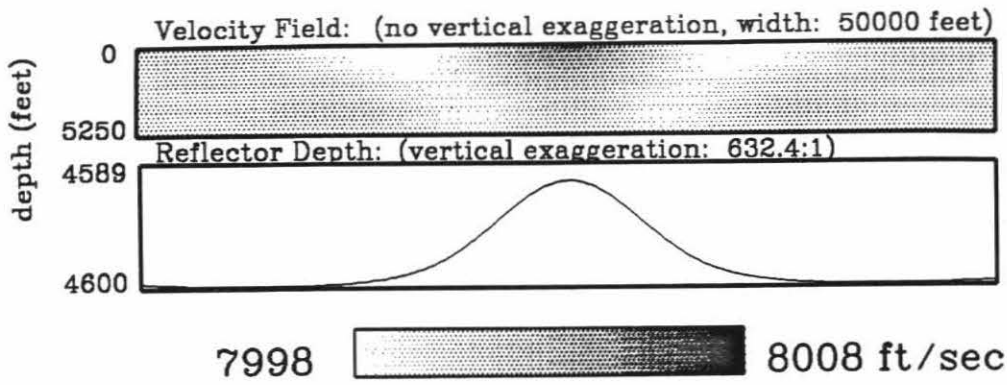

Inversion of Model F
eigenvalue range: (1.0-0.02)

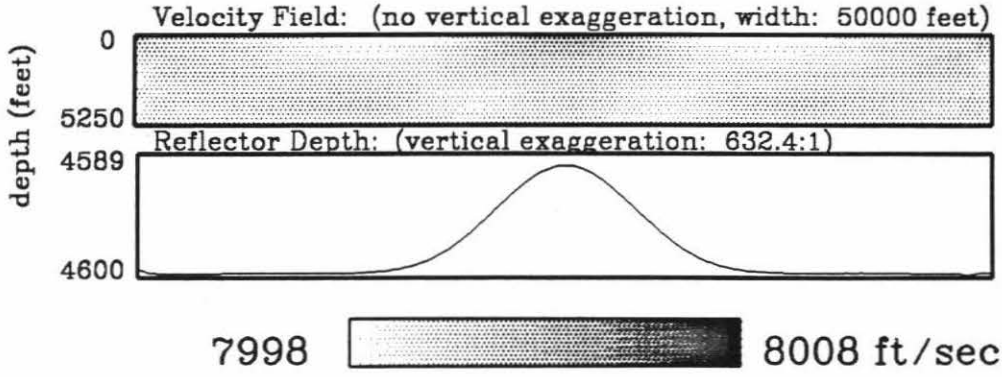

Inversion of Model F with strong velocity emphasis
eigenvalue range: (1.0-0.3)

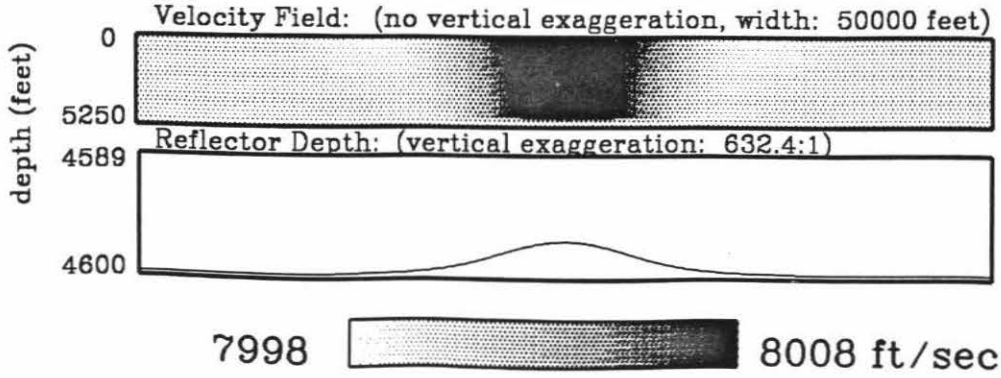

Figures 3.47

G, H, & I: Inversions of broad bump with velocity emphasis to smaller eigenvalues. Improvement can be seen in each inversion. In the final inversion in Figure **I**, the bump is nearly completely inverted and the velocity artifacts are nearly gone. This result contrasts with the identical inversion of a narrow bump in Figure **3.45d & f**. Of the velocity artifact that does remain, most of it is at the top of model and nearly none at the bottom.

Inversion of Model F with strong velocity emphasis
eigenvalue range: (1.0-0.05)

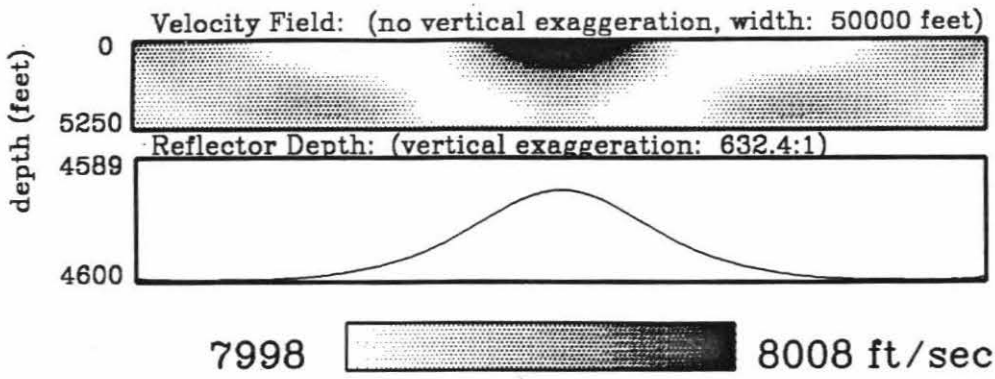

Inversion of Model F with strong velocity emphasis
eigenvalue range: (1.0-0.02)

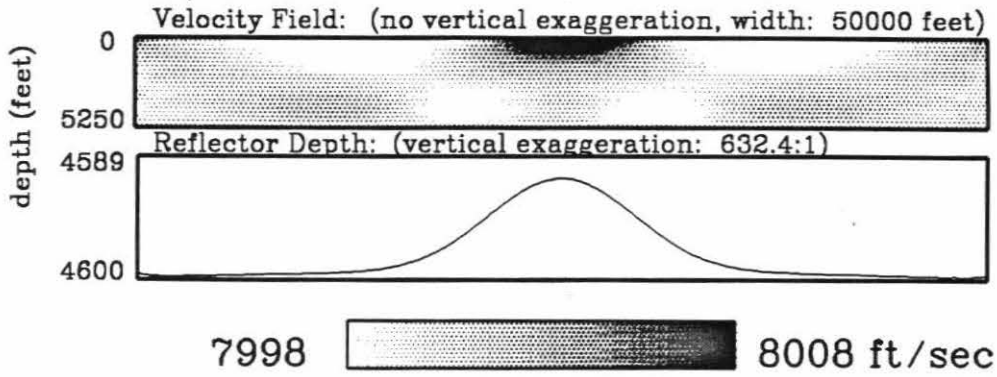

Inversion of Model F with strong velocity emphasis
eigenvalue range: (1.0-0.01)

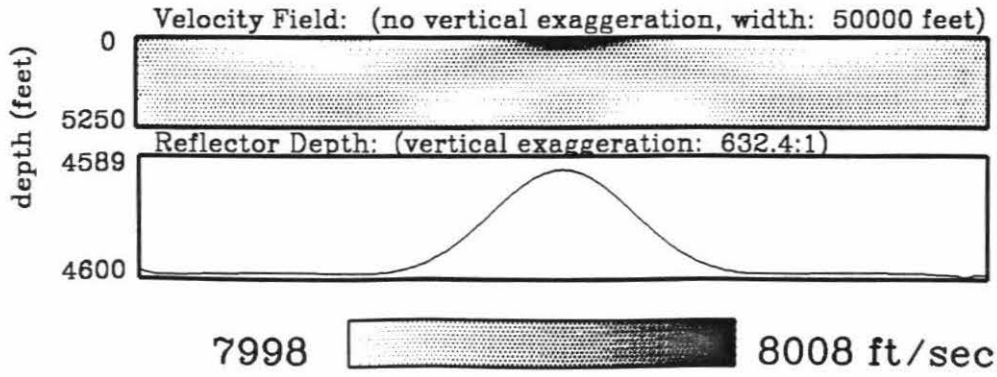

Figure 3.48

Tomographic inversions of velocity variations at different depths.

A: True model used for data collection. Velocity variations have a low amplitude (-50 ft/sec) and smoothed sides to not significantly affect ray paths. Reflector is flat at depth 5000 feet. Maximum ray angle is 45°. The reference model used for later inversion has a constant velocity and a flat reflector at the correct depth.

B: Reflector only inversion of data from model in Figure **A**. The velocity was not allowed to vary in the inversion. This constraint forces the velocity variations into reflector depth variations. This is considered the worst case scenario that can be used for comparison with later inversions.

C: Inversion for reflector and velocity over a small eigenvalue range. The velocity-reflector depth ambiguity has not been inverted. The inversion has placed half of the travel time variation into velocity and the other half into reflector depth variation. Note the reflector structure is similar to that in Figure **B,** but half the amplitude.

True Model G

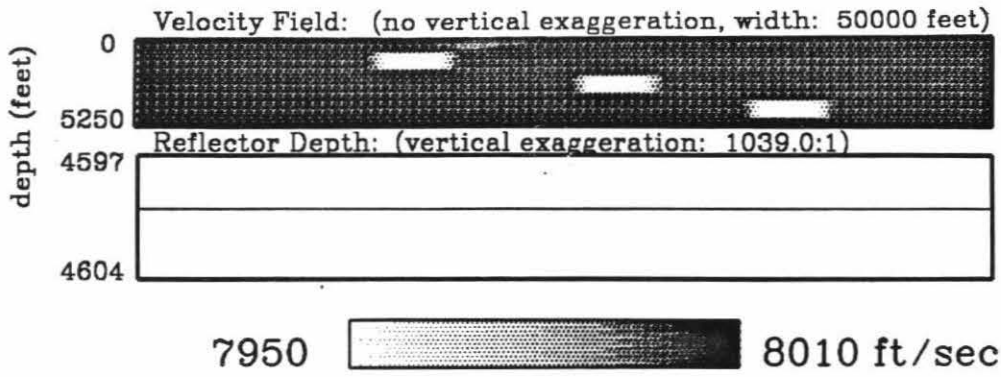

Reflector Only Inversion of Model G

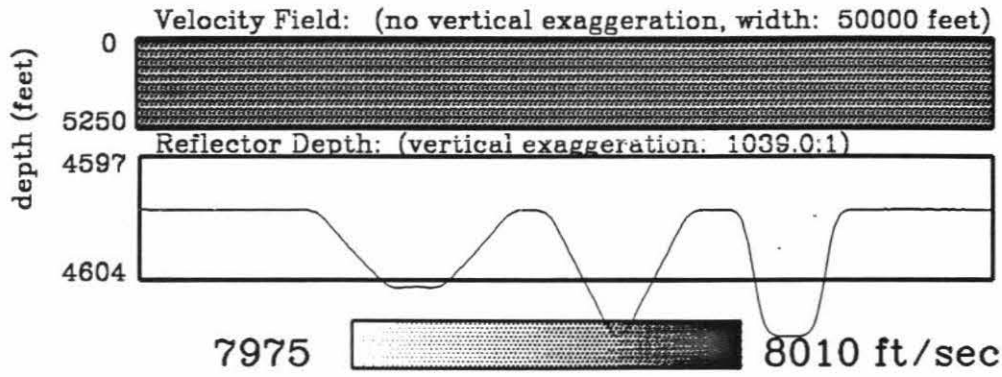

Inversion of Model G
eigenvalue range: (1.0-0.3)

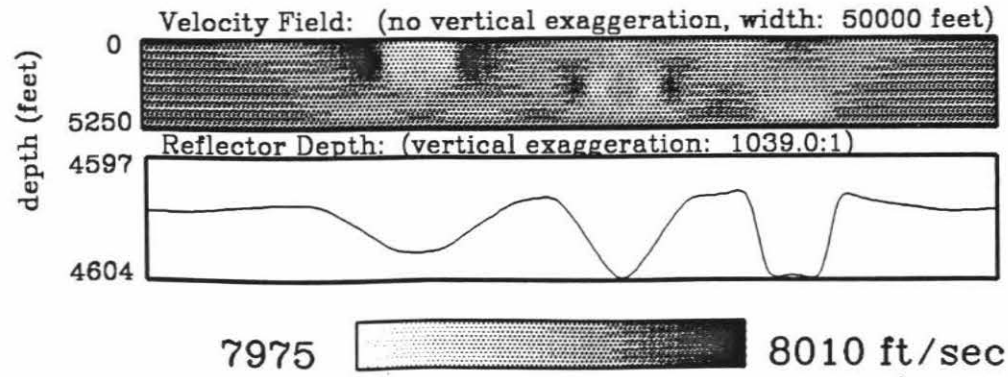

Figures 3.48

D & E: Previous inversion carried out to smaller eigenvalues. Velocity variations are smeared because of the limited angular ray coverage. Reflector artifact on the left side from the upper velocity variation has been removed. Middle artifact has been reduced but not totally removed, while right artifact has not been significantly improved. Note, however, that on the right side, the whole reflector has been raised to the correct average depth.

F: Reference model with an additional, lower, reflector. The rest of the model is identical to the previous reference model. The cable length has not changed, so that maximum ray angle for the upper reflector is 45^{o}, but 27^{o} for the lower reflector.

Inversion of Model G
eigenvalue range: (1.0-0.05)

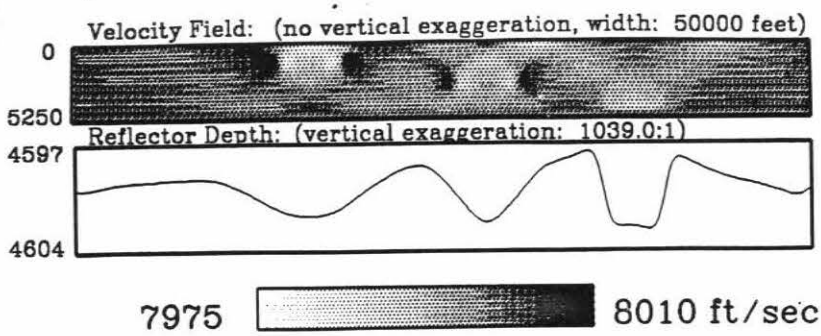

Inversion of Model G
eigenvalue range: (1.0-0.02)

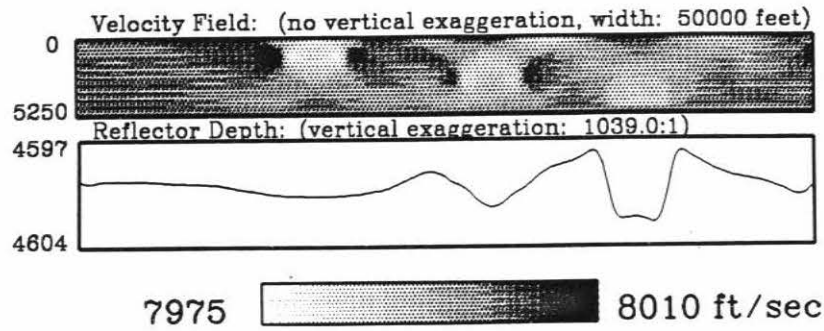

Starting Reference Model with 2 Reflectors

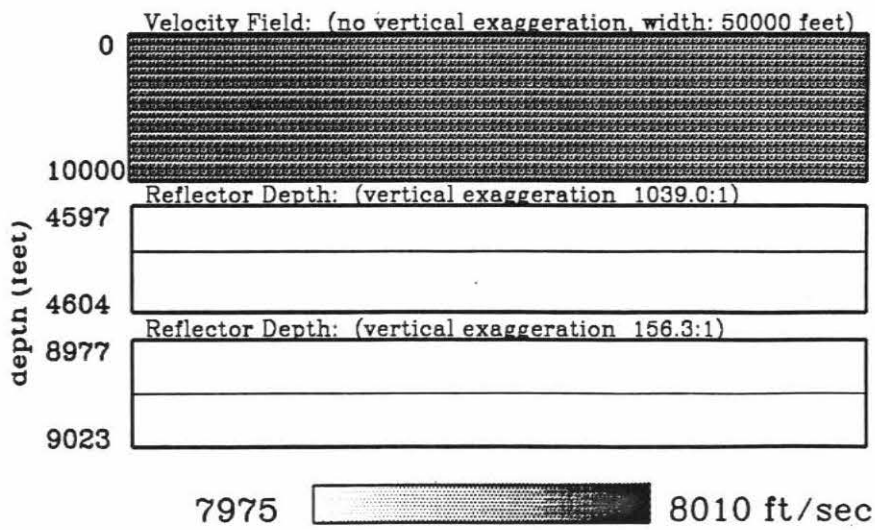

Figure 3.48

G: The true model of Figure **3.48a** is extended in depth to a second reflector with no additional complications. The reference model and true model are identical below the first reflector.

H: The inversion using two reflectors over a small eigenvalue range. The inversion of the upper reflector is not different from the corresponding inversion with only one reflector in Figure **3.48c**.

True Model G with 2 Reflectors

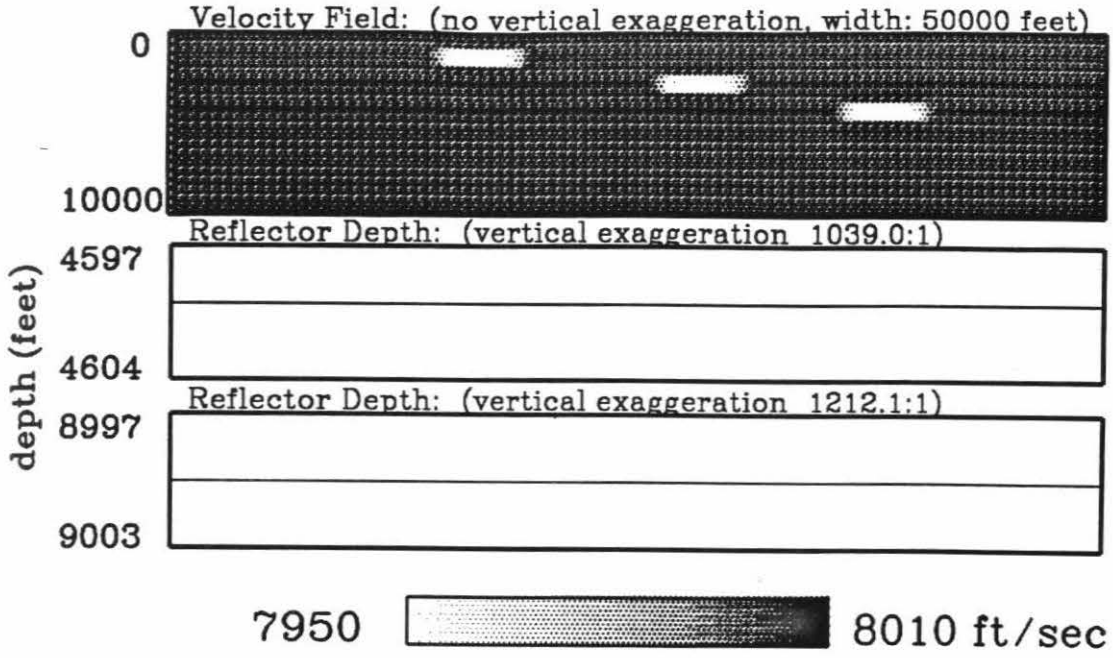

Inversion of Model G using 2 reflectors
eigenvalue range: (1.0-0.3)

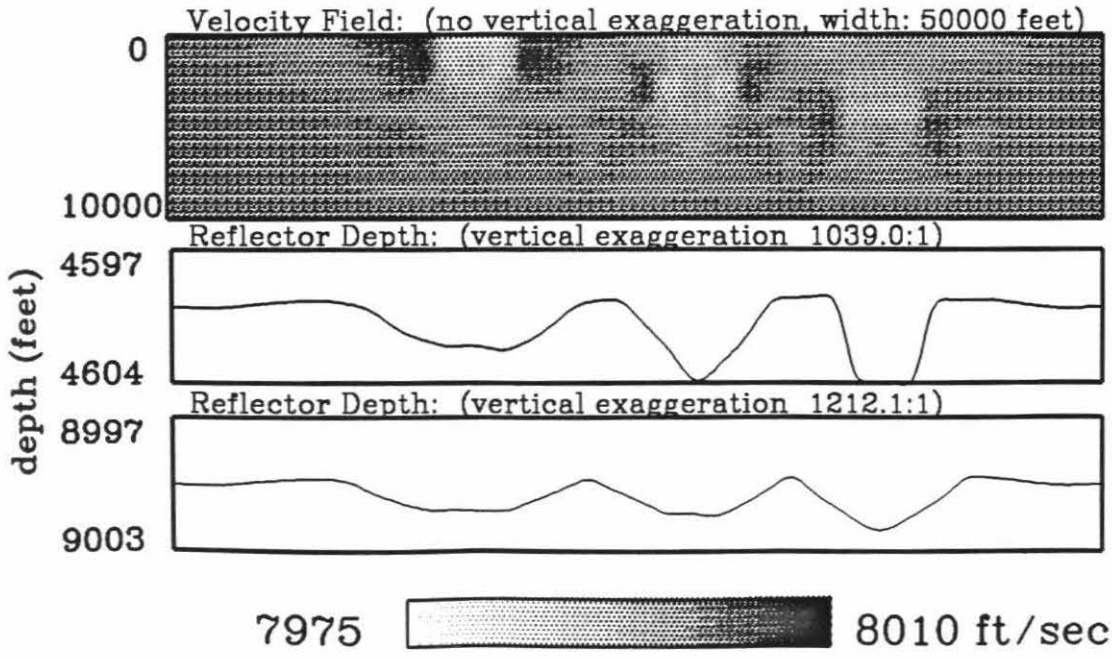

Figures 3.48

I & J: The inversion with two reflectors is carried out to smaller eigenvalues. The result is more accurate than the corresponding inversions with one reflector in Figures **3.48d & e.** However, some bothersome high frequency artifacts remain. They are worse for the right side of model, where the lower velocity variations are.

Inversion of Model G using 2 reflectors
eigenvalue range: (1.0-0.05)

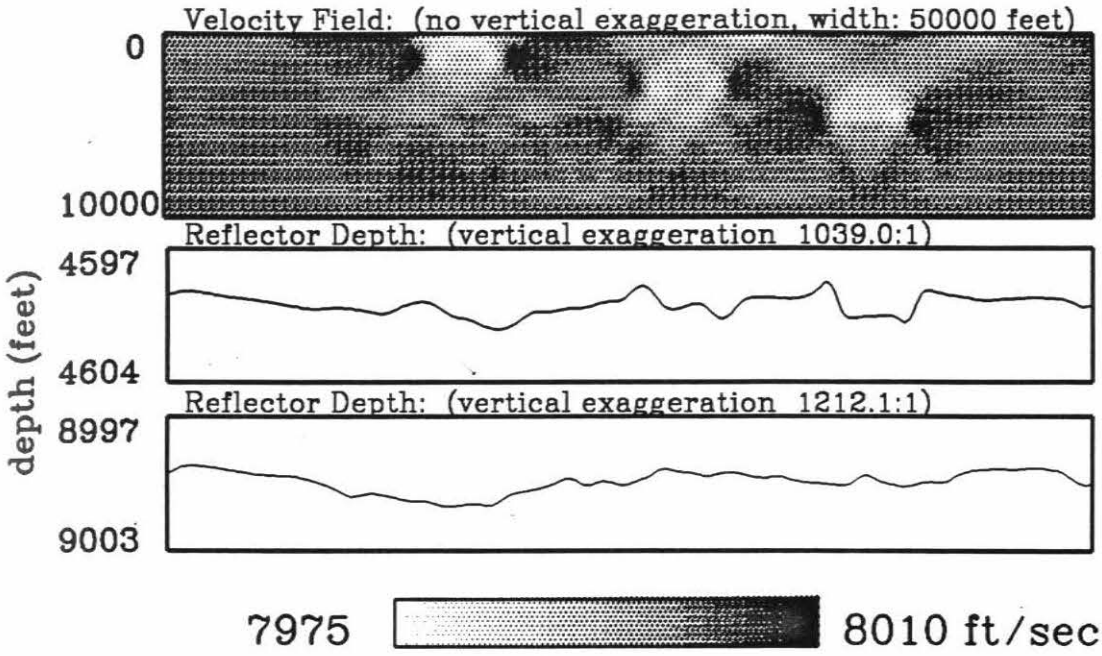

Inversion of Model G using 2 reflectors
eigenvalue range: (1.0-0.02)

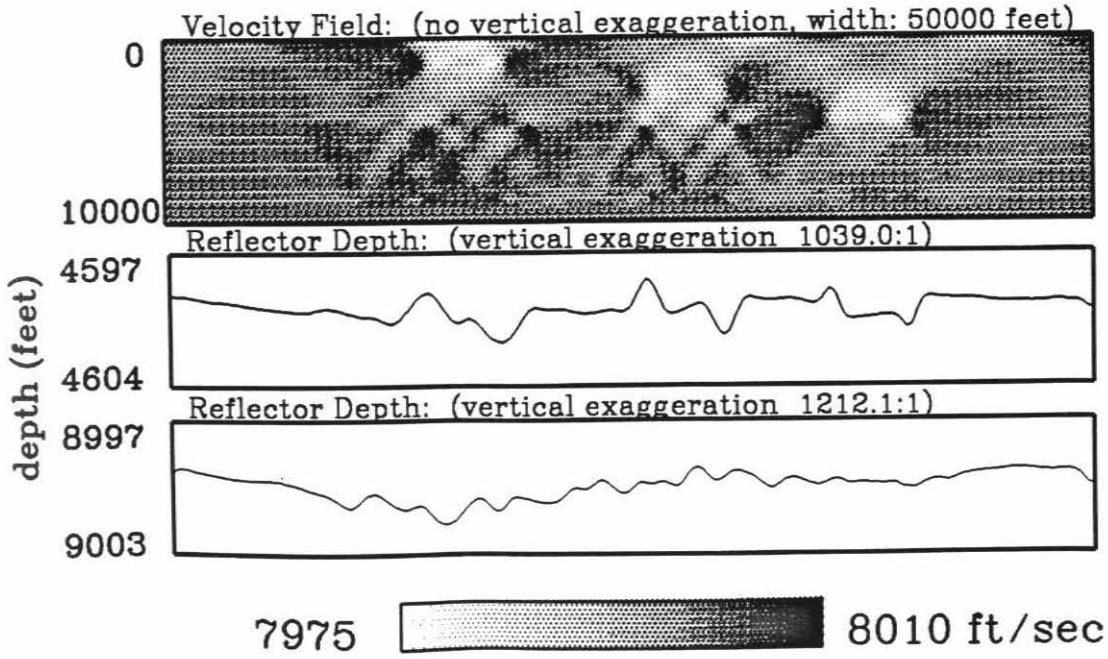

Figures 3.48

K & L: Inversions with two reflectors and the application of constraints. The velocity was not allowed to vary below the upper reflector. The reflector is inverted better in Figure **K** than in the corresponding inversion in Figure **3.48i** without constraints. The high frequency artifacts, however, still exist.

Inversion of Model G using 2 reflectors and Velocity Constraints, eigenvalue range: (1.0-0.05)

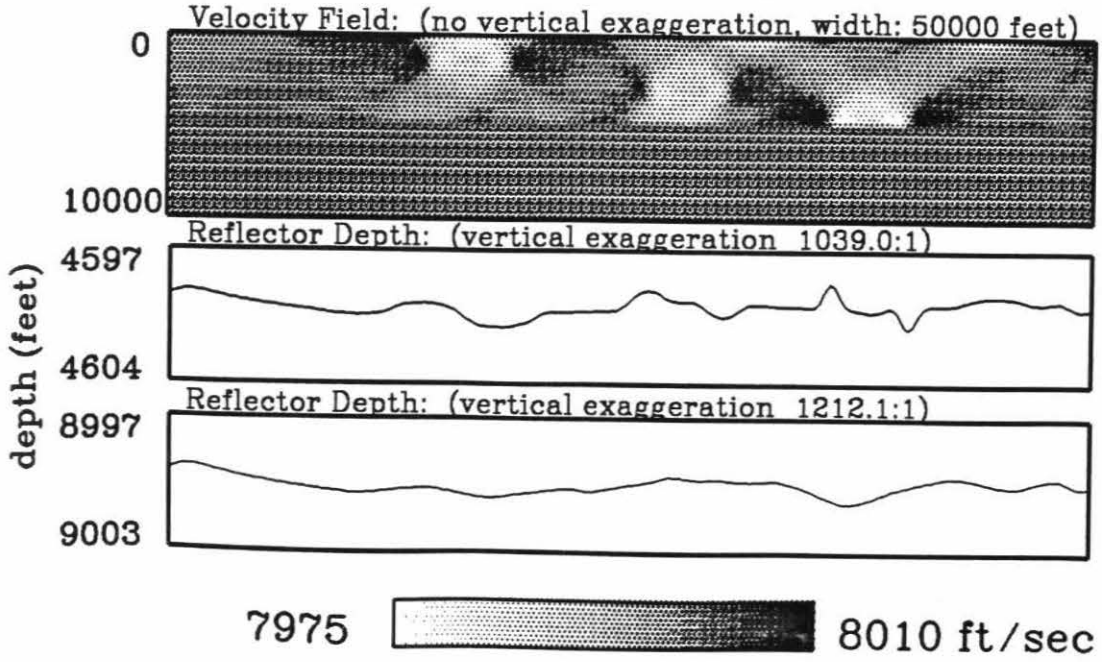

Inversion of Model G using 2 reflectors and Velocity Constraints, eigenvalue range: (1.0-0.02)

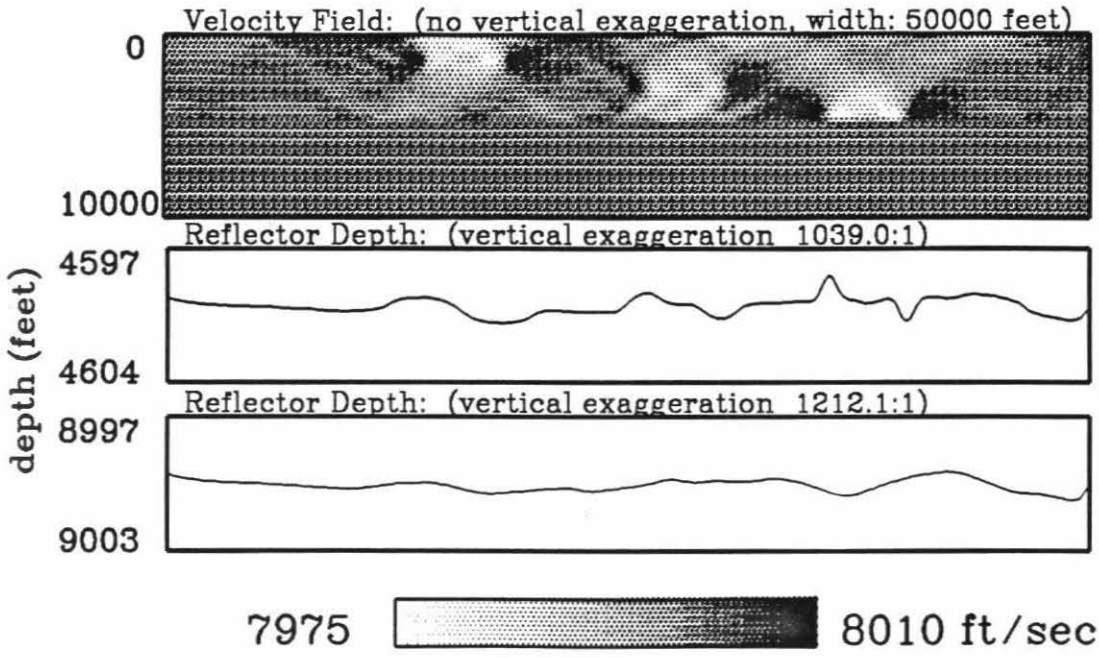

Figures 3.48

M & N: Inversion with one reflector and the application of incorrect velocity constraints. The velocity was not allowed to vary in the lower 40% of the model. This constraint is appropriate for the left, upper velocity variation, but not for the middle and lower, right ones. As a result of this incorrect constraint, server reflector artifacts result.

Inversion of Model G with Velocity Constraints
eigenvalue range: (1.0-0.05)

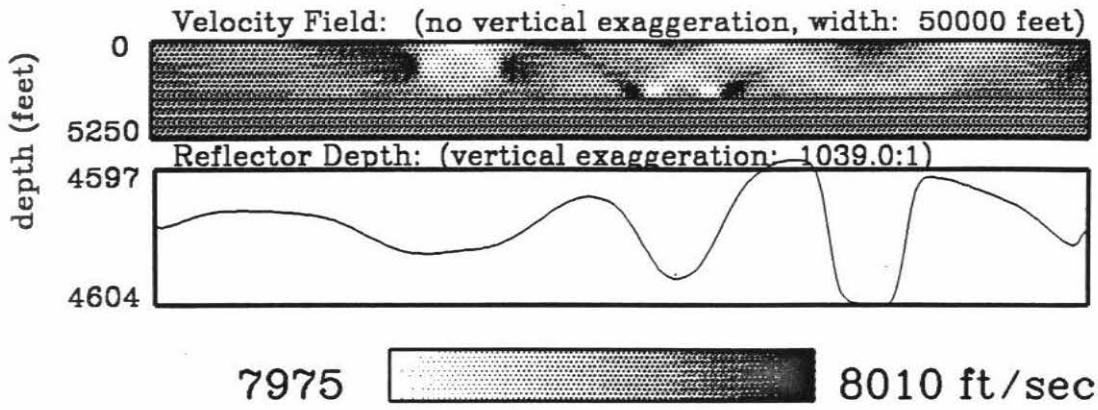

Inversion of Model G with Velocity Constraints
eigenvalue range: (1.0-0.02)

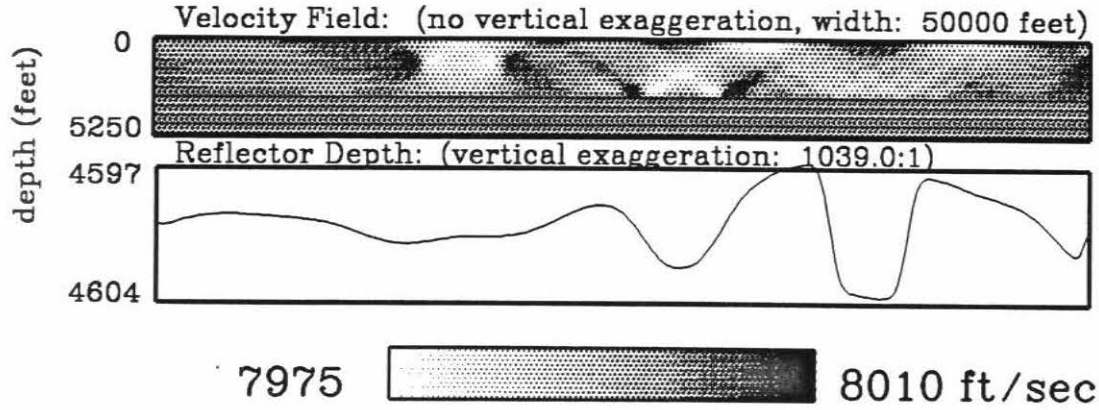

Figure 3.49

Tomographic inversion of velocity variations at the bottom of the model.

A: True model for data collection. The velocity variations are -50 ft/sec in an otherwise constant background field. The velocity variations have smoothed edges and are not strong enough to significantly affect the ray paths. The reference model used for ray tracing had a constant velocity and flat reflector.

B: Inversion over a limited eigenvalue range. Much of the velocity variations have been traded off into reflector artifacts.

C: Inversion to smaller eigenvalue. The reflector artifact on the left side under the small velocity variation has not changed significantly. But the reflector artifact under the wide velocity variation has improved, especially in its center.

True Model H

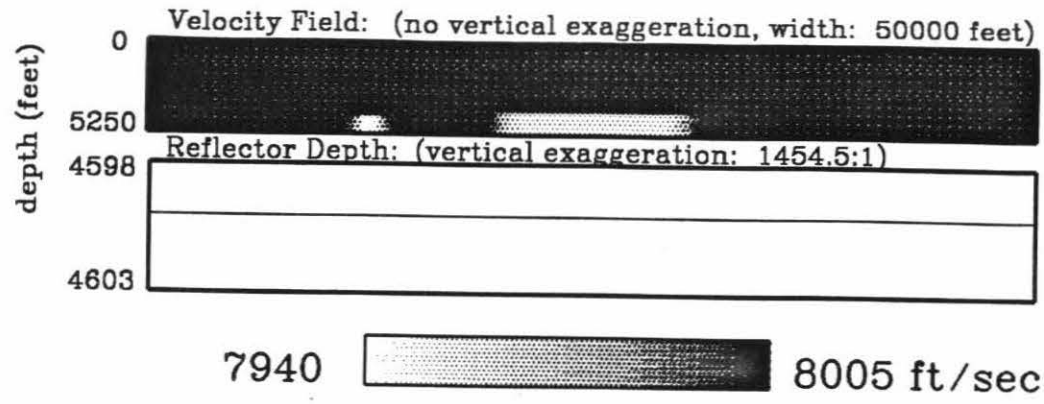

Inversion of Model H
eigenvalue range: (1.0-0.30)

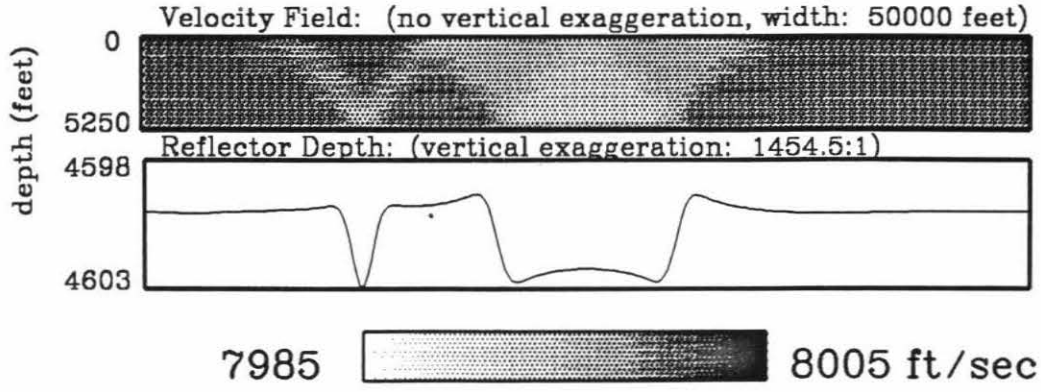

Inversion of Model H
eigenvalue range: (1.0-0.10)

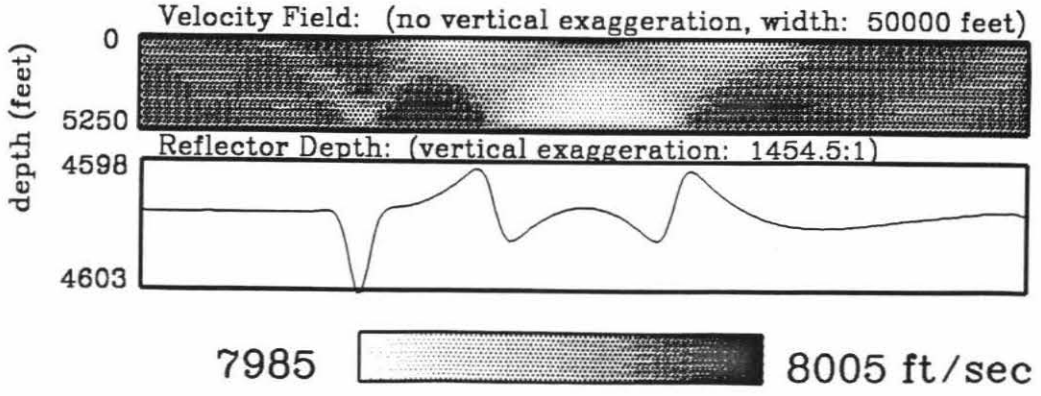

Figure 3.49

D, E, & F: Inversion to successively smaller eigenvalue. The final result has resolved the long wavelength components of the velocity-reflector depth ambiguity, but not the short wavelength components.

Inversion of Model H
eigenvalue range: (1.0-0.05)

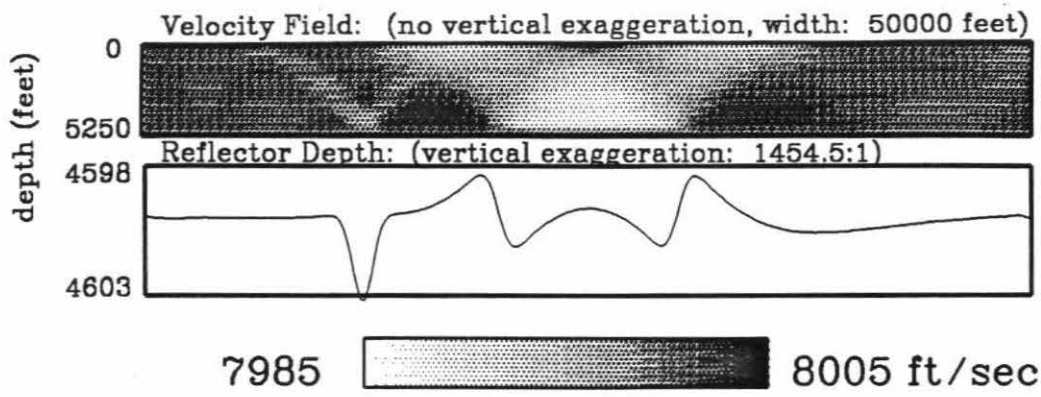

7985 8005 ft/sec

Inversion of Model H
eigenvalue range: (1.0-0.02)

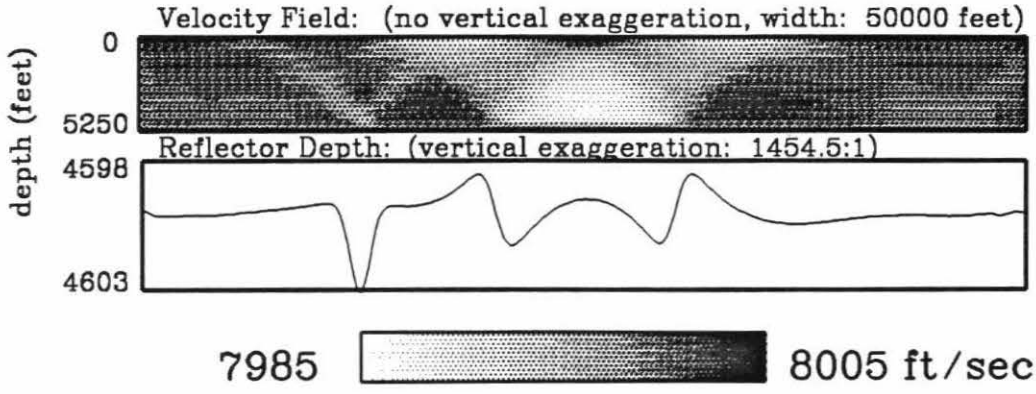

7985 8005 ft/sec

Inversion of Model H
eigenvalue range: (1.0-0.01)

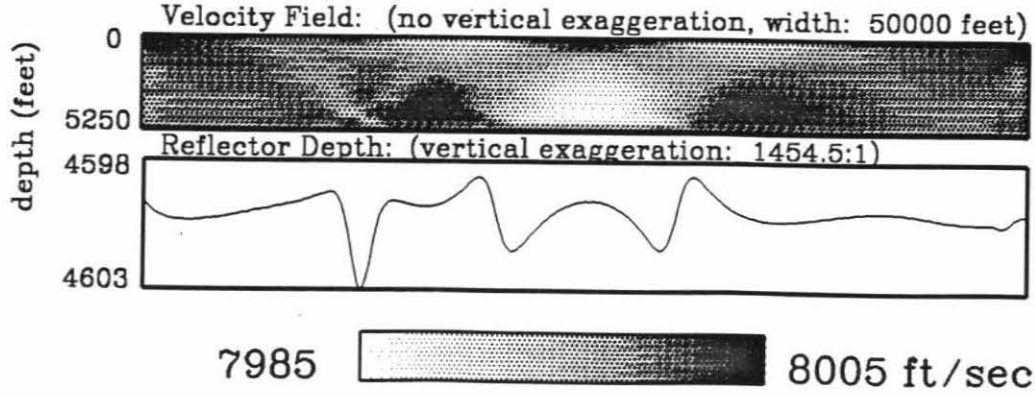

7985 8005 ft/sec

Figure 3.49

G: True model with an additional reflector at depth 9000 feet. The velocity is constant between the two reflectors.

True Model H with 2 reflectors

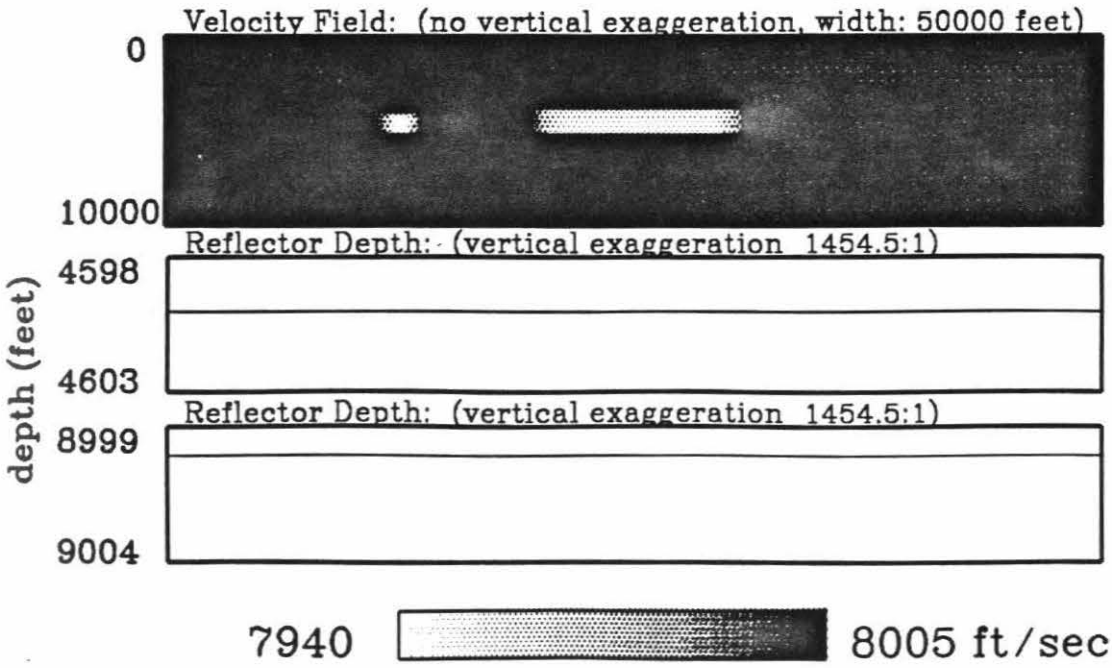

Figure 3.49

H: Reference model with two reflectors used for ray tracing. The only difference is has from the true model is the absence of the two velocity variations.

I: Inversion using two reflectors. The upper reflector is well inverted, even under the small velocity variation. This is markedly better than the corresponding reflector with only one reflector in Figure **3.49d**.

Staring Reference Model with 2 reflectors

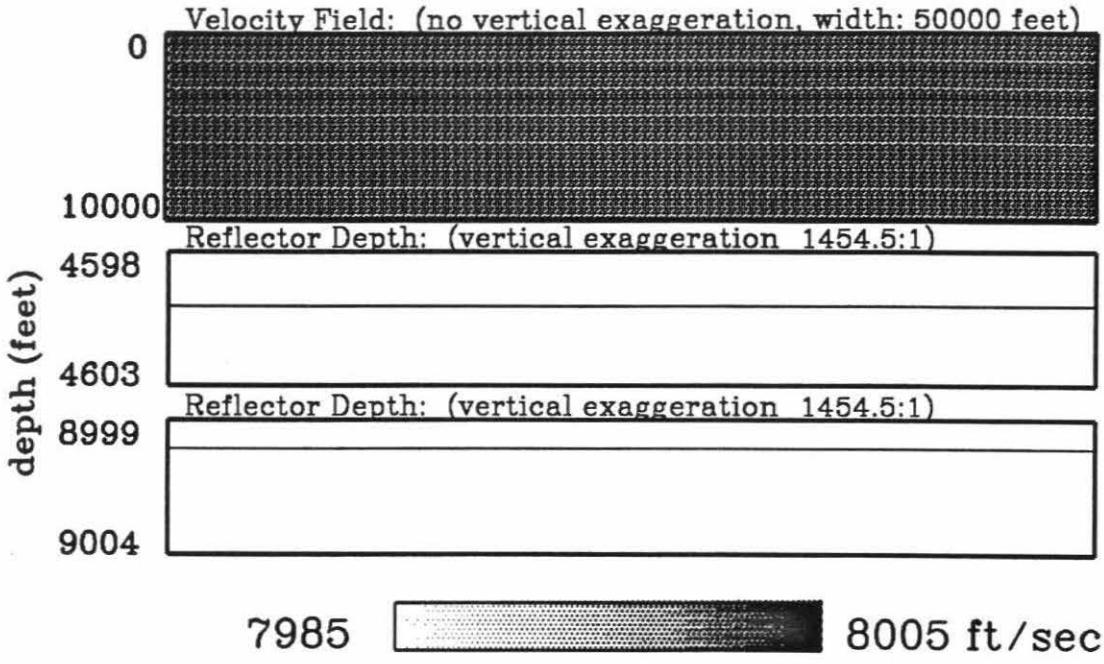

Inversion of Model H using 2 reflectors
eigenvalue range: (1.0-0.05)

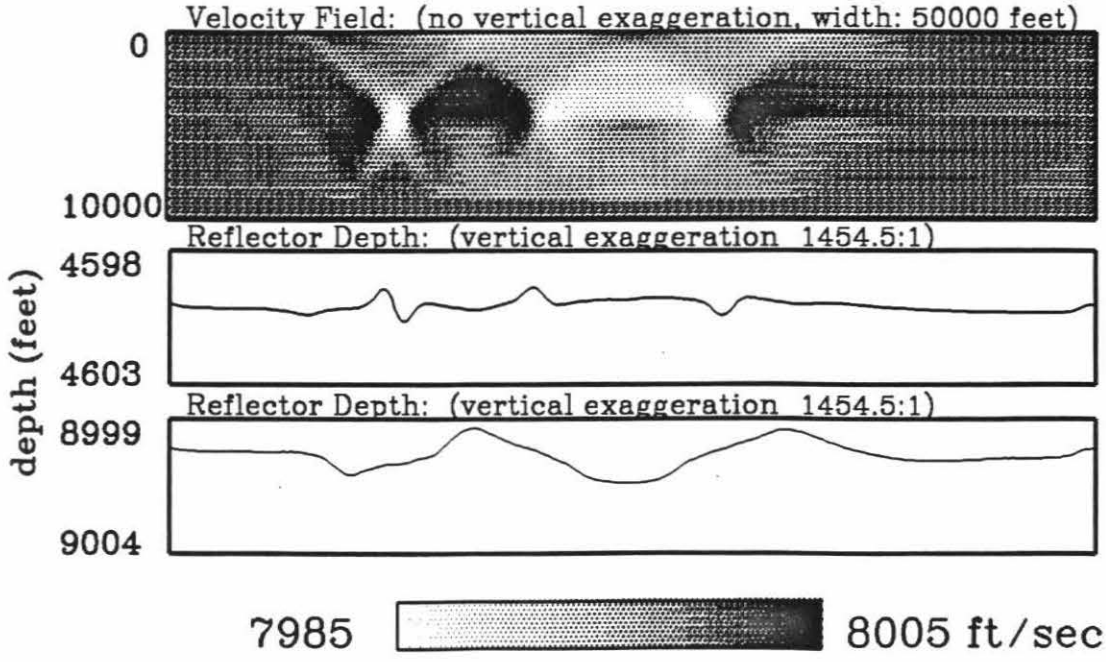

Figure 3.49

J: Inversion using two reflectors to a smaller eigenvalue. The artifact in the lower reflector still remains, as does velocity artifact between the two reflectors. The reference model was correct in these areas, yet the inversion was still corrupted.

Inversion of Model H using 2 reflectors
eigenvalue range: (1.0-0.02)

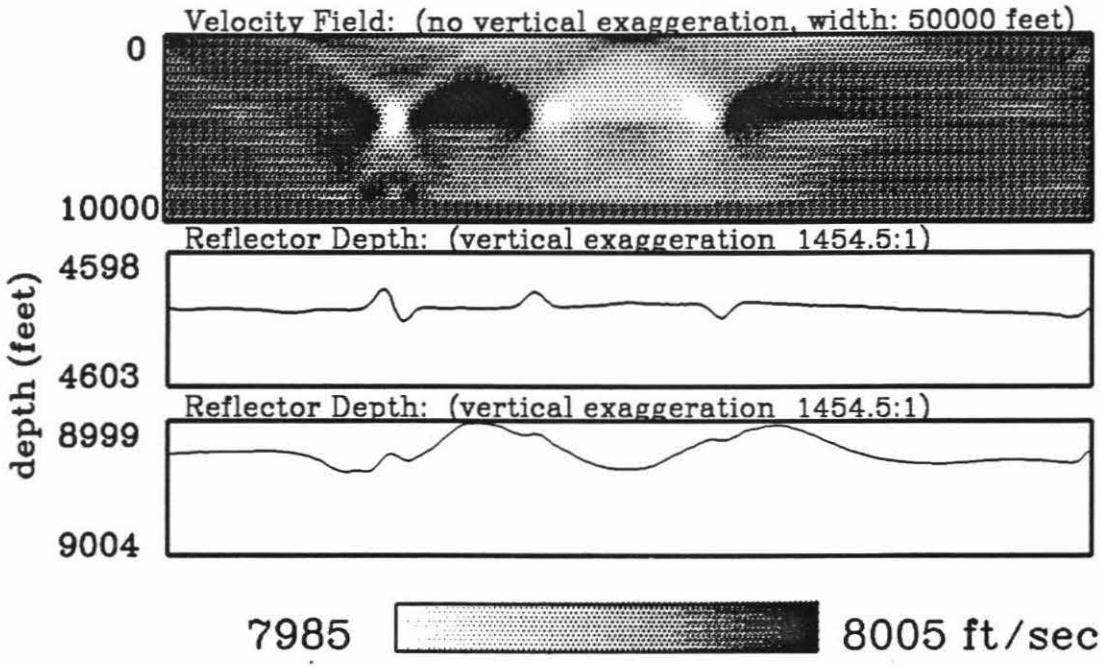

Figure 3.50

Effect of sharp reflector structure on ray paths of shortest travel time is dramatic. Ray path distribution is discontinuous.

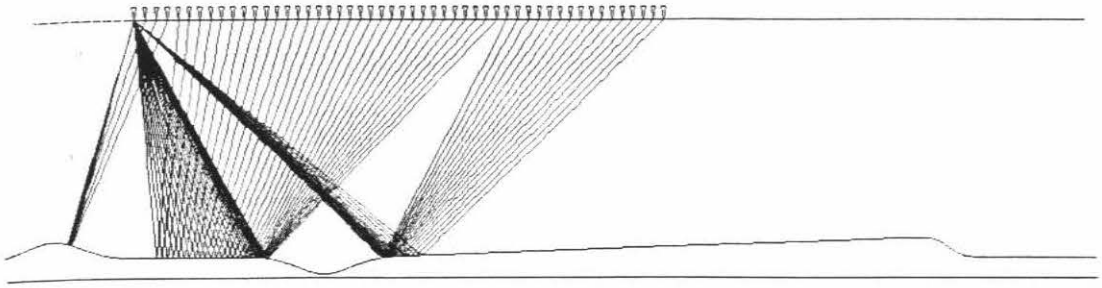

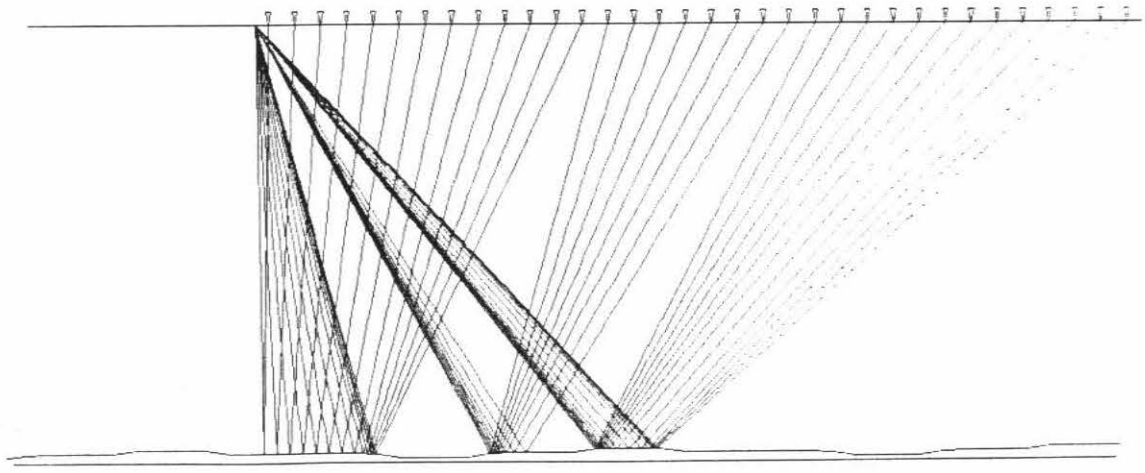

Figure 3.51

Effect of more gradual reflector structure on ray paths. The ray path distribution is continuous, but they are attracted to the hill where a greater density of rays exists.

Ray paths for same reflector position as in previous figure but a different shot location. Ray paths are now discontinuous because wide angle rays are more susceptible to reflector structure.

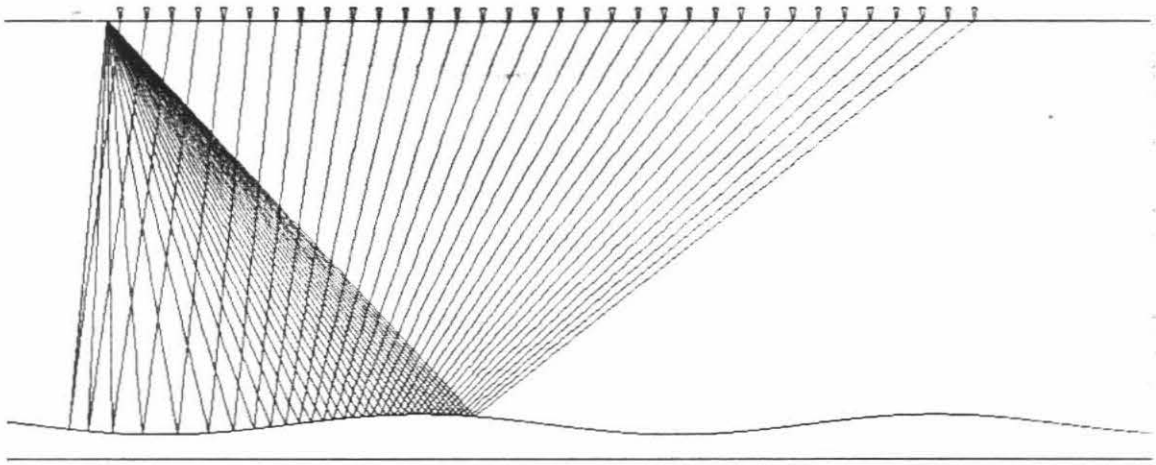

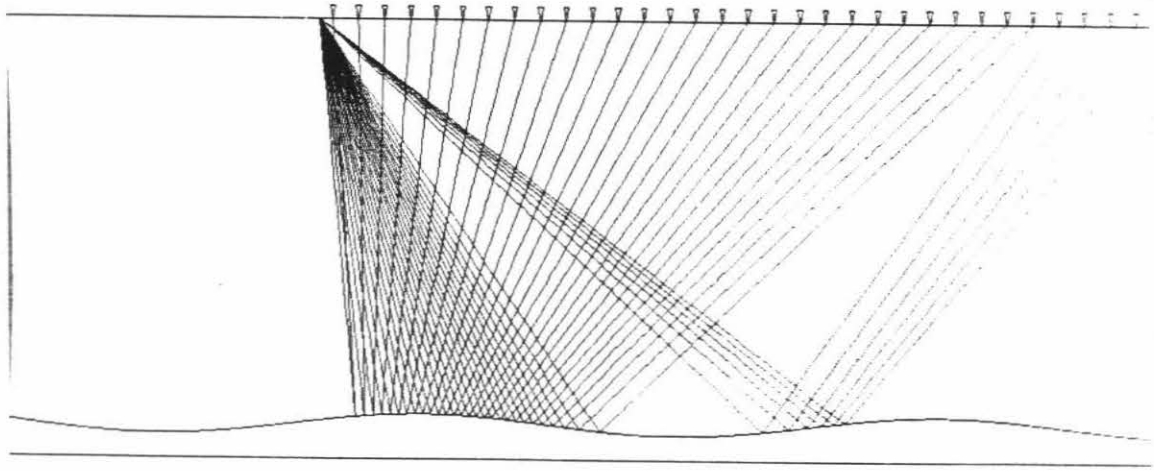

Figure 3.53

A & B: Models with reflector topography large enough to affect ray paths. These two models will be interchanged as true and reference models to test the success of the iterative application of tomography and migration in reducing the non-linear effects from the incorrect reflector structure. Sample ray paths through model in Figure **A** are shown in Figure **3.56**.

C: Density of rays in Figure **B**. Coverage is very smooth.

Model I-1

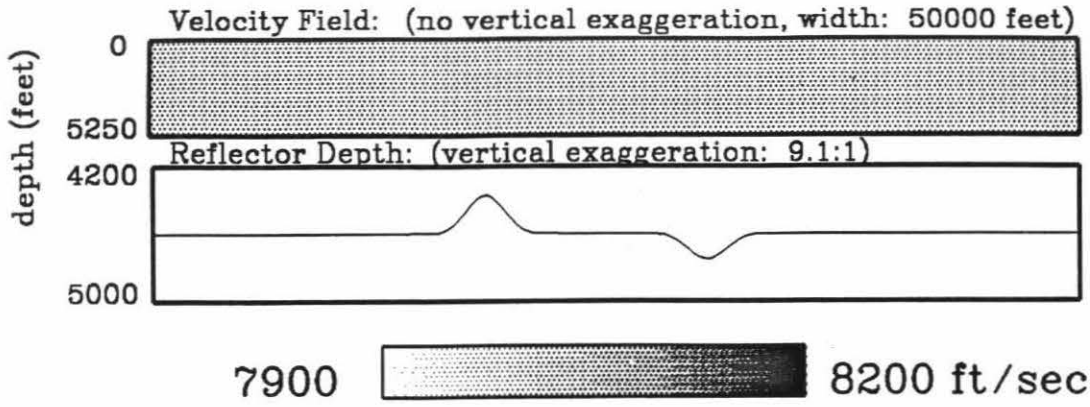

Model I-2

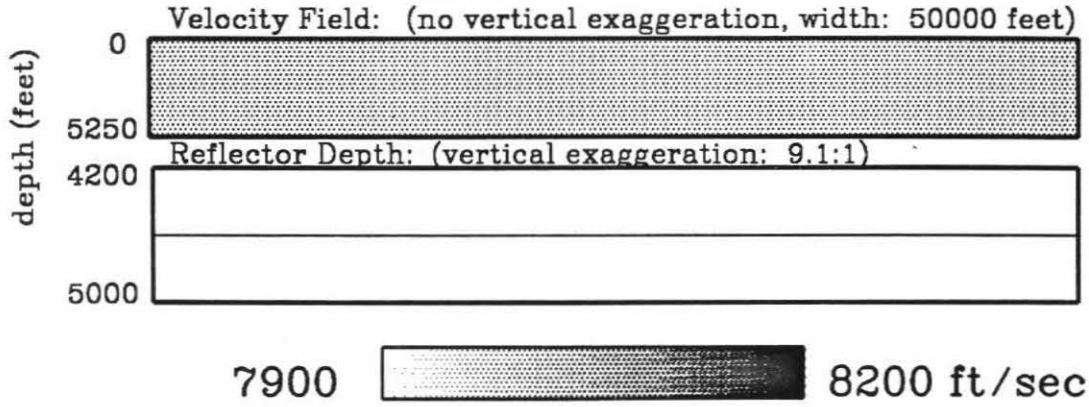

Density of Ray Paths in Model I-2

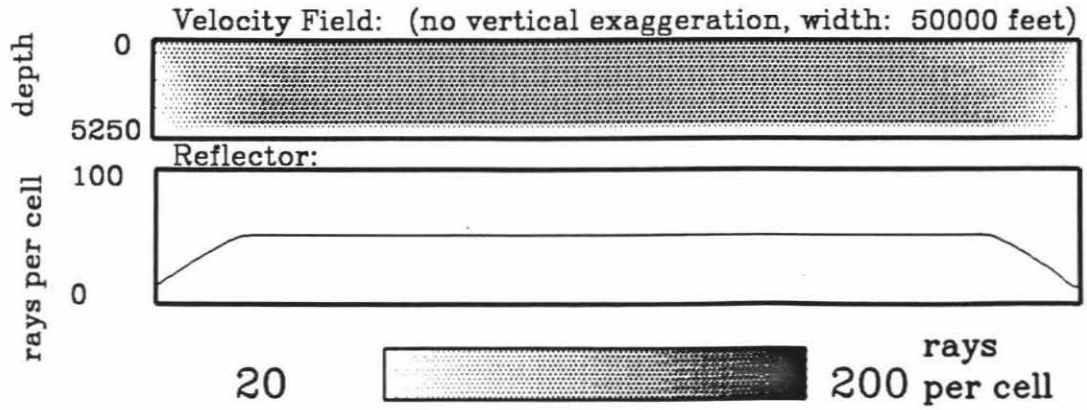

Figure 3.53

D: Density of rays in Figure **A**. The bump causes an increase in ray density to about twice that of the background density. Very few rays reflect off of the bottom of the trough.

E: Reflector only inversion of the bumps using a flat reflector as the reference. The bump has been widened and the trough has been narrowed. The artifacts are solely the result of the non-linearity of the incorrect rays through the reference model.

F: Inversion for velocity and reflector of bumps using flat reflector as reference. Some velocity artifacts appear above the bump.

Density of Ray Paths in Model I-1

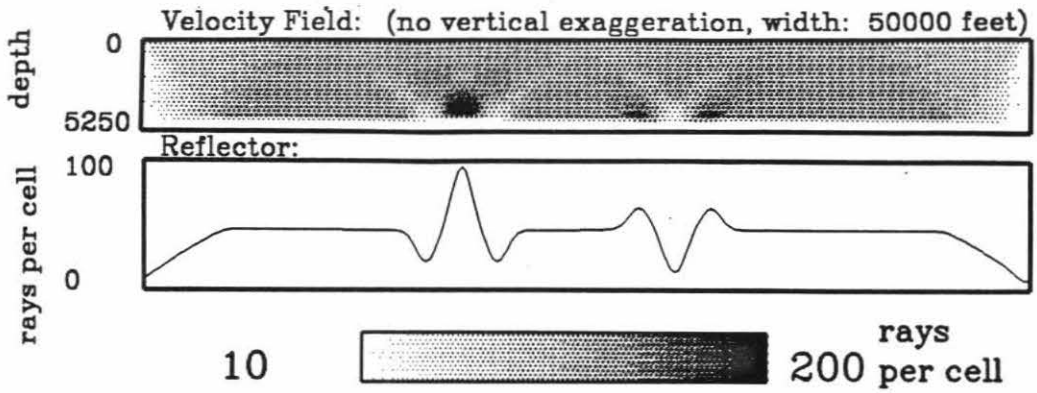

Reflector only Inversion I-3 of Model I-1 using Model I-2 as the Reference Model, eigenvalue range: (1.0-0.05)

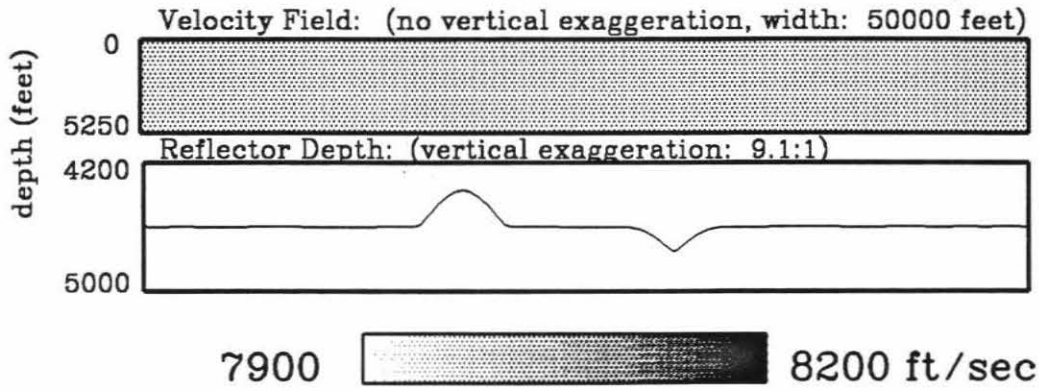

Inversion I-1a of Model I-1 using Model I-2 as the Reference Model, eigenvalue range: (1.0-0.05)

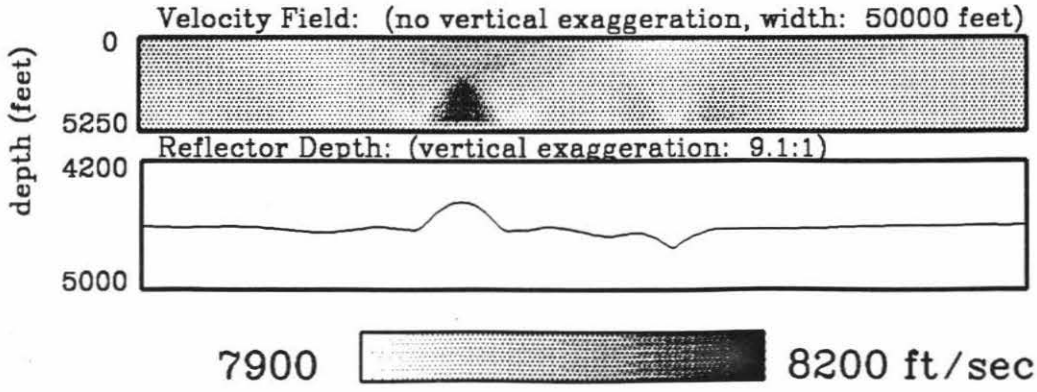

Figure 3.53

G: Previous inversion carried out to smaller eigenvalue. No change is apparent.

H & I: Inversion of flat reflector using reflector with bumps as the reference model. The correct result would remove the bumps and leave a flat reflector. The inversion appears to have partially succeeded. The bump is lower and the trough has been almost totally removed.

Inversion I-1b of Model I-1 using
Model I-2 as the Reference Model, eigenvalue range: (1.0-0.02)

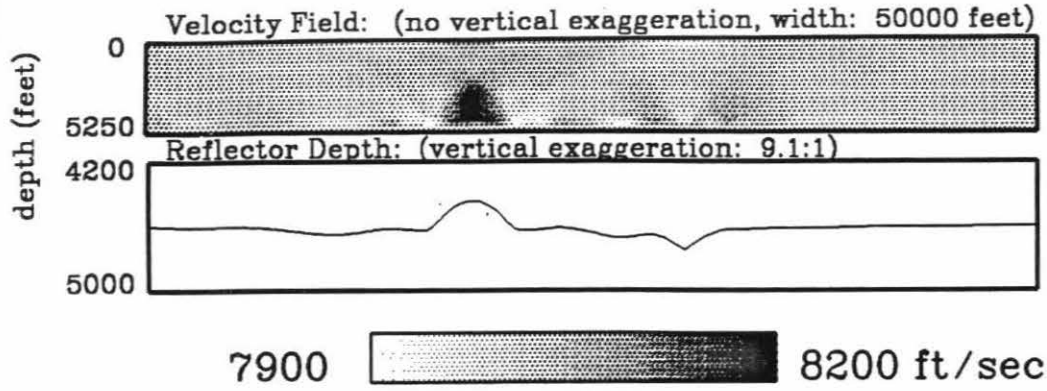

Inversion I-2a of Model I-2 using
Model I-1 as the Reference Model, eignevalue range: (1.0-0.05)

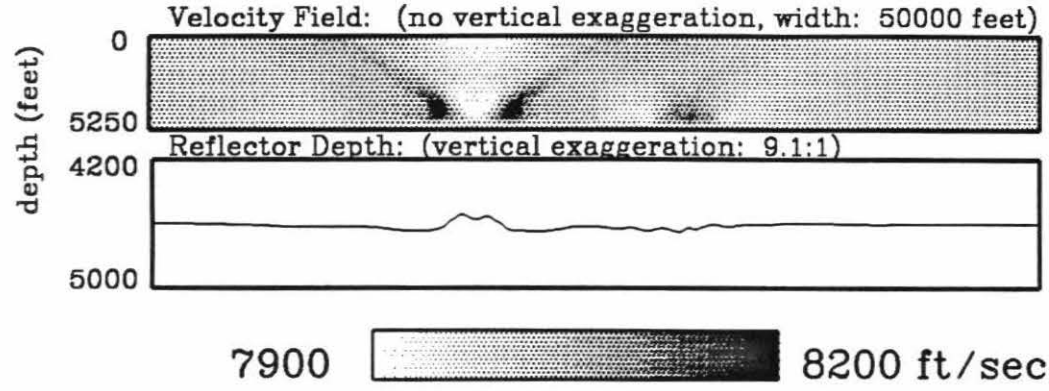

Inversion I-2b of Model I-2 using
Model I-1 as the Reference Model, eigenvalue range: (1.0-0.02)

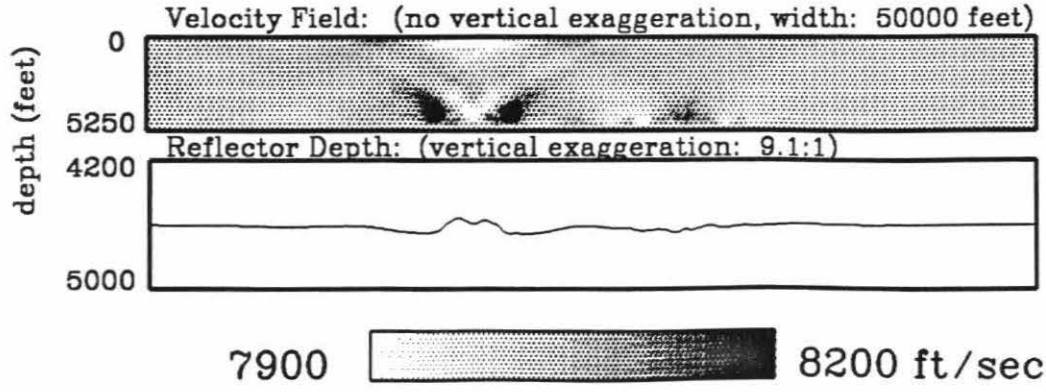

Figure 3.54

Additional inversions after migration through the original inversion and ray tracing through the resulting reflector position and velocity field.

A: Model used for second ray tracing in an attempt to invert the bump model in Figure **3.53a**. Velocity field comes from previous inversion of Figure **3.53f** and reflector position comes from migration of zero offset data through this velocity field. Migration is shown in Figure **3.57c**.

B: Model used for second ray tracing to invert the flat reflector model in Figure **3.53b**. Velocity field comes from inversion in Figure **3.53i**. Reflector comes from migration through velocity field, shown in Figure **3.57f**. The reflector position from the migration is quite different and improved from that of the inversion.

C: Second inversion of bump model in Figure **3.53a** using model in Figure **A** as the reference. Bump has been narrowed and velocity artifacts appear reduced slightly, but no major change has occurred.

Model I-11: Velocity Field of Inversion I-1b with Reflector Picked from Migration through the Velocity

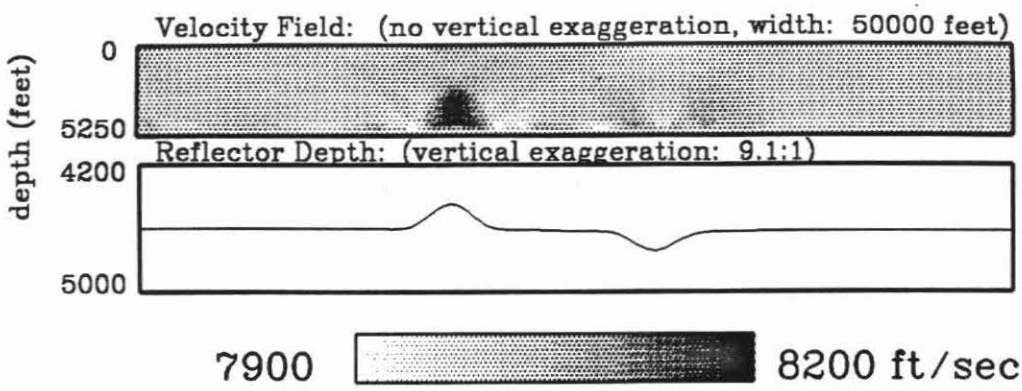

Model I-22: Velocity Field of Inversion I-2a with Reflector Picked from Migration through the Velocity

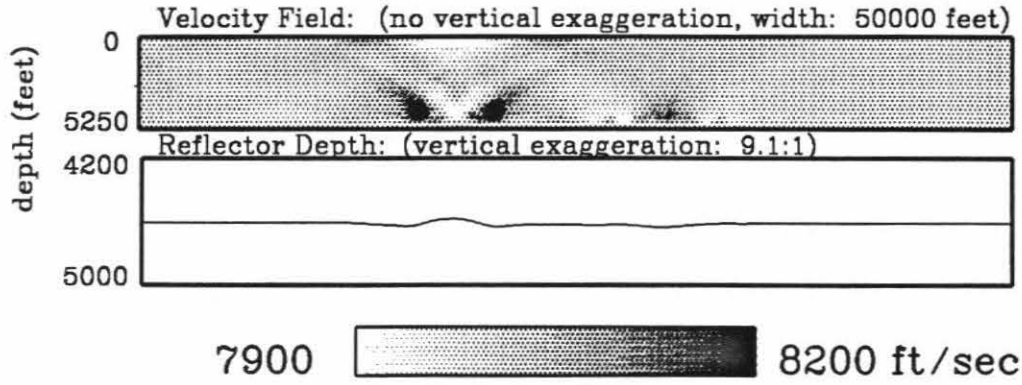

Inversion I-11a of Model I-1 using Model I-11 as the Reference Model, eigenvalue range: (1.0-0.05)

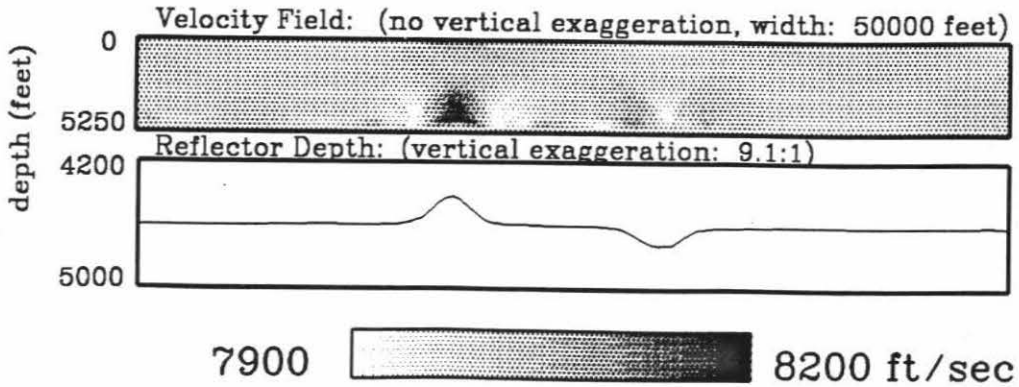

Figure 3.54

D: Previous inversion is continued to smaller eigenvalue. No major change occurs.

E & F: Second inversions of flat reflector model in Figure **3.53b** using Figure **3.54b** as the reference. No significant change has occurred. Reflector position is accurate, but velocity artifacts remain.

Inversion I-11b of Model I-1 using
Model I-11 as the Reference Model, eigenvalue range: (1.0-0.02)

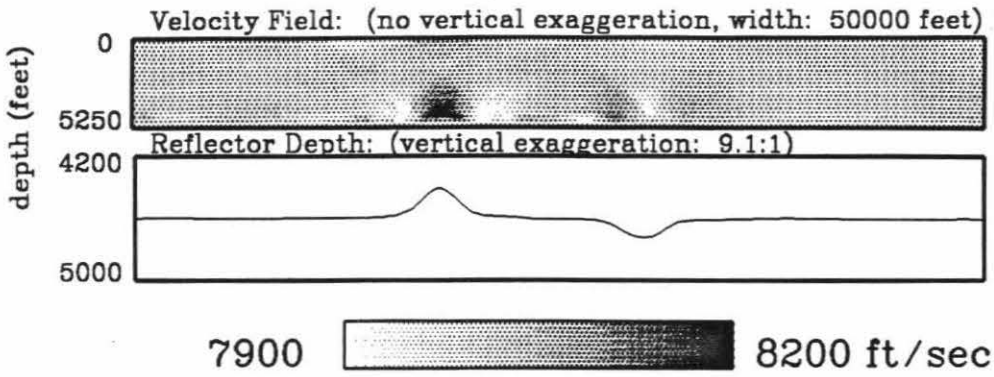

Inversion I-22a of Model I-2 using
Model I-22 as the Reference Model, eigenvalue range: (1.0-0.05)

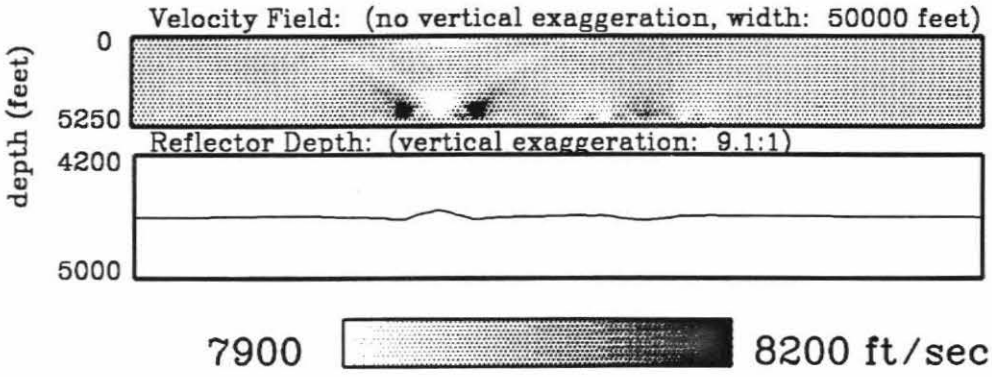

Inversion I-22b of Model I-2 using
Model I-22 as the Reference Model, eigenvalue range: (1.0-0.02)

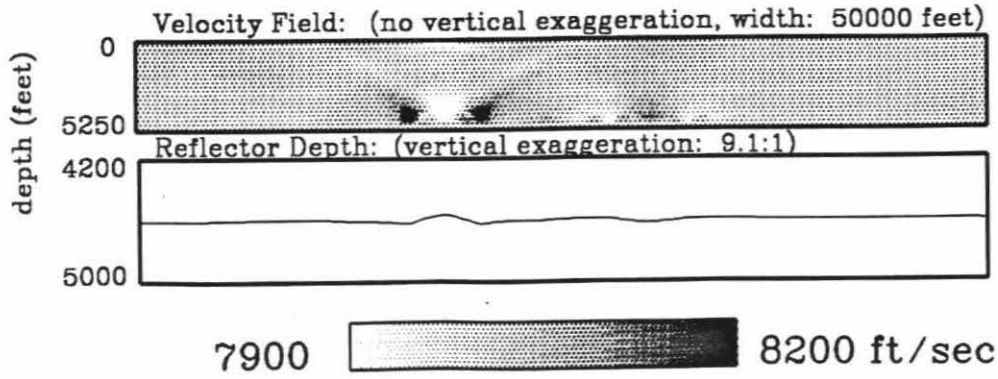

Figure 3.55

Test of the iterative application of tomography for velocity only and migration.

A: Velocity only inversion of bump model of Figure **3.53a** using flat reflector model of Figure **3.53b** as the reference. Severe velocity artifacts have been created.

B: Reflector position picked from migration through velocity field of previous inversion. The migration is shown in Figure **3.57i**. A little structure is discernable, but reflector is still essentially identical to the flat reflector of the reference model.

C: Second inversion for velocity only using Figure **B** as the reference model.

Velocity only Inversion I-4a of Model I-1 using Model I-2 as the Reference Model, eigenvalue range: (1.0-0.05)

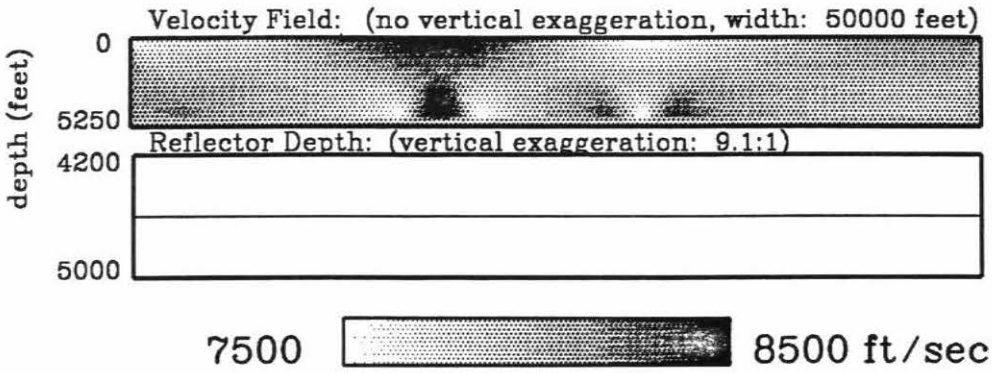

Model I-44: Velocity Field of Inversion I-4a with Reflector Picked from Migration through the Velocity

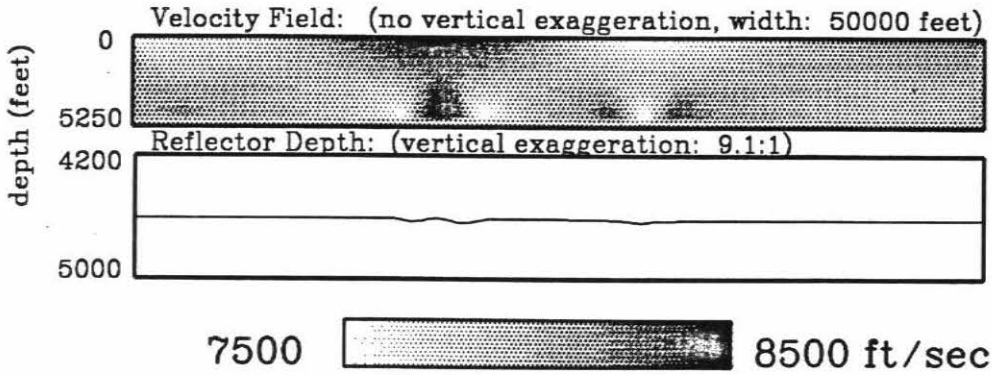

Inversion I-44a of Model I-1 using Model I-44 as the Reference Model, eigenvalue range: (1.0-0.05)

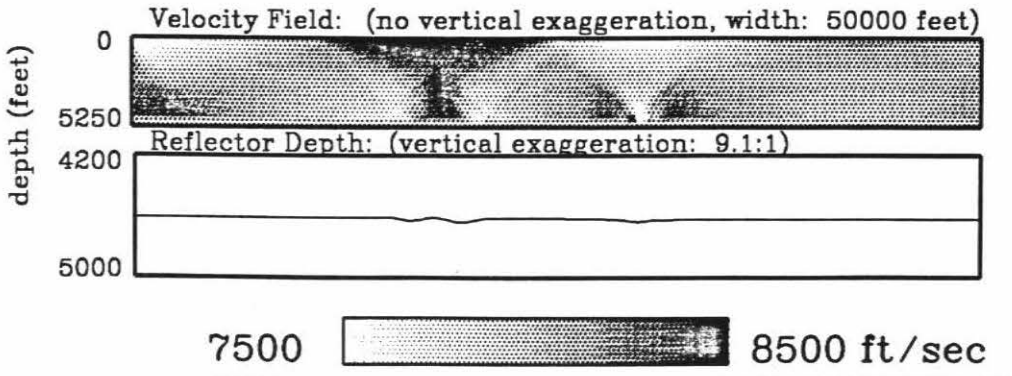

Figure 3.55

D: Second reflector position picked from migration through second inversion in previous Figure C. The migration is shown in Figure **3.57j**.

E: Third inversion for velocity only using previous Figure **D** as the reference model for ray tracing. It is clear this procedure is not effective for this model.

Model I-444: Velocity Field of Inversion I-44a with Reflector Picked from Migration through the Velocity

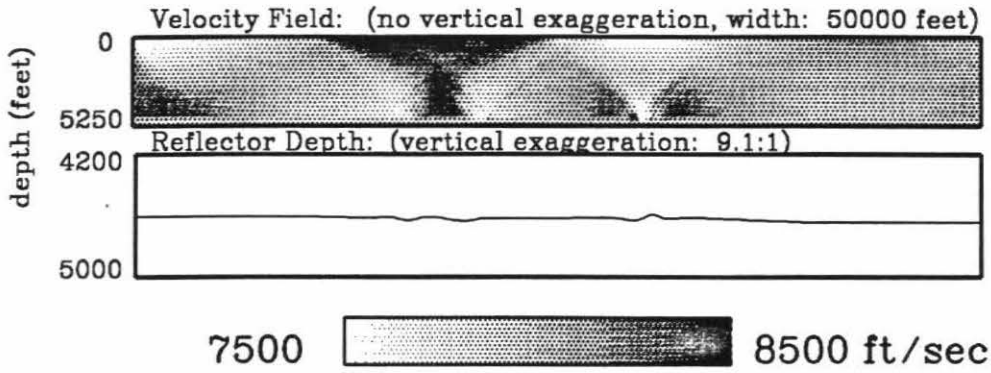

Inversion I-444a of Model I-1 using Model I-444 as the Reference Model, eigenvalue range: (1.0-0.05)

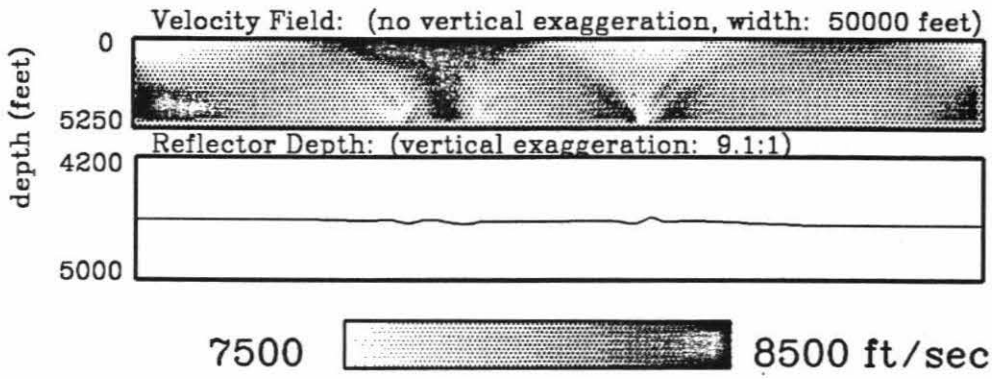

Figure 3.56

A: Sample ray paths through bump model shown in Figure **3.53a** used in previous inversion.

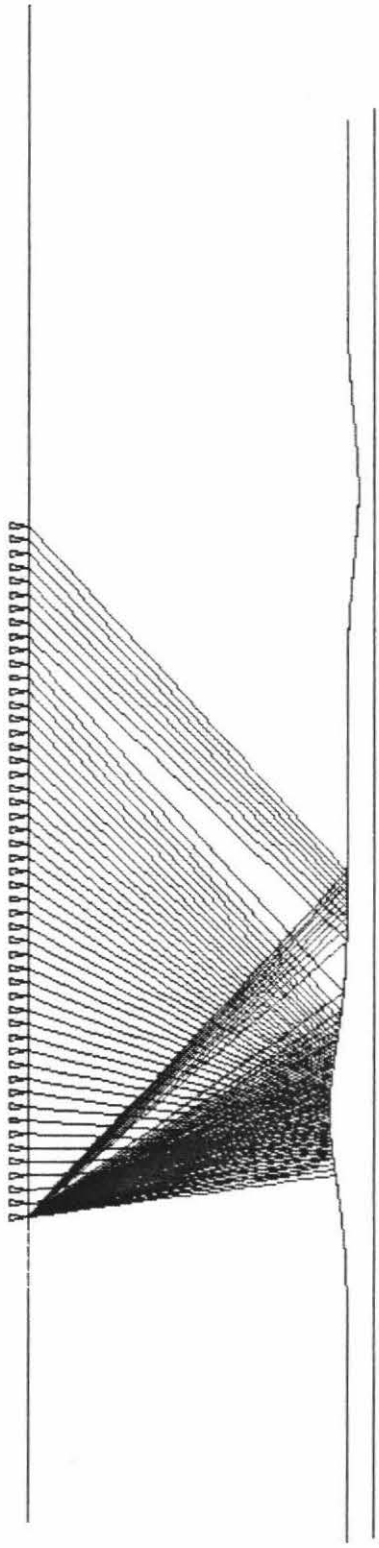

Figure 3.56

B: Sample ray paths over the trough. The ray set is continuous and some rays bounce off of the bottom of the trough.

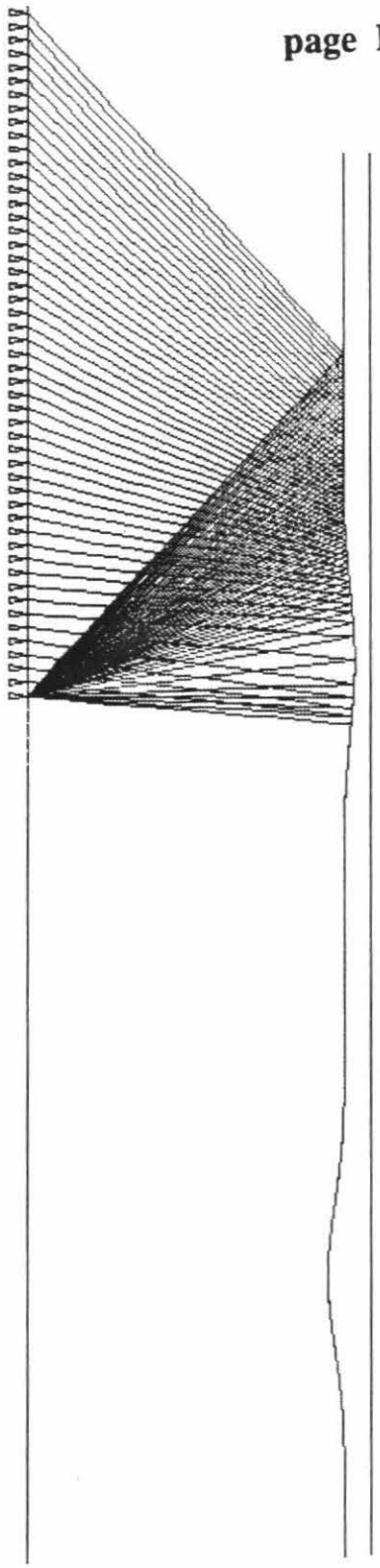

Figure 3.56

C: More sample ray paths over the trough. The ray paths are now discontinuous. The far offset rays are more affected by reflector topography.

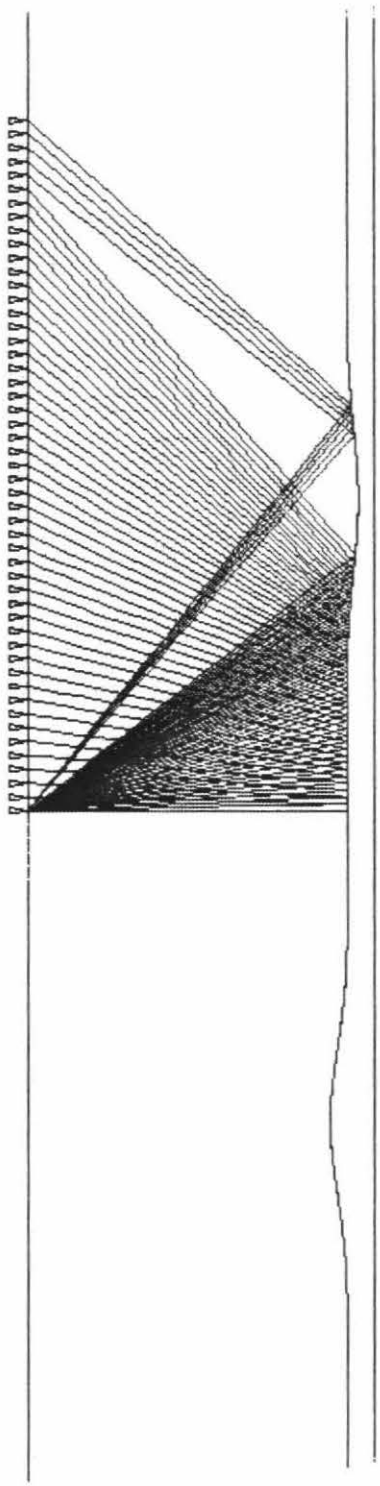

Figure 3.57

A: Zero offset time section from bump model of Figure **3.53a**. Modeling was performed with a 45° frequency domain finite difference modeling program.

B: Migration of previous zero offset data through correct, constant velocity. The bumps have been accurately reproduced.

Zero Offset Time Section of Model I

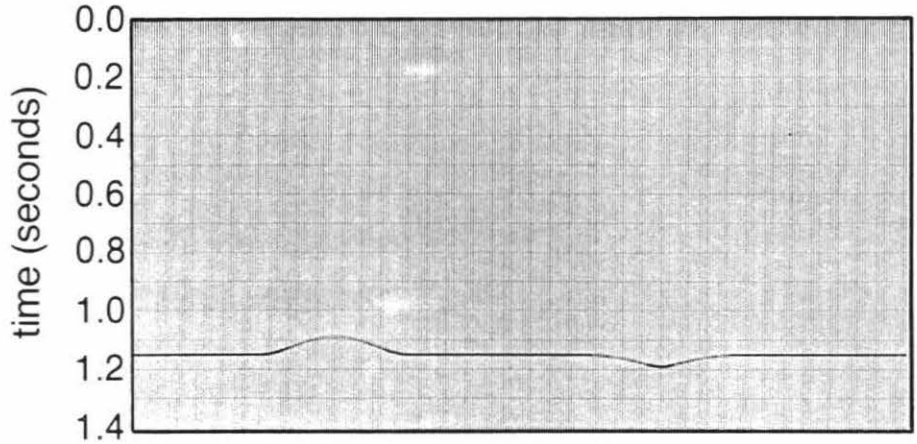

Migration of Model I–1 Time Section Through Correct, Constant Velocity

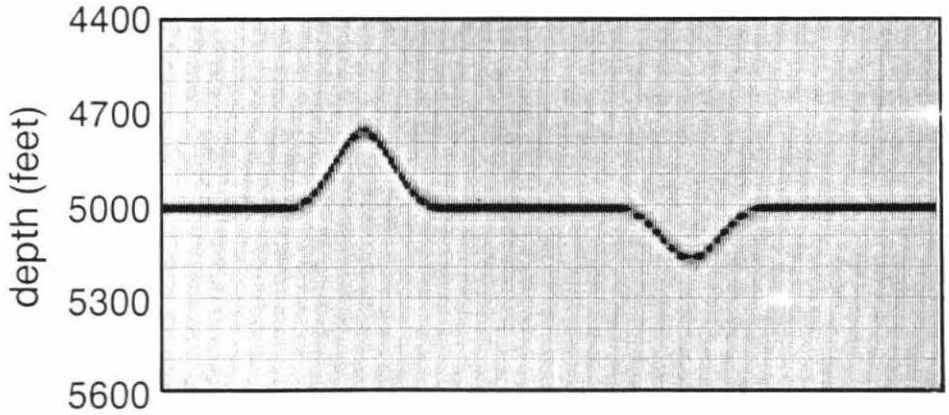

Figure 3.57

C: Migration of bump data through inversion in Figure **3.53f**. The shape of the bump and trough is quite well inverted, but the amplitude of the structure is low.

D: Migration of bump data through second inversion in Figure **3.54d**. Image appears worse than the previous migration through the first inversion.

Migration of Model I–1 Time Section Through Inversion I–1b

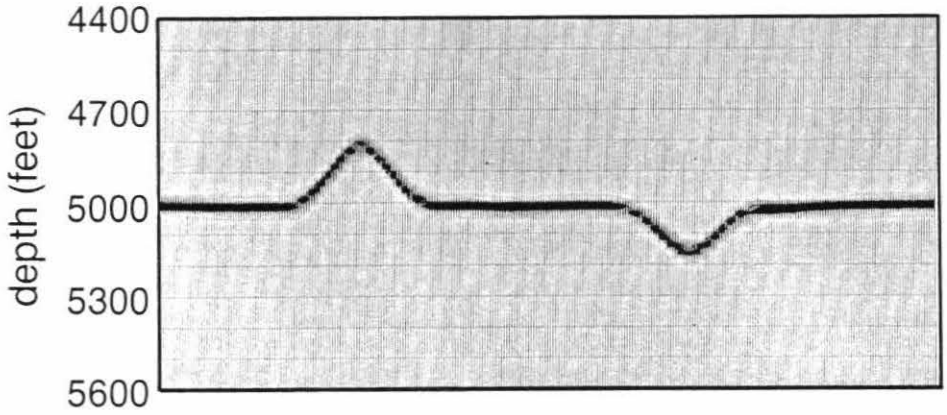

Migration of Model I–1 Time Section Through Inversion I–11b

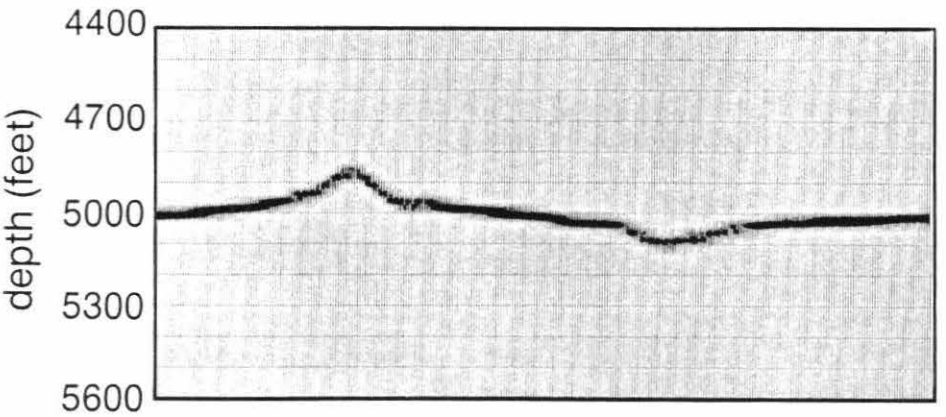

Figure 3.57

E: Difference between the two previous migrations. Figure **3.57c** is subtracted from Figure **3.57d**.

F: Migration of data from flat reflector model in Figure **3.53b** through inversion in Figure **3.53i**. Image is close to the correct result of a flat reflector.

Change between Migrations: Migration Through Model I–11b minus Migration Through Model I–1b

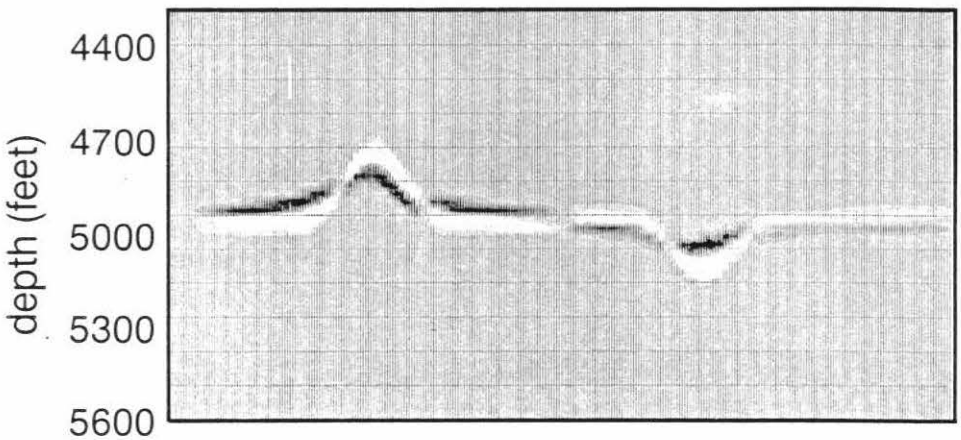

Migration of Model I–2 Time Section Through Inversion I–2b

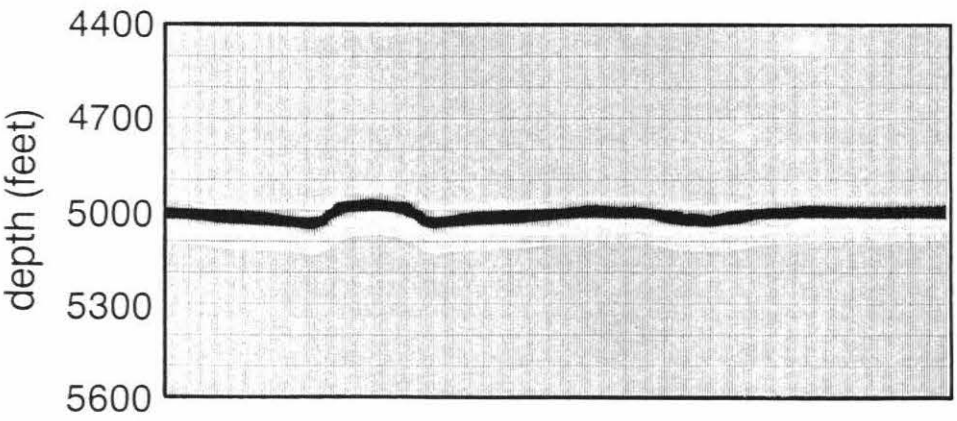

Figure 3.57

G: Migration through second inversion of Figure **3.54f**. There is no significant change from the previous inversion.

H: Difference between the two previous inversions. Figure **3.57f** is subtracted from Figure **3.57g**.

Migration of Model I–2 Time Section Through Inversion I–22b

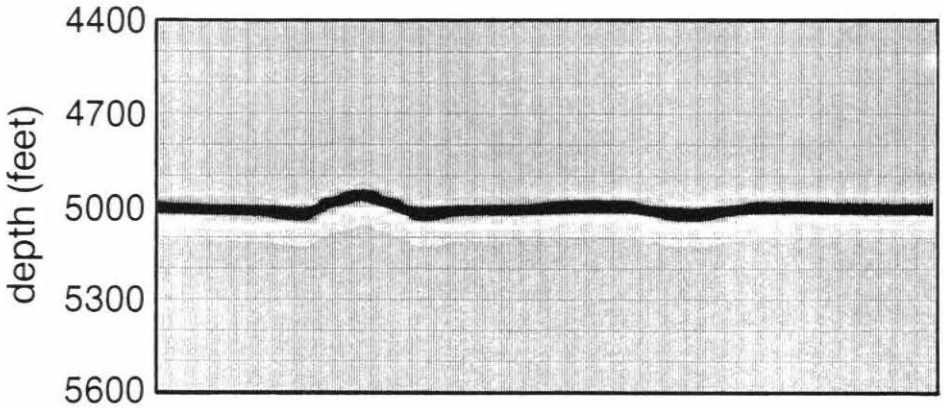

Change between Migrations: Migration Through Model I–22b minus Migration Through Model I–2b

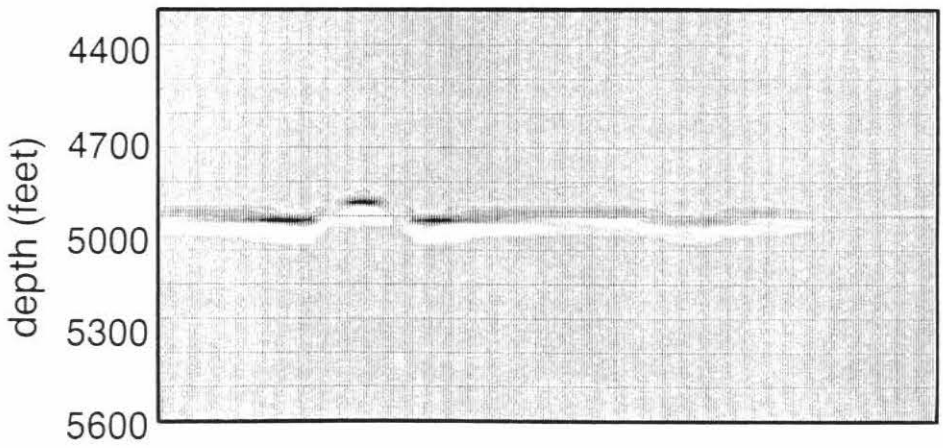

Figure 3.57

I: Migration of bump data from model in Figure **3.53a** through velocity only inversion in Figure **3.55a**. Result is little different from the flat reference model.

J: Migration through second velocity only inversion in Figure **3.55c**.

Migration of Model I–1 Time Section Through Velocity Only Inversion I–4a

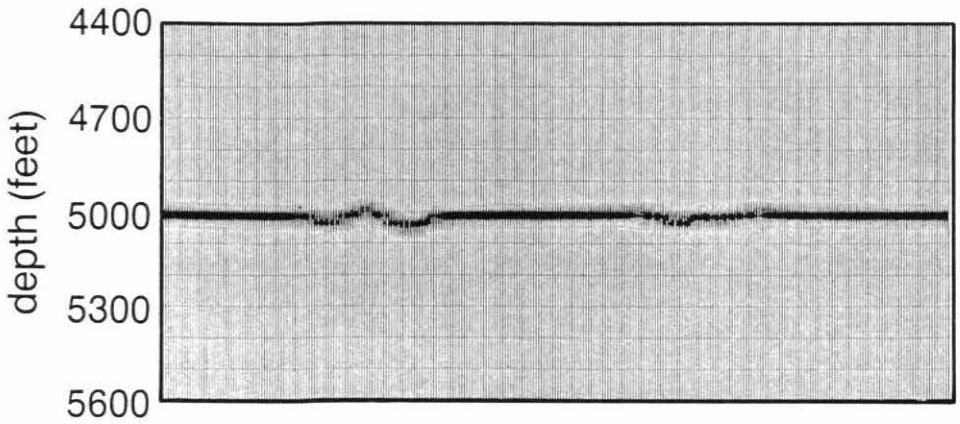

Migration of Model I–1 Time Section Through Velocity Only Inversion I–44a

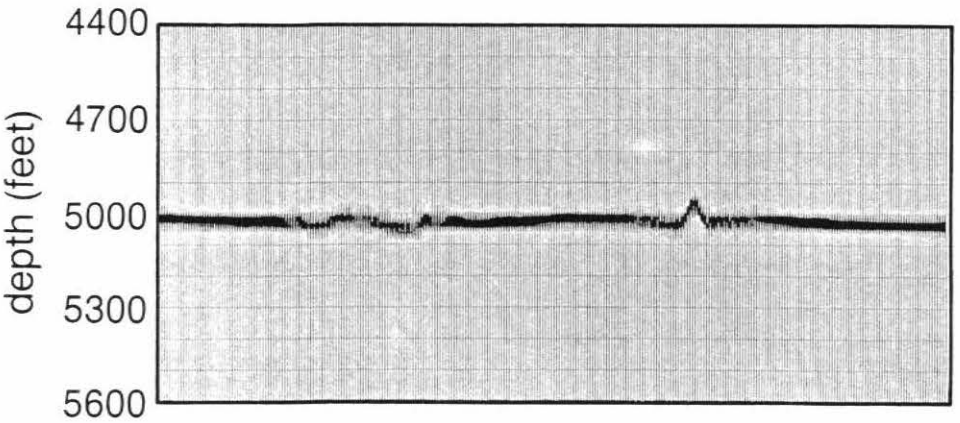

Figure 3.57

K: The difference between the previous two migrations is small.

L: Migration through third velocity only inversion if Figure **3.55e.**

(Figures 3.58 through 3.60 do not exist.)

Change between Migrations: Migration Through Model I–44a minus Migration Through Model I–4a

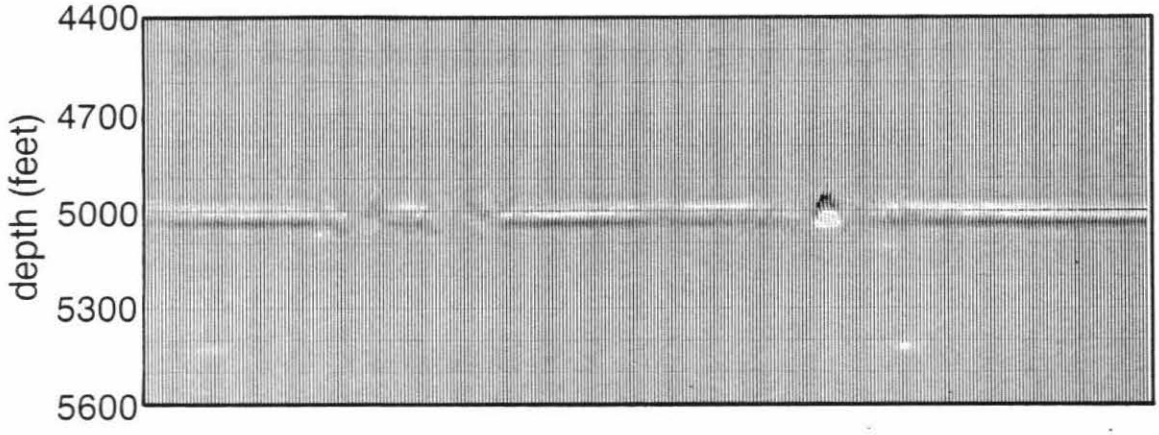

Migration of Model I–1 Time Section Through Velocity Only Inversion I–444a

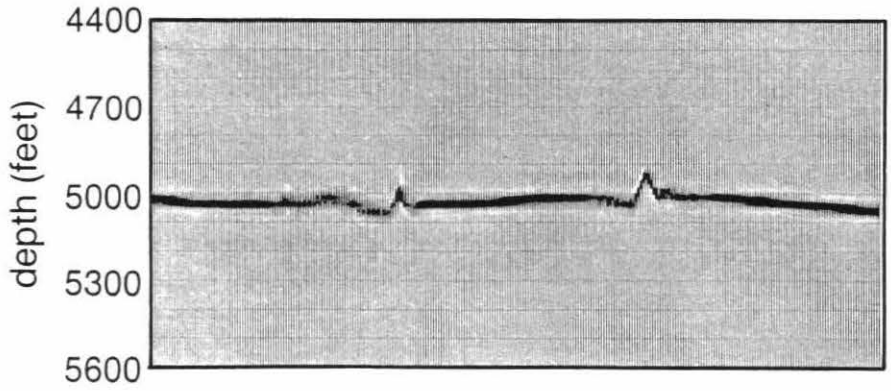

Figure 3.61

Example of the iterative application of tomography and migration using models that have sharp differences between the reflectors only. The two models will be interchanged as true and reference models. The sharp differences seriously affect the ray paths.

A: Model with the three generic sharp reflector structures: bump, trough, and fault. Note vertical exaggeration of the reflector plot. Sample ray paths are shown in figure **3.50**.

B: Density of ray paths for model in previous figure.

C: Plain model for with constant velocity and flat reflector.

Model J-1

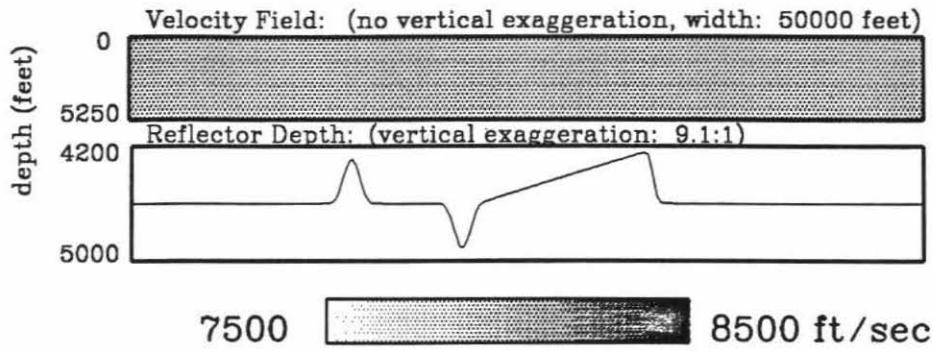

Density of Ray Paths in Model J-1

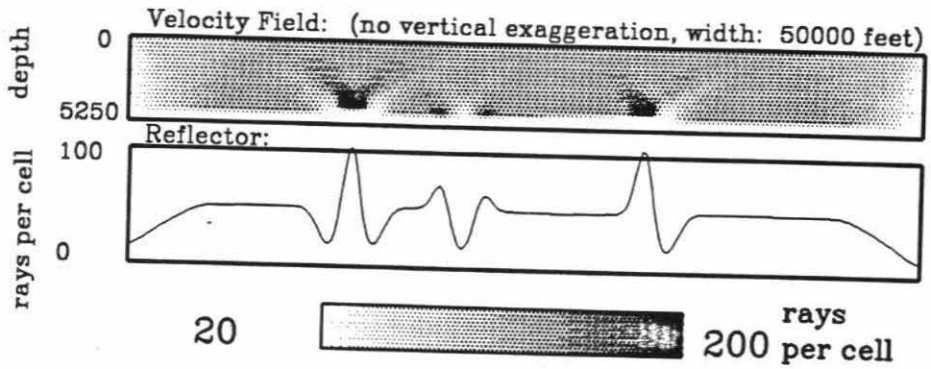

Model J-2

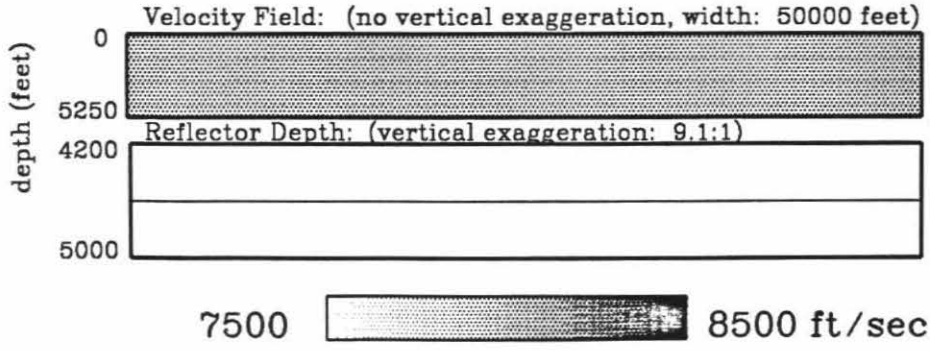

Figure 3.61

D & E: Reflector only inversions of reflector bumps of Figure **3.61a** using plain model of Figure **3.61c** as the reference model. The bumps are widened while the trough is narrowed. Artifacts are only the result of the non-linear effects of the incorrect ray paths of the reference model.

F: Inversion of bump model in Figure **3.61a** using plain model of Figure **3.61c** as the reference model. The general characteristics of the reflector structure are identifiable, but they are contorted.

Reflector only Inversion J-3a of Model J-1 using Model J-2 as the Reference Model, eigenvalue range: (1.0-0.1)

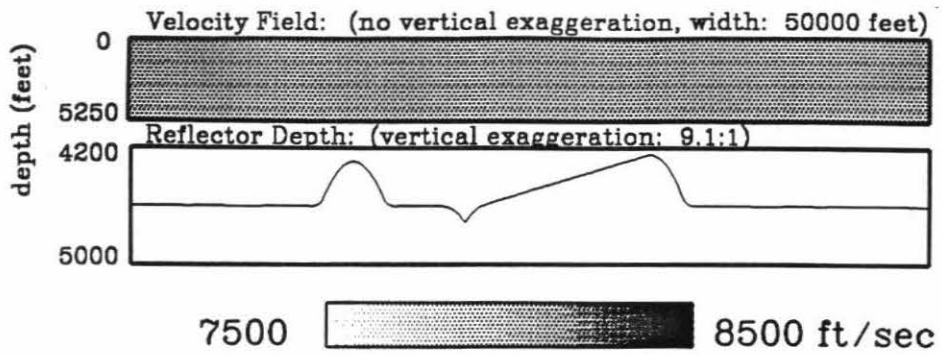

Reflector only Inversion J-3b of Model J-1 using Model J-2 as the Reference Model, eigenvalue range: (1.0-0.02)

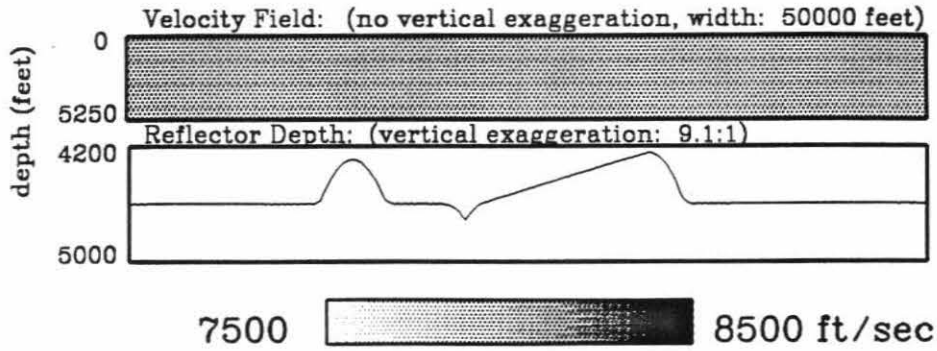

Inversion J-1a of Model J-1 using Model J-2 as the Reference Model, eigenvalue range: (1.0-0.05)

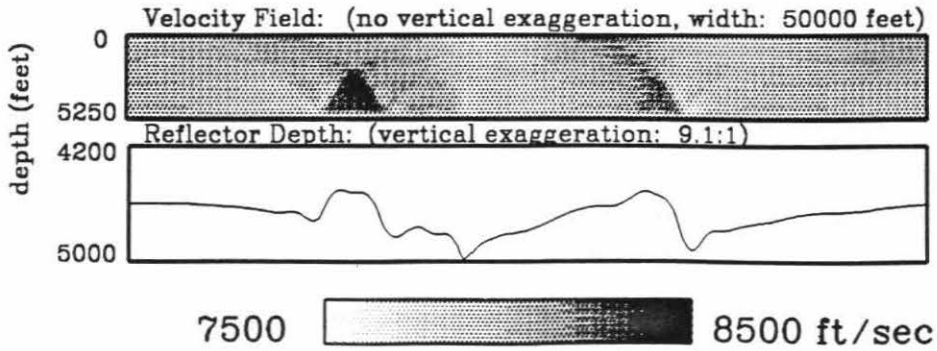

Figure 3.61

G: Previous inversion carried out to smaller eigenvalue. There is no noticeable change.

H: Reference model used for re-ray tracing. Reflector position is picked from migration through velocity field of Figure **G**, shown in Figure **3.63c**. Velocity is the same as Figure **G**.

I: Second inversion of bump model using model in Figure **H** as the reference model. Some small bumps have been introduced on the flanks of the bump and the fault.

Inversion J-1b of Model J-1 using
Model J-2 as the Reference Model, eigenvalue range: (1.0-0.02)

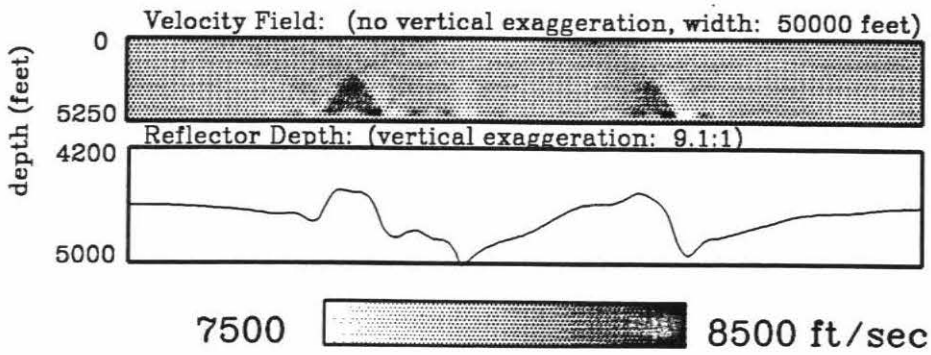

Model J-11: Velocity Field of Inversion J-1b with
Reflector Picked from Migration through the Velocity

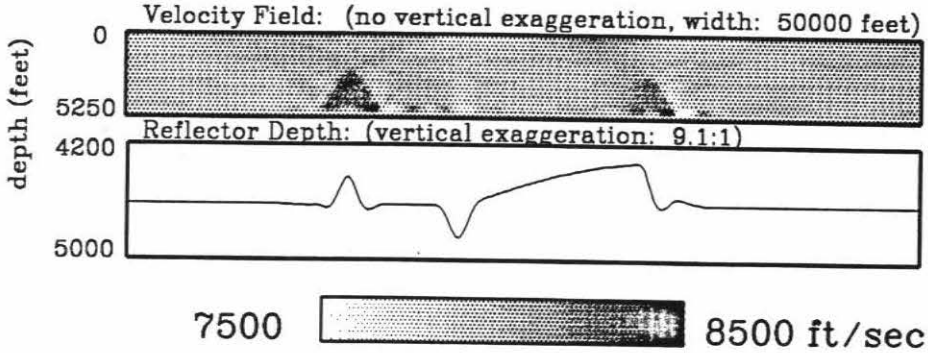

Inversion J-11a of Model J-1 using
Model J-11 as the Reference Model, eigenvalue range: (1.0-0.05)

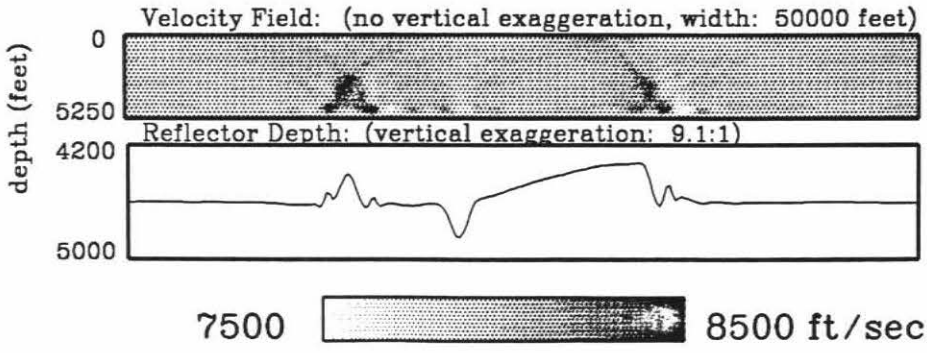

Figure 3.61

J: Previous inversion carried out to smaller eigenvalue. The bumps off the flanks of the bump and fault have increased.

K & L: Inversions of the plain model in Figure **3.61c** using the bump model in Figure **3.61a** as the starting model. The inversion should reduce the bumps and produce a flat reflector. Instead, very unreasonable artifacts have been created that are much larger than the bumps.

Inversion J-11b of Model J-1 using
Model J-11 as the Reference Model, eigenvalue range: (1.0-0.02)

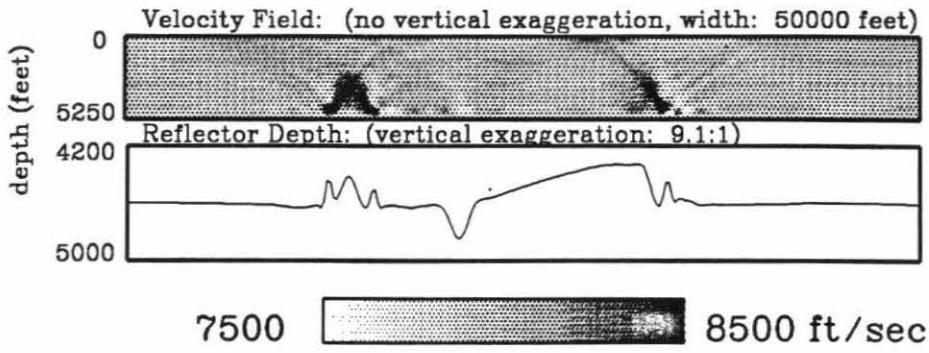

Inversion J-2a of Model J-2 using
Model J-1 as the Reference Model, eignevalue range: (1.0-0.05)

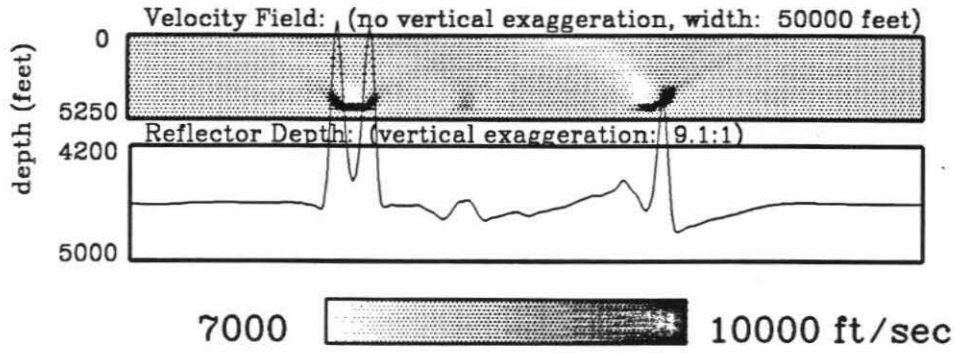

Inversion J-2b of Model J-2 using
Model J-1 as the Reference Model, eigenvalue range: (1.0-0.02)

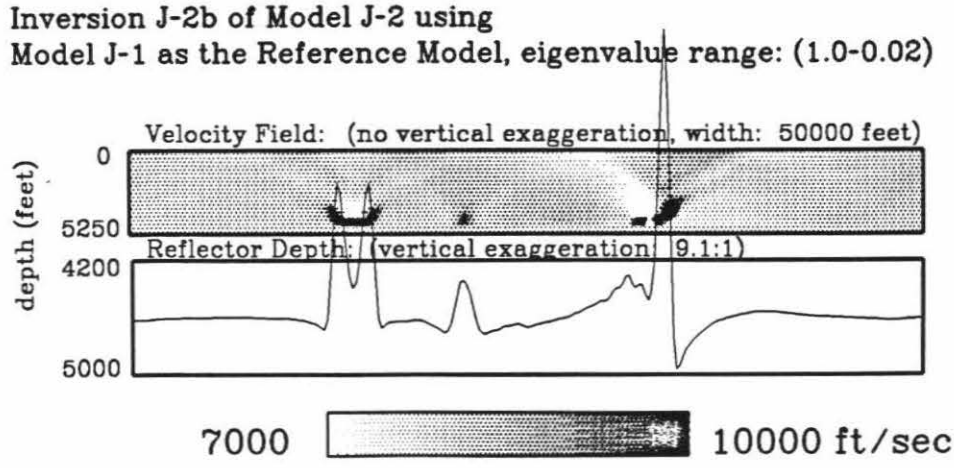

Figure 3.61

M: Reference model used for re-ray tracing. Reflector picked from migration through velocity field of previous inversion, shown in Figure **3.63e**. The reflector position from the migration is smooth and reasonable while the reflector position from the inversion is unstable.

N & O: Second inversion of plain model using previous model as the reference model. The slope leading up to the fault has been removed, but more high frequency artifacts have been introduced.

Model J-22: Velocity Field of Inversion J-2a with Reflector Picked from Migration through the Velocity

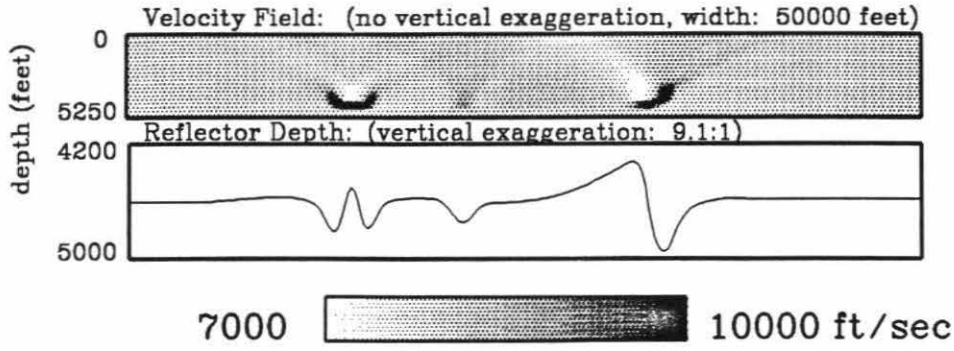

Inversion J-22a of Model J-2 using Model J-22 as the Reference Model, eigenvalue range: (1.0-0.05)

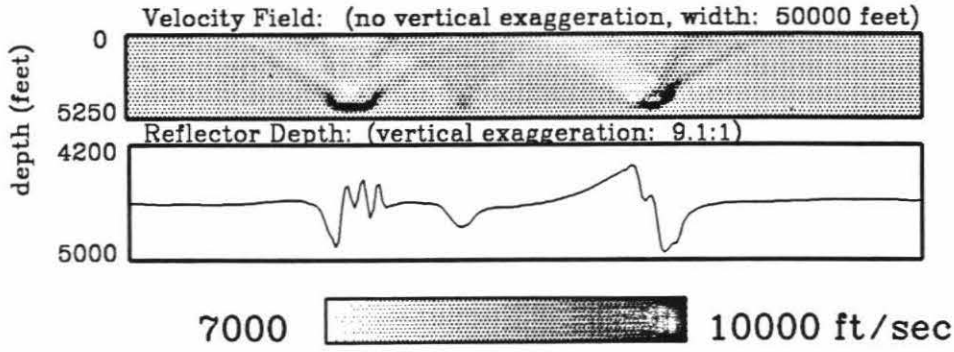

Inversion J-22b of Model J-2 using Model J-22 as the Reference Model, eigenvalue range: (1.0-0.02)

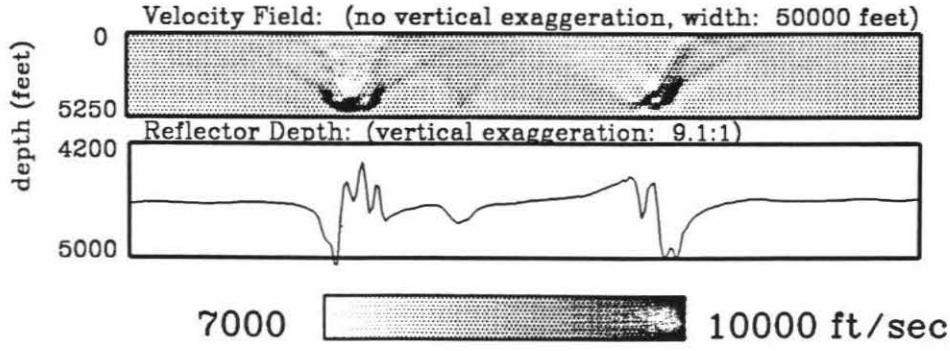

Figure 3.61

P & Q: Constrained inversions of bump model of Figure **3.61a** using plain model in Figure **3.61c** as reference model. Velocity artifacts are much reduced from the corresponding inversion without constraints in Figure **3.61f**. The reflector position is smooth and very similar to the reflector only inversion of Figure **3.61d**.

R: Constrained inversion of plain model using bump model as the reference model. Velocity artifacts are reduced from the corresponding unconstrained inversion in Figure **3.61l**, but the unstable reflector perturbations still exist.

Constrained Inversion J-1c of Model J-1 using Model J-2 as the Reference Model, eigenvalue range: (1.0-0.05)

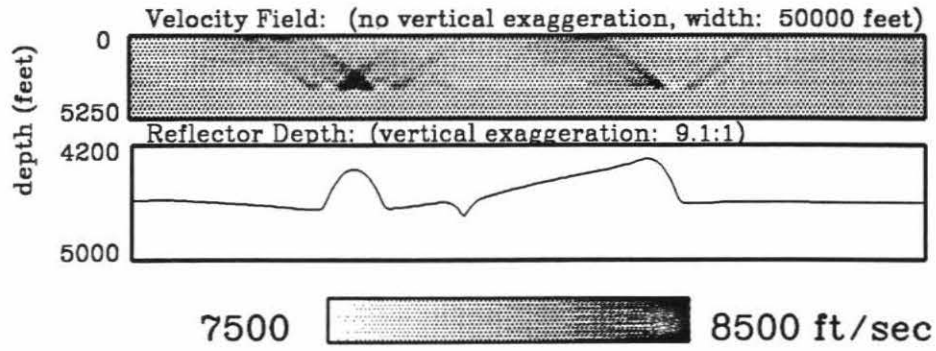

Constrained Inversion J-1d of Model J-1 using Model J-2 as the Reference Model, eigenvalue range: (1.0-0.02)

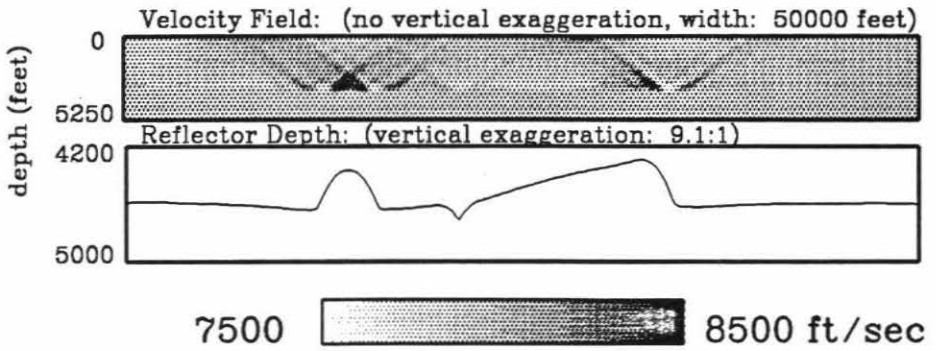

Constrained Inversion J-2c of Model J-2 using Model J-1 as the Reference Model, eignevalue range: (1.0-0.05)

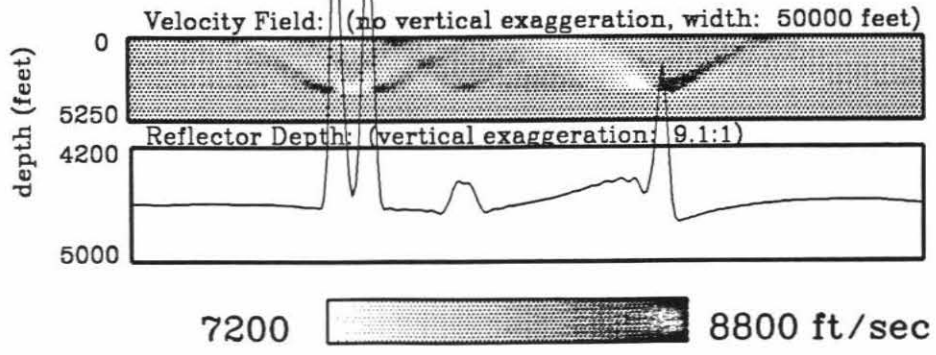

Figure 3.61

S: Previous inversion carried out to smaller eigenvalue.

T: Reflector position picked from migration through velocity field of inversion in Figure **3.61q**, shown in Figure **3.63g**. Reflector is quite accurately inverted.

U: Second inversion of bump model using model of previous figure as the reference model. Artifacts have again cropped up on the flanks of the bump and fault.

Constrained Inversion J-2d of Model J-2 using Model J-1 as the Reference Model, eigenvalue range: (1.0-0.02)

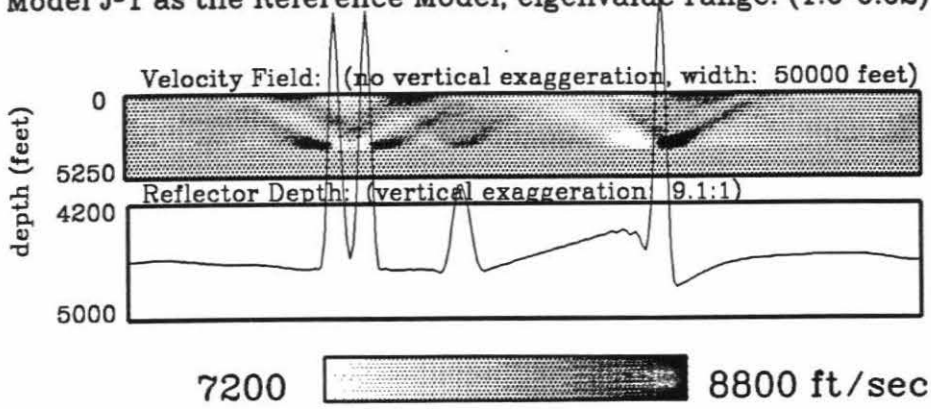

Model J-66: Velocity Field of Inversion J-1d with Reflector Picked from Migration through the Velocity

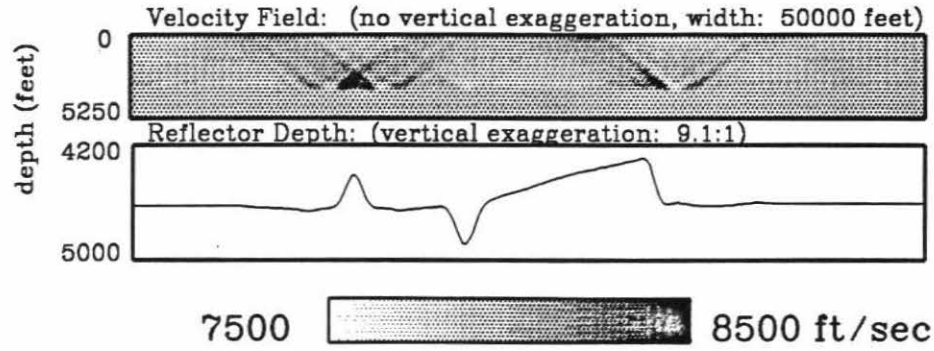

Inversion J-66a of Model J-1 using Model J-66 as the Reference Model, eigenvalue range: (1.0-0.05)

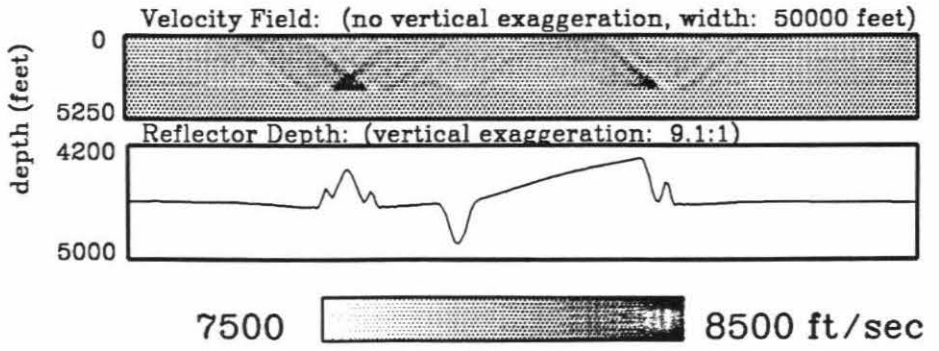

Figure 3.61

V: Previous inversion carried out to smaller eigenvalue.

W: Reflector picked from migration through velocity field of inversion in Figure **3.61r**. Migration is shown in Figure **3.63i**. This reflector position from the migration is very different from the unstable reflector position from the inversion. The bump is lower and the fault has been smoothed. The image is approaching the correct flat reflector.

X: Inversion of plain model using model of previous figure as the reference model. Inversion has improved markedly, with the bump on the left side and the slope leading to the fault reduced in height. This is the first inversion of the plain model that has produced a stable reflector position.

Inversion J-66b of Model J-1 using
Model J-66 as the Reference Model, eigenvalue range: (1.0-0.02)

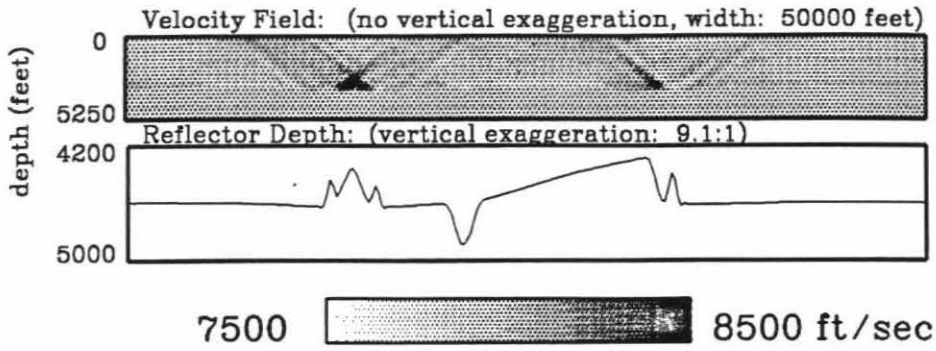

Model J-77: Velocity Field of Inversion J-2d with
Reflector Picked from Migration through the Velocity

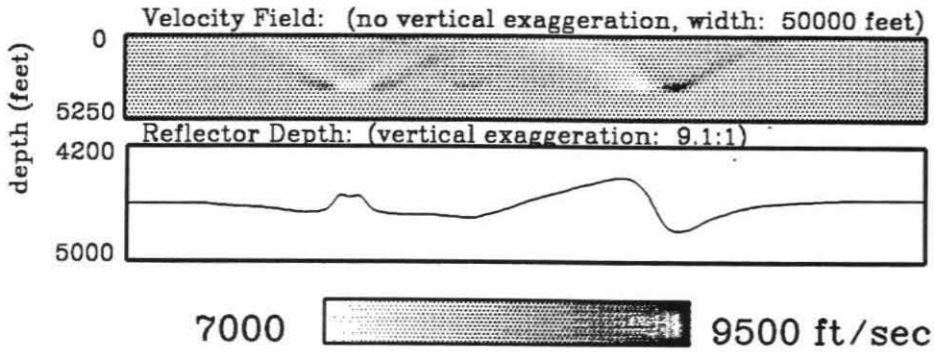

Inversion J-77a of Model J-2 using
Model J-77 as the Reference Model, eigenvalue range: (1.0-0.05)

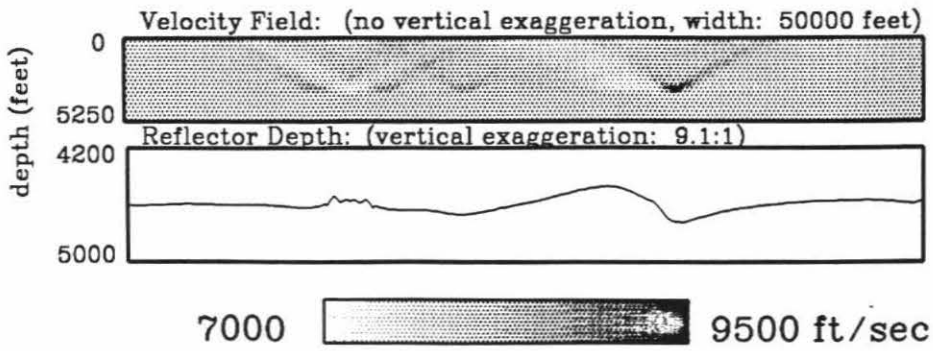

Figure 3.61

Y: Previous inversion carried out to smaller eigenvalue. The reflector position has improved further.

Figure 3.62

Tests of the iterative application of migration and tomographic inversion for velocity only.

A: Velocity only inversion of bump model in Figure **3.61a** using the plain model of Figure **3.61c** as the reference model. Serious velocity artifacts have been recreated.

B: Reflector picked from migration in Figure **3.64a** through velocity field of previous inversion. While the reflector is generally flat, the small scale features of the reflector have been inverted.

Inversion J-77b of Model J-2 using
Model J-77 as the Reference Model, eigenvalue range: (1.0-0.02)

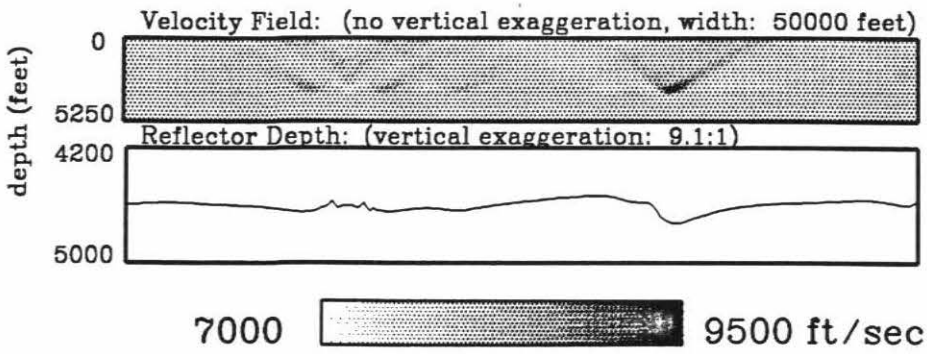

Velocity only Inversion J-4a of Model J-1 using
Model J-2 as the Reference Model, eigenvalue range: (1.0-0.05)

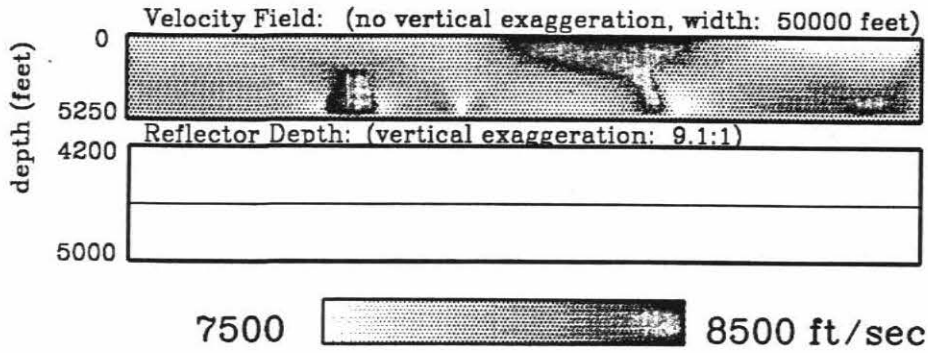

Model J-44: Velocity Field of Inversion J-4a with
Reflector Picked from Migration through the Velocity

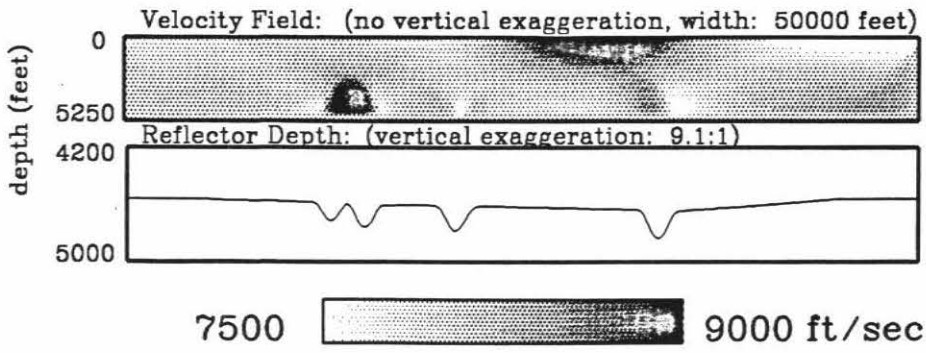

Figure 3.62

C: Second velocity only inversion using model of previous figure as the reference model. The velocity artifacts have changed character.

D: Reflector picked from migration in Figure **3.64b** through velocity field of previous inversion. Some reflector artifacts have been created that do not correspond to any correct reflector structure. None of the broad reflector features have been improved.

E: Third velocity only inversion using model in previous inversion as the reference model. Incorrect high frequency velocity artifacts have been introduced.

Velocity only Inversion J-44a of Model J-1 using Model J-44 as the Reference Model, eigenvalue range: (1.0-0.05)

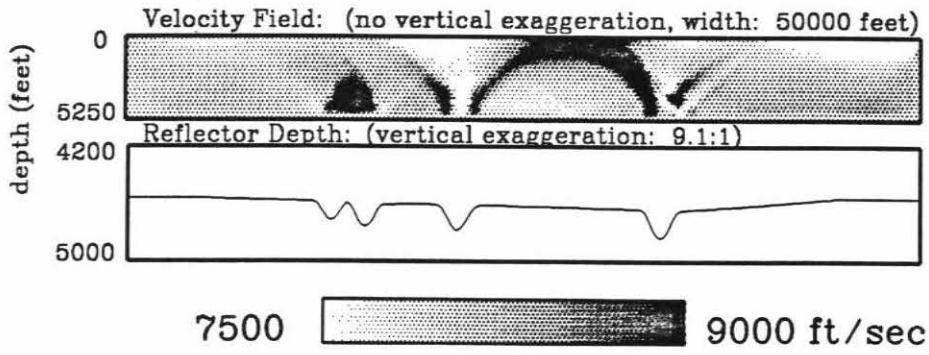

Model J-444: Velocity Field of Inversion J-44a with Reflector Picked from Migration through the Velocity

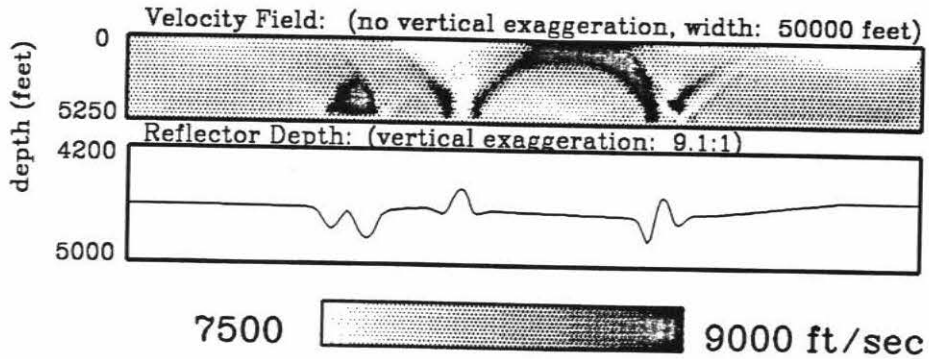

Velocity only Inversion J-444a of Model J-1 using Model J-444 as the Reference Model, eigenvalue range: (1.0-0.05)

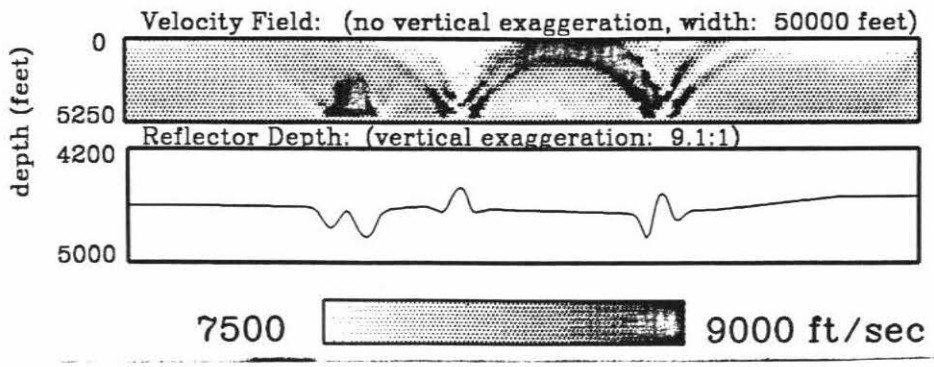

Figure 3.63

A: Zero offset time section from bump model of Figure **3.61a**.

B: Migration of zero offset time section from bump model through correct constant velocity. The correct reflector structure has been reproduced.

Zero Offset Time Section of Model J–1

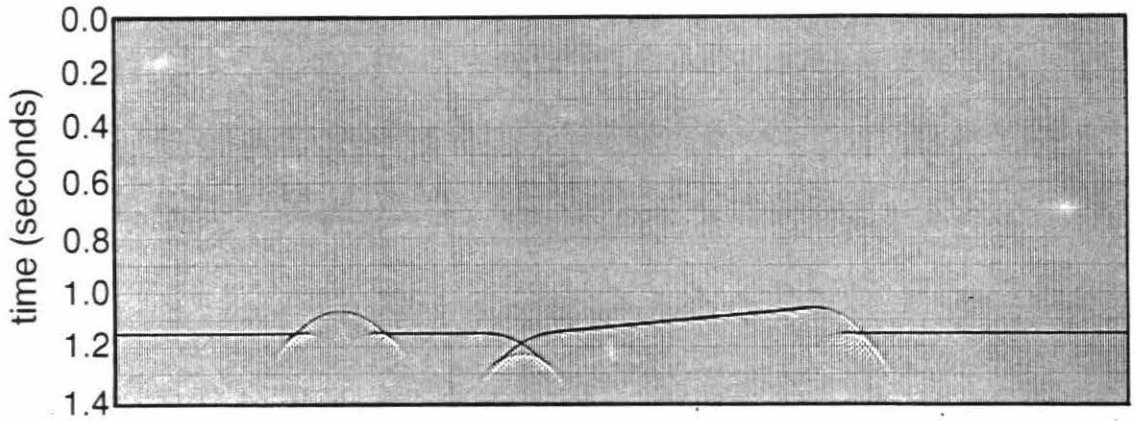

Migration of Model J–1 Time Section Through the Correct, Constant Velocity

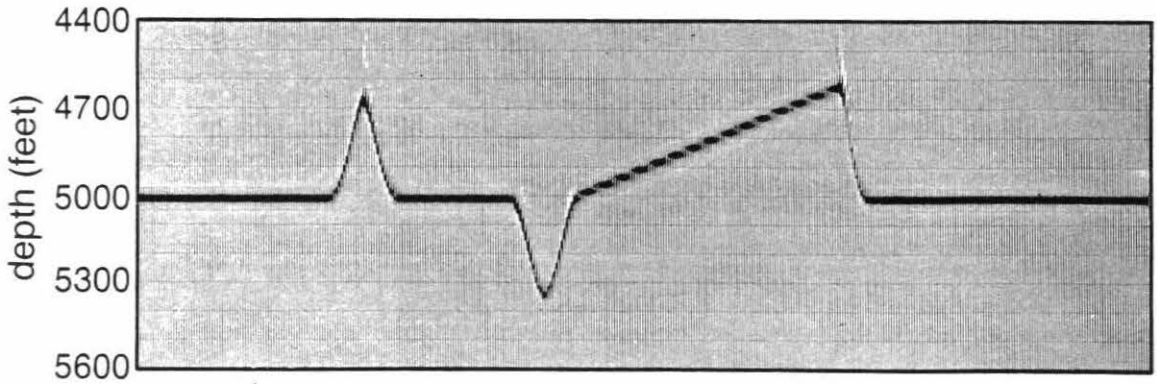

Figure 3.63

C: Migration of bump model data through velocity field of inversion of Figure **3.61f**. Much of the reflector position has been recreated.

D: Migration of bump model data through second inversion in Figure **3.61i**. Result is worse than migration through first inversion in the previous figure.

Migration of Model J–1 Time Section Through Inversion J–1b

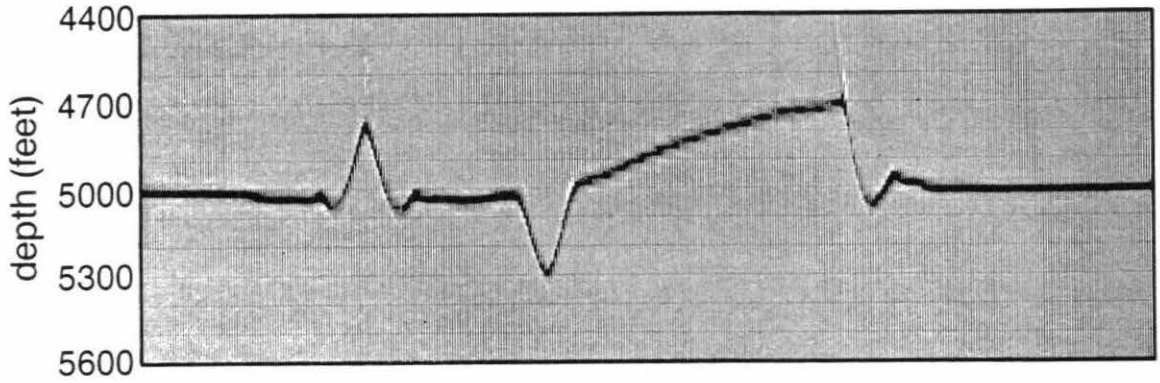

Migration of Model J–1 Time Section Through Inversion J–11b

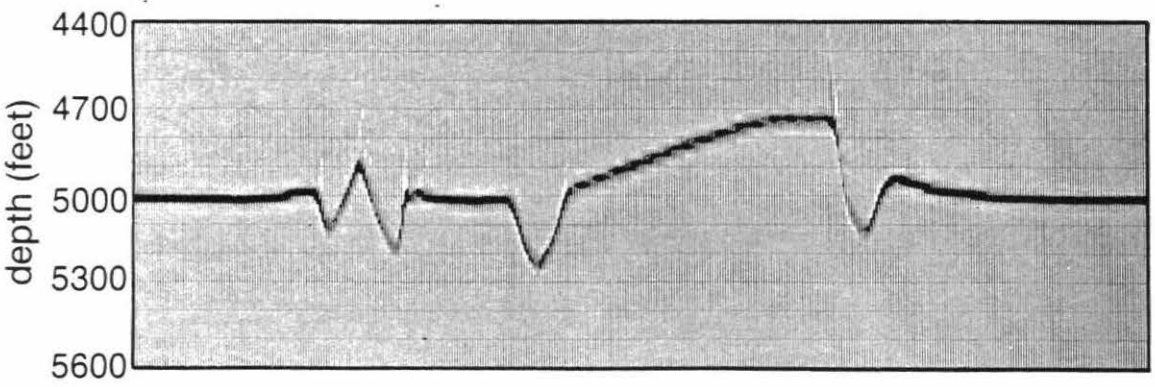

Figure 3.63

E: Migration of plain model data through velocity field of inversion in Figure **3.61k**. The correct result would be a flat reflector. While figure is far from flat, it does not have the instabilities of the reflector position from the inversion.

F: Migration of plain model data through second inversion in Figure **3.61n**. The migration is badly blurred and worse than the one in the previous figure.

Migration of Model J–2 Time Section Through Inversion J–2a

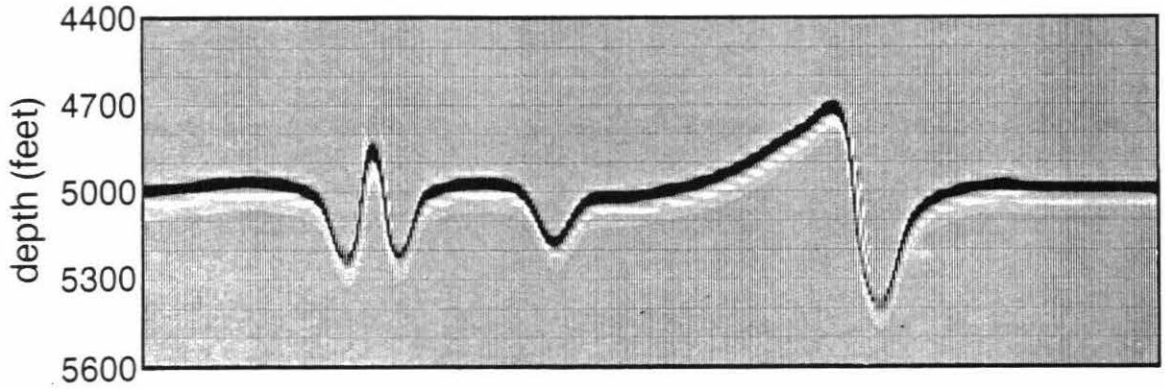

Migration of Model J–2 Time Section Through Inversion J–22b

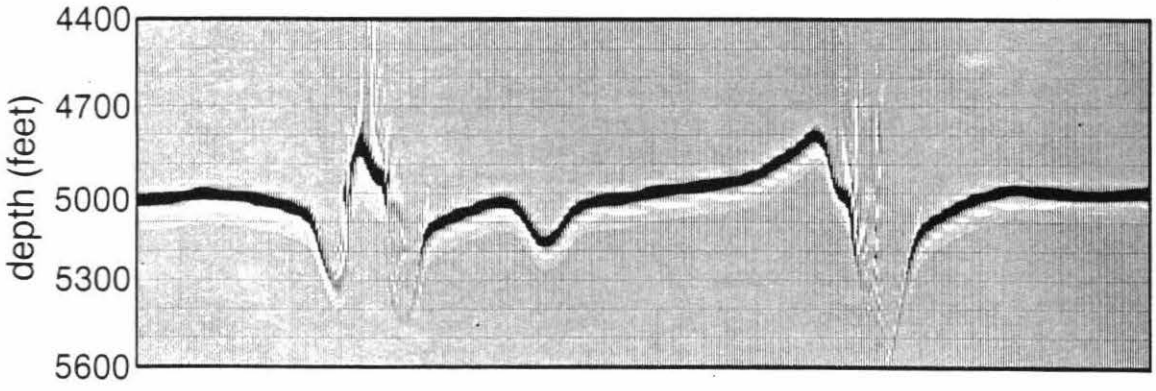

Figure 3.63

G: Migration of bump data through velocity field of constrained inversion in Figure **3.61p**. Result is quite accurate. Many of the artifacts of the reflector position in the inversion no longer exist.

H: Migration of bump data through second constrained inversion if Figure **3.61u**. Result is improved over that in the previous figure.

Migration of Model J–1 Time Section Through Constrained Inversion J–1d

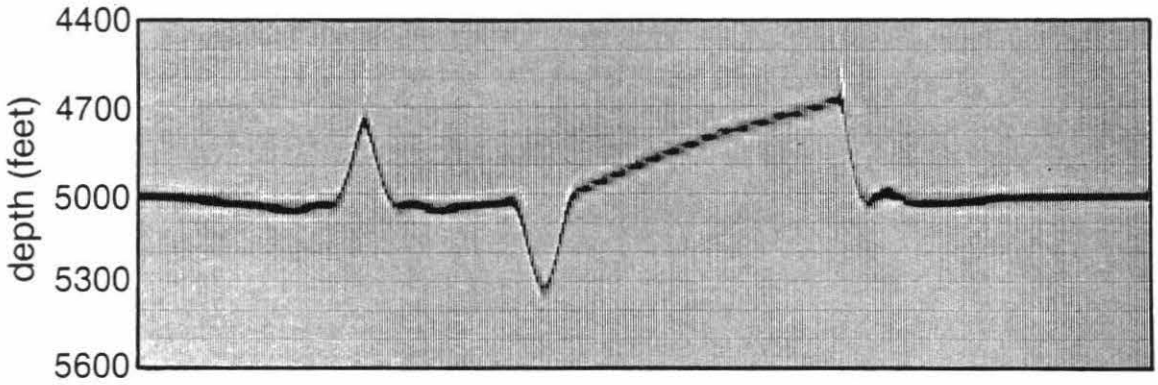

Migration of Model J–1 Time Section Through Constrained Inversion J–66b

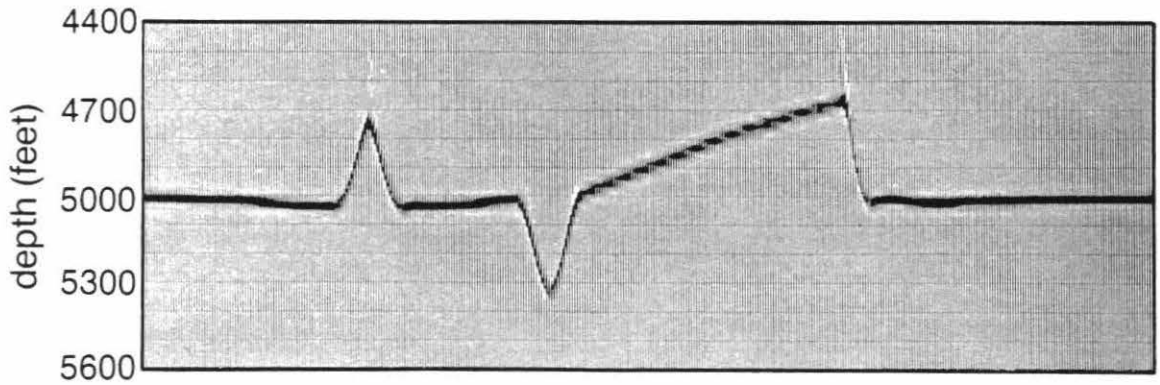

Figure 3.63

I: Migration of plain model data through constrained inversion in Figure **3.61r**. The result is a reasonable, stable, reflector position that is closer to the true flat reflector than that from the reference model. Note that the reflector position in the unconstrained inversion of Figure **3.61k** was unstable.

J: Migration of plain model data through second constrained inversion in Figure **3.61x**. The result is an improvement over the previous migrations. In this case, the reflector position from the migration is similar to that in the inversion.

Migration of Model J–2 Time Section Through Constrained Inversion J–2d

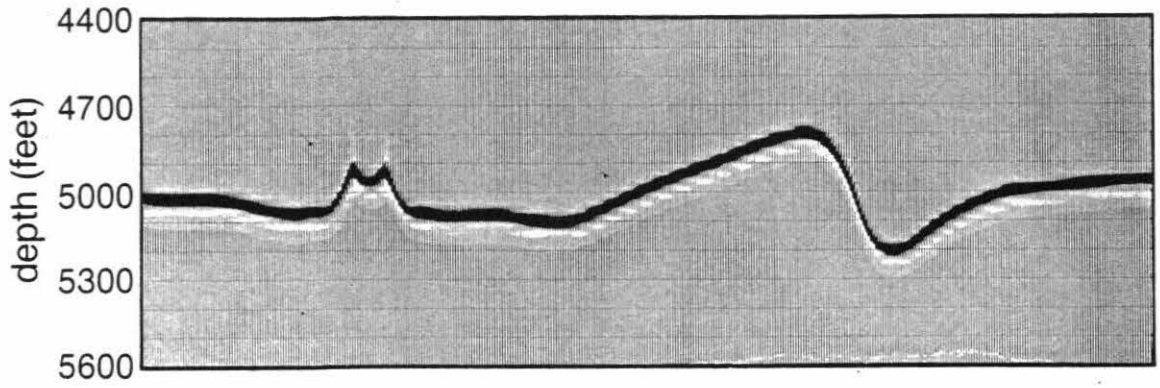

Migration of Model J–2 Time Section Through Constrained Inversion J–77b

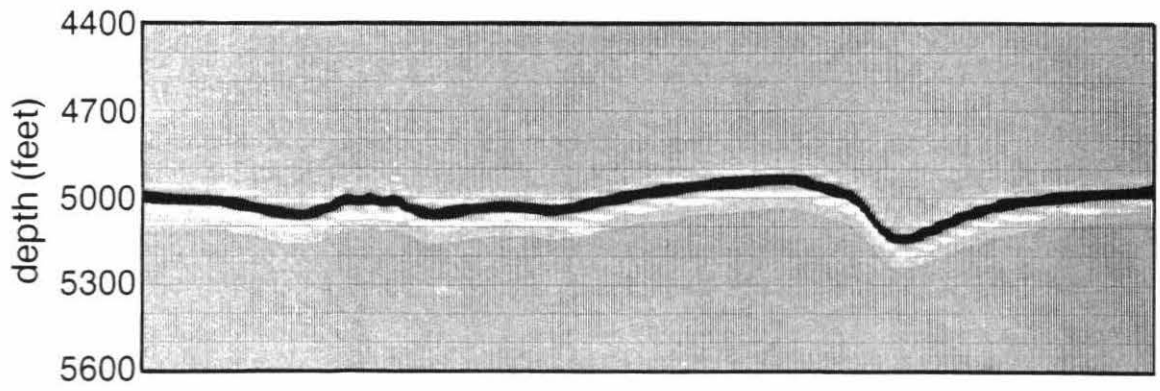

Figure 3.64

A: Migration of bump model data through the velocity only inversion of Figure **3.62a**. Result is similar to the flat reflector of the reference model but the small scale structure of the true reflector has been accurately inverted.

B: Migration of bump data through second velocity only inversion of Figure **3.62c**. Result is considerable worse than the first inversion in the previous figure.

Migration of Model J–1 Time Section Through Velocity Only Inversion J–4a

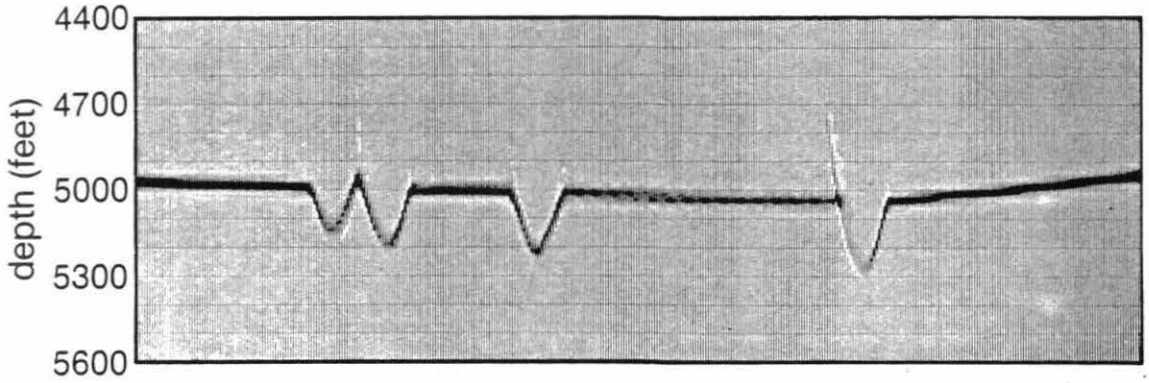

Migration of Model J–1 Time Section Through Velocity Only Inversion J–44a

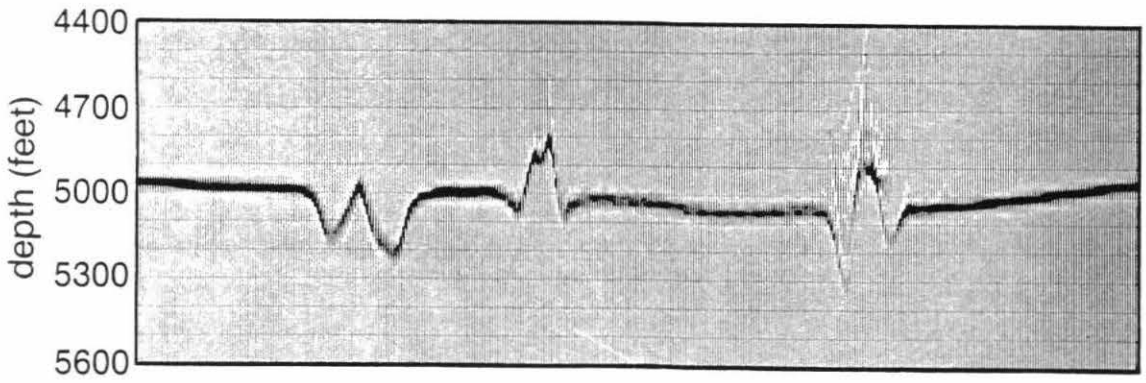

Figure 3.64

C: Migration of bump data through third velocity only inversion of Figure **3.62e**. Result has not improved.

Migration of Model J–1 Time Section Through Velocity Only Inversion J–444a

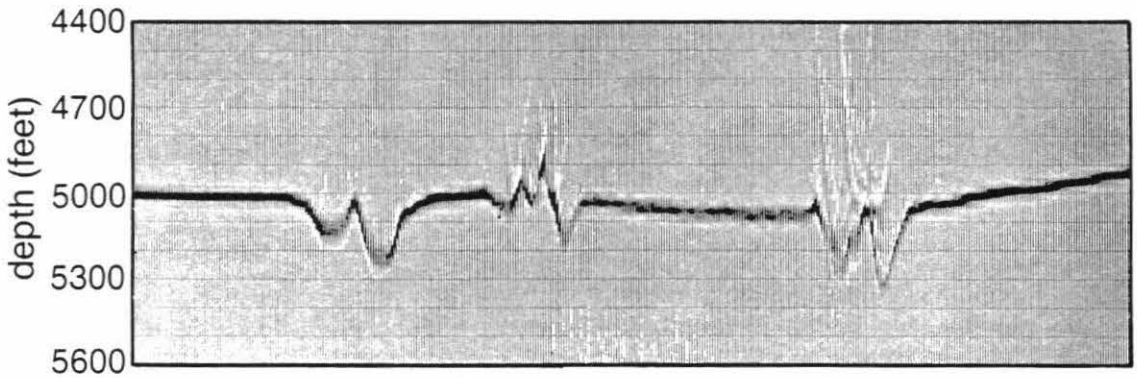

Figure 3.65

Modeling the effect of an incorrect velocity field on pre-stack migration.

A: Model with velocity variations used for pre-stack data collection. The model consists of a low velocity surface layer and vertical velocity channels. The lower 2/3rds of the model has an average velocity of 6500 ft/sec with velocity variations of +/-200 ft/sec. A flat reflector exists at the bottom of the model. The modeling was performed using a 4th order, full wave equation, finite difference scheme of Vidale (1986). The model is periodic to reduce number of modeling runs needed.

Velocity Field Used for Forward Modeling

(no distortion)

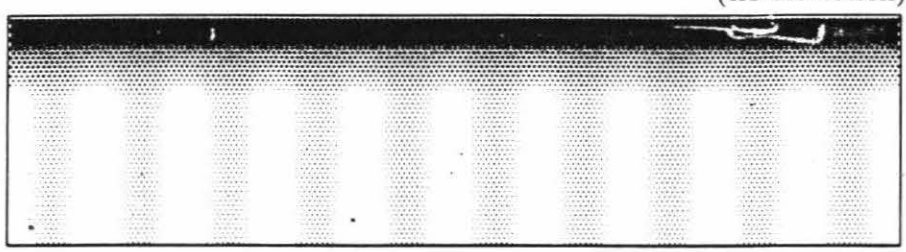

3800 feet

Figure 3.65

B: Shot gather of reflected arrivals over a high velocity channel. First arrival is a low amplitude wave through the high velocity channel followed by a stronger arrival through the low velocity channel. Direct arrivals were removed by subtracting out the data from an identical model without the reflector.

C: Shot gather of reflected arrivals over a low velocity channel.

Shot Gather over High Velocity Channel

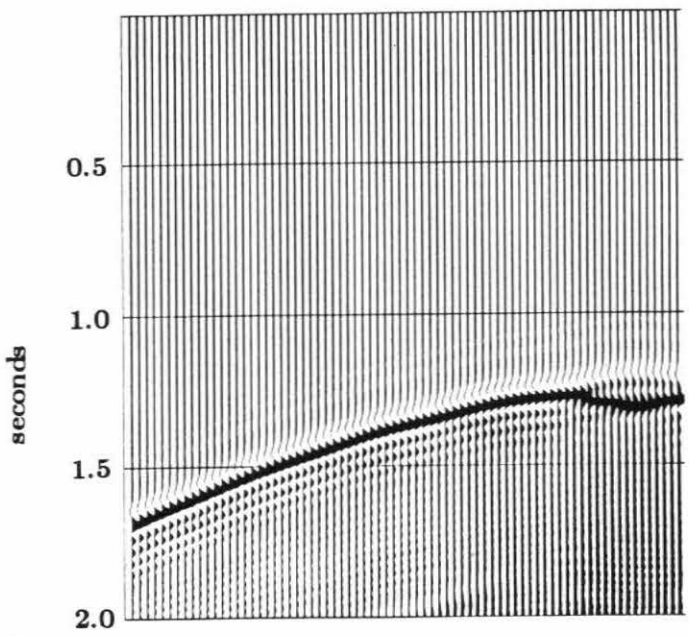

Shot Gather over Low Velocity Channel

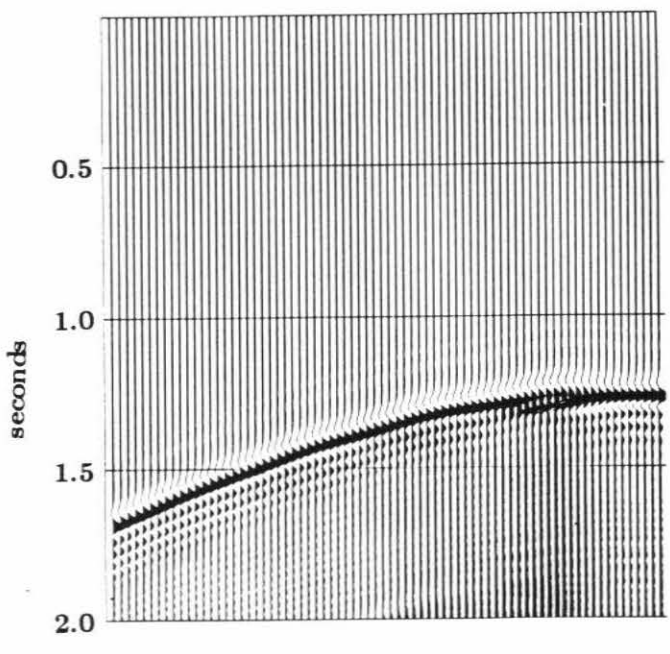

Figure 3.65

D: Zero offset time section from model in figure **3.65a**.

E: Post-stack migration of zero offset data through correct velocity model. The amplitude of the reflector varies because the velocity contrast varies with the velocity channels.

Zero offset section

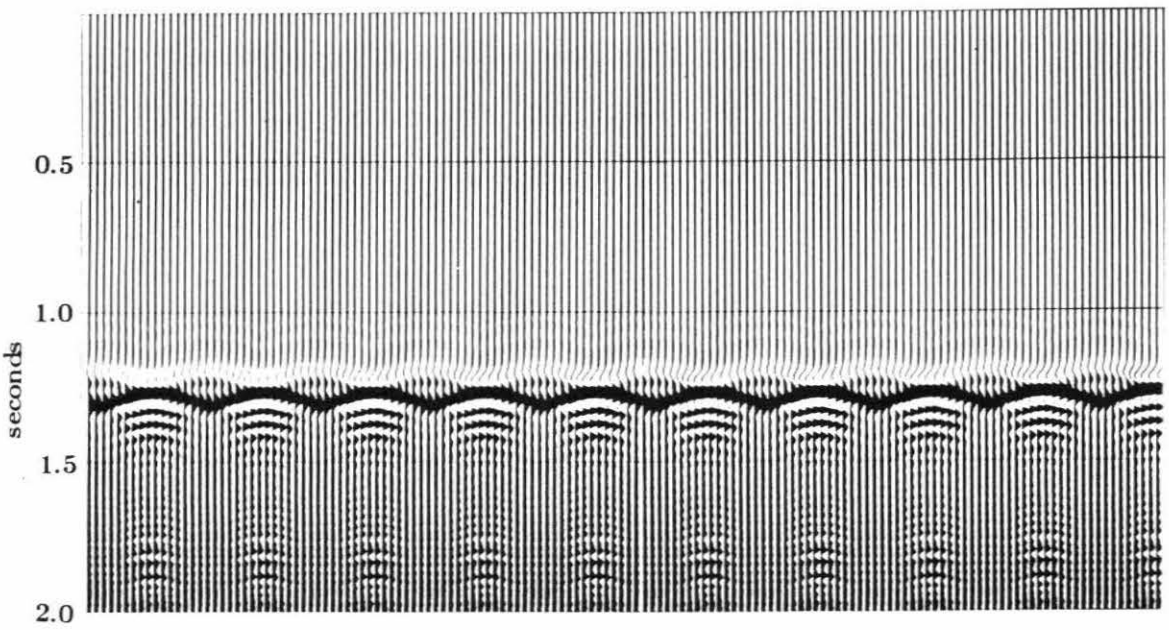

Zero Offset Migration Through Correct Velocity

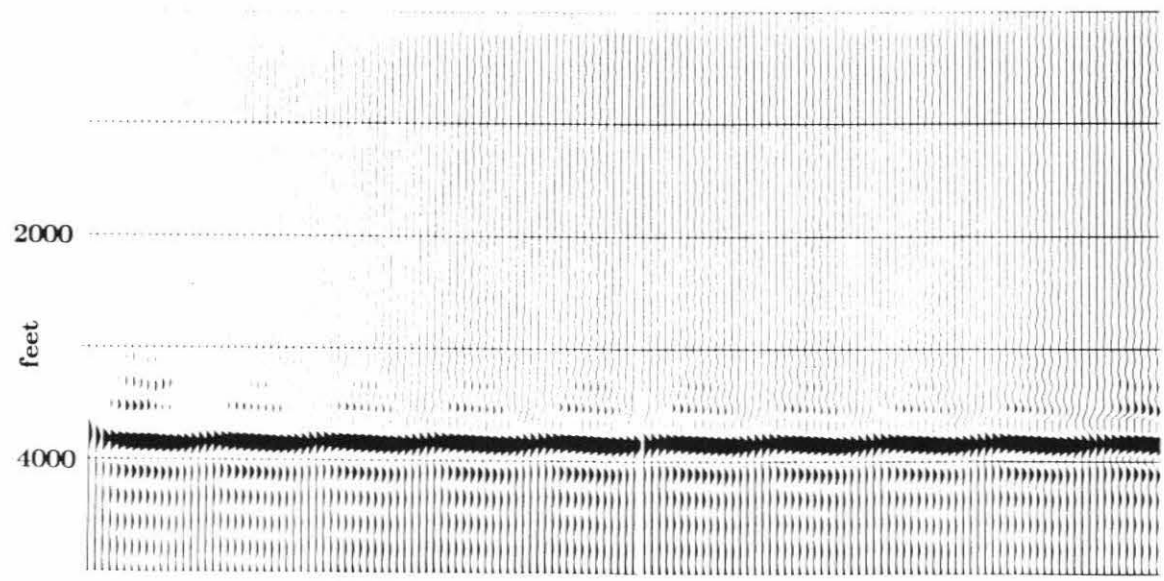

Figure 3.65

F: Pre-stack migration of data through correct velocity model. Migration method used is 45o finite difference, frequency domain algorithm. The program works.

Prestack Migration Through Correct Velocity

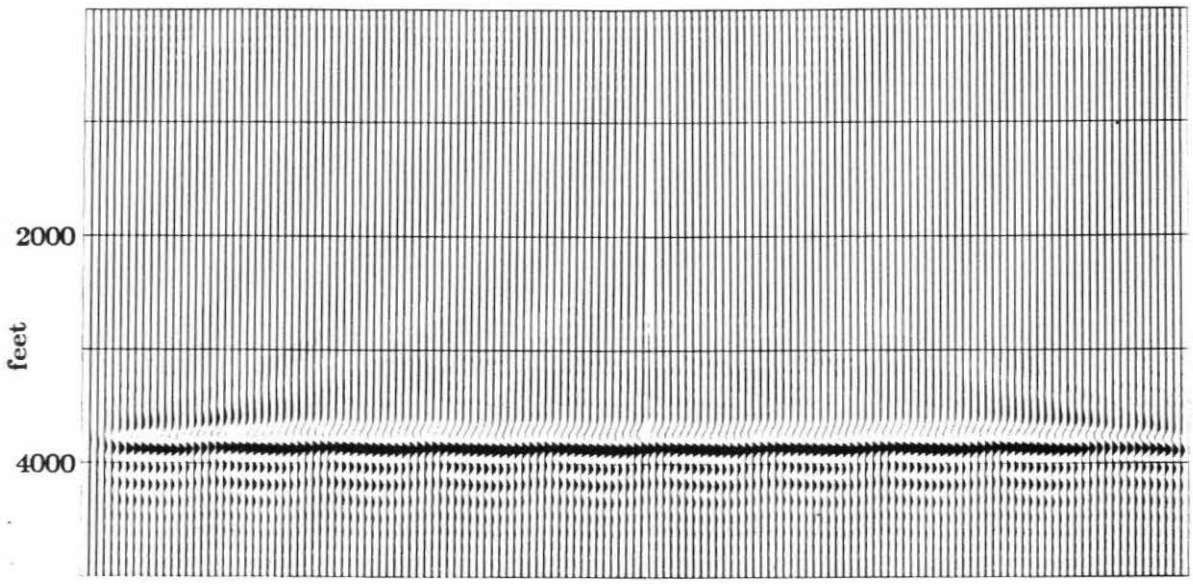

Figure 3.65

G: Model with incorrect velocity used for migration. The vertical gradient represents the horizontal averaging of the original model used for data collection.

False Velocity Field Used for Migration

(no distortion)

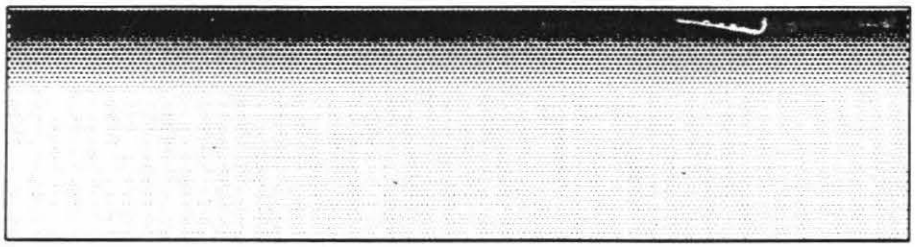

3800 feet

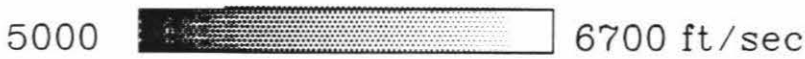

Figure 3.65

H: Post-stack migration of zero offset data through false velocity model of previous figure. The missing velocity variations of the migration model have manifested themselves as reflector variations. No artifacts exist that suggest an incorrect velocity field was used.

I: Pre-stack migration through false velocity of Figure **3.65g**. Reflector is closer to the correct flat reflector than the post-stack migration of the previous figure. Pre-stack migration appears less sensitive to velocity errors than post-stack migration.

Zero Offset Migration Through False Velocity

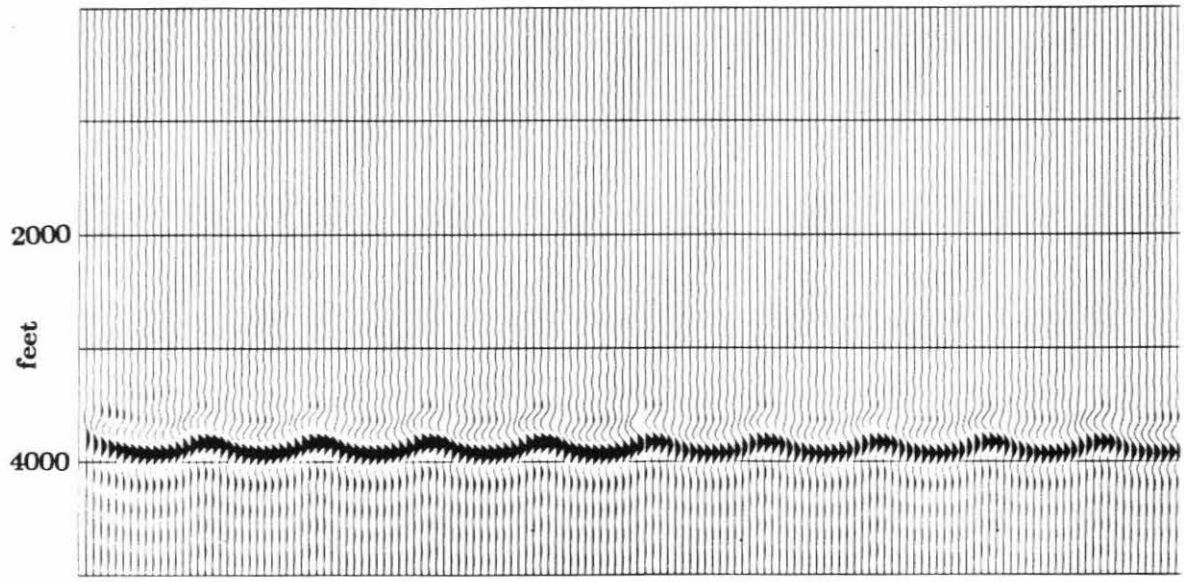

Prestack Migration Through False Velocity

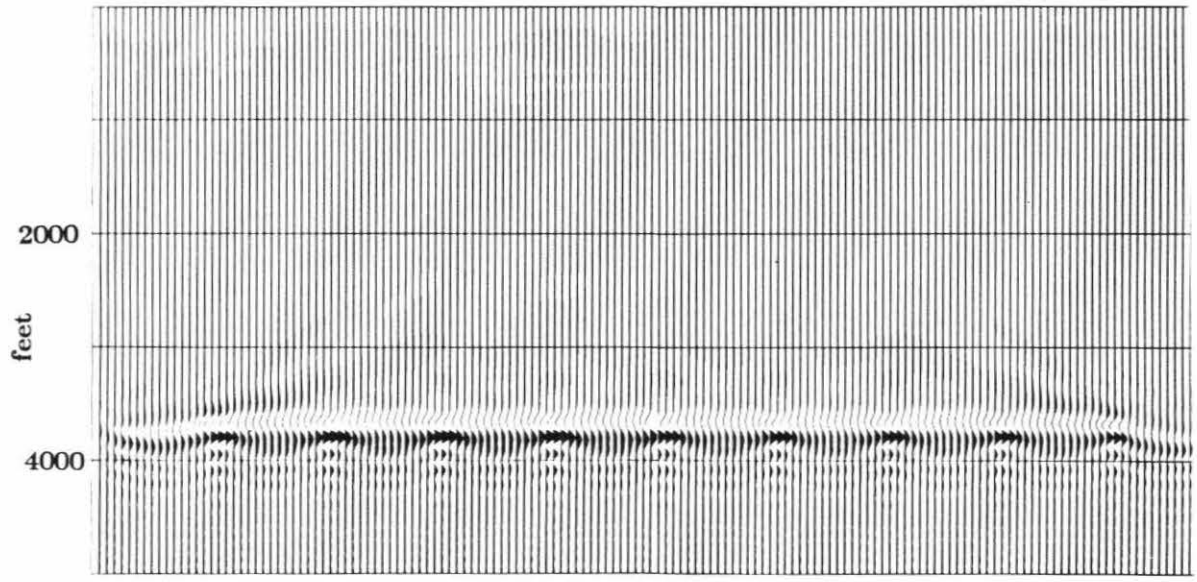

Figure 3.66

A: Model with a sharp velocity contrast used for pre-stack data collection. The data will be migrated through a constant velocity.

Model used for Prestack Data Collection

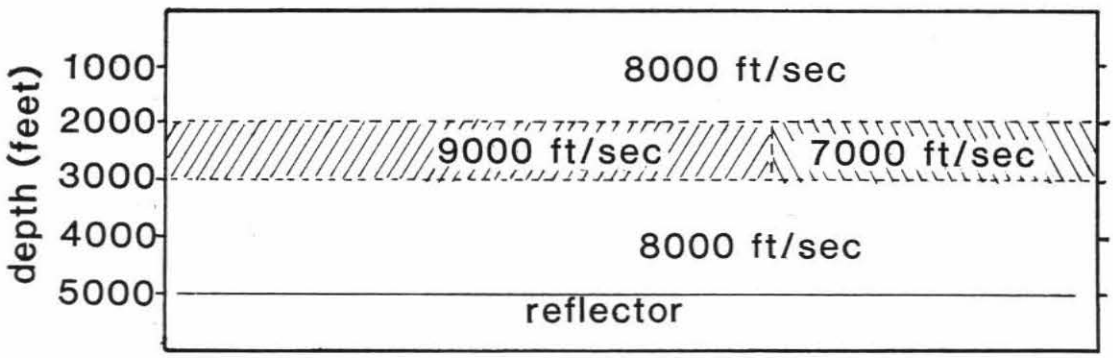

Figure 3.66

B: Pre-stack migration through correct velocity model. Flat reflector is accurately recreated. Low amplitude reflections off of the velocity variations are visible.

C: Pre-stack migration through constant velocity field of 8000 ft/sec. The reflector has been separated into three distinct units: the left side where both the down and up propagation path are in the fast velocity region, the center where the down and up paths are in opposite velocity regions, and the right side where both paths are in the slow velocity variations. Comparing this result with the post-stack migration result in a similar case in Figure **3.76d** suggests that pre-stack migration is less sensitive to velocity errors than post-stack migration.

D: A low pass filter of the pre-stack migration of the previous figure blurs the three segments into one producing a smooth reflector with a gradual transition. The high frequency aspects of the reflector position have been resolved.

Prestack Migration through Correct Velocity Model

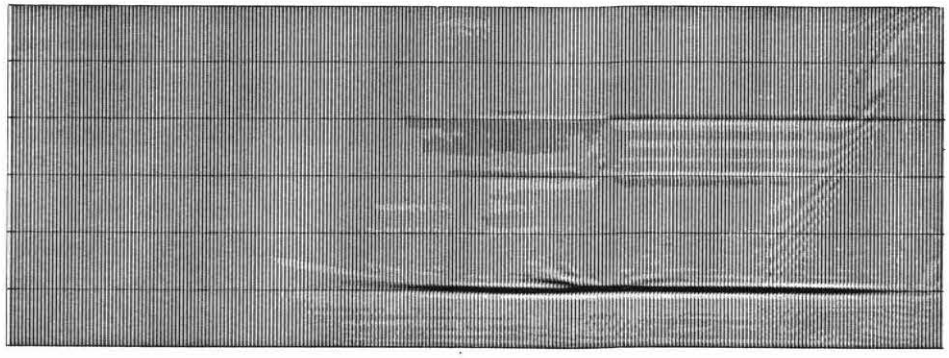

Prestack Migration through Constant Velocity

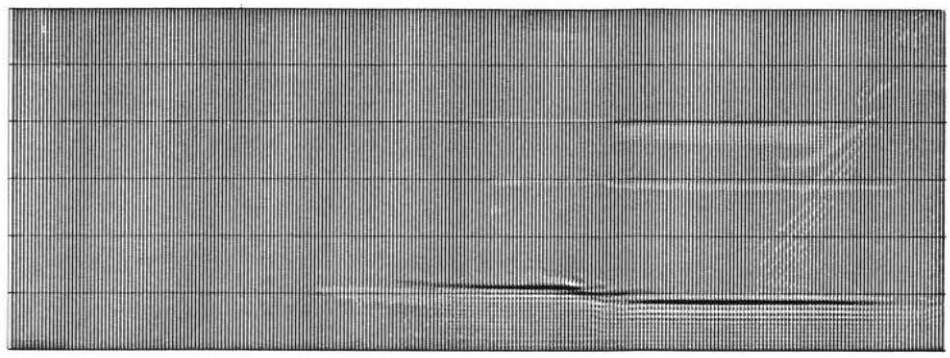

Prestack Migration through Constant Velocity (low frequencies)

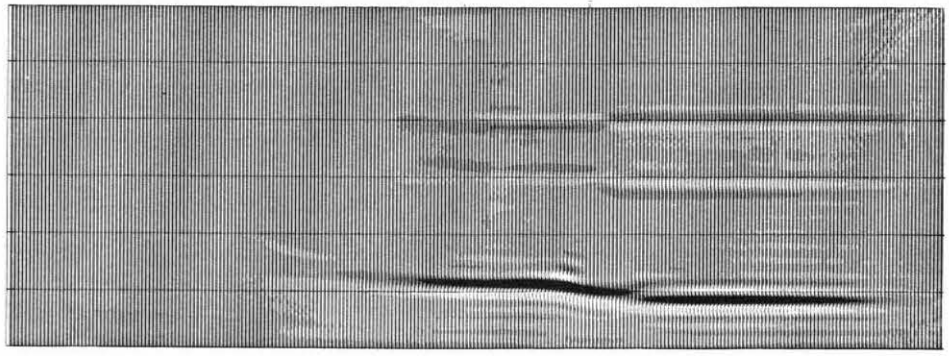

Figure 3.67

True and reference model used for analysis of edge effects.

A: True model used for data collection. Velocity variations are +/-150 ft/sec; the reflector is flat.

B: Reference model used for ray tracing for the inversions. The reflector position is determined by migrating the data from the true model through the constant velocity. Thus, the velocity variations have been manifested as reflector variations. The vertical two-way travel time for the reference model is consistent with the true model in previous figure. The data and migration are shown in the following figures.

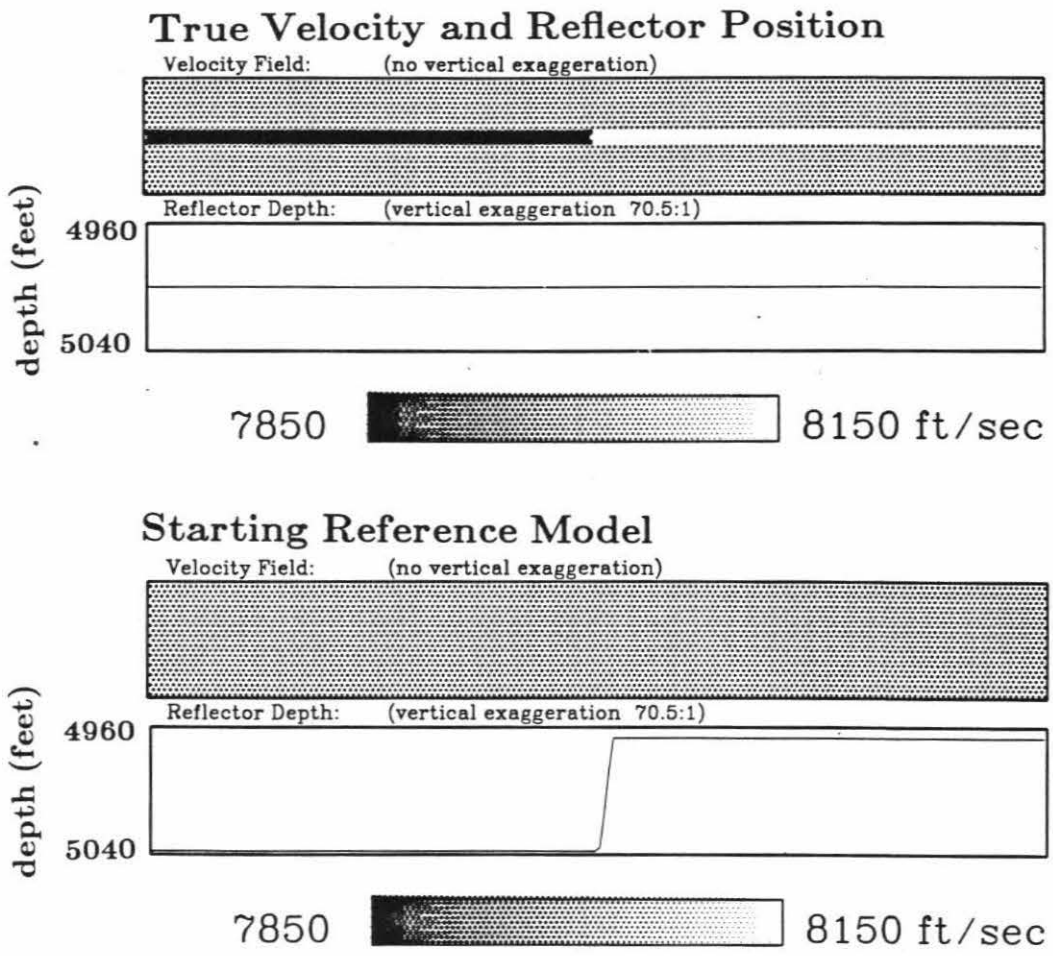
True Velocity and Reflector Position
Velocity Field: (no vertical exaggeration)
Reflector Depth: (vertical exaggeration 70.5:1)
depth (feet)
4960
5040
7850
8150 ft/sec
Starting Reference Model
Velocity Field: (no vertical exaggeration)
Reflector Depth: (vertical exaggeration 70.5:1)
depth (feet)
4960
5040
7850
8150 ft/sec

Figure 3.67

C: Zero offset data from true model.

D: Migration of zero offset data through constant velocity reference model. Reflector of reference model was picked from this migration.

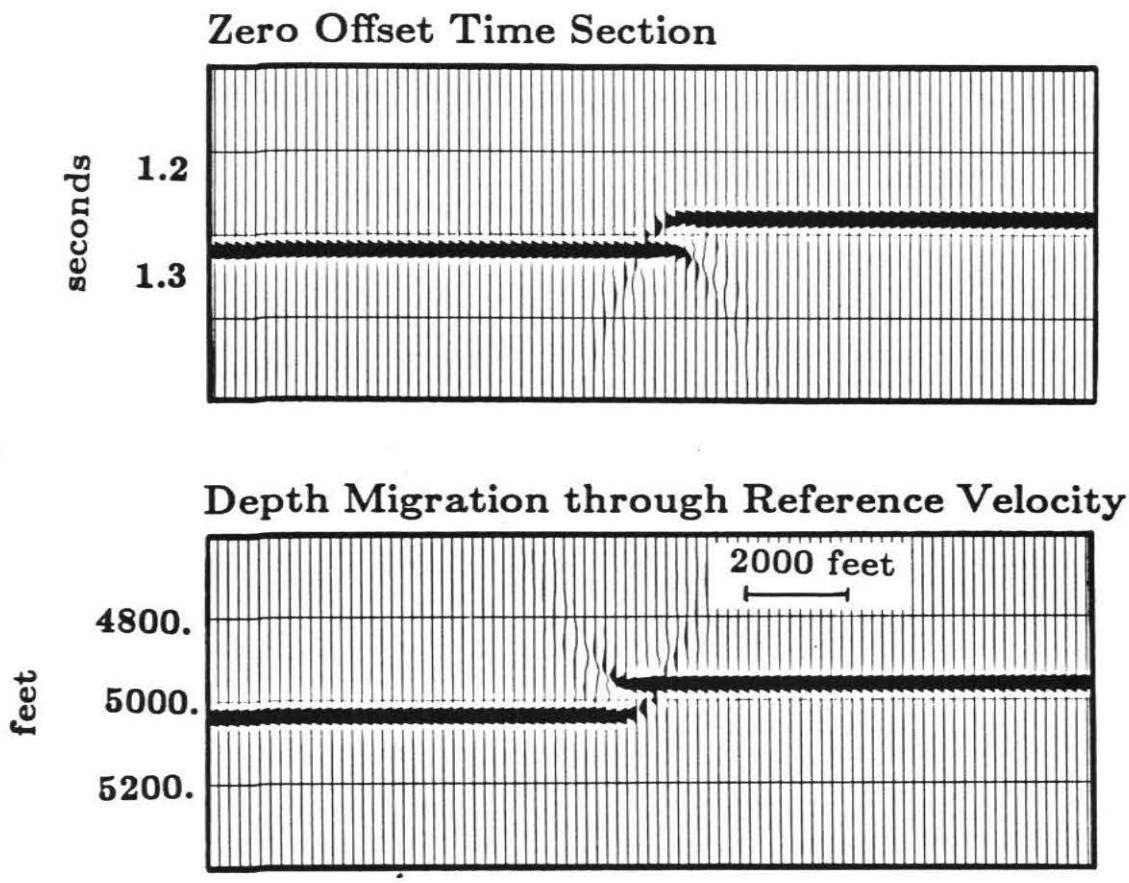
Zero Offset Time Section
seconds
1.2
1.3
Depth Migration through Reference Velocity
feet
4800.
5000.
5200.
2000 feet

Figure 3.67

E: Inversion of true model. The position of the velocity contrast in the center has been resolved. However, the reflector position of the reference model has been hardly improved. Several velocity artifacts associated with the edges exist.

F: The inversion is repeated with the imposition of constraints at the edges that do not allow the velocity to vary laterally. The inversion of the reflector position is now considerably improved.

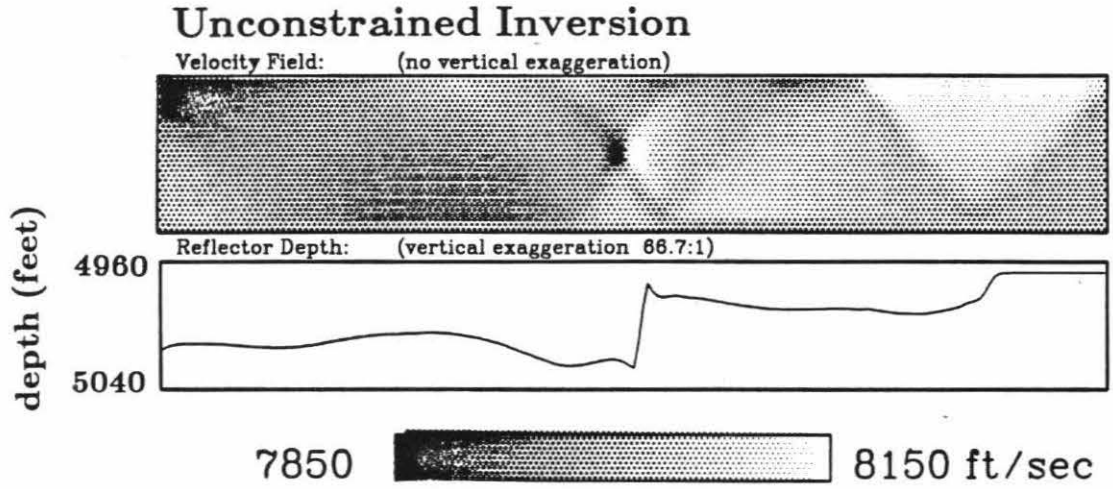
Unconstrained Inversion
Velocity Field: (no vertical exaggeration)
Reflector Depth: (vertical exaggeration 66.7:1)
depth (feet)
4960
5040
7850
8150 ft/sec

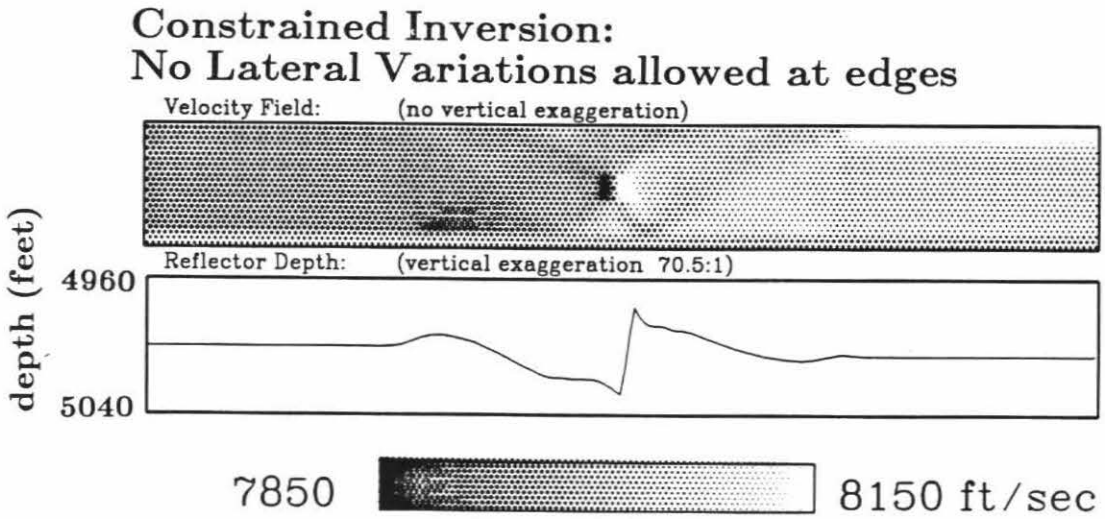
Constrained Inversion:
No Lateral Variations allowed at edges
Velocity Field: (no vertical exaggeration)
Reflector Depth: (vertical exaggeration 70.5:1)
depth (feet)
4960
5040
7850
8150 ft/sec

Figure 3.67

G: The inversion is repeated with a 2nd reflector at twice the depth of the first. There are no differences between the true and reference models besides the original velocity variations. The upper reflector is now well inverted.

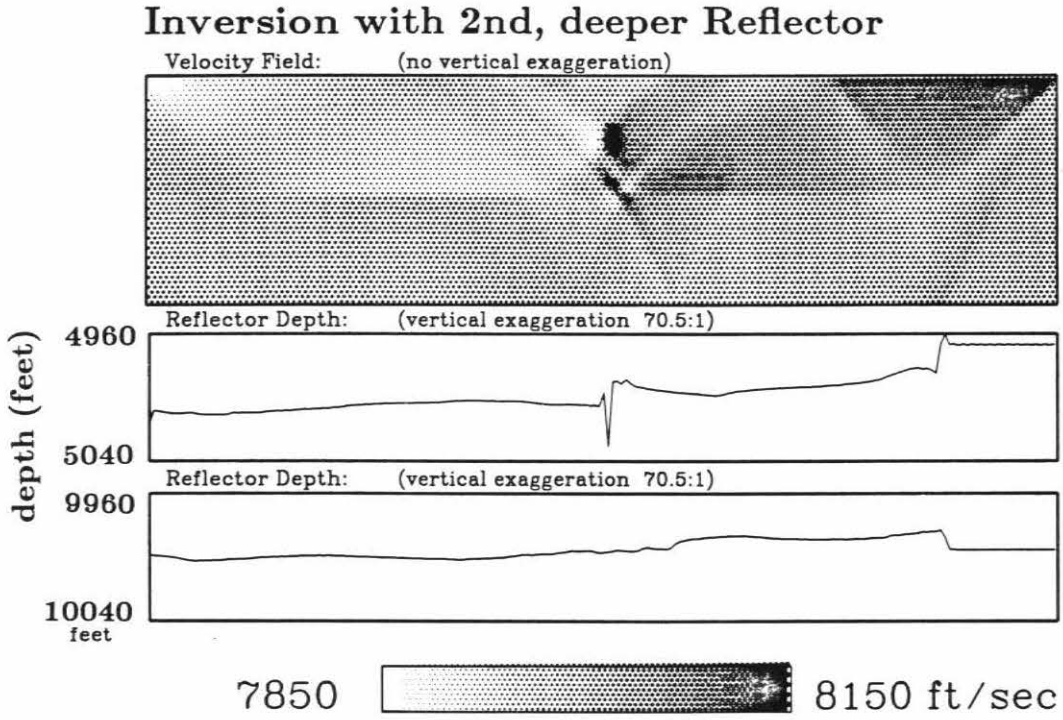
Inversion with 2nd, deeper Reflector
Velocity Field:
(no vertical exaggeration)
Reflector Depth:
(vertical exaggeration 70.5:1)
depth (feet)
4960
5040
Reflector Depth:
(vertical exaggeration 70.5:1)
9960
10040
feet
7850
8150 ft/sec

Figure 3.68

In an effort to improve the unconstrained inversion of Figure **3.67e**, the inversion is repeated with true and reference models that are twice as wide.

A: True model with the same velocity variations as in model **3.67a**.

B: Reference model with the same reflector variations as in model **3.67b**.

C: Inversion using the two previous models. The reflector is better inverted than the corresponding inversion in Figure **3.67c** using narrower models. However, the center and the edges still cause serious problems.

(Figures 3.69 through 3.72 do not exist.)

True Velocity & Reflector Position

A

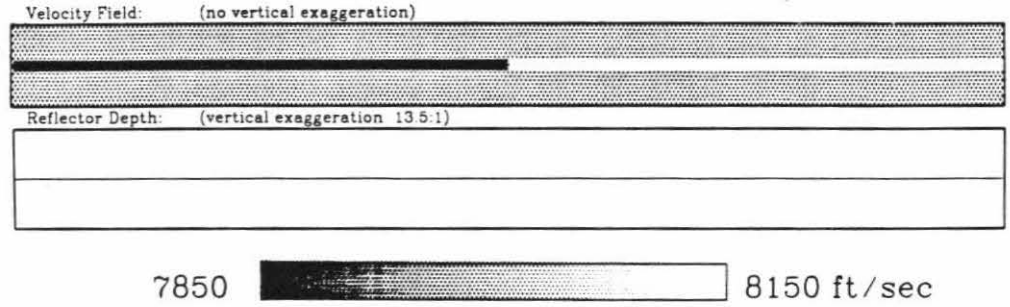

Starting Reference Model for Ray Tracing

B

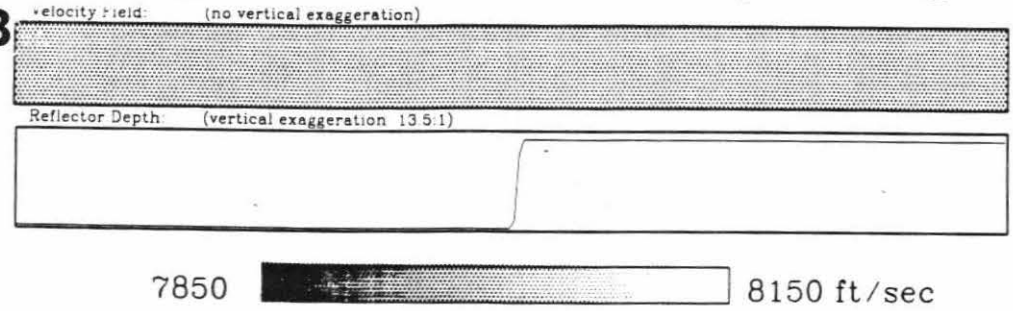

Inversion

C

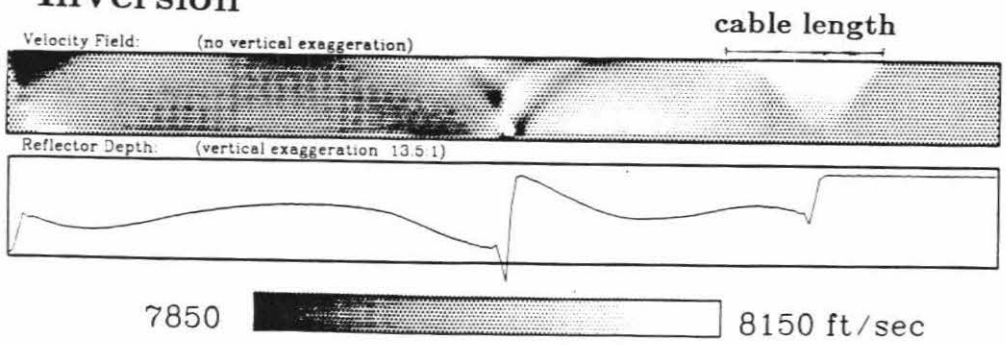

Figure 3.73

Inversion of narrow reflection survey for the analysis of edge effects.

A: True model used for data collection. The velocity is uniform while the reflector has a slope across the model. Note the vertical exaggeration of the reflector scale.

B: Reference model used for ray tracing. It differs from the true model in that the reflector is flat.

True Model K2

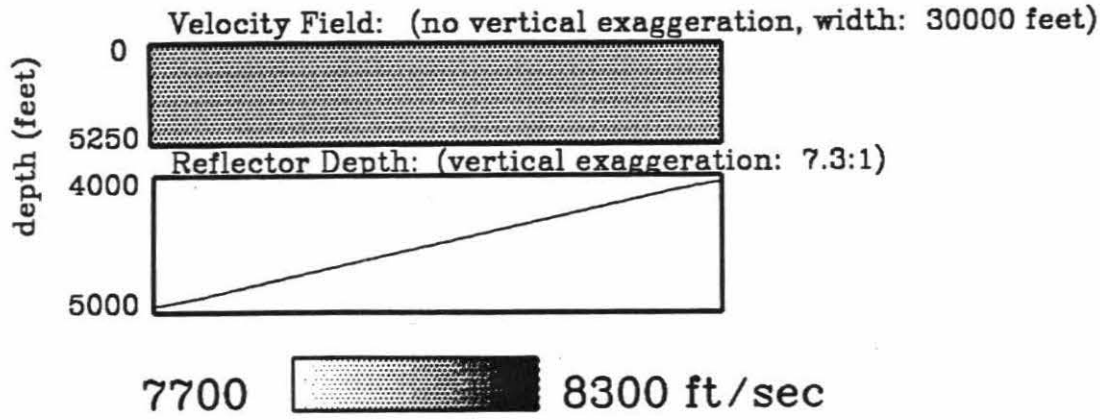

Reference Model K2

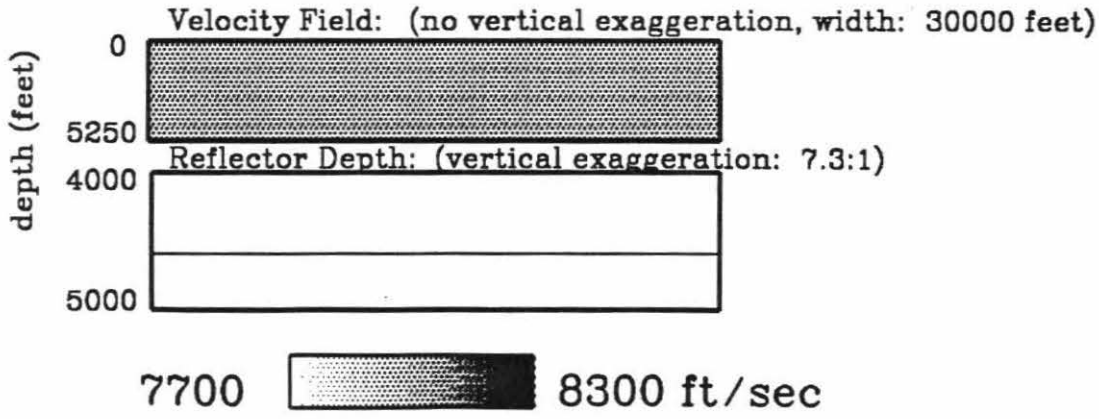

Figure 3.73

C: Plot of ray density in model. The solid black areas are regions of complete ray coverage; the lighter areas give an indication of the region of only partial ray coverage. The ray coverage is not symmetric because the receivers are only to the right of the shot. Thus the far left side contains only vertical rays and the far right side contains only far offset rays.

D: Inversion with low damping. Although the true and reference models had no velocity or reflector structure, this inversion has much false structure. The inhomogeneous ray coverage has seriously distorted the inversion.

Density of Ray Paths in Reference Model

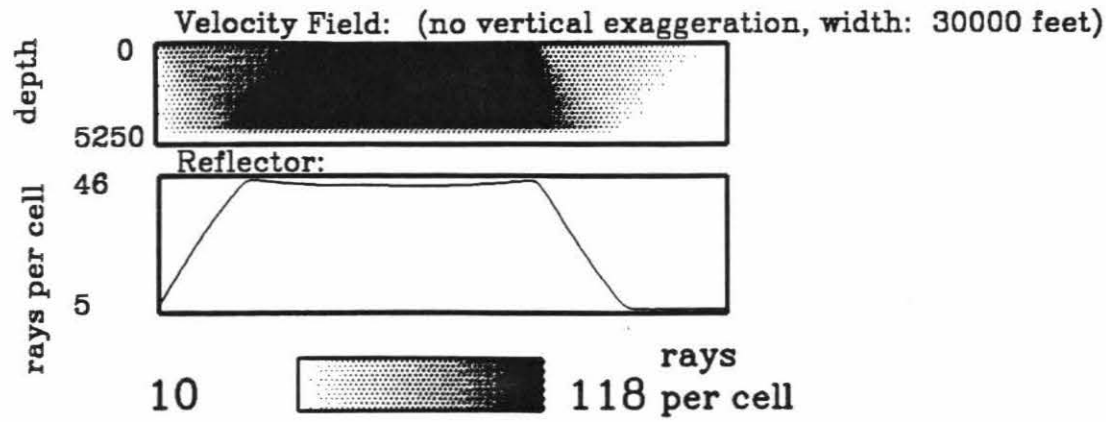

Inversion of Model K2
eigenvalue range: (1.0-0.05)

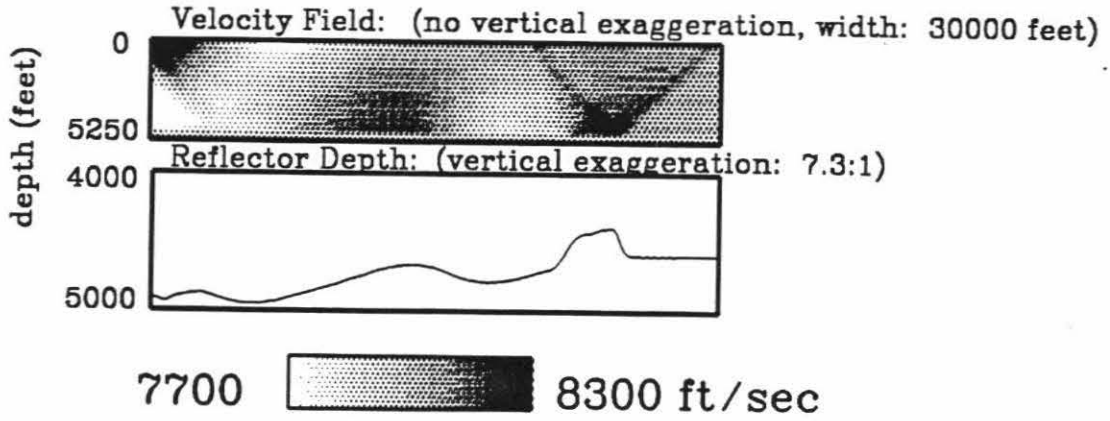

Figure 3.73

E: Inversion to smaller eigenvalue. There is little change from the previous inversion.

F: Inversion with large damping. The reflector and velocity is now somewhat smoother than the inversion with low damping, but still contains many artifacts.

Inversion of Model K2
eigenvalue range: (1.0-0.02)

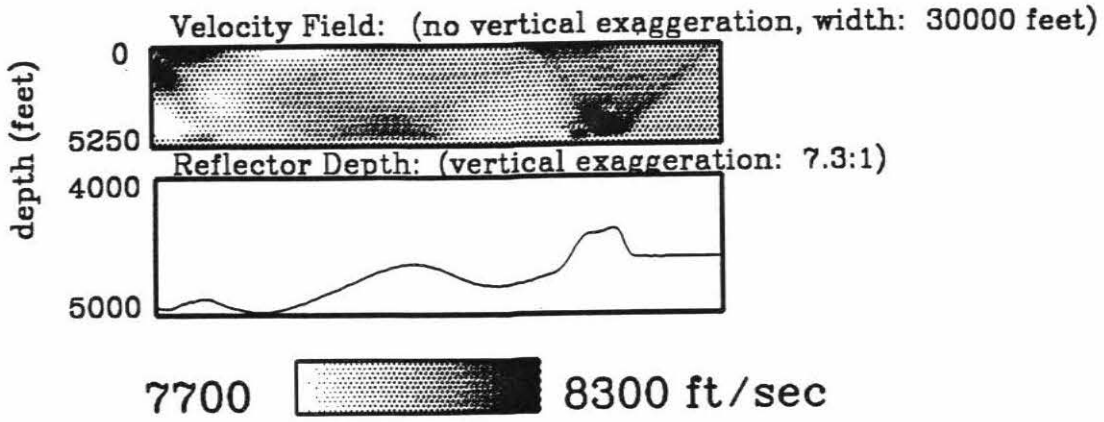

Inversion of Model K2 with large damping
eigenvalue range: (1.0-0.05)

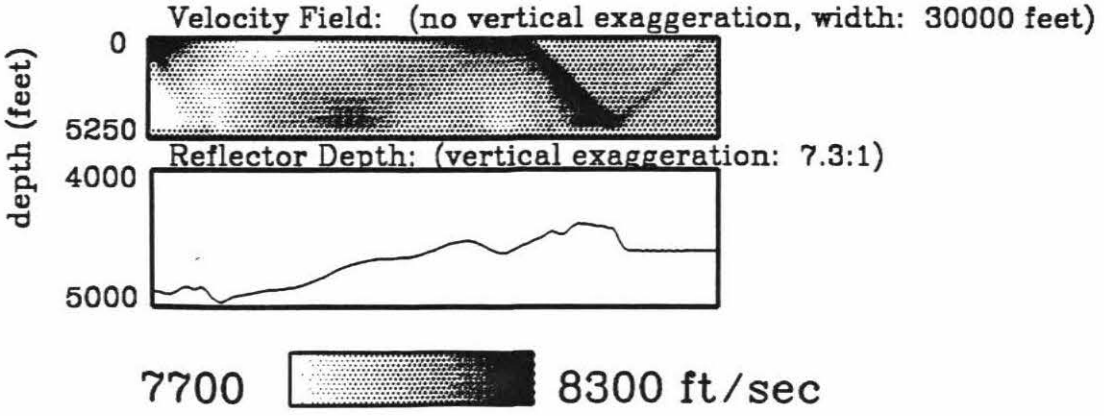

Figure 3.73

G: Inversion with large damping carried out to smaller eigenvalue show little change.

H: Extent of constraints used in attempt to control edge effects. The velocity was not allowed to vary laterally in the black region.

Inversion of Model K2 with large damping eigenvalue range: (1.0-0.02)

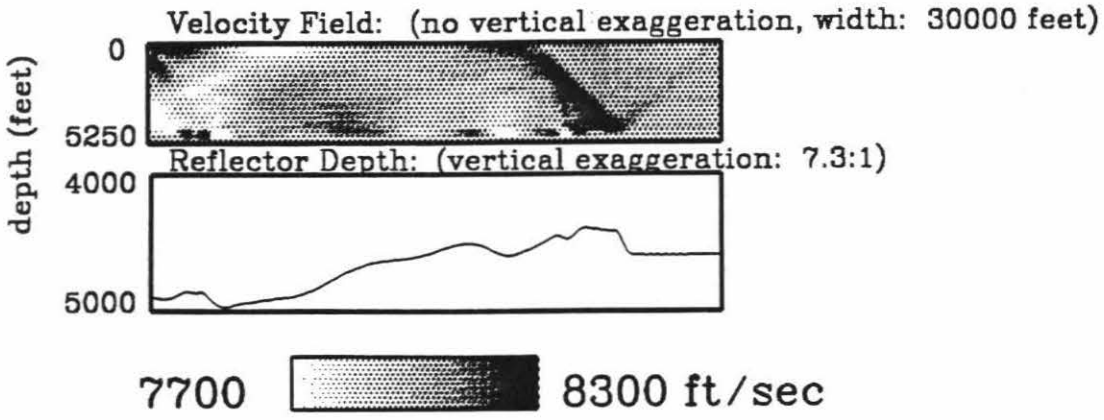

1st set of Constraints used for Inversion
(velocity was not allowed to vary laterally in boxes)

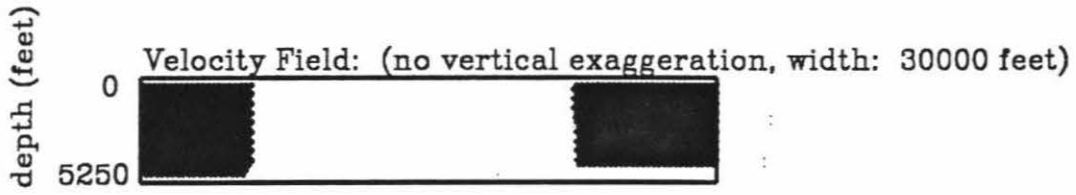

Figures 3.73

I & J: Inversions using constraint described in the previous figure. The results are significantly improved, but still contain some incorrect reflector structure.

1st Constrained Inversion of Model K2
eigenvalue range: (1.0-0.05)

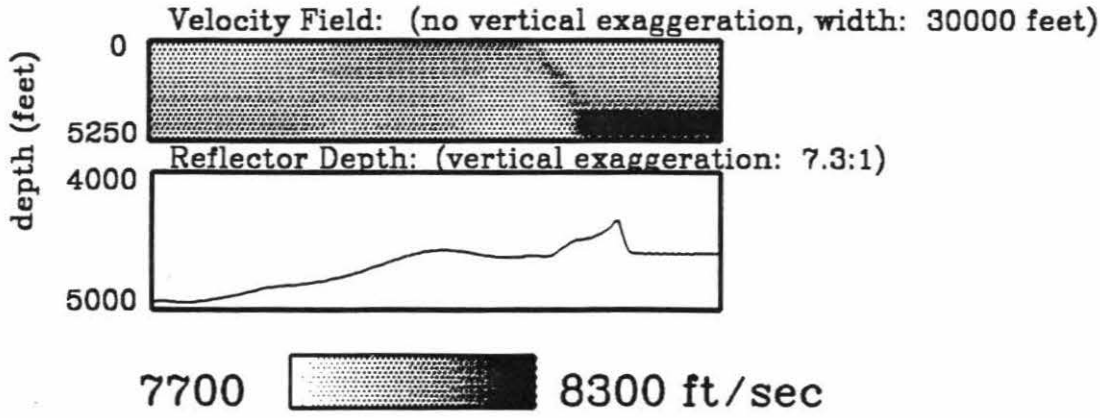

1st Constrained Inversion of Model K2
eigenvalue range: (1.0-0.02)

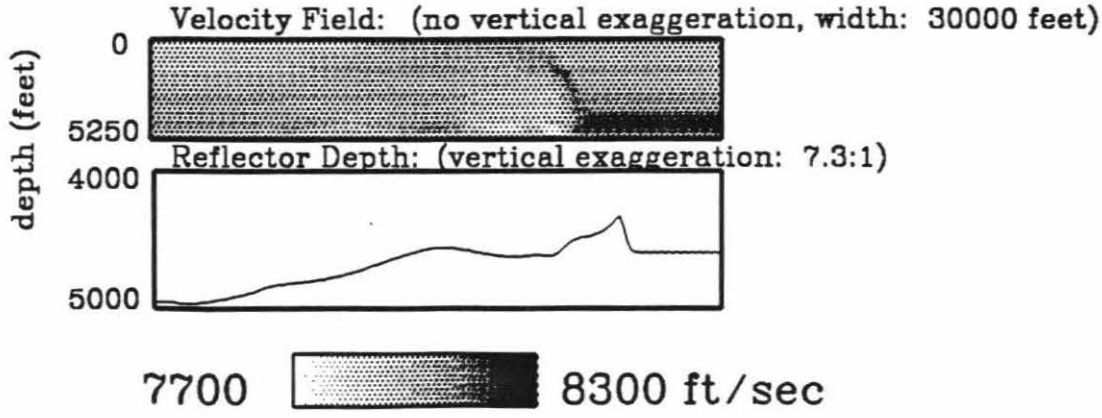

Figure 3.73

K: More severe constraints used to control edge effects. The velocity was not allowed to vary laterally in shaded region.

L: Inversion using more severe constraint of previous figure. The reflector now is the correct gradual slope.

2nd set of Constraints used for Inversion
(velocity was not allowed to vary laterally in boxes)

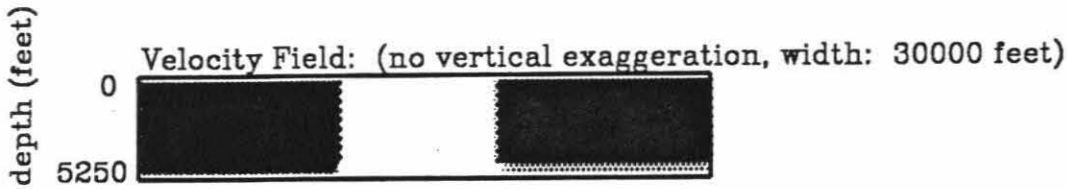

2nd Constrained Inversion of Model K2
eigenvalue range: (1.0-0.05)

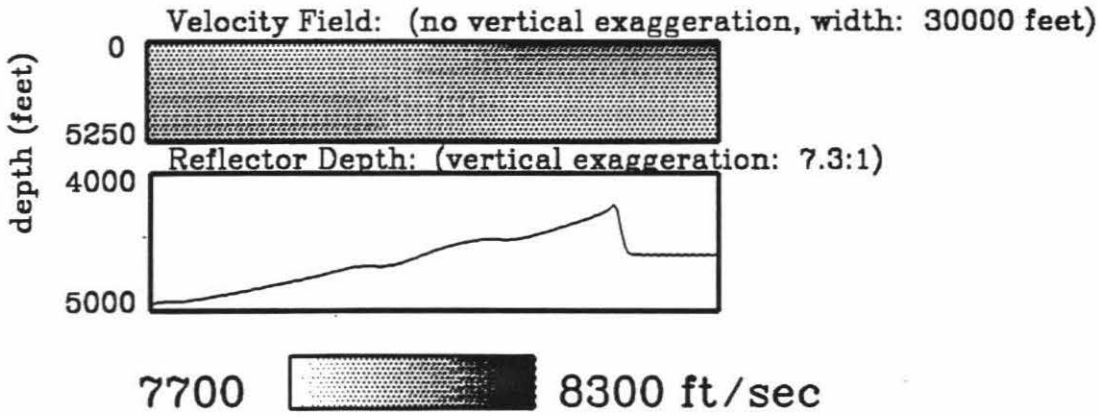

Figure 3.73

M: Previous inversion to smaller eigenvalue. No other artifacts have cropped up.

Figure 3.74

A: True model similar to the one used in Figures **3.73** but significantly wider.

2nd Constrained Inversion of Model K2
eigenvalue range: (1.0-0.02)

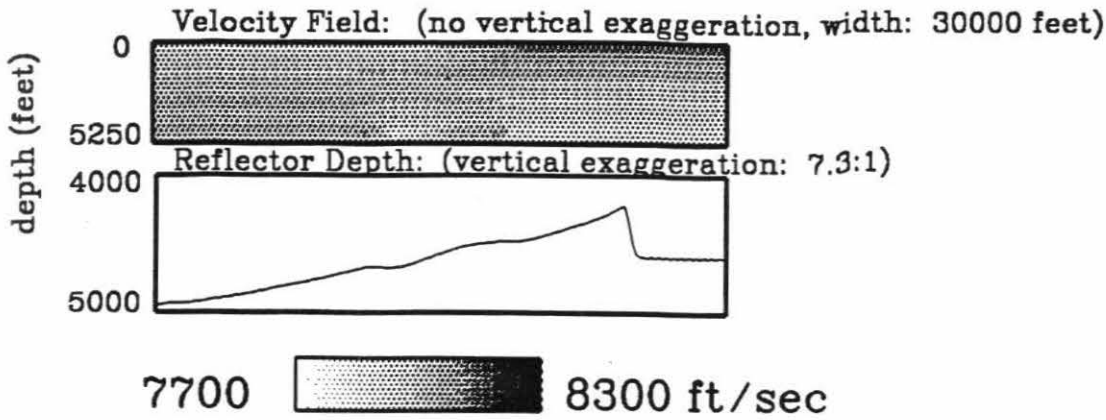

True Model K1

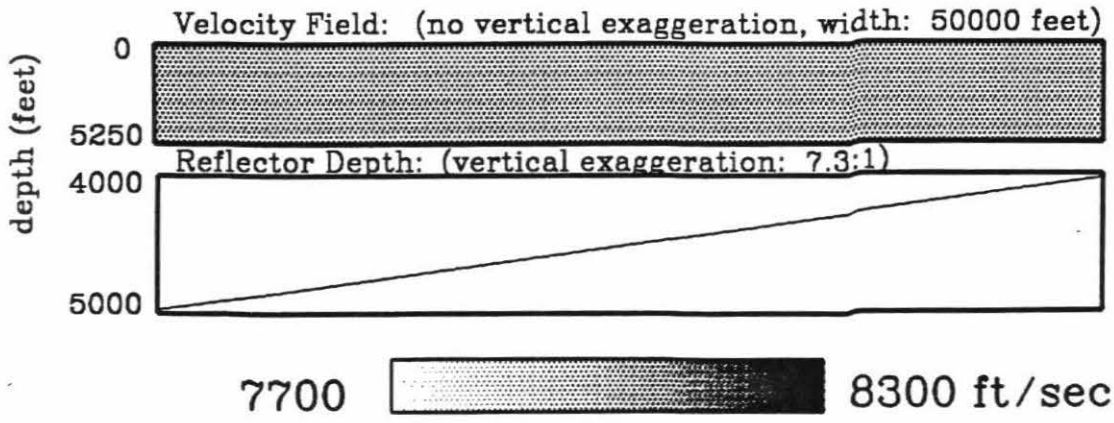

Figure 3.74

B: Reference model used for ray tracing.

C: Density of ray paths showing the region of poor ray coverage at the edges of the survey.

Reference Model K1

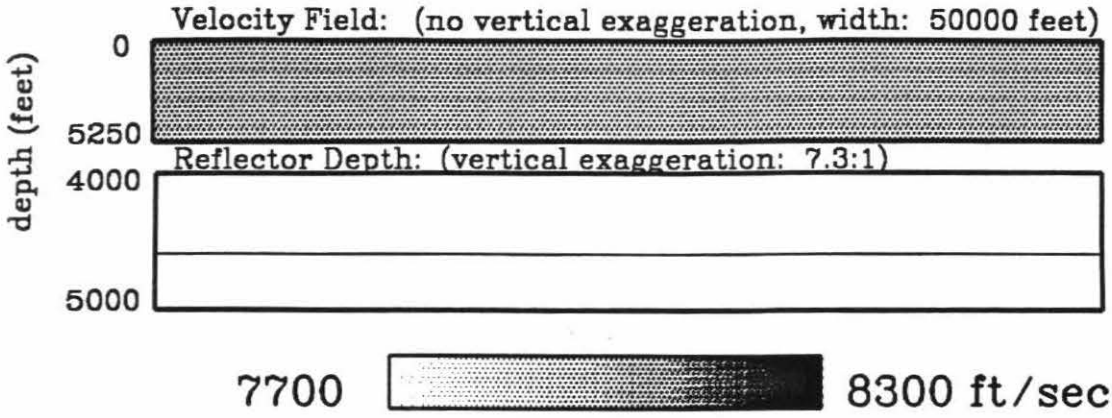

Density of Ray Paths in Reference Model

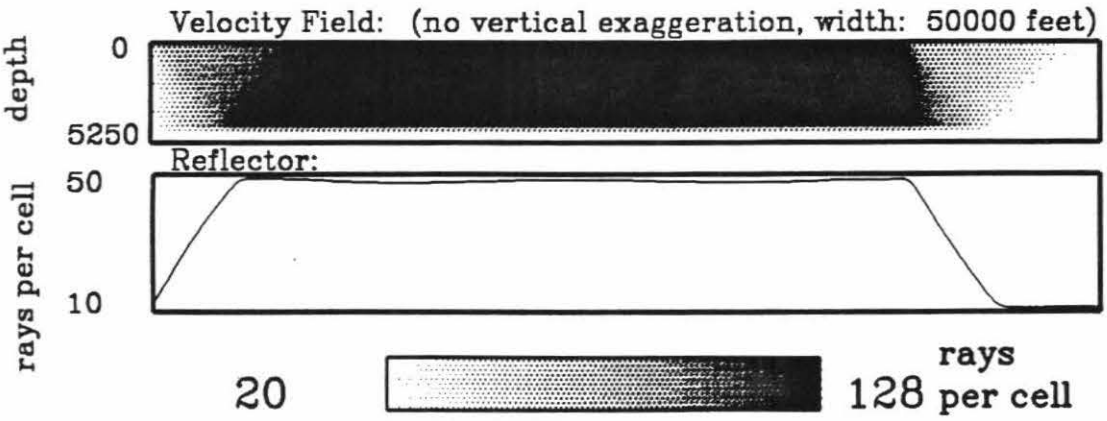

Figure 3.74

D: Inversion of true model in Figure **A** over limited eigenvalue range. A false gradual velocity gradient has been introduced across the model. This is the velocity complement of a sloping reflector.

E: Inversion to smaller eigenvalue. The velocity gradient has been reduced, but some smaller scale artifacts have been introduced. They are still minor, however, compared to the artifacts of the narrow survey in figures **3.73**.

Inversion of Model K1
eigenvalue range: (1.0-0.30)

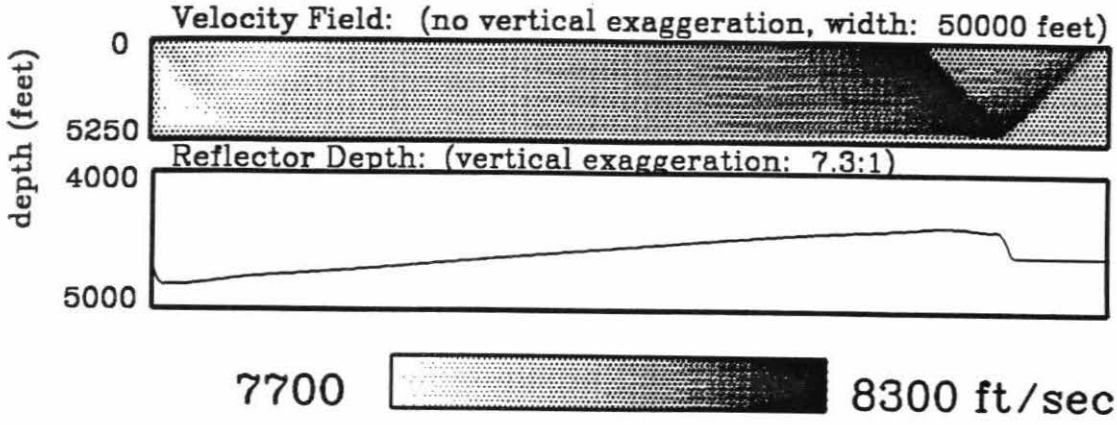

Inversion of Model K1
eigenvalue range: (1.0-0.05)

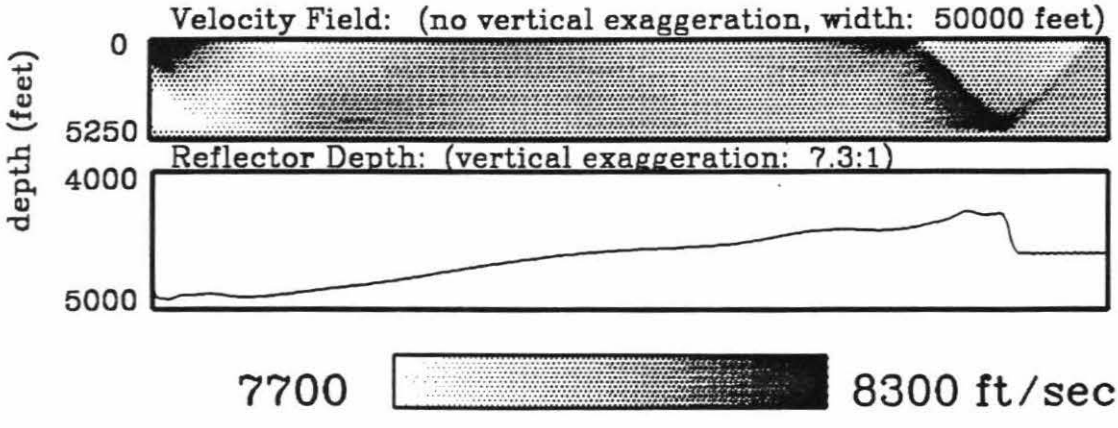

Figure 3.74

F: Inversion to smaller eigenvalue. Most of the artifacts of the edges are within one cable length of the edge of the survey. The reflector, especially in the center, has been well inverted.

Inversion of Model K1
eigenvalue range: (1.0-0.02)

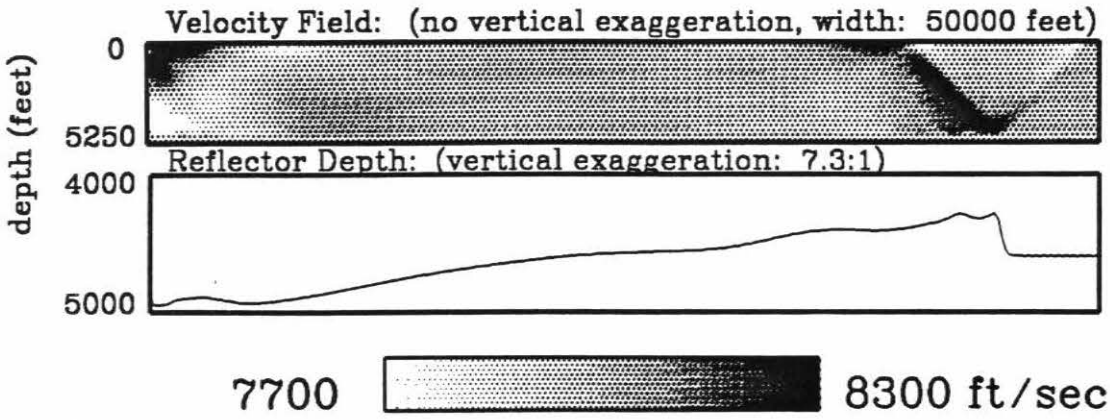

Figures for Chapter 4:

Singular Value Decomposition Analysis of the Travel Times of a Surface Seismic Reflection Survey

Figure 4.1

The generic model used for SVD analysis. Cable length is twice the reflector depth so that maximum ray angle is 45°. Constant velocity produces straight rays. To eliminate the effect of edges, rays exiting the right side of the grid are wrapped around to the left side creating a continuous, circular ray coverage.

Generic Model

128x10 square velocity cells
128 reflector cells

rays are wrapped around to form continuous circular model

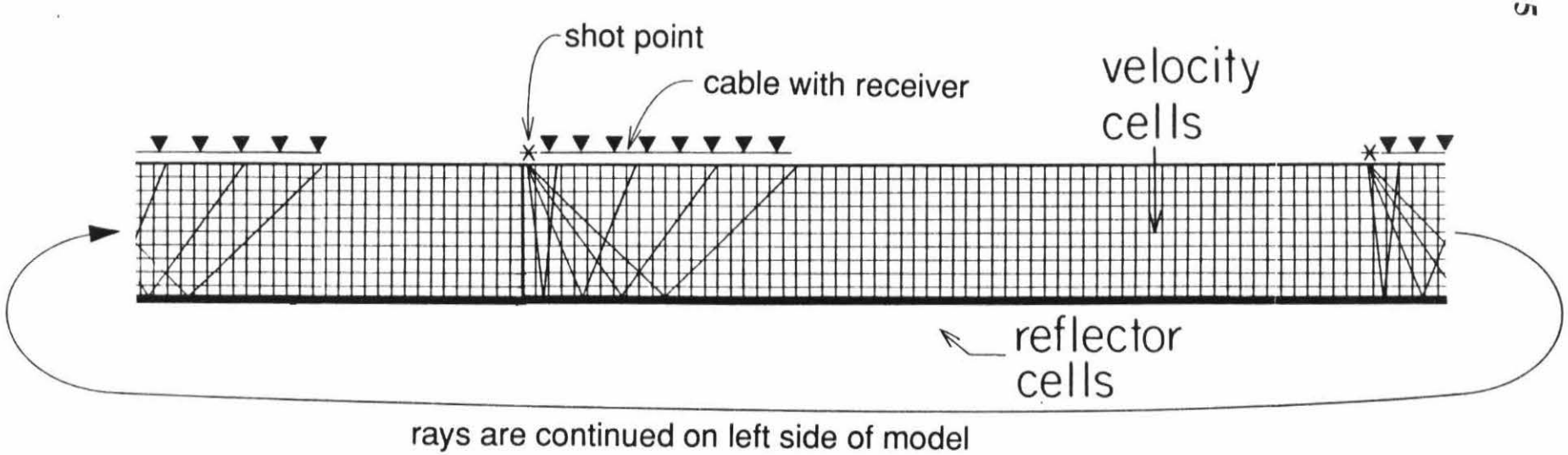

Figure 4.2

A sample velocity variation that is positioned to be ambiguous with a reflector depth variation. The slowness of the marked field can be adjusted to cancel out most all of the travel time variations from the reflector variations. The travel time signature remaining is the move out trend with offset. This is the information that will be used to attempt resole this ambiguity between velocity and reflector depth.

Velocity - Reflector Depth Ambiguity:

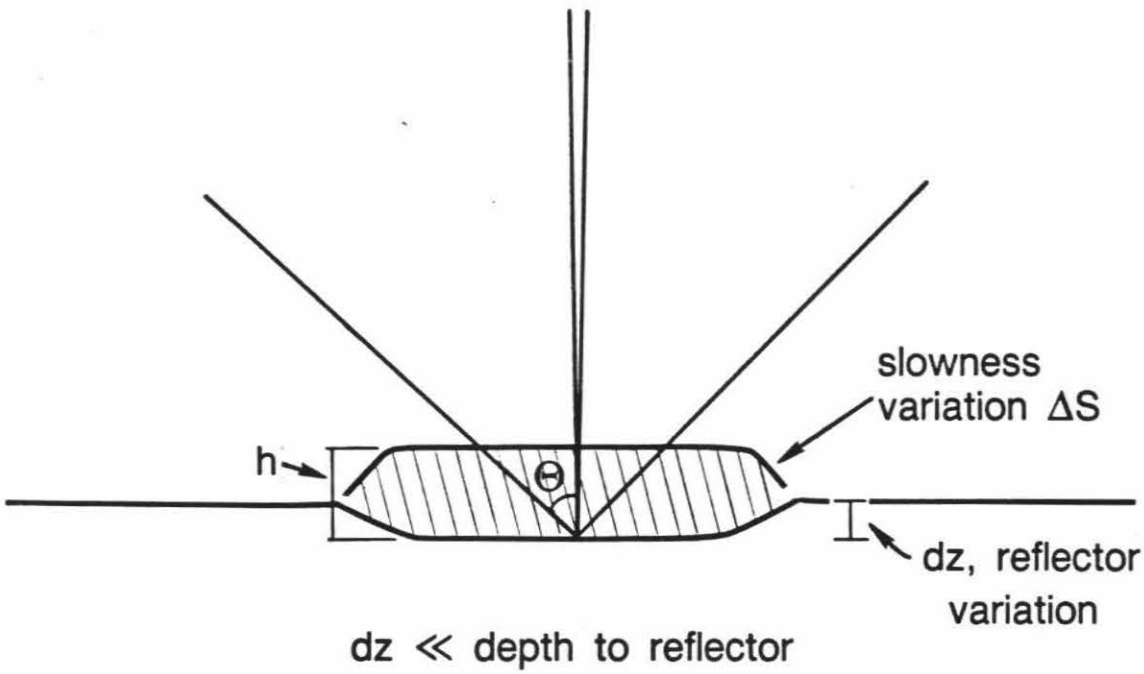

	vertical ray	non-vertical ray
Δt from reflector position:	$-2\cdot\frac{\delta z}{v}$	$-2\cdot\frac{\delta z}{v}\cdot\cos(\Theta)$
Δt from velocity variation:	$2\cdot h\cdot\Delta s$	$2\cdot\frac{h}{\cos(\Theta)}\cdot\Delta s$
net Δt for $(\frac{\delta z}{v} = h\cdot\Delta s)$ **:**	**0.0**	$2\cdot\frac{\delta z}{v}\cdot\left[\frac{1}{\cos(\Theta)} - \cos(\Theta)\right]$

Figure 4.3

Simplified model consisting of only two parameters: a uniform slowness and a flat reflector. This model corresponds to the laterally invariant case that stacking velocity analysis can solve.

The travel time equation is rewritten so both parameters are in unit of two way travel time.

Eigenvector A corresponds to the constructive interference of velocity and reflector depth. Inverting this eigenvector places approximately half of the average travel time variations of the rays into slowness and the other half into the reflector. The amount placed in each is dependent on the relative weight between slowness and reflector.

Eigenvector B corresponds to the velocity-reflector depth ambiguity. The relatively large eigenvalue of 0.105 indicates that this eigenvector can probably be resolved.

2 parameter model

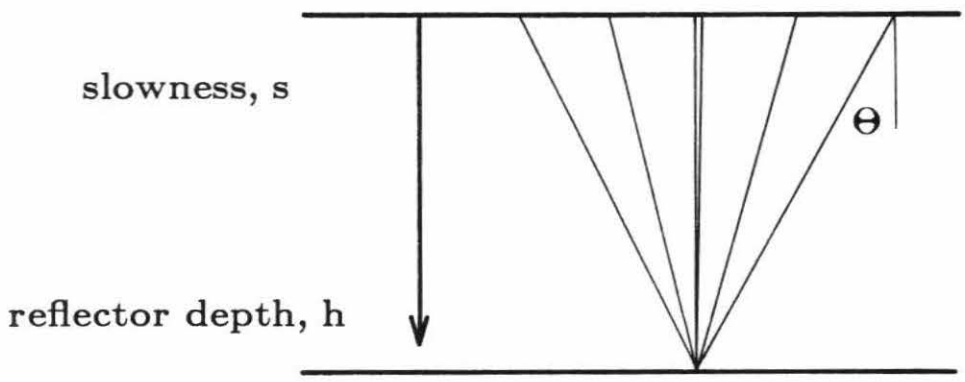

$$\Delta t = \Delta s \cdot 2 \cdot \frac{h}{\cos(\Theta)} + \Delta h \cdot 2 \cdot \cos(\Theta) \cdot s$$

$$= 2 \cdot \left(\cos(\Theta)\right)^{-1} \cdot \left(h \Delta s\right) + 2 \cdot \cos(\Theta) \cdot \left(s \Delta h\right)$$

For maximum ray angle of 45 °
and a reflector weight of 1.0:

Eigenvector A: (1.0, 1.0) eigenvalue= 0.998

Eigenvector B: (1.0, -1.0) eigenvalue= 0.105

Figure 4.4A & B

The data space eigenvectors corresponding to the model space eigenvectors in the previous figure.

A: The upper eigenvector merely takes the average of all the travel time variations.

B: The lower eigenvector is analogous to using the hyperbolic move out curve to properly position the reflector depth.

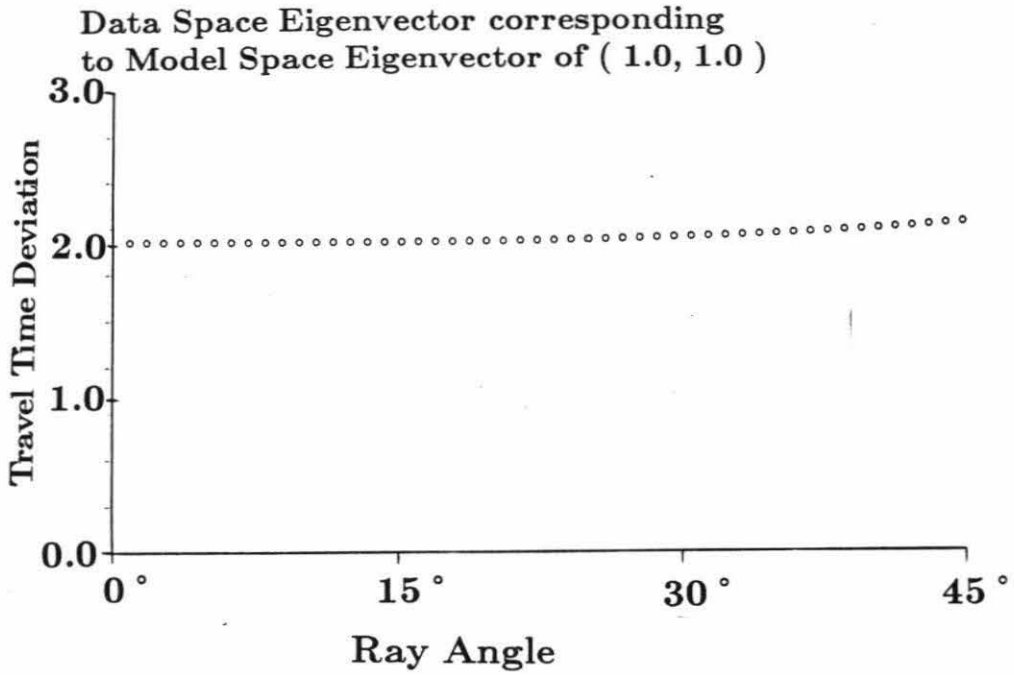
Data Space Eigenvector corresponding
to Model Space Eigenvector of (1.0, 1.0)
Travel Time Deviation
3.0
2.0
1.0
0.0
0 °
15 °
30 °
45 °
Ray Angle

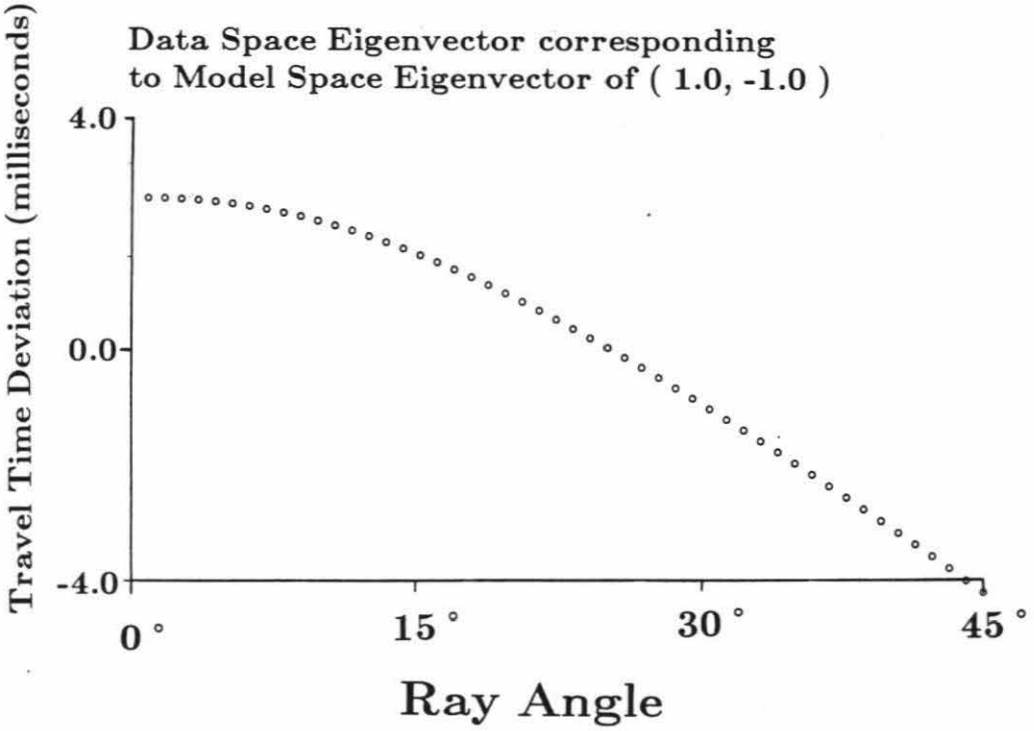
Data Space Eigenvector corresponding
to Model Space Eigenvector of (1.0, -1.0)
Travel Time Deviation (milliseconds)
4.0
0.0
-4.0
0 °
15 °
30 °
45 °
Ray Angle

Figure 4.5

The eigenvalue of the second eigenvector is a strong function of the maximum ray angle available in the data.

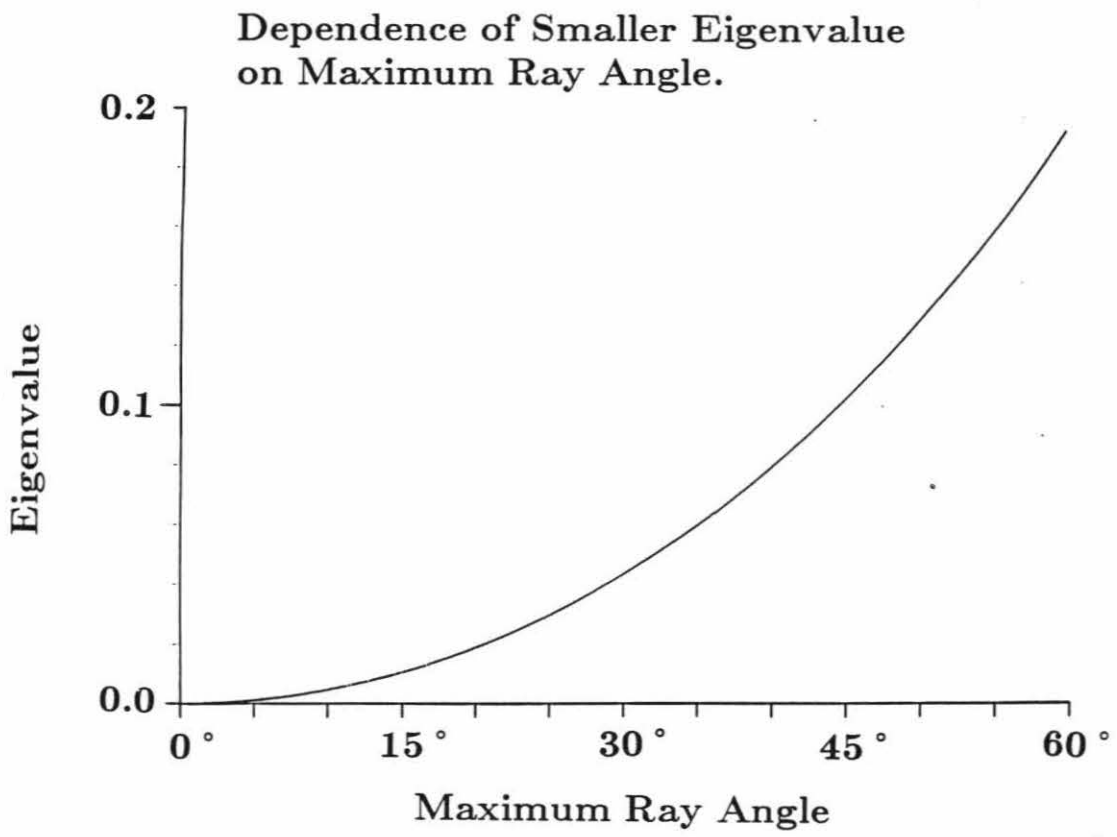
Dependence of Smaller Eigenvalue
on Maximum Ray Angle.
0.2
0.1
0.0
Eigenvalue
0 °
15 °
30 °
45 °
60 °
Maximum Ray Angle

Figure 4.6A & B

The eigenvalue of the second eigenvector is not very sensitive to the relative weighting between velocity and reflector. The eigenvalue is greatest when the net weight for velocity and reflector are equal.

The value of the bottom axis is the relative weight between velocity and reflector for a vertical ray. Since non-vertical rays have longer path length in the velocity field and shorter *simulated* path length in the reflector cell, the net weight between the two fields is achieved at a value of 1.3.

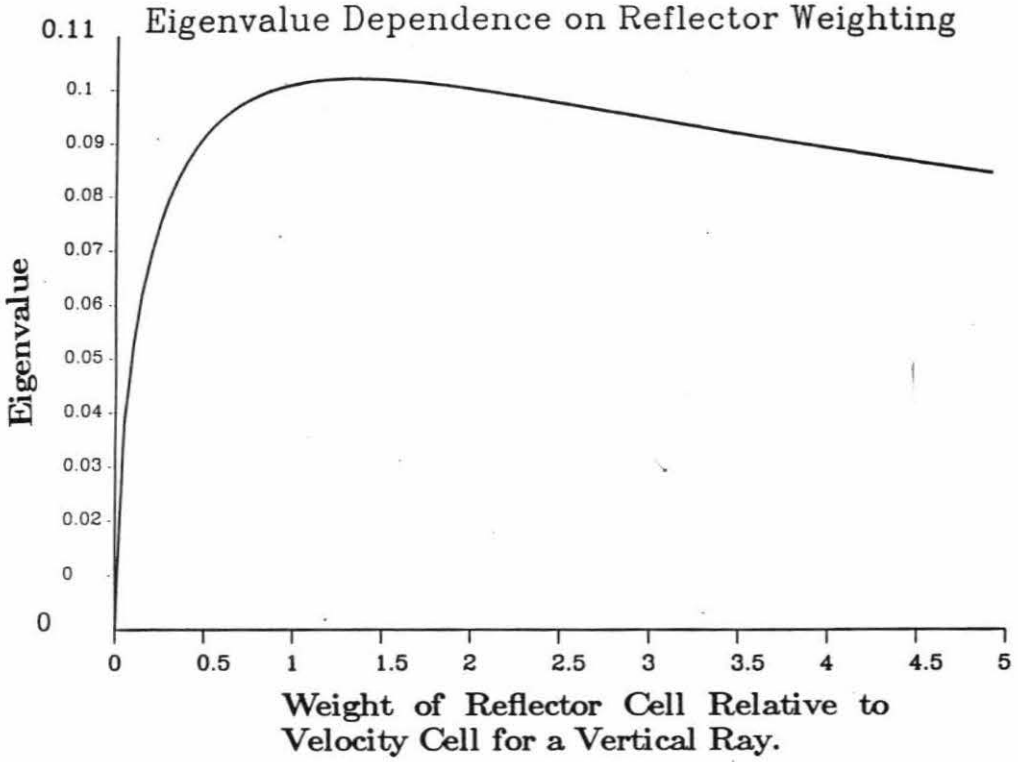
Eigenvalue Dependence on Reflector Weighting
Eigenvalue
0.11
0.1
0.09
0.08
0.07
0.06
0.05
0.04
0.03
0.02
0
0
0
0.5
1
1.5
2
2.5
3
3.5
4
4.5
5
Weight of Reflector Cell Relative to Velocity Cell for a Vertical Ray.

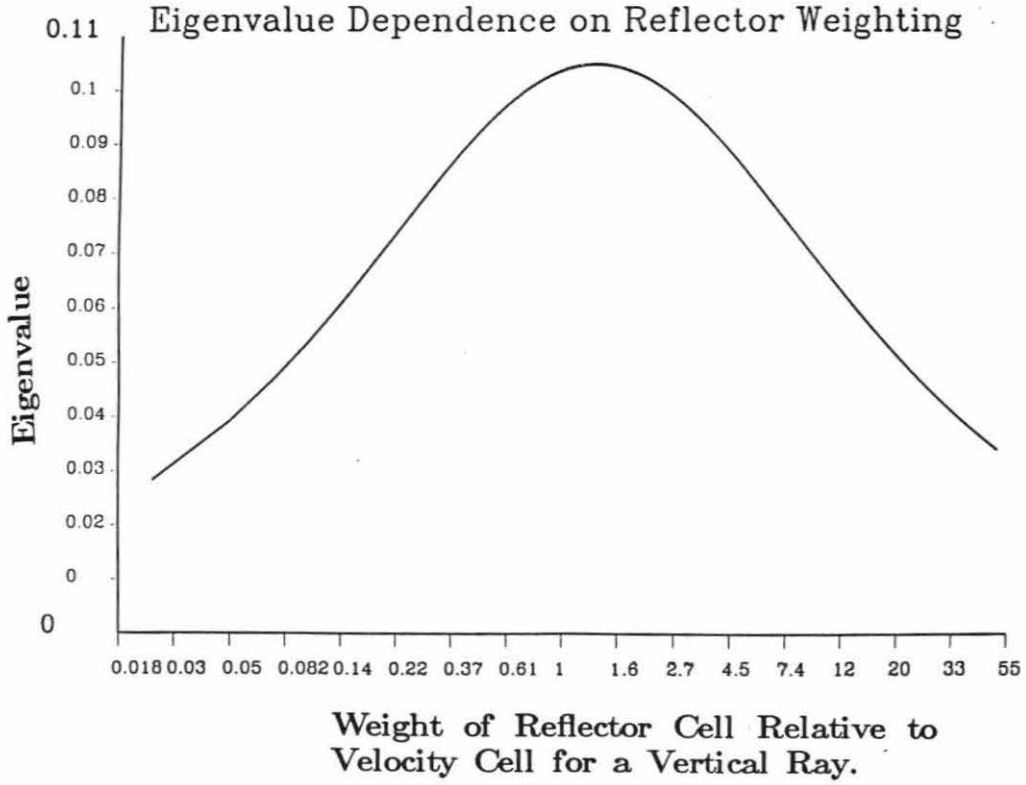
Eigenvalue Dependence on Reflector Weighting
Eigenvalue
0.11
0.1
0.09
0.08
0.07
0.06
0.05
0.04
0.03
0.02
0
0
0.018 0.03 0.05 0.082 0.14 0.22 0.37 0.61 1 1.6 2.7 4.5 7.4 12 20 33 55
Weight of Reflector Cell Relative to Velocity Cell for a Vertical Ray.

Figure 4.7A

Eigenvalue distribution from SVD on the generic model. Two major discontinuities appear at eigenvector 128 & about 750.

Eigenvalue Distribution for a Generic Survey with 128 by 10 square Cells, 128 Reflector Cells 1:1 Velocity to Reflector Weight

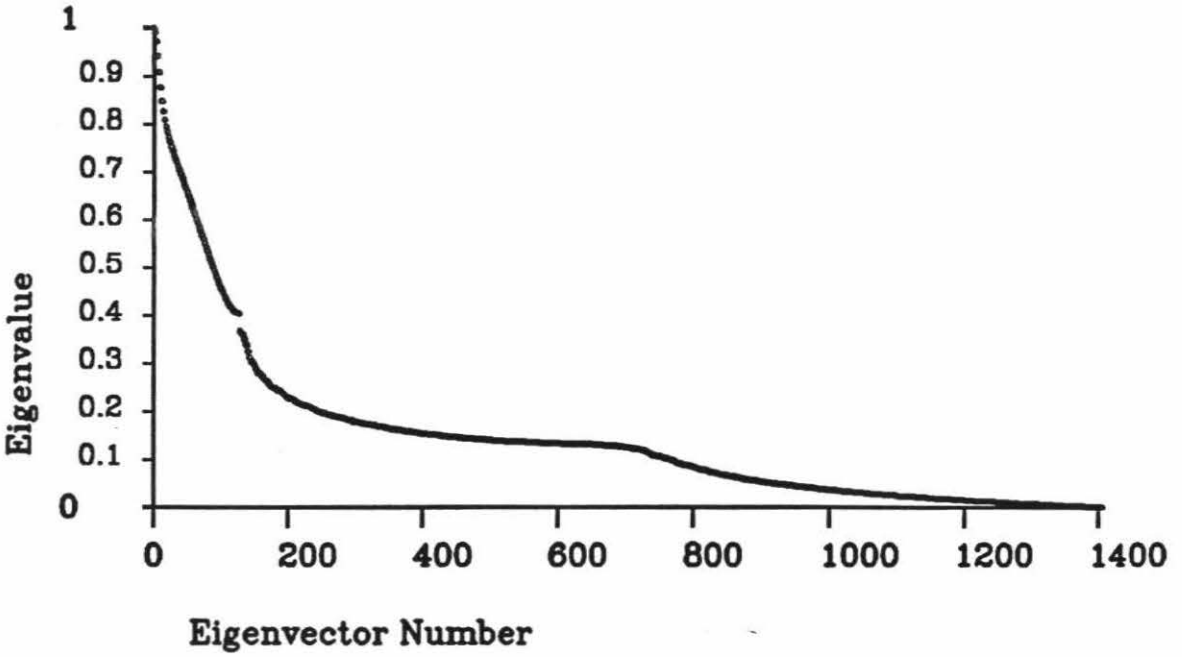

Figure 4.7B & C

Previous eigenvalue distribution plotted at different scales to highlight the discontinuities.

Eigenvalue Distribution for a Generic Survey with
128 by 10 square Cells, 128 Reflector Cells
1:1 Velocity to Reflector Weight

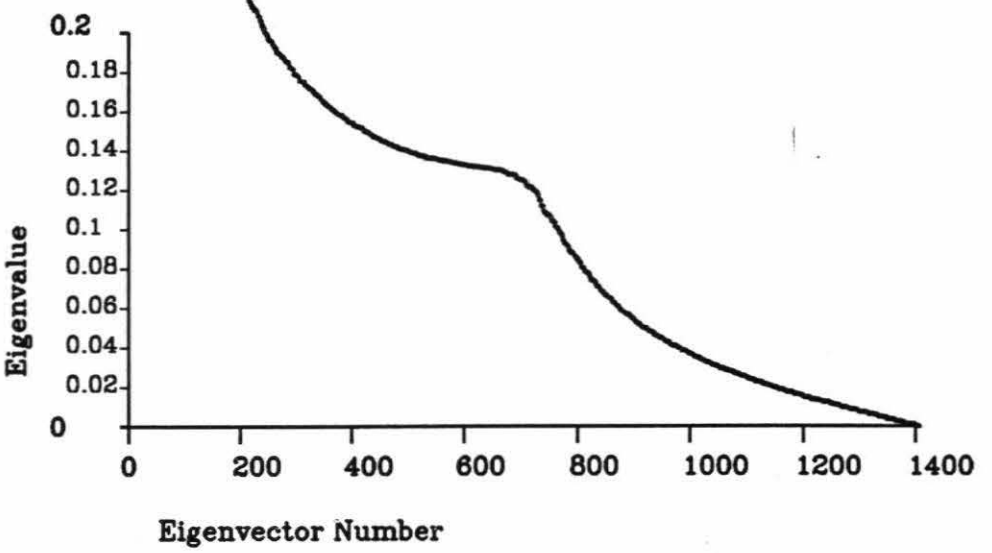

Eigenvalue Distribution for a Generic Survey with
128 by 10 square Cells, 128 Reflector Cells
1:1 Velocity to Reflector Weight

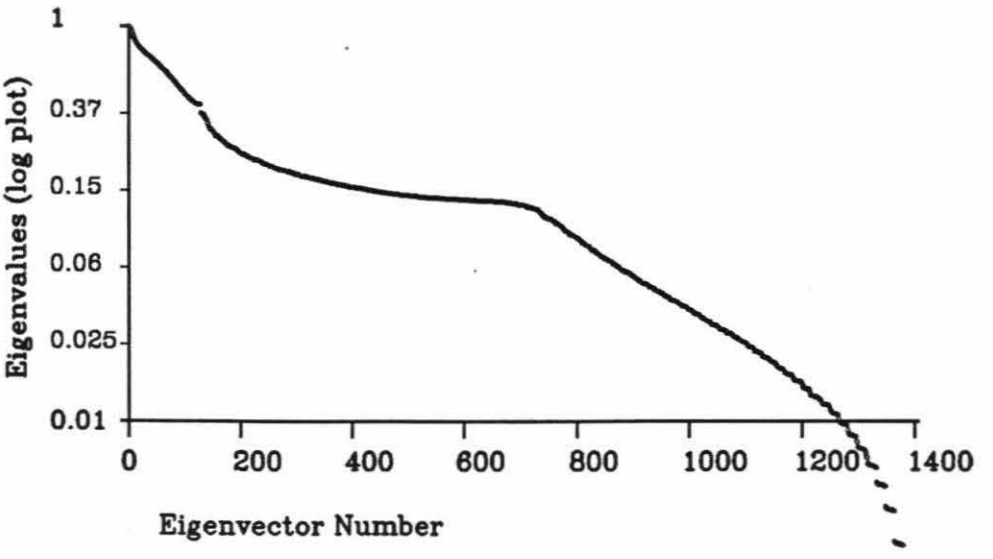

Figure 4.7D & E

The reflector portion of the eigenvectors is plotted against eigenvector. Several groups of eigenvectors are apparent: one with eigenvalues above 0.35 having large eigenvector component in the reflector, another between eigenvalues 0.35 and 0.10 with no reflector components, and two groups below the eigenvalue of 0.10, one with reflector components and another without.

That reflector components exist at very small eigenvalues indicates that some of the reflector cannot be inverted.

Eigenvector Characteristics for Generic Survey with
128 by 10 square cells, 128 reflector cells
1:1 Velocity to Reflector Weight
(all eigenvectors)

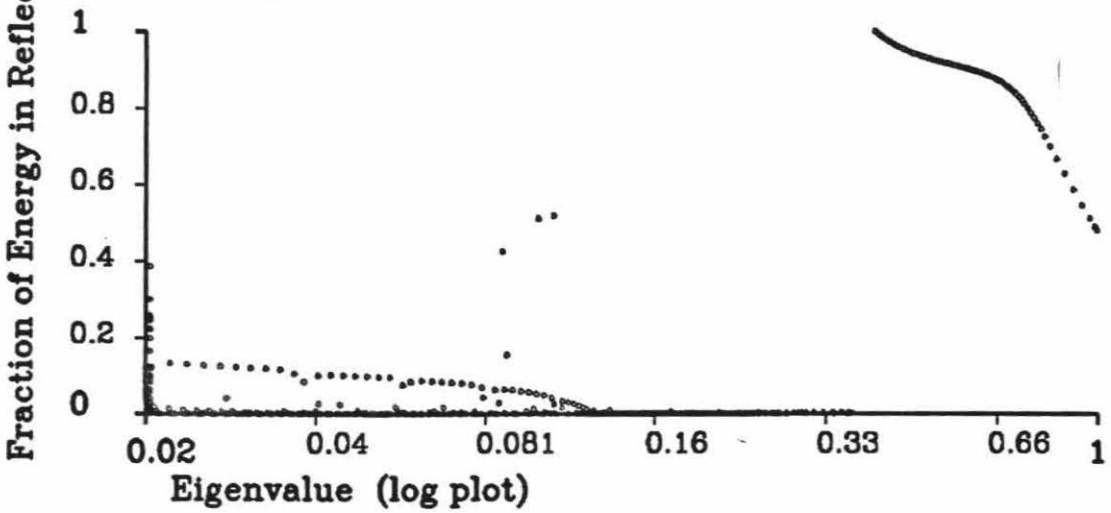

Eigenvector Characteristics for Generic Survey with
128 by 10 square cells, 128 reflector cells
1:1 Velocity to Reflector Weight
(all eigenvectors)

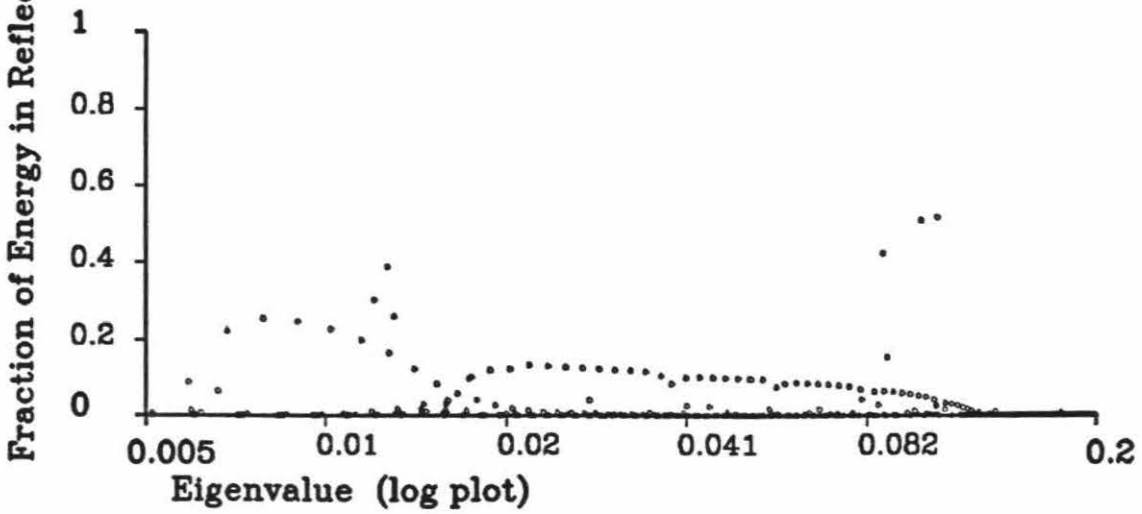

Figure 4.7F

Correlation of the reflector cell with the sum of the slowness column above it. A positive value indicates that the eigenvector represents the constructive interference between velocity and reflector depth. A negative value represents the velocity-reflector depth ambiguity. The four groups of the previous figure are also apparent here.

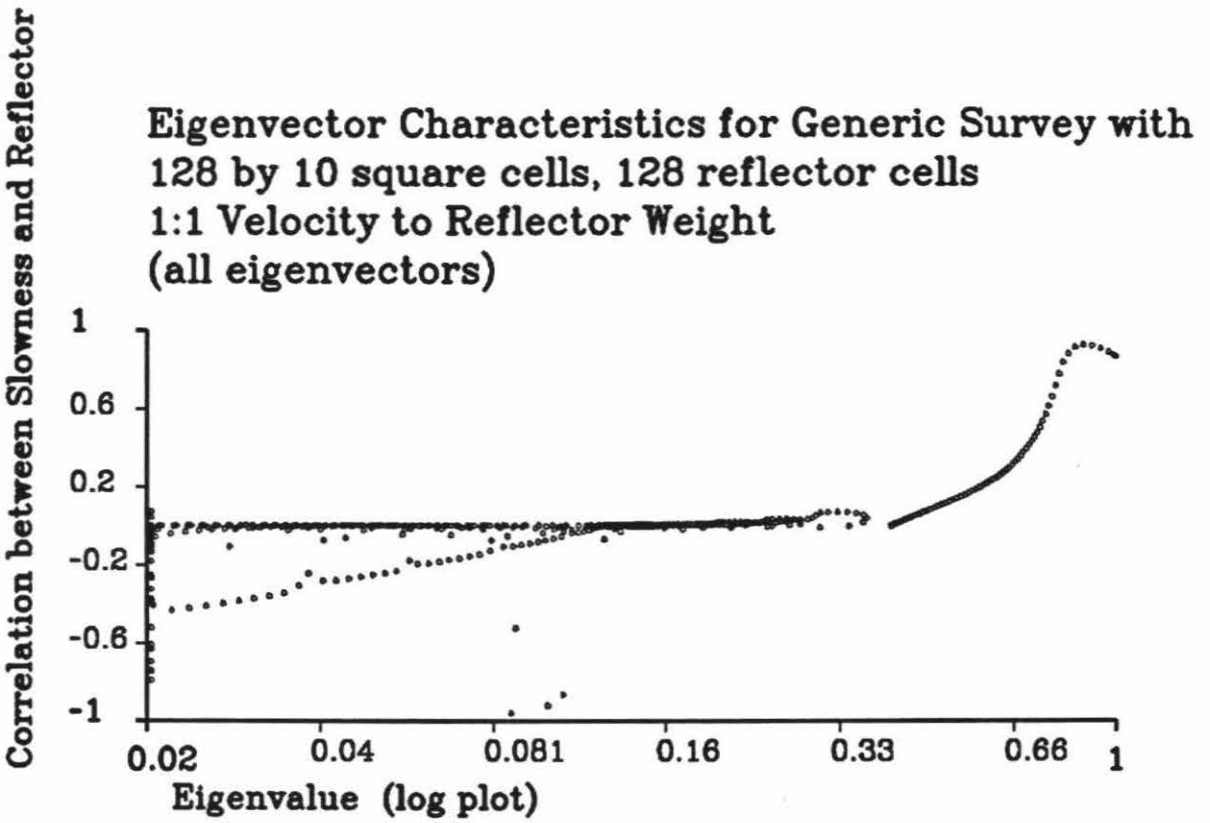
Eigenvector Characteristics for Generic Survey with
128 by 10 square cells, 128 reflector cells
1:1 Velocity to Reflector Weight
(all eigenvectors)
Correlation between Slowness and Reflector
1
0.6
0.2
-0.2
-0.6
-1
0.02
0.04
0.081
0.16
0.33
0.66
1
Eigenvalue (log plot)

Figure 4.7G & H

Vertical wavenumber is plotted versus horizontal wavenumber for each eigenvector. The eigenvectors are separated into those with eigenvalues greater than 0.1 for the upper figure and smaller than 0.1 for the lower figure.

The plots have almost no overlap with the larger eigenvalues having greater horizontal wavenumbers. This result is a manifestation of the smearing from limited angular ray coverage. The eigenvectors of the lower figure correspond to velocity variations that are wider than they are high.

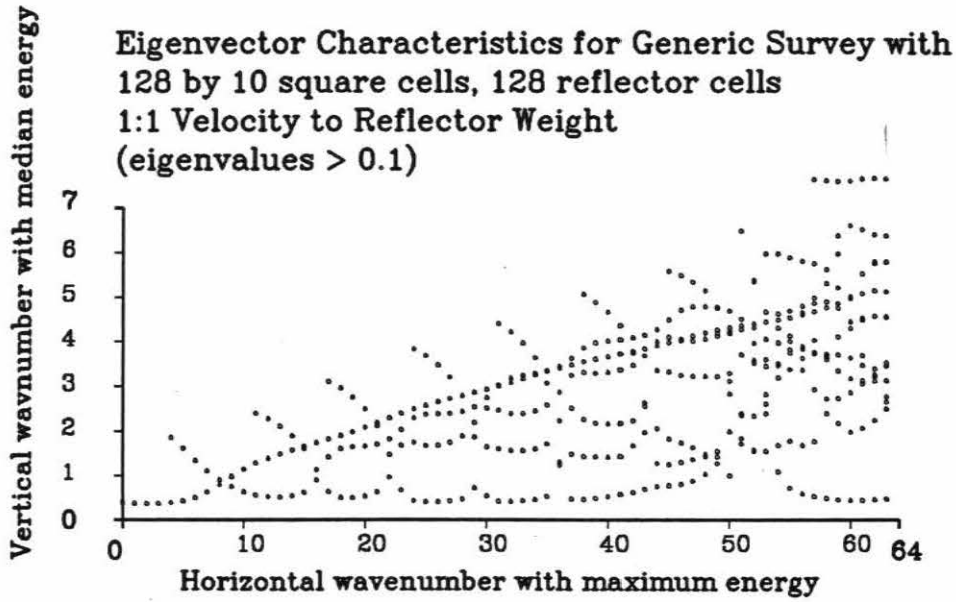
Eigenvector Characteristics for Generic Survey with
128 by 10 square cells, 128 reflector cells
1:1 Velocity to Reflector Weight
(eigenvalues > 0.1)
Vertical wavnumber with median energy
0
1
2
3
4
5
6
7
0
10
20
30
40
50
60
64
Horizontal wavenumber with maximum energy

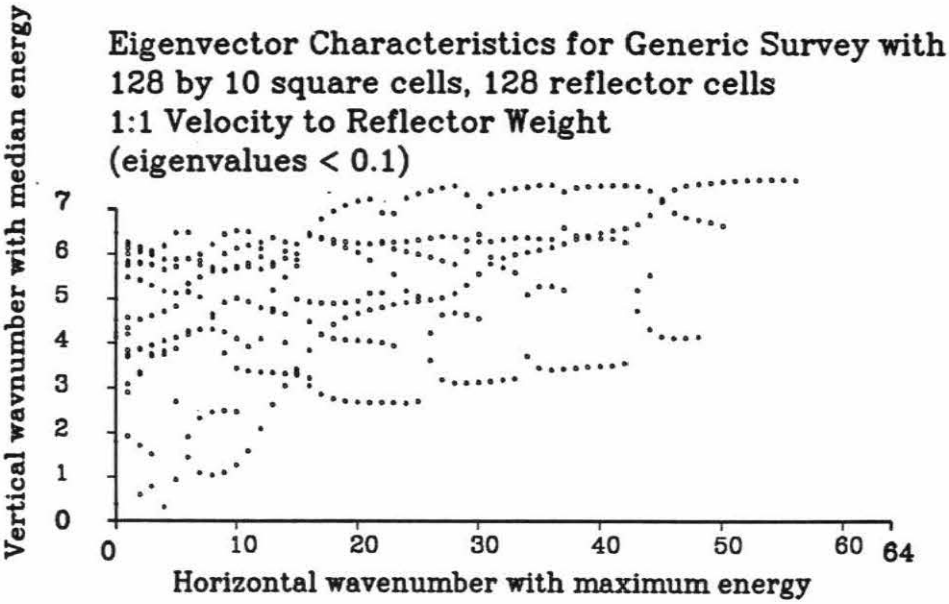
Eigenvector Characteristics for Generic Survey with
128 by 10 square cells, 128 reflector cells
1:1 Velocity to Reflector Weight
(eigenvalues < 0.1)
Vertical wavnumber with median energy
0
1
2
3
4
5
6
7
0
10
20
30
40
50
60
64
Horizontal wavenumber with maximum energy

Figure 4.7I & J

The horizontal wavenumber of each eigenvector plotted against eigenvalue shows clear trends. This plot can be correlated with the four separate groups of eigenvectors in earlier figures. See text for further discussion.

Eigenvector Characteristics for Generic Survey with
128 by 10 square cells, 128 reflector cells
1:1 Velocity to Reflector Weight
(all eigenvectors)

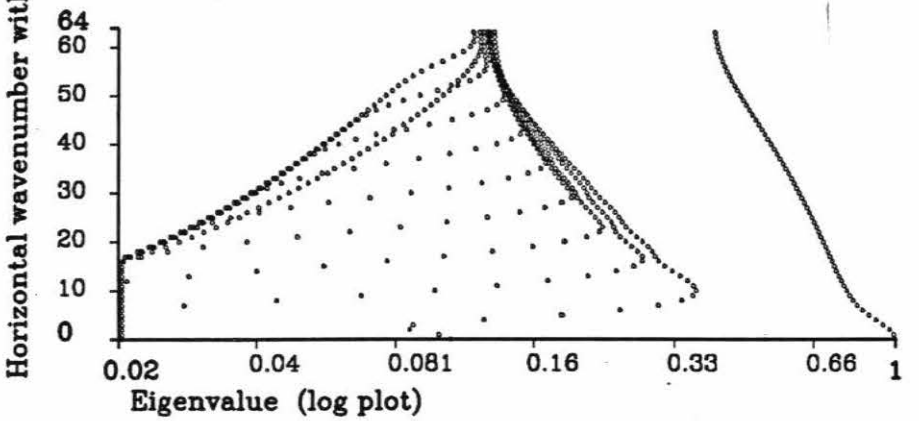

Eigenvector Characteristics for Generic Survey with
128 by 10 square cells, 128 reflector cells
1:1 Velocity to Reflector Weight
(all eigenvectors)

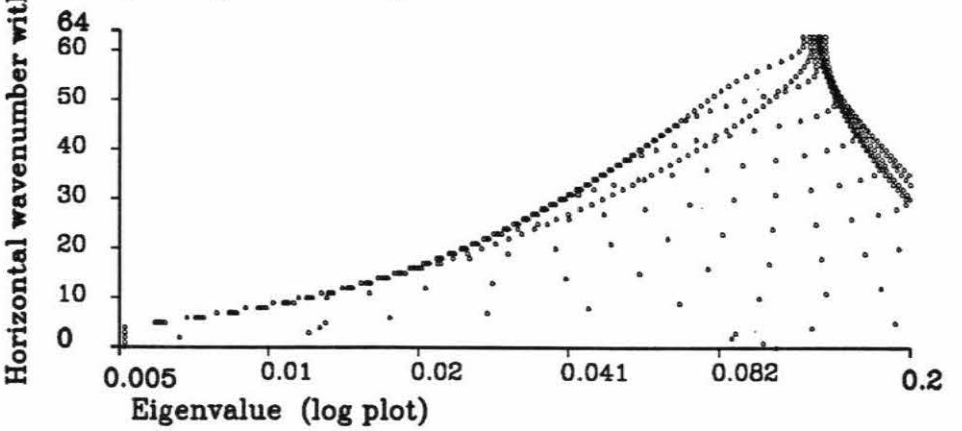

Figure 4.7K & L

The horizontal wavenumbers for only those eigenvectors with a significant reflector component. The group with large eigenvalue in the upper figure represents the constructive interference of velocity and reflector depth. The lower group represents the velocity-reflector depth ambiguity.

The lower figure shows that some eigenvectors with low wavenumbers have very small eigenvalue. Figure **4.12** demonstrates that the increasing eigenvalue of the branch above wavenumber of 6 is an artifact of the large cell sizes since smaller reflector variations cannot have larger eigenvalues than larger ones. Thus most all of the velocity-reflector depth ambiguity has eigenvalues less than 0.01 making them unresolved.

Eigenvector Characteristics for Generic Survey with
128 by 10 square cells, 128 reflector cells
1:1 Velocity to Reflector Weight
(eigenvectors with measurable reflector energy)

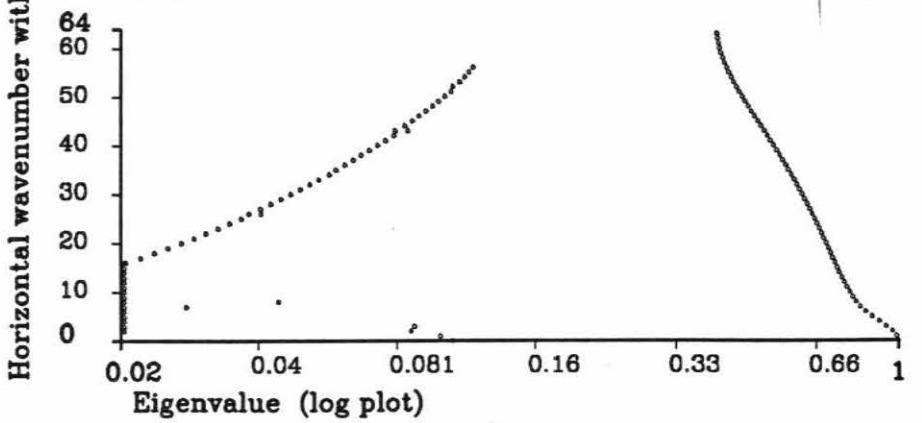

Eigenvector Characteristics for Generic Survey with
128 by 10 square cells, 128 reflector cells
1:1 Velocity to Reflector Weight
(eigenvectors with measurable reflector energy)

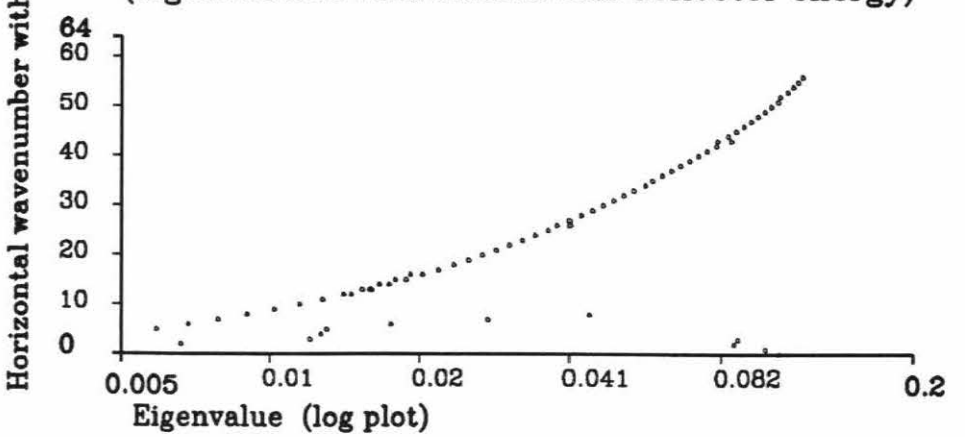

Figure 4.7M & N

The horizontal wavenumbers for those eigenvectors with no reflector components. A possible meaning of individual branches is suggested in the following figures.

Eigenvector Characteristics for Generic Survey with
128 by 10 square cells, 128 reflector cells
1:1 Velocity to Reflector Weight
(eigenvectors with no measurable reflector energy)

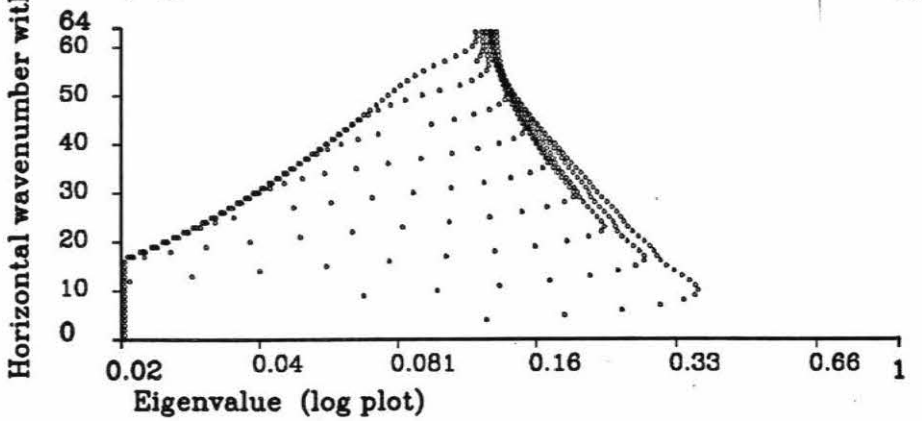

Eigenvector Characteristics for Generic Survey with
128 by 10 square cells, 128 reflector cells
1:1 Velocity to Reflector Weight
(eigenvectors with no measurable reflector energy)

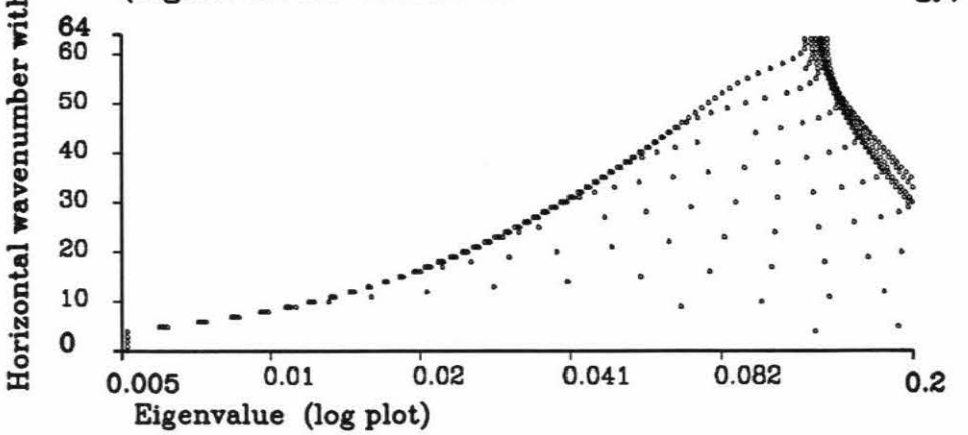

Figure 4.7O & P

The horizontal wavenumbers for only those eigenvectors within a certain range of vertical wavenumbers. The plots suggest that the individual branches of the previous figures correspond to the type vertical variations in the eigenvector.

Vertical wavenumber is well defined for the eigenvectors since they are only 10 points high and are not circular in the vertical direction.

Eigenvector Characteristics for Generic Survey with
128 by 10 square cells, 128 reflector cells
1:1 Velocity to Reflector Weight
(Vertical Wavenumbers < 1.2)

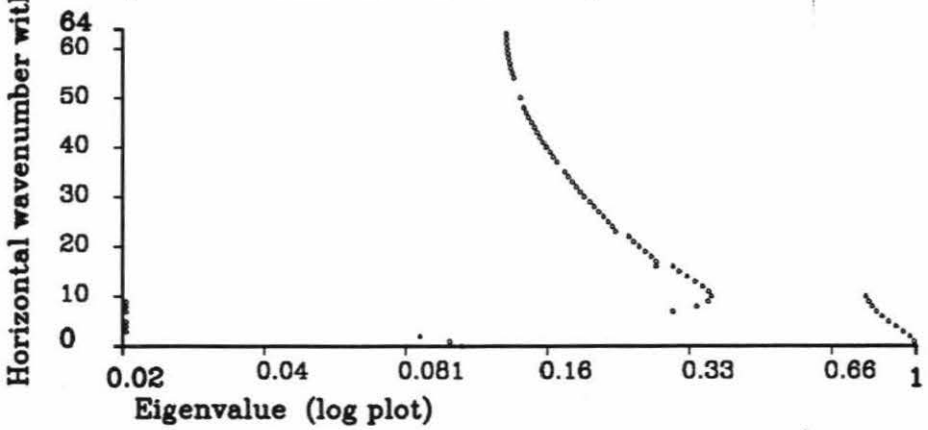

Eigenvector Characteristics for Generic Survey with
128 by 10 square cells, 128 reflector cells
1:1 Velocity to Reflector Weight
(2.1 > Vertical Wavenumber > 1.2)

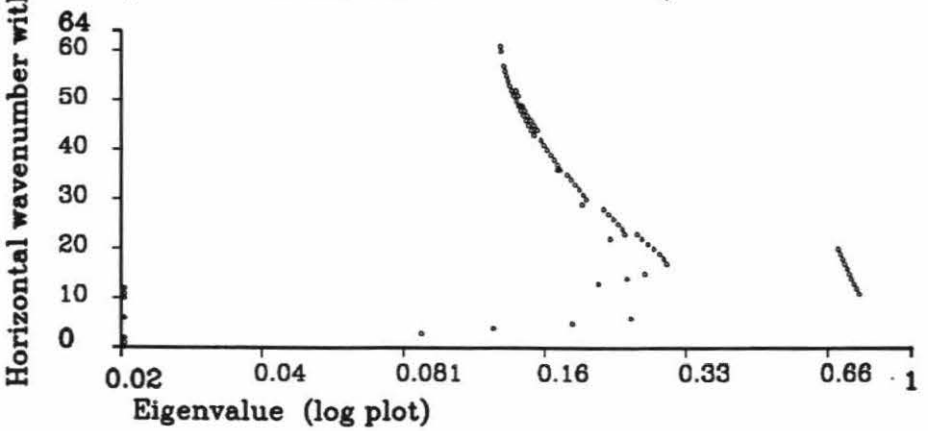

Figure 4.7Q

The horizontal wavenumbers over another range of vertical wavenumber. See previous figure for discussion.

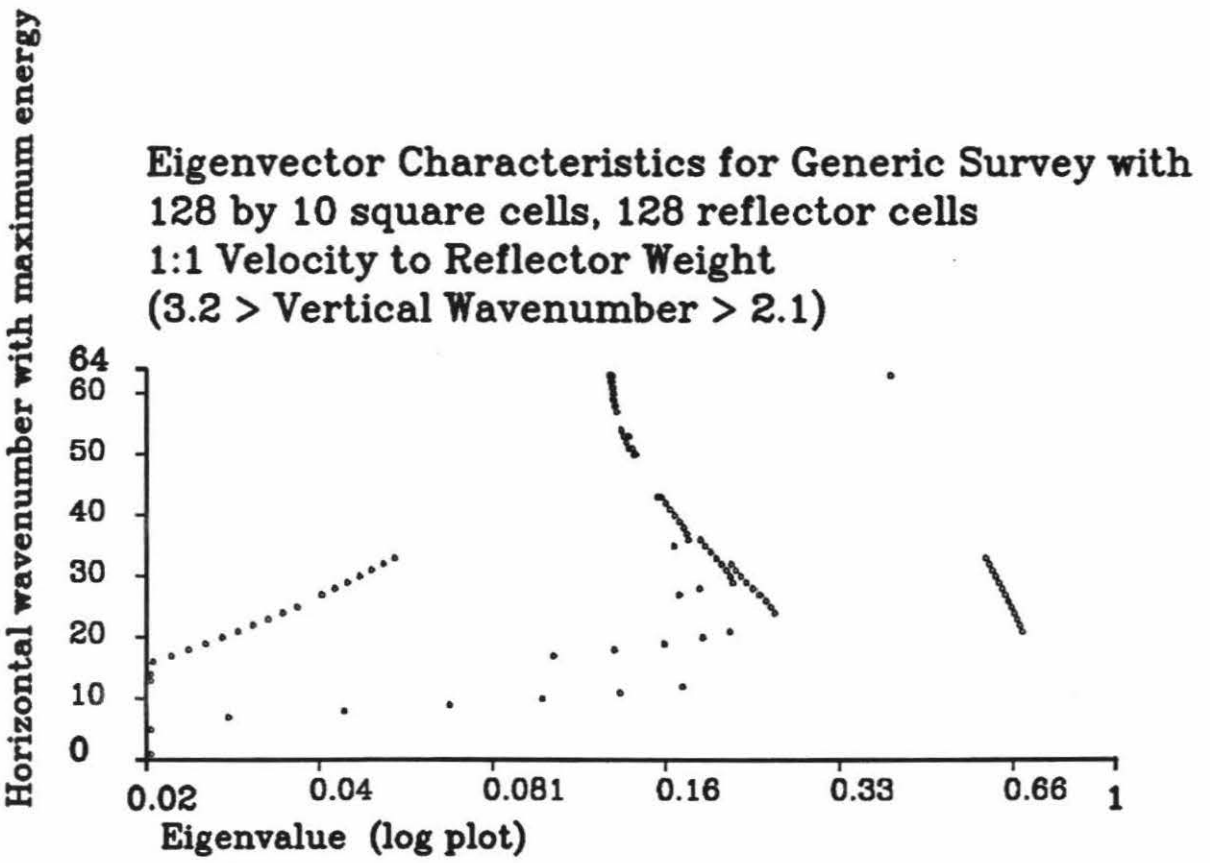
Eigenvector Characteristics for Generic Survey with
128 by 10 square cells, 128 reflector cells
1:1 Velocity to Reflector Weight
(3.2 > Vertical Wavenumber > 2.1)
Horizontal wavenumber with maximum energy
64
60
50
40
30
20
10
0
0.02
0.04
0.081
0.16
0.33
0.66
1
Eigenvalue (log plot)

Figure 4.8A & B

Eigenvectors of the generic model corresponding to the constructive interference between velocity and reflector depth. These eigenvectors are of the first group seen in Figures **4.7d & e**, which is similar to the eigenvector of (1, 1) for the two parameter model.

Eigenvector Number 4 with Eigenvalue: 0.952
for a Generic Survey of 128 by 10 square Cells
& 4:1 Velocity to Reflector Weight

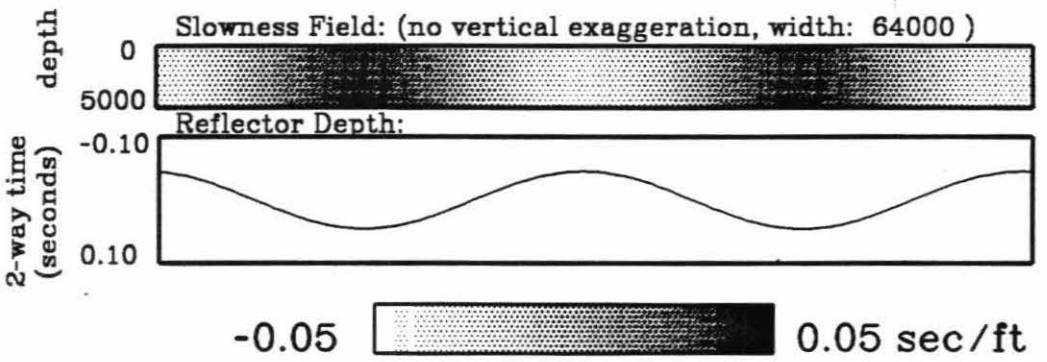

Eigenvector Number 8 with Eigenvalue: 0.845
for a Generic Survey of 128 by 10 square Cells
& 4:1 Velocity to Reflector Weight

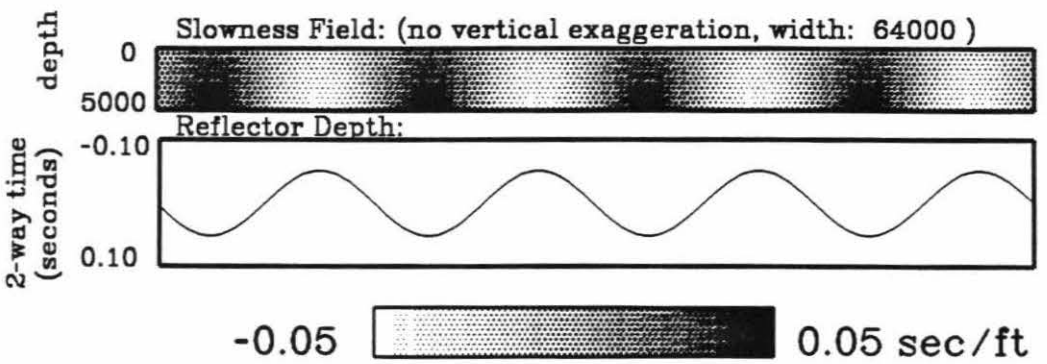

Figure 4.8C

Eigenvector of the generic model corresponding to the constructive interference between velocity and reflector depth.

Eigenvector Number 28 with Eigenvalue: 0.552
for a Generic Survey of 128 by 10 square Cells
& 4:1 Velocity to Reflector Weight

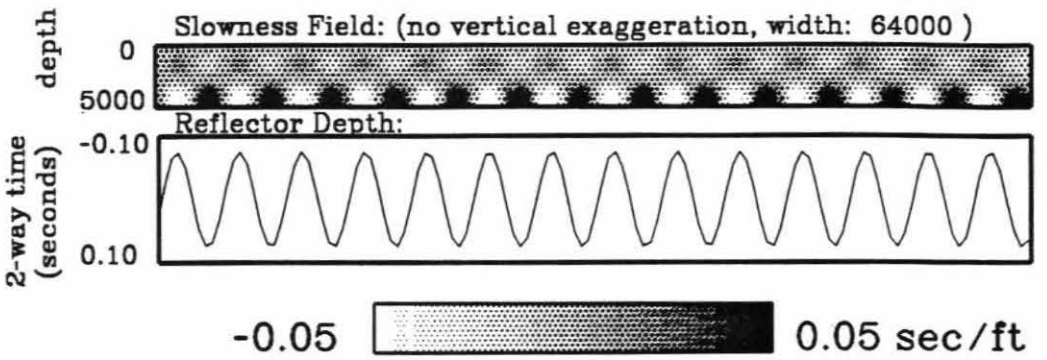

Figure 4.9A & B

Eigenvectors of the generic model of the second group seen in Figures **4.7d & e**. These eigenvectors consist of velocity variations that do not affect reflector depths.

Eigenvector Number 82 with Eigenvalue: 0.392
for a Generic Survey of 128 by 10 square Cells
& 4:1 Velocity to Reflector Weight

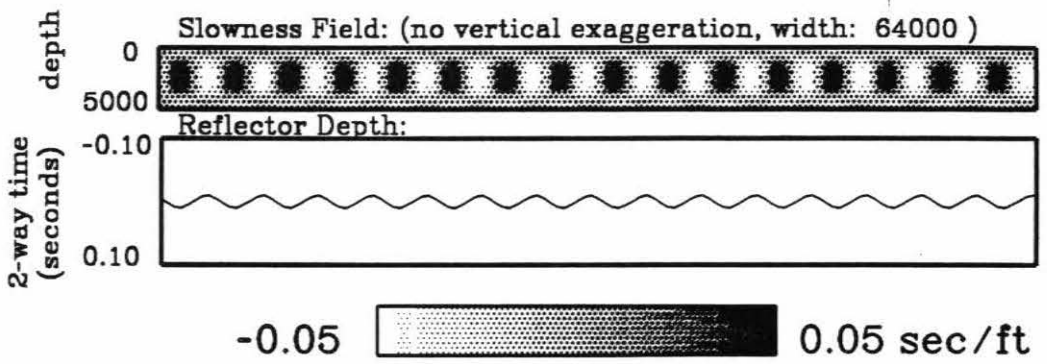

Eigenvector Number 86 with Eigenvalue: 0.382
for a Generic Survey of 128 by 10 square Cells
& 4:1 Velocity to Reflector Weight

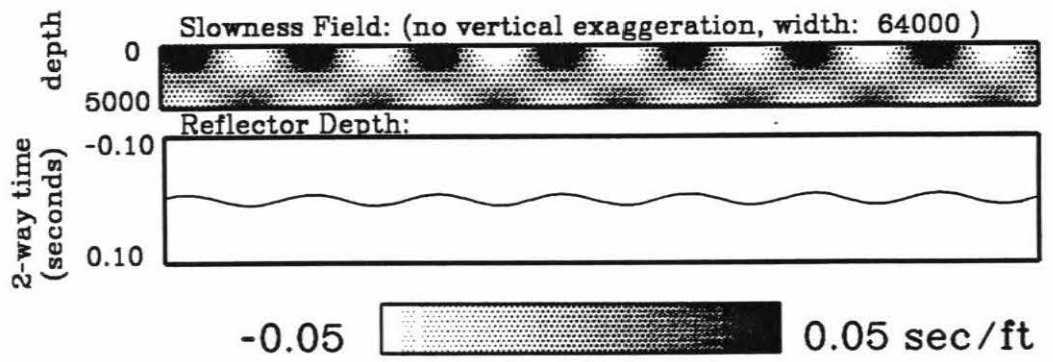

Figure 4.9C & D

Eigenvectors of the generic model with velocity variations that do not affect reflector depths.

Eigenvector Number 691 with Eigenvalue: 0.159
for a Generic Survey of 128 by 10 square Cells
& 4:1 Velocity to Reflector Weight

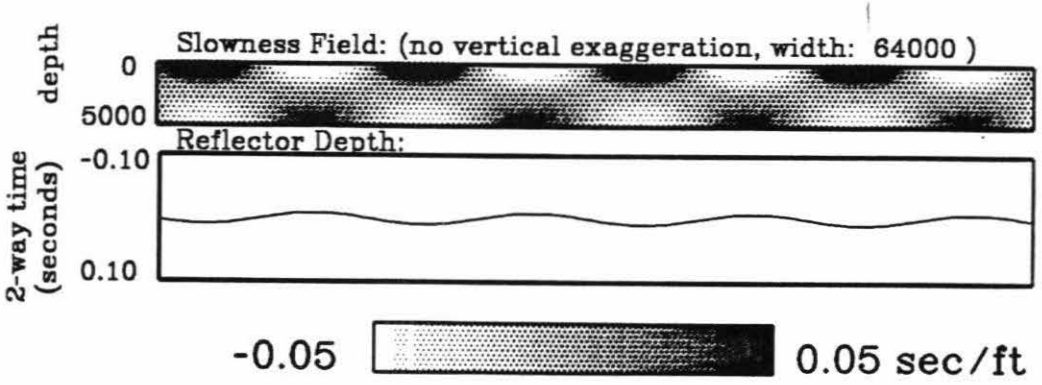

Eigenvector Number 44 with Eigenvalue: 0.47
for a Generic Survey of 128 by 10 square Cells
& 4:1 Velocity to Reflector Weight

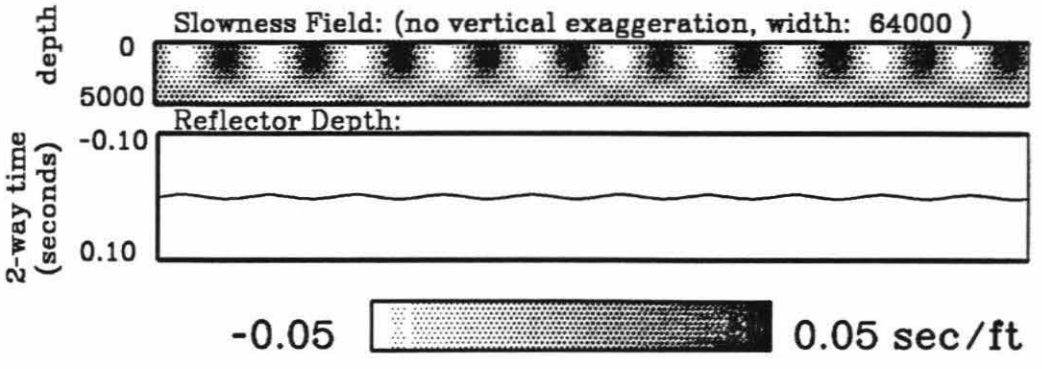

Figure 4.10A & B

Eigenvectors with velocity-reflector depth ambiguity. These correspond to the 2 parameter eigenvector of (1, -1). This group is the one of Figures **4.7d & e** with eigenvalue below 0.1, but with a reflector component of the eigenvector.

Eigenvector Number 804 with Eigenvalue: 0.0982
for a Generic Survey of 128 by 10 square Cells
& 4:1 Velocity to Reflector Weight

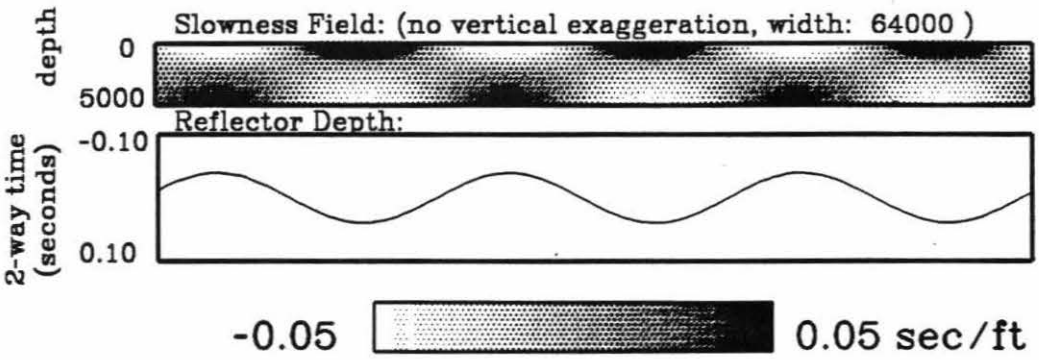

Eigenvector Number 875 with Eigenvalue: 0.0724
for a Generic Survey of 128 by 10 square Cells
& 4:1 Velocity to Reflector Weight

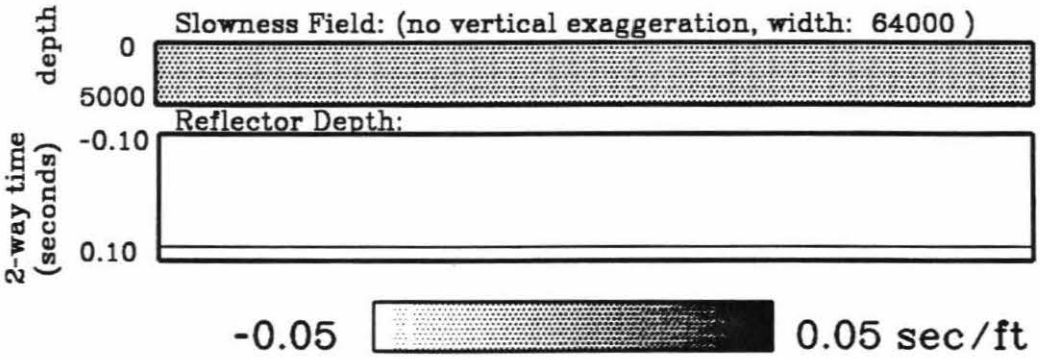

Figure 4.10C & D

Eigenvectors with velocity-reflector depth ambiguity.

Eigenvector Number 895 with Eigenvalue: 0.0689
for a Generic Survey of 128 by 10 square Cells
& 4:1 Velocity to Reflector Weight

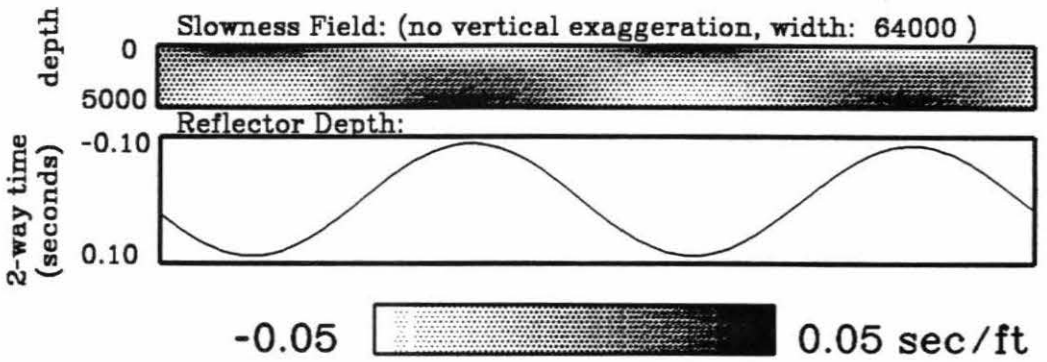

Eigenvector Number 897 with Eigenvalue: 0.0688
for a Generic Survey of 128 by 10 square Cells
& 4:1 Velocity to Reflector Weight

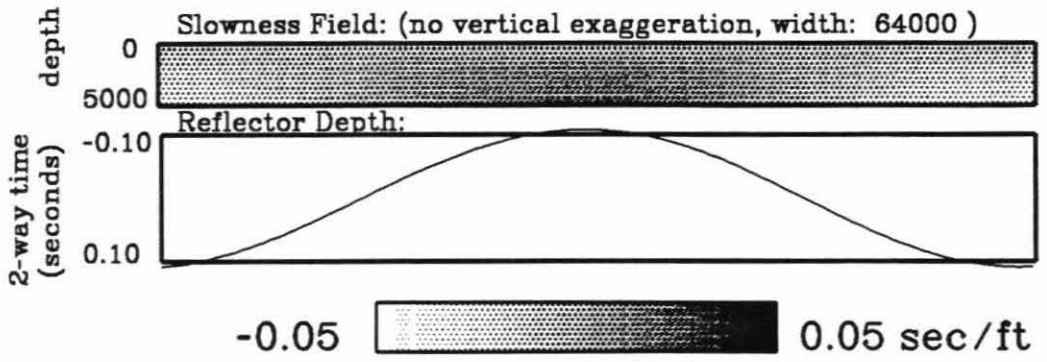

Figure 4.10E & F

Eigenvectors with velocity-reflector depth ambiguity.

Eigenvector Number 1109 with Eigenvalue: 0.0299
for a Generic Survey of 128 by 10 square Cells
& 4:1 Velocity to Reflector Weight

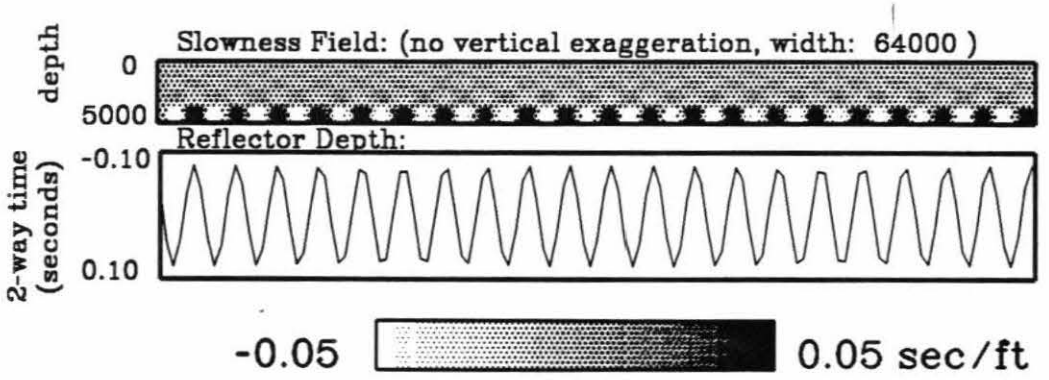

Eigenvector Number 1193 with Eigenvalue: 0.0206
for a Generic Survey of 128 by 10 square Cells
& 4:1 Velocity to Reflector Weight

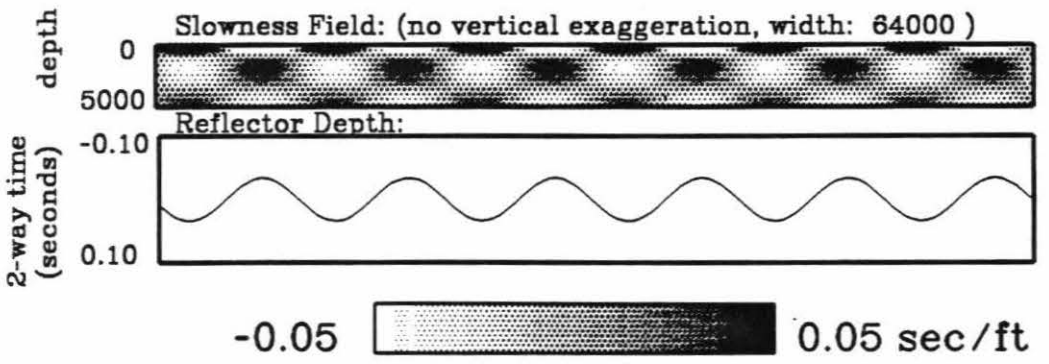

Figure 4.10G & H

Eigenvectors with velocity-reflector depth ambiguity.

Eigenvector Number 1255 with Eigenvalue: 0.0137
for a Generic Survey of 128 by 10 square Cells
& 4:1 Velocity to Reflector Weight

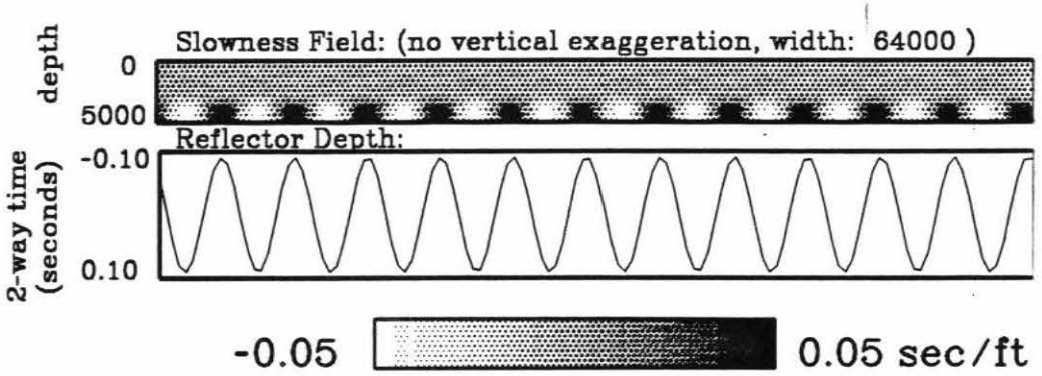

Eigenvector Number 1259 with Eigenvalue: 0.0131
for a Generic Survey of 128 by 10 square Cells
& 4:1 Velocity to Reflector Weight

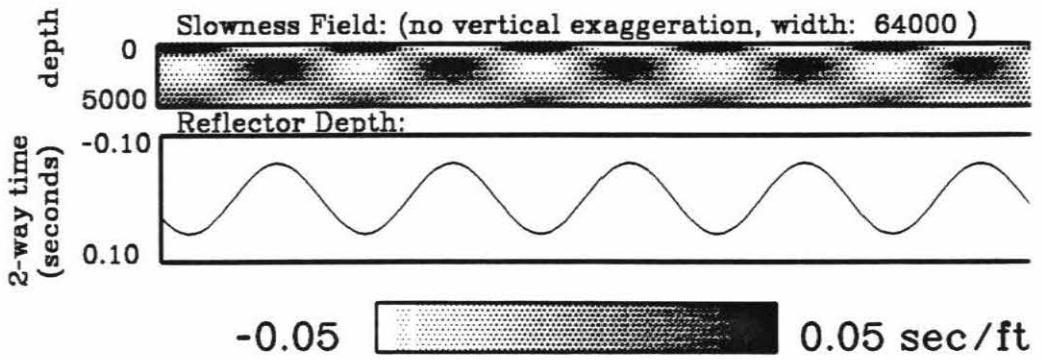

Figure 4.10I & J

Eigenvectors with velocity-reflector depth ambiguity.

Eigenvector Number 1289 with Eigenvalue: 0.0108
for a Generic Survey of 128 by 10 square Cells
& 4:1 Velocity to Reflector Weight

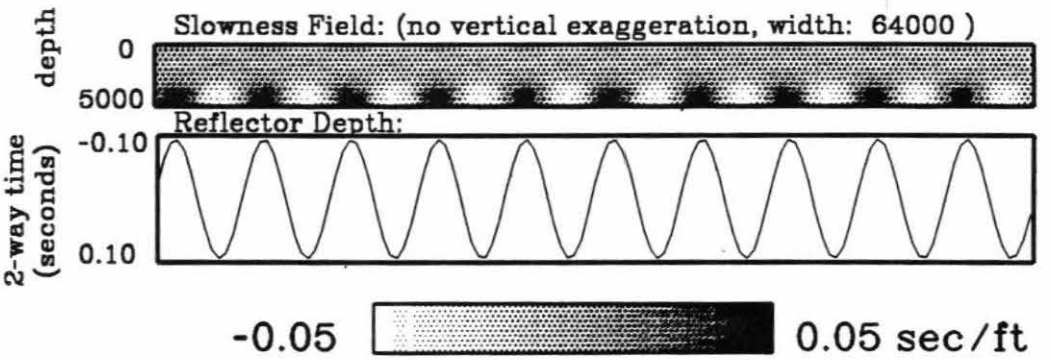

Eigenvector Number 1291 with Eigenvalue: 0.0101
for a Generic Survey of 128 by 10 square Cells
& 4:1 Velocity to Reflector Weight

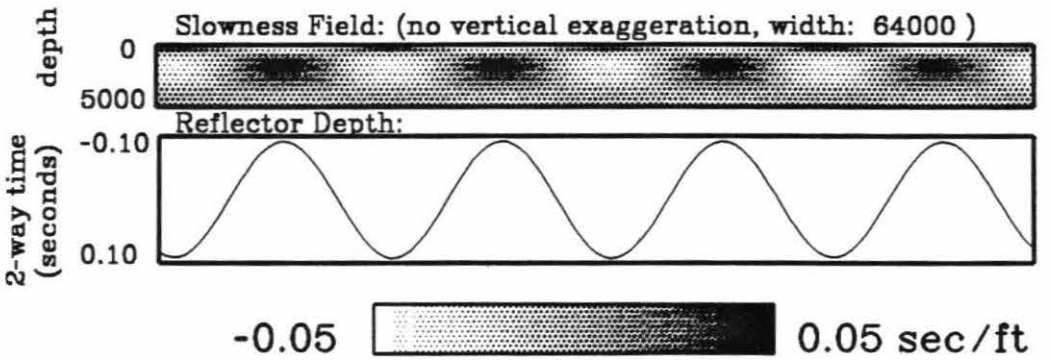

Figure 4.10K & L

Eigenvectors with velocity-reflector depth ambiguity.

Eigenvector Number 1293 with Eigenvalue: 0.00988
for a Generic Survey of 128 by 10 square Cells
& 4:1 Velocity to Reflector Weight

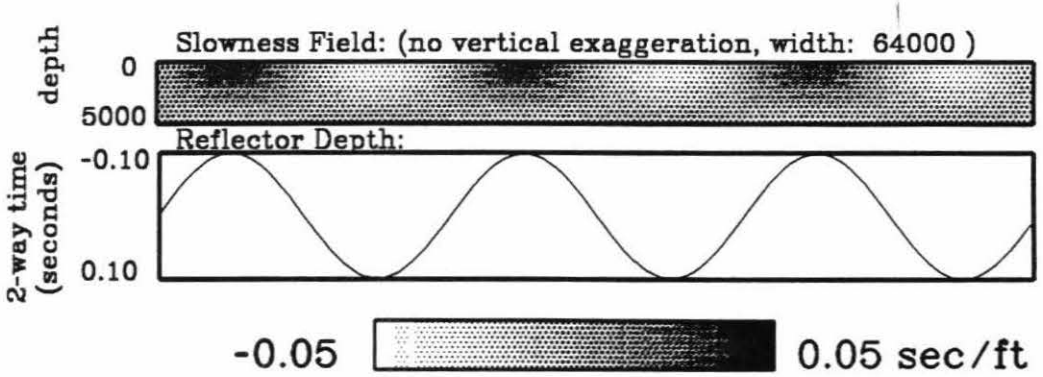

Eigenvector Number 1313 with Eigenvalue: 0.00814
for a Generic Survey of 128 by 10 square Cells
& 4:1 Velocity to Reflector Weight

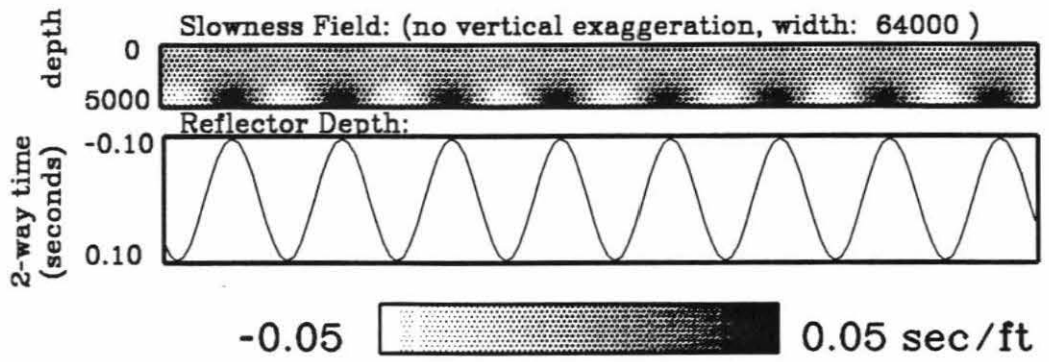

Figure 4.10M & N

Eigenvectors with velocity-reflector depth ambiguity.

Eigenvector Number 1327 with Eigenvalue: 0.00735
for a Generic Survey of 128 by 10 square Cells
& 4:1 Velocity to Reflector Weight

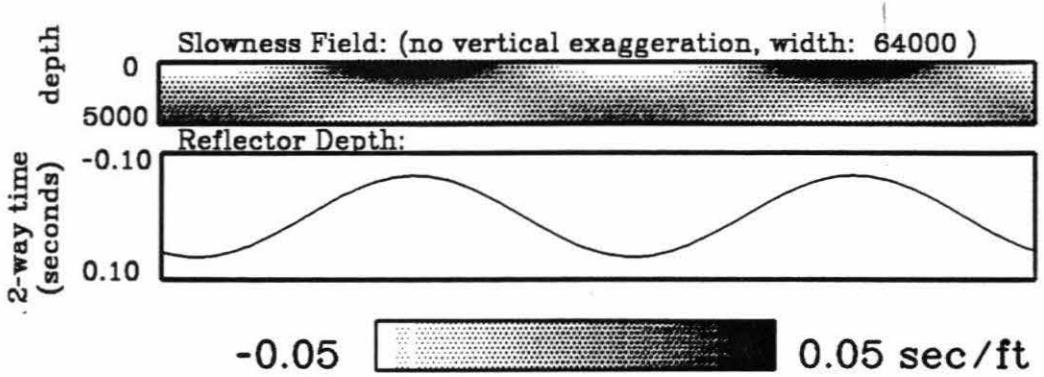

Eigenvector Number 1329 with Eigenvalue: 0.00703
for a Generic Survey of 128 by 10 square Cells
& 4:1 Velocity to Reflector Weight

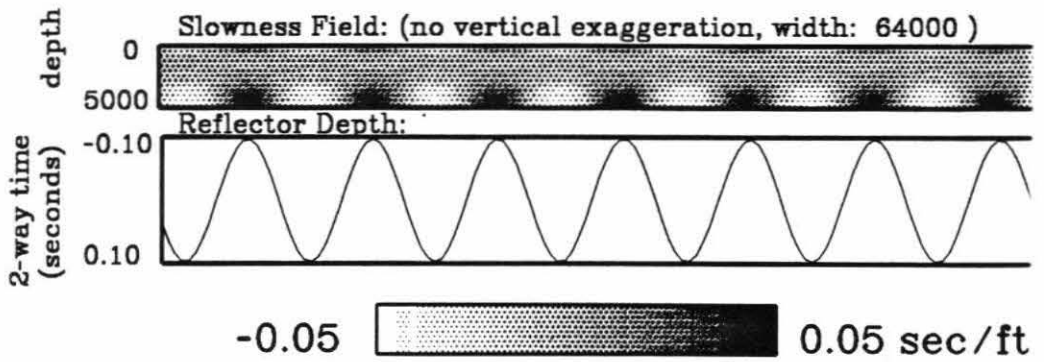

Figure 4.10O & P

Eigenvectors with velocity-reflector depth ambiguity.

Eigenvector Number 1345 with Eigenvalue: 0.00626
for a Generic Survey of 128 by 10 square Cells
& 4:1 Velocity to Reflector Weight

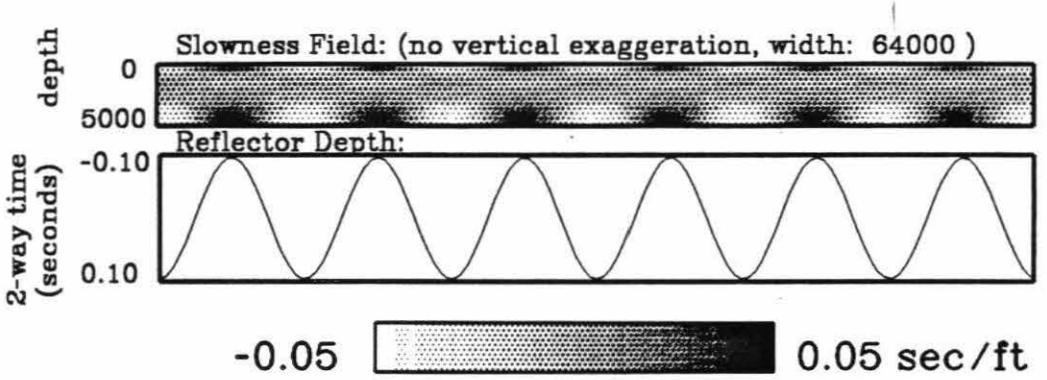

Eigenvector Number 1347 with Eigenvalue: 0.0061
for a Generic Survey of 128 by 10 square Cells
& 4:1 Velocity to Reflector Weight

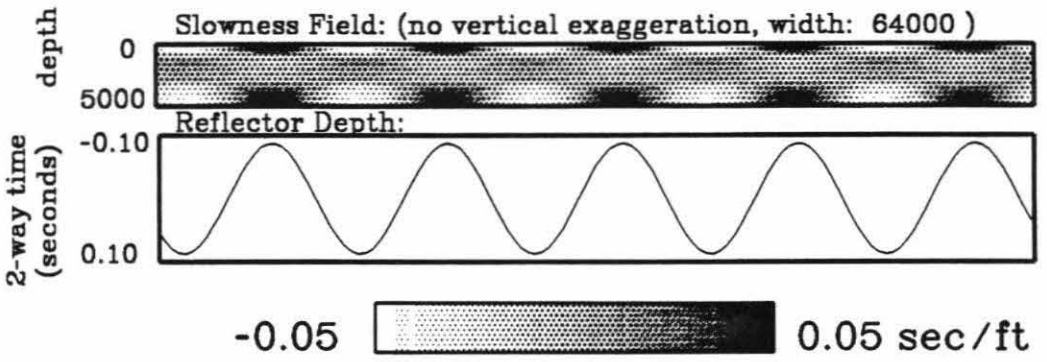

Figure 4.11A & B

Eigenvectors with small eigenvalue and without reflector components. These eigenvectors correspond to the unresolved wavenumber spectrum that cause vertical smearing from the limited angular ray coverage.

The distinction between this group and the other without reflector components but higher eigenvalue is demonstrated by these two eigenvectors. Even though they are very similar, they have very different eigenvalues. The upper eigenvector has 10 horizontal wavelengths across the model, while the lower has only 9. The fewer wavelengths for the lower model corresponds to velocity variations that are slightly wider, demonstrates the boundary between the two groups. The two eigenvectors straddle the transition line in Figure **3.3** between the resolved and unresolved regions.

Eigenvector Number 761 with Eigenvalue: 0.122
for a Generic Survey of 128 by 10 square Cells
& 4:1 Velocity to Reflector Weight

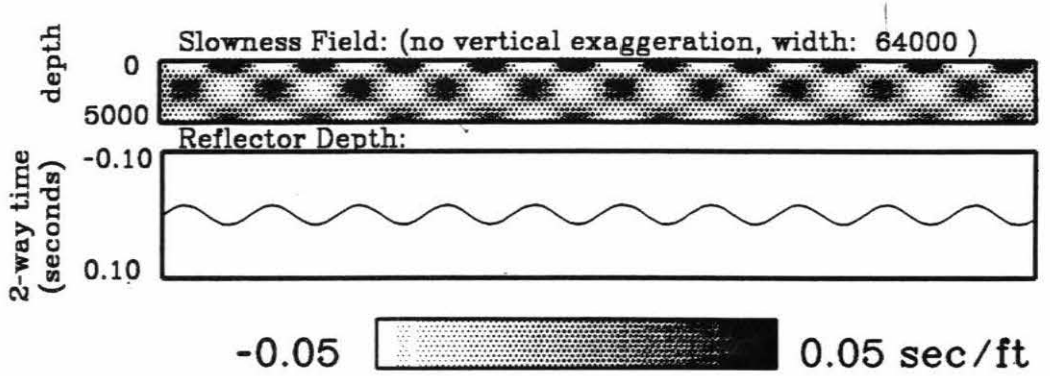

Eigenvector Number 838 with Eigenvalue: 0.0843
for a Generic Survey of 128 by 10 square Cells
& 4:1 Velocity to Reflector Weight

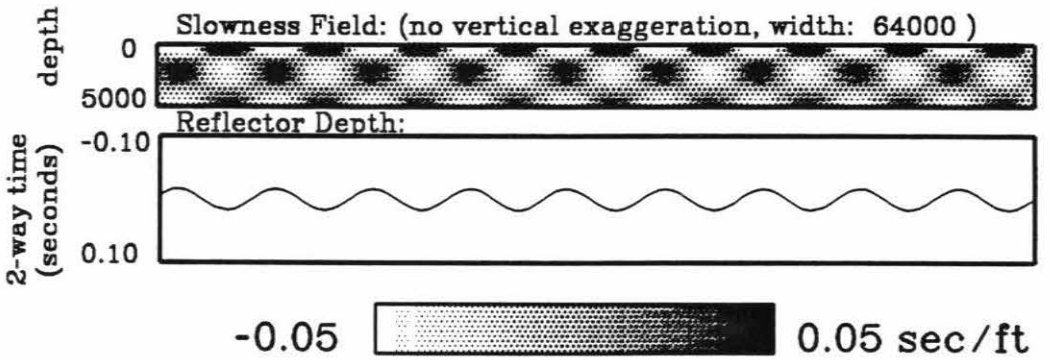

Figure 4.11C & D

Eigenvectors with small eigenvalue and without reflector components.

Eigenvector Number 1063 with Eigenvalue: 0.0364
for a Generic Survey of 128 by 10 square Cells
& 4:1 Velocity to Reflector Weight

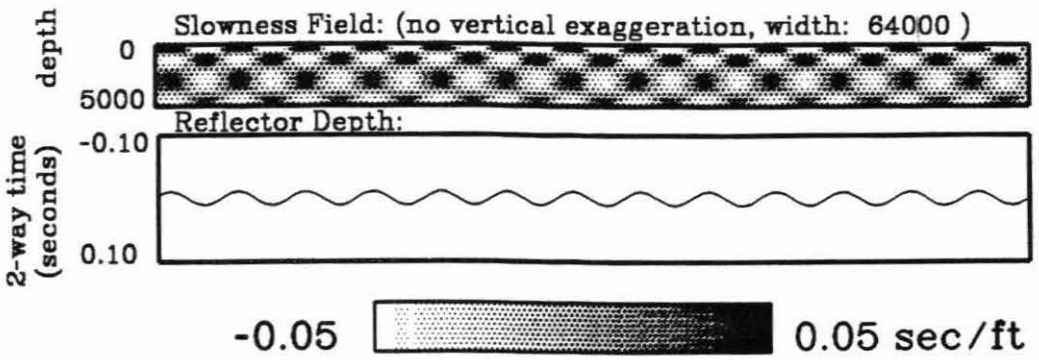

Eigenvector Number 1311 with Eigenvalue: 0.0082
for a Generic Survey of 128 by 10 square Cells
& 4:1 Velocity to Reflector Weight

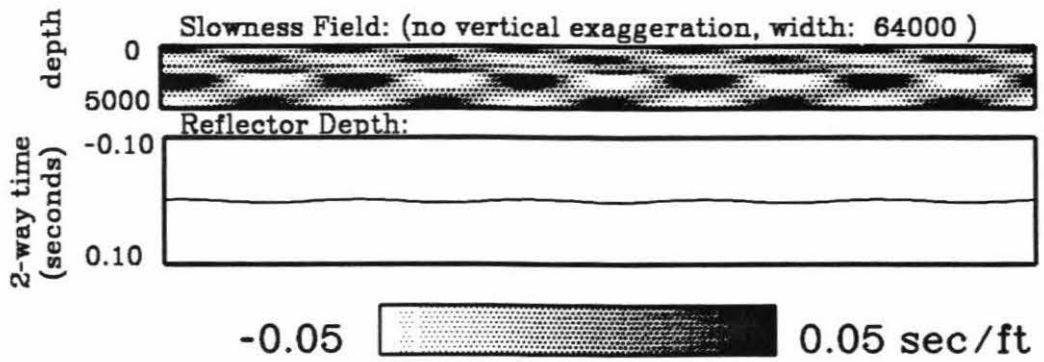

Figure 4.11E & F

Eigenvectors with small eigenvalue and without reflector components.

Eigenvector Number 1354 with Eigenvalue: 0.00483
for a Generic Survey of 128 by 10 square Cells
& 4:1 Velocity to Reflector Weight

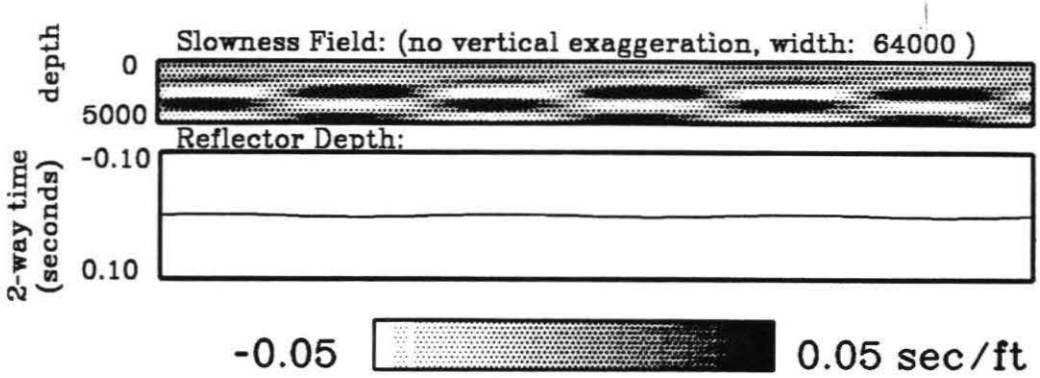

Eigenvector Number 1368 with Eigenvalue: 0.00324
for a Generic Survey of 128 by 10 square Cells
& 4:1 Velocity to Reflector Weight

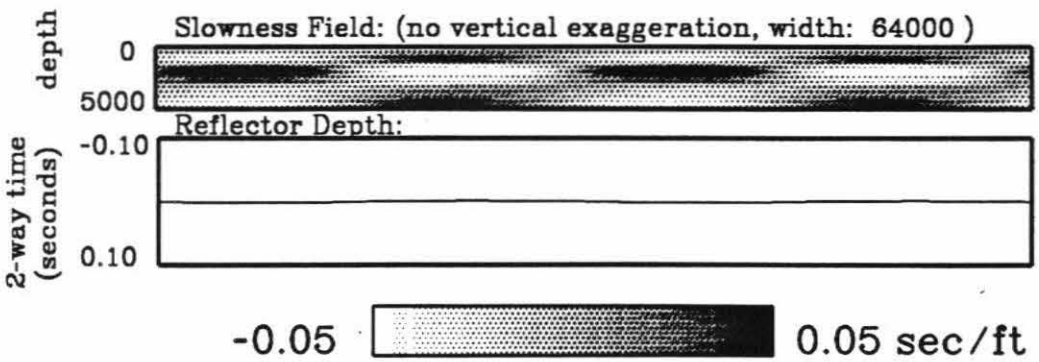

Figure 4.11G & H

Eigenvectors with small eigenvalue and without reflector components.

Eigenvector Number 1382 with Eigenvalue: 0.00245
for a Generic Survey of 128 by 10 square Cells
& 4:1 Velocity to Reflector Weight

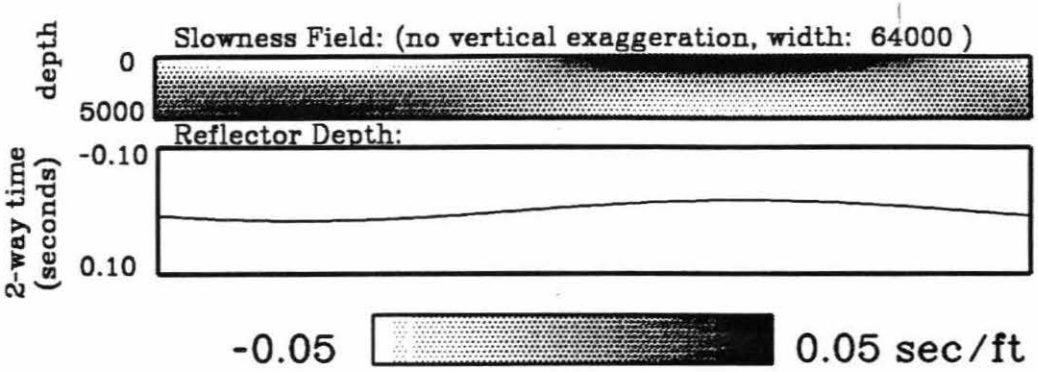

Eigenvector Number 1386 with Eigenvalue: 0.00163
for a Generic Survey of 128 by 10 square Cells
& 4:1 Velocity to Reflector Weight

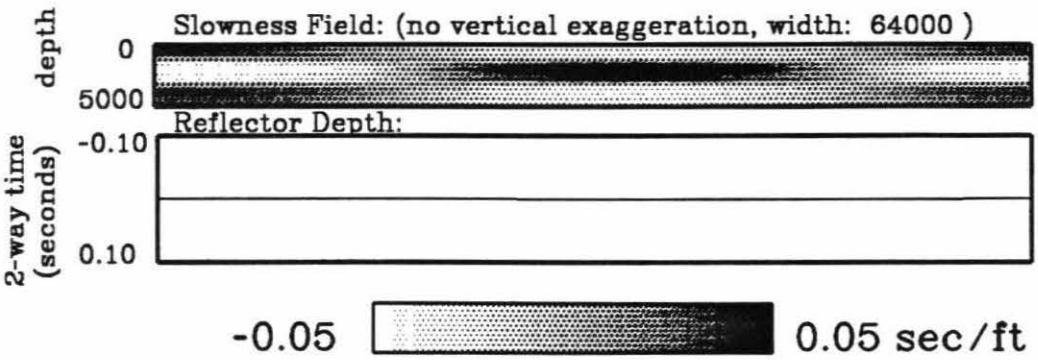

Figure 4.11I & J

Eigenvectors with small eigenvalue and without reflector components.

Eigenvector Number 1400 with Eigenvalue: 0.000249
for a Generic Survey of 128 by 10 square Cells
& 4:1 Velocity to Reflector Weight

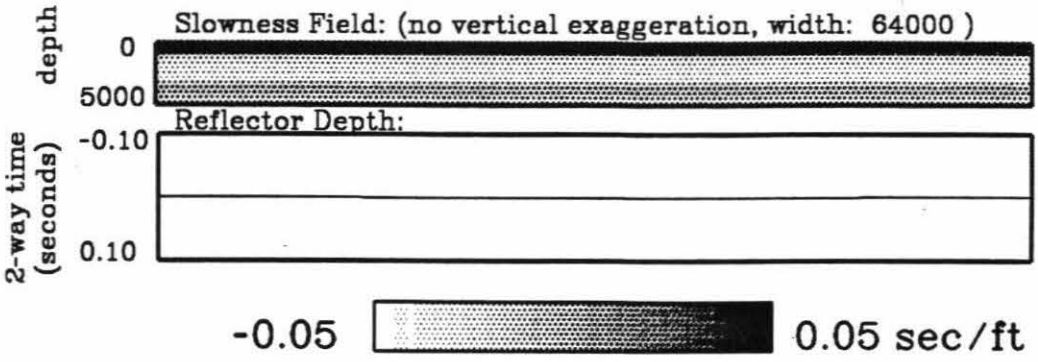

Eigenvector Number 1402 with Eigenvalue: 0.00017
for a Generic Survey of 128 by 10 square Cells
& 4:1 Velocity to Reflector Weight

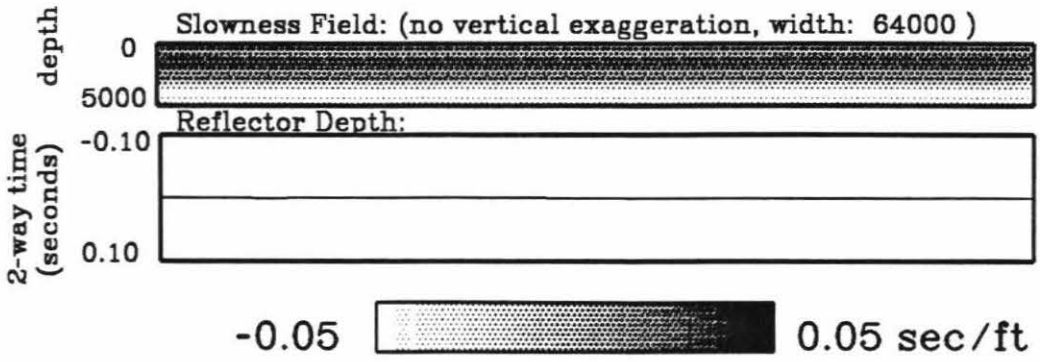

Figure 4.12

Gedanken experiment which demonstrates that smaller scale velocity variations cannot be better resolved than larger ones.

An eigenvector with ambiguous velocity and reflector depth is shrunken in size and additional velocity field is added to fill the void between the surface and reflector. The resolution of the smaller scale velocity variations will be the same if the additional velocity field is not allowed to vary. However, when the velocity field is allowed to vary, it can aid the rest of the velocity field in matching the travel time signature of the reflector variations. Thus the smaller scale reflector variations cannot be better resolved.

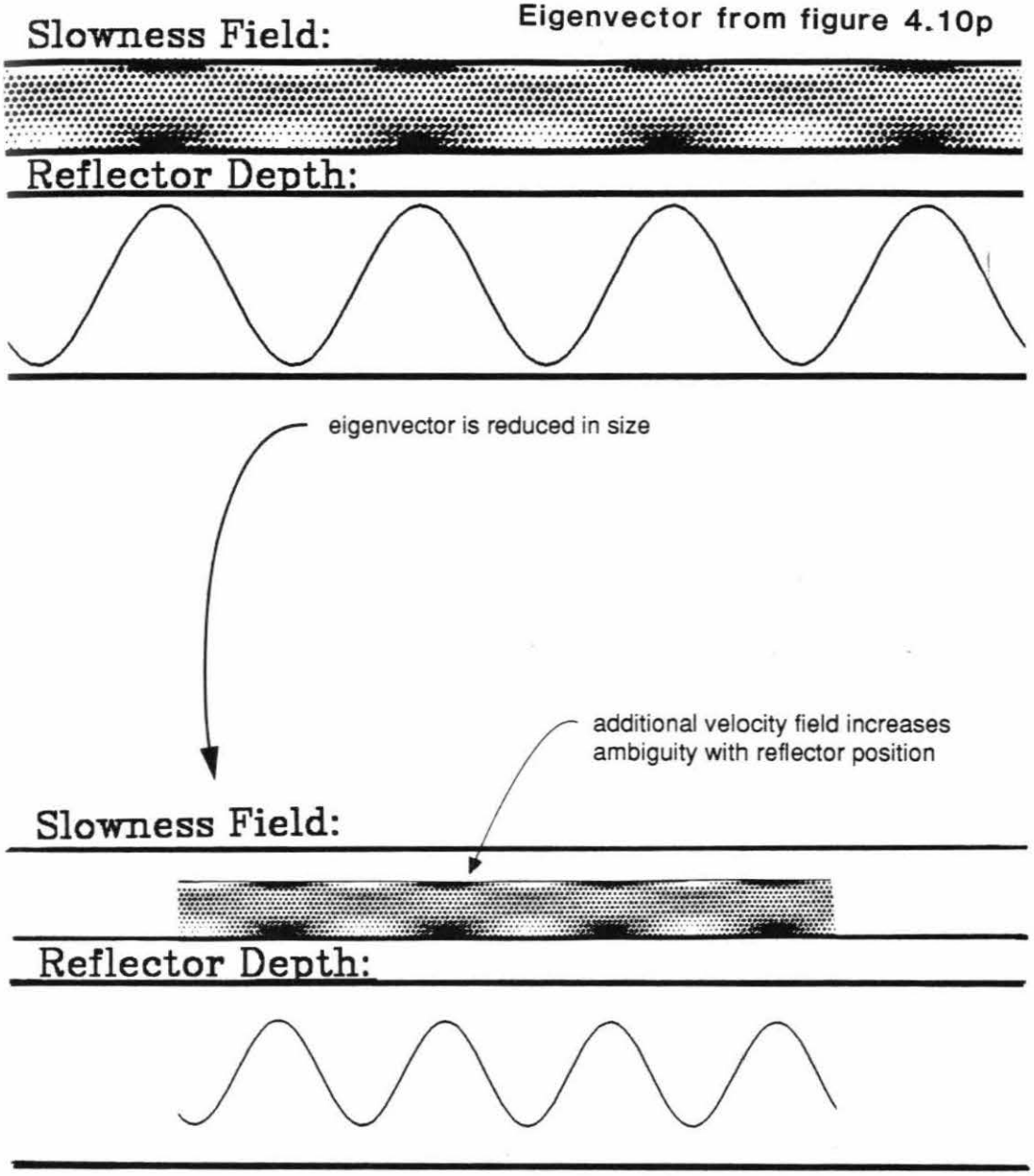

Conclusion: Smaller scale reflector variations cannot be better resolved than larger ones.

Figure 4.13A & B

SVD results using a 4:1 velocity to reflector weight for the generic model. These figures are very similar to those with the 1:1 weight in Figures **4.7i & l.** All of the following models use this 4:1 weight.

Eigenvector Characteristics for Generic Survey with
128 by 10 square cells, 128 reflector cells
4:1 Velocity to Reflector Weight
(all eigenvectors)

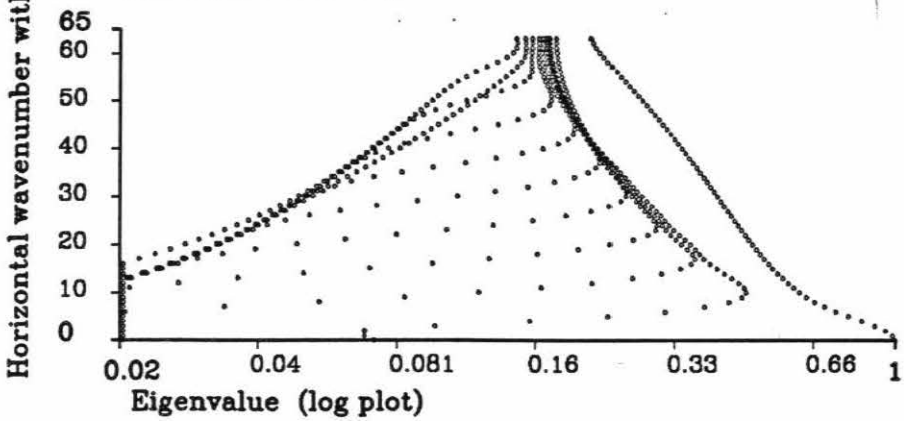

Eigenvector Characteristics for Generic Survey with
128 by 10 square cells, 128 reflector cells
4:1 Velocity to Reflector Weight
(eigenvectors with measurable reflector energy)

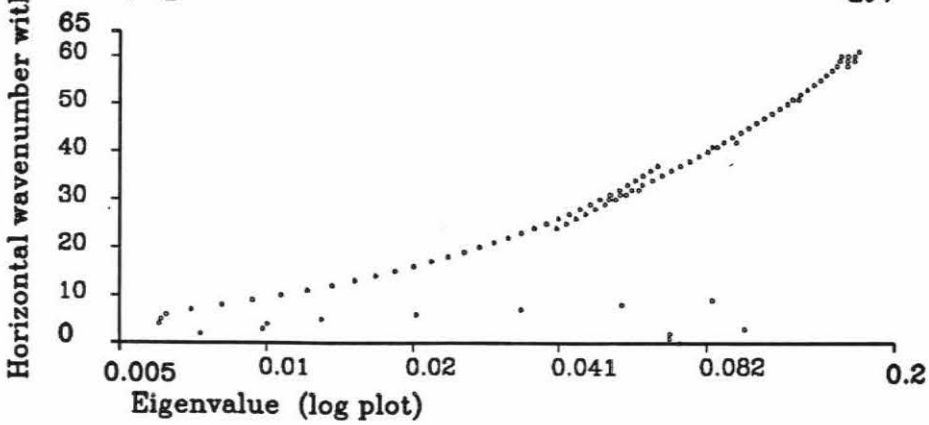

Figure 4.14A & B

SVD results for a model with a strong vertical velocity gradient that doubles the velocity from the surface to the reflector. The cable length is the same as before. The curvature increases the angle of reflection so the maximum is about 60°.

The trends in the upper figure are modified from the previous figure.

The increase of the angles of reflection has increased the eigenvalue of the velocity-reflector depth ambiguity with 0 wavenumber, but reduced those near a wavenumber of 5.

Eigenvector Characteristics for Generic Survey with
128 by 10 square cells, 128 reflector cells
4:1 V-R Weight, Strong Vertical Velocity Gradient
(all eigenvectors)

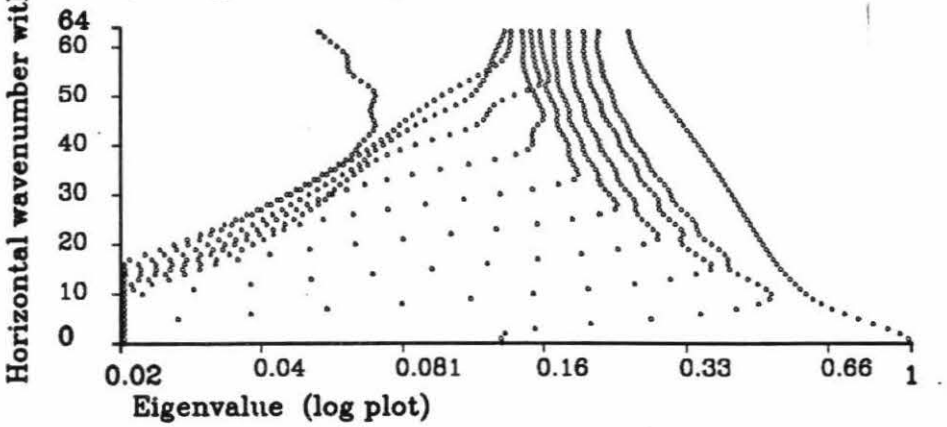

Eigenvector Characteristics for Generic Survey with
128 by 10 square cells, 128 reflector cells
4:1 V-R Weight, Strong Vertical Velocity Gradient
(eigenvectors with measurable reflector energy)

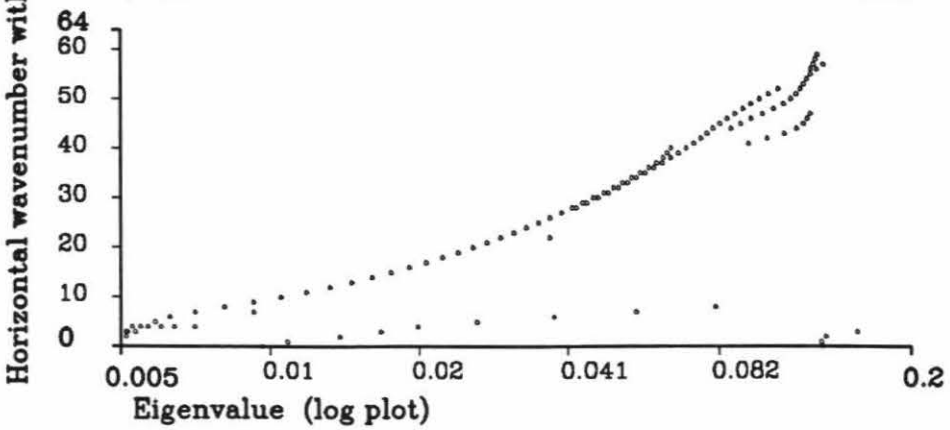

Figure 4.15A

SVD results with the implementation of constraints that did not allow velocity to vary in the lower half of the model. Thus, the lower 128 x 5 velocity cells were effectively removed.

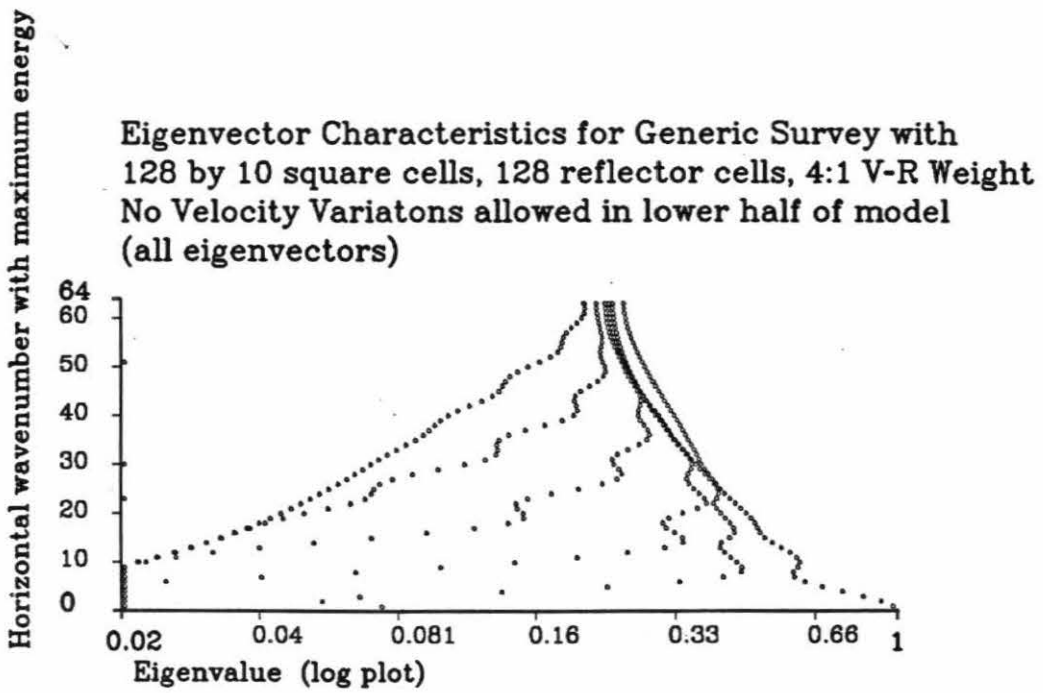
Eigenvector Characteristics for Generic Survey with
128 by 10 square cells, 128 reflector cells, 4:1 V-R Weight
No Velocity Variatons allowed in lower half of model
(all eigenvectors)
Horizontal wavenumber with maximum energy
64
60
50
40
30
20
10
0
0.02
0.04
0.081
0.16
0.33
0.66
1
Eigenvalue (log plot)

Figure 4.15B & C

Analysis of eigenvectors with a reflector component. No high horizontal wavenumbers have small eigenvalues. The eigenvalues of the lower horizontal wavenumbers, although slightly larger than in Figure **4.13b**, still have small eigenvalues.

Eigenvector Characteristics for Generic Survey with
128 by 10 square cells, 128 reflector cells, 4:1 V-R Weight
No Velocity Variatons allowed in lower half of model
(eigenvectors with measurable reflector energy)

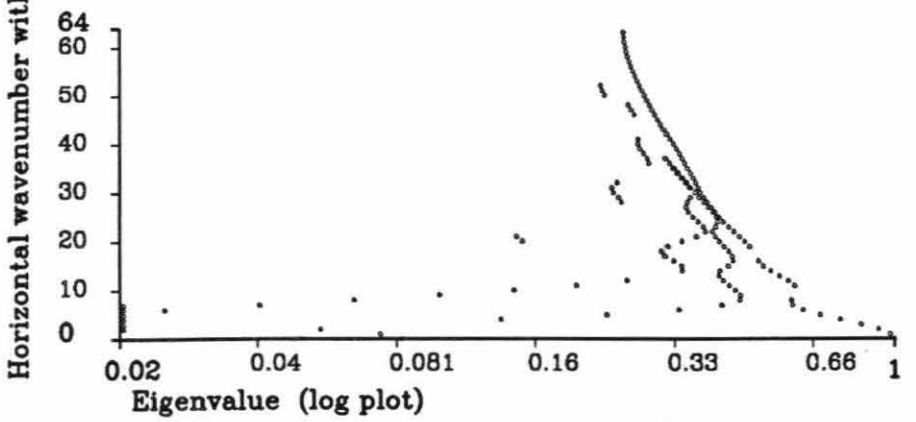

Eigenvector Characteristics for Generic Survey with
128 by 10 square cells, 128 reflector cells, 4:1 V-R Weight
No Velocity Variatons allowed in lower half of model
(eigenvectors with measurable reflector energy)

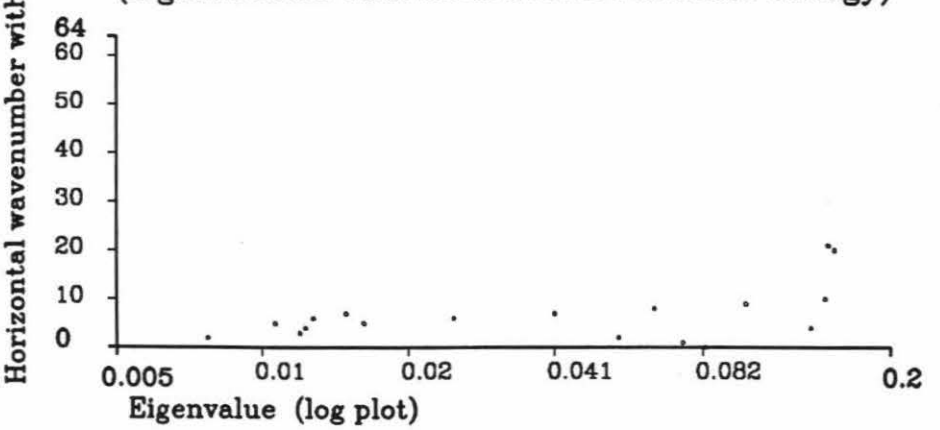

Figure 4.15D & E

Plots of the reflector components in the eigenvectors and its correlation with the column of slowness above it. These figures can be compared with Figures **4.7d** & **4.7f**. Many of the eigenvectors with reflector components, including those with ambiguous velocity and reflector depth variations have been moved to higher eigenvalues.

Eigenvector Characteristics for Generic Survey with
128 by 10 square cells, 128 reflector cells, 4:1 V-R Weight
No Velocity Variatons allowed in lower half of model
(all eigenvectors)

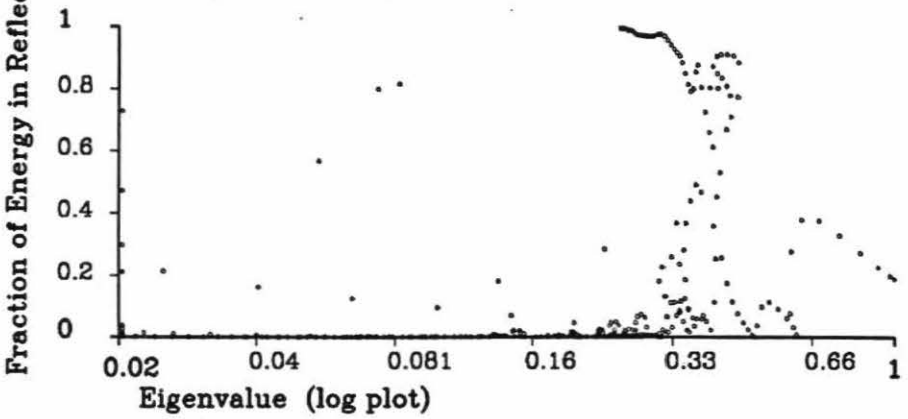

Eigenvector Characteristics for Generic Survey with
128 by 10 square cells, 128 reflector cells, 4:1 V-R Weight
No Velocity Variatons allowed in lower half of model
(all eigenvectors)

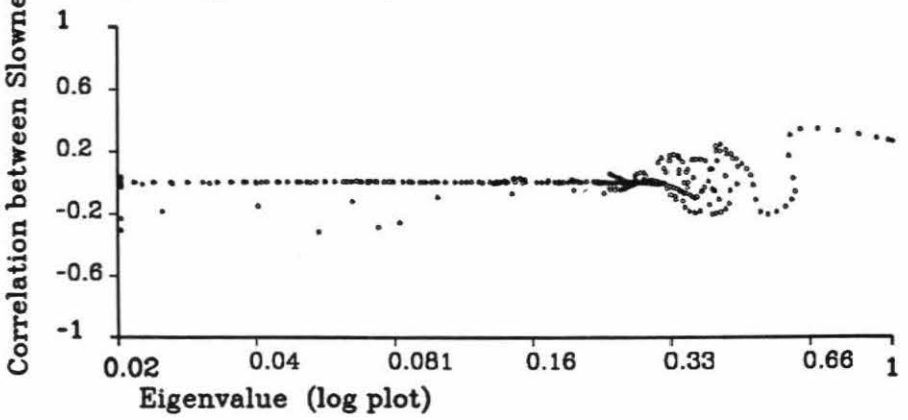

Figure 4.16A & B

SVD results for a model with a shorter cable length such that the maximum ray angle is only 22.5o. The smaller data set should significantly reduce resolution.

Eigenvector Characteristics for Generic Survey with
128 by 10 square cells, 128 reflector cells
4:1 V-R Weight, Maximum Ray Angle of 22.5 degrees
(all eigenvectors)

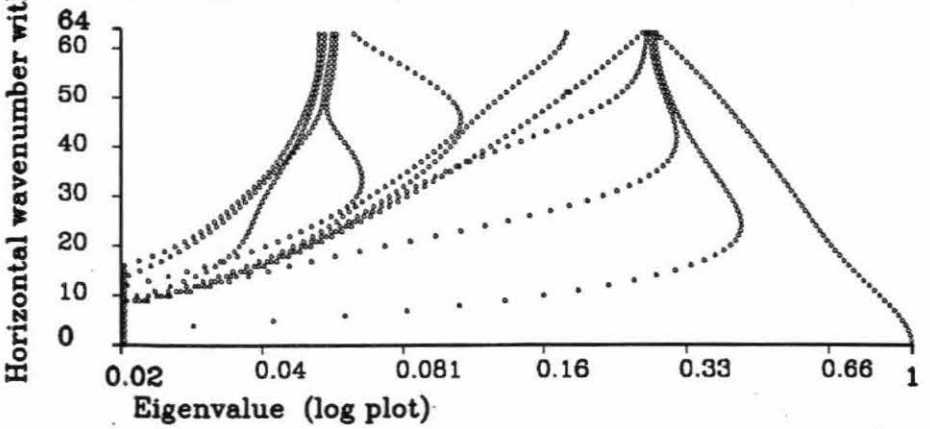

Eigenvector Characteristics for Generic Survey with
128 by 10 square cells, 128 reflector cells
4:1 V-R Weight, Maximum Ray Angle of 22.5 degrees
(eigenvectors with measurable reflector energy)

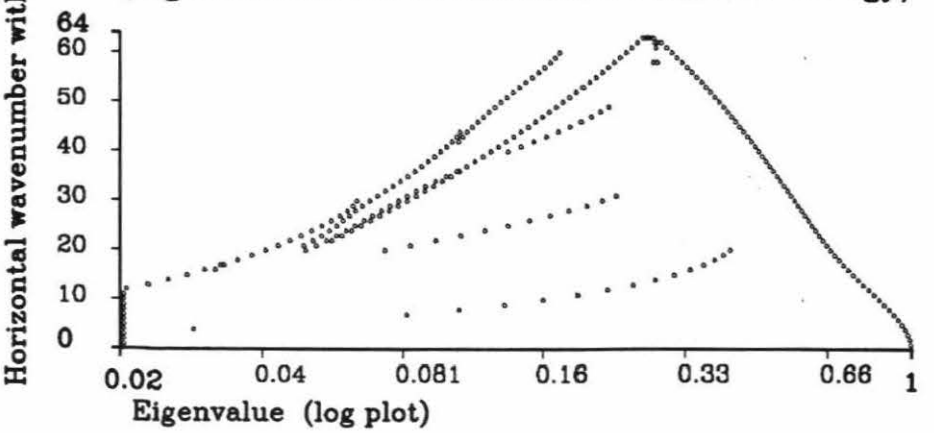

Figure 4.16C

The eigenvalues of the velocity-reflector depth ambiguity should be reduced significantly. They are for very small wavenumbers, but not for larger ones indicating results are corrupted by large cell sizes.

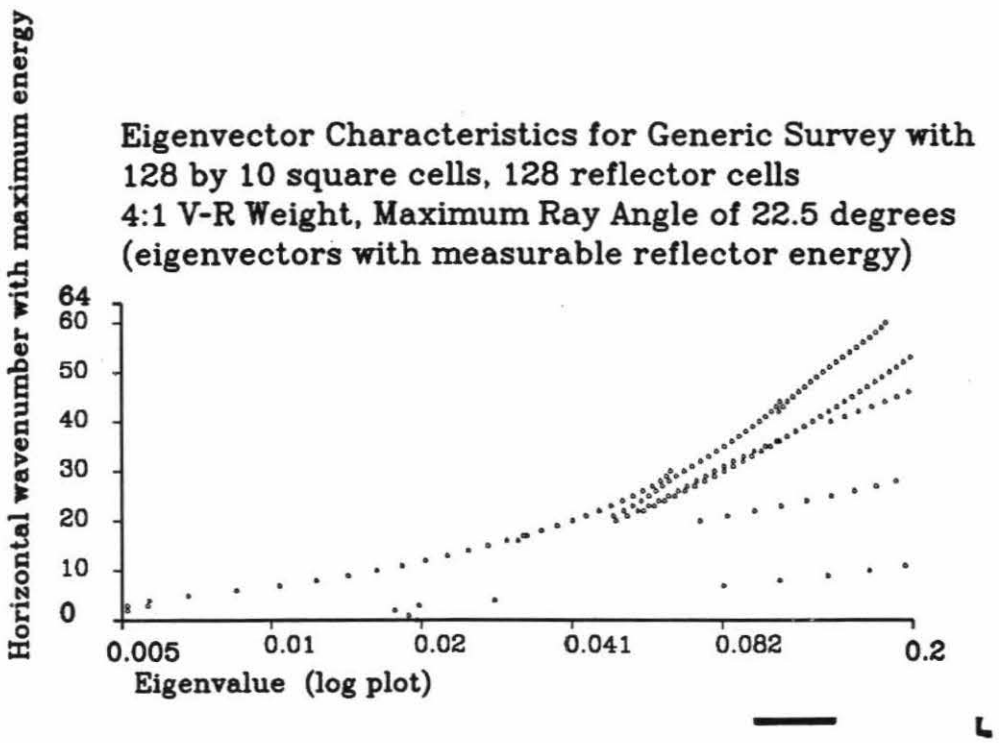
Eigenvector Characteristics for Generic Survey with
128 by 10 square cells, 128 reflector cells
4:1 V-R Weight, Maximum Ray Angle of 22.5 degrees
(eigenvectors with measurable reflector energy)
Horizontal wavenumber with maximum energy
64
60
50
40
30
20
10
0
0.005
0.01
0.02
0.041
0.082
0.2
Eigenvalue (log plot)

Figure 4.17A & B

SVD results with the gaussian damping of high horizontal wavenumbers. As expected, the eigenvalues of the high horizontal wavenumbers have been strongly reduced.

Eigenvector Characteristics for Generic Survey with
128 by 10 square cells, 128 reflector cells
4:1 V-R Weight, Damping of high Horizontal Wavenumbers
(all eigenvectors)

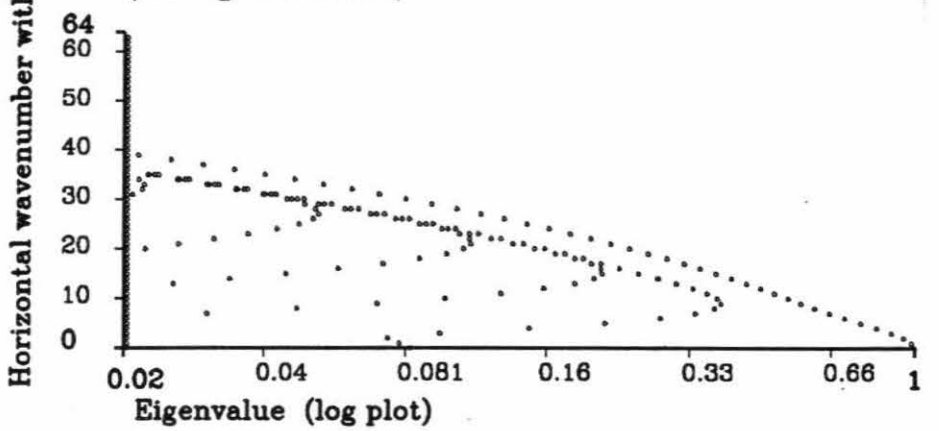

Eigenvector Characteristics for Generic Survey with
128 by 10 square cells, 128 reflector cells
4:1 V-R Weight, Damping of high Horizontal Wavenumbers
(all eigenvectors)

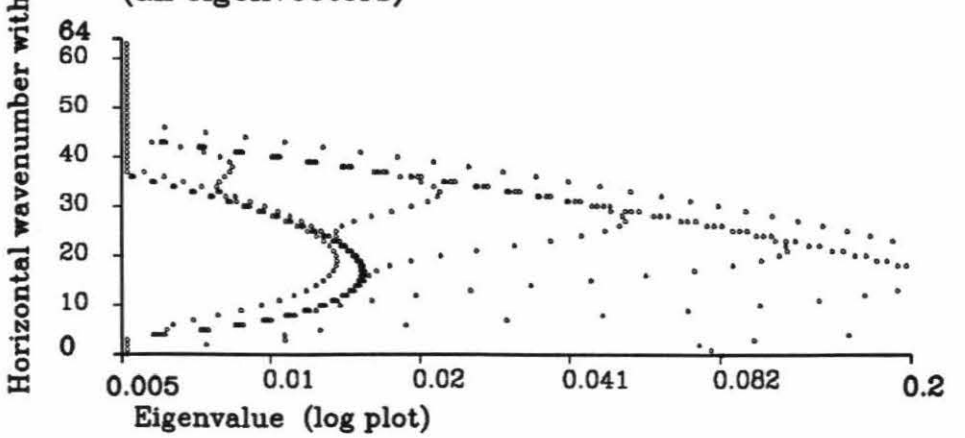

Figure 4.18A & B

SVD results of model with 128 x 16 velocity cells. The cells are smaller and the entire model width is narrower. Upper figure is similar to that in Figure **4.13a** for a 128 x 10 model. Lower figure shows eigenvalues of the velocity-reflector depth ambiguity are smaller than for the 128 x 10 model in Figure **4.13b**.

Eigenvector Characteristics for Generic Survey with
128 by 16 square cells, 128 reflector cells
4:1 Velocity to Reflector Weight
(all eigenvectors)

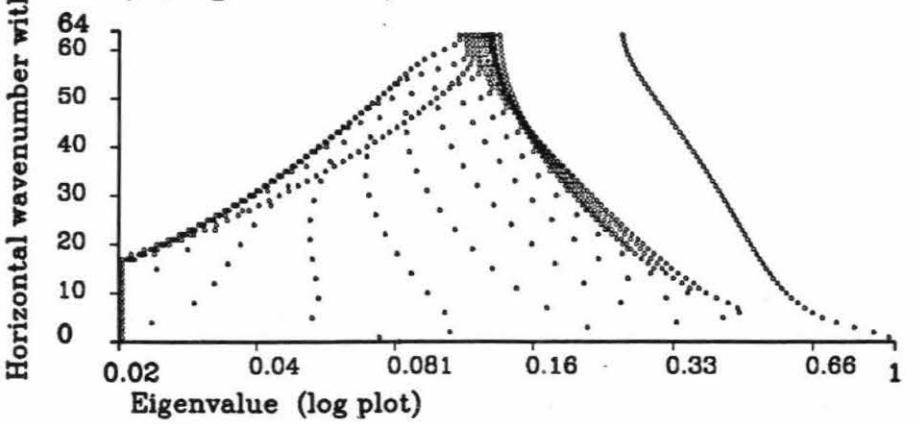

Eigenvector Characteristics for Generic Survey with
128 by 16 square cells, 128 reflector cells
4:1 Velocity to Reflector Weight
(eigenvectors with measurable reflector energy)

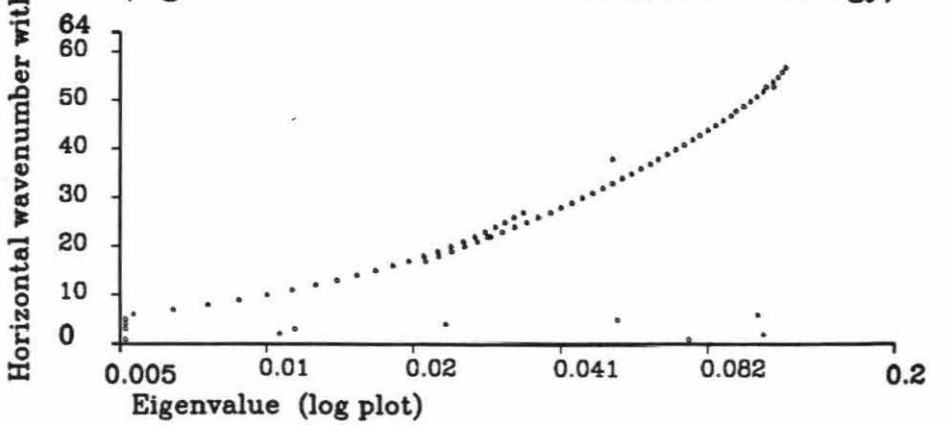

Figure 4.19A & B

SVD results for a model with 128 x 10 rectangular cells three times wider than high which makes the circumference of the circular model very large, but increases possible effects from the finite cell sizes.

Eigenvector Characteristics for Generic Survey with 128 by 10 rectangular cells 3 times wider than high, 128 reflector cells, 4:1 V-R Weight
(all eigenvectors)

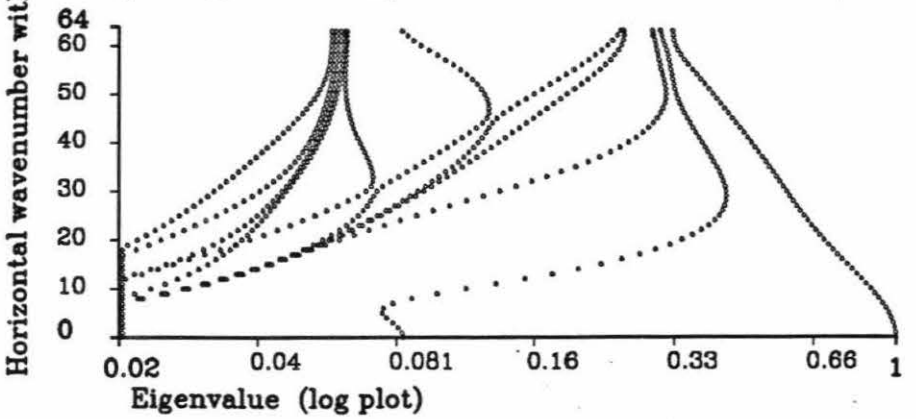

Eigenvector Characteristics for Generic Survey with 128 by 10 rectangular cells 3 times wider than high, 128 reflector cells, 4:1 V-R Weight
(eigenvectors with measurable reflector energy)

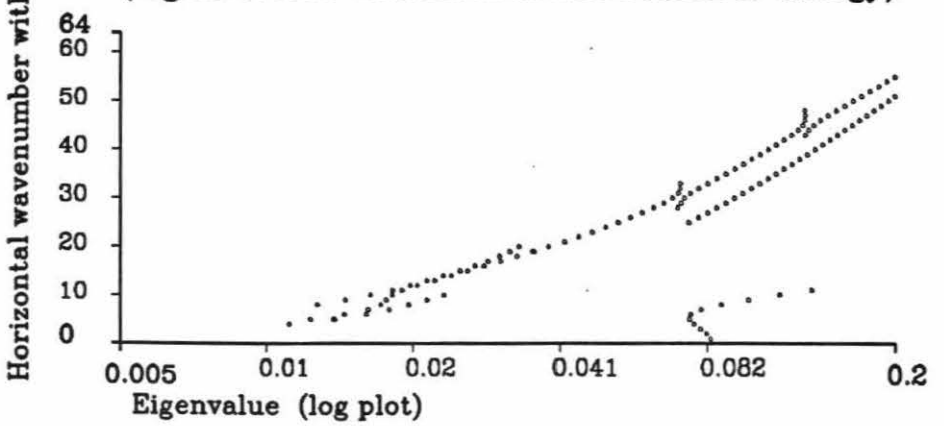

Figure 4.20A & B

SVD results for a model with 256 x 5 rectangular cells two times higher than wide which also increases the circumference of the model. Since velocity is smeared vertically from the limited angular ray coverage, this type of cell should not significantly affect results. Both figures are similar to their corresponding ones for square cells in Figures **4.13a & b**

Eigenvector Characteristics for Generic Survey with
256 by 5 rectangular Cells two times higher than wide
256 Reflector Cells, 4:1 V-R Weight
(all eigenvectors)

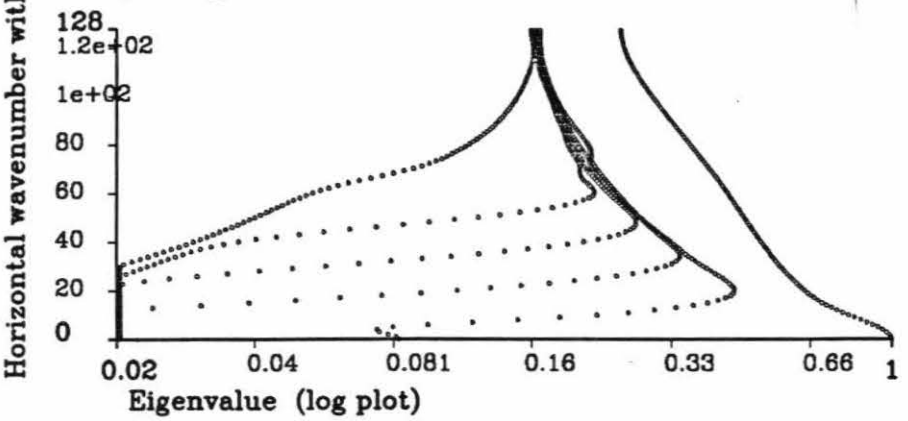

Eigenvector Characteristics for Generic Survey with
256 by 5 rectangular Cells two times higher than wide
256 Reflector Cells, 4:1 V-R Weight
(eigenvectors with measurable reflector energy)

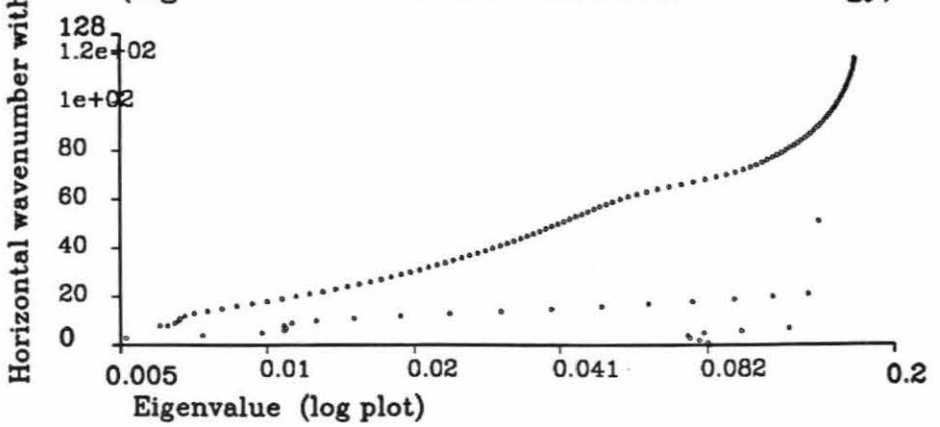

Figure 4.21A

SVD results for model with an additional reflector at twice the depth. 128 x 10 rectangular velocity cells twice as high as wide were used. There are now two branches of eigenvectors on the far right side, one corresponding to each reflector. The main interest is whether the addition of the second reflector has helped resolve the first one. Since the cable length has not been changed, the maximum angular ray coverage for the second, deeper reflector is about 25^{o}.

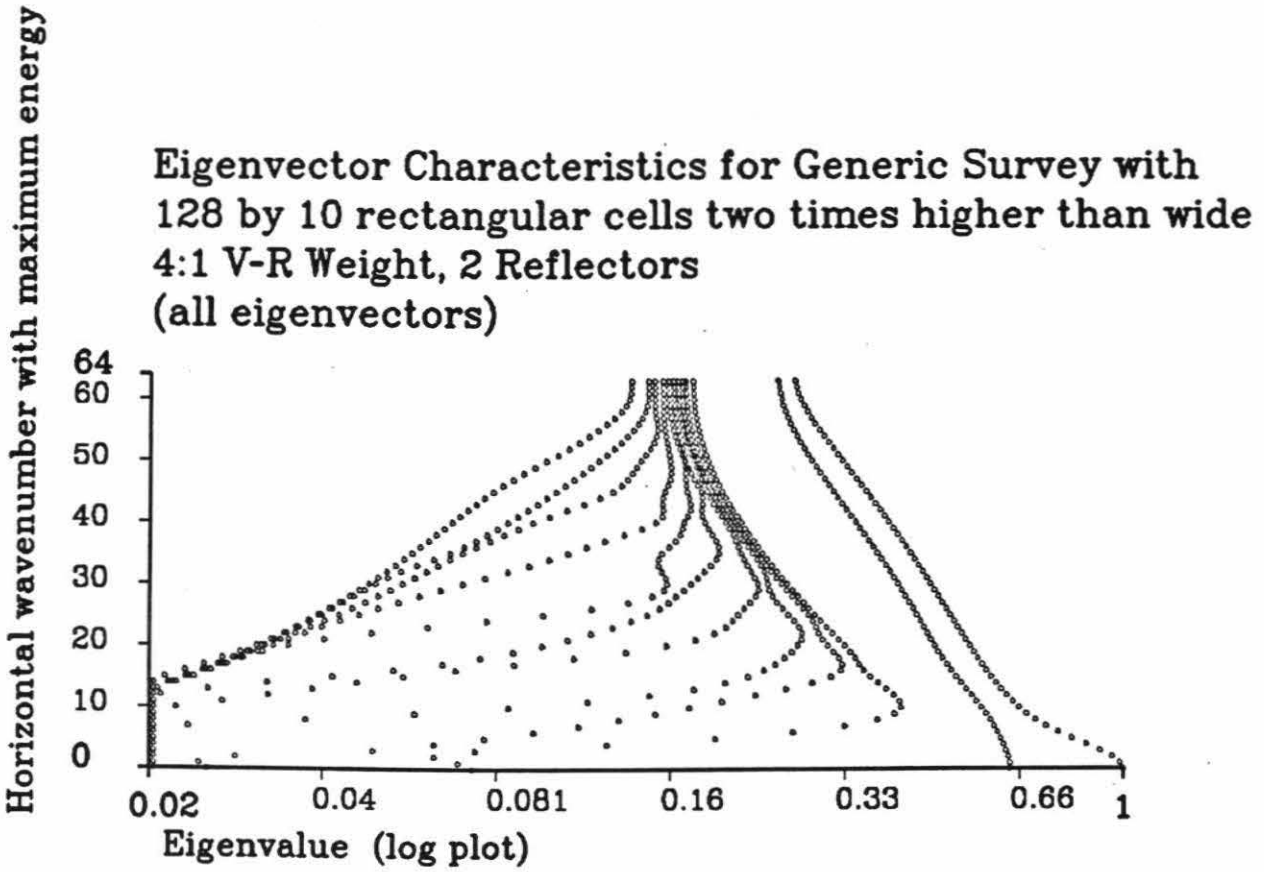
Eigenvector Characteristics for Generic Survey with
128 by 10 rectangular cells two times higher than wide
4:1 V-R Weight, 2 Reflectors
(all eigenvectors)
Horizontal wavenumber with maximum energy
64
60
50
40
30
20
10
0
0.02
0.04
0.081
0.16
0.33
0.66
1
Eigenvalue (log plot)

Figure 4.21B & C

Analysis of the eigenvectors with upper reflector components shows the reflector is generally better resolved but some eigenvalues still exist below 0.01.

Eigenvector Characteristics for Generic Survey with
128 by 10 rectangular cells two times higher than wide
4:1 V-R Weight, 2 Reflectors
(eigenvectors with measurable upper reflector energy)

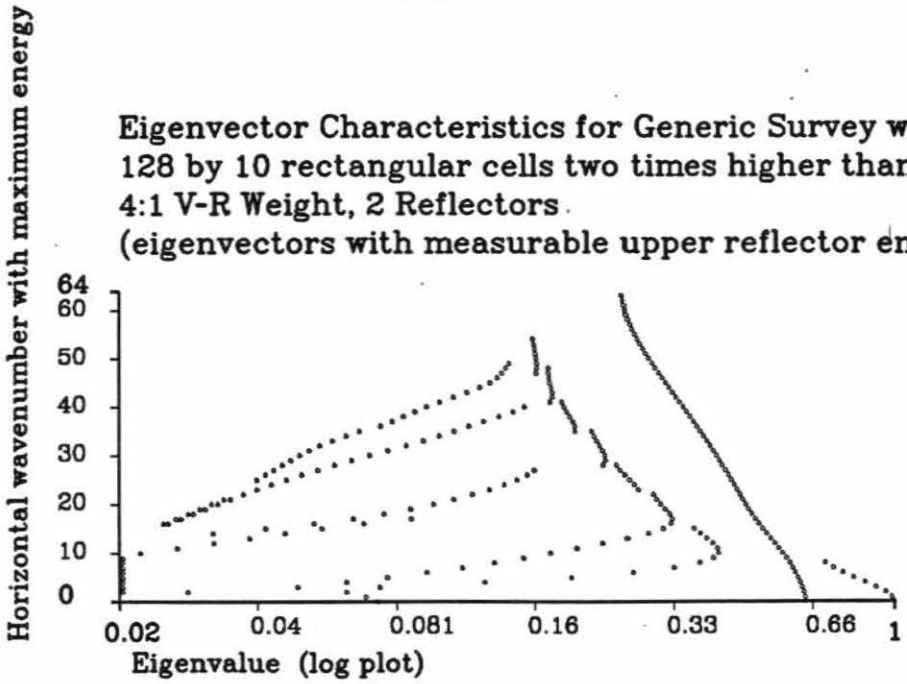

Eigenvector Characteristics for Generic Survey with
128 by 10 rectangular cells two times higher than wide
4:1 V-R Weight, 2 Reflectors
(eigenvectors with measurable upper reflector energy)

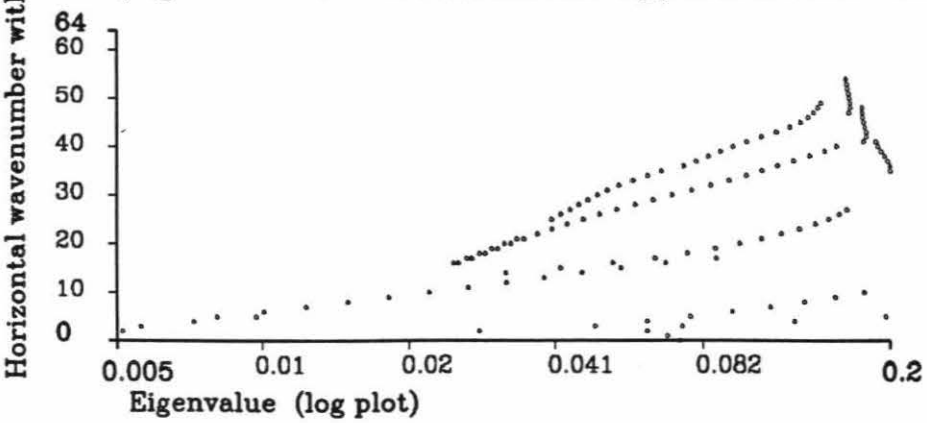

Figure 4.22A

Eigenvalue distribution of a cross bore hole pure transmission experiment. The original generic circular model simulates the cross hole geometry on its side when sources placed at the bottom shoot up to receivers at the surface. 128 x 8 rectangular velocity cells two times higher than wide were used.

The plot shows two groups with a discontinuity after eigenvector number 800.

Eigenvalue Distribution for a Cross Borehole Experiment
128 by 8 rectangular Cells 2 times higher than wide
Sources are at bottom of field, Receivers at top

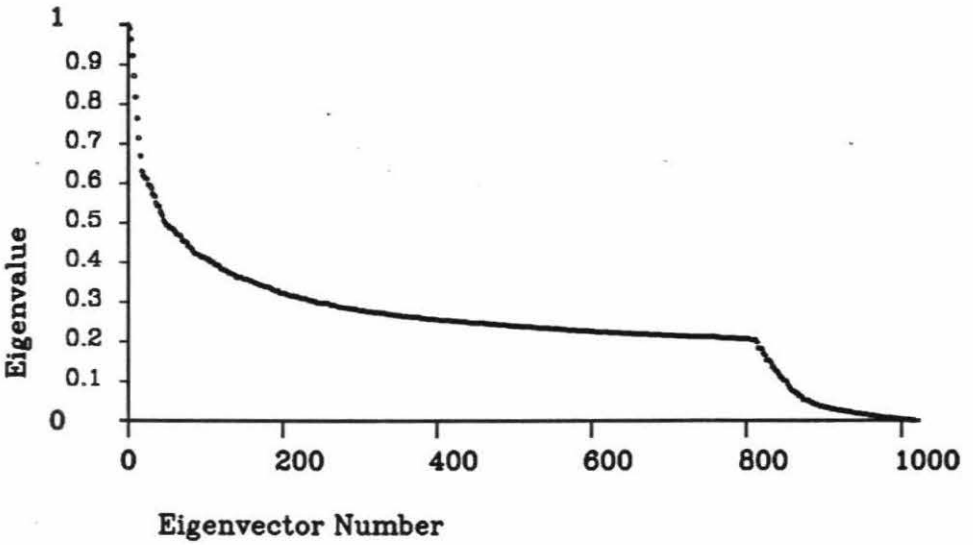

Figure 4.22B & C

Horizontal wavenumbers of pure transmission experiment display similar features as the similar plot in Figure **4.7m & n**.

Eigenvector Characteristics for Cross Hole Experiment
128 by 8 rectangular cells 2 times higher than wide
Sources are at bottom of field, Receivers at top
(all eigenvectors)

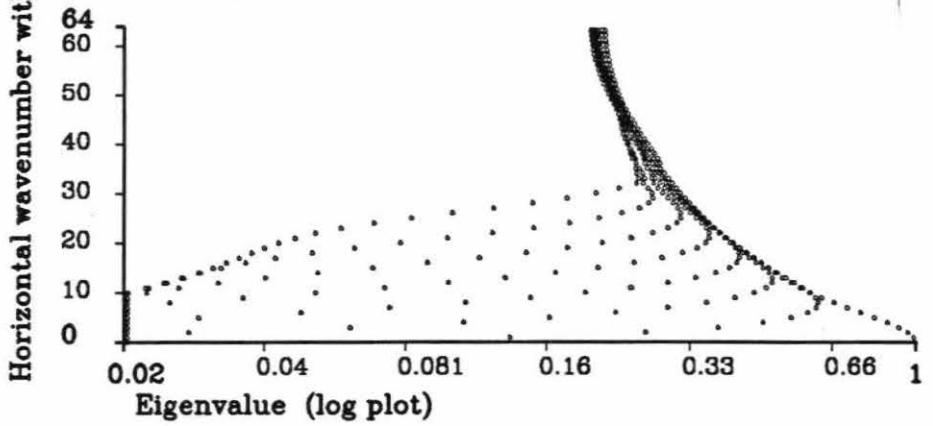

Eigenvector Characteristics for Cross Hole Experiment
128 by 8 rectangular cells 2 times higher than wide
Sources are at bottom of field, Receivers at top
(all eigenvectors)

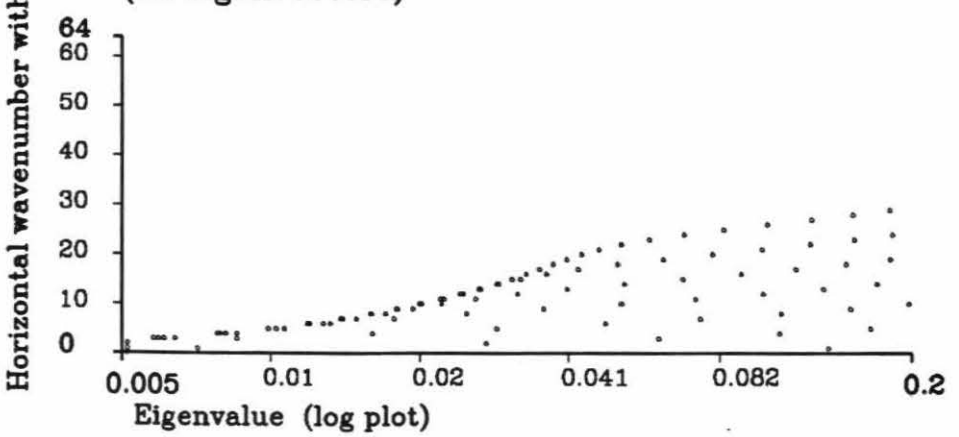

Figure 4.22D & E

Previous plot of only those eigenvectors with certain vertical wavenumbers produces one branch of the previous figure.

Eigenvector Characteristics for Cross Hole Experiment
128 by 8 rectangular cells 2 times higher than wide
Sources are at bottom of field, Receivers at top
(Vertical Wavenumbers 0)

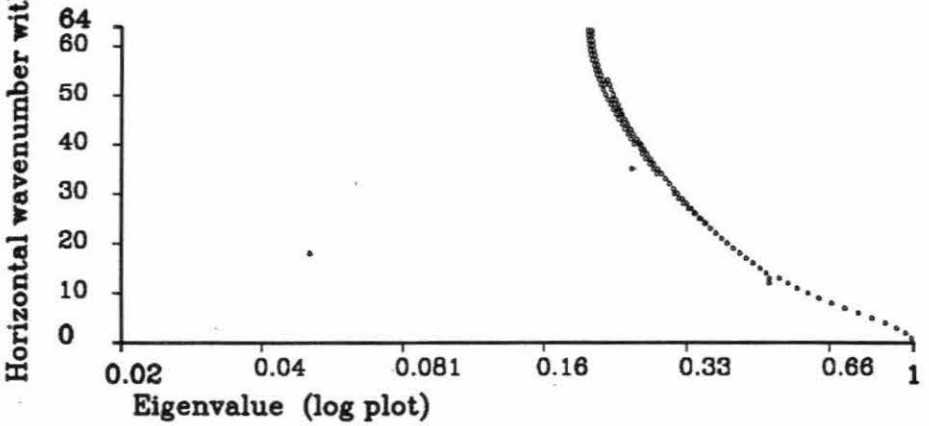

Eigenvector Characteristics for Cross Hole Experiment
128 by 8 rectangular cells 2 times higher than wide
Sources are at bottom of field, Receivers at top
(Vertical Wavenumbers 1)

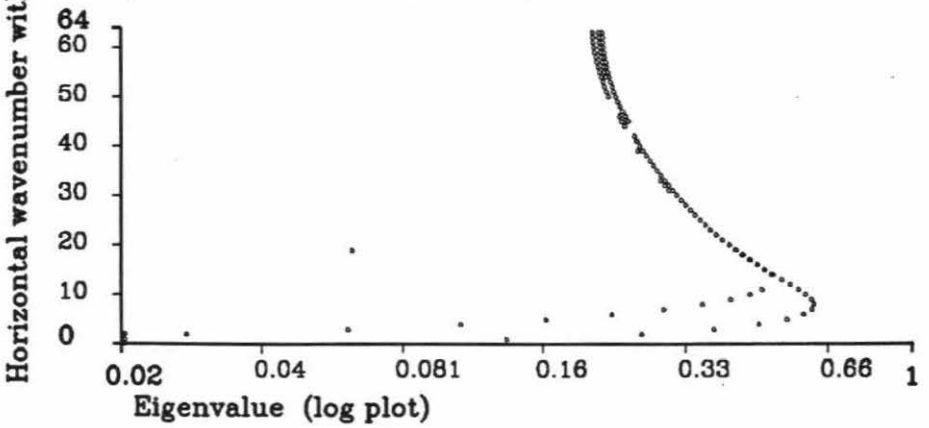

Figure 4.23

Model used for the analysis of edge effects. A single spread was used which produces a different limited ray coverage on the left side from the right.

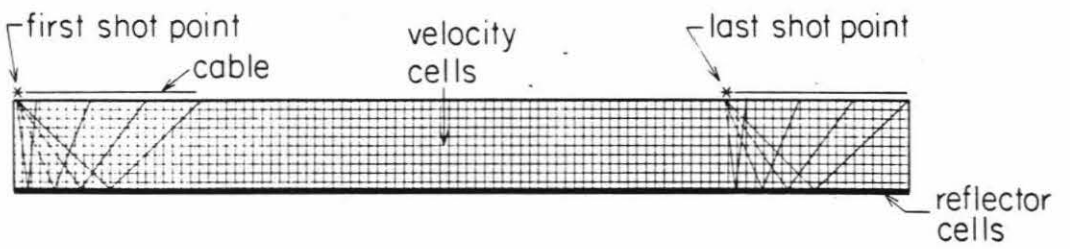
first shot point
cable
velocity
cells
last shot point
reflector
cells

Figure 4.24A & B

Eigenvectors from model with edge effects with ambiguous velocity and reflector depth that are not significantly affected by the edges. They share many similar properties to the eigenvectors of the generic model. The eigenvectors are no longer only one horizontal wavenumber as with the generic model with wrap around.

**Eigenvector Number 763 with Eigenvalue: 0.0778
for a Generic Survey of 128 by 10 square Cells
& 4:1 V-R Weight, No Wrap around**

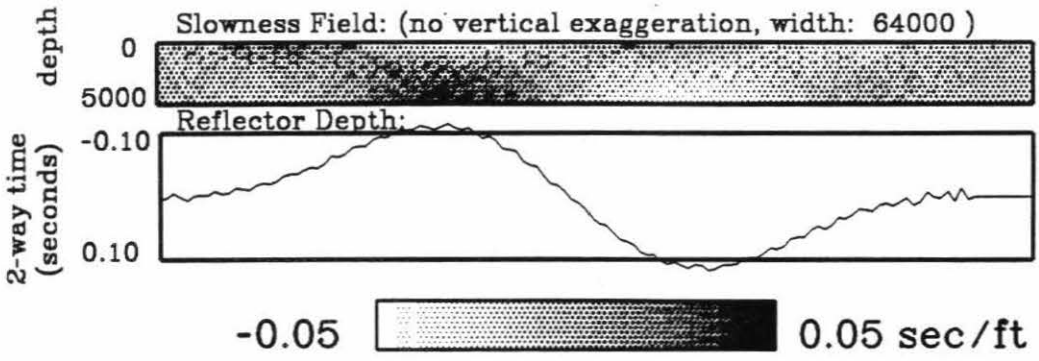

**Eigenvector Number 1140 with Eigenvalue: 0.0147
for a Generic Survey of 128 by 10 square Cells
& 4:1 V-R Weight, No Wrap around**

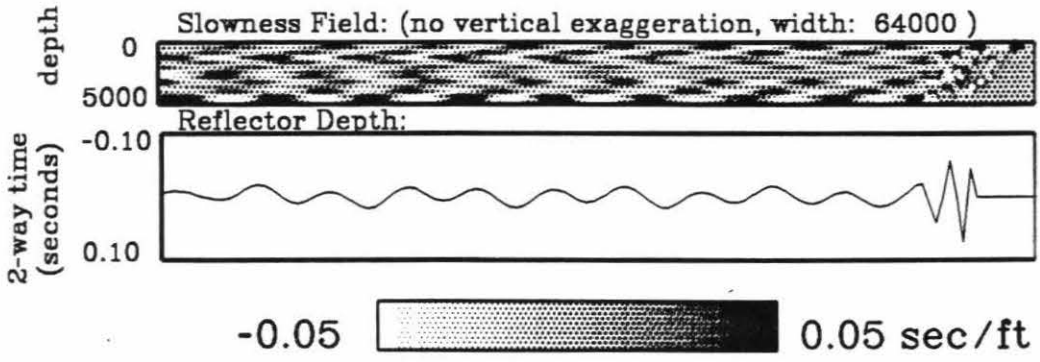

Figure 4.24C & D

Eigenvectors for model with edge effects that are not significantly affected by the edges.

Eigenvector Number 1148 with Eigenvalue: 0.0139
for a Generic Survey of 128 by 10 square Cells
& 4:1 V-R Weight, No Wrap around

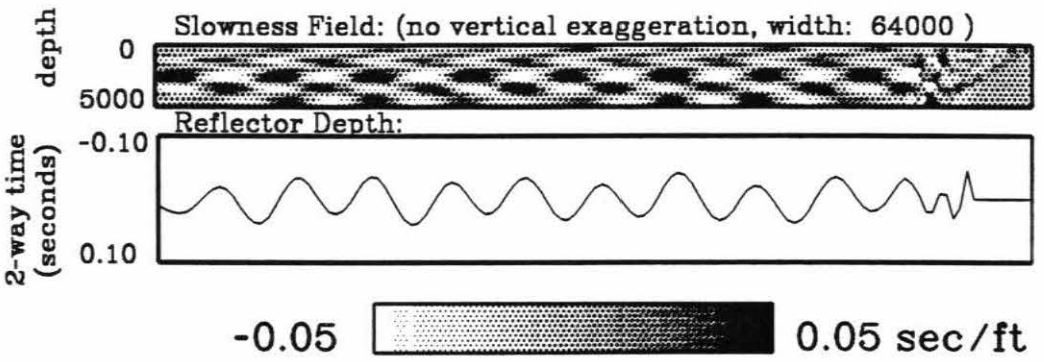

Eigenvector Number 1152 with Eigenvalue: 0.0135
for a Generic Survey of 128 by 10 square Cells
& 4:1 V-R Weight, No Wrap around

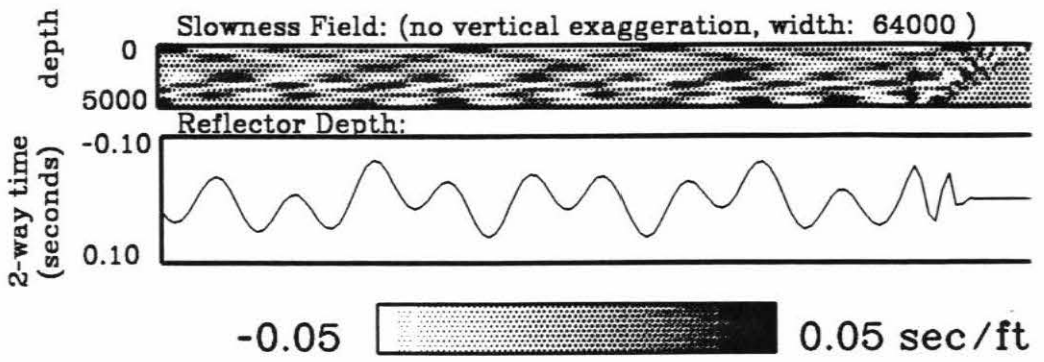

Figure 4.24E & F

Eigenvectors for model with edge effects that are not significantly affected by the edges.

Eigenvector Number 1175 with Eigenvalue: 0.0114
for a Generic Survey of 128 by 10 square Cells
& 4:1 V-R Weight, No Wrap around

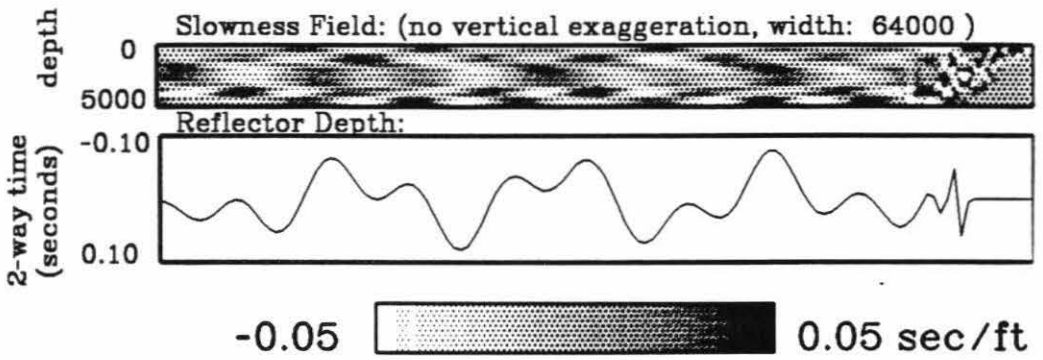

Eigenvector Number 1179 with Eigenvalue: 0.0112
for a Generic Survey of 128 by 10 square Cells
& 4:1 V-R Weight, No Wrap around

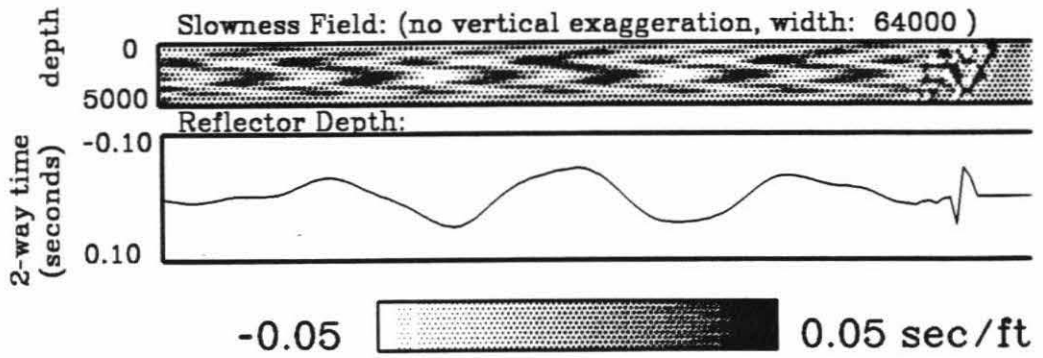

Figure 4.24G & H

Eigenvectors for model with edge effects that are not significantly affected by the edges.

Eigenvector Number 1178 with Eigenvalue: 0.0112
for a Generic Survey of 128 by 10 square Cells
& 4:1 V-R Weight, No Wrap around

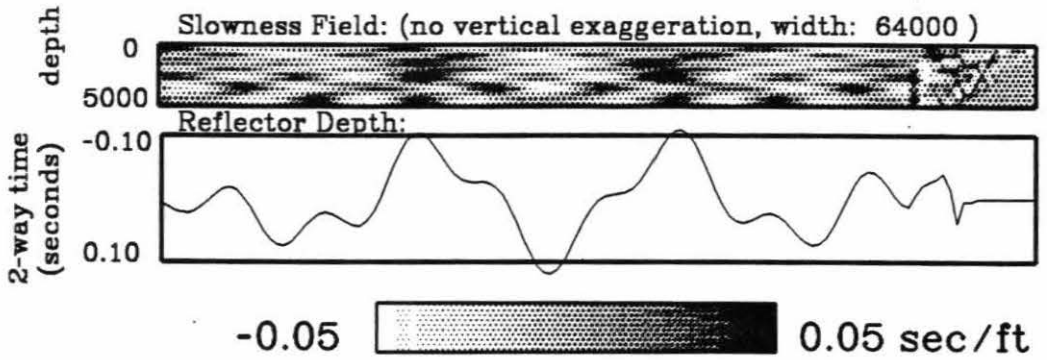

Eigenvector Number 1237 with Eigenvalue: 0.00667
for a Generic Survey of 128 by 10 square Cells
& 4:1 V-R Weight, No Wrap around

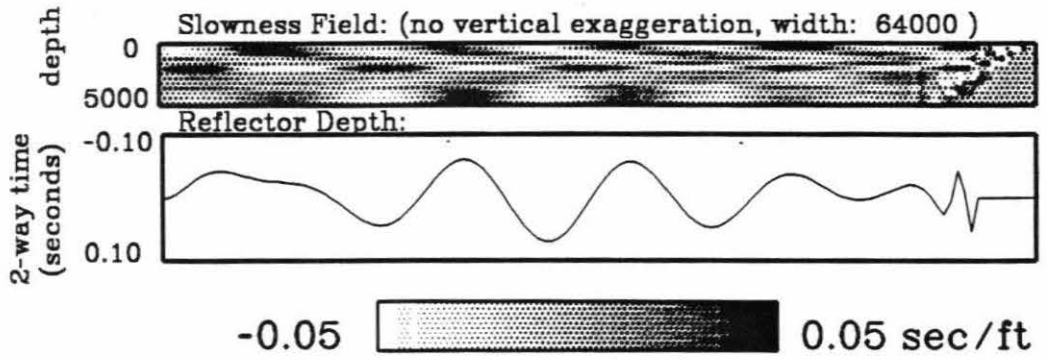

Figure 4.24I & J

Eigenvectors for model with edge effects that are not significantly affected by the edges.

Eigenvector Number 1243 with Eigenvalue: 0.00634
for a Generic Survey of 128 by 10 square Cells
& 4:1 V-R Weight, No Wrap around

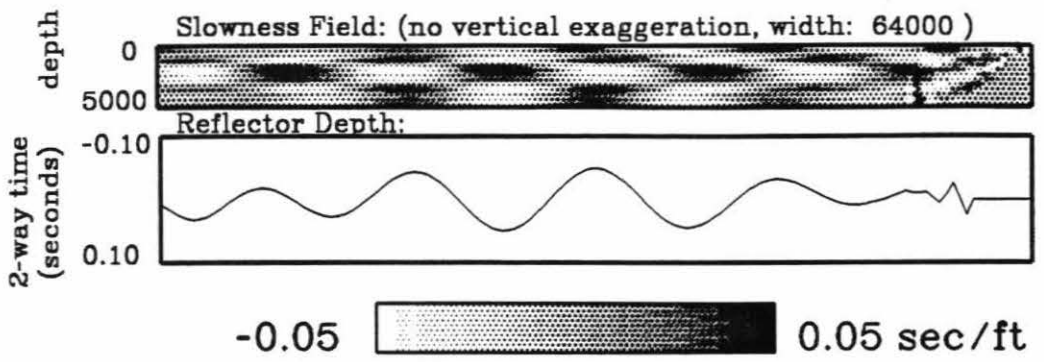

Figure 4.25A & B

Eigenvectors with a significant component near the edges.

Eigenvector Number 1236 with Eigenvalue: 0.00669
for a Generic Survey of 128 by 10 square Cells
& 4:1 V-R Weight, No Wrap around

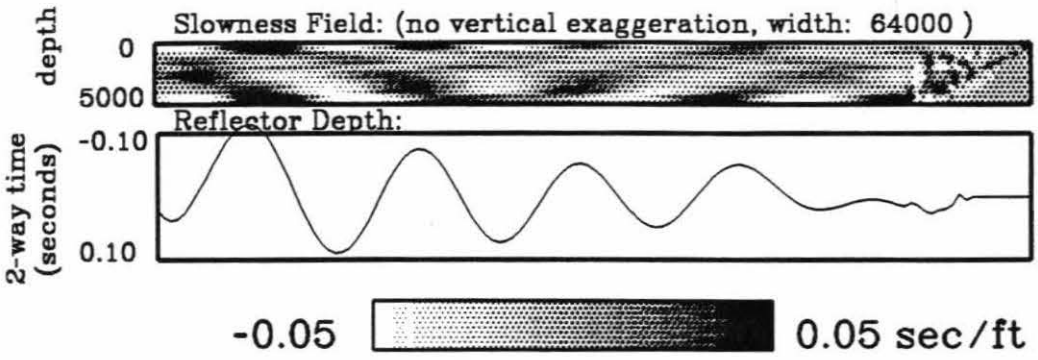

Eigenvector Number 1250 with Eigenvalue: 0.00584
for a Generic Survey of 128 by 10 square Cells
& 4:1 V-R Weight, No Wrap around

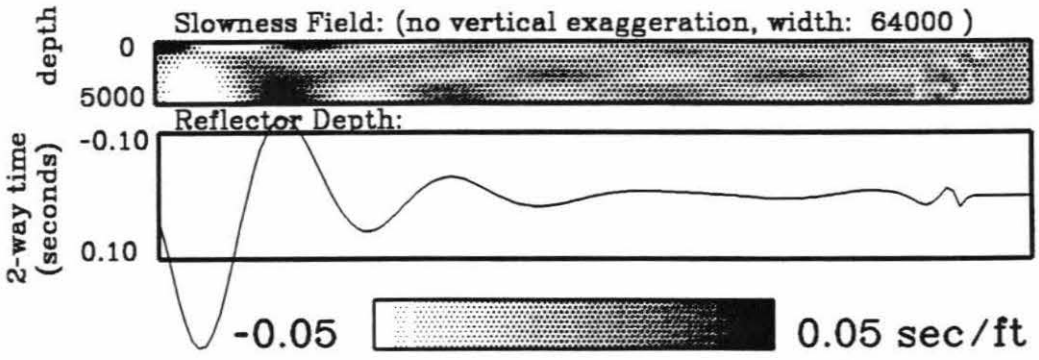

Figure 4.25C & D

Eigenvectors with a significant component near the edges.

**Eigenvector Number 1251 with Eigenvalue: 0.00574
for a Generic Survey of 128 by 10 square Cells
& 4:1 V-R Weight, No Wrap around**

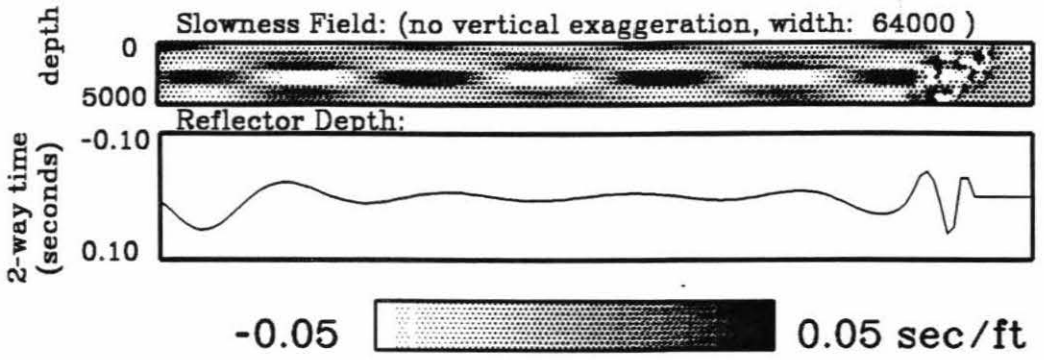

**Eigenvector Number 1253 with Eigenvalue: 0.0056
for a Generic Survey of 128 by 10 square Cells
& 4:1 V-R Weight, No Wrap around**

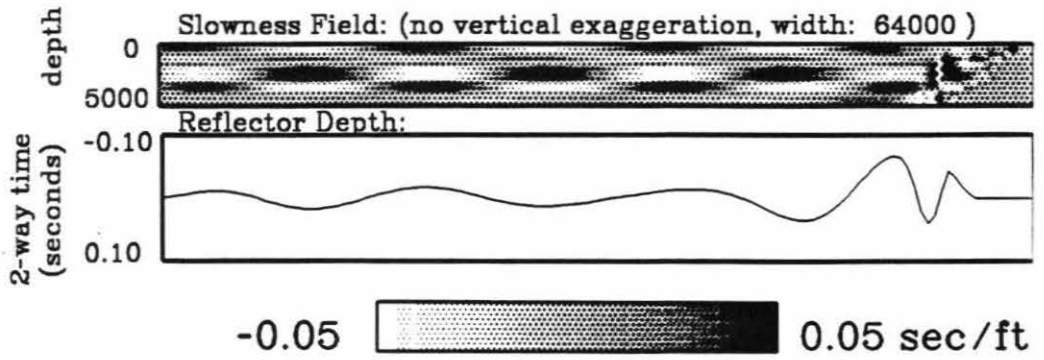

Figure 4.25E & F

Eigenvectors with a significant component near the edges.

Eigenvector Number 1255 with Eigenvalue: 0.00553
for a Generic Survey of 128 by 10 square Cells
& 4:1 V-R Weight, No Wrap around

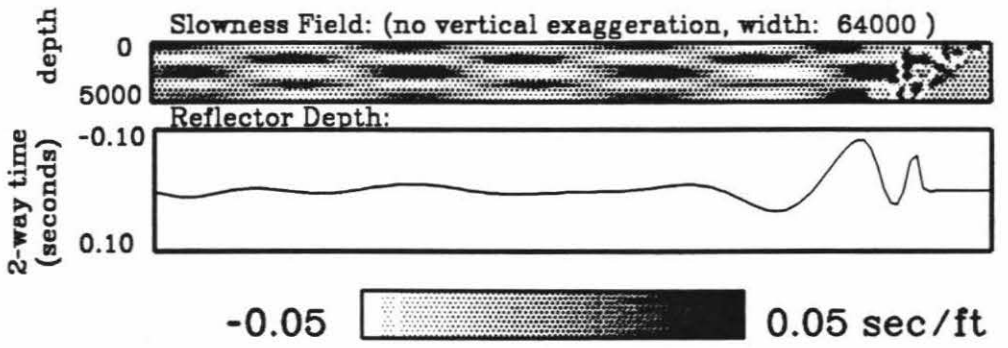

Eigenvector Number 1270 with Eigenvalue: 0.00454
for a Generic Survey of 128 by 10 square Cells
& 4:1 V-R Weight, No Wrap around

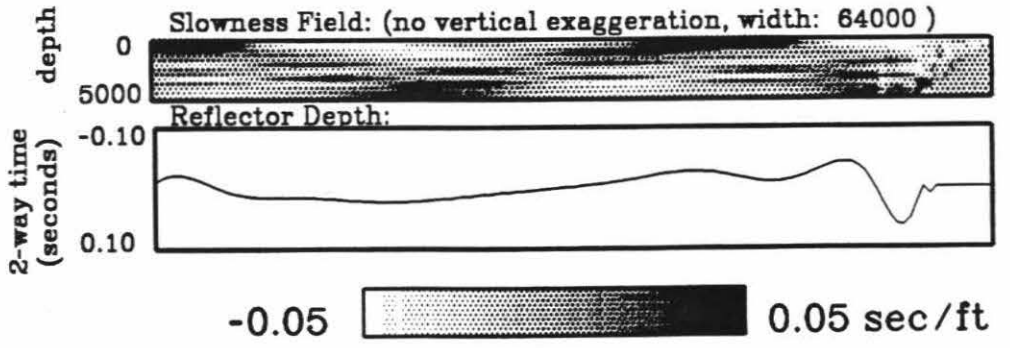

Figure 4.25G & H

Eigenvectors with a significant component near the edges.

Eigenvector Number 1275 with Eigenvalue: 0.00424
for a Generic Survey of 128 by 10 square Cells
& 4:1 V-R Weight, No Wrap around

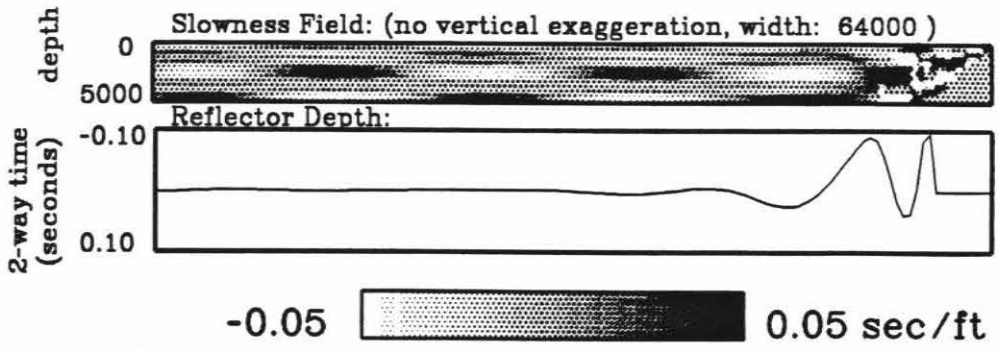

Eigenvector Number 1303 with Eigenvalue: 0.00232
for a Generic Survey of 128 by 10 square Cells
& 4:1 V-R Weight, No Wrap around

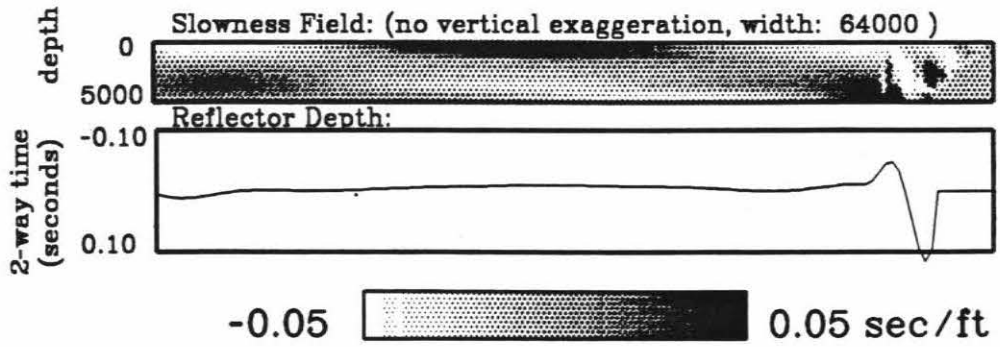

Figure 4.26A & B

The horizontal wavenumbers of the eigenvectors no longer show distinct trends because the eigenvectors are no longer as pure as with the generic model with wrap around.

Eigenvector Characteristics for Generic Survey with
128 by 10 square cells, 128 reflector cells
4:1 V-R Weight, No Wrap around (edge effects exist)
(all eigenvectors)

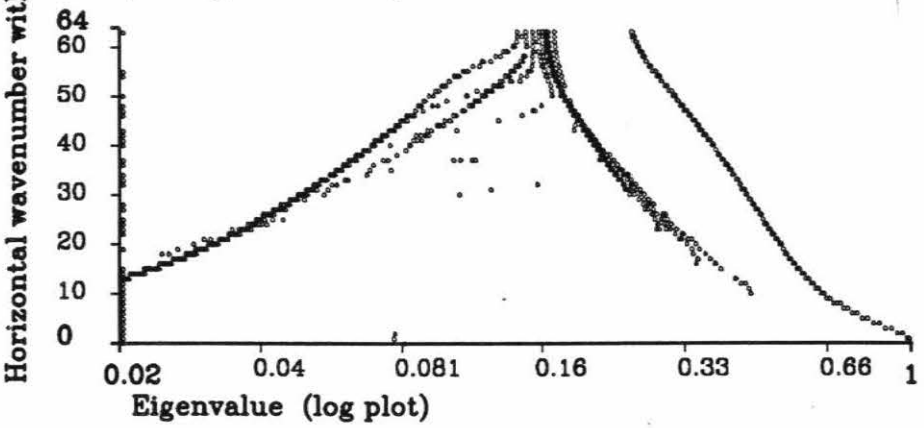

Eigenvector Characteristics for Generic Survey with
128 by 10 square cells, 128 reflector cells
4:1 V-R Weight, No Wrap around (edge effects exist)
(eigenvectors with no measurable reflector energy)

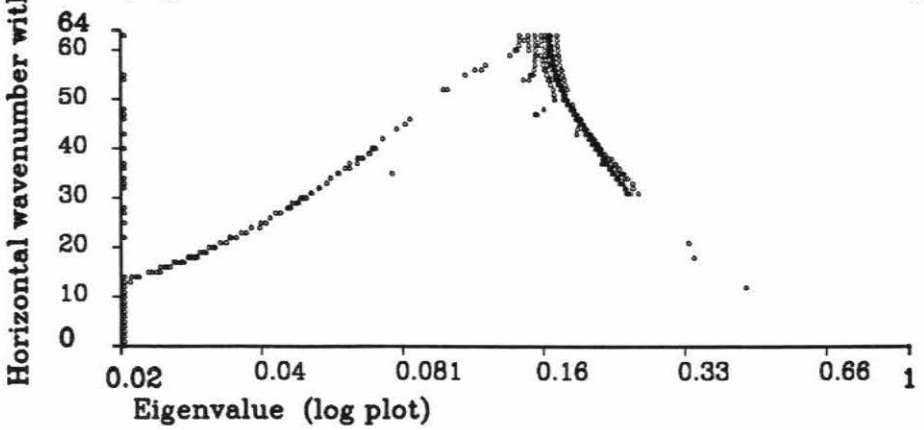

Figure 4.26C & D

Eigenvectors with measurable reflector components away from the model edges. Except for three points near eigenvalue 0.08, there are no other eigenvectors with low wavenumber and eigenvalues greater than 0.02. For comparison see Figure **4.13a & b** for model with wrap around.

Eigenvector Characteristics for Generic Survey with
128 by 10 square cells, 128 reflector cells
4:1 V-R Weight, No Wrap around (edge effects exist)
(eigenvectors with measurable reflector energy)

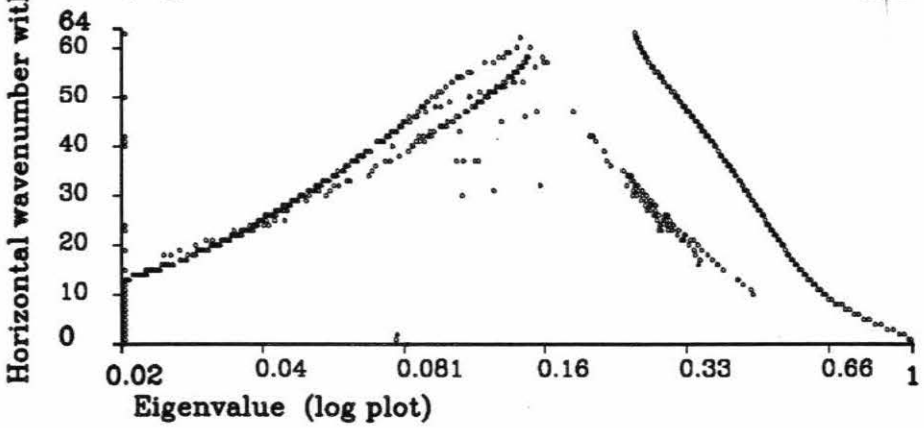

Eigenvector Characteristics for Generic Survey with
128 by 10 square cells, 128 reflector cells
4:1 V-R Weight, No Wrap around (edge effects exist)
(measurable reflector energy away from model edges)

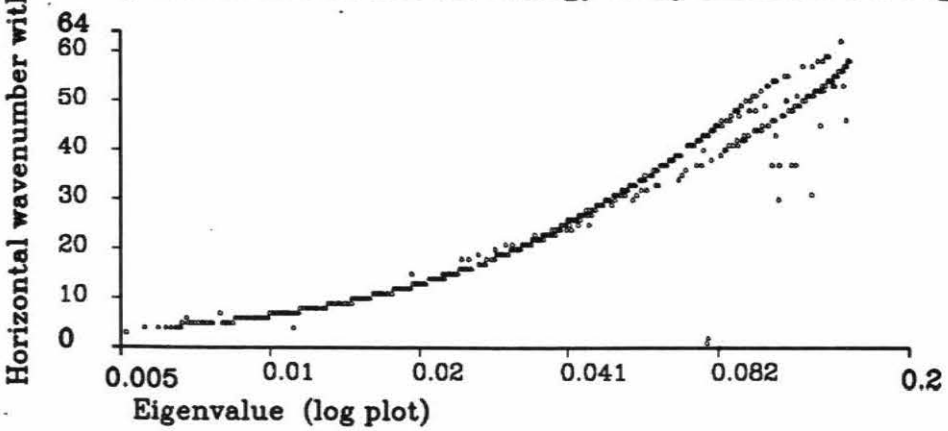

Figure 4.26E & F

Fraction of eigenvector in reflector shows many to have very small components. Several distinct groups appear. Figure can be compared with Figure **4.7d & e** for model with wrap around.

Eigenvector Characteristics for Generic Survey with
128 by 10 square cells, 128 reflector cells
4:1 V-R Weight, No Wrap around (edge effects exist)
(all eigenvectors)

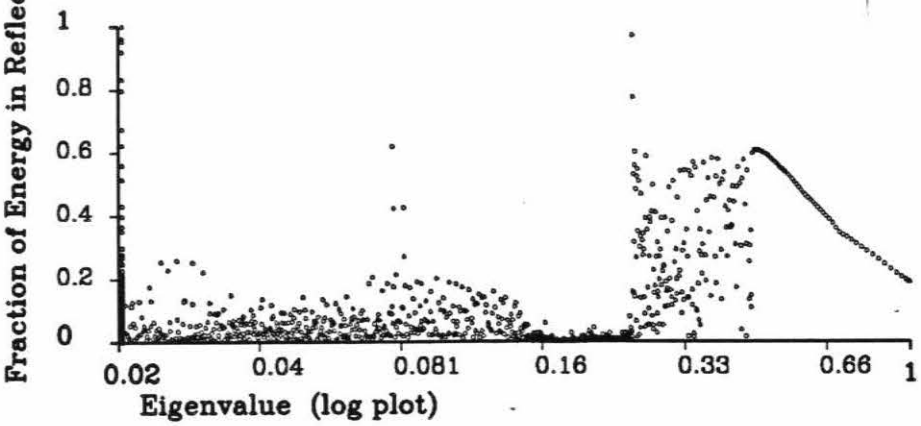

Eigenvector Characteristics for Generic Survey with
128 by 10 square cells, 128 reflector cells
4:1 V-R Weight, No Wrap around (edge effects exist)
(all eigenvectors)

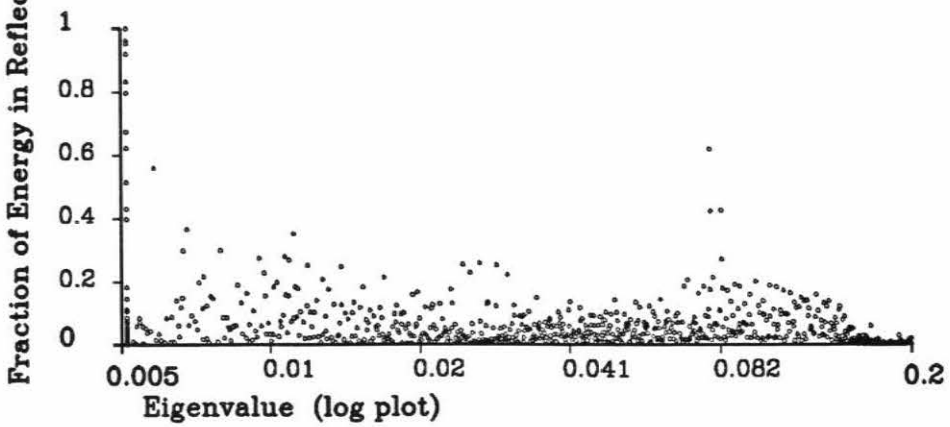

Figure 4.26G

Correlation between reflector and column of slowness above it. Eigenvectors with larger eigenvalues have positive correlation while those with smaller eigenvalues have lower correlation.

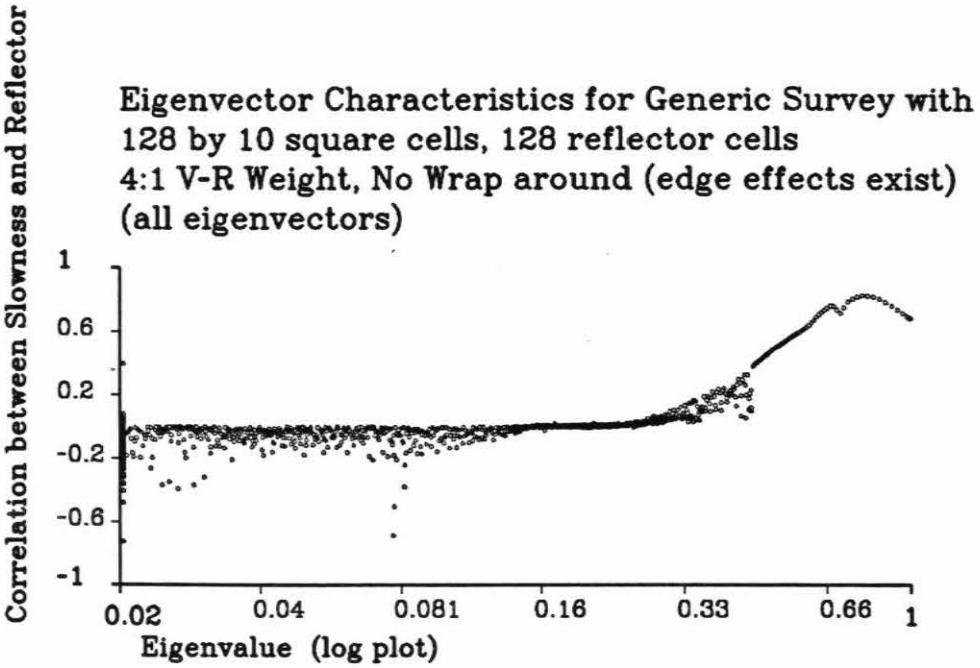
Eigenvector Characteristics for Generic Survey with
128 by 10 square cells, 128 reflector cells
4:1 V-R Weight, No Wrap around (edge effects exist)
(all eigenvectors)
Correlation between Slowness and Reflector
1
0.6
0.2
-0.2
-0.6
-1
0.02
0.04
0.081
0.16
0.33
0.66
1
Eigenvalue (log plot)

Figure 4.26H & I

Proximity of eigenvalue components to the edges is computed by using a linear weight with a value of 1 at the edges and -1 at the center. Most eigenvectors have most of their components either very near to the edges or spread throughout the model with a slight bias toward the center.

Eigenvector Characteristics for Generic Survey with
128 by 10 square cells, 128 reflector cells
4:1 V-R Weight, No Wrap around (edge effects exist)
(eigenvectors with measurable reflector energy)

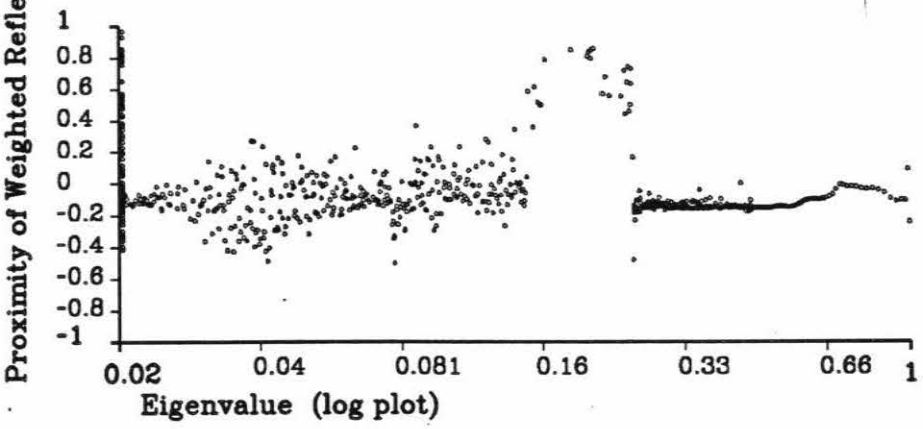

Eigenvector Characteristics for Generic Survey with
128 by 10 square cells, 128 reflector cells
4:1 V-R Weight, No Wrap around (edge effects exist)
(eigenvectors with measurable reflector energy)

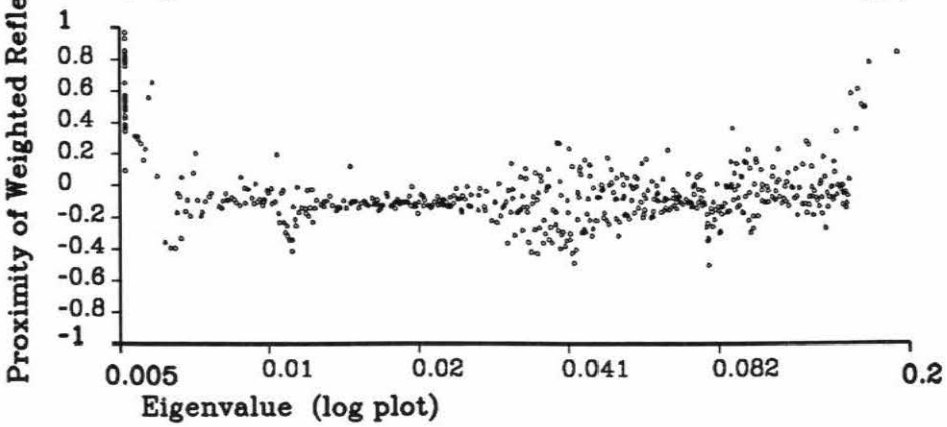

Figures for Chapter 5:

Application of Tomography to Two Data Sets Containing Lateral Velocity Variations

Figure 5.1

Seismic section over an ice lake from the North Slope of Alaska. An ice lake is a lake in the surrounding permafrost that has not frozen because of a high concentration of salts. It is a strong slow velocity anomaly.

Even though static corrections have been applied to remove the effects of the anomaly, a broad general slump remains. Travel times will be picked off of the two marked reflectors. The reflectors are labeled incorrectly and should be switched.

Stacked Seismic Section
(with static corrections)

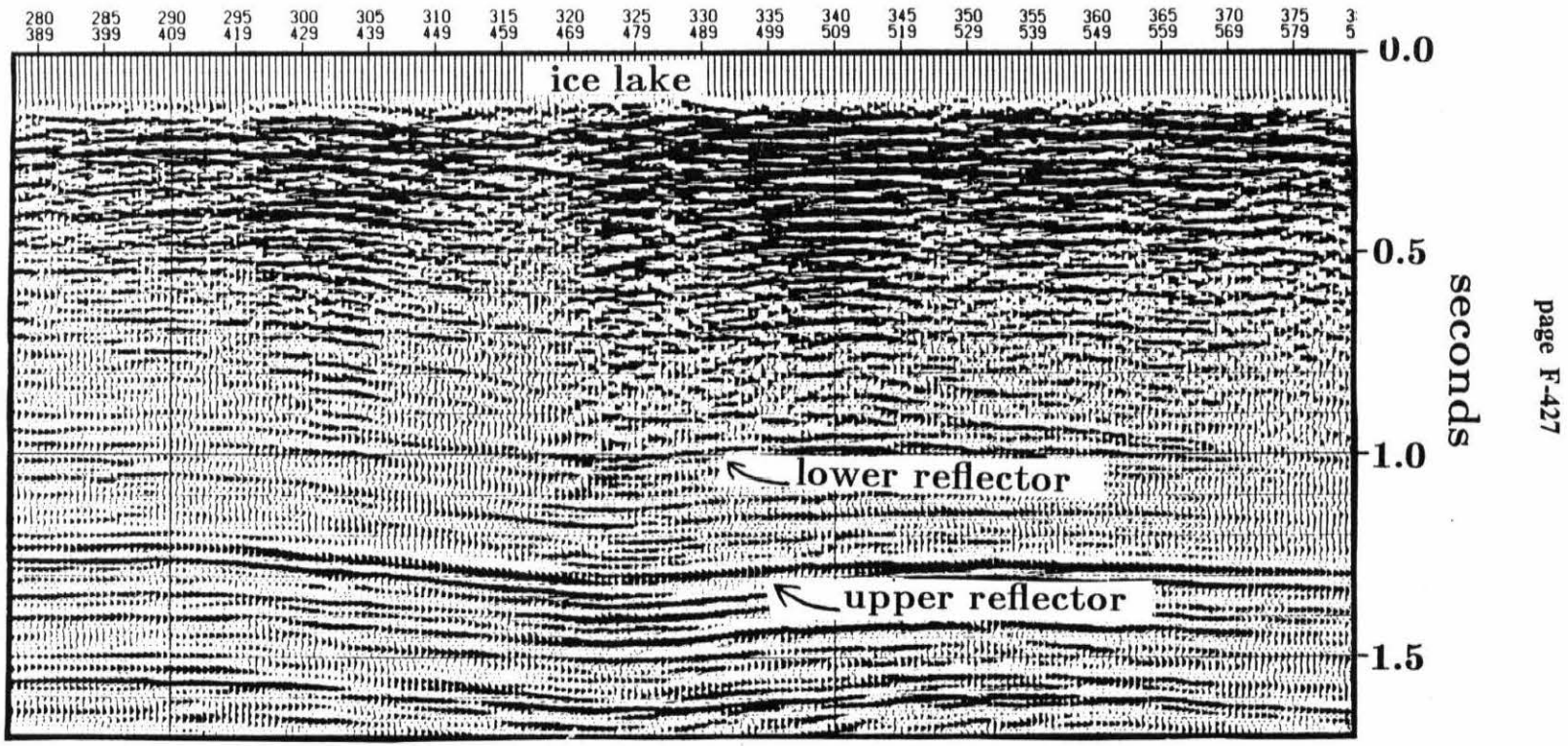

Figure 5.2A & B

Near and far offset sections of the prestack data. NMO has been applied. The difference between the plots suggests that the broad slump of the previous figure is indeed an artifact of the ice lake. Between the two lobes on the far offset section, the ice lake has been under shot and not produced a negative anomaly.

This data is an example of the pre-stack data from which travel times were picked.

Near Offset Section
seconds
0.8
1.0
1.5
1.7
upper reflector
lower reflector

Far Offset section with NMO
seconds
0.8
1.5
1.7
mute
lower reflector

Figure 5.3

Examples of travel time picks from the pre-stack data. Picks are the dots at the peaks of the wave forms.

A: A common mid-point (CMP) section over the ice lake disrupts the hyperbolic moveout path. Arrivals are the most continuous on CMP sections.

B & C: Common offset sections near the ice lake. A few of the picks are questionable. The arrivals are not as continuous as in the CMP section.

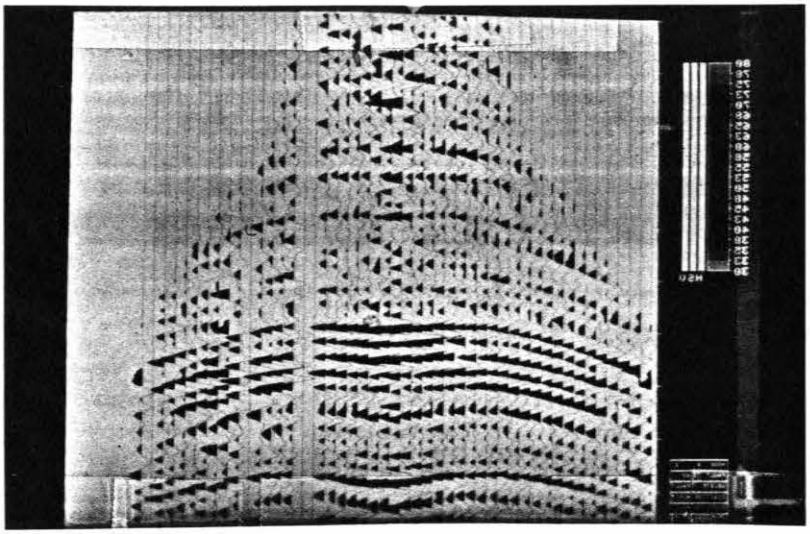

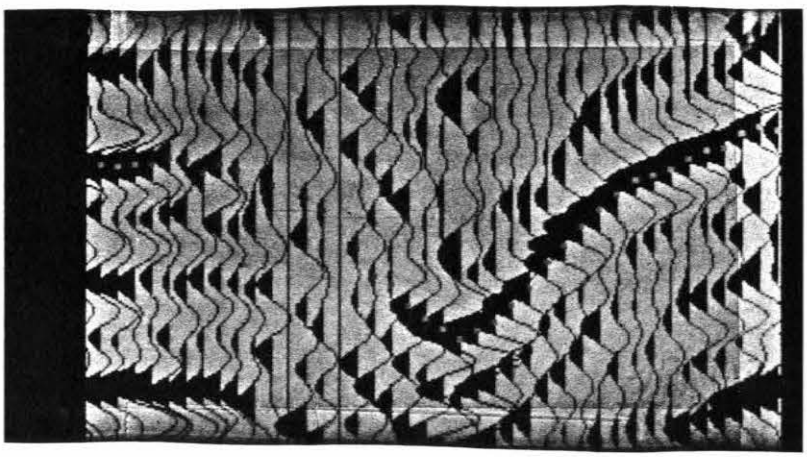

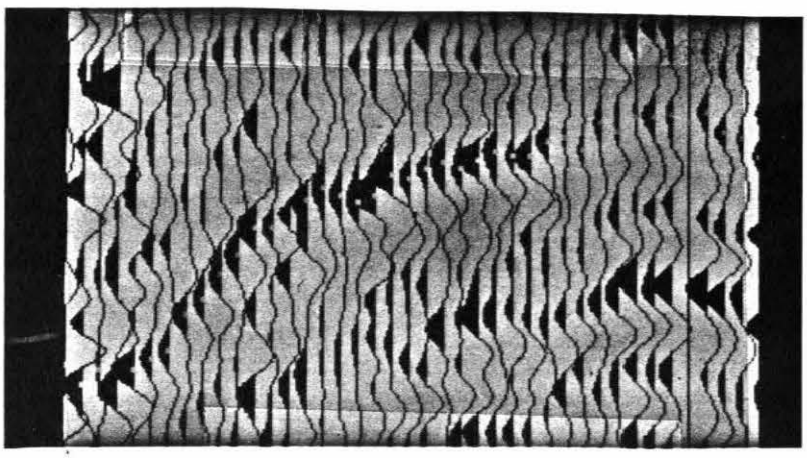

Figure 5.4

Reference model used for tracing rays. Reflectors are plotted on a separate scale so that they can be vertically exaggerated to emphasize their structure. Their actual location in the velocity model can be seen on the following figure.

The ice lake was not included in the reference model. The reference model contained a velocity field that varied only with depth. The permafrost zone was 1000 feet thick with a velocity of 11,000 ft/sec. The velocity then dropped to 7611 ft/sec and continued with a linear velocity gradient to 10,000 ft/sec at the bottom of the model.

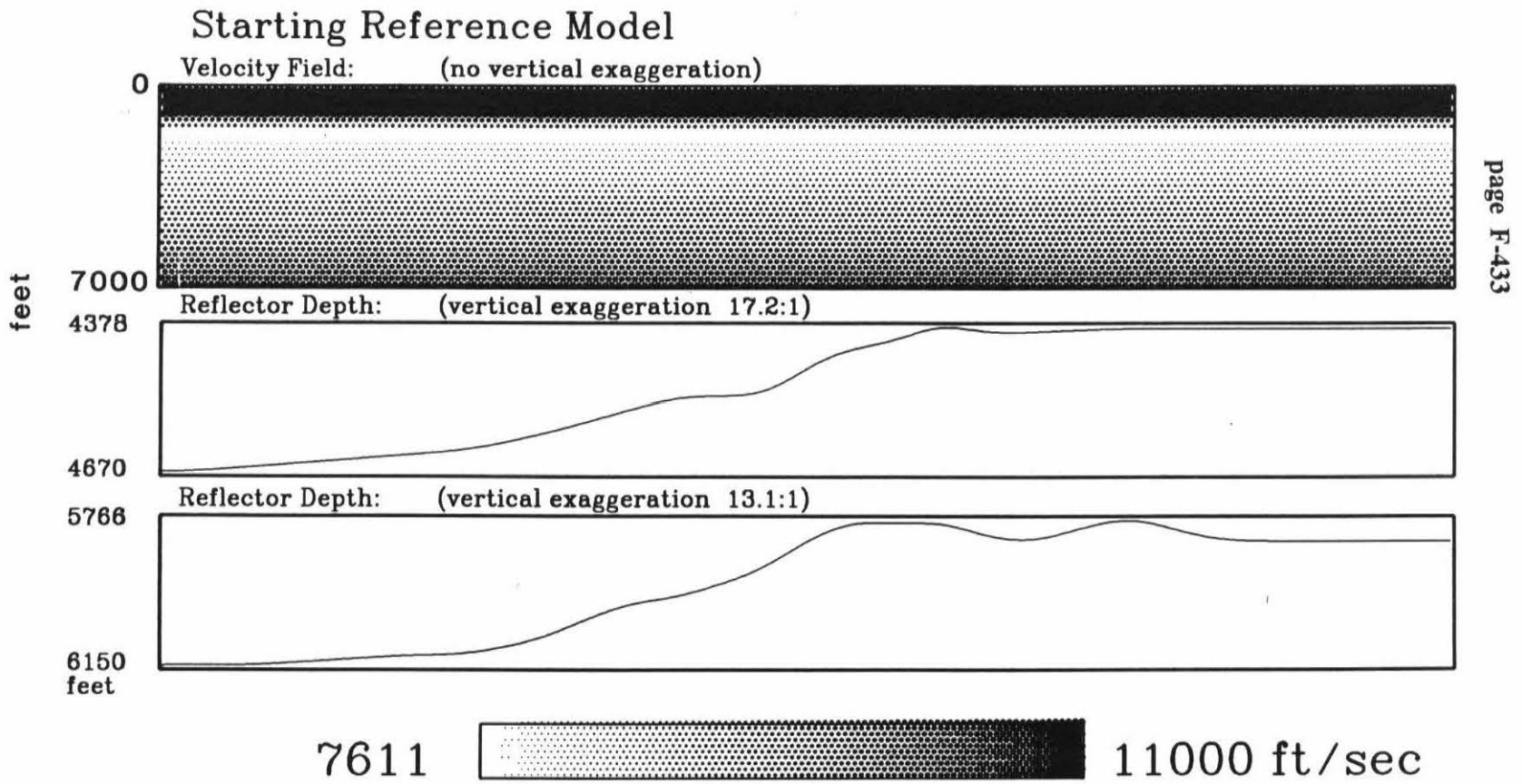
Starting Reference Model
Velocity Field: (no vertical exaggeration)
0
7000
feet
Reflector Depth: (vertical exaggeration 17.2:1)
4378
4670
Reflector Depth: (vertical exaggeration 13.1:1)
5766
6150
feet
7611
11000 ft/sec

Figure 5.5

Density of rays through the reference model. This plot shows the width of the ray coverage and location of the regions of limited ray coverage where there might be edge effects. The location of the two reflectors is obvious from the sudden change of ray density.

Ray density is actually the sum of the path lengths for each cell. The scale of "Rays per Cell" is only approximate since rays at different angles have different average path lengths in the cells.

Ray Density

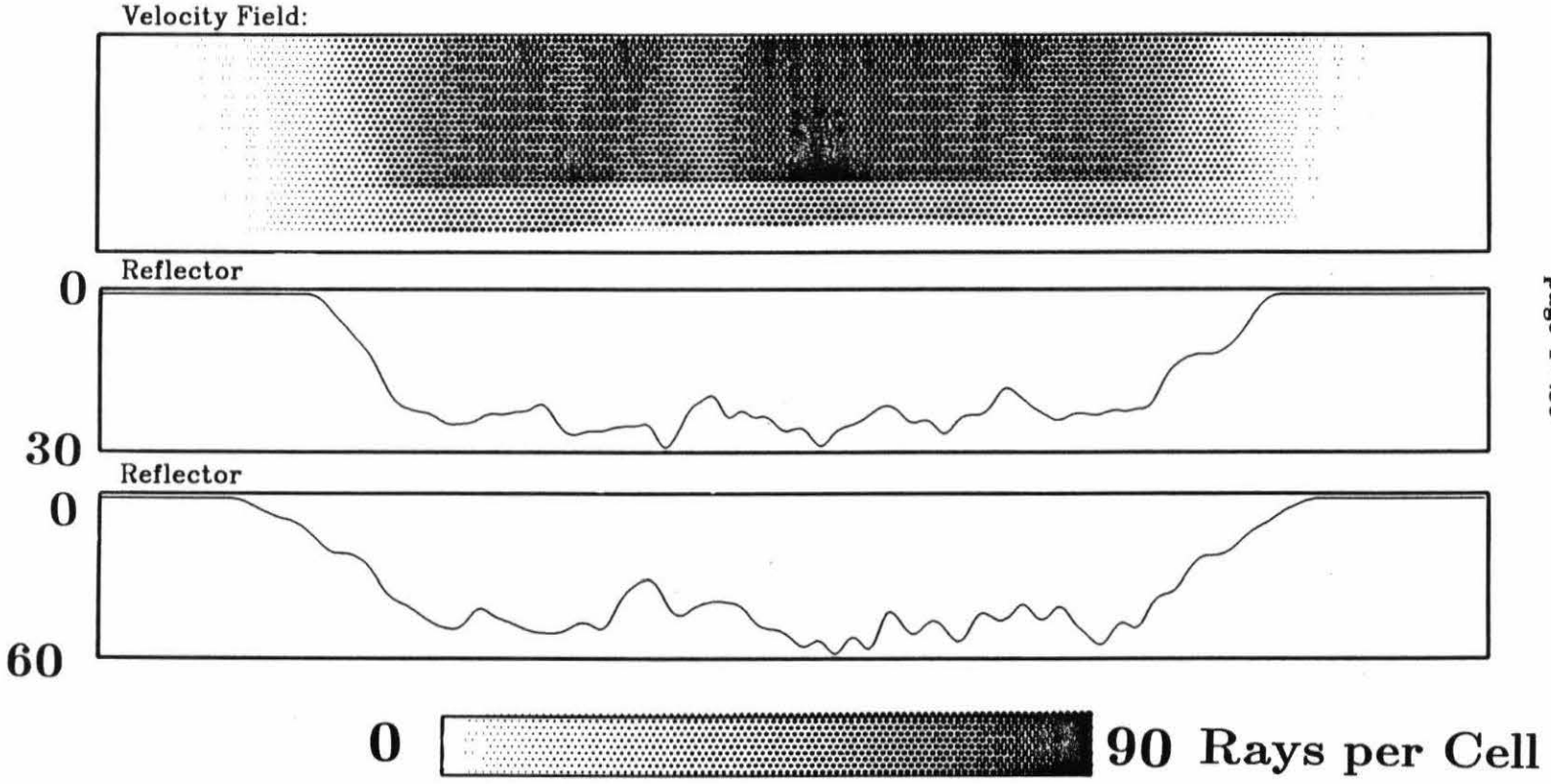
Velocity Field:
Reflector
0
30
Reflector
0
60
0
90 Rays per Cell

Figure 5.6

Two types of plots of the travel time variation between the data and reference model. The left two plots are for the upper reflector, the right two for the lower one. Since a split spread recording geometry was used, the near offset is in the center.

The upper plots emphasize the broad features in the travel time variations. The signature of the ice lake is apparent as the "**X**". One branch of the "**X**" is the common shot line, the other is the common offset line.

The lower plots emphasize the high frequency aspect of the data, which may represent noise. The travel time picks from the upper reflector on the right side appears to be much noisier than that for the lower reflector on the left side.

Travel Time Variations between data and model

permafrost model

Figure 3

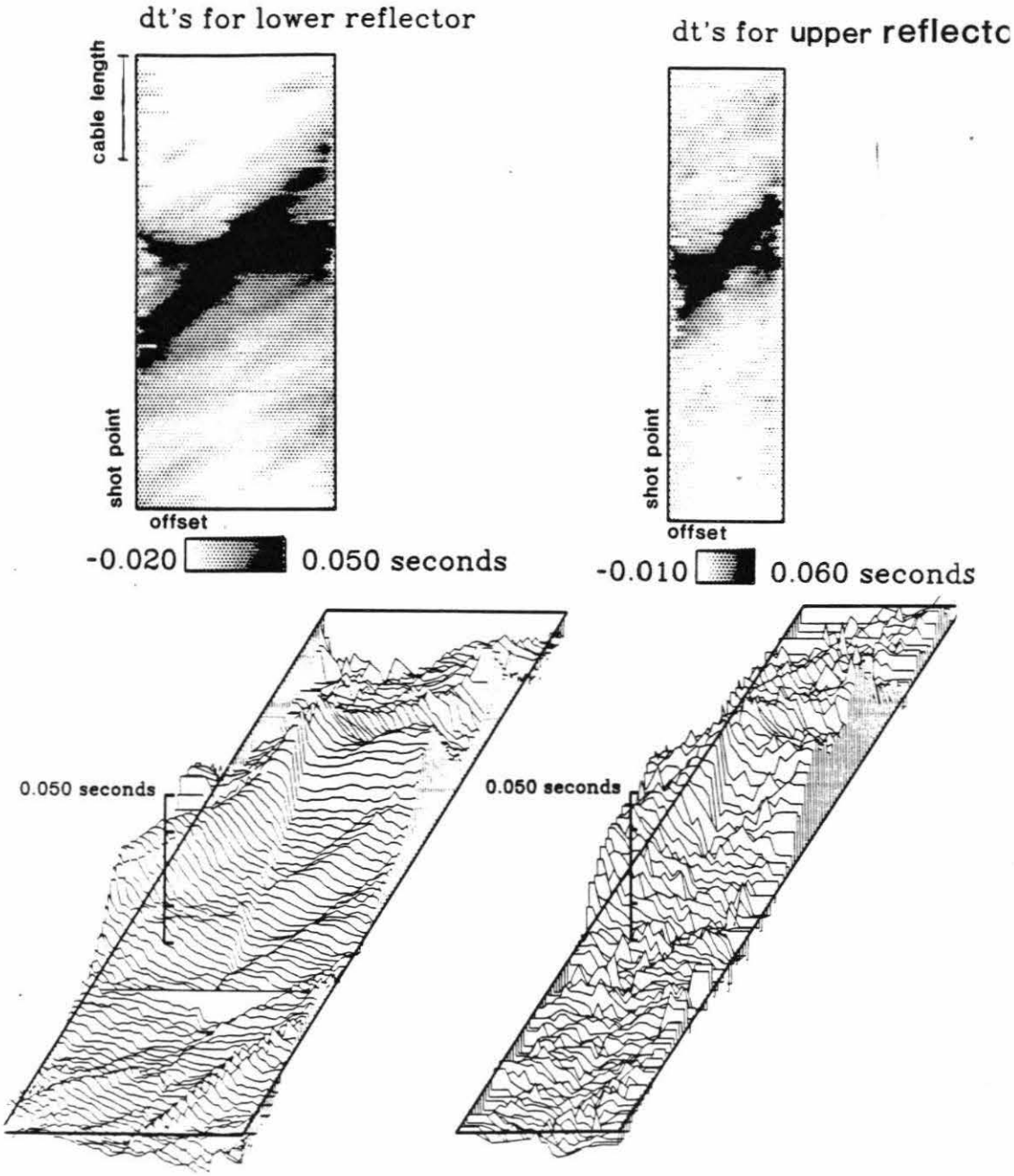

Figure 5.7A & B

Constrained inversions that only allow the permafrost layer in the top 1000 feet and the reflector to vary. The inversion is different from statics in that the ray bending in the high velocity permafrost layer, the linear velocity gradient with depth, and reflector structure is taken into account.

A: Inversion of data with a reflector bias. A reflector bias tries to adjust the reflector position to match the travel times and only adjusts the velocity when warranted by the data. Thus, velocity-reflector depth ambiguities that cannot be resolved over the eigenvalue range are placed in the reflector. This biased inversion is achieved by first back projecting the travel time deviations into reflector depth and then continuing the inversion allowing both the reflector and velocity to vary.

There is a strong negative velocity anomaly at the position of the ice lake. However, the reflector underneath the ice lake exhibits a strong slump. Other, lower amplitude structure which was not apparent in the raw data has also appeared.

The cable length for one side of the split spread is marked at the top of the model.

B: Another inversion of the permafrost data, except biased toward velocity. The velocity anomaly associated with the ice lake is now significantly larger and the slump under the ice lake is smaller than the reflector biased inversion. Much of the other structure does not appear to have changed.

Eigenvalue range: (1.0–0.05)

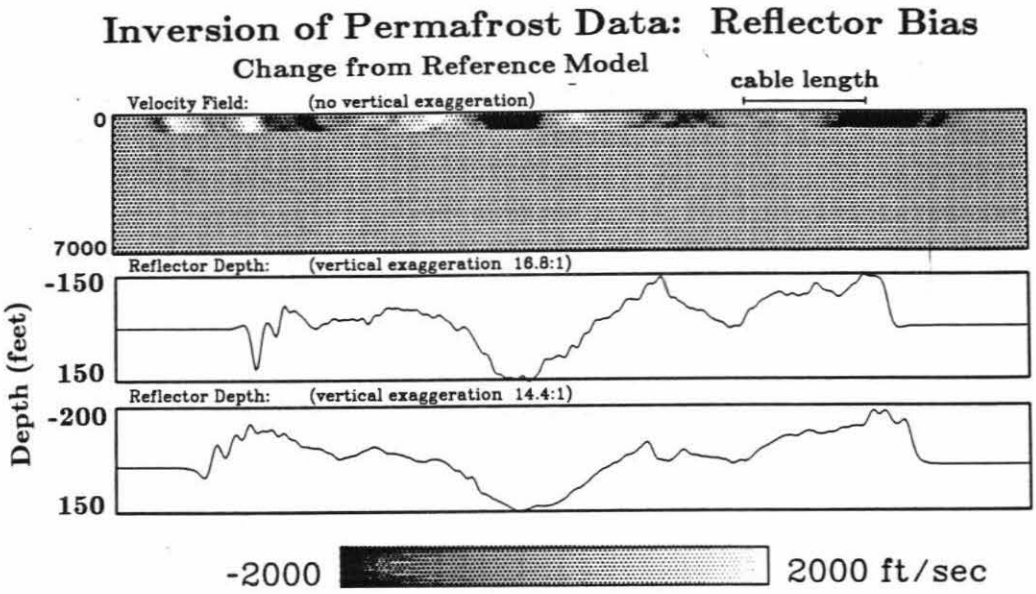

Eigenvalue range: (1.0–0.05)

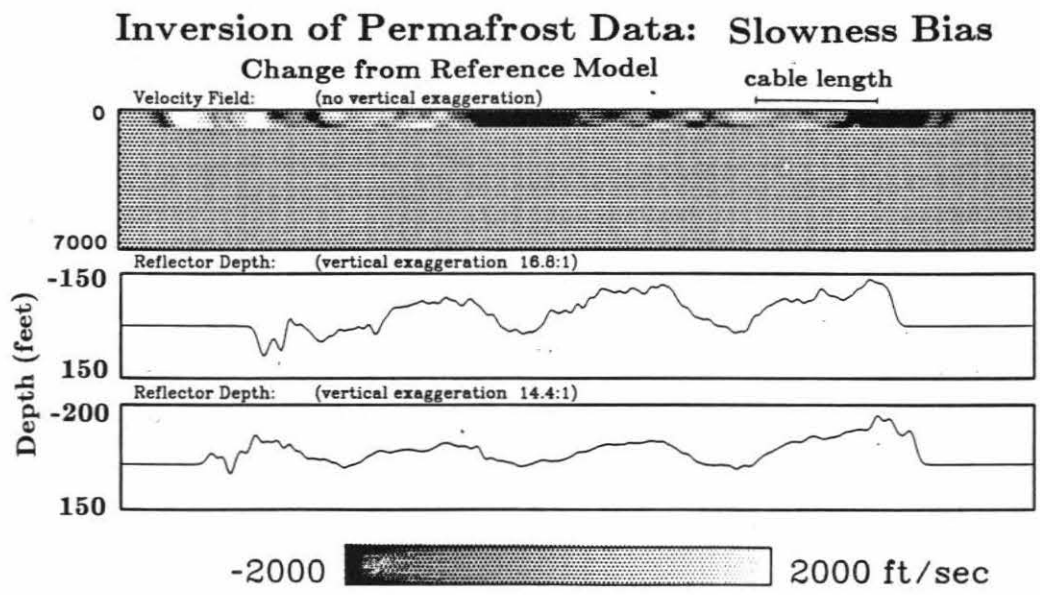

Figure 5.8

The previous two figures are subtracted from each other to clearly show the differences between them. The difference is the velocity-reflector depth ambiguity that could not be resolved over the eigenvalue range of the inversions. The ambiguity consists of mainly one broad bump that is identical in both reflectors. The lack of the high frequency aspects in the inversion demonstrate that they are well inverted with the constraint of only allowing the surface layer to vary.

Difference between Reflector Biased Inversion and Velocity Biased Inversion eigenvalue range: (1.0-0.05)

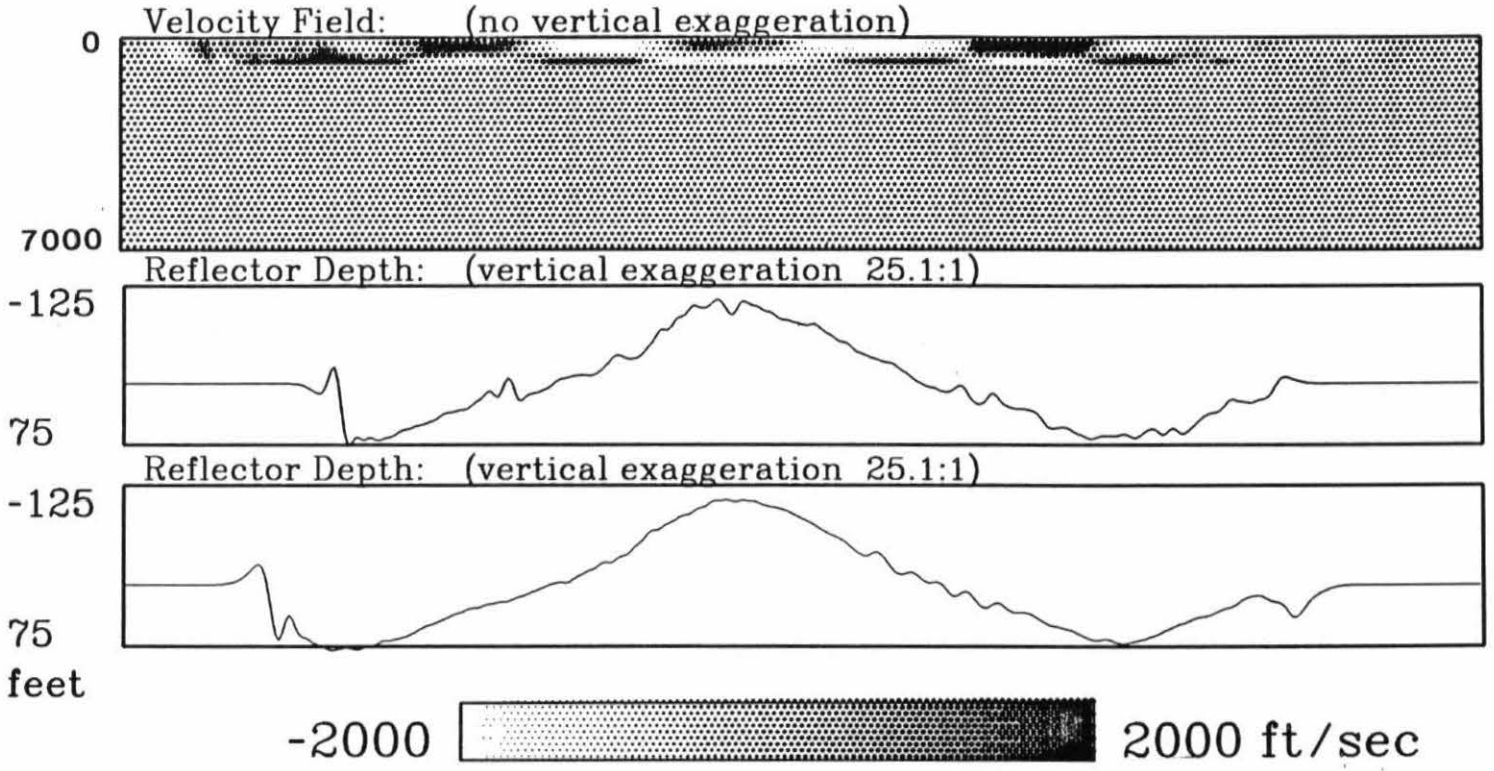

Figure 5.9A & B

To confirm that the unresolved velocity and reflector depth of the two biased inversions is indeed the result of the ice lake, a sample ice lake is modeled.

A: Model of ice lake. Travel times are computed for this model and used as data in the identical inversion procedure as before.

B: Identical plot as in Figure **5.8** except using synthetic data. The figure is nearly identical to Figure **5.8** confirming that the ambiguous velocity and reflector depth is caused by the ice lake.

Velocity Field used for Modeling Ice Lake

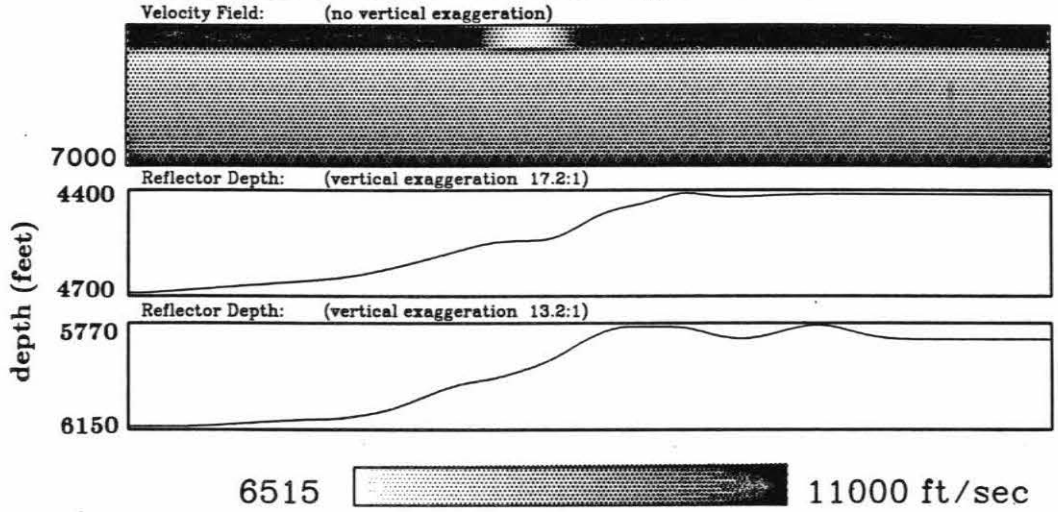

Difference between Reflector Biased Inversion and Velocity Biased Inversion of Simulated Ice Lake

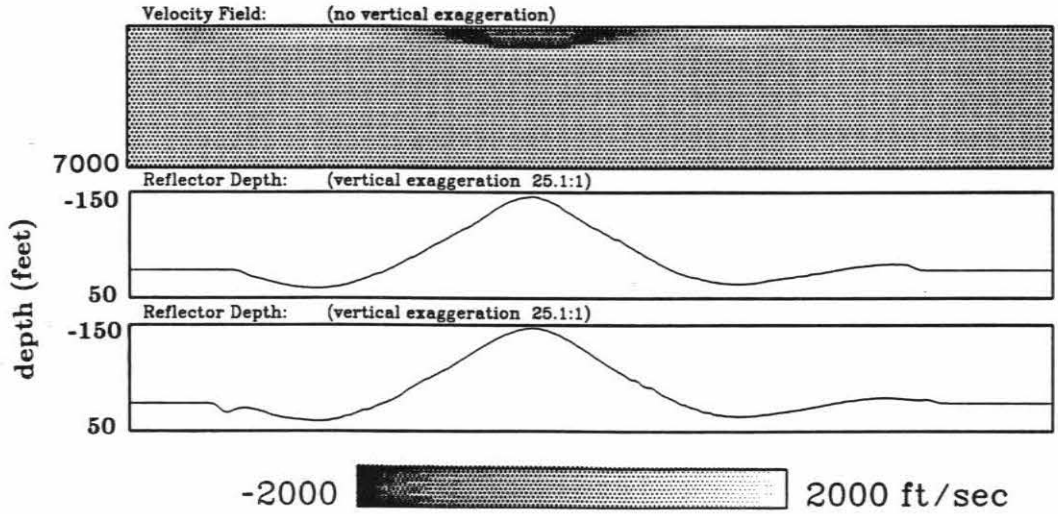

Figure 5.10A & B

The biased inversions are continued to smaller eigenvalue. Shown here are the subtractions similar to Figure **5.8**.

The velocity-reflector depth ambiguity has been resolved in the inversion down to the eigenvalue 0.01. The two biased inversions have converged.

Difference between Reflector Biased Inversion and Velocity Biased Inversion eigenvalue range: (1.0-0.02)

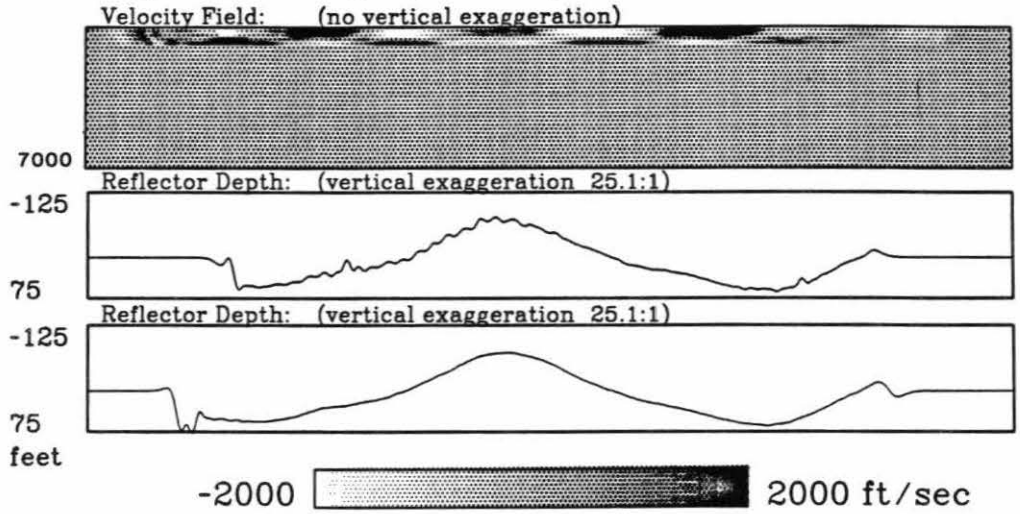

-2000 2000 ft/sec

Difference between Reflector Biased Inversion and Velocity Biased Inversion eigenvalue range: (1.0-0.01)

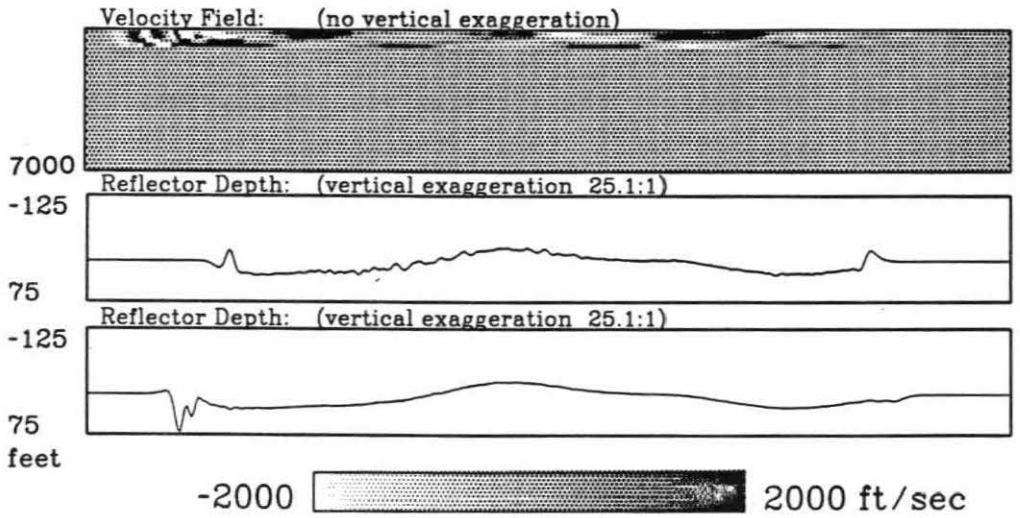

-2000 2000 ft/sec

Figure 5.11A & B

To analyze the noise in the travel time picks, inversions of different halves of the data are compared. The data was split in half by shot gathers, so each half contained alternate shot points. With the two data sets sharing no common data, they represent two independent surveys. The difference between the inversions of the independent surveys is a measure of the noise in the data. Since each inversion used only half the data and the differences are subtracted, the results here are twice the actual noise level.

The amplitude of the reflector variations does not increase significantly in the inversion to smaller eigenvalue because a reflector bias was used in the inversions and some of the reflector variations have traded off into velocity variations. Note the scale change of the velocity variations.

The reflector variations in these figures is markedly low, on the order of only 10-20 feet. The errors from the travel time picks are not a serious problem for this data set. The greater variations of the upper reflector indicate that the travel time picks from it were less accurate.

In contrast to Figure **5.10b**, the high frequency reflector variations are more of a concern at smaller eigenvalues. Thus, what eigenvalue range one choses to carry out the inversion is dependent on whether the objective is to resolve smaller scale structure or broader scale structure.

The long wavelength pattern in the inversion to smaller eigenvalue is bothersome and will be investigated in the following figure.

Difference between Inversions of Alternate Halves of the Travel Times. eigenvalue range: (1.0-0.05)

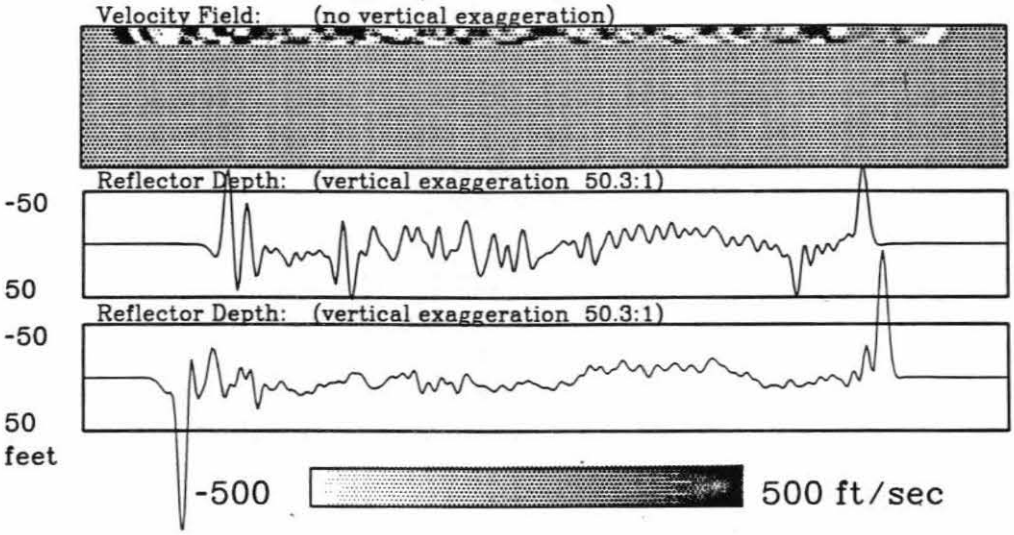

Difference between Inversions of Alternate Halves of the Travel Times. eigenvalue range: (1.0-0.01)

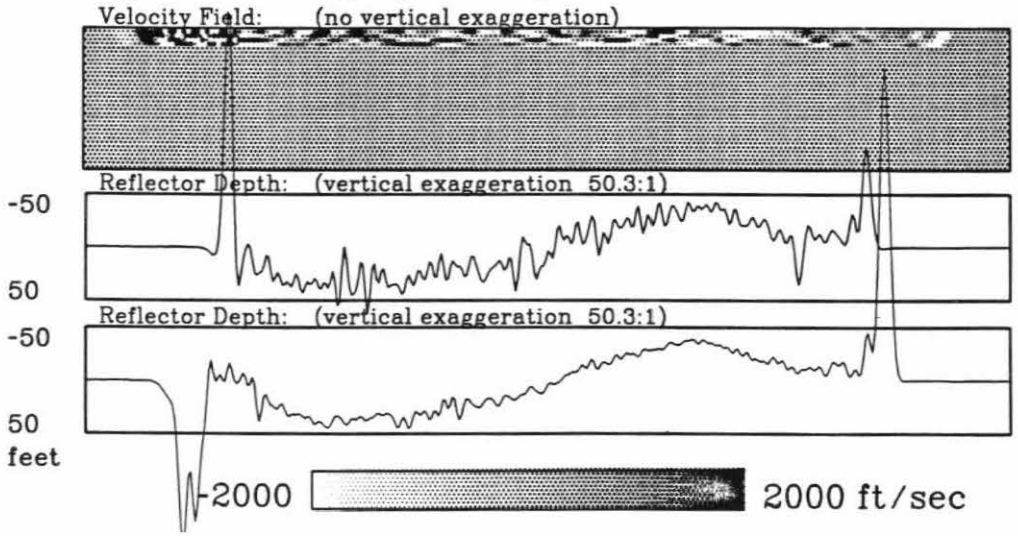

Figure 5.12

Change of the velocity biased inversion when carried from a minimum eigenvalue of 0.02 to 0.01. The change in inverting to a smaller eigenvalue is a large bothersome pattern that dominates the inversion. This pattern also dominates the reflector biased inversion and therefore does not appear in the difference between the inversions.

This component is clearly unreasonable and results from some noise in the data. It most likely is an artifact from the strong travel time deviations near the edges of the survey. Data quality at the edges is poor which can be seen from the inversions in Figures **5.7a & b**. The edges effect the central part of the survey presumably because of the limited width of the survey.

This artifact is not considered to be serious since it does not bear on the main objective: the resolution of the velocity-reflector depth ambiguity underneath the ice lake. The two patterns are essentially orthogonal to each other. Moreover, the inversions could be rerun with some of the travel times deviations at the edges removed.

Difference between Inversions over eigenvalue ranges: (1.0-0.02) & (1.0-0.01)

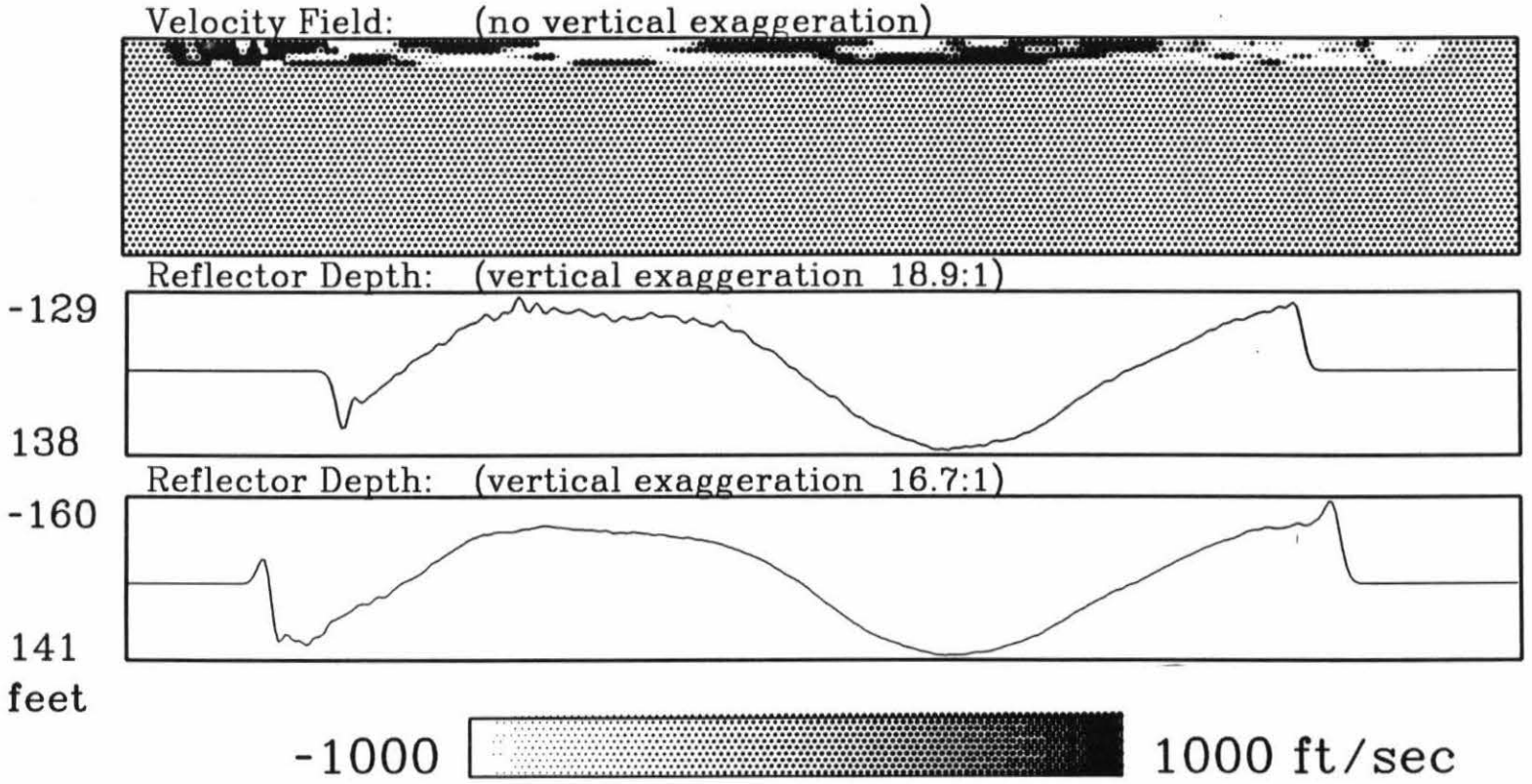

Figure 5.13

Seismic section from the Central Valley of California over a gas pocket. The effect of the gas pocket is quite clear in the center where the upper reflectors exhibit a deep slump and the lower reflectors are washed out.

Edges are distorted because section was produced by performing a pre-stack migration through a laterally invariant velocity field.

This data set is the same as that used by Toldi (1985).

Stacked Section
Central Valley Data

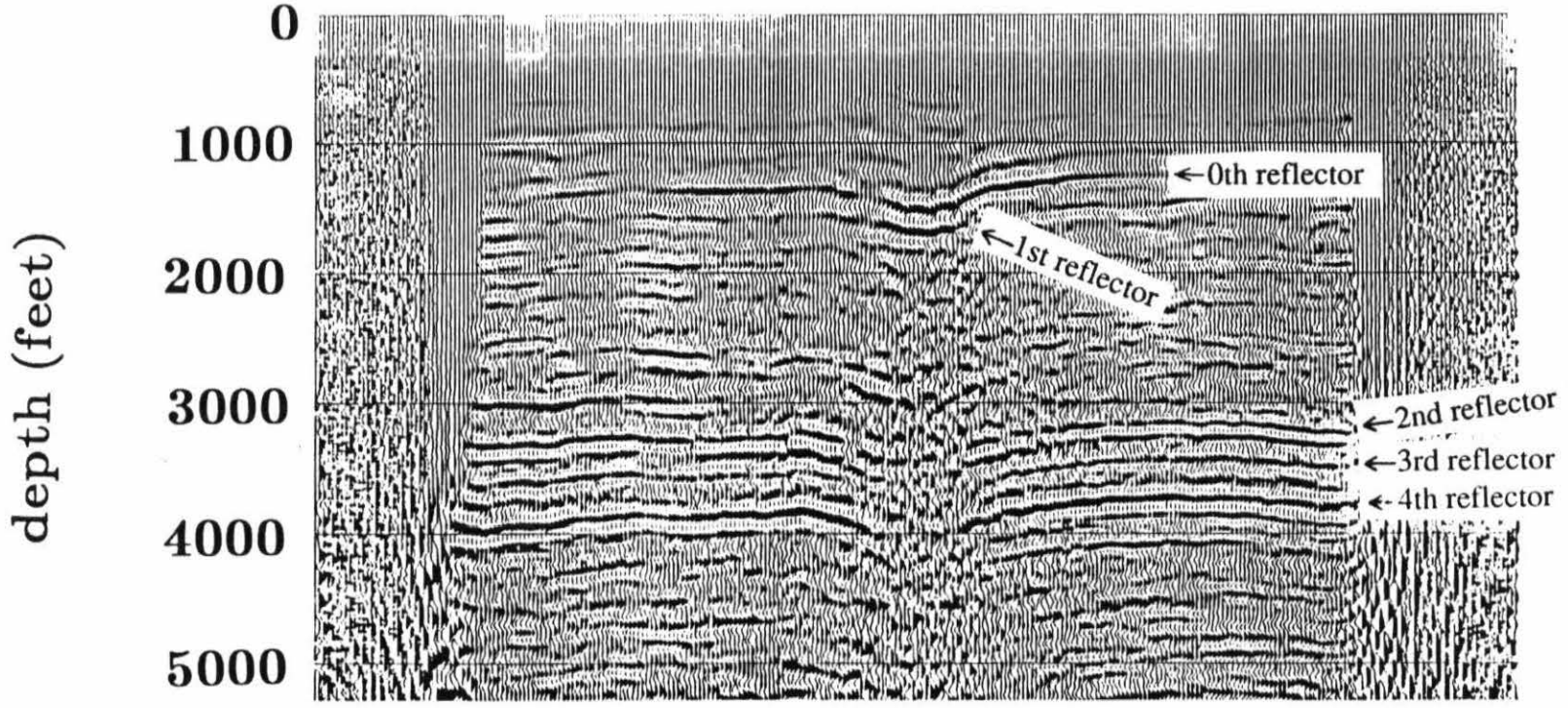

Figure 5.14A & B

Examples of travel time picks on shot gathers. Picks in both figures are high quality. The lower figure has more variations between neighboring traces.

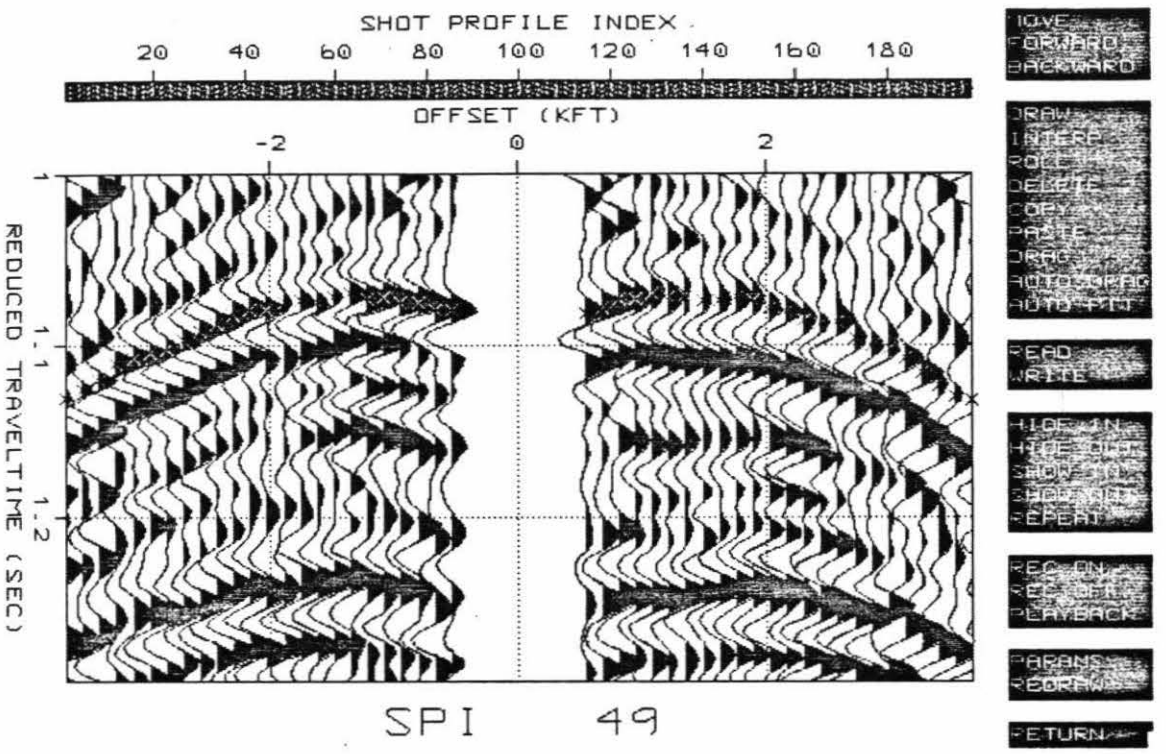
SHOT PROFILE INDEX
20 40 60 80 100 120 140 160 180
OFFSET (KFT)
-2 0 2
REDUCED TRAVELTIME (SEC)
1 1.1 1.2
SPI 49
MOVE
FORWARD
BACKWARD
DRAW
INTERP
DELETE
COPY
PASTE
DRAG
AUTO DRAG
AUTO FIT
READ
WRITE
HIDE IN
HIDE OUT
SHOW IN
SHOW OUT
REPEAT
REC ON
REC OFF
PLAYBACK
PARAMS
REDRAW
RETURN

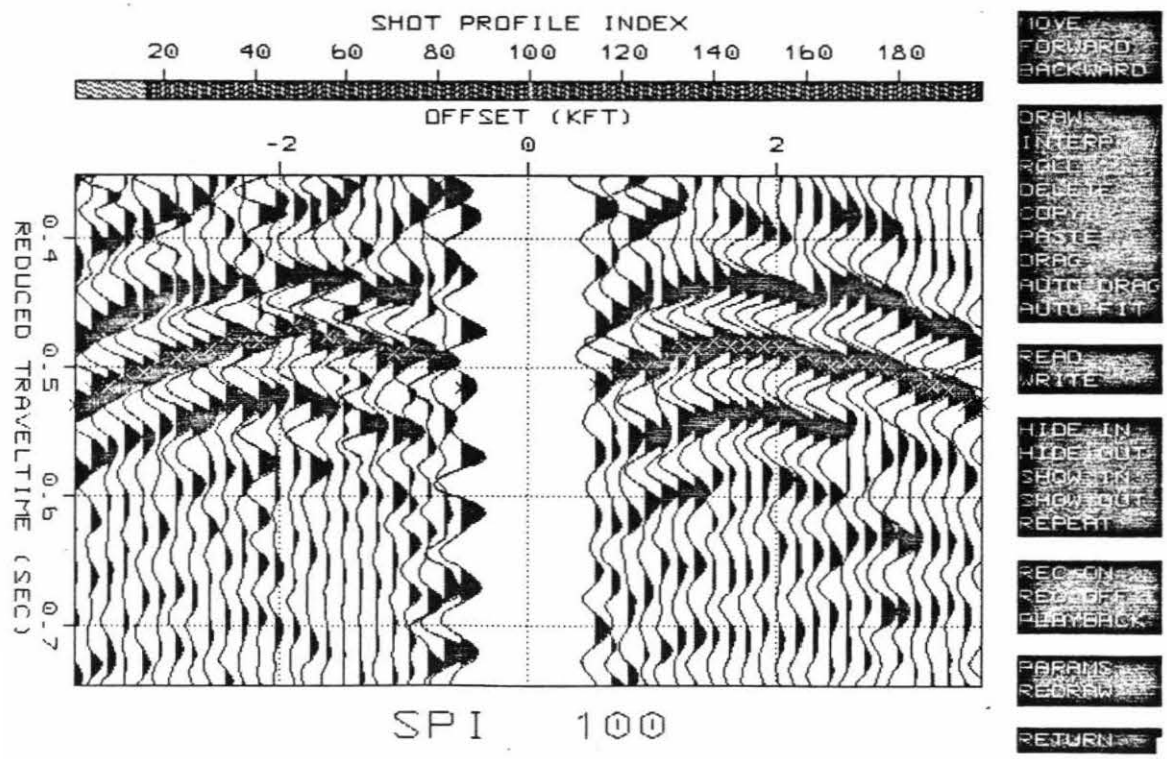
SHOT PROFILE INDEX
20 40 60 80 100 120 140 160 180
OFFSET (KFT)
-2 0 2
REDUCED TRAVELTIME (SEC)
0.4 0.5 0.6 0.7
SPI 100
MOVE
FORWARD
BACKWARD
DRAW
INTERP
DELETE
COPY
PASTE
DRAG
AUTO DRAG
AUTO FIT
READ
WRITE
HIDE IN
HIDE OUT
SHOW IN
SHOW OUT
REPEAT
REC ON
REC OFF
PLAYBACK
PARAMS
REDRAW
RETURN

Figure 5.14C & D

Examples of travel time picks that suggest problems. A clear arrival at far offset bifurcates as one moves to near offset. Which of the two branches to take is not entirely clear.

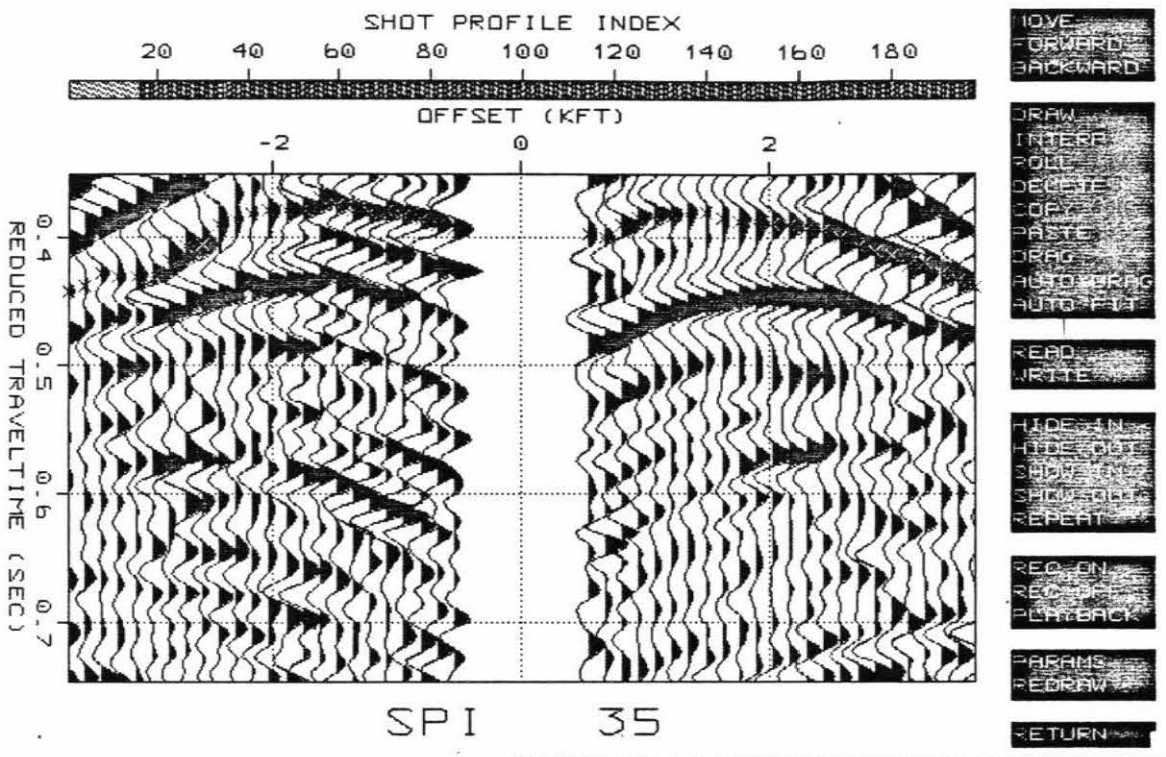
SHOT PROFILE INDEX
20 40 60 80 100 120 140 160 180
OFFSET (KFT)
-2 0 2
REDUCED TRAVELTIME (SEC)
0.4 0.5 0.6 0.7
SPI 35
MOVE
FORWARD
BACKWARD
DRAW
INTERP
ROLL
DELETE
COPY
PASTE
DRAG
AUTODRAG
AUTO FIT
READ
WRITE
HIDE IN
HIDE OUT
SHOW IN
SHOW OUT
REPEAT
REC ON
REC OFF
PLAYBACK
PARAMS
REDRAW
RETURN

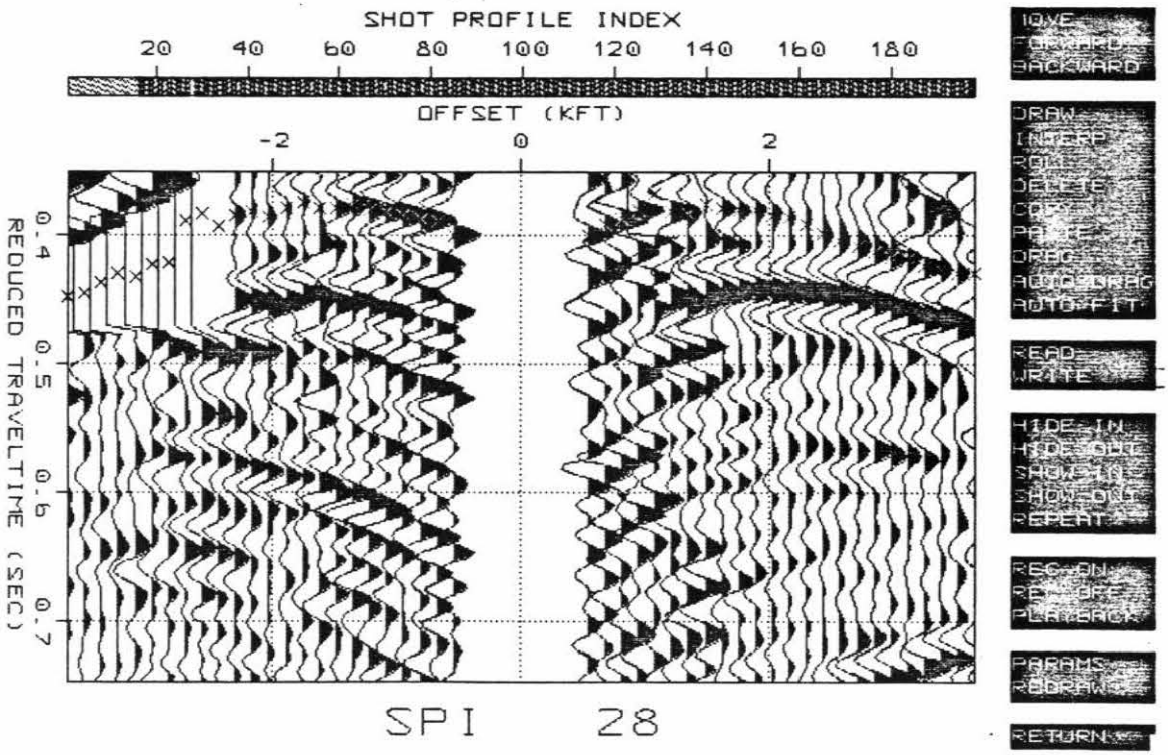
SHOT PROFILE INDEX
20 40 60 80 100 120 140 160 180
OFFSET (KFT)
-2 0 2
REDUCED TRAVELTIME (SEC)
0.4 0.5 0.6 0.7
SPI 28
MOVE
FORWARD
BACKWARD
DRAW
INTERP
ROLL
DELETE
COPY
PASTE
DRAG
AUTODRAG
AUTO FIT
READ
WRITE
HIDE IN
HIDE OUT
SHOW IN
SHOW OUT
REPEAT
REC ON
REC OFF
PLAYBACK
PARAMS
REDRAW
RETURN

Figure 5.15

Ray density from ray traced through reference model. Reference model consisted of flat reflectors and a laterally invariant velocity taken from Toldi (1985). The figure shows the extent of ray coverage, and the location of the ray coverage edges where artifacts are expected.

Ray Density in Velocity Cells

(no vertical exaggeration)

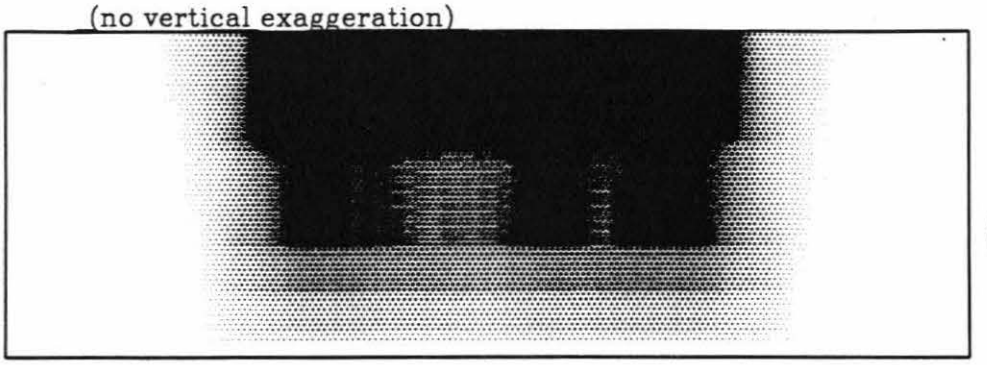

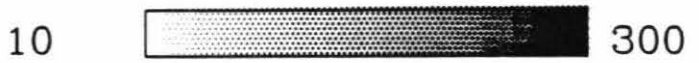

Ray Density in Reflector Cells

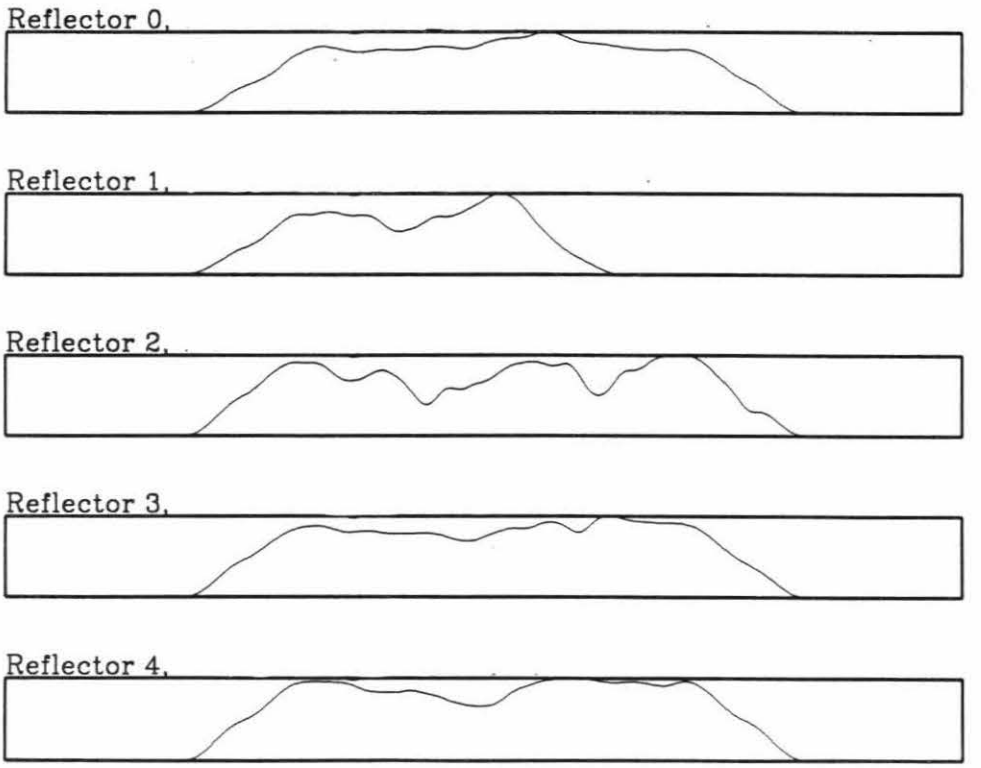

Figure 5.16

An initial inversion was performed to guide the result based on some simple geologic assumptions: That a gas pocket exists near the surface at the center of the model and that the remaining broad variations are mainly the result of reflector variations. This inversion was used as input to the following inversion but without the retracing of rays.

Initial Controlled Inversion to Implement Simple Geologic Knowledge

(change from reference model)

(no vertical exaggeration)

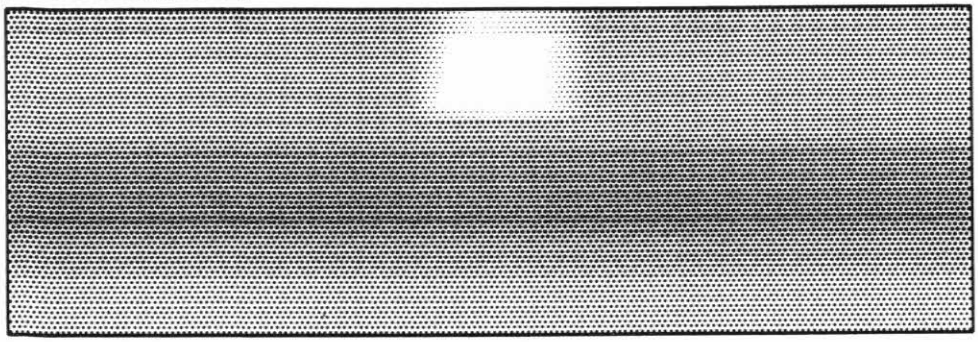

Reflector depths:

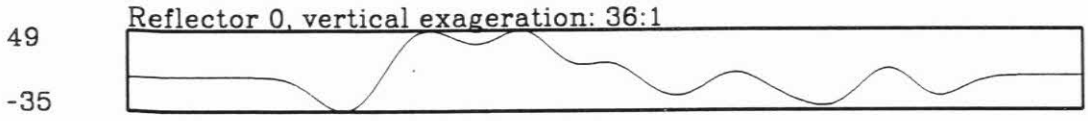

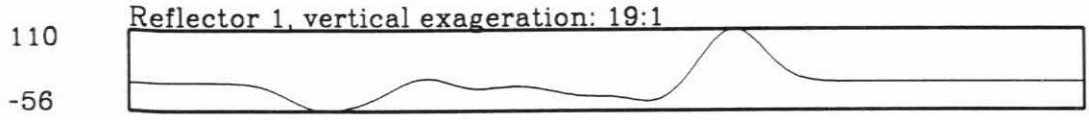

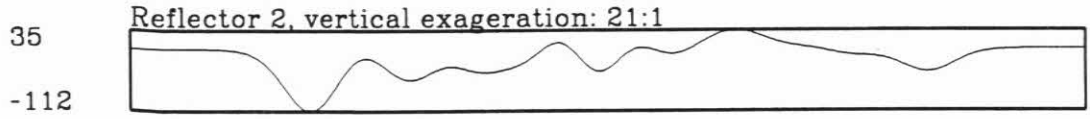

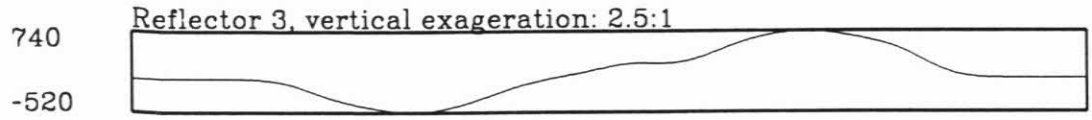

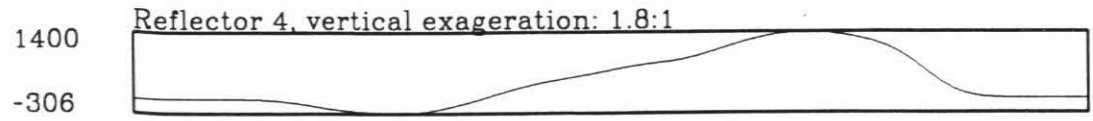

Figure 5.17

Inversion to a very small eigenvalue. Gas pocket has been inverted in the center at the top of the model.

Many other velocity variations appear. Most are expected to be artifacts from the inability to resolve the velocity-reflector depth ambiguity without constraints and the small maximum ray angle. However, since the goal of tomography is to produce a sharp image from migration rather than the correct reflector depth, these artifacts are not considered to be serious.

Inversion over Eigenvalue Range: (1.0-0.01)

Change from Reference Model

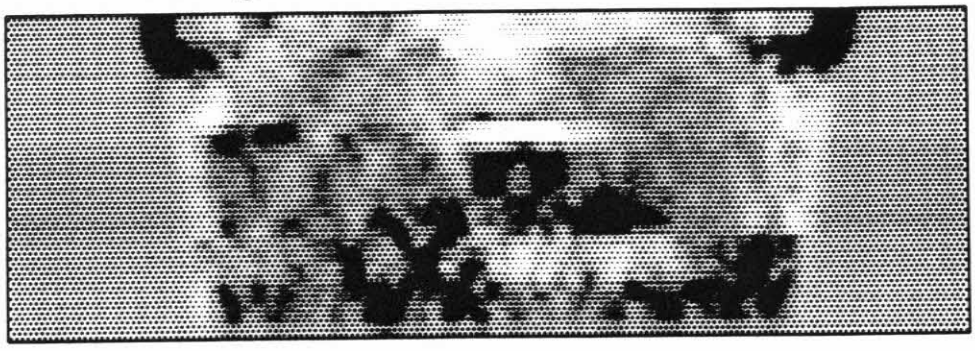

-1000 1000 ft/sec

Reflector Position

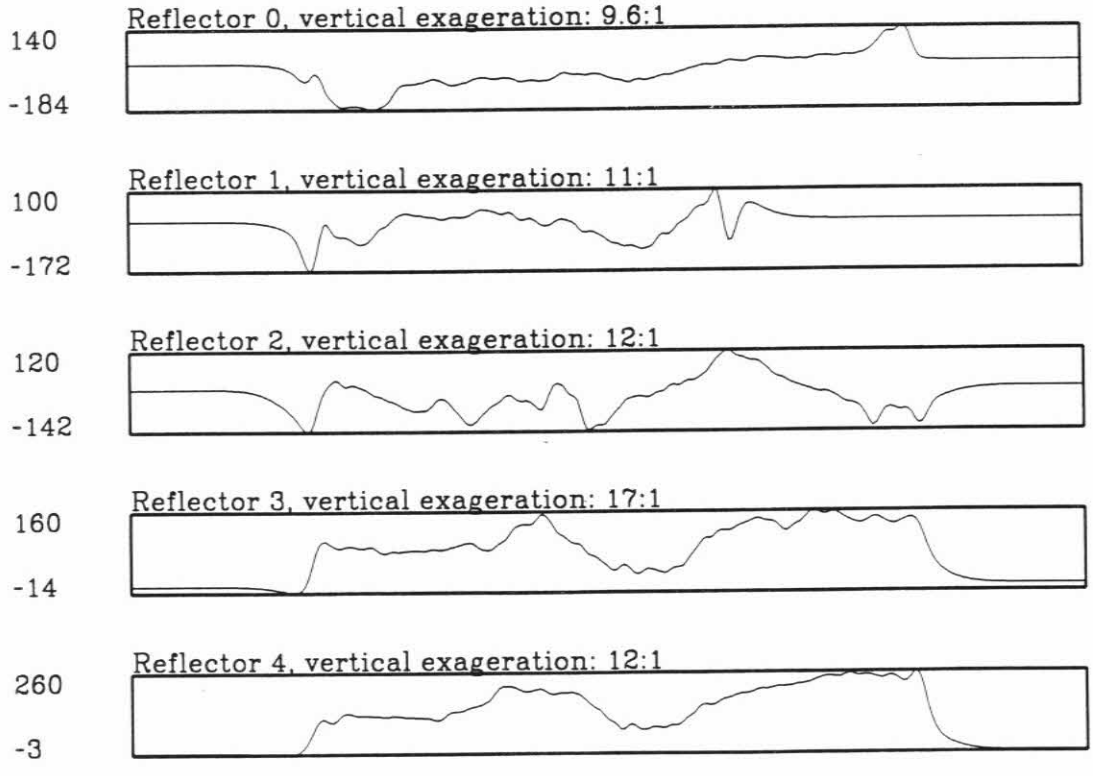

Figure 5.18

Prestack migration through velocity field of inversion in previous figure. Code used is 45°, finite difference, frequency domain.

The reflector is now imaged underneath the gas pocket. That the upper reflectors now have a lower amplitude than in the original section in Figure **5.13** is the result of two possible factors: 1) the migration is plotted in real amplitude without AGC & 2) the travel time picks for the upper reflectors may be seriously corrupted. The lower reflectors may have increased in amplitude so much that the relative amplitude of the upper ones have been reduced. The sample travel time picks from the upper reflectors are shown above in Figures **5.14c & d**. The wrong cycle may have been picked.

Prestack Migration through best Inversion
Central Valley Data

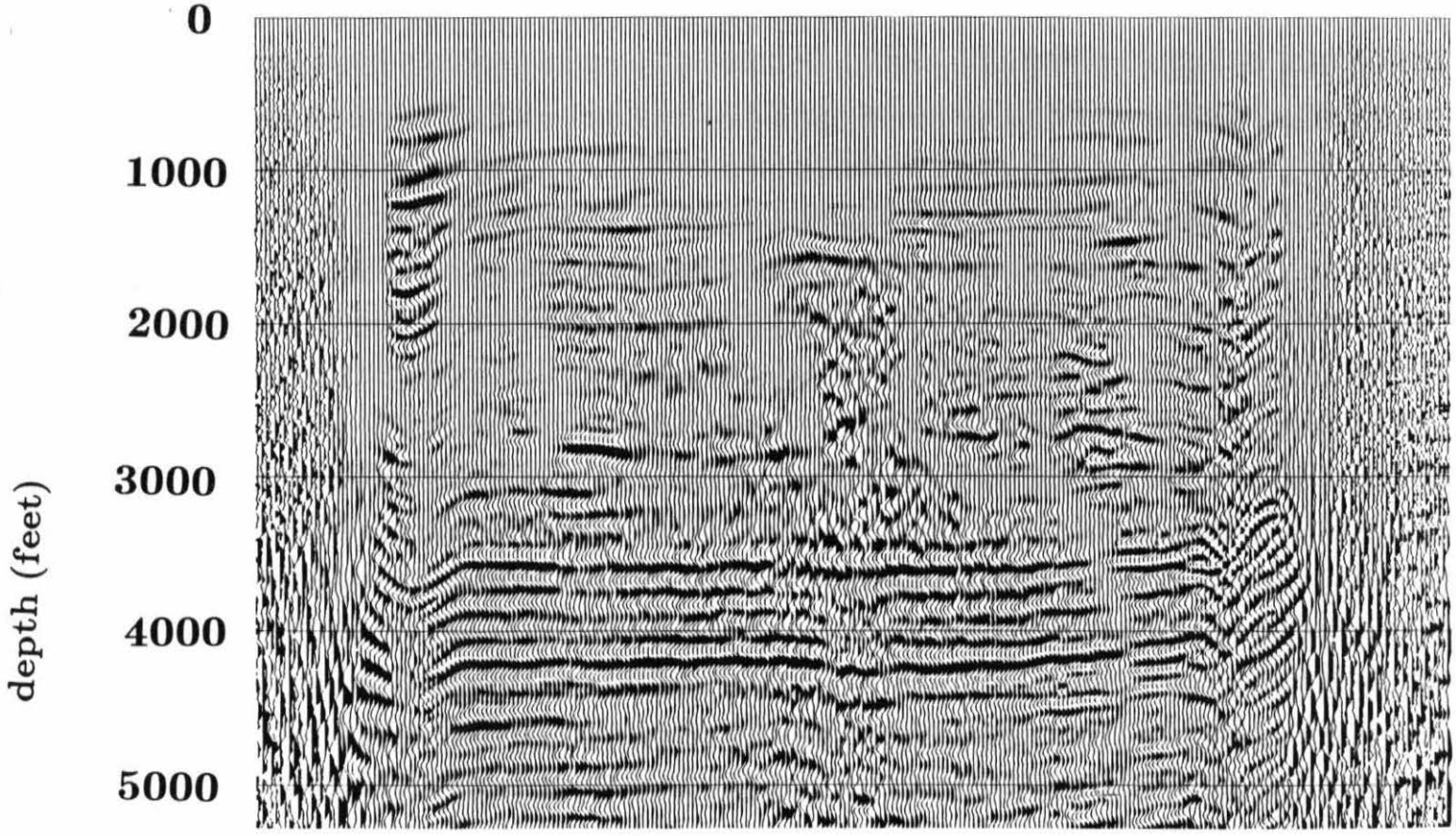

Figure 5.19

Inversion for velocity only. The reflectors were kept at their original depth and flat shape. The different velocity scale make this figure difficult to compare with the corresponding one in Figure **5.17**.

The objective here is to analyze the effect of a more restricted, simpler inversion.

Velocity-only Inversion over Eigenvalue Range: (1.0-0.01)

Change from Reference Model

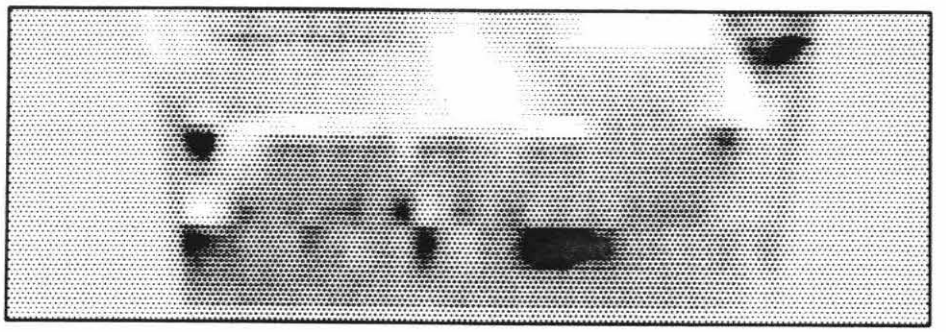

-500 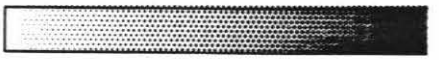 2000 ft/sec

Reflector Position

Reflector 0, vertical exageration: 1500:1

0 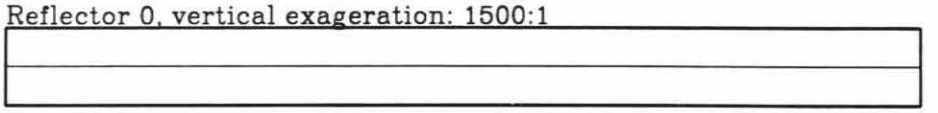

Reflector 1, vertical exageration: 1500:1

0 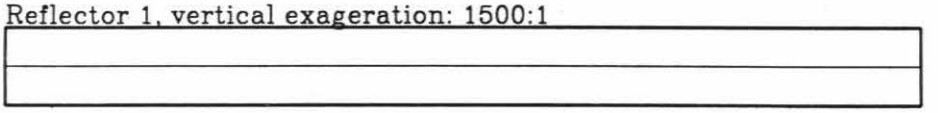

Reflector 2, vertical exageration: 1500:1

0 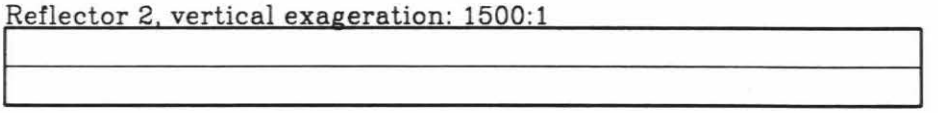

Reflector 3, vertical exageration: 1500:1

0 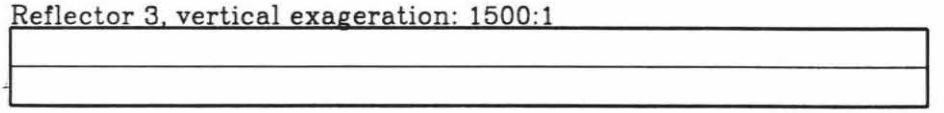

Reflector 4, vertical exageration: 1500:1

0 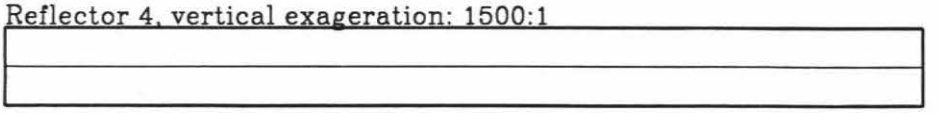

Figure 5.20

Prestack migration through velocity field of inversion in previous figure. The reflectors are nearly perfectly flat. This result is not surprising since, the velocity model was adjusted to match the flat reflectors of the reference model.

The reflector is continuous under the gas pocket.

Prestack Migration through Velocity Only Inversion
Central Valley Data

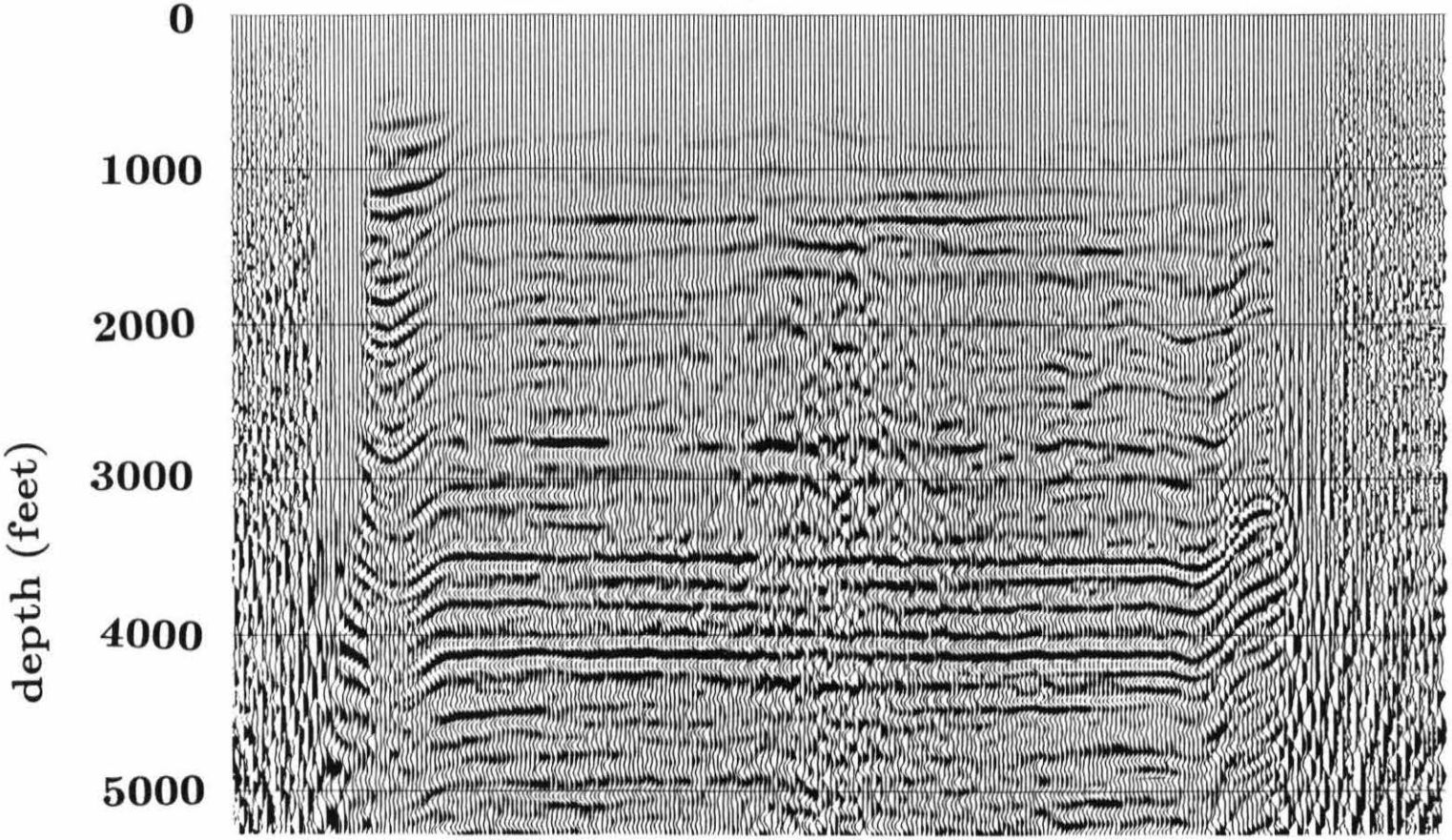

Figure 5.21

The two migrations are compared by the energy in each trace. The migration through the combined inversion for velocity and reflector depth produces a uniformly stronger image than the migration through the inversion for velocity only.

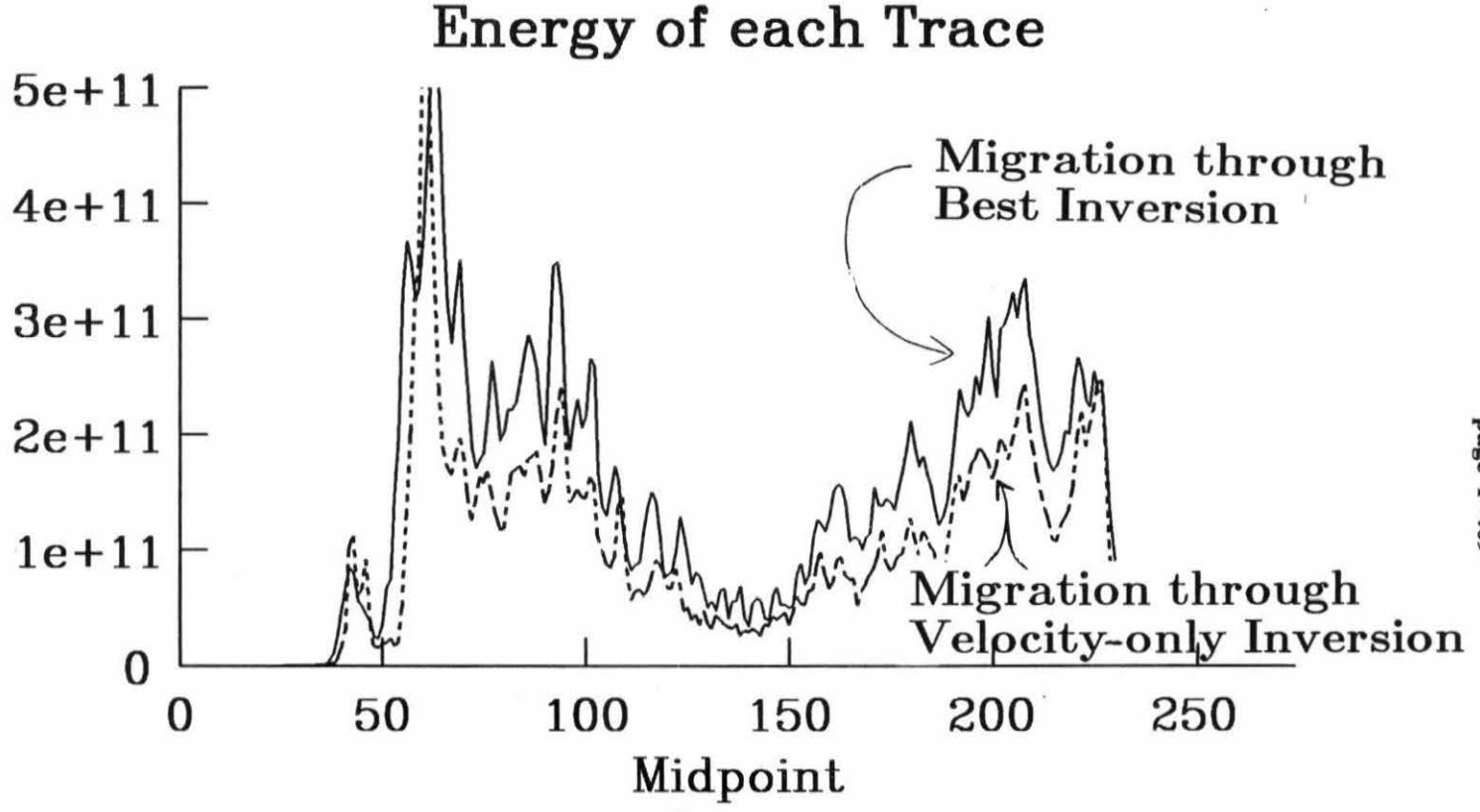
Energy of each Trace
5e+11
4e+11
3e+11
2e+11
1e+11
0
0
50
100
150
200
250
Midpoint
Migration through
Best Inversion
Migration through
Velocity-only Inversion